Genome-wide Microscopy Screening Identifies Links Across Processes Including a Conserved Connection Between DNA Damage Control and the Microtubule Cytoskeleton

a dissertation submitted to the

University of Cambridge

for the degree of

Doctor of Philosophy

presented by

JONATHAN LUKE DONE LAWSON

BA MSci MPhil MA (Cantab.)

a member of

Jesus College

born 17th November 1987

Supervisor: Dr. Rafael Edgardo Carazo Salas

June 2015

To my family.
We did it!


CELL
MICROTUBULE
CELLS
ALET
DNA
HITS
MICROTUBULES
DIFFERENT
LENGTH
CYCLE
RESPONSE
SHAPE
DAMAGE
FIGURE
MAY
WITHIN
HIT
AVERAGE
STRAINS
PROGRESSION
FACTORS
INVESTIGATION
USING
REPAIR
TREATED
IMAGES
POMBE
NUMBER
ALSO
KNOWN
TUBULIN
GENES
WILD-TYPE
SCREENING
HU
USED
MUTANTS
PLATES
MUTANT
PROTEINS
PROTEIN
TREATMENT
SCREEN
RESULTS
AMO1
DATA
IMAGING
GFP-ATB2
CLUSTER
GROWTH
PROCESSES
ADDITION
DELETION
MEDIUM
FOUND
WELL
PHENOTYPE
TYPICALLY
INTERPHASE
EFFECT
POLYMERISATION
TIME
LINKELY
LONGER
POSSIBLE
ANALYSIS
GENOME
GRANL
SINCE
ACROSS
OBSERVED
USE
SHOWED
ONE
MM
PLATE
NEW
DIVISION
REPORTED
SCREENS
MANY
EXPERIMENTS
COMPLETE
FEATURES
GENETIC
SEVERAL
TWO
GENE
FLUORESCENCE
WHILST
INCREASE
HOWEVER
ELONGATION
SPINDLE
CHROMOSOME
NUCLEAR
BUNDLE
METHODS
BUNDLES
DYNAMICS
ABLE
EXPECTED
IMAGE
LIBRARY
ALTHOUGH
FIRST
HOURS
PHENOTYPES
DDR
POPULATIONS
HAYLES
DUE
END
SIGNIFICANT
SMALL
SHOW
ENDS
PER
MUCH
SUGGEST
MT
OCCUPANCY
SPECIFIC
THREE
TOTAL
DENSITY
CONTROL
TABLE
PHASE
APPROACH
HR
WORK
NURSE
STUDY
CHANGES
RESULT
HIGH-THROUGHPUT
LONG
PROTEIN
UNTREATED
PROTEINS
RATE
ORGANISATION
STRAIN
KINASES
TREATED
JUST
HENCE
BASED
HIGH
MIN
COMPLEX
REPAIR
USING
WITHIN
HIT
MAY
ALSO
ET
AL
CELLS
DNA
MICROTUBULES
MICROTUBULE
CELL

DECLARATION

This dissertation is the result of my own work and includes nothing which is the outcome of work done in collaboration except as declared in the Preface and specified in the text.

It is not substantially the same as any that I have submitted, or, is being concurrently submitted for a degree or diploma or other qualification at the University of Cambridge or any other University or similar institution except as declared in the Preface and specified in the text. I further state that no substantial part of my dissertation has already been submitted, or, is being concurrently submitted for any such degree, diploma or other qualification at the University of Cambridge or any other University of similar institution except as declared in the Preface and specified in the text.

It does not exceed the prescribed word limit of 60 000 words, required by the Biological Sciences Degree Committee.

Jonathan Luke Done Lawson

The high-throughput/high-content screening aspect of the work presented in this thesis is the result of close collaboration with others. The full details of the approaches and methods used will be explored in **Chapter 3**. Collaborators were:

Dr Xenia Studera, Carazo Salas Group, 2008-2012

Xenia, is an experimental biologist. She researched and defined the biological aspects of the screening pipeline that form the basis of our approach to screening. She performed much of the preliminary work, the first round of screening, a genome-wide visual screen used to define computational hit detection thresholds and some aspects of low-throughput validation and quality control.

PhD Thesis: *'Establishment of a genome-wide, microscope-based functional genomics screen to identify microtubule regulators in fission yeast'* 2012, ETH Zürich (Studera, 2012)

Dr Veronika Graml, Carazo Salas Group, 2008-2013

Veronika is a computational biologist. She created, developed and implemented the computational pipeline that was applied to all images collected throughout all screening work. This includes image correction, segmentation, feature extraction and hit detection. In addition, Veronika was responsible for hit classification and clustering work.

PhD Thesis: *'An automated, 3D image-based functional genomics screen for microtubule and cell shape regulators in fission yeast'* 2012, ETH Zürich (Graml, 2012)

Dr Anatole Chessel, Carazo Salas Lab, 2010-2015

Anatole is a Post-doctoral Researcher in the Carazo Salas group and a specialist in image processing and statistical analysis. He performed mathematical investigations of the screening data – most specifically Bayesian analysis of cell shape and microtubule features to infer biologically significant relationships (**Section 4.4**) – and developed SYSGRO (**Section 4.5.2**).

In addition, Miriam Börtfeld-Miller (Lab Manager, Carazo-Salas Lab, 2008-2009) contributed to initial screening preparation work at ETH Zürich and Dr Eugenia Piddini (Research Fellow, Gurdon Institute) and Dr Laura Wagstaff (Post-doctoral Researcher, Piddini Lab, 2010-2015) contributed parts of the human tissue culture work as reported in **Section 5.10**. Dr Balint Antal (Post-doctoral Researcher, Carazo-Salas Lab, 2014-2015) primarily developed the Mineotaur tool (**Section 4.5.3**).

Work presented in **Section 3.8** contributed to a collaboration between several labs (Jeffares et al., 2015), with most of the research performed and coordinated by Dr Daniel Jeffares (Senior Research Fellow, UCL) and Professor Jürg Bähler (Chair in Molecular Systems Biology, UCL).

Acknowledgements

So here it is. The very last part of my PhD thesis. The last blank page waiting to be written. I never thought it'd happen and, on reflection, it's been really fun, although I haven't always appreciated that. I've put a lot of thought into all the people I want to thank. I hope I don't forget anyone.

First I want to thank Rafael, it's not always been easy but I honestly don't think I could have made it this far in any other lab. I've learnt so much and had the chance to rediscover some long forgotten skills. I'm also eternally grateful for all of your support with everything I've been involved in outside the lab. Special thanks also to my advisor, Julie Ahringer, and David Glover for their guidance and insights.

I'd like to thank everyone else I've worked with in the lab, Xenia, Veronika, Marco, Anatole, JuanFra, James, Balint, Tara, Yung-Chin and the one who keeps the wheels on, Kathy. I will think of you all on Tuesday afternoons. Thanks too to 'the other half' of the lab, though we are apart, the Piddini's are not forgotten. Special thanks to Eugenia for letting me hide-out in her tissue culture room and to Laura (Flora) for, well, a lot. Massive thanks to all of the staff at the Gurdon Institute that have kept us supplied and up and running, especially Juanita and the Kitchenettes, Nicola & Alex, the IT guys and everyone in the offices.

Further thanks to everyone in Pharmacology for welcoming a poor outcast lab and giving us somewhere out of the rain, as well as all of the help you gave in pulling together the best Christmas beach party ever. Special thanks to Mike, Ruth, Ewan and Dervila for all of the help, support and advice.

I'm also really thankful for the amazing scientists I've collaborated with over the last few years, particularly Daniel J. and Jürg for asking us to join their screening work, Daniel O. and Ludovic for letting us play with stem cells and Attila and Fede for speed dating. Possibly the greatest joy of working with the Opera has been the chance to learn about other people's science, so thanks to everyone who's tried screening work and to Martin for fixing her every time she broke. Thanks too

to Christine for all of her help and advice on the best ways to inflict DNA damage and for reading parts of this thesis.

Thanks to the ones who backed the whole thing too, The Wellcome Trust for being the best science funding body there is and to Daniel, Sarah, Clare and the rest of the Develomental Mechanisms committee for agreeing to let me have that money and then making sure I did something sensible with it. Also to Steve for making sure I check-in with Genetics sometimes and Claire for dealing with all of the various frantic e-mails.

I want to show my appreciation to everyone else I've worked with outside the lab too. First and foremost to Lou and Eva for being such great role models for how to do some science communicating, for being great friends and for all of the opportunities you've given me. Big thanks to everyone I worked with at *BlueSci* – particularly Tim, Tom and Fliss – the Jesus College MCR committee 2011/12 and everyone in college who supported us – Ian & Margaret, Sheena, Madeleine, Tim and Lisa – and the fantastic team that put together the Cambridge Science Festival every year. Additionally, thanks to Djuke and all of the FameLab International 2014 finalists for two frantic but truly inspiring days and also to everyone I've got to know through Twitter, tweetups, SpotOn, SciBarCamb etc.

Big thanks to the students I've had the pleasure to work with: the school groups that I've lectured and the undergraduates that I've demonstrated to and supervised. Teaching has been a rewarding and surprisingly educational experience.

Thanks to all of the friends I've shared the PhD years with, especially my many fantastic housemates and everyone that I've known through college. Special mentions to Poul and his love of comic book films, Megan for supporting the Twilight addiction, Lucy & James for Zelda nights, Hannah for 'the usual meal at the usual place' and Cheryl for tea and penguins. Much love to all of my friends that predate PhDs but that still deserve a mention: Fiona, my darling 'wife' Lauren and dearest Dr Lally ("Remember...you are what you eat").

On the topic of ancient history, I want to recognise the work of the dedicated doctors, nurses and staff of Alder Hey Children's Hospital – Professors Tam & Lloyd, Ann Black, Annie, Jane, Geraldine, Lesley etc. – none of this would have happened without your years of hard work.

To all of my wonderful, loving family – genetic or otherwise – you have always supported my choices and helped me to achieve my goals, and for that I am

eternally grateful. I did this to make you proud and I love you all. Thank you for helping me get this far. It's amazing what you can do without ever learning to hold a pen properly.

Sincerest thanks to one of the more recent additions to my life, Stuart. You've been more fantastic that I could have asked for as I've faced the dreaded thesis beast. You mean so much to me and I'm hoping that having a real job will give me more time to show you how important you are. Also, thanks for fixing all of my commas.

The final thanks should probably go to those who put the most time into getting me this far: to Mum, Simon and Adam. I don't really know what to say but I hope you know that you mean the world to me and that I'm very proud to be part of your family. You've stood by me through everything and I'm pleased to be able to achieve so much with the gifts you have given me. I hope I can keep on making you happy.

Abstract

Genome-wide Microscopy Screening Identifies Links Across Processes Including a Conserved Connection Between DNA Damage Control and the Microtubule Cytoskeleton – Jonathan Luke Done Lawson

Previous PhD students in the lab created a method for large-scale, high-content microscopy screening of a cell library consisting of over 3000 single mutant strains of the fission yeast, *Schizosaccharomyces pombe*. Each strain has one non-essential gene knocked-out, allowing investigation of the resulting phenotypes. I report the implementation and completion of this screen; developing methods to ensure reliable and accurate results through inclusion of many controls across multiple screening repeats. In total, over 4.5 million images from approximately 19 000 biologically independent cell populations were imaged and analysed.

All strains screened contained GFP-labelled tubulin (GFP-Atb2) allowing visualisation of the microtubule polymer network and its organisation in cells, a feature that is conserved across eukaryotes and simplified in *S. pombe*, making it easy to study. Examination of cell outlines and microtubule patterns was used to study three cell processes: the shape of cells, the organisational pattern of interphase microtubules and the cell cycle stage of cells, as judged by microtubule pattern. Comparison with extensive data from wild-type cells led to the identification of 262 factors that influence one or more of these cell processes.

I go on to biologically validate some of the outcomes from the screen, leading to a publication in *Developmental Cell* reporting the screen, its findings and the online genomic resource SYSGRO. I then focus on a group of mutants that suggest a connection between the DNA damage response (DDR) and microtubule organisation. From here I show that the DDR induces elongation of microtubule bundles in response to the DDR kinases, ATM and ATR. I begin to reveal factors that may mediate this response and finally, I provide evidence to suggest that the same mechanism is conserved in cultured human cells (Hc3716-hTERT), which may go some way to explaining clinical results showing a beneficial effect of microtubule destabilisation in conjunction with cancer therapies.

Thesis Digest

I believe public access to research is important. As such, I include this Thesis Digest as a summary of my work that is hopefully accessible to scientists and non-scientists alike.

The ability to sequence genomes has allowed us to learn how many genes living things have, but it has not helped us to learn what any of those genes do. Using automated microscopy and bespoke computer programs, I have attempted to uncover the functions of some of the genes in the fission yeast *Schizosaccharomyces pombe*. I have used yeast because it is much easier to grow and study than humans, but is biologically similar and has many of the same genes.

We are able to use genetic techniques to individually remove each one of over 3000 genes from yeast cells. These cells can then be examined to discover what effect the loss of a particular gene has on the life of the cell.

In my work I have looked to specifically identify genes that affect three key cell processes. The first is cell shape. The second is the cell cycle, the process by which cells grow and divide to produce new cells. The third is called the cytoskeleton, which is a network of fibres inside living cells that is responsible for giving the cell structure and helping to organise the many biological processes that take place inside all cells. As a result of this study, I have identified new functions for over 250 genes, many of which appear to play interesting roles in linking cell shape, the cytoskeleton and the cell cycle to each other and to other vital cellular processes.

In particular, I have discovered that a group of genes that are known to be important in repairing damaged genes also affect the shape of cells and the organisation of the cytoskeleton. Previous clinical research has shown that cancer treatments are often more effective when drugs are also used to impair the cytoskeleton. Cancer cells typically have a lot of damaged genes. My work may help to explain the connection between the cytoskeleton and damaged genes in cancer cells. In the long term this could provide new insights that may help to develop more effective cancer treatments.

Contents

CONTENTS

List of Figures

1 Introduction

"We're all stories, in the end. Just make it a good one, eh?!"
—THE 11^{TH} DOCTOR (*The Big Bang*, 2010)

All known life on Earth derives from a common ancestor that is thought to have lived more than 3.5 billion years ago (Schopf, 2006; Schopf et al., 2007). Divergence from one origin means that several key aspects are common to all life. Most fundamentally, the form, behaviour and activities of living things are governed by genetic codes, stored as DNA (Alberts, 2002). All life, with the debatable exception of viruses, also consists of cells (Cooper and Hausman, 2013; Lodish, 2008), which are created by the division of existing cells (Virchow, 1855).

As such, understanding how genes give rise to cells and how cells adapt to, and interact with, their environment is essential to understanding life as a whole. Cells consist of many interrelated processes that are necessary to maintain life (Alberts, 2002; Cooper and Hausman, 2013; Lodish, 2008). Hence, dissecting the connections between genes and their expression in cells and larger organisms, is a long running biological aim.

Three of the most conserved and significant cell processes concern the ability to produce new cells (the cell cycle); the capacity to maintain an evolutionarily optimised shape, or to change shape on the basis of contextual or environmental cues (cell shape); and the ability to organise and structure different cell components to ensure optimal functionality (cytoskeleton). Such activities are, to greater or lesser extent, present in all living cells and are primarily under genetic control.

This work focuses on the study of cell cycle, cell shape and the cytoskeleton in eukaryotic cells, as opposed to prokaryotic or archaeal systems, so will particularly focus on cytoskeletal elements known as microtubules, which are exclusive to eukarya (Bermudes et al., 1994).

1.1 Early genetics

Shortly after the publication of the theory of evolution by natural selection (Darwin and Wallace, 1858; Darwin, 1859), the basics of genetics were laid down by Gregor Mendel (Mendel, 1865). Mendel found that traits could be passed down through the generations, and described the units and mechanics of this transmission. These units are now known as genes (Johannsen, 1909). Mendel's work helped to reveal that many organisms carry at least two copies of each gene – giving rise to genetic dominant and recessive traits – and inherit one genome copy from each parent (diploid). Several model systems, including some yeasts, have only one copy of most genes (haploid), whilst some plant crops have more than two gene copies (polyploid).

Freidrich Meischner placed genes in the nucleus of eukaryotic cells, in a substance called nuclein (Meischner, 1869); later known as DNA. Walter Sutton proposed this as the means for carrying genetic information (Sutton, 1902, 1903). In 1953, Watson and Crick, on the basis of unpublished work by Franklin and Wilkins, described the structure of DNA as two strands arranged in a double helix. They explained how this allowed DNA to replicate by separating the strands and using each as a template to create a duplicate of the other (semi-conservative replication). This explained how genes were able to carry and perpetuate information (Watson and Crick, 1953).

As the study of genetics has continued, it has become possible to assign physical traits to specific genes – to specific pieces of DNA – and it is now possible to read the genetic code through DNA sequencing (Sanger and Coulson, 1975; Sanger et al., 1977b). Modern genetic techniques even make it possible to synthesise new genes (Khorana et al., 1972; Itakura et al., 1977; Edge et al., 1981; Bartlett and Stirling, 2003) and introduce them into living cells (Alberts, 2002; Lederberg, 1994). One of the key experimental techniques that has contributed to this advancement of our understanding of genes has been genetic screening, which allows us to link genes to their effects (Hartwell et al., 2008).

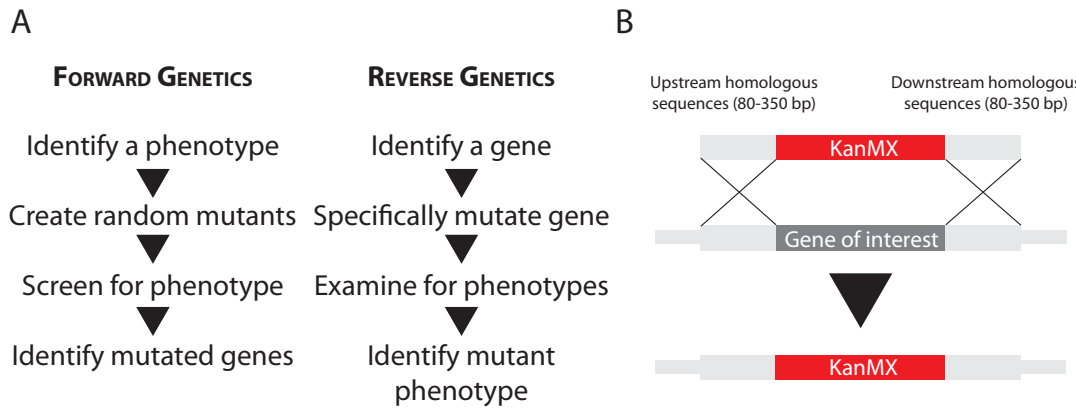

Figure 1.1: Overview of genetic screen methodologies - **(A)** A comparison of forward and reverse genetic screen approaches. **(B)** Illustration of the method of targeted gene knock-out by homologous recombination for reverse screening, as used by Kim et al. (2010).

1.2 Development of forward genetic screens

Genetic screens were some of the first approaches used to study gene functions (Hartwell et al., 2008). The first screens – now called forward genetic screens (**Figure 1.1A**) – started by identifying an unusual physical trait (phenotype) and then examining organisms with variations in this trait to work out which genes caused it (genotype). From here it was possible to infer that genes which caused similar phenotypes probably had related functions.

Screening was an extension of the original forward genetics methods, where study of natural variation within species was used to infer genetic variation, as with Mendel and his pea plants. Genetic screening used treatments that caused genetic variation, eliminating the need to identify naturally occurring variation.

Each forward genetics screen would generally start off with hundreds or thousands of randomly created mutants in order to identify just a few new genes. Perhaps some of the most significant early experiments identified cell division cycle-regulating mutants (cdc) in the budding yeast, *Saccharomyces cerevisiae* (Hartwell et al., 1970), and the fission yeast, *Schizosaccharomyces pombe* (Nurse, 1975).

1.3 Reverse genetic screens

Methods for genetic screening have advanced significantly in recent decades, especially since the development of genomic DNA sequencing. The screen reported here is a reverse genetic screen (Griffiths, 2000) and requires detailed prior knowledge of genes in a genome. A screen of this scale also depends upon the prior creation of techniques and equipment for the mass handling of large numbers of parallel samples, which have allowed the production of genome-wide libraries of gene mutants for study (Giaever et al., 2002; Kim et al., 2010).

True reverse genetic screens are a recent occurrence because they depend upon, at least partial, knowledge of the genome sequence and the ability to manipulate it (**Figure 1.1A**), something which has only been possible since the advent of gene sequencing towards the end of the 20^{th} Century (Hartwell et al., 2008). Although the first complete DNA genome, from bacteriophage ϕX174, was published in 1977 (Sanger et al., 1977a), full genome sequencing of model organisms primarily started in the 1990s, with *S. cerevisiae* (Goffeau et al., 1996), *Escherichia coli* (Blattner et al., 1997) and *Caenorhabditis elegans* (Consortium, 1998). Other key species followed: *Drosophila melanogaster* (Adams et al., 2000), *S. pombe* (Wood et al., 2002) and the Human Genome Project, which finally completed in 2006 (Gregory et al., 2006), after initial drafts (Venter et al., 2001; Lander et al., 2001). Since then DNA sequencing has become faster and cheaper, expanding the potential for application of reverse genetic approaches.

In reverse genetics, a gene that has been identified in the genome but that does not have a known function, is targeted (Griffiths, 2000). That gene is then mutated – deleted, knocked-out, over-expressed or suppressed – and the resulting organism is assessed, in an attempt to discover what effect the gene has on the organism. Hence, reverse genetics starts with an altered genotype and searches for a phenotype, whilst forward genetics starts with a mutant phenotype and searches for the corresponding genotype.

When reverse genetics is expanded to study many genes at once, this is reverse screening. It is generally impractical to examine all possible phenotypes for a large number of genes, so reverse screens tend to examine just a few phenotypes. For every mutant in a reverse screen, the mutations are known before-

hand. In a forward screen, extensive follow-up work is required simply to identify the genes affected by each mutation.

Successful screening, either forward or reverse, relies upon having a large number of mutants to test. In forward screens, many random mutants are needed to give a reasonable probability that every gene will be mutated at least once, this is called genome coverage (Brown and Balling, 2001). In reverse screens, the more genes that are mutated, the greater the likelihood of identifying some with an interesting phenotype. Reverse screens now are generally genome-wide, although they have previously been restricted to certain parts of the genome, or known functional groups of genes. The more mutants in a screen, the more time and resources are required to complete it. Initially this made many large-scale screens impractical.

The easiest phenotype to assess is typically viability. If a gene is essential for life then deleting it leads to death and it is generally relatively easy to tell whether something is dead or alive. However, in all organisms, the vast majority of genes are not essential for life under optimal conditions and a more extensive search is needed to identify the role of these non-essential genes.

Perhaps one of the most relevant, genome-wide reverse genetic screens that relied upon relatively straightforward phenotype analysis was performed by Kim et al. (2010) and was the source of the *S. pombe* genome-wide gene knock-out (KO) library (**Figure 1.1B**). Their work examined the viability and growth fitness of different gene-deletion mutants and compared them to their *S. cerevisiae* orthologues (Giaever et al., 2002; Winzeler et al., 1999; Huh et al., 2003).

The development of more advanced screening tools has allowed both the scale of screens undertaken and the complexity of the phenotypes being screened to increase (Friedman and Perrimon, 2004). In particular, this has progressively enabled reverse genetic screens to explore increasingly complex phenotypes in increasing numbers of genes, offering a thorough, if not totally comprehensive, overview of gene functions in an organism.

These high-throughput techniques generally employ robotics, where possible, to speed experimental procedures and computers, to accelerate the process of phenotype identification (Hieter and Boguski, 1997; Galperin and Koonin, 2000; Eisenberg et al., 2000). Procedures using microarrays (Brown and Botstein, 1999; Duggan et al., 1999), next-generation sequencing (Schuster, 2008; Mardis,

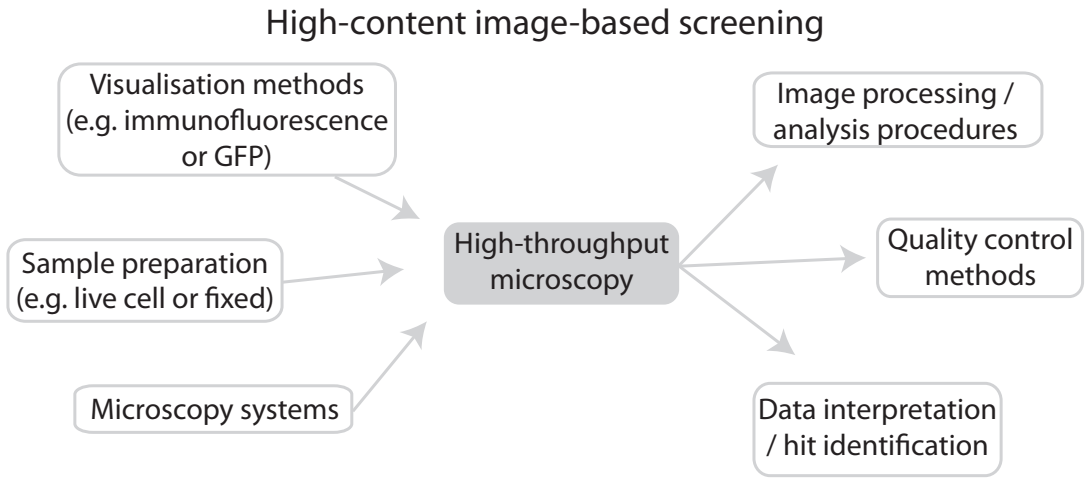

Figure 1.2: Overview of high-content image-based screening - An illustration of the key considerations in planning and implementation of a high-content genetic screen using automated microscopy and computerised image analysis. Figure adapted from Studera (2012).

2008; Metzker, 2010) and spectrometry (Rauch et al., 2006; Matthiesen, 2007; Munck et al., 2001), for example, are able to rapidly analyse the abundance of different cell components from large numbers of samples.

However, many components and phenotypes are best studied through direct observation by microscopy (Neumann et al., 2010; Boutros et al., 2004; Pepperkok and Ellenberg, 2006). Furthermore, the use of microscopy allows for more direct assessment of variation within a population of cells, by contrast to the chemical profiling approaches above that typically only produce population-averaged data. Hence progress in genetic screening has also led to great advancements in microscopy (Pepperkok and Ellenberg, 2006; Glory and Murphy, 2007; Wollman and Stuurman, 2007).

1.3.1 Image-based screening

Image-based screening is clearly a key approach when searching for understated phenotypes, but it is limited. To find something using microscopy you need a powerful enough microscope, you need to know what to look at, what to look for and, in most cases you need suitable molecular labelling techniques. You also need time (**Figure 1.2**). Deciding conclusively, with repeats, whether a mutant is

dead or not, is much quicker and easier than deciding if one group of cells is, for example, on average 5% bigger or smaller than another. The first image-based screens were not genome-wide and studied features that were easy to detect with relatively low power microscopy (Fraser et al., 2000; Gonczy et al., 2000). These early screens were visually assessed and phenotypes were qualitatively determined. One major drawback of visual assessment is that small changes or changes that are not present in all cells/organisms may be too subtle to be noticed.

Other sub-genome screens have limited themselves to studying genes with known functional connections. For example, studying kinases and phosphatases in the regulation of the DNA damage response (Cotta-Ramusino et al., 2011).

1.3.1.1 High-content screening

The great potential of image-based screening is that it is able to produce a much richer dataset – many different spatially and temporally resolved parameters can be automatically extracted from an image simultaneously – making it possible to measure several different phenotypes or aspects of phenotypes at the same time, this is called high-content screening (HCS).

One of the first screens to make effective use of HCS approaches used 11 different labelling techniques to visualise different aspects of wild-type cells treated with around 100 different drugs (Perlman et al., 2004). What was distinctive about this paper was its use of computers to collect multiple quantitative parameters for each cell studied (multi-dimensional). This meant large amounts of data could be collected from just a few cells. However, in this study, all 11 labels were used on separate cell populations, they were never used together on the same cells, meaning that it was not possible to detect correlated changes across multiple cell processes within individual cells.

The Perlman et al. screen, as with many subsequent screens, made use of fixed cells only. The difficulties of preparing many live samples in parallel for high-throughput imaging have only recently begun to be addressed (Oheim, 2011; Evensen et al., 2013; Neumann et al., 2006). In addition, the use of fixed samples allowed labelled antibodies to be used to mark specific features of the organism being studied that would not otherwise be visible.

There are other limitations to using fixed cells too. Fixation can result in imaging artefacts, certain cell structures can be difficult to preserve and it prevents the study of dynamic processes (Himes et al., 1982; Kozubek et al., 2000; Melan, 1995; Giepmans et al., 2006). It would later become possible to use fluorescent markers, such as green fluorescent protein (GFP) (Prendergast and Mann, 1978) to study the same features in live cells. Whilst GFP was known about before the origin of HCS, the more practically applicable variants (such as enhanced GFP; eGFP) were still relatively new (Heim et al., 1995; Giepmans et al., 2006) and genetic constructs for gene labelling in different organisms were not widely available.

1.3.1.2 Computer-assisted screening

Subsequent advances in automated microscopy and computational image processing now make image-based screening on a larger scale much more viable (Gough and Johnston, 2007; Taylor et al., 2007). We are able to study phenotypes in many thousands of mutants, examining much finer biological details, in a fraction of the time that would be possible manually (Forsburg, 2001; Jorgensen and Mango, 2002; Sommer and Gerlich, 2013). In addition, a computer algorithm is 100% consistent throughout the entire screen, whereas human opinion varies from person-to-person and day-to-day. High-throughput, genome-wide, image-based computational screening is still relatively new (Taylor et al., 2007; Sommer and Gerlich, 2013).

The approach of Bakal et al. (2007) is of particular interest for this study. Their screen made use of over-expression constructs to effectively increase the level of some genes within cells and studied the effects of these genetic manipulations on cell shape. Most importantly, although this screen extracted many computational measures of cell shape, these were then combined into probability scores by comparison to a small number of distinctive stereotyped cell morphologies (**Figure 1.3**). This used machine learning approaches and meant that results could be biologically represented as a measure of likeness to known cell shape classes. This was particularly relevant as cell shape within populations of cultured animal cells is typically thought to be inherently variable and intuitive assessment of shape similarity is almost impossible. This work was later continued to infer

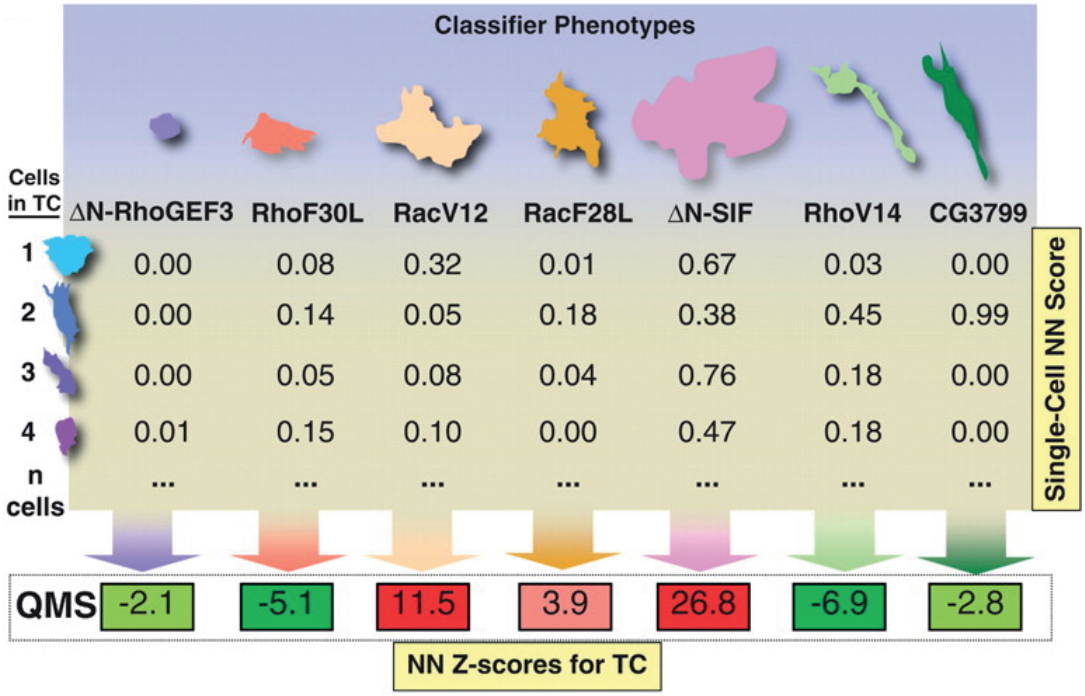

Figure 1.3: Classification of cells based upon stereotyped shapes - A demonstration of the use of computerised classifiers (in this case neural networks (NN)), to assign individual cells (left), on the basis of a large number of quantitative features, into a small number of easily interpreted morphological classes (top) on a probabilistic basis. This was then used to create a quantitative morphological signature (QMS) for each cell population (treatment condition; TC). Figure from Bakal et al. (2007).

that a preference for certain cell shapes, even in cells where morphology seems to be variable, may be biologically predetermined (Yin et al., 2013).

A similar approach was also undertaken to study mitotic spindle pattern (Goshima et al., 2007). Both of these screens used RNA interference (RNAi) to effectively reduce the expression of certain genes (Boutros and Ahringer, 2008; Krausz, 2007; Krausz and Korn, 2008). RNAi introduces small RNA fragments into cells that are integrated into an endogenous cell process, causing the suppression of mRNA sequences that are complementary to the introduced small RNAs; effectively silencing the gene that produced the mRNA (Agrawal et al., 2003). Whilst this is not direct genetic manipulation, it fundamentally serves the same purpose and is more practically applicable in cells from diploid organisms (flies, rodents and humans). Other screens have used RNAi in human cells to specifically study endocytosis (Pelkmans et al., 2005; Mercer et al., 2012; Collinet et al., 2010),

actin (Rohn et al., 2011) and the Golgi apparatus (Chia et al., 2012).

1.3.1.3 Live-cell screening

Shortly after the origin of genome-wide image-based screening, studies using live cells began to emerge. The leading screen in this area is probably the MitoCheck project (Neumann et al., 2006, 2010), which performed rapid imaging and processing of live, RNAi-treated human cells. In total, around 21 000 genes were suppressed and labelled chromosomes were used to assess mitotic cell division phenotypes (see **Section 1.6**). Since mitosis represents such a small fraction of each cell cycle, at any one time very few cells can be expected to be undergoing mitosis. Hence, it would be very difficult to accurately study cell division from static images of fixed cells, as it would be prohibitively labour intensive to collect sufficient data on such a rare occurrence. The MitoCheck methodology was also adapted to a fixed cell screen for secretory proteins (Simpson et al., 2012).

1.3.1.4 Screening multiple phenotypes

All of these factors: genetically labelled proteins, live-cell processing and multi-dimensional computational analysis, have recently combined to allow image-based screening to study multiple phenotypes within the same cell (Bakal and Perrimon, 2010). So far this has included genome-wide studies of cytoskeletal components (see **Section 1.5**) in human cells (Fuchs et al., 2010); an examination of epigenetic regulation in cancer cells (Laufer et al., 2013) and a double RNAi screen of signalling factor genes (Horn et al., 2011). Notably, these previous studies used immunostained fixed cells and examined related aspects of single cell processes. In this screen we will move beyond this to live-cell multi-process screening, examining three related but separate cell processes.

Many of the screens mentioned used RNAi to suppress genes and have used population averages to draw conclusions. As explained, RNAi is a useful tool for studying gene activity, especially in diploid organisms. However, results can be unpredictable, gene suppression is rarely 100% and typically varies between repeats (Sledz and Williams, 2005; Boutros and Ahringer, 2008). Furthermore, RNAi encounters issues with off-target effects – where RNAi constructs may also suppress other genes. As such, most RNAi screens require testing of multiple

RNAi constructs per gene and need large numbers of repeats to compensate for variability in suppression.

Few true gene-deletion or knock-out screens, which would overcome the limitations of RNAi, have been performed (Winzeler et al., 1999; Kelly et al., 2001). This is probably because it is much easier to create and apply RNAi constructs to cells than it is to create thousands of different mutants – an issue that is particularly true in diploid organisms. Parallel mass manipulation of strains has made this more plausible in recent years, hence the occurrence of *S. cerevisiae* and *S. pombe* gene-deletion libraries (Kim et al., 2010; Winzeler et al., 1999; Kelly et al., 2001).

One further aspect to note is that, although images from screens have often been collected in three-dimensions using multiple focal plane z-stacks, image analysis has generally been performed in just two-dimensions, using stack projections. This approach limits the information that can be obtained and can easily lead to issues when studying complex structures such as microtubules. Two-dimensional projections may create inaccuracies in detection that three-dimensional analysis can overcome (Applegate et al., 2011; Graml, 2012).

As such, in this work, we have attempted a genome-wide, image-based, reverse genetics screen of true gene-deletions – in which individual genes have been completely and specifically removed. We have used computational methods to analyse the information collected, in three spatial dimensions, and extract numerous independent features to give a rich, multi-dimensional high-content dataset simultaneously exploring three biological processes: cell shape maintenance, microtubule organisation and cell cycle progression. To study these processes, we also use more detailed imaging-approaches than have been previously applied, using higher magnification to more precisely visualise individual cell structures, and more accurately reconstruct them in three-dimensions.

1.4 Cell shape

Cell shape is perhaps the most intuitive of the processes investigated here. All cells are encased within a cell membrane, consisting of a lipid bilayer, which defines the outline of the cell and creates a semi-permeable barrier between the

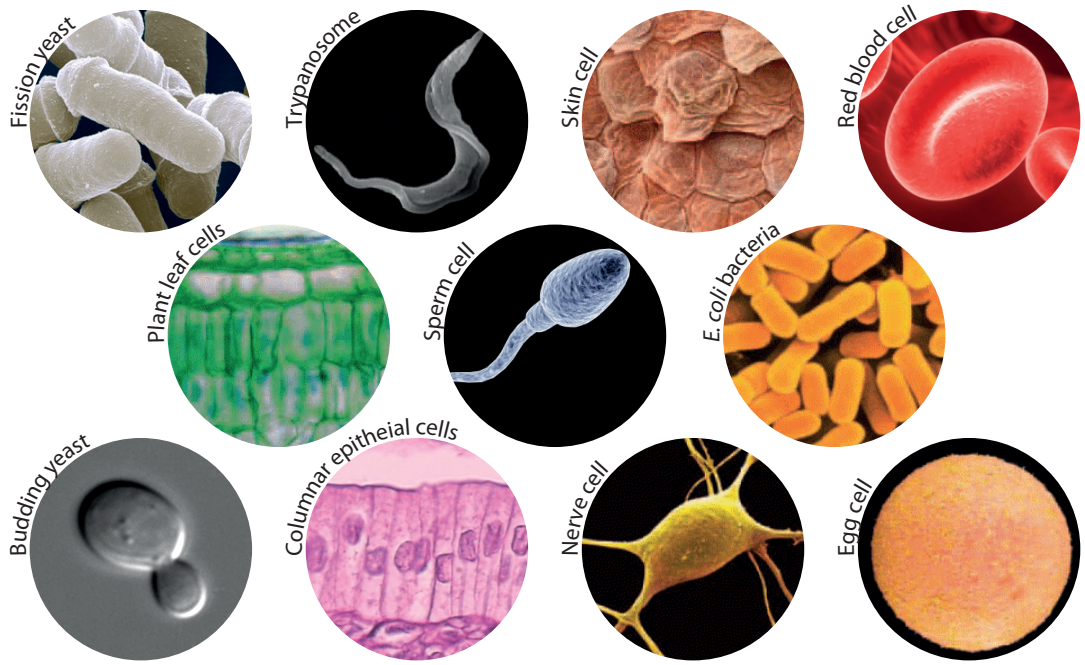

Figure 1.4: Examples of cell shape variation - A collection of images illustrating variation in cell shape. Human sperm, egg, skin, blood, nerve, and epithelial cells are shown along with plant leaf cells, bacterial (*E. coli*) cells, fungal budding (*S. cerevisiae*) and fission (*S. pombe*) yeasts and the protist parasite trypanosome (*T. cruzi*) in its bloodstream form.

environment and the cytoplasm (Cooper and Hausman, 2013; Lodish, 2008; Alberts, 2002). Observation of the variety of shapes and forms that different cells can adopt is suggestive of the huge significance and impact that cell shape has on the fitness and functionality of cells (Shah, 2010; Cabeen and Jacobs-Wagner, 2005; Ben-Ze'ev, 1985; Carthew, 2005; Hayles and Nurse, 2001; Stein and Bonner, 1989). Furthermore, given its visual nature, cell shape is probably one of the most obvious aspects of cell biology to study using a multi-dimensional, image-based screen (Bakal et al., 2007).

Distinctive cell shapes are perhaps most apparent in multi-cellular organisms (**Figure 1.4**). Blood cells have a biconcave shape that allows for optimal oxygen transport (Diez-Silva et al., 2010). Columnar epithelia adopt an angular cuboid-like shape that allows them to fit closely together to form tight protective barriers around the body (Leptin, 1994; Knust, 2000, 2002). Sperm cells demonstrate a streamlined shape, dominated by a long highly motile flagellum, ideal for swimming (Dresdner and Katz, 1981; Coetzee et al., 1998). Brain and nerve cells

have long thin, wire-like projections that allow them to span long distances and form complex neural networks (Patel and Shen, 2009; Stein and Bonner, 1989). Even unicellular organisms, like yeasts and bacteria, exhibit a wide array of different shapes that are adapted for their chosen habitats and activities (Cabeen and Jacobs-Wagner, 2005; Hachet et al., 2012; Harold, 1990).

The origins of cellular life are unknown. It is generally thought that self-replicating nucleotides, protein chains and metabolic reactions may have originated in warm, aqueous pools containing organic molecules that probably closely mirrored the internal composition of modern cells (Cavalier-Smith, 1987a,b). However, understanding how this collection of biological processes, structures and metabolites came to be encased in a lipid layer is non-trivial. The protein coat observed in modern viruses may represent an intermediate step in this process, but this is not certain and may equally represent a separate parallel branch of evolution.

Some of the earliest cells were probably spherical, representing a physically defined property of lipids to form spherical droplets on the basis of the need to minimise contact surface area with the environment (Koch, 1996; Hiltmann and Lory, 1983). It may have taken some time to move beyond this stage, until cells developed the ability to actively manipulate their own shapes (Drubin and Nelson, 1996). Spherical cells limit the possible size of cells. As cells get larger the distance between the environment and the cell centre also increases. Keeping the whole cell alive relies upon the ability to keep it fully supplied, this is limited by the speed of diffusion of molecules through the cell from the surface to the centre. As cell radius increases, diffusion takes more time and eventually cells become too large to survive without creating faster means of internal transport or developing the ability to adopt different shapes (Koch, 1996; Hiltmann and Lory, 1983).

Rod-shaped cells, such as those seen in bacterial *E. coli* and eukaryotic *S. pombe* may have been one of the earliest solutions to increasing cell size, without increasing the maximum distance between any part of the cell and the environment (Cava et al., 2013; Snell and Nurse, 1994; Verde et al., 1995).

The existence and diversity of cell shape in current biological systems has been apparent since the first direct studies of cells by Robert Hooke and Antoni van Leeuwenhoek in the late 17th century (Hooke, 1665; Leuwenhoek, 1693, 1722). It is beyond the scope of this work to cover all of the explanations for the diversity of cell shapes that have been reported across biology. It is sufficient to say that the shape of different cell types is so distinctive, highly developed and precisely

maintained that correct shape must be under significant evolutionary selective pressure and must thence be of great importance to the fitness of cells (Hayles et al., 2013). The shape of cells is widely accepted to be one of the most important factors in development of multi-cellular organisms (Paluch and Heisenberg, 2009) and the means by which it is defined and maintained by different cell types has been a leading question for developmental biology for at least 100 years (Thompson, 1917).

One of the great attractions of cell shape is that it is the product of the interplay between many other cell processes. Cell shape can change rapidly and respond to environmental cues and physical stresses (Davies and Tripathi, 1993; Pilizota and Shaevitz, 2014; Adams, 1992; Lecuit and Lenne, 2007; Butler et al., 2009). However, cell shape also clearly has genetic components, although this encompasses many separate pathways (Carthew, 2005; Cabeen and Jacobs-Wagner, 2005; Hayles et al., 2013; Oppenheimer, 1998). In many cells the cytoskeleton – a network of protein fibres throughout most cells that influences cell shape and structure (see **Section 1.5**) – is attributed a significant role in cell shape, as in cell motility (Pollard and Cooper, 2009; Helfand et al., 2003; Nakamura, 2015; Wells and Bonetta, 2005; Hayles and Nurse, 2001). Extension of cytoskeletal elements can create protrusions and outgrowths of the cell as the membrane is pushed outwards by the cytoskeleton (Luo, 2002; Haimo and Rosenbaum, 1981). Yet some evidence suggest that cell shape can be retained even when cytoskeleton is lost (Beinhauer et al., 1997).

Genetics can also influence cell shape by controlling aspects of cell growth and polarity (Nelson, 2003; Pruyne and Bretscher, 2000; Amano et al., 2010; Nelson et al., 1990). Genes can alter, and are altered by, the extracellular matrix composition (Jones et al., 1993; Mott and Werb, 2004; Yeung et al., 2005) – the scaffolding of proteins that tissues are assembled around – and genes can affect the localisation and interaction of membrane bound proteins (Simons and Toomre, 2000), to name just a few key genetically encoded processes. In addition, cell shape is responsive to signals from other cells (Boudreau and Jones, 1999; Davy and Robbins, 2000; Stolz and Michalopoulos, 1994) and is closely linked to cell division processes (Verde et al., 1995; Hayles et al., 2013; Effler et al., 2006, 2007). Hence, whilst cell shape definition is fundamental, it is also elusive.

Interestingly, studies appear to show that cell shape, even when mutated, adopts very specific alternate phenotypes (Yin et al., 2013; Hayles et al., 2013). It favours a small number of stable states over a wide ranging continuum of different forms. Given the apparent complexity of the factors determining cell shape, it would be expected that many subtly different phenotypes should be observed. This may serve to highlight the importance of self-reinforcing feedback mechanisms within cell shape that help to buffer against minor perturbations within the system (Ursell et al., 2014; Takeda et al., 2008). Such an extreme and intricate network of maintenance and control is reminiscent of the cell cycle and further suggestive of the value of correct cell shape to biological success.

Despite this apparent resistance to slight change, it is sensible to study cell shape in a biological system where shape is well-defined and consistent (Piel and Tran, 2009; Nurse, 1975; Verde et al., 1995). Doing so makes it much easier to detect subtle deviations in cell shape, resulting from different mutants and thus is more reliable in detecting genes that alter cell shape definition and maintenance. In particular, certain unicellular organisms that have little natural wild-type shape plasticity and can easily be imaged individually, can be particularly useful in allowing reliable automated cell identification and accurate cell shape measurement.

1.5 Microtubule cytoskeleton

Cytoskeletal components occur on a number of scales in eukaryotic cells (Lodish, 2008; Alberts, 2002; Fletcher and Mullins, 2010). Actin microfilaments are probably the simplest in terms of molecular structure, known for their roles in contractile tissues (Lodish, 2008; Alberts, 2002; Small, 1988). Intermediate filaments include proteins such as keratin and lamins, which play structural roles throughout the body (Herrmann et al., 2007; Leduc and Etienne-Manneville, 2015; Chernyatina et al., 2015; Gruenbaum and Aebi, 2014). The most structurally complex component is the microtubule cytoskeleton, which has roles in cell organisation, transport, structure, signalling, motility and division (Olmsted and Borisy, 1973; Nogales, 2000; Cooper and Hausman, 2013).

The ability of microtubules to span long distances within cells makes them ideal for organisation and transport roles. Many organelles are known to associate

with microtubules, which allows them to maintain distinct identities, position themselves within cells and allows transfer of components between different cell compartments (Bornens, 2008; Pon, 2011; Stephens, 2012). Mitochondria, Golgi, endosomes, vesicles and ribosomes are all known to interact with microtubules in at least some cases. Most distinctively, in neural cells, microtubules are essential to keep the distal growth cones supplied with cell components manufactured in the cell body (Franker and Hoogenraad, 2013; Goldstein and Yang, 2000; Welte, 2004). This can involve reliable, regulable, directional transport of factors over distances of a metre or more (Lodish, 2008). Microtubules are also known to be hijacked by some viruses, providing fast transit to the nucleus (Niehl et al., 2013; Sodeik et al., 1997; Roohvand et al., 2009; Greber and Way, 2006).

Microtubules are a key structural element in eukaryotic cell projections. The most specialised of these are perhaps cilia and flagella, both of which consist of elaborate arrangements of parallel microtubules, which are able to move relative to each other, creating waving or swimming motions (Lodish, 2008; Snell et al., 2004). The vast majority of cells in higher eukaryotes include at least one primary cilium, which is thought to be a significant structure in the reception of cell-cell chemical signals (Singla and Reiter, 2006; Gerdes et al., 2009; Goetz and Anderson, 2010).

The earliest observed microtubule function, and the most studied, is in the bipolar mitotic spindle that microtubules form in almost all cells as they undergo cell division (Bütschli, 1876; Flemming, 1878). The role of the spindle is to ensure that all cells produced from cell division receive a full complement of genetic information (Alberts, 2002; Lodish, 2008).

1.5.1 Structure

Microtubules were first described visually during cell division in 1876 (Bütschli, 1876), although they were not imaged in detail until a study of nerve cells in 1953 (De Robertis and Franchi, 1953), and it was another 10 years until the name 'microtubule' was coined (Slautterback, 1963). A microtubule is a 25 nm diameter, hollow tube made up of many globular units of tubulin protein heterodimers; α- and β-tubulin (**Figure 1.5A**; Olmsted and Borisy (1973); Amos and Schlieper

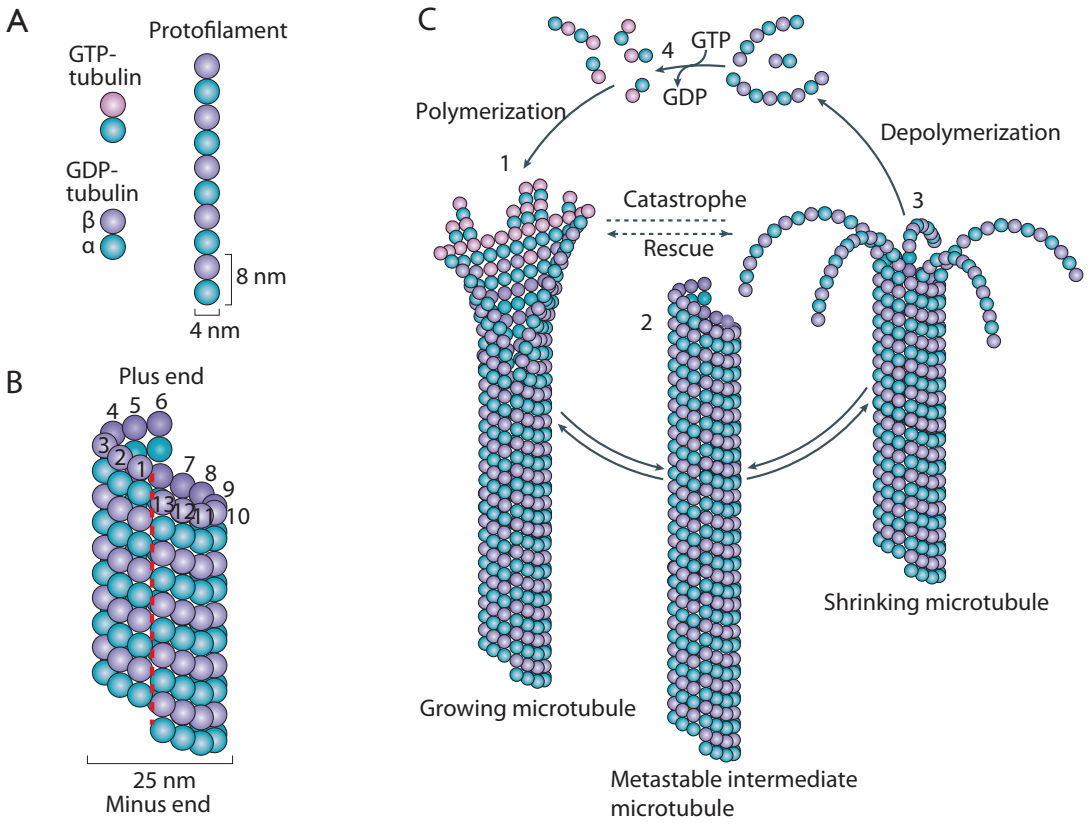

Figure 1.5: Microtubule structure and dynamics - The structure and organisation of a microtubule from GTP-regulated tubulin heterodimers **(A)** to polarised 13 protofilament tubes **(B)**. Microtubules demonstrate dynamic instability where they undergo reversible switching between states of growth by tubulin polymerisation **(C1)** and shrinkage by depolymerisation **(C3)**. These switching events are referred to as catastrophe and rescue. Figure from Akhmanova and Steinmetz (2008).

(2005)). Both proteins bind to the ATP-like small molecule regulator, GTP, although only β-tubulin undergoes repeated GTP hydrolysis cycles, which regulate microtubule formation (Mitchison and Kirschner, 1984a; Spiegelman et al., 1977).

A microtubule is generally formed *in vivo* by a nucleation complex containing γ-tubulin, which is thought to provide a structural template for microtubule initiation (Mitchison and Kirschner, 1984b; Dammermann et al., 2003; Wiese and Zheng, 2006). GTP-bound tubulin dimers then bind to the nucleation complex in a head-to-tail conformation with α-tubulin closest to the nucleators (nearest the -end of the microtubule) (Mitchison and Kirschner, 1984b). The opposite end of the microtubule exposes β-tubulin and is called the +end (Fan et al., 1996; Mitchison,

1993). As such, microtubules are inherently polar, with a distinct directionality throughout their entire structure (**Figure 1.5B**). Microtubules will form *in vitro*, in the absence of any other factors, and can still create a polarised structure (Olmsted and Borisy, 1973).

Each microtubule typically consists of a ring of 13 parallel protofilaments of head-to-tail tubulin dimers (Evans et al., 1985; Amos and Schlieper, 2005), although other numbers have been reported in some cases (**Figure 1.5B**; Desai and Mitchison (1997); Savage et al. (1989); Fukushige et al. (1999)). Each filament is slightly offset from its neighbours creating an overall three-start helix of tubulin monomers, with a 10° rise between adjacent protofilaments around the microtubule (Mitchison and Kirschner, 1984a). This helical conformation creates a slight discontinuity along one side of the microtubule, where two adjacent protofilaments are forced to adopt unusual lateral interactions, this is called the seam (Kikkawa et al., 1994).

1.5.2 Dynamics

Microtubules are in a constant stochastic state of change, which never reaches a stable equilibrium. This is an intrinsic property of the tubulin polymer called dynamic instability (Mitchison and Kirschner, 1984a; Kirschner and Mitchison, 1986b,a). Microtubules will constantly undergo extended periods of polymerisation (addition of dimers) and depolymerisation (loss of dimers; **Figure 1.5C**). The switch to depolymerisation is called catastrophe (Brun et al., 2009), whilst recovery of polymerisation is rescue (Gardner et al., 2013). A paused state where there is no change at microtubule ends has been reported in cells (Bouissou et al., 2009; Amos and Schlieper, 2005; Shelden and Wadsworth, 1993), but does not seem to be intrinsic to tubulin, as it is rarely observed *in vitro* (Walker et al., 1988).

Microtubules can gain and lose dimers from either end *in vitro*. However, the -end is always less dynamically active and is further stabilised in cells, by association with nucleation factors (Mitchison and Kirschner, 1984a; Amos and Schlieper, 2005).

Polymerisation is thought to be a relatively uncoordinated process whereby dimers independently bind to the +ends of existing protofilaments. With dimers binding randomly to the end of the first protofilament they encounter. Although lat-

eral interactions between new dimers and neighbouring longer protofilaments are thought to promote the addition of dimers to shorter protofilaments, helping to maintain all protofilaments at a similar length (Mitchison and Kirschner, 1984a,b; van der Vaart et al., 2009). The switch to depolymerisation is thought to be linked to hydrolysis of GTP. GDP bound tubulin dimers curve away from the microtubule core by an estimated 11°-15° (Amos and Schlieper, 2005). GTP hydrolysis is thought to occur rapidly upon integration into microtubules, as polymerised tubulin dimers facilitate GTP hydrolysis in the adjacent tubulin dimer along the microtubule (Nogales et al., 1998). As such, it is thought that most tubulin dimers in microtubules are in the GDP form. Although this is not sufficient to cause collapse, it places the microtubule lattice under tension (Amos and Schlieper, 2005).

Although the theory has not been fully proved, it is believed that a cap of GTP-tubulin at the +end ensures microtubules remain stable. Should GTP-hydrolysis occur spontaneously within this cap region, then the whole microtubule will rapidly undergo highly coordinated collapse (Drechsel and Kirschner, 1994; Janosi et al., 2002). It is observed that a collapsing microtubule shows curled protofilament fragments peeling away from it, which leads to the idea that GTP hydrolysis puts the microtubule polymer lattice under intense strain (Desai and Mitchison, 1997; Arnal et al., 2000). Loss of the GTP-cap releases all of this stored energy, causing the microtubule to spring apart.

How rescue occurs is not known. It has been proposed that regions of GTP-tubulin that have been somehow retained within the microtubule lattice may offer distinct points of stability where it is possible to halt depolymerisation (Dimitrov et al., 2008). Similarly, microtubule pausing is not well-studied.

1.5.3 Organisation within cells

Microtubules are found to some extent in almost all eukaryotic cells. The stereotypical view of their organisation is that of a microtubule aster – a star-shaped arrangement of microtubules radiating outwards in three-dimensions from one point. In this model, microtubules are nucleated from a central location in the cell, close to the nucleus (Vorobjev et al., 2001). Nucleation sites are generally referred to as microtubule organising centres (MTOCs) (Zheng et al., 1995). The primary MTOC in animal cells is the centrosome. From here microtubules grow

outwards in all directions dynamically exploring the full volume of the cell (Hayles and Nurse, 2001).

The arrangement and associated dynamic properties of microtubules are known to differ in many cell types. Most distinctively, the axonal and dendritic outgrowths of neural cells are shaped by stable arrangements of microtubules throughout each process (Patel and Shen, 2009; Amos and Schlieper, 2005). Eukaryotic flagella and cilia are persistent microtubule structures (Lodish, 2008; Snell et al., 2004). Columnar epithelial cells maintain a transverse planar matrix of short microtubules just below their apical surfaces, with a separate set of parallel longitudinal microtubules running between the basal and apical surfaces (Musch, 2004).

In addition, if we look beyond animal cells, many other interesting microtubule arrangements become apparent. The protist, *Trypanosoma brucei* – of interest as the leading cause of African sleeping sickness – maintains a dense, strongly polarised microtubule corset around the cell periphery just below the cell membrane (Schneider et al., 1987; Vedrenne et al., 2002). This corset is even retained during cell division, leading to an extremely geometrically complex cytokinetic event. Plant cells also predominantly maintain a circumferential arrangement of microtubules, which is known to be significant for the correct deposition of cell wall fibres (Wasteneys, 2002; Hamada, 2014; Liu et al., 2015). Note that, in contrast to the single nucleation site required by a microtubule aster, both of these arrangements highlight the existence of cells with multiple microtubule organising centres (Luders and Stearns, 2007).

Most notably, all cells undergo drastic changes in microtubule activity as part of the cell cycle. Although microtubules have many other functions within cells perhaps their most vital is in cell division (Alberts, 2002; Lodish, 2008). During mitosis, cells duplicate their centrosomes, which then separate to opposite sides of the cell. These two centrosomes form the poles of the mitotic spindle, producing microtubules directed towards the cell centre. They capture chromosomes and align them to the cell centre – a structure called the metaphase plate – before rapidly undergoing catastrophe to reliably segregate a full complement of chromosomes into each new cell (see **Section 1.6**). During the early stages of division, microtubules must complete a rapid and thorough search for chromosomes within the cell volume, yet upon chromosome capture their dynamic activity must instantaneously stabilised and not reactivate until all chromosomes are captured and

aligned (Neumann et al., 2010; Wollman et al., 2005; Kline-Smith and Walczak, 2004; Holy and Leibler, 1994).

These reversible, time-dependent organisational changes are even observed in simple eukaryotes. The yeast *S. pombe* demonstrates at least three distinct microtubule patterns. An interphase pattern, similar to the aster, where microtubules are nucleated close to the nucleus by multiple MTOCs (interphase MTOCs; iMTOCs) – one of which is the spindle pole body (SPB); functionally equivalent to the mammalian centrosome – and reach out towards the cell ends (Hayles and Nurse, 2001; Sawin and Tran, 2006). During division, microtubules form a spindle, whilst shortly after division the microtubules adopt a highly transient and dynamic organisation called the post-anaphase array (PAA) nucleated from the division site at the cell middle (equatorial MTOC; eMTOC) (Heitz et al., 2001). It is probable that this helps to keep the two new nuclei clear of the forming septum as cells divide. In *S. pombe* interphase microtubules are bundled together, so predominantly project specifically towards one of the two cell ends.

1.5.4 Regulation of microtubules

Although microtubules are intrinsically dynamically active, they cannot completely regulate their own activity. Microtubules exhibit constant activity *in vitro*, responding only to changes in overall tubulin concentration and GTP availability. Yet a great variety of behaviours have been observed *in vivo*. Hence, it is apparent that other factors must control microtubule activity *in vivo* (**Figure 1.6**).

Confirmed microtubule regulators, in any species, are few and far between, with many microtubule behaviours currently unexplained (Amos and Schlieper, 2005; Akhmanova and Hoogenraad, 2005). What work has been done generally focuses on the role of microtubules in cell division, overlooking their distinct activities during interphase and in different cell types.

Regulators have been explored and reviewed extensively elsewhere (Amos and Schlieper, 2005; Akhmanova and Hoogenraad, 2005; Glotzer, 2009), including my own review (Lawson and Carazo Salas, 2013). Typically they breakdown into five groups; nucleators, stabilisers, destabilisers, motors and bundlers (Desai and Mitchison, 1997).

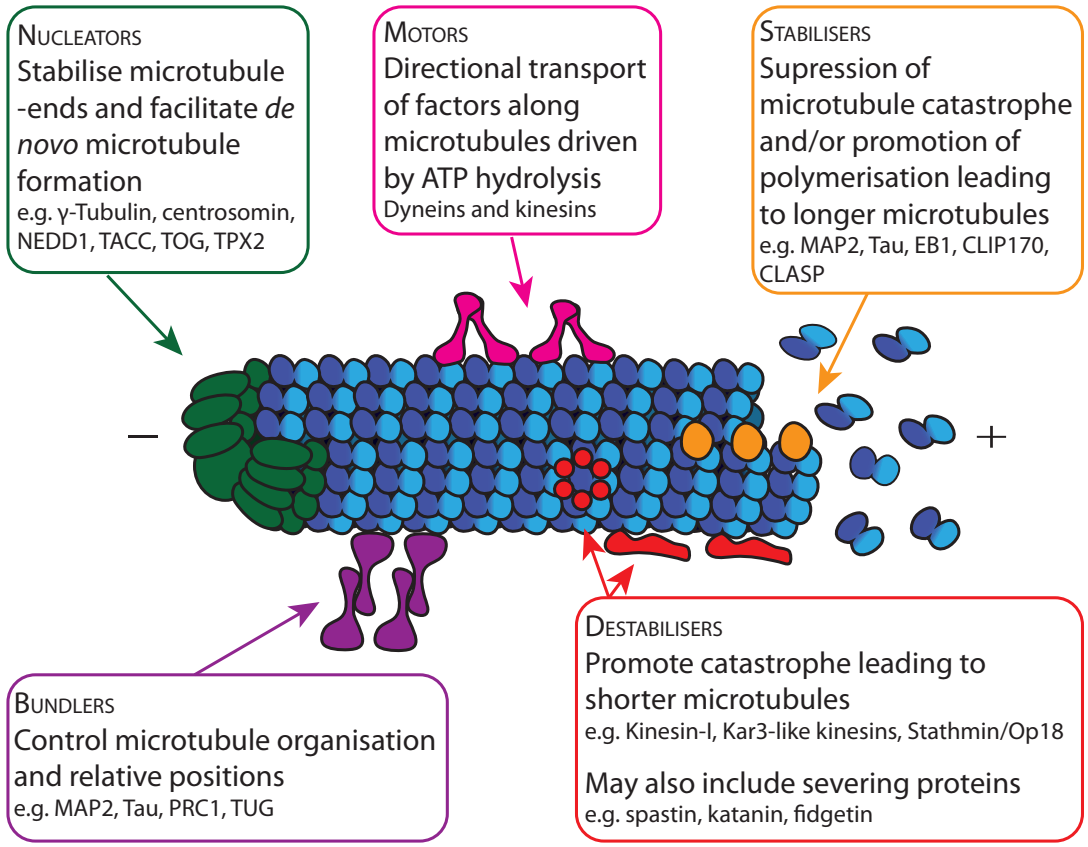

Figure 1.6: Factors that regulate microtubule dynamic instability - Microtubule regulators are primarily categorised into five groups according to their effect in relation to microtubules: nucleators (green), motors (magenta), stabilisers (orange), destabilisers (red) and bundlers (purple). Figure adapted from Studera (2012) and Lawson and Carazo Salas (2013).

1.5.4.1 Nucleation factors

Microtubule nucleators, epitomised by γ-tubulin (Stearns et al., 1991), have already been mentioned and provide structures and points for the initiation of new microtubules and the stabilisation of -ends (Dammermann et al., 2003; Wiese and Zheng, 2006). In many cell types, nucleators are necessary, as the endogenous tubulin concentration within cells is below the level necessary for spontaneous microtubule initiation (Amos and Schlieper, 2005). In animal cells, many components of the centrosome are assigned nucleator functionality, although their precise roles are not always clear (Pereira and Schiebel, 1997; Schiebel, 2000; Wiese and Zheng, 2006).

At the core of nucleation is the γ-tubulin ring complex (γ-TuRC), which includes several factors which help to activate and organise γ-tubulin for nucleation and ensure localisation to MTOCs. Accessory factors include centrosomin from *D. melanogaster* or Mto1 in *S. pombe* (Wiese and Zheng, 2006; Fujita et al., 2002).

1.5.4.2 Stabilising and destabilising factors

Stabilisers and destabilisers, unsurprisingly, are antagonistic to each other (Desai and Mitchison, 1997; Amos and Schlieper, 2005). They act to affect the average length of microtubules within a cell. Stabilisers typically either promote polymerisation or suppress catastrophe and are typically found at the microtubule +ends – so-called +TIPs – where these processes occur (Amos and Schlieper, 2005; Akhmanova and Hoogenraad, 2005; Akhmanova and Steinmetz, 2008). Several factors that influence microtubule stability are known, although some have their effect indirectly through others.

Some of the earliest microtubule regulators were stabilisers, simply called microtubule associated proteins (MAPs). Unusually, MAPs are found throughout the microtubule lattice, particularly in neuronal cells (Amos and Schlieper, 2005; Mandelkow and Mandelkow, 1995). +TIP proteins include the conserved EB1 (end binding 1), CLIP170 (cytoplasmic linker protein 170) and CLASP (CLIP-associated protein) families, which suppress catastrophe and may aid rescue, as well as XMAP215, which facilitates microtubule polymerisation (Akhmanova and Hoogenraad, 2005; Glotzer, 2009; Carvalho et al., 2003).

Destabilisers are not as well-studied, those that are known are often structurally related to motor proteins and may promote microtubule collapse by causing distortions in the microtubule lattice. This includes Kinesin-I (Kinesin-13; Wordeman and Mitchison (1995); Desai et al. (1999)), Kinesin-14 (Amos and Schlieper, 2005) and some members of the Kinesin-8 family (Kip3 in *S. cerevisiae* (Varga et al., 2006) and Klp5/6 in *S. pombe* (Erent et al., 2012)).

Stathmin/Op18 was one of the first destabilisers to be identified; it is also a known oncoprotein (Belmont et al., 1996). Stathmin is able to bind two tubulin dimers and forces them into a curved arrangement that further favours microtubule catastrophe. Due to its ability to bind multiple tubulin dimers in microtubules and in the cytoplasm, it also effectively sequesters free tubulin dimers, preventing their integration into microtubules.

In addition, a few microtubule severing factors are known – including katanin, spastin and fidgetin – which, through unknown mechanisms, are able to break microtubules in the middle (Quarmby, 2000; Roll-Mecak and McNally, 2010). They have been reported as destabilisers as the unprotected microtubule ends they create – lacking GTP-tubulin caps – are prone to depolymerisation. They are also believed to be important in the production of microtubules for axon formation in neurons (Roll-Mecak and Vale, 2006).

1.5.4.3 Microtubule motors

Motor proteins are an interesting element of cytoskeletal processes, which are also found in relation to actin (Lodish, 2008). Motors primarily operate as transporters, hydrolysing ATP to facilitate the movement of cargoes along cytoskeletal elements. By binding between two microtubules they can also affect their relative positioning allowing them to fulfil a microtubule organising role in some cells (Jolly and Gelfand, 2010; Carazo-Salas and Nurse, 2006).

Motors typically consist of head domains that interact with the cytoskeleton and 'walk' along the repeating units of the cytoskeleton like a track. Tail regions then interact with cargoes allowing them to be transported. Microtubule motors divide into two superfamilies: dyneins and kinesins (Hirokawa, 1998).

There are a small number of dyneins, which typically form large complexes (1.2 MDa) of several units (Hirokawa, 1998; Lodish, 2008; King, 2000). Notably, in contrast to actin motors (myosins) and kinesins, the ATP hydrolysing motor units in dyneins do not contact the microtubule directly. Dyneins were first identified in cilia and flagella as the driving unit for motion of these structures (Gibbons and Rowe, 1965). By attaching to one microtubule and then walking along another, they are able to induce twisting between two microtubules, creating cilia/flagella motion.

There are many kinesins (14 families), which typically form dimers or tetramers (Hirokawa, 1998). They were first identified through study of neural axons (Vale et al., 1985). All motors are directional, dyneins travel from +ends to -ends, whilst kinesins typically move in the opposite direction. However some kinesins have opposite polarity, which correlates with a reversal of domains organisation; placing their motor domains at the C-terminus (Hirokawa et al., 2009).

1.5.4.4 Bundling factors

Bundler proteins generally occur in specific contexts, helping to stably associate microtubules and fix their relative positions (Walczak and Shaw, 2010). These include some of the MAPs (specifically Tau and MAP2), which are thought to be able to cross-link microtubules and control their spacing in neurons (Dehmelt and Halpain, 2005). Another bundler, PRC1, forms rigid homodimers that promote the antiparallel bundling of microtubules (Subramanian et al., 2010).

As mentioned above, motors can also help in the bundling of microtubules; the Kinesin-5 family cross-link microtubules from opposite spindle poles during cell division (Ferenz et al., 2010) and a Kinesin-14, Klp2, in *S. pombe* is known to collaborate with the PRC1 homologue Ase1 in creating antiparallel microtubule bundles during interphase (Carazo-Salas and Nurse, 2006, 2007).

1.5.4.5 Regulation by post-translational modification

Others have reported that microtubules undergo extensive post-translational modification within cells, accumulating a variety of acetylations, glycylations and glutamylations, as well as losing a few C-terminal amino acids and gaining the occasional phosphorylation (Wloga and Gaertig, 2010; Westermann and Weber, 2003; Janke and Bulinski, 2011). It has been proposed that this 'tubulin code' may be as complex and elaborate as the 'histone code' of histone modification as part of epigenetic regulation (Verhey and Gaertig, 2007). As such, there may also be an array of protein modifying factors that have notable influence on microtubules, although few have yet been identified.

1.5.4.6 Other ways to control microtubules

In addition, tubulin folding is aided by chaperone cofactors, which ensure association with GTP and correct dimer assembly (Melki et al., 1993; Gao et al., 1993; Lewis et al., 1996). The prefoldins are known to be chaperones specific to cytoskeletal protein assembly, although tubulin assembly is also likely to be supported by many other accessory factors (Eisenberg et al., 2002; Simons et al., 2004; Vainberg et al., 1998).

In many species, several tubulin isoforms also exist, even *S. pombe* includes two α-tubulin genes (*nda2* and *atb2*; Adachi et al. (1986)), whilst mammalian species may have more than ten tubulin isoforms (Janke and Bulinski, 2011).

One additional complication that comes with the investigation of microtubule regulating factors is that since these factors affect a process that is already highly variable and responsive to change, the effects of over-expressing or deleting one regulator proteins are generally much more complex than might be expected (Mitchison and Kirschner, 1984a; Desai and Mitchison, 1997). For example, deleting a potential nucleation factor may reduce the number of microtubules, but it will also cause remaining microtubules to become longer – as there will be more free tubulin available for polymerisation – this may then, in turn, affect the arrangement or organisation of the microtubule network within the cell. As such, identifying the effects of mutating a specific gene on the microtubule cytoskeleton may be trivial, but establishing the actual method of action can be much more complex.

1.5.5 Reason to believe in more

The microtubule network, being particularly well-defined in terms of core molecular constituents, is probably the best context in which to ask the question: what do we hope to find? As previously mentioned, we know that we do not know everything about microtubule behaviour in cells, therefore it is intuitive to believe that there are many microtubule regulators yet to be discovered.

This assertion can be further supported by biochemical studies that suggest the existence of many more regulators than those that are known. Several studies have used microtubules as bait for the biochemical enrichment of proteins by association (Mack and Compton, 2001; Liska et al., 2004; Sauer et al., 2005). Many proteins identified through such studied may be found to non-specifically or indirectly interact with proteins, and an association is not proof of a functional interaction. In one case, 250 interactors were proposed, of which 100 were already known (Hughes et al., 2008). Of the new hits that were tested further, only 25% showed an actual effect on microtubules. Whilst this highlights the need for caution in the analysis of screening results, it also serves to show that many functional microtubule regulators remain undiscovered.

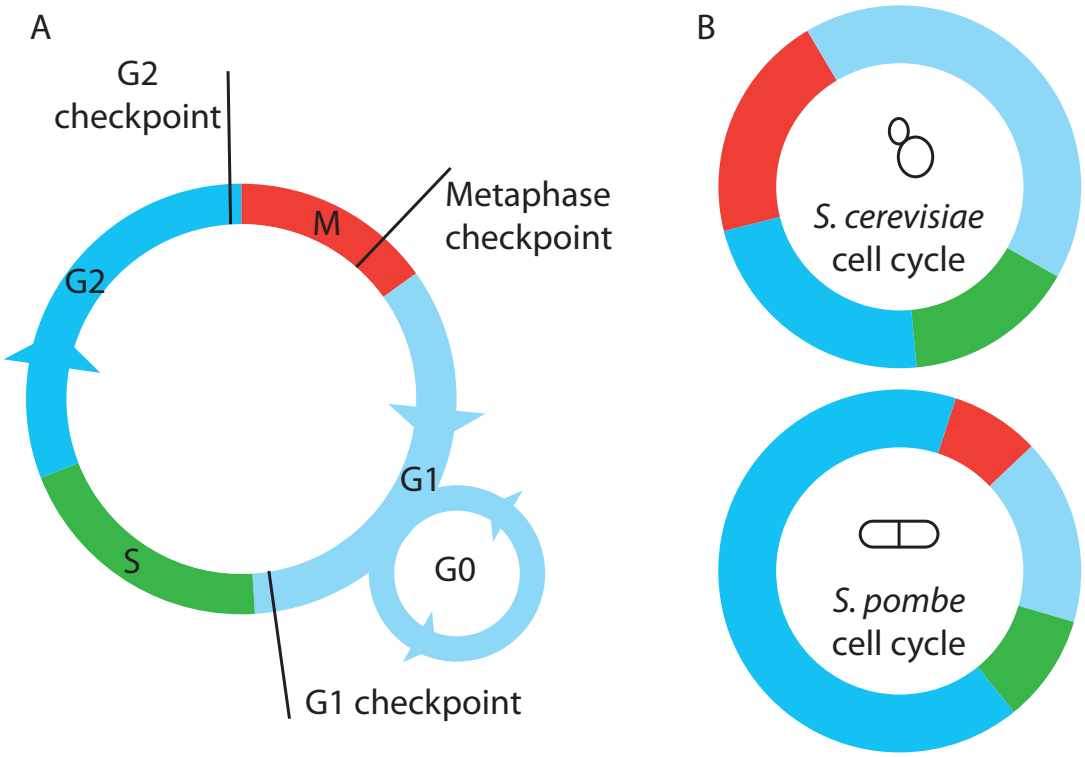

Figure 1.7: The cell cycle, its checkpoints and progression - **(A)** A generalised representation of a cell cycle, indicating key regulation checkpoints and featuring the quiescent/senescent state (G0). Figure derived from Alberts (2002). **(B)** Comparative illustrations of cell cycle progression in two common model organisms, the budding yeast *S. cerevisiae* and the fission yeast *S. pombe*. Figure adapted from Langerak and Russell (2011).

1.6 Cell cycle

Biologically, life exists to make more life. Therefore, the division of cells to produce more cells is probably the most fundamental, and therefore significant, aspect of any living system. The cell cycle is the process that controls the division of cells by ensuring that events occur consistently in the correct order to duplicate all genetic information and maintain sufficient cell mass through each round of cell division, producing two complete new cells from one parent cell (Alberts, 2002; Lodish, 2008).

With some exceptions, the cell cycle consists of four phases: gap 1 (G1), synthesis (S), gap 2 (G2) and mitosis (M). The four phases are progressed through in order and key checkpoints must be reached before each phase can be com-

pleted (**Figure 1.7A**). The actual duration of cell cycles varies greatly between species. Bacteria can complete a full cycle in 20-30 min, yeasts may take 2-5 hours, whilst human cells typically take 1-2 days. In addition, cells may enter a quiescent or senescent phase (G0), where they can persist indefinitely without undergoing further division (Burns and Tannock, 1970). This is a common state in adult multi-cellular organisms where the need to produce new cells is restricted to preserve the correct form and function of organs and tissues.

1.6.1 Cell cycle phases

The gap phases are primarily stages at which the cell grows with the goal of doubling cell mass in each cell cycle. In different species these phases represent very different portions of the cell cycle, although together they typically constitute the majority of time in any given cell cycle. In *S. cerevisiae*, G1 tends to be longer than G2, whereas in *S. pombe* G1 is very short and G2 can be around 70% of the total cell cycle duration (**Figure 1.7B**; Alberts (2002)). In mammalian cells relative durations vary in different tissues and at different stages (Lodish, 2008). Where an increase in mass is not needed, gap phases are completely dispensable. During early embryogenesis in many multi-cellular organisms, the egg cell, which is often very large, may undergo several rounds of division without any growth, passing directly between S and M phases (Graham and Morgan, 1966; Masui and Wang, 1998; Noatynska et al., 2013).

The primary aim of S phase is synthesis of new DNA. Every cell carries all of its genetic information in DNA and after division both new cells must still contain a complete copy. Hence, a complete new copy must be created. This is an intricate, carefully regulated process, with many checks to prevent damage to DNA and to avoid introducing errors into the genetic code (Hennessy and Botstein, 1991; Sclafani and Holzen, 2007).

M phase is the point at which the cell actually divides and represents a point of no return. It is essential to ensure that any errors within a cell, particularly in the genome, are corrected before division, or they may cause irreparable damage. Visually and biochemically, this is probably the most active and disruptive phase of the cell cycle, including many rapid transitions in a very short space of time (Alberts, 2002; Cooper and Hausman, 2013). As such, it is probably also amongst the most closely studied.

In M phase chromosomes condense and become distinct (prophase), the microtubule spindle forms and captures chromosomes (metaphase). Once all chromosomes are captured they are aligned at the cell centre to a point called the metaphase plate. Once all chromosomes are correctly aligned and securely attached to both spindle poles, microtubules elongate the spindle and pull one complete genome copy to each spindle pole (anaphase) (Goshima and Scholey, 2010; Alberts, 2002). The chromosomes then decondense within the two new nuclei (telophase) and the cell divides precisely between the two spindle poles (cytokinesis). Notably, both *S. pombe* and *S. cerevisiae* undergo closed mitosis, where the nuclear envelope remains *in situ* throughout cell division. Most animal cells undergo open mitosis, breaking down the nuclear envelope in early M phase and reconstructing it following anaphase (Guttinger et al., 2009).

1.6.2 Order and directionality

The order of events in the cell cycle is controlled by the cyclic accumulation, activation and degradation of specific protein factors. These factors are called cyclins, because the levels of cyclins within cells, cycle in line with the cell cycle (Evans et al., 1983). Cyclins are necessary to allow the cell to enter certain cell cycle phases. The most well-studied, control entry into M phase and are members of the Cyclin B family (Clb1/2 in *S. cerevisiae* and Cdc13 in *S. pombe*), alternatively called M phase cyclins (Hunt, 1991; Norbury and Nurse, 1992; Pines, 1993).

Cyclins are produced slowly throughout the cell cycle, accumulating within the cell until a critical level is reached, which permits initiation of the corresponding cell cycle phase. Towards the end of that phase all of the cyclins are rapidly destroyed; this prevents the same cell cycle phase from being repeated until another full cell cycle is complete. Cyclins act by regulating the activity and specificity of cyclin-dependent kinases (CDKs), which phosphorylate many other proteins to affect their activity (Alberts, 2002; Nurse and Thuriaux, 1980). Notably, cyclins from different phases are able to cross-influence the accumulation and degradation of others, ensuring that each cell cycle phase maintains a distinct character and progression (Cooper and Hausman, 2013; Li et al., 2004).

The activation of CDKs also depends upon phosphorylation and degradation events. These signals are outputs from other cell processes. In order for a cy-

clin:CDK complex to become active, all of these processes must signal that the cell is ready to progress to the next phase (Gu et al., 1992; Obaya and Sedivy, 2002; Koepp et al., 1999; Nakayama and Nakayama, 2005). These events that regulate cell cycle progression are known as checkpoints.

1.6.3 Checkpoints

In order to ensure that the cell cycle fulfils the goal of fully duplicating all aspects of a cell to successfully produce two new cells many tasks must be completed. Every stage of the cell cycle has certain requirements to meet before it can be completed. These must be fulfilled in order to continue to subsequent cell cycle stages.

There are generally agreed to be three key checkpoints in each cell cycle: G1 (DNA damage), G2 (DNA replication) and Metaphase (spindle assembly) (Kastan and Bartek, 2004; Elledge, 1996; Lukas et al., 2004; Houtgraaf et al., 2006).

The G1 checkpoint, variously known as the restriction point in mammals and the start point in yeast, is the event where a cell commits to another round of division. Up to this point G1 can still be prolonged and the cell can become quiescent or enter senescence. The precise requirements that must be fulfilled to pass this check can vary between species, but typically include attaining a sufficient size and containing a complete and error-free genome (Skotheim et al., 2008; Bartek and Lukas, 2001).

Similarly, the G2 checkpoint permits transition from G2 into M phase. It assesses the completion of DNA replication during S phase, complete with resolution of any errors. It also ensures that the cell has attained sufficient size for division (Lobrich and Jeggo, 2007).

Both of these checkpoints are sensitive to DNA damage through the actions of DNA damage response kinases (see **Section 4.7**; Smith et al. (2010); Yang et al. (2003); Rhind and Russell (2000)). These kinases typically integrate with a wider stress detection signalling network. Hence cells will typically also halt cycling at one of these checkpoints if stressed in other ways, including changes in osmolarity, oxygen availability or temperature (Hammond et al., 2003; Alao and Sunnerhagen, 2008; Bakkenist and Kastan, 2004; Pearce and Humphrey, 2001).

Finally, the metaphase checkpoint occurs in the metaphase stage of M phase. This checkpoint is highly precise, preventing the cell from progressing to anaphase until every chromosome in the cell is securely attached by microtubules to both spindle poles and has been aligned to the metaphase plate (Lara-Gonzalez et al., 2012; Pinsky and Biggins, 2005).

1.6.4 New approaches

The cell cycle is especially interesting because, due to its nature, it affects every part of the inner workings of a cell. Logically, it must affect every major structure and process as part of the upheaval of driving cell division. The checkpoints that control the cell cycle must also be sensitive to the activities of every part of the cell, ensuring that everything is prepared in advance of each new cell cycle phase. Whilst it has been extensively studied in its own right, it is also a prime subject for investigation within a wider context. The inclusion of the cell cycle in any multi-process study is likely to be particularly informative because no matter what else is being studied, connections are probable.

1.7 Cell shape, microtubules and the cell cycle together

Whilst cell shape, microtubules and the cell cycle are interesting in their own rights, the value of our approach is in the ability to study all three together. Classically, we have been forced to take a reductionist approach to biology, focusing on one small part, or one pathway, all too often losing sight of the bigger picture in the process.

Biological systems are built on coordinated activities and interactions; there are no biological pathways, no isolated protein complexes, just vast, complex networks of thousands of components, all of which change subtly in response to any stimulus, environmental adjustment or genetic manipulation. The need for all of this communication and cross-communication suggests that many genes may bridge processes and have several different functions, yet very few of these have been identified (van de Peppel and Holstege, 2005; Dudley et al., 2005). This

concept ultimately leads to pleiotropic genes, which influence several, seemingly unrelated phenotypes, and are theorised to be key to understanding complex genetic diseases, and the ageing process (Chavali et al., 2010; Sivakumaran et al., 2011; Kirkwood and Austad, 2000; Kirkwood, 2005).

The large-scale and high-throughput technologies that have developed in recent years are now making it possible to study biological systems as a whole, without the need to pick and choose individual phenotypes, functions or genes. By doing so we can begin to probe the genetic and molecular nature of the interconnectedness of biological systems in new and diverse ways.

Our existing knowledge of these three chosen processes makes them an interesting test case for studying connection between processes, as all three have significant connections to each other.

1.7.1 Cell shape and microtubules

The connection between processes is perhaps most apparent in relation to cell shape and microtubules where cells are known to change their shape significantly in response to the actions of cytoskeletal structures. In general, cell shape is primarily coordinated by the actin cytoskeleton, which forms a dense sub-membrane network (the cell cortex) (Salbreux et al., 2012; Pollard and Cooper, 2009). However, in addition to structures formed directly by microtubules, the microtubule network is able to influence cell shape in other ways (Wells and Bonetta, 2005; Nakamura, 2015). Through its role as a transport system, the microtubule network can affect the delivery of polarity and growth factors to specific regions of the cell surface (Matter and Mellman, 1994; Nelson, 2003; Siegrist and Doe, 2007). This can vary from the delivery of actin organising factors, affecting cell protrusions, to directing polarity factors that coordinate other processes for membrane expansion and cell outgrowth or the direct delivery of new membrane components in vesicles, which then cause local expansion of the cell membrane (Feierbach et al., 2004; Schmoranzer and Simon, 2003; Basu and Chang, 2007; Browning et al., 2003). The recycling of membrane factors, by microtubule guided vesicles, also helps to ensure that different membrane regions maintain molecularly distinct characteristics, which are often important for the maintenance of polarised cell shape (Apodaca, 2001; Musch, 2004).

It is notable, even in simple systems such as *S. pombe*, that disorganisation of microtubules can lead to bending of the classic rod-shaped cell and may lead to redefinition of cell polarity, with the initiation of new growth zones (Chang and Martin, 2009; Niccoli et al., 2003).

1.7.2 Microtubules and cell cycle

The significance of microtubules in the cell cycle is apparent through the role of microtubules in the mitotic spindle. Microtubules undergo drastic rearrangements in coordination with cell cycle progression to ensure correct spindle construction and reliable chromosome segregation (Ding et al., 1993; Lodish, 2008). In addition, microtubule attachment is a key input to the metaphase checkpoint, with the cell cycle halting until spindle construction is complete (Pinsky and Biggins, 2005; Foley and Kapoor, 2013). These procedures indicate the necessity for cross regulation of both processes and make it clear that processes must exist that directly relate to both microtubules and the cell cycle.

1.7.3 Cell shape and cell cycle

Linking cell shape and cell cycle is perhaps less apparent in some biological contexts, yet these connections are still vital. Many cell types undergo a significant shape change prior to division, commonly called ‘rounding up’, where they become more spherical. This is likely to be an adaptation to aiding chromosome capture by the spindle – it is easier to capture chromosomes in a spherical volume where the area of space to be explored in each direction is approximately equal (Lancaster et al., 2013). However, this poses several problems, as cells must be able to resume their previous cell shape rapidly after division. More importantly, within multi-cellular organisms, cells form well-defined layers, structures and barriers, which must be maintained throughout cell divisions, hence each division event may require several cells to change shape in order to preserve correct organisation (Baker and Garrod, 1993; Ragkousi and Gibson, 2014; Pugacheva et al., 2006).

Furthermore, during development, attaining a correct mature cell shape, and fate, can depend upon the completion of a certain number of cell cycles and the ac-

cumulation of specific factors into daughter cells (Fuerstenberg et al., 1998; Gi-ansanti et al., 2001). In some tissues, cell shape changes noticeably throughout the cell cycle, neural precursor cells maintain a pseudo-stratified organisation, with cell shape changes reflecting cell cycle progression. This is thought to allow the production of a greater number of neurons in a smaller space. Noticeably, the retention of an attachment to the basal membrane is also critical to avoiding terminal differentiation (Fish et al., 2008; Schenk et al., 2009).

Conversely, the cell cycle is required to wait for cells to attain a certain size before division, which is another important input to the cell cycle checkpoints. Size can be considered as an aspect of cell shape (Cadart et al., 2014; Fantes, 1977). Particularly in *S. pombe*, attaining suitable cell size for division is thought, by some, to be measured by assessing the cell length through a diffusion gradient of Pom1 kinase from cell tips to the cell centre (Martin and Berthelot-Grosjean, 2009; Moseley et al., 2009; Saunders et al., 2012).

1.7.4 All three together

Perhaps one of the most interesting points at which all three processes intersect is in the aligned division of cells during development (Thery and Bornens, 2006; O'Connell and Wang, 2000; Siller and Doe, 2009; Lu and Johnston, 2013). The alignment of the spindle in a dividing cell can be key to ensuring the correct formation of two daughter cells. The spindle must be perpendicular to the division plane of the cell, ensuring that each genome is gathered separately into each daughter cell. In tissues, the alignment of the spindle and division plane within a tissue can have a major effect on the fates of the two cells produced (Siller and Doe, 2009; Noatynska et al., 2013; Panbianco and Gotta, 2011). Positioning of the spindle is dependent upon sensing of cell shape and cell polarity and is driven by the cytoskeleton.

Orientation of the spindle is perhaps most obvious in *S. cerevisiae*, which divides by budding, producing a small side cell from an existing cell (**Figure 1.8A**). Due to this method of division, the position of cell division is predetermined and the spindle must follow suit (Yin et al., 2000; Beach et al., 2000; Segal et al., 2002). Hence the spindle undergoes a search of the cell periphery to find the bud and migrates one spindle pole into the bud before initiating cell division.

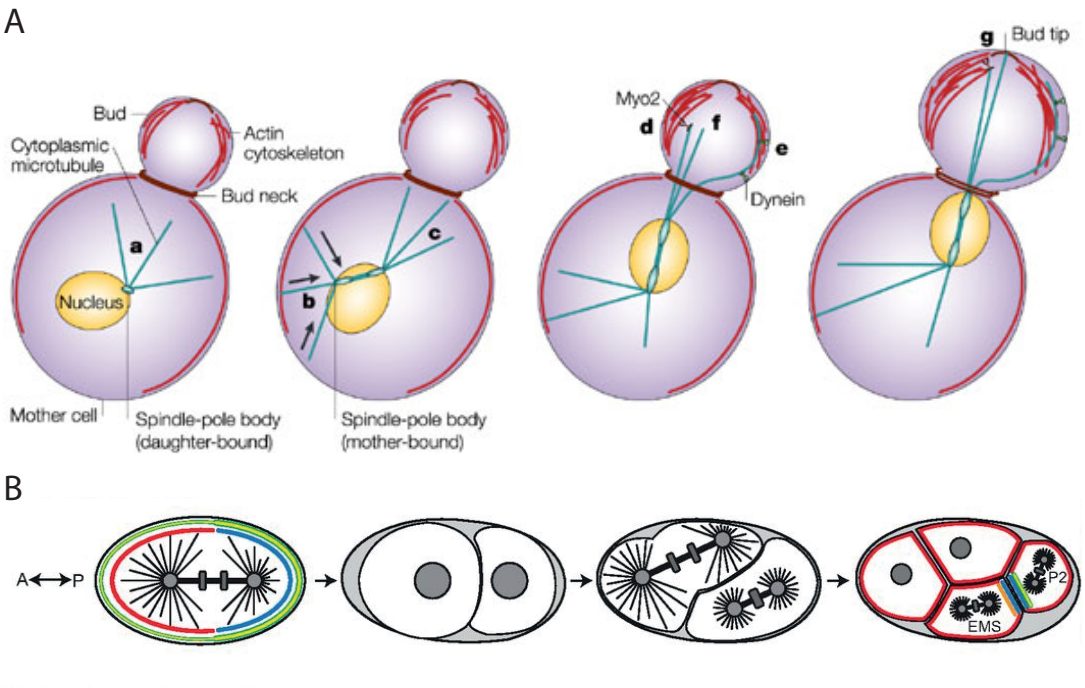

Figure 1.8: Examples of links between cell shape, microtubules and the cell cycle - **(A)** The process of spindle alignment in *S. cerevisiae*. Cortical markers and forces affecting cell shape are detected by the dynamic activity of microtubules. Microtubules guide entry of one spindle pole into the bud, enabling cell division to proceed. Figure from Pearson and Bloom (2004) **(B)** Early cell divisions in *C. elegans* embryos. Centrosome position establishes the anteroposterior (AP) axis, affecting the localisation of PAR (red) and PKC3 (blue). This ultimately influences spindle alignment resulting in two cells with different shapes, sizes and fates. Figure from Lu and Johnston (2013).

Spindle alignment in most cases is microtubule-dependent. In addition to the inward-facing spindle microtubules that bridge between spindle poles and form attachments to chromosomes, there are also microtubules that radiate outwards, called astral microtubules. These project towards the cell cortex and periphery, detecting markers of cell shape and polarity and engaging with motor proteins to rotate the spindle into the correct orientation (Lee et al., 2000; Giansanti et al., 2001).

Hence, aligned cell division depends upon microtubules to detect and respond to cell shape, which positions the spindle and division plane and ensures the correct completion of the cell cycle.

In addition, cooperation of all three processes can ensure correct developmental programming. Microtubules are key to the delivery of specific cell fate-determining factors to specific parts of the cell in a number of contexts. The alignment of these microtubules is often dependent upon cell shape and then relies upon the cell cycle to divide the cell accordingly to produce two new cells that are now molecularly distinct.

In one-cell *C. elegans* embryos, the MTOC from the sperm determines the antero-posterior axis of the embryo, affecting cell fate determinant localisation, spindle orientation and division plane alignment, creating two cells with different shapes, sizes and fates (**Figure 1.8B**; Wallenfang and Seydoux (2000)). Similarly, microtubules in the *D. melanogaster* oocyte are first responsible for accumulation of factors from nurse cells into the spatially-defined oocyte. However, a subsequent, drastic near-reversal of microtubule polarity is then used to drive repositioning of the oocyte nucleus from the cell posterior into one anterior corner, this serves to define the dorsoventral axis of the embryo, affecting subsequent cell cycles and fates (Roth and Lynch, 2012; St Johnston, 2005).

These are three intricately connected processes and we can only hope to fully understand their activities by attempting to establish all of the factors involved in each process and by studying them together in context, to understand how they interact with other cell processes and relate to each other. The fission yeast, *S. pombe*, provides an ideal context in which to study these processes and their relationships. It has a highly stereotyped cell shape that is reported to adopt a limited number of mutant phenotypes (Hayles et al., 2013) and it has a greatly simplified interphase microtubule network. In addition, *S. pombe* is a well-established model organism for study of the cell cycle (Nurse, 1975) and all three of these processes interact to sustain the wild-type phenotypes as cells grow and divide (Hayles and Nurse, 2001). Furthermore, yeast is well-suited to high-throughput screening because of its small size, rapid generation time and ease of genetic manipulation.

1.8 The goals of high-content screening

The initial goals of this project were laid down in 2008; to apply novel computational image processing methods to high-throughput biological microscopy and

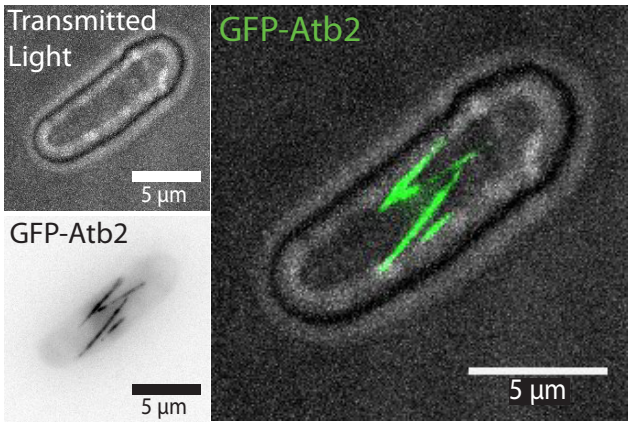

Figure 1.9: ***Schizosaccharomyces pombe*** - A stereotypical wild-type cell of *S. pombe* showing spherocylindrical shape and interphase microtubule array consisting of four antiparallel microtubule bundles, approximately aligned to the major cell axis.

develop a rapid and efficient pipeline for the simultaneous screening of multiple-biological processes for specific visual phenotypes.

In particular, we have set out to explore the genes that influence a trio of visual phenotypic traits that are well-studied, but not fully understood. These processes all have central, conserved roles in basic eukaryotic cell biology; the determination of cell shape, the arrangement of the microtubule cytoskeleton and progression through the cell cycle.

Since the intention was to apply high-throughput methods, a biological system was needed that would allow for genome-wide exploration of the chosen cell processes and would provide clear three-dimensional images for automated segmentation and analysis.

1.8.1 The fission yeast *Schizosaccharomyces pombe*

To address these goals, a simple and easily manipulated model system was chosen, the fission yeast *S. pombe*. This unicellular organism is well-established as a laboratory model and offers the added benefit of the commercially available KO library (Kim et al., 2010) of haploid total gene-deletion, true knock-out (KO) mutants for the vast majority of non-essential genes (In version 2 of the library, coverage is 3004/3576; Hayles et al. (2013)).

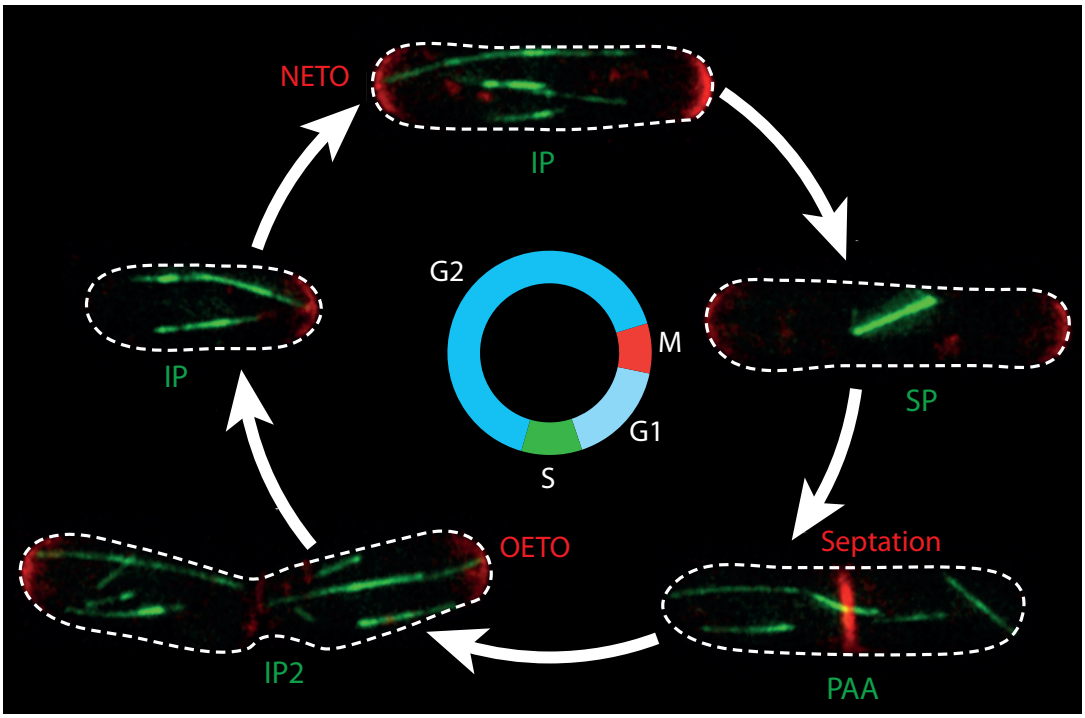

Figure 1.10: The cell cycle of *S. pombe* - Changes in microtubule organisation (green; GFP-Atb2) and cell growth pattern (red; RFP-Bgs4) through the cell cycle of *S. pombe*. Cells transition from the microtubule spindle (S) during M phase, to the post-anaphase array (PAA). Microtubules adopt interphase organisation before the completion of septation (interphase2; IP2). Eventually cells separate becoming individual cells with interphase microtubules (IP). After sepatation, cells undergo old end take-off (OETO) leading to monopolar growth. Subsequent new end take-off (NETO) permits bipolar growth. Image credit to R. Carazo Salas.

In addition, this species has a well-defined and highly stereotyped cellular morphology (**Figure 1.9**). By virtue of the cell wall, yeast cells are unable to adopt the highly variable and irregular shapes observed in most metazoan cells, making it much easier to study the roles of specific genetic elements in regulating cell shape (Chang and Martin, 2009; Hayles et al., 2013). Wild-type *S. pombe* cells typically maintain a spherocylindrical or capsule shape, consisting of a cylinder capped with approximately hemispherical ends. The cells have a near constant diameter of $\approx$4 μm during exponential growth and elongate from $\approx$7 μm to $\approx$14 μm as they progress through the cell cycle (Hayles and Nurse, 2001).

Similarly, unlike some other model yeast species, *S. pombe* maintains microtubules throughout all stages of the cell cycle. Again, the microtubule organisation

of wild-type cells is extremely well-characterised and has a considerably simpler form, that is much more easily studied and quantified, than in the cells of higher organisms (Hagan and Yanagida, 1997). For the majority of time, cells make use of an interphase microtubule formation, which features 2-5 microtubule bundles approximately aligned to the major axis of the cell. Within these bundles, several individual microtubules are positioned such that their stable -ends are located close to the cell centre (and the nuclear envelope), whilst +ends project towards the cell tips (an antiparallel microtubule array) (Drummond and Cross, 2000; Tran et al., 2001).

It was the changes in microtubule patterns that allowed us to also examine progression through the cell cycle as a later addition to our screen (**Figure 1.10**). Perhaps the most vital role of microtubules is in cell division, where they form a spindle to separate chromosomes into daughter cells. In *S. pombe* this takes the distinctive form of a single, very large microtubule bundle spanning the cell centre. This is closely succeeded by the post-anaphase array (PAA), nucleated from the apparent site of septation and consisting of many relatively disorganised, short microtubules projecting into both presumptive daughter cells. The interphase microtubule organisation is then resumed in both new cells, prior to the total separation of the cells, giving the appearance of two conjoined interphase cells (interphase2; IP2) (Chang and Martin, 2009).

After division, *S. pombe* cells initiate cell growth from their old end (old end take-off; OETO) and then undergo monopolar growth. At some point before the end of G2 most cells will activate growth from the new cell end (new end take-off; NETO) and continue to grow from both cell ends until cell division causes the cell to undergo septation.

2 Methods

"This is my timey-wimey detector. It goes ding when there's stuff. Also, it can boil an egg at 30 paces, whether you want it to or not, actually, so I've learned to stay away from hens."
—THE 10^{TH} DOCTOR (*Blink*, 2007)

2.1 Working with *S. pombe*

2.1.1 Fission yeast strains

Strain	Genotype	Source
PN556	*leu1-32, ura4-D18, ade-M216, h+*	Paul Nurse
PN557	*leu1-32, ura4-D18, ade-M210, h-*	Paul Nurse
MS1404	*leu1-32, ura4-D18, gfp-atb2-KanR, h-*	Masamitsu Sato
RCS001	*leu1-32, ura4-D18, gfp-atb2-NatR, h-*	Miriam Börtfeld-Miller
RCS1088	*leu1-32, ura4-D18, cdc2Δ::NatR, cdc2-as(F84G)-HphR*	Marco Geymonat
XS014	*mcherry-atb2-hph, ase1-gfp-KanR, h-*	Xenia Studera
MP339/PN4739	*ade-M210, amo1-gfp-KanMX6, h+*	Mercedes Pardo
MJ95	*leu1-32, ura4-D18, mcherry-atb2-Hph, h-*	Masamitsu Sato
JL024	*amo1-gfp-KanMX6, mcherry-atb2-Hph*	This study
LL5	*ade-M210/M216 leu1- cut11-gfp-ura4+, mcherry-atb2-Hph*	Luca Lorenzi
JL028	*amo1-gfp-KanR, sad1-dsred-leu2+*	This study
M38	*leu1-32, ura4-D18, his-, ade-M216, cdc13-gfp-leu1+*	Marco Geymonat
JCR978	*leu1-32, ura4-D18, his3-D1, bgs4Δ::ura4+, Pbgs4+-RFP-bgs4-leu1+, h-*	Marco Geymonat

Table 2.1: *S. pombe* strain list - List of all individual strains used in this research.

All haploid deletion library strains (Kim et al., 2010) were purchased from Bioneer corporation (`www.bioneer.com`) as the version 2 library (3004 strains) or version 2 to version 3 (v2v3) update (547 strains: 206 upgraded strains, 341 additional

strains). All deletion strains (xΔ; where x is the name of any non-essential gene) have one of two possible genotypes:

- *xΔ::KanMX4 ade-M210, ura-D18, leu32 h+*
- *xΔ::KanMX4 ade-M216, ura-D18, leu32 h+*

The complete library was then crossed with RCS001 to create a library of GFP-Atb2 labelled strains. When working with individual library strains, the presence of the reported gene deletion was assessed directly by PCR, as described in Studera (2012), before any further experimental work.

2.1.2 Growth medium & selection methods

All medium was made using purified water that had been filtered, deionised and autoclaved.

2.1.2.1 Rich YES medium

Most strains were subject to selection using drug resistance (Sato et al., 2005) and were grown in rich yeast extract plus supplements (YES) medium:

- 5 g/L bacto yeast extract (BD, USA)
- 0.25 g/L SP supplements (50 mg/L each of adenine, L-histidine, L-leucine, L-lysine & uracil; Formedium, UK)

Medium is initially made up to ⅘ the final volume. Before use the remaining volume is made up with:

- 150 mL/L 20% (w/v) glucose
- 50 mL/L water

Solid YES medium for making plates was made by adding 20 g/L agar (Formedium, UK). When grown in liquid culture, cells were typically suspended in YES medium + carbenicillin to suppress bacterial growth.

2.1.2.2 Edinburgh minimal medium (EMM)

Some strains were selected using auxotrophy, the inability to grow in the absence of an external source for a specific biological component. Selection on the basis of auxotrophy requires that strains are grown on Edinburgh minimal medium (EMM) agar plates lacking the key auxotrophic factor. This medium was also used to select for a combination of auxotrophic and drug selection markers. Basic EMM + Agar consisted of:

- 24.6 g/L EMM without dextrose mix (MP Biomedicals, USA)
- 17 g/L agar (Formedium, UK)

Medium is initially made up to 7/10 the final volume. Before use the remaining volume is made up with:

- 100 mL/L 20% (w/v) glucose
- 200 mL/L water + supplements (see below)

Supplements for EMM, are given below. Medium should contain all of these factors, other than the ones being selected against.

- 50 mL/L adenine (Formedium, UK)
- 33.3 mL/L histidine (Formedium, UK)
- 33.3 mL/L leucine (Formedium, UK)
- 33.3 mL/L lysine (Formedium, UK)
- 33.3 mL/L uridine (Formedium, UK)

Liquid EMM was not used in this study, auxotrophic strains selected for on EMM plates were then grown for experiments in liquid YES medium.

2.1.2.3 Selection drugs

Selective drugs were added to medium to isolate specific genotypes:

- **Geneticin** (G418; Roche, Switzerland) Selects for Kan cassettes, such as those found in the KO library. It was used for selection at 200 mg/L. During screening it was used at 100 mg/L to suppress bacterial contamination ('G418/2')

- **Nourseothricin** (clonNAT; Werner BioAgents, Germany) Selects for Nat resistance cassettes, such as the gfp-atb2::Nat construct of RCS001. Used at 100 mg/L, stored as 1000x aliquots at -20℃.
- **Carbenicillin** (Carb; Applichem, Germany) A non-selective drug used to limit bacterial contamination of yeast cultures. All liquid yeast cultures that did not include selective drugs contained 50 mg/L unless specifically stated.

2.1.2.4 Mating medium

Yeast strains will cross when deprived of nitrogen, this was done by growing strains together on agar plates containing Edinburgh minimal medium (EMM) minus nitrogen:

- 27.3 g/L EMM broth without Nitrogen (Formedium, UK)
- 0.35 g/L SP supplements (Formedium, UK)
- 17 g/L agar (Formedium, UK)

2.1.2.5 Freezing medium

For long term storage at -80℃, cells were suspended in 50% (v/v) medium and 50% (v/v) yellow freezing medium (YFM) consisting of:

- 5 g/L Bacto yeast extract (BD, USA)
- 0.25 g/L SP supplements (Formedium, UK)
- 30 g/L glucose
- 30% (v/v) glycerol

2.1.3 Low-throughput *S. pombe* handling

2.1.3.1 Long term storage and recovery

Fission yeast strains can be stored near indefinitely in a high glycerol solution at -80℃, assuming they are not subjected to regular refreezing. Typically cells

are stored in 2 mL cryotubes (Sigma-Aldrich, USA) suspended in a 50/50 mix of growth medium and YFM.

To minimise damage to the stocks, cells were recovered from frozen by scratching away some of the surface ice with an inoculation loop and streaking it onto selective YES agar plates. The plates were then incubated at 32℃ for at least 3 day to allow colonies to develop.

2.1.3.2 Growing cells in liquid culture

Yeast strains were kept, in the short term, on YES agar plates and subject to appropriate selection pressures to prevent the loss of required genetic features. Prior to experiments, cells were maintained in exponential phase by suspending some in 10 mL of medium in 50 mL tubes (Cellstar, Greiner Bio-One, Austria) and incubating at 32℃ with shaking, for at least 48 hours. To maintain exponential growth, these liquid cell suspensions were diluted approximately every 12 hours. Continued culturing for 48 hours is required to ensure that all cells are in the exponential growth phase and have adopted the corresponding steady-state cell morphology.

The dilutions needed to maintain exponential growth can be calculated by assessing the optical density (OD) of strains. This was measured using a spectrophotometer (Ultraspec 2100 Pro, Amersham Biosciences, UK) to record the absorbance of light at 595 nm (OD_{595}).

An OD_{595} of 0.5 was approximately equal to 10^7 cells/mL, where exponential growth phase was considered to be between OD_{595} 0.05 (10^6 cells/mL) and OD_{595} 1.0 (2x 10^7 cells/mL). Equivalent OD_{595} and cell density readings were assessed using a haemocytometer to count cell number in samples with varying ODs, creating a calibration curve for conversions. Since the doubling rate of *S. pombe* is approximately $2\frac{1}{4}$ hours at 32℃ it is easily possible to calculate the necessary dilution factor for a given length of time. For a given final OD_{595} (C_F), a known time period (Δt; in hours) and a known current OD_{595} (C_C) the required dilution factor (D) can be found.

$$D = 2^{\left(\frac{\Delta t}{2\frac{1}{4}}\right)} * \frac{C_C}{C_F} \tag{2.1}$$

As an example, if the current OD_{595} is 0.5 and the desired OD_{595} after 12 hours is also 0.5 then the required dilution factor would be 40, meaning that a 1:40 dilution is needed.

2.1.3.3 Liquid culture drug/analogue treatments

All strains were grown, as described above, for the minimum 48 hours before treatment.

Treatments with hydroxyurea (HU) typically started 6 hours before filming and used a final, non-lethal 15 mM concentration. Since cells were grown in small volumes, a 300 mM stock solution in water was made fresh for each round of treatments. Cells adapt to HU exposure after 3-4 hour (Parker et al., 1997), hence the dose was renewed every three hours during treatment.

Cdc2-AS strains were treated with the kinase-inhibiting analogue 3-BrB-PP1 (Ab-Cam; ab143756) at final concentration 5 μM, typically for 6 hours prior to imaging (Cipak et al., 2011).

Phleomycin treated cells were also exposed for 6 hours prior to filming, with re-treatment every 3 hours (Belenguer et al., 1995; Toczyski, 2006) . Doses ranged from 2 μg/mL to 10 μg/mL, all of which were sufficient to cause cell elongation.

2.1.4 Low-throughput *S. pombe* imaging

Cultures were diluted to reach approximate OD_{595} 0.5 in time for imaging. Cells were typically imaged in glass-bottomed microwell dishes (35mm dish, 1.5mm coverglass, MatTek, USA). Dishes were pre-coated with lectin (1 mg/mL pure *Glycine max* lectin (Patricell, UK) in 10mM phosphate plus 150 mM NaCl). 100 μl were used to coat the glass and the excess subsequently removed, leaving a fine coating which was allowed to dry (30 min) before cells were added.

300 μl of the exponential cell suspension were added to the lectin-coated glass for 20 minutes, allowing the cells to attach to the glass, due to binding between lectin and cell wall sugars. When the medium was removed a high density coating of cells was left on the glass. To give a sparse monolayer for easy imaging of individual cells, the cell-coated glass was mildly washed 2-3 times with YES

medium. Finally 3 mL of YES medium were added to keep the cells alive during imaging.

All low-throughput imaging was performed on a DeltaVision System (Applied Precision, USA), built around an Olympus IX81 wide-field microscope, coupled to a CCD coolSNAP HQ2 camera (Photometrix, USA). Images were collected using a 100x/1.4 N.A. UPLSapo Oil immersion lens, using transmitted light plus FITC (ex 490/20 nm; em 528/38 nm), TRITC (ex 555/28 nm; em 617/73 nm) and DAPI (ex 360/40 nm; em 457/50 nm) filters linked to LED light sources.

2.1.4.1 Static imaging

S. pombe strains were typically imaged using transmitted light (Intensity 32%; Exposure 0.025 s) and the FITC filters (GFP imaging; 100%; 0.3 s) . Occasionally TRITC filters (mCh/RFP imaging; 100%; 0.3 s) were also used. 16 plane z-stacks were collected with a separation of 0.4 μm, covering a total of 6 μm above the glass surface. Since *S. pombe* cells are $\approx$4 μm thick, this ensures that the complete volume of all horizontal or near-horizontal cells can be imaged.

Maximum intensity projections of z-stacks were typically used for manual image analysis, as this offers the greatest contrast between microtubules and cytoplasm. Raw image stacks were used in combination with projections to study Amo1 localisation across the spherical nuclear envelope. Sum projections were used when quantifying total cell GFP-Atb2 content.

2.1.4.2 Microtubule kymographs

Individual focal planes were filmed every two seconds for 10 min (Tran et al., 2001) using FITC filters (32%; 0.2 s). The focal plane was manually selected to focus on the +end of one interphase microtubule bundle. Throughout imaging, the focus was continually manually adjusted to keep the moving microtubule end in focus at all times. To avoid excessive bleaching of surrounding cells, the aperture on the light path was closed down so that only the focal cell was illuminated.

To form a kymograph, the complete timelapse video was converted into a z-stack by altering the image metadata. The stack was then rotated about the z-axis to align the microtubule to the vertical axis. Images were then cropped to give

the minimum possible volume that contained the focal microtubule at all times. Projection of this volume on the yz plane produced a view of the fluorescent signal over time, with each time point condensed into a near two-dimensional slice. These were later analysed to give polymerisation, depolymerisation and catastrophe rates for microtubules.

2.1.4.3 Measuring growth rate

For image-based assessment of changes in growth rate in response to HU treatment, several strains were grown in separate wells of a LabTek 8-well plate, allowing for parallel automated filming of several treated and untreated strains. Plates were pre-treated with lectin in the same way as described for other experiments.

Cells were imaged using the same Olympus DeltaVision microscope, but using a 60x/1.42 N.A. PlanApoN Oil immersion lens to rapidly capture a greater number of cells. Fluorescence signals were not collected for these cells, and images were collected as 5-plane z-stacks with a separation of 1 μm between planes. The use of a z-stack ensured that cells should stay in focus throughout prolonged imaging even if there was a shift in the focal plane during imaging. Samples were imaged every 10 min for 6 hours.

2.1.5 Other low-throughput methods

2.1.5.1 Hydroxyurea sensitivity testing

Solid YES plus agar plates were prepared containing 3 mM, 10 mM or 15 mM HU. Strains for testing were grown to high density in YES liquid medium for 2-3 days. 100 μl samples from each strain were then arranged in the first column of a 96-well plate and then subjected to six rounds of serial dilutions by addition of 10 μl from the first well into 90 μl of fresh medium in the second well, then taking 10 μl from the second and adding to 90 μl medium in the third, and so on.

4-5 μl from each well was then pipetted onto the pre-prepared plates of agar medium. To aid in arrangement of drops from each well, an 8-well multi-tip pipette was used. Care was taken to avoid allowing adjacent drops to merge and plates

were then left to dry completely before inverting and incubating at 37℃ for 2-3 days.

Resistance to different doses of HU was measured by how many dilutions a strain could withstand and still produce colonies. Comparison was also made between the number of colonies that survive in the most diluted surviving samples. Wild-type dilutions were included as a control.

2.1.5.2 Western blotting for SQ/TQ phosphorylation

Western blotting primarily made use of the Amo1-GFP strain. Using the GFP label as a way to detect Amo1 in blots. Control dark cells (PN557) or other GFP labelled cells (MS1404) were used in some experiments as controls. As for imaging, cells were previously maintained in exponential growth phase for 48 hours in a small volume (10-20 mL) liquid YES medium. The night before treatment, cells were transferred into a larger volume (250 mL) to allow enough cells to be collected for testing.

At the start of treatment samples were diluted to OD_{595} 0.3-0.5 and HU was added. Due to the larger culture volumes here, HU was weighed and added directly, not pre-diluted in water. Cultures were re-treated with HU every 3 hours. Note that since the volume of each sample reduced throughout the experiments, the amount of HU added was corrected accordingly.

Every two hours, a 50 mL culture was removed and centrifuged (3 000 rpm, 3 min), to pellet cells. Pellets were resuspended in 1 mL PBS, transferred to small volume freezing tubes and centrifuged again (13 200 rpm, 1.5 min) to recover the cell pellet. Pellets were then snap frozen in dry ice and stored at -80℃. Samples were stored for at least 24 hours before protein extraction.

Initially, trichloroacetic acid (TCA) extraction of proteins was attempted. All centrifugation steps were 13 200 rpm, 1.5 min, unless otherwise stated. Samples were kept on ice as much as possible throughout. Frozen samples were thawed and resuspended in 1 mL 20% (w/v) TCA, then centrifuged and resuspended in 400 μL 20% TCA. Glass beads (0.5 mm diameter, BioSPec Products) were added to samples to fill the liquid volume. Cells were lysed using a Ribolyser (Hybaid), with three 10 second treatments, with 1 min cool-down periods in ice between each.

A further 400 μL 5% (w/v) TCA was added to each sample and left for 3 min to equilibrate. The aqueous layer above the beads was then removed to a new tube and centrifuged for 10 min to pellet precipitated proteins. The supernatant was removed completely and 50 μL Tris buffer (pH 7) and 100 μL Laemmli buffer (62.5 mM Tris-HCl pH 6.8, 10% (v/v) glycerol, 2% SDS, 5% β-mercaptoethanol, 0.001% (w/v) Bromophenol blue) were added. The pellet was resuspended by vortexing and the suspension incubated at 100℃ (5 min). The samples were centrifuged and the supernatant removed to new tubes for storage at -20℃.

From each sample 5 μL was subjected to electrophoresis in a 10% (v/v) polyacrylamide gel (200V, 50 min). Gels were blotted onto nitrocellulose using a semi-dry transfer method (15V, 1 hour). Each sample was typically run in two lanes on the same gel, this allowed each gel to be cut in half, with one side probed for the presence of Amo1 (anti-GFP) and the other probed for Amo1 phosphorylation (anti-pSQ/TQ).

Membranes were blocked using PBST + 5% (w/v) milk powder for 1 hour. Primary antibody treatment was overnight in PBST + 5% milk powder at 4℃. Membranes were washed six times with PBST (5 min each) then treated with HRP conjugated secondary antibodies in PBST + 5% milk powder. Membranes were then washed a further six times in PBST (5 min each) and developed using Amersham ECL Western Blotting Detection Reagents (GE Healthcare). The membrane was coated with the reagents then sandwiched within transparent plastic film for development onto photographic film. Films were exposed for 15 min to 1 hour.

TCA extraction did not produce any distinct signals for phosphorylated Amo1. It is not the best method for conserving phospho-proteins and does not enrich for Amo1, which has relatively low abundance (Asakawa et al., 2014), so this is not surprising. After consulting with Jesus Carballo, who has experience of studying ATM/ATR phosphorylation targets, I moved to an alternative method known to have better results in isolating phosphorylated proteins.

In this approach, frozen cell pellets were resuspended in 300 μL lysis buffer (30 mM Tris pH 7.5, 150 mM NaCl, 0.1% (v/v) triton X-100, 10 mM NaF, 1 mM sodium orthovanadate, 10% (v/v) glycerol, 50 mM β-glycerophosphate, 2 mM EDTA, 1x PMSF (Life Technologies, 100x stock) and 1x c***O***mplete EDTA-free protease inhibitors (Roche; 1 tablet per 50 mL) in water). Glass beads were added and cells lysed as for TCA. A hot, sterile needle was used to pierce the base of each sample tube. Tubes were placed atop a new 2mL tube inside a 15 mL tube and

centrifuged (1000 rpm, 30 sec), transferring the lysed cell suspension into the new tubes.

Samples were centrifuged (13 200 rpm, 5 min) to remove cell debris. Supernatant was moved to a new tube, centrifuged again (13 200 rpm, 10 min) and supernatant moved to a new tube again. A protein assay kit (Bio-rad) was used to test the protein concentrations in each sample and standardise them by dilution in water. Typically samples were standardised to 2-4 mg/mL.

Amo1 was enriched using 30 μL GFP-Trap magnetic beads (ChromoTek) per sample. Beads were prewashed in 1 mL breaking buffer (30 mM Tris pH 7.5, 150 mM NaCl, 0.1% (v/v) triton X-100) and vortexed. A magnetic tube stand was used to separate the beads from the buffer. The buffer was removed and replaced with the samples. Samples were incubated with the beads (1 hour, 4℃, rotation). Beads were then washed rapidly four times with breaking buffer then resuspended in 70 μL Laemmli buffer, heated at 100℃ (5 min) and stored at -20℃ before electrophoresis and blotting. This procedure was as before, however 5% (w/v) milk powder was replaced with 1% (w/v) BSA (Sigma), which J. Carballo reported gives better results when blotting for phospho-proteins.

Primary antibodies used for blotting were rabbit anti-phospho-SQ/TQ (AbCam, 1:200) and mouse anti-GFP (Roche, 1:1000). Secondary antibodies were goat anti-mouse (BioRad, 1:300) and anti-rabbit (BioRad, 1:300).

2.1.6 High-throughput *S. pombe* handling

2.1.6.1 Library handling & storage

The haploid deletion collection is provided from Bioneer Inc. arrayed in 33 96-well plates (plus 6 for the v2v3 upgrade). To aid in mass handling of these strains, a 96-tip pipette system (Rainin liquidator 96, Mettler-Toledo, Switzerland) was used. This device may be referred to as the 'liquidator'.

In addition to the original 'dark' library, lacking any fluorescent markers, a '*gfp-atb2*' library was created for the purposes of this screen, by crossing the library strains *en masse* with our RCS001 (*gfp-atb2-NatR*) strain. The original and variant libraries are both stored in 96-well plates at -80℃. For high-throughput procedures, 200 μL aliquots were frozen in shallow plates (Polypropylene Microplates,

Greiner Bio-One). Individual strains can also be recovered from 1 mL aliquots in deep well plates consisting of 96 separate tubes (1 mL Matrix 2D Barcoded ScrewTop Storage Tubes, Thermo Scientific, USA)).

The details of how the *gfp-atb2* library was produced and stored has previously been described for the version 2 library in the thesis of X. Studera (see Collaborations; Studera (2012)). I subsequently reproduced this approach for the v2v3 update, with minor technical modifications. In place of the semi-automated methods previously used, this work was entirely manual, making use of the liquidator.

To perform strain crossing, cells from agar plates (both RCS001 and deletion strains) were suspended at high density in 96-well plates in 50 μL/well water. Sequentially 4 μL droplets of RCS001 and then deletion strains were deposited onto EMM without nitrogen (EMM-N) agar plates. The droplets of RCS001 suspension were allowed to dry completely before adding the deletion strains on top. After incubating high temperature was used to remove vegetative cells (6 day, 42℃) and spores were germinated and subjected to selection prior to being grown in liquid medium for freezing and long term storage.

2.1.6.2 Screening preparation

In preparation for screening, each library plate was thawed from long-term storage, grown on selection medium to ensure all cells were of the correct genotypes and then underwent a series of serial dilutions over 48 hours to ensure all strains were in a suitable growth phase for imaging. Our preliminary work paralleled that of others (Kim et al., 2010) in showing that different mutant strains grow and divide at different rates. Serial dilution of strains provided a way of ensuring that, irrespective of growth rates, all 96 mutants in each plate could be maintained in exponential growth phase without needing to treat each strain individually. This was important as we were specifically interested in examining cells during rapid growth and division, where cells are constantly adapting to change and hence where the connections between cell processes are probably most apparent.

Plates were thawed from shallow plates (**Table 2.2**; Day -17) by leaving at room temperature for 20 min. 20 μL of cell suspension was then added to 180 μL of fresh YES medium and allowed to grow to high density stationary phase (room temperature with shaking, 5 days), ensuring as many strains as possible recovered fully from freezing.

	Task
Day -17	thaw plate
Day -16	incubate at room temperature
Day -15	
Day -14	
Day -13	
Day -12	transfer to selection medium
Day -11	incubate at 30℃
Day -10	
Day -9	
Day -8	transfer to liquid culture, grow to high cell density
Day -7	incubate at room temperature
Day -6	
Day -5	
Day -4	
Day -3	dilution 1
Day -2	dilution 2
Day -1	dilution 3
Day 0	imaging

Table 2.2: Preparation for screening - Schedule of tasks performed on plates prior to high-throughput imaging.

Strains were subjected to selection (**Table 2.2**; Day -12) by transferring 4 μL of the high density liquid culture onto solid YES plus agar 96-well compatible plates (OmniTray, Nunc, USA) containing G418 & Nat.

This was a technically challenging stage as care was needed to ensure that the separate droplets of cell suspension did not run together, merging different mutant strains. It was important to ensure the surface of the agar was not excessively damp by leaving plates at room temperature for at least 24 hours prior to use, this helped keep the cell cultures separate. Multiple copies of each plate were usually created.

Droplets were allowed to dry at room temperature for at least 1 hour before incubating at 30℃ for 4 days. This helped to ensure that all cells had the desired genotype when imaged.

Cells from the resulting colonies were transferred to 200 μL liquid G418/2 YES medium (**Table 2.2**; Day -8) and grown to high density again (room temperature with shaking, 5 days). It was during the transfer back to liquid that control strains were added to empty wells and, in the case of the second genomic screen, that plates were divided into two half-plates. The different locations of control strains across different screens can be seen in **Figure 3.11B, D & E**.

Control strains included the negative control *gfp-atb2* wild-type strain (MS1404), *mal3*Δ 'dark cells' lacking fluorescent markers, as well as GFP-Atb2-labelled positive controls *mal3*Δ, *mto1*Δ, *ase1*Δ – which demonstrate distinctive high penetrance microtubule phenotypes – plus *tea1*Δ – which has a more subtle phenotype. The occurrence, frequency and positions of different control strains in different screening rounds varied, as explained in **Section 3.3.2**. To permit computational subtraction of background signals, the last well (H12) in every 96-well plate was left empty of cells, containing only imaging medium (**Section 2.1.6.4**).

2.1.6.3 Growth phase alignment

It has previously been observed that different *S. pombe* mutants can vary greatly in growth rates, with the vast majority showing growth deficiency compared to wild-type strains (Kim et al., 2010). Since each screening plate contains 96 different randomly arrayed deletion mutants, this creates a significant challenge in ensuring that all strains are imaged during comparable states of exponential growth.

To address this issue in a manner compatible with high-throughput procedures, a method was developed based upon serial dilution of strains, which should ensure that all strains can be imaged during exponential growth. The basic method has been described in full elsewhere: Graml et al. (2014); Studera (2012). This protocol creates multiple parallel copies of the same plate subject to different degrees of dilution. In principle, fast growing strains will require a high degree of dilution to maintain exponential growth over 48 hours. If insufficiently diluted, they will enter a different physiological state and will not be comparable to other strains. Conversely slow growing strains only require a small amount of dilution and excessive dilution will result in too few cells for imaging. By creating multiple copies of each plate it is possible to have low dilution factors for slower strains and higher dilution factors for faster strains without needing to dilute each strain individually.

From the high density G418/2 plate described in **Section 2.1.6.2**, initial dilutions were created to re-initiate exponential growth (**Table 2.2**; Day -3). These first dilutions were typically created ≈60 hours prior to the start of filming. The first plate was created by diluting 15 μL of the high density cell cultures into 235 μL of fresh G418/2 YES medium. This same medium was used for all subsequent steps, up to and including imaging. This plate was typically called a 1:20 dilution. The second dilution took 50 μL from each well of the 1:20 plate and added it to 150 μL of medium, creating a 1:80 dilution. Plates were incubated at room temperature with shaking (**Figure 2.1**).

24 hours later (**Table 2.2**; Day -2), the absorbance OD_{570} was measured for all 96 strains in both dilution plates by resuspending the cells and using a plate compatible spectrophotometer (microplate reader, Bio-Rad, USA). Here, the empty H12 wells were used for the reference background reading. A reading of OD_{570} 0.3 was equivalent to 2 x 10^7 cells/mL.

Optimal growth was taken to be between OD_{570} 0.09 and 0.3. Whichever plate gave readings where most strains were in the optimal range was then used for a

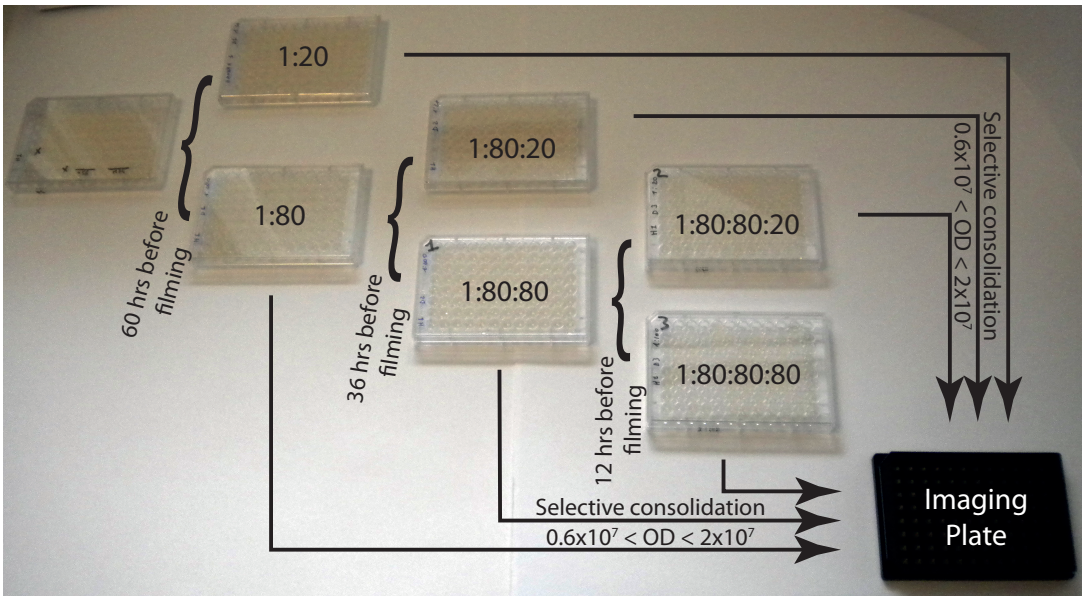

Figure 2.1: Alignment of strains by serial dilution - Photograph illustrating how multiple 96-well plates of different dilutions are created from one source plate, over a 48 hour period, to ensure that all 96 strains are in optimal physiological condition for imaging.

second round of dilutions. Typically this was the 1:80 plate. The same procedure of adding 15 μL to 235 μL and then adding 50 μL from this to 150 μL was used to create two new plates, referred to by the rounds of dilution that produced them, e.g. 1:80:20 and 1:80:80. The same procedure of measuring and diluting was performed once again (**Table 2.2**; Day -1), diluting one of the four pre-existing dilution plates, after a further 24 hours (12 hours before filming).

This procedure ensured that almost all strains were present in the optimal growth state at the time of filming. Most strains, with wild-type-like growth rates, had optimal density in the most dilute plates. As a minimum, 6 dilutions were produced from each screening plate, however sometimes more were required.

2.1.6.4 Imaging

The final preparation for filming (**Table 2.2**; Day 0) entailed taking a final set of OD_{570} from all dilution plates. The imaging plate (perfect edge, flat glass-bottom, 96-well plate; Swissci, Switzerland; PS96BG175) was also pre-coated with lectin (as in **Section 2.1.4**) using 80 μL per well, removing the excess and allowing to

dry completely.

From all of the serial dilution plates created in **Section 2.1.6.3**, it was necessary to compile a final plate of all 96 strains in optimal growth conditions for filming. Thus, for each mutant strain the best dilution was selected and individually transferred to the final plate.

Previously the process of selecting which copy of each strain to use was performed manually, by assessing the OD_{570} readings. This was changed in this work, to use a bespoke Microsoft Excel tool that I created, which automatically compared and selected the most optimal dilution (Lawson, 2011). The selected copies were then manually moved to a final plate before all being transferred together into the imaging plate.

If multiple plates were imaged in the same day, or if it was not possible to image straight away, the final plate could be subjected to additional small dilutions (1:2 or 1:5) to preserve optimal conditions until filming.

Once 100 μL of each cell culture was added to the lectin-coated filming plate they were allowed to adhere to the lectin for at least 30 min. As for low throughput imaging (**Section 2.1.4**), the medium was then removed and cells washed at least twice with fresh medium to remove excess cells. The same liquidator tips were used throughout washing, with 3-4 rinses each of 70% (v/v) ethanol and then pure water between each wash.

Once a suitable cell density was attained (as assessed visually), 100 μL of fluorescent imaging medium (0.1 mg/mL Dextran Blue in G418/2 YES; Dextran Cascade Blue 10 000 MW, Invitrogen, USA) was added per well.

Cells were imaged using the OperaLX, high-throughput, autofocusing, spinning disk, confocal microscope (PerkinElmer, USA) with 60x water immersion objective and CCD camera, collecting images using the 488nm (GFP; 120 ms, $\approx$5000 μW) and 405nm (Cascade Blue; 80 ms, $\approx$1000 μW) laser channels.

Images were collected as 16 z-plane stacks upwards from the glass face, with a separation of 0.4 μm, ensuring the full volume of most cells close to the glass could be captured. To ensure that enough cells were imaged in most wells for meaningful statistical analysis, six different locations were imaged in each well. This meant six separate image stacks of different cell were collected for each mutant studied.

The six locations could all be filmed together as one experiment, but this would mean the microscope would spend a longer time imaging each well before moving on to the next, so the time difference between the first and last well would be very large (≈4.5 hours). This reduces the ability to compared between strains as such a large difference in imaging time between strains may result in a difference in physiological condition. As these are live cells, they continue to grow during imaging, so reach higher cell density at later times and are more likely to enter stationary phase. Instead, plates were imaged six separate times, with one location per well each time (≈40 min per run). This approach ensures that the images from all 96-wells in each experiment are in more comparable physiological states, separated by a maximum of just 40 min. Scheduling these six consecutive experiments used the remote control interface (RCI) feature of the OperaLX.

To ensure at least some cells in every well were imaged at an appropriate cell density for reliable image processing, the six imaging fields were chosen with five broadly distributed across the centre of the well, and one in the region of higher cell density nearer to the well edge (which was occasionally useful for very slow growing mutants).

Images were automatically transferred overnight to the lab server where they could be stored long term and accessed for analysis.

2.1.6.5 Rearraying candidate hits for (re-)rescreening

Initially, two complete genome-wide screens of 3004 mutants were performed, which gave rise to 763 candidate hits. These 763 mutants were filmed another eight times (rescreening), giving a total of ten independent datasets for each mutant. It was impossible to acquire sufficient data from these ten repeats to perform statistical analysis of 92 strains. Hence, these were imaged a further eight times in an attempt to enrich these datasets (re-rescreening).

To perform screens of subsets of the library, the selected strains needed to be separated from all other strains and re-arrayed into new 96-well plates.

For rescreening, Solid G418/Nat YES selection plates of library strains were generated in the same way as during preparation for the genomic screening. Inoculation loops were used to transfer selected strains from these plates into new

96-well plates, containing 100 μL G418/2 YES liquid medium. 88 strains were arrayed on each plate as shown in **Figure 3.11D**, allowing some space for controls. This created nine new plates.

These new plates were treated like freshly thawed screening plates. They were grown to high density, subjected to selection on solid medium and then regrown in liquid prior to dilutions. Since the rescreen consisted of eight independent repeats, two copies of the solid selection plates were made. This allowed the solid plates to be used as the source for cells in all eight imaging repeats, rather than repeatedly thawing frozen stocks.

For long term storage of these re-arrayed plates, during the first round of re-screening, 100 μL of the cells that remained in the high density plate after the start of serial dilutions were combined with 100 μL YFM in shallow plates (Polypropylene Microplates, Greiner Bio-One, Germany) and stored at -80℃.

The same procedure, using the solid plates from the rescreen, was used to create one plate of 92 'difficult' strains for which re-rescreening was needed (**Figure 3.11E**). This was also grown and imaged eight times.

2.2 Working with cultured cells (Hc3716-hTERT)

2.2.1 Cell lines

The cells used in this work are Hc3716-hTERT (Hc3716) immortalised human fetal hepatocyte cells (Waki et al., 2010), which have been immortalised through the activation of the telomerase reverse transcriptase (hTERT), permitting continued growth and division without detectable cancer-like phenotypes.

These cells are always incubated under constant conditions of 37℃ and 5% CO_2

2.2.2 Growth medium

Cells were grown in modified hepatocyte culture medium.

The basic culture medium is made up of:

- 500 mL hepatocyte basal medium (HBM) (Lonza, USA)
- 1 SingleQuots™ Kit (Lonza, USA)
  - 0.5 mL ascorbic acid
  - 10 mL bovine serum albumin – fatty acid free (BSA-FAF)
  - 0.5 mL hydrocortisone
  - 0.5 mL human epidermal growth factor (hEGF)
  - 0.5 mL transferrin
  - 0.5 mL insulin
  - 0.5 mL gentamicin/amphotericin-B

To the hepatocyte culture medium were added:

- 10% (v/v) human serum (Gibco, USA)
- 5% (v/v) fetal bovine serum (FBS) (Lonza, USA)
- 2% (v/v) DMSO

2.2.3 Storage & recovery

For long-term storage, cells in 100 mm Petri dishes (Nunc, USA) were treated with 2 mL/dish 0.05% trypsin-EDTA (Gibco, USA) for 10-20 min, diluted in 6 mL/dish of HCM and counted (Countess cell counter, Invitrogen, USA). Cells were then centrifuged (1000 rpm, 3 min) and the pellet resuspended in freezing medium (90% (v/v) FBS, 10% (v/v) DMSO) to give 10^6 cells/mL. This was divided into 1 mL aliquots in screwcap cryotubes (Greiner Bio-One, Germany) and frozen slowly by encasing in polystyrene and storing at -80℃ for at least 24 hours before transferring to liquid nitrogen.

Cryotubes of cells were rapidly thawed by immediate immersion in a 37℃ water bath, 1 mL cell suspension was then diluted in 7 mL HCM and centrifuged to pellet cells (1000 rpm, 3 min). Cells were resuspended in 8 mL HCM and added to a 100 mm Petri dish.

24 hours after thawing, the cell medium was replaced by fresh HCM to remove any dead cells. Cells were maintained for at least a week after freezing to allow for complete recovery before attempting any experimental work.

2.2.4 Cell maintenance

Cells were maintained at, or below, 50% confluence in 100 mm Petri dishes (Nunc, USA) in 8 mL HCM. To maintain suitable density, cultures were diluted approximately twice per week, with dilution factors based upon an estimated 24 hour doubling time.

Cells were released for dilution by removing medium and incubating with 2 mL/dish 0.05% trypsin-EDTA (Gibco, USA) for 10-20 min. The cells, suspended in trypsin, were added to 6 mL HCM and centrifuged to pellet the cells. The pellet was re-suspended in a variable volume (3-5 mL) of HCM in accordance with the required dilution factor (typically 1:3 of 1:5). 1 mL of resuspended cells was added to 7 mL HCM in fresh 100 mm dishes.

2.2.5 DNA damage induction

2.2.5.1 Preparing cells for induction of DNA damage

60 mm Petri dishes (Nunc, USA)) were prepared with 4 mL HCM covering six 13 mm diameter coverslips (VWR, USA) per dish. The coverslips were spread across the base of the dish as the cells that adhere to the coverslips are the ones that can be fixed and imaged.

Cells in 100 mm dishes were released by trypsin treatment as in **Section 2.2.4**, once the cell pellet was resuspended in 3 mL HCM, 10 μL were added to 10μL trypan blue (Invitrogen, USA) and the cell number measured (Countess cell counter, Invitrogen, USA). 2.5 x 10^5 cells/mL cells were then seeded onto each of the prepared plates. This gave $\approx$70% density of cells after 24-48 hours.

2.2.5.2 Induction of DNA damage and cell fixation

Conditioned medium was removed and kept during UVC treatment of cells. A non-lethal dose of 30 J/m^2 (Graml et al., 2014) was used, unless otherwise stated (Bespoke UVC device; Jackson Lab, Gurdon Institute, Cambridge, UK). After treatment the medium was returned to the plates. For ionising radiation (IR) treatment, medium was not removed and cells were exposed to doses of 2, 5 or 10 Gy, as described in the text (CellRad, Faxitron; Su et al. (2010); Bao et al. (2006)). Control coverslips were given equivalent treatment but without UVC/IR exposure.

After treatment, cells were typically incubated for a further eight hours, unless otherwise stated. The cells were then fixed using a -20℃ methanol fixation procedure on the coverslips to preserve microtubules for immunofluorescence and imaging.

Prior to fixation, all coverslips were briefly washed in PBS. Where cold-induced depolymerisation of microtubules was used, coverslips were then incubated in 4℃ PBS for 10 min (Kirschner et al., 1974; Delphin et al., 2012) before permeabilisation by immersion in OPT buffer (100mM PIPES/KOH pH 6.75, 1mM $MgCl_2$, 1 mM EGTA, 10% (v/v) glycerol, 0.5% (v/v) Triton X-100) for 1 min at room temperature, then rinsed in PBS and fixed in methanol at -20℃ for 6 min. Coverslips were stored under PBS at 4℃ until stained for immunofluorescence (Delphin et al., 2012).

2.2.5.3 Immunofluorescence and imaging

All incubations for this procedure were performed at room temperature.

Fixed cells on coverslips were treated with 50 mM NH_4Cl in PBS for 10 min and then permeabilised by incubating for a further 10 min with 0.1% (v/v) Triton X-100 (Sigma-Aldrich, USA) in PBS.

The cells were then treated with blocking solution (2% (v/v) FCS, 2% (v/v) BSA in PBS) for 30 min. Then primary antibodies were added in 50% blocking solution/PBS for 30-60 min. Coverslips were then washed 3-4 times in PBS for at least 5 min each, then incubated with secondary fluorescent antibodies and DAPI (1:5000) together in 50% blocking solution/PBS for 20-30 min. Finally cells were washed in PBS again (3-4 times, 5 min) and mounted on slides in a drop of

Fluorsave (Calbiochem, USA). The slides were then incubated overnight at 4℃ to allow mounting medium to set before imaging.

Primary antibodies used were:

- β-tubulin (1:100, Rabbit, AbCam Ab6046)
- α-acetylated tubulin (1:250, Mouse, AbCam Ab24610)
- γH2AX (1:100, Rabbit, Cell Signalling Technology #2577)

Secondary antibodies were conjugated with Alexa Fluor-555 (1:500, red, Invitrogen, USA) or Alexa Fluor-488 (1:500, green, Invitrogen, USA)

Imaging used the same DeltaVision System as used for *S. pombe*. Images were collected using a 60x/1.42 N.A. PlanApoN Oil immersion lens, using transmitted light plus FITC (ex 490/20 nm; em 528/38 nm), TRITC (ex 555/28 nm; em 617/73 nm) and DAPI (ex 360/40 nm; em 457/50).

Cells were typically imaged using the FITC filters (Tubulin/γH2AX imaging; 32%; 0.2 s), TRITC filters (Ac-Tubulin imaging; 32%; 0.2 s) and DAPI filters (Nuclei; 10%; 0.05 s). 8 plane z-stacks were collected with a separation of 0.4 μm covering the total nuclear volume of each cell.

2.3 Image analysis tools

2.3.1 Low-throughput/manual analysis

FIJI (Fiji is just ImageJ) (`fiji.sc/Fiji`) was used for all manual processing of images collected in low-throughput experiments.

Cell length was measured in maximum intensity projected stacks, as the length of a line from one cell tip to the other, running through the centre of the cell width. This line was typically straight, although occasionally segmented lines were used for cells with a high degree of curvature. Cell width was measured similarly across the cell centre. Cell boundaries were judged to be the dark outline that surrounds each cell in transmitted light images.

Microtubules were also measured using a segmented line of one pixel width along each fluorescent microtubule bundle, these measurements were later used to measure microtubule fluorescence intensity.

Total cell fluorescence intensity was measured by outlining the cells, using the dark outline in transmitted light images and then using the outline as a mask to measure average intensity in fluorescent channels.

2.3.2 High-throughput/computational analysis

All computational analysis software for image correction, segmentation, feature extraction and hit detection used in this work was custom developed by V. Graml and explained in her thesis (see Collaborations; Graml (2012)). These tools make use of MatLab (MathWorks) and R (R development core team) software environments. A general overview of the approach used is given in **Chapter 3**. Note that the application of these methods and some of the subsequent data processing were performed by A. Chessel.

2.4 Other computational tools

I have created additional data handling tools using MatLab and the Visual Basic for Applications (VBA) element of Microsoft Excel. Tools created during my previous studies (Lawson, 2011) include spreadsheets that automatically compare and combine cell density measurements for parallel serial dilutions of 96-well plates, used in preparation of all high-throughput imaging plates. They also include an Excel based histogram generation tool.

I have made use of MatLab in the analysis of genome positions, extracting positional information from PomBase and comparing it to hit list information. It has been used extensively in statistical testing of datasets. The tool for basic phosphorylation site analysis, used in the investigation of DDR kinase targets was created in MatLab, using regular expressions, and can easily be adapted to search for any consensus sequence. MatLab was also used in the preparation of this thesis to produce many of the graphics.

Hit clustering was performed by V. Graml. I performed the functional analysis of phenotypic gene clusters using the online functional annotation tool DAVID (`david.abcc.ncifcrf.gov`) to suggest groupings. The potential interest of these groups was then manually assessed by myself in discussion with other lab members.

3 High-throughput Screening

"...there's something you'd better understand about me 'cause it's important, and one day your life may depend on it: I am definitely a mad man with a box!"
—THE 11^{TH} DOCTOR (*The 11^{th} Hour*, 2010)

3.1 Overview of screening pipeline

Previous work performed by X. Studera and V. Graml established much of the general procedure that was implemented in this screen (Studera, 2012; Graml, 2012; Graml et al., 2014). Together they also performed the first iteration of this screening procedure, which established much of the methodology. This pipeline consists of four stages; two experimental and two computational, which are: Input, acquisition, processing & output (**Figure 3.1**). Initially the screen was devised to only explore cell shape and microtubule organisation. As I will show, cell cycle progression was added retrospectively based upon the results of the first screen, where evaluation showed that accurate prediction of the four cell cycle-linked microtubule patterns was possible and could also improve the clarity of the results in the analysis of microtubule phenotypes.

Notably, there is evidence to suggest that the phenotypes studied are highly temperature sensitive (Sawin and Nurse, 1998), so it is important to highlight that all screening work presented was performed at ambient temperature, a decision primarily made for technical reasons. This may mean that some more extreme phenotypes have been suppressed and that some expected phenotypes may not be present. It provides a test for the detection sensitivity of the computational image analysis methods used.

3.1.1 Screening input

Each strain in the KO library has one non-essential open reading frame (ORF) that has been replaced with a KanMX drug selection cassette. For this study, the KO

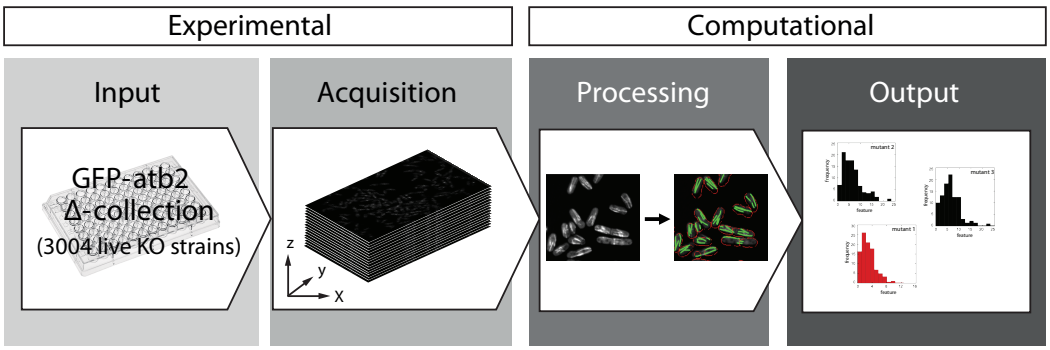

Figure 3.1: Established high-content microscopy workflow - Previously established four-step screening workflow consisting of high-throughput manipulation of yeast strains (Input), automated microscopy (Acquistion), computational image processing and feature extraction (Processing) and hit selection (Output)

library strains were crossed, in 96-well format, with another strain which produced a GFP-Atb2 construct from the endogenous gene locus (RCS001; *Patb2::gfp-atb2-NatR*). Atb2 is one of two α-tubulin proteins in *S. pombe* which contributes to microtubule construction. This construct was chosen, as its endogenous location within the genome, using the natural promoter, gave it more consistent expression across cells compared to plasmide expression vectors and exogenous expression sites that were considered by X. Studera. It also meant the total GFP signal could more accurately be used as a proxy for total protein level (Studera, 2012) and showed a higher cell viability than alternatives, particularly as the other tubulin genes (*nda2* & *nda3*) in *S. pombe* are essential (Adachi et al., 1986; Hayles et al., 2013; Kim et al., 2010). By labelling α-tubulin with GFP it was possible to visualise the microtubules in live cells, with fluorescence microscopy. In this way, a complete library of labelled microtubule strains was produced.

Genetic crossing of the library was performed once by X. Studera and M. Bortfeld-Miller, prior to the commencement of this project. The method used was taken from (Dixon et al., 2008) which uses 42℃ heat to eliminate remnant vegetative cells prior to spore germination. The complete, modified library was stored at -80℃ and used to provide source material for all subsequent screens.

A small scale version of this procedure (six 96-well plates) was performed by myself and X. Studera in 2012, upon the acquisition of an upgraded KO library (v2v3 upgrade), see **Section 2.1.6.1**.

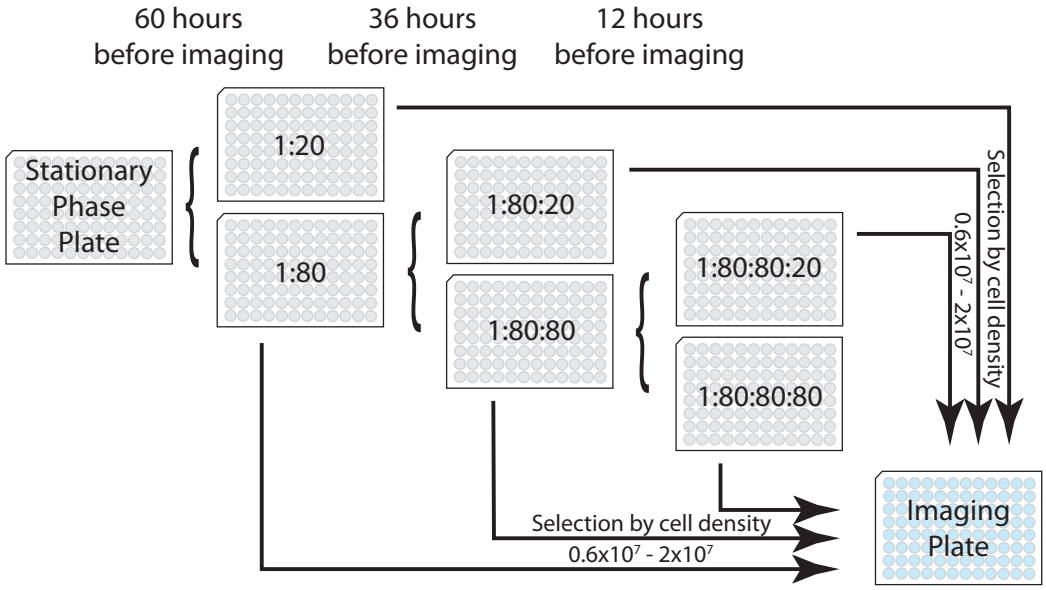

Figure 3.2: Serial dilution preparation for high-throughput imaging - An initial 96-well plate, in which all strains were at high-density in stationary phase, was diluted to give two new plates of differing cell densities ≈60 hours before imaging. One of these was then diluted again after 24 hours. A third dilution round followed after another 24 hours. The figure depicts the most typical dilution series, with 1:20 and 1:80 dilutions, producing six plates. The exact dilutions used varied between plates, in response to the observed cell density readings recorded at each dilution (see **Section 2.1.6.3**). Before imaging, the most optimal replicate of each strain was selected, based upon optical density measurements, for transfer into the imaging plate.

3.1.2 Screening acquisition

Strains were subjected to selection after being thawed for imaging. After this, they were grown to high density (detailed in **Section 2.1.6.2**) until all strains entered the stationary growth phase. A novel method, described briefly below and further in Section **2.1.6.3**, was then applied to ensure all strains were in physiologically comparable mid-logarithmic growth states during imaging.

The challenge at this stage was that the different gene-deletions possessed by each mutant strain had subtle and varied effects on the growth proficiencies of the cells. This is similar to the effect previously demonstrated in heterozygous diploid cells (Kim et al., 2010). As a result, some strains grew faster or slower

than others, and showed asynchronous exit from and entry into stationary phase. Since we were interested in studying cells during active growth and division, in mid-logarithmic phase, a way was needed to ensure all strains would be in comparable physiological conditions during filming. Also, since the cell shape and microtubule organisation is different in exponentially growing cells and stationary phase cells, it was important to keep the cells growing constantly for at least 48 hours prior to filming. In addition, the method needed to be compatible with high-throughput manipulations.

The method selected, involved diluting an initial high cell density plate multiple times by different dilution factors in the 60 hours prior to imaging. From this collection of (at least six) plates, all with different cell densities, it was possible to identify a replicate of each mutant strain that was in the correct growth phase for filming, see **Section 2.1.6.3** and **Figure 3.2**. To make this selection faster, easier and more high-throughput compatible, during my early work I produced a spreadsheet containing VBA code capable of comparing cell densities across multiple plates and selecting the best growth phase (Lawson, 2011).

All high-throughput imaging was performed using an OperaLX microscope, with cells imaged in fluorescent medium to provide contrast for easy computational segmentation of cell outlines. In total each imaged location included a 2-channel stack of 32 individual greyscale images (**Figure 3.3**). For each mutant, six separate cell fields were imaged, giving 192 images per strain or over 500 000 images of deletion mutants per screen. Each plate was imaged for approximately 4½ hours.

The high resolution collection of images in three dimensions allowed cells to be computationally reconstructed and analysed, giving a more accurate and detailed measure of individual cell states.

3.1.3 Screen image analysis

At this stage the process becomes much more computational, and was handed over to our image analysts. All of the processes used were designed and implemented by V. Graml and are detailed in her thesis (Graml, 2012). During later stages, these same processes were applied to new datasets by A. Chessel.

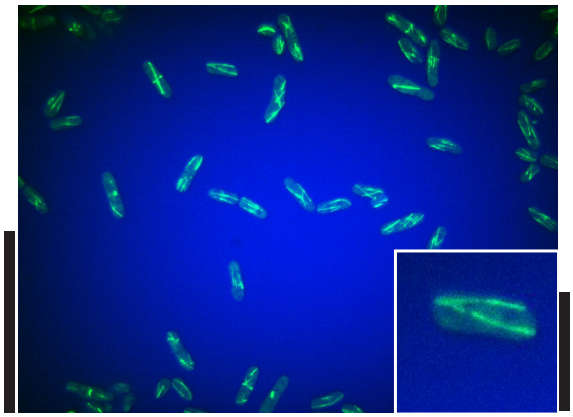

Figure 3.3: Example screen image - Maximum projection of a control 16-plane z-stack of GFP-Atb2 labelled wild-type cells. Inset shows enlarged image of one cell. Microtubules appear in green, due to GFP, cell outline contrast is provided by fluorescent Cascade Blue dextran in the growth medium. Left scale bar represents 50 μm on main image. Right scale bar represents 10 μm on inset.

Technical limitations of the way in which images were collected, meant that the first stage of analysis involved pre-processing of images to remove noise and other aberrations. The major issue results from inhomogeneous illumination of the cell fields by the microscope. To address this, a background subtraction algorithm was created to flatten the background signal across all images by using a reference empty image to visualise the inconsistency.

3.1.3.1 Defining cell outlines

From here, it was possible to define cell outlines (cell segmentation) in two-dimensional projections of the three-dimensional image stacks. This involved projecting the central part of the stacks, from the 405 nm channel (blue; cell outlines). Only part of each stack was used as this showed the maximal extent of all in-focus cells (i.e. those cells lying flat on the glass surface) and increased contrast between the dark cell cytoplasm and bright fluorescent medium.

An adaptive thresholding approach was used to distinguish cells from the background, as it allowed for more reliable segmentation of the full variety of cells. The results were cleaned using hole filling and watershed algorithms (Meyer, 1994; Sethian, 1999) to define solid objects and separate multiple objects that are close

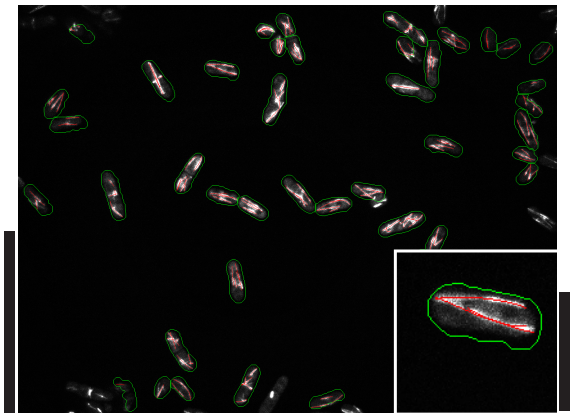

Figure 3.4: Example processed image - Overlay of computationally detected cell outlines (red) and microtubules (green) onto original microtubule image (grey). One cell shown enlarged in inset. Note, microtubules were detected and reconstructed in three-dimensions and have subsequently been projected to give a two-dimensional image. Detection procedures are explained fully by V. Graml (Graml, 2012). This image shows all detected objects, not just the ones judged to accurately represent cells. Left scale bar represents 50 μm on main image. Right scale bar represents 10 μm on inset.

together. A final round of cleaning tried to separate any remaining unusually large objects, severely misshapen objects and objects in contact with the edges of the image.

From the detected objects (**Figure 3.4**), 81 numerical features were measured. These features varied from intuitive geometrical properties, such as cell length & width, to more abstract feature sets, including Zernike moments (Khotanzad and Hong, 1990) and Haralick features (Haralick, 1979). They were used as the basis for the subsequent validation of objects as cells and later as the criteria for hit identification and grouping.

Features were first used to define true, in-focus cells that were correctly segmented. A supervised machine learning approach, specifically a Random Forest classifier, was used for this. Large numbers of segmented images were manually assessed, by myself and others, to determine which objects were true cells. The features extracted from this 'training set' were then used to educate the classifier, which was then able to automatically identify cells throughout the rest of the screens. Many different, extreme shape mutants were included in the training set, to avoid biasing the classifier towards cells with wild-type morphology.

3.1.3.2 Detecting microtubules within cells

Microtubules could only be processed once the cell outlines had been determined. The unique challenge of this project was the detection of individual microtubule structures, in three dimensions, within the volume of each cell. To do this, well-established two-dimensional line detection methods were applied to parts of the whole z-stack images. These two-dimensional fragments were then joined and smoothed, in three dimensions, to reconstruct the complete microtubule arrays (**Figure 3.4**). Line detection algorithms were only applied within the cell outlines. Out of several methods trialled, this was found to be the most accurate at segmenting microtubules (89% well detected) with minimal creation of additional structures (<1%).

Numerical feature measurements for microtubules were then collected, again featuring an assortment of 39 intuitive and abstract features.

As explored later, in **Section 3.2.1**, we found that it was easiest to identify mutants that affected interphase microtubule pattern by sub-selecting for cells in interphase before analysing microtubule features and selecting hits.

3.1.4 Screening output

Detecting mutants with aberrant cell shape or microtubule patterns used two parallel feature comparison methods, with slightly different applications. Fundamentally these are a statistical 'p-value based method,' considering each feature independently and a 'multi-parametric profile method,' (Collinet et al., 2010) which considers all cell shape or microtubule features simultaneously, and is thus more able to detect complex but subtle phenotypes. The establishment of hit detection methods has been explained in full in Graml (2012).

Since hit detection relies on statistical tests, we also defined a minimum required population size for each mutant, which was required in order for it to be analysed in each screen. For cell shape, there needed to be at least 30 well-segmented cells, for microtubules we required 30 cells with interphase microtubule arrays. These number requirements were developed on the basis of initial test screening that showed a minimum of 30 cells was required for reliable distinction of wild-type cells from positive controls. For cell cycle, due to the division of the cells

analysed into sub-populations by microtubule state, we required 50 cells with detectable microtubule arrays.

3.1.4.1 p-value based hits

The distribution of feature measurements for every cell shape or microtubule feature, across every mutant screened, was compared to the distribution of the same feature measured in a large number of wild-type control cells using the Kolmogorov-Smirnov (KS) non-parametric statistical test. Each test generated a p-value of similarity between a mutant and the wild-type for each feature. Values were quality controlled using a random sampling method (bootstrapping) and the smallest p-value from each mutant was used for hit detection. All of these were ranked and the mutants with the smallest p-values were called as hits for cell shape or microtubule patterns.

It proved challenging to determine a cut-off point for this ranked list of p-values, and so a series of lists with different thresholds were generated. By comparing these with a list of visually detectable hits, produced by X. Studera, cut-offs of 5% and 10% were defined for cell shape and microtubules respectively. This produced computational lists that had a high degree of overlap with the visual lists but minimised the number of computational-only hits.

The visual screening of images from the first screen, after validation and cleaning, produced 79 shape hits and 74 microtubule hits (overlap 49, (Studera, 2012)). Some of these visual hits were also detected based upon very few cells, which is visually but not computationally feasible. To give an accurate comparison with the pre-validation data used in the computational analysis, a raw visual hit list, based solely on the imaging data (without subsequent biological validation), but subject to the same population size requirements as the computational analysis (i.e. ignoring visual hits with small populations), was used.

Thus a visual list of 129 hits (87 shape, 87 microtubule, overlap 49) was used to determine thresholds for computational hit detection by maximising overlap whilst minimising additional computational hit discovery.

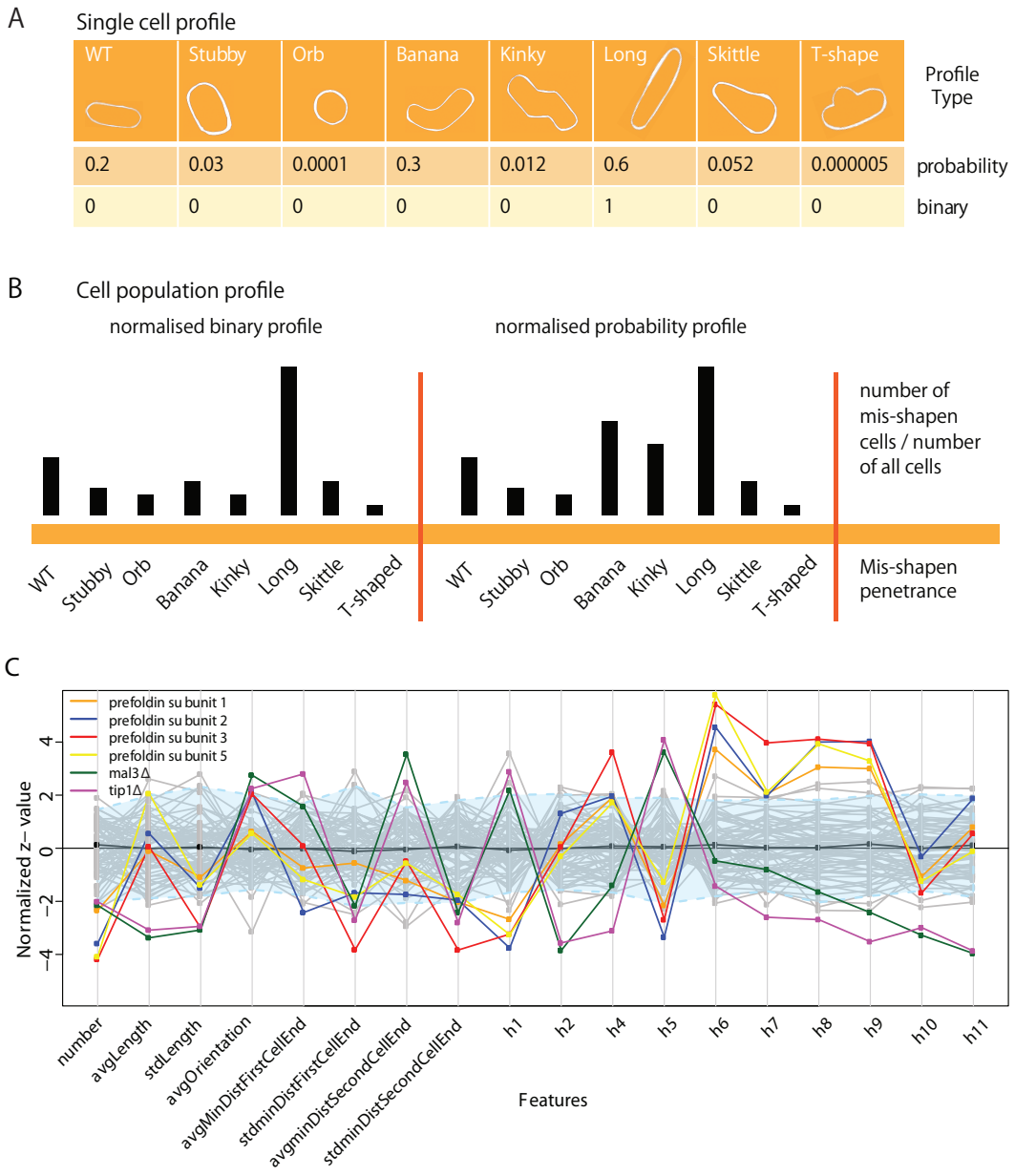

Figure 3.5: Feature profiles used in hit detection - Cell shape feature profiles were constructed by using SVM classifiers to assign a probability that each individual cell belongs to each of eight stereotyped cell shape classes. The results of this were also binarised, assigning each cell uniquely to just one shape class, based upon the highest probability (binary profile). An example cell shape feature profile is shown in **(A)**. The results from individual cells could then be combined to represent a population of cells **(B)**. Microtubule feature profiles **(C)** used extracted features directly, hits (coloured lines) regularly deviate outside of the 95% confidence interval (green region) defined from wild-type cells (grey lines). Figure adapted from Graml et al. (2014), cell shape artwork credit to C. Stocker

3.1.4.2 Multi-parametric profile hits

For cell shape, support vector machine (SVM) classifiers were trained to independently assign each cell a probability of belonging to one of eight well-defined shape classes (wild-type, stubby, orb, banana, kinky, long, skittle or t-shape; see **Figure 3.5A**) on the basis of the raw quantiative parameters. This created an easily interpreted, probabilistic profile of the likelihood that each cell belonged to each of the eight shape classes.

Cells from the same mutant populations could then be combined in two ways to give population-wide data. In the first instance, raw probabilistic values could be averaged across all cells. In the second approach, the values for each cell were binarised; each cell was assigned uniquely to the shape class that had the highest probability. This meant that each cell had a value of 1 for the most probable shape and 0 for all others. The binarised values were then combined across each mutant population (Graml, 2012). For each mutant population, this gave 16 values, eight from each method.

In addition to the 16 values above, an assessment of the penetrance of mutant shape phenotypes in each population, was included. This phenotypic fingerprint (phenoprint) of 17 values for each mutant could then be compared with the wild-type phenoprint to detect hits independent from KS-test p-values (**Figure 3.5B**).

Multi-dimensional feature profiles were also created for microtubule phenotypes, using a different approach. In place of 17 SVM-derived shape values, each microtubule profile value was one of the features directly extracted from screening images. Only features that are intuitively interpretable and the Haralick features were included. Microtubule intensity measures were found to vary too extensively between screen repeats, so could not be effectively compared in the absence of a fixed standard for normalisation.

In both cases, a multi-dimensional vector, which can also be represented as a two-dimensional profile, was produced describing each mutant relative to wild-type (**Figure 3.5C**). Measurement of the Euclidean distance between the mutant and wild-type then provided an assessment of the divergence of each mutant. Hits were called by using different wild-type populations in comparison to the mean of all wild-type cells to define a 95% statistical confidence interval. Euclidean distances greater than this were considered as hits.

3.1.5 Pipeline testing

This screening pipeline was tested with a pair of proof-of-principle test plates (**Figure 3.6A**) that I designed and imaged. I arranged different strains within these plates to explore any plate location effects that may need to be considered during screening. The initial plate consisted of wild-type GFP-Atb2 cells, in addition to three positive control KO mutants:

- *tip1*Δ a CLIP170 homologue, mutant cells have very short microtubule bundles (Brunner and Nurse, 2000; Busch and Brunner, 2004)
- *mto1*Δ a centrosomin related microtubule nucleation mutant, each cell has a single long microtubule bundle (Lynch et al., 2014; Samejima et al., 2010; Sawin et al., 2004; Venkatram et al., 2004)
- *ase1*Δ a microtubule bundling factor and PRC1 homologue, cells have many, individual, disarrayed microtubules and generally longer cells (Bratman and Chang, 2007)

In our second test plate, a different layout of strains was used. In addition to the strains from the first plate, a negative control strain (pkl1Δ; a kinesin-like protein with no reported phenotypic effect; Pidoux et al. (1996)) was included.

When V. Graml performed comparisons between different populations of the same mutant strains in these wells, she was able to demonstrate 100% accuracy in detection of positive controls by comparison to wild-type cells. An assessment of heterogeneity between distinct populations of the same mutant strain ranged between 75% and 100% (**Figure 3.6B**).

3.2 Cell cycle progression

Initial computational investigation of mutants based upon microtubule features showed a high degree of noise, due to the intrinsic change of microtubule patterns known to exist throughout the cell cycle (Hagan, 1998). We decided that by sub-selecting for cells with interphase microtubule arrays only, before looking to identify hits, we could more meaningfully identify mutants with roles in interphase. This required the development of a method to assign cell cycle stages

A

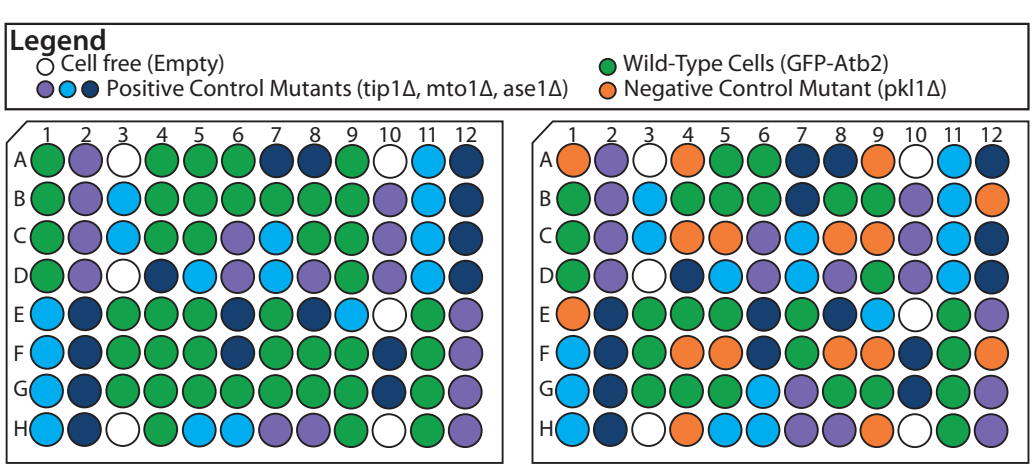

B

Mutant	Correct Detection Rate (Plate 1)	Similarity Between Like Populations (Plate 1)	Correct Detection Rate (Plate 1)	Similarity Between Like Populations (Plate 1)
Wild-type	93%	86%	85%	92%
tip1Δ	100%	100%	100%	75%
mto1Δ	100%	80%	100%	100%
ase1Δ	100%	100%	100%	88%

Figure 3.6: Proof-of-principle plate layouts - **(A)** Arrangement of strains within test plates designed to calibrate and establish the accuracy and reproducibility of the screening method and investigate potential plate effects. Each plate contained 16 populations for each GFP-Atb2-labelled deletion mutant and 6 empty wells with the remaining space occupied by GFP-Atb2 wild-type populations. **(B)** Evaluation of correct mutant vs. wild-type phenotype assignments for the two plates and assessment of phenotypic homogeneity between different populations of the same genotype.

based upon microtubule patterns, using an automated method that could effectively distinguish the different microtubule arrays observed throughout the cell cycle, reliably across different mutants.

3.2.1 Assigning cell cycle states

The assignment of the four microtubule-determined cell cycle phases used the microtubule features collected above. These were used with a manually annotated training set of cells to program an SVM classifier to recognise whether the microtubule array in each cell appeared to represent ‘Interphase’, ‘Spindle’, ‘PAA’ or ‘Interphase2’ (**Figure 3.7**).

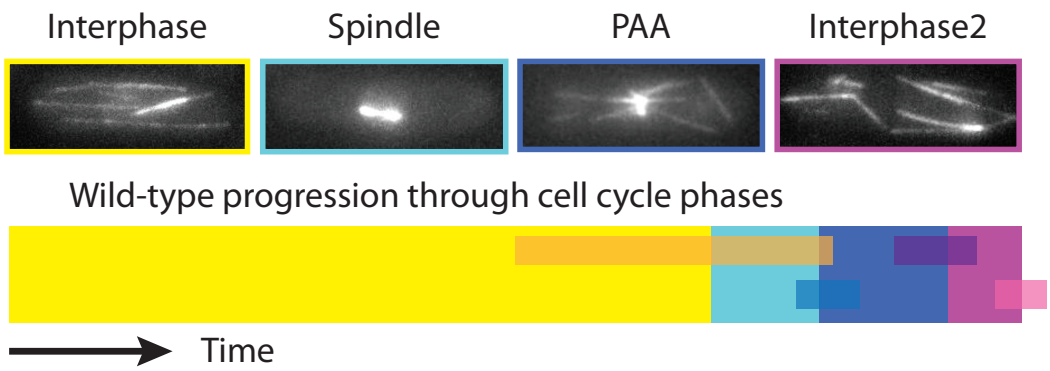

Figure 3.7: Cell cycle progression stages - The four microtubule patterns linked to cell cycle progression: Interphase (IP; yellow), Spindle (SP; cyan), Post-anaphase array (PAA; blue), Pre-septation interphase/Interphase2 (IP2; purple). The proportion of an average wild-type population at room temperature that occupies each stage, equivalent to the duration of each stage is shown by the coloured bars. The narrower overlaid transparent bars represent the wild-type 95% confidence interval for each stage.

This allowed us to focus our investigation of microtubule hits based only on the interphase array, but it also provided extra data about the proportion of different cell cycle states within each mutant population. Ergodic analysis could then be used to assume that the proportion of cells in a static population in a specific state is representative of the proportion of time that each cell in that population spends in that state. Hence we could infer changes in progression through the cell cycle by changes in the proportion of a population occupying each state.

3.2.2 Validation of cell cycle assignment

Previously, cell cycle assignment within *S. pombe* has used features such as cell length and cyclin protein accumulation. Microtubule organisation, although well-characterised, has not typically been used (Hagan, 1998).

To demonstrate that microtubules can be used as *bona fide* reporters of the cell cycle state in high-throughput and that the progression through microtubule states is consistently linked to cell cycle progression, I performed low throughput analysis of cells carrying a *cdc13-gfp* expressing construct, alongside red fluorescent mCherry labelled microtubules (mCh-Atb2). Cdc13 is one of the M phase-

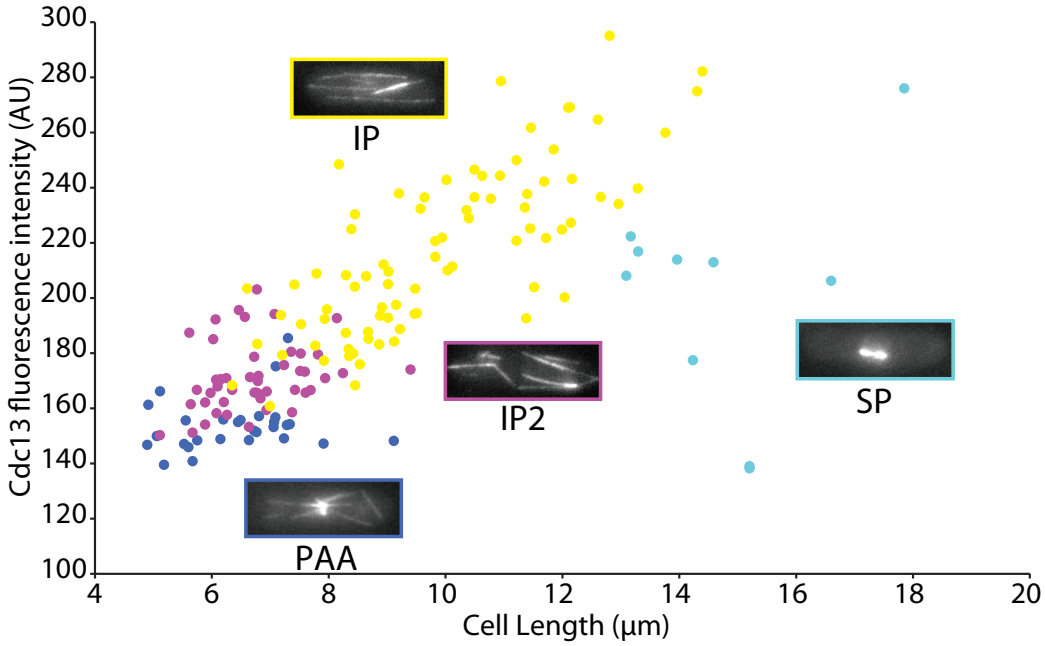

Figure 3.8: Validating the link between microtubule pattern and the cell cycle - Comparison of cell length and Cdc13-GFP intensity measurements – as classical markers of cell cycle progression – to annotations of microtubule patterns. Thus demonstrating a strong, regular and rapid progression: from PAA, through to IP2 cells in the early cell cycle, followed by an extended period with IP microtubule organisation, before adopting SP patterns concomitantly with nuclear division.

regulating B cyclins in *S. pombe*, which accumulates throughout the cell cycle and rapidly degrades at the time of division (Alfa et al., 1989; Booher and Beach, 1987).

I showed that cells assigned a PAA microtubule array, have the lowest levels of cdc13 and are generally shortest. From this we infer that PAA cells likely link to early G1 phase, as expected. Cdc13 levels and cell length increase through IP2 cells (late G1/S phase) and into cells with interphase microtubule arrays (S/G2 phase). Cdc13 then drops rapidly during mitosis, where the cells demonstrate a spindle microtubule array (M phase). See **Figure 3.8**.

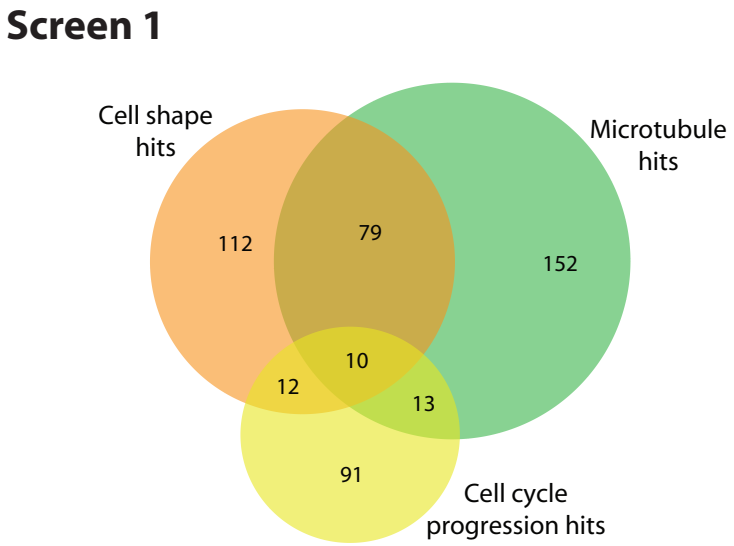

Figure 3.9: Hits from first screen - Venn diagram representing the 469 mutants proposed as hits by the first complete genome-wide screen, performed by X. Studera.

3.2.3 Cell cycle progression hits

Detection of cell cycle progression mutants used a different method to cell shape and microtubules. Here, hits were called by examining the proportion of each mutant population allocated to each cell cycle state. Again, by using bootstrap sampling of wild-type cells, it was possible to generate a 95% statistical confidence interval for the proportion of the population in each cell cycle state (**Figure 3.7**). If a mutant was outside these intervals for two or more of the four states, it was determined to be a cell cycle progression mutant.

3.2.4 Further screening overview

From the first screen the final hit list contained 213 shape, 254 microtubule and 126 cell cycle progression hits representing a total of 469 mutants (**Figure 3.9**).

To enrich and validate the findings of this first screen I went on to perform several further screens, detailed throughout the rest of this chapter. First, a second complete screen of 3004 mutants plus a large number of control populations was undertaken (**Section 3.3**). On the basis of the results from these two screens, a subset of 763 possible hits was rescreened a further eight times (**Section**

	Screen 1	Screen2	Rescreens	Rerescreens	TOTAL
Plates	33	66	9	1	179
Repeats	1	1	8	8	
Mutants	3004	3004	763	92	
Wild-type	33	2046	144	8	2231
Positive controls	33	1056	216	16	1321
Timepoints	1	2	1	1	
Cell fields	19 008	38 016	41 472	4608	103 104
Greyscale 2D images	608 256	2 433 024	1 327 104	147 456	4 515 840
Imaging time (hours)	149	561	324	36	1070
Data generated (Tb)	1.58	6.33	3.45	0.38	11.74

Table 3.1: Screening numbers - Comparison of the two genome-wide screening repeats, and subsequent sub-screens, indicating scale of data produced and effect of alterations made through subsequent screening rounds. Numbers reflect screening of Bioneer library Version 2 as reported in Graml et al. (2014).

3.4.1). After all of this, there was still insufficient data for meaningful analysis of 92 strains, so these were re-rescreened a further eight times (**Section 3.4.3**). Full information on all of these screens is provided in **Table 3.1**.

3.3 Second genome-wide screen

High-throughput approaches, particularly image-based screens, are known to have quite poor reproducibility between independent repeats (Barr and Bakal, 2012). Having successfully completed a genome-wide screen of our GFP-Atb2 labelled library, it was decided that further screening was required to validate the initial findings.

3.3.1 Improving library coverage

Due to the requirement for a minimum population size for computational analysis of mutant strains, 554 of the 3004 mutant strains imaged could not be processed

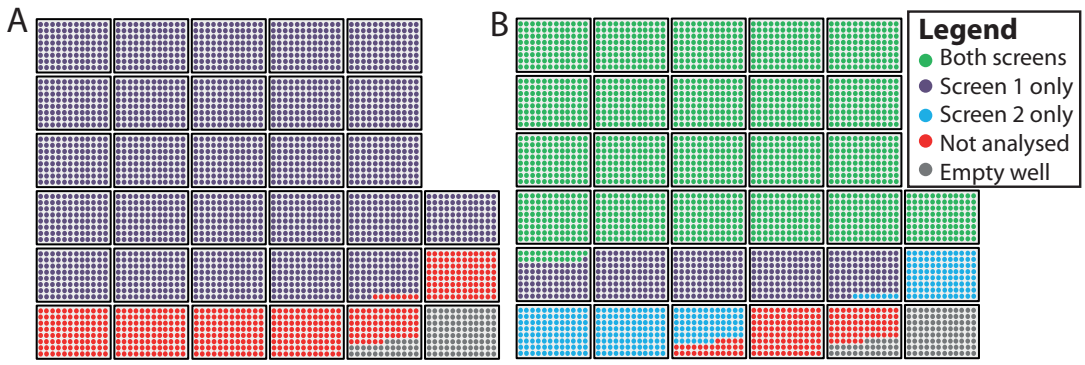

Figure 3.10: Library screening coverage - Each well from the 33 plates of the version 2 Bioneer gene-deletion library is represented as a coloured point, based upon the results from our first genome-wide screen **(A)** or both genome-wide screens together **(B)**. 554 (17%) mutant strains were missed in the initial screen, reduced to just 191 (6%) missed after both screens.

following the first screen (**Figure 3.10A**), giving a high chance that some interesting hits may have been missed. Whilst some strains are likely have been lost due to defects during mating of the KO library with the GFP-Atb2 stain, we reasoned that it should still be possible to improve library coverage through a second biologically independent screening repeat.

3.3.2 Additional control strain data

An additional problem came from the lack of internal controls within the first screen. The arrangement of strains within 96-well plates in the KO library leaves only four wells per plate empty (**Figure 3.11A**). One of these wells must remain empty as part of our background correction procedure, leaving just three for internal controls. These three were dark (non-GFP) cells, wild-type (GFP-Atb2 expressing; MS1404) cells and a positive control (*mal3*Δ*, gfp-atb2*). Mal3 is a homologue of the +TIP microtubule end binding protein, EB1, with well-established microtubule-stabilising effects. Deletion of *mal3* results in very short microtubule bundles (des Georges et al., 2008; Katsuki et al., 2009; Beinhauer et al., 1997; Sandblad et al., 2006).

Three wells per plate was considered insufficient for reliable data collection, from a screen of this type. It was not always possible to collect enough data from one

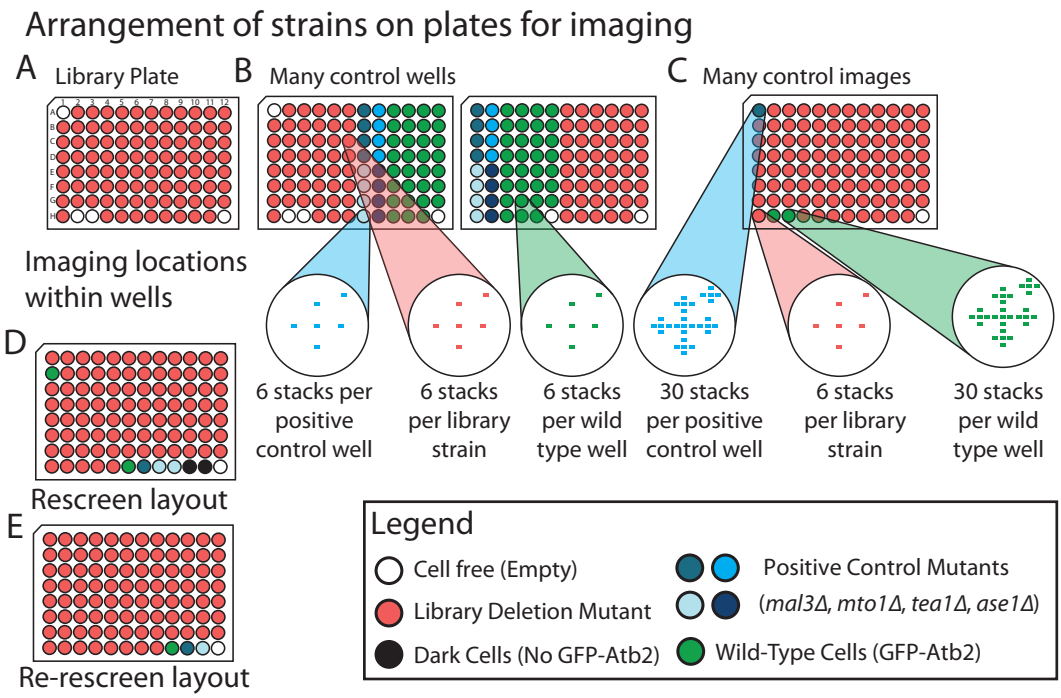

Figure 3.11: Inclusion of controls in screening - 96-well plate in the deletion library only include four empty wells **(A)** limiting the number of control populations that can be added during screening. To allow better comparison with wild-type and known positive controls, two methods were considered to introduce additional control populations for the second genome-wide screen. In the first, each library plate was split across two imaging plates **(B)**, with the remaining half of each plate given over to control strains. Ultimately this was the method used. An alternative method considered using the same number of control populations as the first screen but with more images collected from those control populations than from the experimental wells **(C)**. **(D)** shows the arrangement of control strains for rescreening and **(E)** shows control wells for re-rescreening. The empty/cotrol well shown at position A1 (top left) in these plates is used as an example, the location of this empty position changes for each plate within the library.

well for statistical analysis and it was not possible to assess the degree of plate-to-plate variation on the basis of so few control populations. In addition, having a large number of independent controls in each plate would allow us to better assess variation in microtubule fluorescence intensity between mutants. This was necessary because, as mentioned in **Section 3.1.4.2**, microtubule intensity features showed a high degree of plate-to-plate variation.

I tested two methods to increase the number of controls included in the second

screen. I investigated increasing the number of control wells by splitting each 96-well plate of strains, from the library, across multiple imaging plates (**Figure 3.11B**). In an alternative approach, the number of control wells remained unchanged but more fields of cells were imaged within those wells, relative to the experimental wells (**Figure 3.11C**). This approach was not possible in the first screen due to technical limitations of the microscope, which were removed due to a subsequent software upgrade of the OperaLX.

Comparison of these methods found, as expected, that increasing the number of control fields without changing the number of control wells only addressed the issue of insufficient cell population, which was found to be a relatively minor improvement. This approach could not address wells where control populations did not grow well and also did not increase the number of independent control populations, so could not be used to explore microtubule intensity variation.

As such, the decision was taken to use the first approach, requiring additional investment of time and resources to complete the screen. Hence, the second screen consisted of 66 experimental plates for the KO library. Each KO library plate was split across two imaging plates, with remaining wells containing over 30 wild-type populations and 16 positive control populations. The additional benefit of having so many positive control populations was that it was possible for every plate to include several different control strains. Positive controls were evenly divided between four mutants:

- *mal3*Δ also present in the first screen (microtubule stabiliser)
- *mto1*Δ included in proof-of-principle plates (microtubule nucleator)
- *ase1*Δ included in proof-of-principle plates (microtubule bundler)
- *tea1*Δ a polarity factor. Deletion cells may have slightly elongated microtubules and cells can appear curved (banana) or branched (t-shaped). This mutant was included because it has a well-characterised but subtle phenotype, with low penetrance in the population (Behrens and Nurse, 2002; Feierbach et al., 2004; Glynn et al., 2001; Mata and Nurse, 1997).

3.3.3 Examining microtubule dynamics

The upgraded capacities of the OperaLX microscope also allowed us to attempt investigation of microtubule dynamics by inclusion of timelapse in the screening procedure. It is known that some microtubule regulators, when deleted, do not give rise to detectable phenotypes in static images, but have a pronounced effect on microtubule organisation when visualised over time (Carazo-Salas and Nurse, 2007; Tischer et al., 2009). Several possible approaches were considered to implement timelapse imaging, as it is not a default capability of this system.

In particular, we needed to reconcile the long timeframes needed for each screening experiment with the very short time intervals needed to collect meaningful data on microtubule dynamics. We hoped that, if a large number of microtubules could be imaged at just two timepoints separated by only a short time window, this would be sufficient to infer rates of microtubule polymerisation and depolymerisation.

Of the different methods considered, almost all gave a time difference that was either difficult to consistently control or was far too long to give any useful data relating to microtubule dynamics. The eventual solution consisted of creating experiments that imaged two different locations within each well sequentially and then manually altering the coding of these experiment files so that both locations were in fact the same location. As such, a complete z-stack was collected for each field of cells and then another was collected directly afterwards. This approach gave the highest possible time resolution of 20 seconds, comparable to the 16 second gaps used in previous low-throughput studies (Tischer et al., 2008). This approach additionally made it easy to correctly align images from the two time points as the objective lens did not move laterally between timepoints, so retained the correct position more accurately.

Although, these data have been collected for the entire KO library, as part of the second genome-wide screen, it has not yet been possible to develop a computational approach to analyse the time resolved information. As such there are no further results to report on the high-throughput investigation of microtubule dynamics.

3.3.4 Outcomes from two genome-wide screens

The second complete genome-wide screen consisted of 66 experimental plates including 3004 KO mutants, 2046 wild-type populations and 264 independent populations for each positive control. In total this included 36 636 fields of cells, each imaged in two channels, 16 focal planes and two time points. Thus a total of 2 344 704 individual greyscale images were collected. This equates to around 561 hours of imaging time and 6.33 Tb of image data across the entire screen (**Table 3.1**).

Following analysis of the screening data 418 hits (200 shape, 213 microtubule and 84 cell cycle progression; **Figure 3.12A**) were identified. As predicted, total overlap between the two screens was found to be quite poor, including just 124 (16%) hits, encompassing 60 (17%) shape, 37 (9%) microtubule and 11 (6%) cell cycle progression hits (**Figure 3.12B**). The second screen also greatly improved coverage of the KO library, although a total of 640 strains were not computationally assessed in the second screen, only 191 strains were missed by both screens when considered together (**Figure 3.10B**).

3.4 Additional screening repeats

In total 763 hits were identified across all three processes, between the two complete screens of the KO library. Whilst the poor overlap between screens was anticipated it was still disappointing and meant that many of the hits proposed were still suggested on the basis of just one dataset.

It was considered an infeasible use of resources to continue to pursue complete screens of the KO library until a stable and complete set of proposed hits could be defined, thus an alternative screen-based solution was devised to create a list of high-confidence hits.

3.4.1 Eight rounds of rescreening

All 763 proposed hits (**Figure 3.12C**) were rearrayed into a new set of nine plates for additional screening rounds. These plates were each imaged an additional

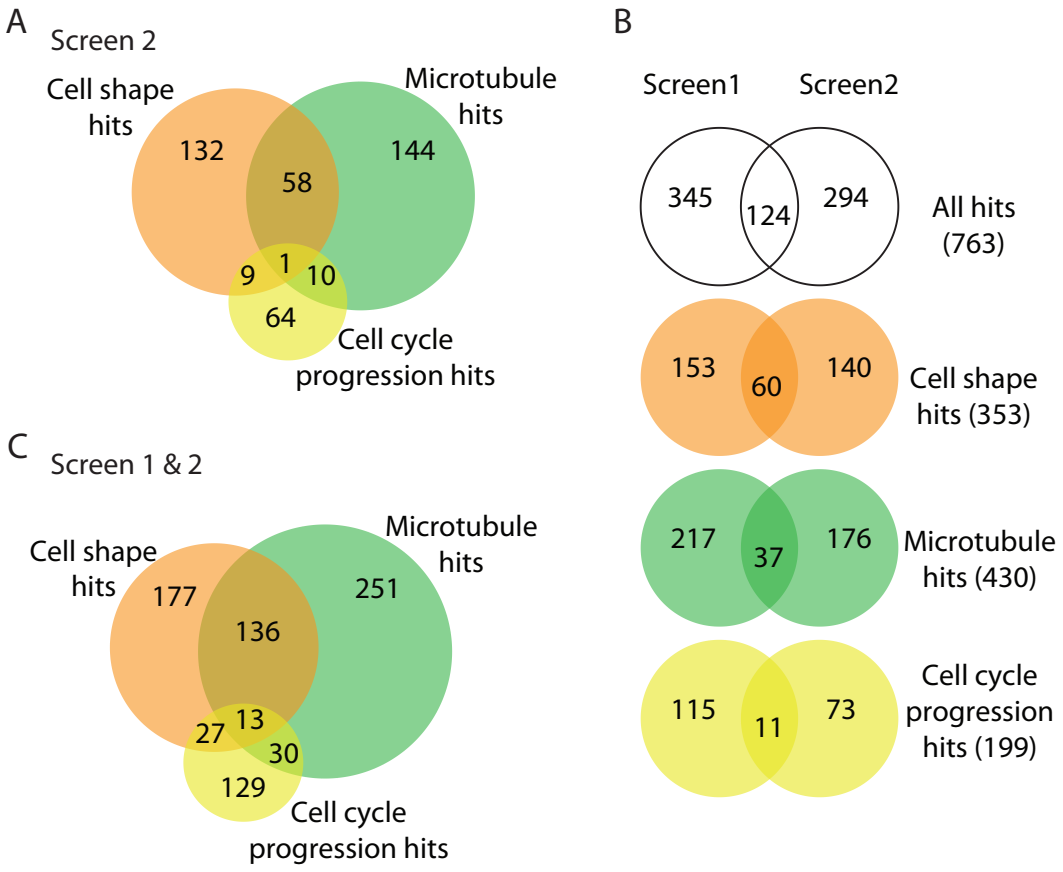

Figure 3.12: Initial screening results - **(A)** Venn diagram representing the 418 mutants proposed as hits by the second complete genome-wide screen. **(B)** Comparison between screens for all hits and each cell process separately. **(C)** Composite Venn diagram showing all 763 hits proposed by one or both of the genome-wide screens and included in subsequent screening rounds.

eight times, providing a total maximum of 10 independent datasets for each candidate hit. Rescreening plates contained 88 mutants per plate, allowing additional space for control strains (**Figure 3.11D**). Extensive inclusion of controls was not needed at this stage, as the previous screen demonstrated a high degree of consistency across plates for most features, other than microtubule intensity.

To generate the rescreen plates, library plates were thawed, grown and plated on selection medium as performed previously. Required strains were individually selected from these solid medium plates and resuspended in 96-well plates of liquid medium. Each plate was then grown to high density and replated onto solid

selection medium. This provided source material for each round of reimaging. Shallow-well, liquid medium copies of these plates were also prepared for long term cold storage.

It was possible to use the same selection plates for all rescreening repeats because they all occurred within a short space of time, so it was not necessary to continually freeze and thaw the strains.

Over 1.25 million new greyscale images of cells were collected during refilming (**Table 3.1**; Rescreens).

3.4.2 Methods for selecting high-confidence hits

Each independent screening repeat produced a separate subset of suggested hits, with very few (<3%) consistently detected across all ten screens. We devised a series of rules to determine which hits we could select with a high degree of confidence.

First, we required that, for a candidate to be a high-confidence hit, it must have been computationally analysed in at least three of the ten imaging rounds (≈88% of candidates). Assuming this to be true, we also required that, out of all of the screening repeats where data had been analysed for a specific mutant, that mutant must have been determined to be a hit in at least 35% of cases.

The need for rescreening and the definition of a 35% threshold for high-confidence hit detection was based upon the large amount of control data collected during the second screen (**Figure 3.13**). The three control mutants with distinctive phenotypes (*mal3*Δ, *mto1*Δ and *ase1*Δ) were correctly identified as mutants in >85% of the populations imaged. By contrast, across all control populations, *tea1*Δ was only identified as mutant in ≈35% of populations, due to its low penetrance, subtle phenotype. This meant that hits like *tea1*Δ, only had a 12% (0.35^2) chance of being correctly identified as a hit in both genome-wide screens. This demonstrates the probabilistic nature of hit detection, which made it necessary to pursue many rounds of screening and set a threshold for high-confidence hit detection.

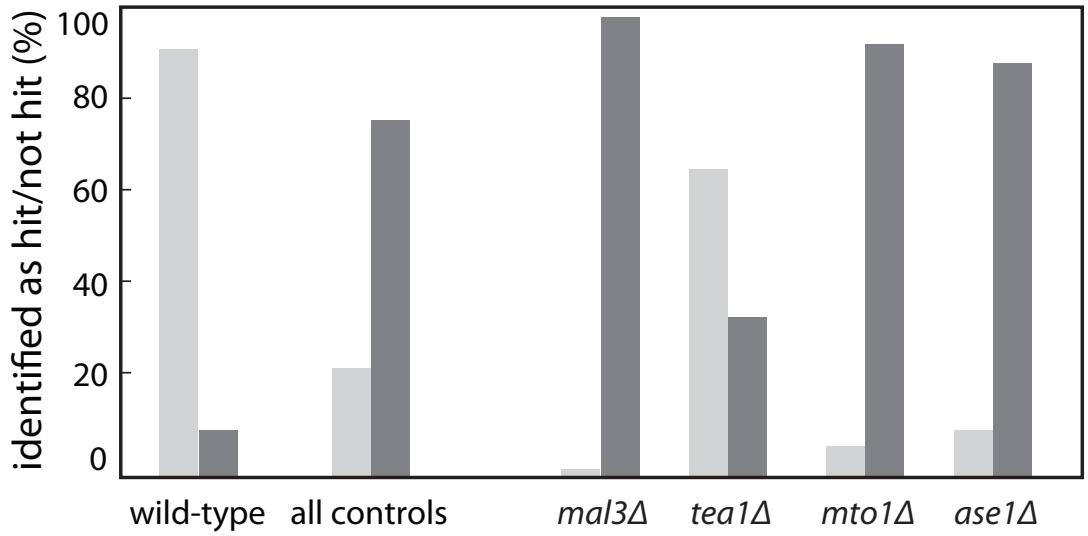

Figure 3.13: Detection rates of control populations - Percentage of control populations from the second genome-wide screen identified as having wild-type (light grey) or mutant (dark grey) phenotypes. The 'all controls' section represents pooled data from all populations of the four positive control mutant strains.

3.4.3 Enriching poor datasets through re-rescreening

Whilst defining high-confidence hits, we found that 92 of our 763 candidates did not fulfil the first requirement. This was likely due to issues with growth of individual strains during the process of thawing or replating prior to rescreening. Hence, to reduce the issue of missed strains, these 92 were rearranged into one further 96-well plate (**Table 3.1**; Rerescreens). Where possible, strains were collected from the solid selection plates, used during rescreening, or were individually thawed from cold storage. These strains were collected into one shallow 96-well liquid culture plate, grown to high density and then plated onto new solid selection plates. These plates were then processed as in the main screen. The remaining four wells in each plate included a small number of control populations (**Figure 3.11E**).

A further eight screenings of this remaining plate helped to improve the coverage of the candidate hits, although some (≈50%) remained intractable, which may suggest poor mating capacity or recovery from cold storage.

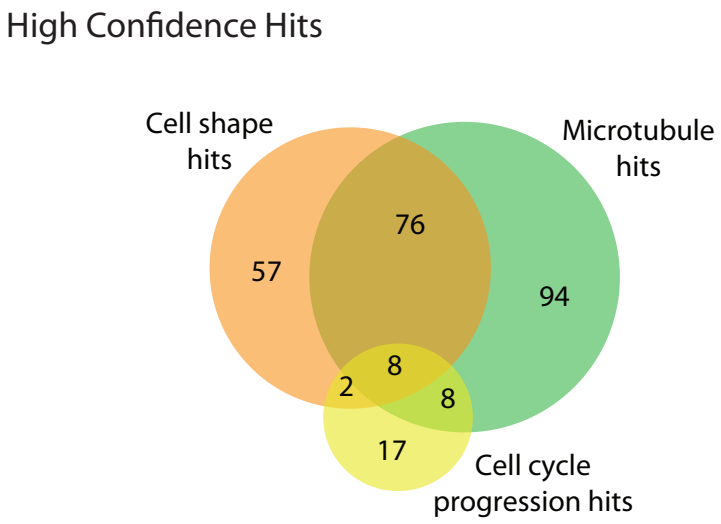

Figure 3.14: High-confidence hits - Finalised high-confidence hit list resulting from the combination of results from all screening repeats. All hits were analysed in at least three of ten repeats. When analysed, they were detected as hits at least 35% of the time.

3.5 Finalising high-confidence hits

Ultimately a list of 262 high-confidence hits (**Figure 3.14**; 143 cell shape, 186 microtubule and 35 cell cycle progression) was finalised, which showed particularly significant overlap between cell shape and microtubules (76 hits). Thus the high-confidence hit list represents 34% of the candidate hits (41% shape, 43% microtubule, 18% cell cycle progression).

Note that consistency within the cell cycle progression list is particularly low. This is the product of a number of factors. Firstly, the method of detection for the different cell cycle states was less mathematically robust, based directly upon just four numerical measures. In addition, due to the dominance of the interphase state within the *S. pombe* cell cycle, the sample populations within different mutants for the other three states were likely to be very small and hence have a high degree of noise, even with our minimum population requirements. Finally, this is compounded by our requirement that a hit must be deviant in at least two of the four cell cycle states.

Hence, it is unsurprising to find that our 35 high-confidence hits for this property

generally showed strong deviance in the proportion of cells in interphase, as this would be the most stable phenotype to detect. It is, in fact, satisfying that we were able to successfully verify any high-confidence hits under these conditions (estimate from random sampling: ≈0.65 hits).

3.6 Comparing results across screen repeats

Comparing different screening repeats pairwise, reveals an average overlap for shape hits of 48% and for microtubule hits of 33%. The lower overlap and larger number of microtubule hits in each repeat, is reflective of the difference in thresholds used during hit selection for these processes. A higher threshold for microtubule phenotypes allows for more hits and permits a greater degree of noise between repeats. On average, high-confidence cell shape hits were hits in 5.48±2.06 screening repeats. For microtubules this was 4.27±1.90.

The cell cycle progression average overlap is only 10%, with each high-confidence hit proposed by 2.80±1.08 repeats. The greater noise here results from the subdivision of cell populations into different cell states, resulting in smaller sample sizes for each phase as stated earlier. This is especially true for the shorter cell cycle phases. The variation between screens is also compounded by the small number of cell cycle progression hits that were detected in each screening repeat. Further biological investigation is required to fully validate these hits and explore their relationship to the cell cycle machinery.

3.7 Screening subsequent library versions

As mentioned earlier, additional plates of deletion mutants were made available by Bioneer during this work. This constituted an upgrade of the KO library, from version 2 to version 3. All data presented here are based upon data from the version 2 library. The upgrade brought total coverage by the library to 92.5% ($^{3308}/_{3576}$) non-essential genes. These additional plates were also imaged in accordance with the protocol for both the first and second genomic screens. However, due to the abundance of data already generated from the version 2 library and

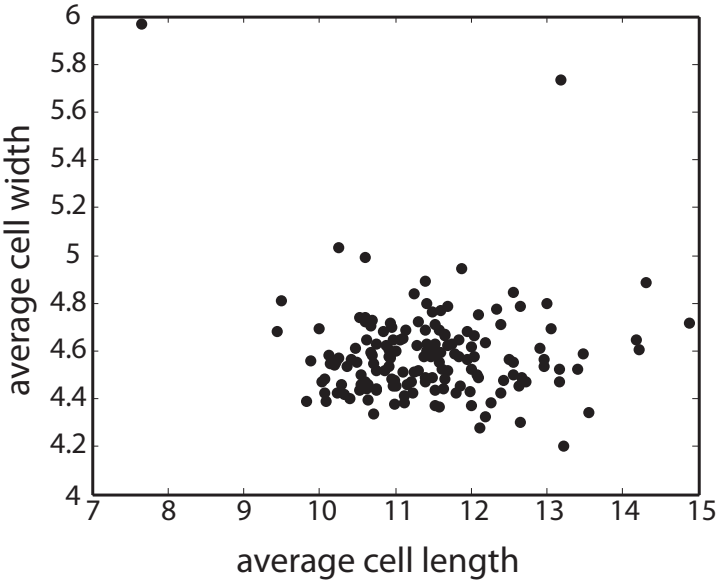

Figure 3.15: Example data generated from wild-type strains - Graphical representation of the variation in average population-level cell length and width measurements for different wild-type strains. These were two of the 11 parameters provided by myself and A. Chessel for inclusion in Jeffares et al. (2015).

due to lack of available resources within the lab, the analysis of these plates was not completed and so cannot be discussed further.

3.8 Collaborative work: Cell shape screening of wild-type *S. pombe* strains

In addition to screening deletion mutants, I also became engaged with a large multi-lab collaboration to characterise the nature of wild-type *S. pombe* cells (Jeffares et al., 2015). Members of the Bähler lab (University College London, UK) had compiled a collection of 161 natural *S. pombe* isolates. These samples were originally collected, from sites across the world, by different scientists at different times, spanning decades (1912-2002). The goal of the project was to assess the variation within wild-type populations, their rate of evolution, the efficacy of genome-wide association studies (GWAS) and to explore the history of this species, including how and when it spread around the world.

The analysis of these strains has included meta-analysis of historical, geographical, genomic, metabolic and phenotypic data. My contribution to this project was to perform six repeated screenings of the wild-type collection, alongside some of our own wild-type controls and subtle shape mutants. We then used our established image processing and analysis methods to extract cell shape features and applied our cell shape class SVM classifiers to create shape phenoprints for comparison between different mutants. This has been used by the collaboration as one of many factors for comparing the wild-type strains and assessing the effects of genome variation.

Of the 161 strains studied, 57 genetically distinct isolates were identified ($\geq$1900 single nucleotide polymorphisms (SNPs)). Analysis showed that crosses between more genetically distinct strains demonstrated reduced spore viability, suggesting that enough genetic diversity has developed to create a partial barrier to efficient reproduction. Estimation of the rate of genome evolution, based on both mitochondrial and nuclear estimates, made it possible to predict that the most recent common ancestor of all of these strains probably existed around 2300 years ago, with *S. pombe* most likely arriving in the Americas around the 17th century (95% confidence interval: 1422-1752). From this, a European origin for *S. pombe* was inferred, by contrast to the neolithic spread of *S. cerevisiae*.

Our screening procedure provided 11 parameters to the GWAS studies of these strains. In total 74 traits from five experimental methods were included. Our automated screening dataset included outputs from the eight SVM classifiers for each cell shape class, including wild-type, as well as three of the most strongly determinant cell shape features (cell length, width & width ratio i.e. the relative width of the two cell ends; **Figure 3.15**).

The GWAS study found links between almost 1500 regions of genetic variation and specific phenotypic traits. This included 1% of SNPs and 2% of larger insertion/deletion (indel) mutations, thought to occur primarily within non-translated gene regulatory sequences. Whilst the sample size was small for this analysis, it was possible to effectively apply GWAS and produce significant genome-phenotype associations, some of which our collaborators went on to validate. The results demonstrate the significance of subtle non-coding genome mutations and highlight the natural variation present within this model species.

4 Screening Hit Validation & Investigation

"Never ignore coincidence. Unless, of course, you're busy. In which case, always ignore coincidence."
—THE 11^{TH} DOCTOR (*The Pandorica Opens*, 2010)

As described in **Section 3.5**, our multi-process, high-throughput screen of over 3000 haploid *S. pombe* KO mutants produced 262 high-confidence hits. This included 143 factors influencing cell shape, 186 affecting microtubules and 35 with cell cycle progression effects. Of these, 94 mutants were linked to more than one of the three processes. Surprisingly, many mutants were identified as only affecting cell shape (60/143) or microtubules (106/186) suggesting these processes are not entirely co-dependent, as has previously been thought and can be influenced separately.

Precisely half (131) of the screening hits had previously annotated functions in *S. pombe*, as reported by the genome resource PomBase (`www.pombase.org`; McDowall et al. (2015); Wood et al. (2012)), whilst 102 had only predicted functions and 29 were previously completely unknown. Of the genes with previously known or predicted functions, 13 cell shape hits had existing cell shape annotations, whilst 12 microtubule hits had microtubule annotations. Just one cell cycle progression hit had previously been linked to the cell cycle. However, this is unsurprising given our novel approach to identifying cell cycle perturbations, using microtubule patterns.

Notably, our hits showed some enrichment for genes conserved in other species, which is plausibly reflective of the evolutionary significance of the three processes being investigated. In total, 232 hits (88%) are reported to be conserved to *S. cerevisiae* whilst 77% are found in vertebrates and 50% in humans, this is by comparison to the KO library, which respectively shows 86%, 68% and 42% conservation in the same comparisons.

Full information on all hits, including conservation and clustering data can be found in **Appendix Chapter A**.

4.1 Hit clusters & functions

As reported by V. Graml (Graml, 2012) and in Graml et al. (2014). it was possible to organise the hits from high-throughput screening by using hierarchical cluster analysis. This approach links genes together on the basis of their feature similarity. This can be considered as iteratively linking each gene or group of genes to their nearest neighbours in multi-dimensional space, where each dimension represents one numerical feature. This creates a relational tree linking all genes in a hitlist together on the basis of the distance between them. This tree can then be cut at any given position to give a number of separate clusters. Here, V. Graml typically cut each tree at ⅓ its full height. Simply put, clustering grouped hits on the basis of phenotypic similarity. The online functional analysis tool, DAVID (`david.abcc.ncifcrf.gov`), allowed me to look for functionally related genes within each cluster and begin to identify pathways and cell processes that may be linked to specific phenotypes.

4.1.1 Cell shape hits

The 143 cell shape hits were clustered based upon the results of the SVM classifiers used to create probabilistic cell shape phenoprints (**Section 3.1.4.2**). Hence clustering was performed based up on comparison between the average occurrence of seven intuitive cell shape classes within each mutant population (**Figure 4.1**). The majority of hits showed enrichment for long or stubby (disproportionately wider) cells, with a smaller number featuring a greater number of cells that were banana (bent/curved), skittle (one end wider) or kinked (‘z’ or ‘s’ shaped). No hits showed an enrichment for t-shaped (branched cells), which typically occur rarely, especially in the conditions used for this screen. There was also no enrichment for orb (round) cells, which goes some way to support the idea that such a significant loss of cell polarity is highly detrimental to cell viability. This is reflected in the fact that the *orb* mutants in *S. pombe*, identified for demonstrating this phenotype in temperature sensitive strains (Snell and Nurse, 1994; Verde et al., 1995), are all essential genes.

Overall functional enrichment analysis for the cell shape hit list revealed enrichment for genes involved in histone modification (13), transcription (25) and cell

morphogenesis (9). Cluster analysis of these hits produced 5 clusters:

- Cluster 1: 16 hits, high in stubby & skittle cells. Enriched for genes with related functions in cell wall construction & meiosis (6).

aah3, arf6, ecm6, met14, meu29, pit1, rps1701, sgf29, tea3, trm112, zds1, zfs1, SPAC16E8.08, SPAC323.05c, SPBC19C2.10, SPBC19F8.03c

- Cluster 2: 66 hits, high in stubby cells. Genes involved in vesicle transport (9), polarised growth & cytoskeleton (11) and protein ubiquitination (4).

are2, arp42, ccr1, ccr4, cgs1, clr3, cps3, csn1, csn2, cys11, did4, dip1, efc25, end4, gdh1, gpa2, hem14, lsd1, mga2, mug132, myo1, nab3, pka1, png1, pom1, pop3, ppk26, pub1, rad57, rpl2102, rpl901, rpn10, scd2, sft1, shd1, sin1, tom7, ubi1, ura3, usb1, vac7, vps25, vps32, vps36, wis1, ypa1,

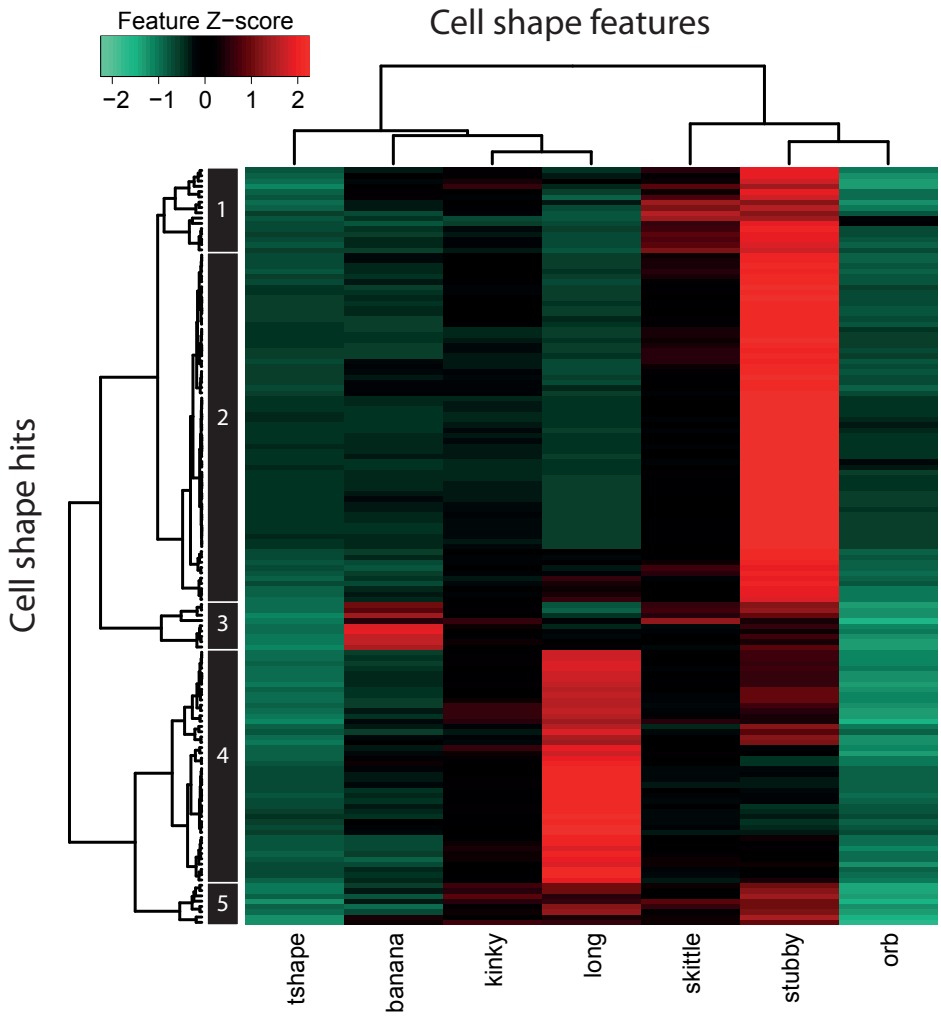

Figure 4.1: Hierarchical clustering of cell shape hits - All 143 cell shape hits clustered using population averaged probability values for each mutant belonging to each cell shape class as defined in **Section 3.1.4.2**. Figure adapted from Graml et al. (2014).

ypa2, *SPAC14C4.10c*, *SPAC1610.02c*, *SPAC1F3.03*, *SPAC1F5.05c*, *SPAC227.17c*, *SPAC25B8.19c*, *SPAC2C4.10c*, *SPAC31G5.19*, *SPAC328.04*, *SPAC3A12.13c*, *SPAC6G9.14*, *SPAC8C9.19*, *SPAP14E8.02*, *SPBC23G7.06c*, *SPBC25B2.08*, *SPBC409.19c*, *SPBP35G2.04c*, *SPCC1322.03*, *SPCC584.11c*, *SPCC965.06*

- Cluster 3: 9 hits, high in banana cells. Includes ribosomal proteins (4).

  amk2, *cbf12*, *php5*, *rpl1702*, *rps1002*, *rps2201*, *tea2*, *SPAC3F10.17*, *SPBC25H2.15*

- Cluster 4: 44 hits, long cells. Highly enriched for chromatin regulators (20), RNA processing (7) and DNA damage/stress response (9) genes.

  apl4, *brl2*, *ccq1*, *cdt2*, *cph1*, *cph2*, *csx1*, *ctp1*, *ctu2*, *cuf1*, *dep1*, *dph3*, *elp3*, *elp4*, *elp6*, *mcl1*, *med20*, *mms1*, *pep3*, *pmt1*, *pof3*, *rad32*, *rad50*, *rad55*, *rep2*, *rga2*, *rtr1*, *rxt2*, *sal3*, *sbh1*, *sec2302*, *sep11*, *set1*, *spf1*, *swd1*, *vps16*, *SPAC27D7.06*, *SPAC30.02c*, *SPAC664.03*, *SPBC16G5.07c*, *SPBC17A3.05c*, *SPBC18H10.07*, *SPCC1450.03*, *SPCC553.08c*

- Cluster 5: 8 hits, high in long & stubby cells. Enriched for genes with functions in the nucleus (4).

  cwf12, *erd1*, *rsc4*, *sce3*, *srs2*, *tup12*, *upf1*, *SPAC630.10*

The groups of genes, particularly in Clusters 2 and 4, are particularly interesting for providing validation of this screening method. Both contain groups of genes that would be expected to have effects on cell shape, and even produce predictable phenotypes.

The genes present in Cluster 2 are the most logical; components of cell growth and intracellular transport, which would directly affect cell growth through delivery of cell membrane and cell wall components. An inability to correctly distribute materials to the growing tips would intuitively stunt the capacity for polarised cell growth. It is unsurprising then that these cells demonstrate stubby phenotypes. A similar explanation may apply to meiotic cell wall factors in Cluster 1, indicating a more diverse role for those factors, which have previously been confined to the meiotic cell cycle, in cell growth.

The relationship between gene groups in Cluster 4 and cell shape is less immediately apparent. One of the earliest reasons for using *S. pombe* as a model organism, especially for studies of the cell cycle, was the linkage between cell length and the cell cycle (Fantes, 1977; Mitchison and Nurse, 1985). Mutants in DNA repair mechanisms are logically prone to accumulating DNA damage (Lydall and Weinert, 1995). Hence, even when DNA damage is not artificially induced, they are more likely to enact the DNA damage response in response to natural causes, leading to cell cycle delay to give more time to repair DNA damage caused by natural environmental factors. A higher probability of cell cycle delay

will result in an increase in average cell length. Chromatin modifying factors in this cluster could theoretically also accumulate DNA damage due to impaired ability to alter chromatin structure leading to defective DNA repair.

Whilst these expected gene groups may seem more interesting as validation rather than new scientific interest, they may provide leads to suggest new functions for other unknown genes found within the same cluster.

Other groups, such as the link between ribosomal deletion mutants and bent cells in Cluster 3, are apparently novel and may provide interesting new avenues for future research. It is difficult to predict how ribosome mutations may affect other aspects of the cell, as so many cell processes are directly dependent upon correct translation of proteins. Yet the specificity and consistency of this cell shape phenotype, across multiple ribosomal mutants, would suggest a specific connection.

4.1.2 Microtubule hits

The 186 microtubule hits were clustered using a subset of the feature measurements extracted from screening images (**Figure 4.2**). The features selected were those that showed the least cross-correlation with other features, this included average and standard deviation measures of intuitive physical microtubule properties, such as length, orientation (angle between microtubule and major cell axis) and number per cell, as well as Haralick textural features (h1, h4, h5, h8, h10 & h11). Feature enrichment analysis for all 186 hits revealed many chromatin/transcription regulators (30) and intracellular transport proteins (33). In total, 12 hits had known or predicted microtubule associations, including microtubule regulators (*tea1*, *tea2*, *mal3*, *tip1*, *gfh1*) and the prefoldin complex (e.g. *pfd1*, *pac10*, *bob1*). Hits were clustered on the basis of 12 parameters to give 8 distinct clusters:

- Cluster 1: 50 hits, more, longer & more variable microtubules. Genes involved in response to DNA damage/stress (11).

  apl4, *arf6*, *ccq1*, *cdt2*, *cph2*, *csn1*, *ctp1*, *cuf1*, *dep1*, *elp4*, *erd1*, *gcn5*, *kap113*, *mcl1*, *med20*, *met14*, *mft1*, *mms1*, *pep3*, *pka1*, *png1*, *pof3*, *rad32*, *rad50*, *rad51*, *rad55*, *rep2*, *rpl3001*, *rpl801*, *rps1002*, *rxt2*, *sal3*, *sbh1*, *sep11*, *spf1*, *tup12*, *ubi1*, *vps16*, *yox1*, *ypa1*, *SPAC12B10.10*, *SPAC22H10.11c*, *SPAC27D7.06*, *SPAC30.02c*, *SPAC3F10.17*, *SPAC630.10*, *SPBC17A3.05c*, *SPBC543.08*, *SPCC1450.03*, *SPCC553.08c*

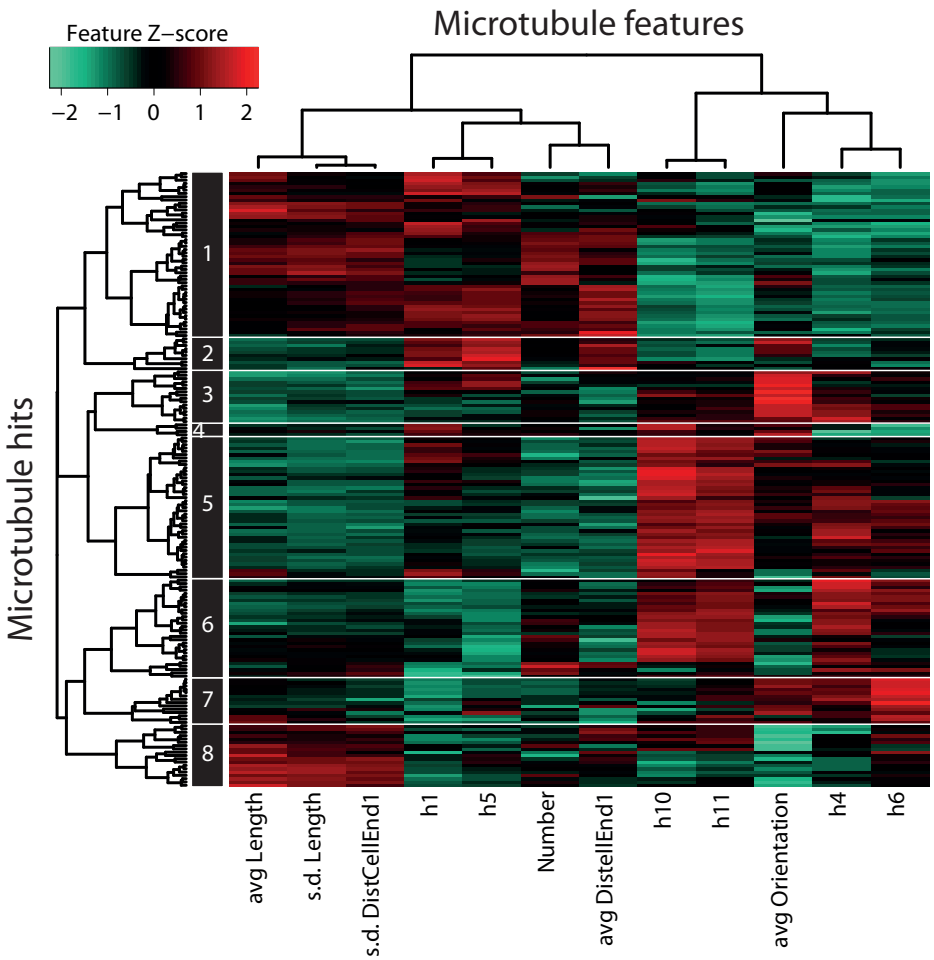

Figure 4.2: Hierarchical clustering of microtubule hits - All 186 microtubule hits clustered using average and standard deviation values of non-correlated biologically interpretable and Haralick textural features. Figure adapted from Graml et al. (2014).

- Cluster 2: 10 hits, shorter microtubules. Includes genes known to affect microtubules & polarity (5).

  ada2, *arp42*, *csn2*, *mal3*, *nab3*, *rsc4*, *tea2*, *tea4*, *tip1*, *wis1*

- Cluster 3: 16 hits, shorter, mis-oriented microtubules. Golgi & vacuolar proteins (5).

  aah3, *apl5*, *aps3*, *cbp1*, *efc25*, *fkh2*, *gas5*, *vps1*, *SPAC17A5.08*, *SPAC27E2.03c*, *SPAC4G8.07c*, *SPAC6G9.14*, *SPBC16E9.15*, *SPBC20F10.07*, *SPBC29A10.12*, *SPCC1322.03*

- Cluster 4: 4 hits, mis-oriented microtubules. Combines exonuclease (*exo2* (Szankasi and Smith, 1996, 1992)), polarity (*tea1*), transport (*vps32* (Iwaki

et al., 2007)) and mitochondrial (*mss116* (Matsuyama et al., 2006)) factors. No known connections reported by DAVID.

exo2, *tea1*, *vps32*, *SPBC691.04*

- Cluster 5: 43 hits, fewer microtubules. Features proteolytic proteins (5) and kinases (4).

  bag101, *cao2*, *cps3*, *did4*, *fft2*, *git3*, *liz1*, *lon1*, *mak1*, *meu34*, *mok11*, *mug81*, *nif1*, *pex5*, *ppk13*, *qcr6*, *red1*, *rpl3702*, *rpn10*, *snz1*, *sol1*, *spo7*, *ssa1*, *tel1*, *ulp2*, *vps36*, *zfs1*, *SPAC15E1.02c*, *SPAC1687.08*, *SPAC589.09*, *SPAC5H10.04*, *SPAC5H10.09c*, *SPAC890.05*, *SPBC13G1.02*, *SPBC16A3.10*, *SPBC1734.07c*, *SPBC23E6.02*, *SPBC29A10.16c*, *SPBC685.03*, *SPBP8B7.18c*, *SPCC1183.11*, *SPCC1672.04c*, *SPCC24B10.19c*

- Cluster 6: 30 hits, highly oriented microtubules. Includes transport (8) and mitochondrial (8) genes.

  ago1, *ccr1*, *coq5*, *cys11*, *ecm6*, *naa30*, *pop3*, *rrf1*, *ryh1*, *sat1*, *sco1*, *sin1*, *sts1*, *tdh1*, *tlg2*, *tom7*, *usb1*, *vps25*, *vps66*, *SPAC1610.02c*, *SPAC1F3.03*, *SPAC227.17c*, *SPAC343.20*, *SPAC6C3.08*, *SPAC823.10c*, *SPAC8C9.19*, *SPBC106.07c*, *SPBC1861.05*, *SPCC584.11c*, *SPCC965.06*

- Cluster 7: 14 hits, fewer, mis-oriented microtubules. Strongly enriched for the cytoskeleton-specific prefoldin chaperones (4).

  bob1, *cid12*, *clr5*, *elp2*, *gfh1*, *hem14*, *oxa102*, *pac10*, *rdh54*, *tsf1*, *SPAC227.10*, *SPAPB1A10.08*, *SPAPB21F2.03*, *SPBC1D7.01*

- Cluster 8: 19 hits, longer, highly oriented microtubules. Enriched for histone modification (6) and RNA metabolism (4) genes.

  ash2, *cph1*, *csx1*, *dph3*, *elp3*, *elp6*, *gma12*, *pmt1*, *sce3*, *ser2*, *set1*, *swd1*, *tup11*, *upf3*, *SPAC664.03*, *SPBC1604.12*, *SPBC16G5.07c*, *SPBC18H10.07*, *SPBC2F12.03c*

Here again the screening approach used is validated by the presence of several predictable groups of genes. Most obviously, Cluster 2 contains several (4) of the well-characterised microtubule regulating mutants (*mal3*Δ, *tip1*Δ, *tea2*Δ (Browning et al., 2000) and *tea4*Δ (Tatebe et al., 2005; Martin et al., 2005)) that are already known to have shorter microtubules, in-keeping with the characteristics of this cluster.

Similarly, Cluster 7 includes the predicted prefoldin proteins (e.g. *pac10*, *pfd1*), which were explored in detail by X. Studera. The prefoldin complex, in other species, is known to be involved in the correct assembly of α/β-tubulin dimers (Simons et al., 2004). As such, deletion of prefoldins is expected to reduce the efficiency of tubulin production. Less tubulin will mean less polymerised microtubules in each cell, agreeing with the lower number of microtubules observed in this cluster.

Some of the other hit groups in these clusters are much less predictable. Groups of factors involved in gene expression and protein turn-over are found in Clusters 3 (Golgi), 5 (proteolysis/kinases) and 8 (histones/RNA). That these factors cluster suggests that their phenotypes are not simply the result of disregulation in core cellular machineries, but point to a more specific, although not necessarily direct or desirable, link with the microtubule cytoskeleton.

Clusters 1 and 6 offer probably the most distinctive and interesting set of results. Factors involved in vesicle transport have well-established links with microtubules in many organisms (Hehnly and Stamnes, 2007; Nelson, 1991; Banks, 1976), but most evidence suggests this is not the case in *S. pombe* (Höög et al., 2007), where vesicle delivery to the cell ends is thought to be dependent upon actin cable formation and not microtubule arrays (Chang and Martin, 2009). Additionally, we may expect microtubule mutants to affect intracellular transport but it is less clear how transport proteins may come to affect microtubule organisation.

Cluster 6 contains two prominent functional groups of genes, intracellular transport and mitochondria. This may suggest that these two functions in *S. pombe* are tightly linked, which may explain why both groups appear to give similar mutant phenotypes. A relationship between mitochondrial function and microtubules has been reported before (Fu et al., 2011), where the protein Mmb1 was identified as a linker necessary to prevent mitochondrial aggregation.

It is easiest to consider that a reduction of ATP production by mitochondria may influence tubulin GTP hydrolysis, or affect the ATP hydrolysis rate of microtubule associated motors, yet neither of these possibilities provide an adequate explanation for the observed phenotype in these mutants. A shortage of purine nucleotides would be expected to result in a loss of microtubules as GDP-tubulin dimers are less able to regenerate into GTP-tubulin and reincorporate into microtubules. The majority of genes in this cluster do not show marked microtubule reduction. By contrast, Fu et al. (2011) went on to show an apparent reduction in microtubule depolymerisation rate in *mmb1*Δ cells, yet this appears to be a specific molecular interaction and does not appear to relate to the hits or phenotypes reported here.

Since association of mitochondria with microtubules, in many species, is thought to affect mitochondrial location within cells this may suggest that microtubules and mitochondria are functionally linked (Tepp et al., 2014; McDaniel and Roberson, 2000; Wu et al., 2013; Murphy, 2012; Heggeness et al., 1978). However, again,

the mitochondrial factors identified in this screen are localised throughout the different mitochondrial compartments, so cannot predictably influence microtubules.

The largest gene group of interest is found in Cluster 1 and includes a number of genes also found in the cell shape hit list. This is the group of genes related to DNA damage/repair and cell stress; the DNA damage response (DDR) hits. These hits have a variety of roles ranging from transcriptional regulation and chromatin remodelling (e.g. *csn1* (Mundt et al., 2002; Zhou et al., 2001), *set1* (Kanoh et al., 2003; Noma and Grewal, 2002)) to DNA digestion and resynthesis (e.g. *ctp1* (Akamatsu et al., 2008; Williams et al., 2009), *mcl1* (Williams and McIntosh, 2002, 2005; Tsutsui et al., 2005)). Loss of these factors would most likely result in delayed or defective DNA repair mechanisms and increased activity of the DDR. Little is currently known about any possible link between persistent DNA damage and microtubule organisation, although this cluster analysis suggests that DNA repair defects may be linked to an increase in total microtubule polymer mass within cells.

4.1.3 Cell cycle progression hits

Our initial data on cell cycle progression was limited by the fact that it used ergodic reasoning to study a dynamic process over time, by looking at a static snapshot of a population of cells.

Ergodic rate analysis (ERA) (Kafri et al., 2013) of the number of cells in each cell cycle stage, implemented by A. Chessel, used the proportion of cells in each cell cycle linked microtubule state (**Figure 4.3A**) to create a measure of the rate of transition from each state into the next, relative to the wild-type population (**Figure 4.3B**). The results of this analysis were used in clustering the cell cycle progression hits. As such, enrichment (red) in the cluster diagram (**Figure 4.3C**) represents accelerated transition from the named cell cycle microtubule state into the subsequent state.

The complete list of 35 cell cycle progression hits shows weak enrichment for RNA binding factors (6), ribosomes (4) and transcriptional regulators (5). The hits form four clusters:

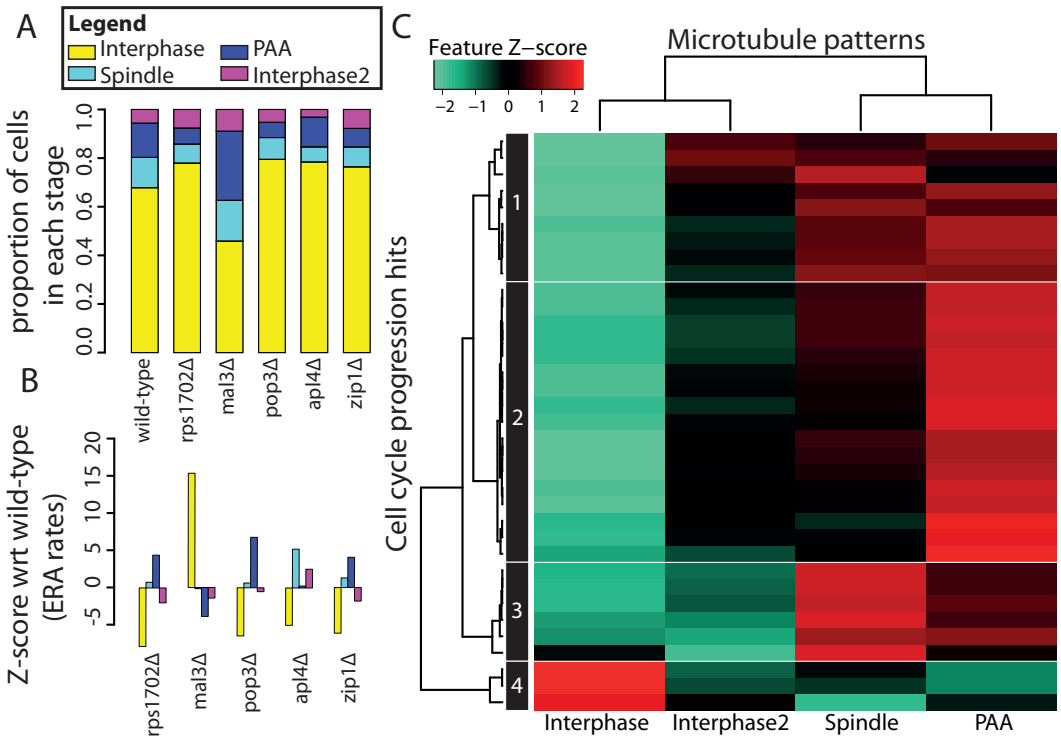

Figure 4.3: Hierarchical clustering of cell cycle progression hits - **(A)** Stacked bar graphs showing the proportion of different cell cycle progression hit cell populations assigned to each cell cycle-linked microtubule phenotype. **(B)** Results of ergodic rate analysis (ERA) of **(A)** inferring rate of exit from each state relative to wild-type. **(C)** All 35 cell cycle progression hits clustered using ERA values. Figure adapted from Graml et al. (2014).

- Cluster 1: 9 hits, delayed exit from interphase, rapid exit from spindle and PAA states. Includes ncRNA processing factors (3).

  apl4, dph3, gar2, rep1, trm112, twf1, vps66, SPAC8C9.19, SPBC106.07c

- Cluster 2: 17 hits, delayed interphase exit, acceleration through PAA. Enriched for ribosome (4) and transcription factors (3).

  cbp1, ccr1, cgi121, cys11, dbp7, elf1, pop3, rpl502, rpl801, rps1702, snz1, zip1, SPAC1610.02c, SPAC823.10c, SPBC8D2.12c, SPBPB7E8.01, SPCC1322.03

- Cluster 3: 6 hits, delayed interphase exit, faster exit from spindle state. Stress responses (3).

  iws1, pcr1, pmp3, pxa1, SPAC3A11.13, SPCC645.12c

- Cluster 4: 3 hits, accelerated interphase. Cytoskeleton & polarity (3).

  mal3, pac10, pom1

With such a small number of hits it is difficult to come to many conclusions about new processes involved in cell cycle progression. Unsurprisingly, given that it typically represents over 70% of the cell cycle, the cluster diagram is dominated by the interphase microtubule state. The vast majority of hits show an extension of interphase, a clear indicator of checkpoint-induced cell cycle delay. Surprisingly, as reported in Graml et al., we found that these strains rarely correlated with cell elongation, another commonly accepted indicator of cell cycle delay (see **Section 6.2.3**).

Several of the functional groups I identified in this cluster analysis agree with the observed phenotypes, again supporting the validity and accuracy of these hit lists. In particular, defects in transcription and translation are likely to delay cell cycle progression as it takes more time for all of the necessary factors to be synthesised in each cell cycle. Similarly loss of factors involved in cytoskeleton organisation and cell polarity may reasonably be expected to have connections to the cell cycle, affecting reorganisation of the microtubule cytoskeleton. For example, the *pom1*Δ mutant behaves as expected (Martin and Berthelot-Grosjean, 2009; Moseley et al., 2009; Saunders et al., 2012). Since Pom1 is thought to be required to measure the elongation of a cell and determine when it is large enough to divide, its loss is tightly linked to more rapid, premature cell division.

4.1.4 Functional groups across processes

As mentioned at the start of this chapter, over a third (36%; $^{94}/_{262}$) of hits in this screen were found to affect more than one of the three cell processes studied. The majority of these ($^{84}/_{94}$) overlap between cell shape and microtubule hits, indicative of the close relationship between these two processes. By comparison, overlap with the cell cycle progression hits was much lower, suggesting a greater degree of independence, but also greater stringency in hit detection.

As may be expected from common themes in the cluster analysis of cell shape and microtubule hit lists individually, the overlap region includes many genes assigned roles in transcription (18), chromatin organisation (18) DNA damage & stress (16) and intracellular transport (13). The fact that these functional groups also tend to cluster phenotypically within each hit list goes some way to suggest that certain cell shape and microtubule properties may be strongly linked and hence more dependent on common factors, whilst others are more independent.

Transport genes, for example, are linked to stubby cells and greater microtubule disorientation, whilst chromatin regulators show links to longer cells and longer microtubules. Whilst these relationships may be more physical than biological, more work is needed to investigate them fully.

The other genes that span between processes in this screen are in much smaller groups, rendering functional analysis pointless. The smallest group, between cell shape and cell cycle progression, contains just *pom1*Δ and *trm112*Δ – two highly functionally and phenotypically distinct genes. The eight genes in both microtubule and cell cycle progression lists include several microtubule related genes (*mal3*, *cbp1* and *pac10*) in addition to ribosomal (*rpl801*), mitochondrial (*SPAC823.10c*, *SPBC106.07c*) and transport (*vps66*) associated genes. These genes span different phenotypic clusters in both cell processes.

Interestingly, the eight genes present in all three hit lists contain a diverse array of genes, several with indirect links to translation (*cys11*, *ccr1* and *dph3*) as well as signalling pathways (*pop3*) and transport (*apl4*). These genes are often found in the same clusters across hit lists. Four of the eight occupy Cell Shape Cluster 2, Microtubule Cluster 6 and Cell Cycle Progression Cluster 2, representing stubby cells with highly oriented microtubules and a greater proportion of interphase cells with fewer PAA cells.

It may be interesting to use the functional annotations and phenotypic information for these cross-process hits to identify other genes currently present in just one hit list that may have been assigned to more than one hit list if more data had been available. Furthermore it may, in future, be possible to make use of what is known, functionally and phenotypically, about the 262 hits reported here to re-examine the original 763 hit candidates and infer new true hits that were called as false negatives on the basis of the data collected here. This would create an iterative process that may help to produce more comprehensive hit lists that can offer more complete insights into the connections between different gene functional groups.

Whilst this cluster analysis has primarily reported on the known functions of hits, it is important to point out that each cluster also contains several poorly characterised or unknown genes. By revealing genes that phenocopy others of known functions we may be able to use screens like this one, to not only uncover factors

influencing several processes of interest but also provide evidence to connect unknown genes to other cell processes not being studied, based upon phenotypic similarities.

4.1.5 Hits of previously unknown function

The 29 hits with no previously existing annotations divide proportionally between the three hit lists; 15 cell shape (9.7%), 18 microtubule (10.5%) and three cell cycle progression (8.6%). Of these, six are found in both cell shape and microtubule lists, of which one (*SPAC8C9.19*) appears in all three hit lists. These hits are proportionally distributed throughout the different clusters, although nine of the unknown cell shape hits appear together in Cluster 2.

4.2 Analysis of position within the genome

Using MatLab and information about gene positions from PomBase, I created code that could be used to examine the distribution of hit genes within the genome and begin to uncover whether there were any locational effects of the genes themselves that may explain the phenotypes observed in this screen in a way that is separate from considering the activities of the different gene products. The work presented here considers the relative position of genes by extracting the start positions for different genes, plotting their positions within the genome and using statistical tests to examine any clustering of genes within specific regions. Midpoints and endpoints of genes were also considered but gave very similar results, hence are not shown as this work is not the main focus of subsequent investigations.

4.2.1 Hits with close linkage to tubulin genes

Gene regulation is complex and often involves regulatory sequences located around the gene, in nearby genes, or even in totally independent parts of the genome (Pennacchio et al., 2013; Cooper and Hausman, 2013). It may be that some of our hits were not discovered because the protein they produce has any impact on cell shape microtubules or cell cycle progression, but simply because

they happen to also contain sequences that act as gene regulation sites for other genes.

The fact that gene regulation can act over large distances, meant that I could not examine these effects fully with the data currently available. It was also not possible to comprehensively examine the region around every gene with a potential link to cell shape, microtubules and cell cycle progression to see if any hit genes maybe nearby. Instead, I decided to focus on the three tubulin genes because of their central roles in this screen, the microtubule cytoskeleton and the cell in general. This was particularly interesting because it was impossible to investigate deletion of any of these genes directly since one (α-tubulin 2; *atb2*) was needed to provide the fluorescent readout in the screen and the other two (β-tubulin; *nda3* and α-tubulin 1; *nda2*) are essential for viability.

All three tubulin genes occur on chromosome II in *S. pombe*, with *atb2* on the reverse strand around 0.26 Mb from the start of the chromosome, *nda3* on the reverse strand at 3.97 Mb and *nda2* on the forward strand at 4.27 Mb. Overall, there are 91 hits across the $\approx$4.5 Mb of chromosome II, an average of one every 49.5 kb, slightly lower than the average across the whole genome (47.7 kb). Hits around the tubulin genes appear to be uniformly distributed and show no enrichment relative to the rest of the chromosome. The nearest genes to *nda3* are *SPBC1604.12*, a microtubule hit 54.5 kb away and *vps36*, a shape and microtubule hit 37 kb away (**Figure 4.4B**). For *nda2* these are *fkh2*, 27 kb away and *SPBC16A3.10*, 12.6 kb away, both microtubule hits. It is interesting to note that all four neighbouring genes are microtubule hits, although they do not appear in the same phenotypic clusters.

In addition, this investigation was enlightening because it led me to examine genetic linkage between *atb2* and nearby gene deletions. When two gene loci are close together on the same chromosome, they typically stay together during genetic crosses because a meiotic recombination event is needed to separate them. The closer two genes are, the stronger this genetic linkage.

When strains were crossed to create the GFP-Atb2 library, if the *GFP-atb2* gene from one parent was closely linked to the gene that was deleted in the other parent then a relatively unlikely recombination event would have been needed to bring both mutations together in the same haploid cell. If the genetic linkage was close enough then it is possible that recombination may have disrupted either the

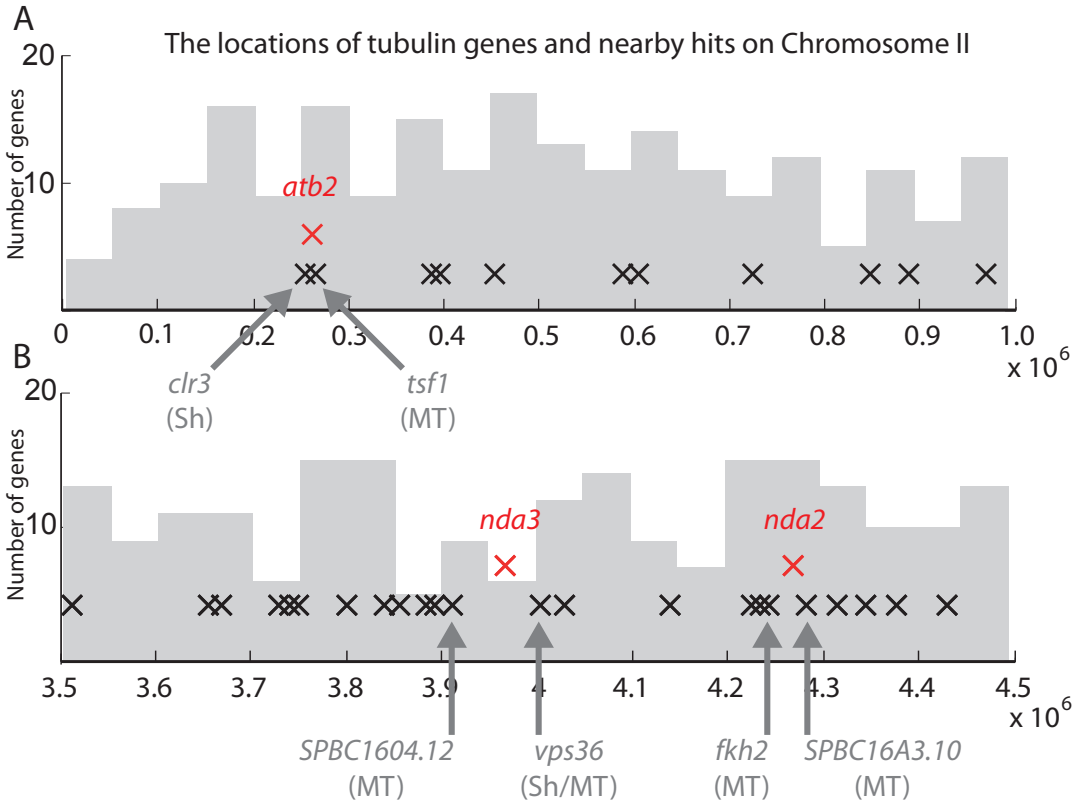

Figure 4.4: Genomic positions of tubulin genes and screening hits - Start positions for hit genes from all hit lists (black crosses), overlaid onto histograms showing the positions of all genes deleted in the KO library located on Chromosome II in the areas surrounding the tubulin genes (red crosses). **(A)** The area around *atb2*. **(B)** The area encompassing *nda2* and *nda3*.

gfp-atb2 or gene deletion constructs and so the resulting genotype may not be as expected.

This meant that it was interesting to investigate whether hits occurred near to *atb2* and whether the observed phenotypes were as expected. Two hits were closely linked to *atb2*. *clr3* is a cell shape hit just 2.6 kb away and *tsf1* is a microtubule hit 7.4 kb away (**Figure 4.4A**). Notably, the screening images from both of these mutants contain a large number of cells lacking GFP signal.

Assuming that the kanamycin and nourseothricin selection cassettes are both still present and in the correct genetic loci, this suggests that surviving cells are the result of meiotic recombination events, bringing each gene-deletion together with *gfp-atb2* on the same chromosome. Over such a short distance it is possible re-

combination may have occurred within the *atb2* gene. Recombination within *atb2* could result in GFP-negative cells that are still resistant to both drugs. Relative gene positions mean that, *tsf1*Δ is especially prone to *atb2* disruption. Notably, both genes are well within the average 21 kb linkage disequilibrium distance reported for *S. pombe* (Jeffares et al., 2015) and therefore meiotic recombination events within the region between these genes is predictably unlikely.

As *clr3* is not a microtubule hit, its phenotype (wider cells) may yet be linked to the role of the Clr3 protein as a histone deacetylase, whereby it may act to regulate other genes that influence cell shape. There may also be a role for *clr3* in microtubule regulation but, because so few cells retained GFP labelling, it is not possible to assess this computationally. Enough *clr3*Δ cells with microtubules were available for statistical analysis in one screen repeat, in which it was not a hit.

There is no apparent role for Tsf1 in microtubule regulation, hence the phenotype observed may be due to genome positions more than protein functions. Interestingly, *tsf1*Δ cells were found to have longer than normal microtubules in cells where GFP-positive microtubules were present. If we assume that this is due to the position of the *tsf1* gene and not due to the activity of Tsf1 then this may suggest the presence of an *atb2* transcription inhibitory site within the *tsf1* gene or may suggest that *tsf1* transcription is somehow inhibitory to *atb2* expression.

4.2.2 Distribution of hits across the genome

Associated with the study of tubulin loci, I went on to investigate the location of hits within the genome more broadly. I was able to produce code that could make use of PomBase data to plot histograms of the positions of genes and hits along all three chromosomes (**Figure 4.5**). Using this approach, it was possible to compare the physical distribution of hits – both for all hits, and each of the three process hit lists – on each chromosome to the background distribution of all Bioneer genes and investigate whether genomic location could affect hit occurrence.

First, I looked to see whether hits showed a particular preference for any one chromosome (**Table 4.1**; top). Assuming random distribution of hits across each chromosome it was possible to predict the expected number of hits for each, these could then be compared to the actual number of hits on each chromosome using

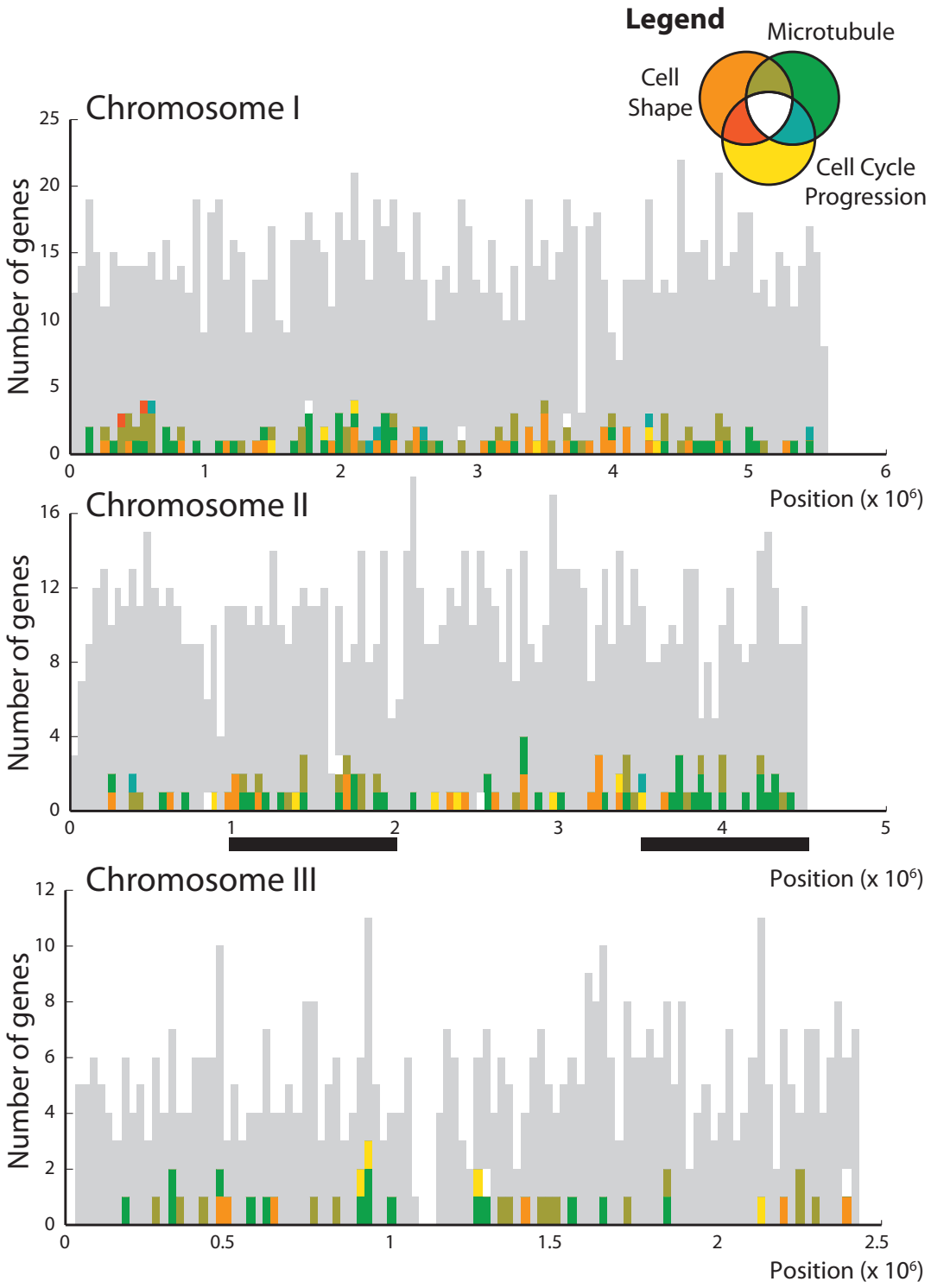

Figure 4.5: Genome locations for all hits - Stacked histograms showing start positions for hit genes from all hit lists (see legend for colour code), overlaid onto histograms (grey) showing genes in the KO library. Each histogram bar represents 1% of total chromosome length. Regions of Chromosome II enriched for microtubule hits, as identified in **Table 4.2**, are indicated by black bars beneath the graph.

Hit list	Chromosome I	Chromosome II	Chromosome III	
Number of hits (observed/expected)				χ^2 p-value
All	$^{129}/_{117.4}$	$^{91}/_{94.3}$	$^{42}/_{50.3}$	0.27
Shape	$^{76}/_{64.0}$	$^{44}/_{51.5}$	$^{23}/_{27.5}$	0.13
Microtubule	$^{89}/_{83.3}$	$^{65}/_{67.0}$	$^{32}/_{35.7}$	0.66
Cell Cycle Progression	$^{17}/_{15.7}$	$^{12}/_{12.6}$	$^{6}/_{6.7}$	0.90
Hit vs. Bioneer KS-test p-value				
All	0.54	0.22	0.24	
Shape	0.34	0.74	0.60	
Microtubule	0.19	**0.03**	0.30	
Cell Cycle Progression	0.63	0.58	0.35	

Table 4.1: Assessing gene distribution - Observed and expected numbers of gene hits per chromosome and the results of χ^2 assessment of hit distribution across chromosomes (top). KS-test p-values assessing distribution of hits within each chromosome relative to the background distribution of genes covered by the Bioneer deletion library (bottom).

the chi-squared (χ^2) test. This test revealed no significant biases (p>0.13). The greatest deviation from the expected values occurred amongst the shape hits, which were slightly more common than expected on chromosome I (76 observed, 64 expected).

I went on to employ the non-parametric KS-test to compare the distribution of Bioneer genes along each chromosome to the distribution of hits (**Table 4.1**; bottom). Here again, most results were not significant (p>0.19). However, I found that microtubule hits on chromosome II did not appear to represent a random sampling of the Bioneer genes along the chromosome (p=0.025).

I returned to chi-squared testing to dissect how the location of microtubule hits on chromosome II differed from the expected distribution. Expected number of microtubule hits for different sections of the chromosome were calculated based on the distribution of the 1044 genes deleted in the KO library on chromosome II. Expected values ranged between 6.23 and 7.97 hits per 0.5 Mb (**Table 4.2**). Testing revealed a significant deviation from expectation (p=0.01) with 21 genes

	Position on Chromosome II (Mb)									
	<0.5	0.5-1.0	1.0-1.5	1.5-2.0	2.0-2.5	2.5-3.0	3.0-3.5	3.5-4.0	4.0-4.5	χ^2 p-value
Observed	4	3	**10**	**11**	1	7	6	**11**	**12**	0.01
Expected	7.2	6.5	7.5	6.4	7.9	7.7	7.9	6.2	7.7	

Table 4.2: Microtubule hits on Chromosome II - Observed and expected numbers of microtubule hits per 0.5 Mb stretch of chromosome II. Enriched regions highlighted in bold.

occurring between 1 and 2 Mb along chromosome II (expected 13.9) and 23 genes between 3.5 and 4.5 Mb (expected 14.0). Since the centromere is apparent in the distribution of KO library genes – as an area of low gene abundance around 1.6 Mb into the chromosome – and since the total chromosome length is ≈4.5 Mb, these two positional gene clusters can be respectively referred to as the Centromeric and Sub-telomeric Clusters.

I then used the phenotypic clustering to consider whether there was any similarity in microtubule phenotypes between the genes that occur within these positional clusters. I again employed chi-squared testing to compare the actual number of genes within each positional cluster that were also assigned to each microtubule phenotypic cluster and showed no significance ($p>0.18$), however these results are questionable given the small number of genes involved in each cluster.

4.2.3 Relating genetic position clusters and phenotypic clusters

Within the Centromeric Cluster, 29% of genes (6/21; expected 2.1/21) are also part of Microtubule Cluster 8 (19 hits; long, strongly oriented microtubules), almost one third (32%; 6/19) of that cluster (**Table 4.3**; top). Studying these six more closely, all of them occur within 0.2 Mb of each other (positions 1.67-1.87 Mb). Notably, there are 9 members of Microtubule Cluster 8 (47%, 9/19) on chromosome II; the other 3 are contained within the Sub-telomeric Cluster.

Functional annotations for Cluster 8 included RNA processing and chromatin

	Cell shape cluster								
	1	2	3	4	5	6	7	8	
Hits:	50	10	16	4	43	30	14	19	χ^2 p-value
Centromeric cluster (Chr II, 1.0-2.0 Mb)									
Observed	4	2	1	1	3	3	1	**6**	0.18
Expected	5.6	1.1	1.8	0.5	4.9	3.4	1.6	2.1	
Telomeric cluster (Chr II, 3.5-4.5 Mb)									
Observed	4	1	2	0	**9**	2	2	3	0.68
Expected	6.2	1.2	2.0	0.5	5.3	3.7	1.7	2.3	

Table 4.3: Phenotype clustering of hits from chromosome II clusters - χ^2 analysis of the distribution of microtubule hits from enriched regions of chromosome II. Although no significance is shown for due to small sample size, apparent enrichments are highlighted in bold.

modification gene groups. The six Cluster 8 genes also found in the centromeric region of chromosome II include two of the four RNA processing genes but show no other functional connections. This suggests the interesting possibility that their phenotypic similarities may be due to their genetic loci, rather than their protein function. However, one of these six genes is *elp6*, which is tightly functionally and phenotypically linked to another microtubule hit *elp3*. The *elp3* gene is found on chromosome I suggesting that the effects of *elp3* and *elp6* on microtubules are more likely to depend on protein function rather than genetic location.

Moving to consider the Sub-telomeric Cluster, 39% of hits (9/23; expected 5.3) are also part of Microtubule Cluster 5 (43 hits; fewer microtubules), representing 21% (9/43) of that cluster (**Table 4.3**; bottom). In addition, a further 2 members of Cluster 5 can be found within 0.1 Mb of the Sub-telomeric Cluster. There are a total of 17 Cluster 5 hits across the whole chromosome, which is in line with expectation. As discussed in the previous section, this region of chromosome II also contains both *nda2* and *nda3* tubulin genes and two of the four neighbouring hits mentioned are present in Microtubule Cluster 5 (*vps36*Δ and *SPBC16A3.10*Δ).

This may suggest that several of the hits found in Microtubule Cluster 5 have a shared phenotype because of their genomic position, not because of functional similarity. This is supported by the relatively small number of functionally related

hits in this cluster. Cluster 5 contains groups of proteins annotated for functions in proteolysis or annotated for kinase activity, only one hit from each functional group is present in this region of chromosome II. Performing functional enrichment studies specifically on these 11 genes reveals only weak enrichment for zinc-finger proteins (3) and nucleotide binding proteins (4), neither of which are particularly revealing or specific functions.

It has not been the focus of this work to pursue these findings further, however they may provide an interesting alternative approach to studying some of the hits identified in this screen. A significant number of genes within Microtubule Clusters 5 and 8 may be hits due to a genomic effect on other genes, in that they may contain regulatory sequences or enhancer regions that influence the activity of other genes. Alternatively, the clustering of these phenotypically related genes may suggest that they have been clustered through evolution due to related functions or co-regulation, which may help to shed some light on their observed phenotypes.

4.3 Comparing shape hits to other screens (Hayles et al.)

In 2013, Hayles et al. (2013) published the results of their own genome-wide screen for cell shape mutants. The screen encompassed 4843 gene-deletion, haploid *S. pombe* cell lines – including essential and non-essential gene-deletions – as they underwent germination from spores on rich YES+agar medium. It was possible for them to include essential genes in their screen because spores were formed from meiosis of viable heterozygous diploid cells (Kim et al., 2010). I have examined the results of this screen in relation to our own findings to further validate our results and explore the conservation of phenotypic effects across different growth conditions.

The Hayles et al. screen used entirely manual visualisation techniques to examine each mutant and assign visually interpreted cell shape classifications, akin to our SVM determined cell shape classes. Each mutant was uniquely assigned to one class rather than being assigned probabilistic values for several classes as we have done here. The classes used are described in **Table 4.4** and compared to

Shape class	Description	Hayles et al. (2013)	Graml et al. (2014)
Wild-type		3041	60
Miss E	Mis-shapen cells, essential	0	1
Miss V	Mis-shapen cells, viable	31	3
Miss weak V	Mildly mis-shapen cells, viable	191	13
Long HP	Many long cells	131	33
Long LP	Few long cells	30	3
Long Br	Long branched cells	11	4
Rounded	Spherical cells	34	10
Stubby	Shorter & wider cells	44	9
Curved	Bent/banana cells	39	3
Small		11	3
Skittle	Cells wider at one end	13	1
TOTAL		3576	143

Table 4.4: Comparing shape hits - Cell shape classifications of non-essential gene deletions as reported by Hayles et al. (2013) and the number of cell shape hits from Graml et al. (2014) belonging to each class.

the shape hits from this screen, note that only the 3576 non-essential deletions from Hayles et al. are included in the comparison.

Whilst there are similarities between the results of the two screens there are also many differences, much of this results from the different experimental procedures used and physiological cell conditions studied. In particular, cells germinating on solid medium are generally found to explore a wider range of more severe phenotypes than cells during exponential growth in liquid medium (Snell and Nurse, 1994; Verde et al., 1995).

The analysis of the results from these two screens also varies. Whilst here we use 7 shape classes and each strain (including wild-type) can belong partially to several of them, Hayles et al. report more shape classes (11) but assign each mutant exclusively to one. Their additional shape classes were mainly the result of rearrangement of the same shape classes we have used. For example, in place of long and t-shaped classes, they use long LP (low penetrance), long LP (high penetrance) and long Br (branched/t-shape). They also include three

qualitative, 'misshapen' classes to collect strains that could not be placed into one or other stereotyped cell shape class. Our probabilistic, quantitative approach to classifying each cell circumvents this need for a general term.

Definitions of some classes also varied, the Hayles et al. 'short' class was created as an opposition to long classes and taken to have a cell cycle connection akin to *wee1* mutants. They also had a requirement for stubby cells to be shorter and wider than wild-type. Stubby cells in our screen were those with a lower aspect ratio than wild-type irrespective of absolute length, this would encompass stubby and short cells from Hayles et al., as well as potentially some long cells, which could be simultaneously counted as long and stubby (as seen in Cell Shape Cluster 5).

In addition, Hayles et al. report that, as classically assumed, long cells in *S. pombe* are not so much indicative of shape disregulation but are a sign of delayed cell cycle progression through interphase. This is a more valid assumption for Hayles et al. because of the inclusion of essential genes in the screen, since essential genes commonly include cell cycle regulators. In the paper, 66.5% of the deletion mutants annotated as long are deleted for essential genes, leading to a different interpretation than for our non-essential gene screen.

In Graml et al. (2014), we reported a low correlation between our long shape hits and our cell cycle progression hits, indicating that the connection between cell length and the cell cycle is not completely obligate. Continuing from this, our correlation analysis of cell cycle progression hits appeared to suggest a cryptic compensation mechanism, whereby extension or contraction of the interphase state was often linked to an inverse change in the presence of the PAA state within a population. This supports previous findings describing a second cell size checkpoint during the G1/S cell cycle transition (Fantes, 1977; Fantes and Nurse, 1978; Mitchison, 2003).

The many differences between these papers give limited scope for clear comparison. However there are some conclusions to be drawn. The most obvious finding is that agreement between these screens is not total, suggesting that differences in environment and physiological state do indeed have a strong effect on cell shape across different mutants.

What is less immediately apparent is that our cell shape hit list shows a preferential bias for cell shape mutants reported by Hayles et al. Of the non-essential

Graml et al. (2014)		Hayles et al. (2013) phenotypes												
			Misshapen			Long								
Cluster	Phenotype	WT	E	V	Weak V	HP	LP	Br	Round	Stubby	Curved	Small	Skittle	TOTAL
1	Stubby/Skittle	8	0	1	2	0	0	0	3	1	0	1	0	16
2	Stubby	32	0	1	9	7	1	0	7	6	0	2	1	66
3	Bent	6	0	0	0	1	0	0	0	0	2	0	0	9
4	Long	10	1	1	2	23	1	4	1	0	1	0	0	44
5	Long/Stubby	4	0	0	0	2	1	0	0	1	0	0	0	8
	TOTAL	60	1	3	13	33	3	47	11	8	3	3	1	**143**

Table 4.5: Comparing shape phenotypes - Cell shape hits from Graml et al. (2014) categorised by phenotypic cluster (left) compared to cell shape annotations from Hayles et al. (2013) (top).

genes they explored, only 535 (15%) were annotated as cell shape mutants. Of our 143 cell shape mutants, 83 (58%; expected 22) also had cell shape phenotypes according to Hayles et al. Whilst our cell shape hits were dominated by long and stubby cells, Hayles et al. reported mainly long or misshapen strains.

This can be examined more closely using the broad definitions of our cell shape clusters (**Table 4.5**), particularly the two largest clusters (2 & 4; stubby & long). In total, 48% ($^{40}/_{143}$) of our cell shape hits were reported as long by Hayles et al., of which 70% ($^{28}/_{40}$) are found in Cluster 4 and include strong enrichment for chromosome organisation/transcription (13) & DNA damage (6). The fact that cells shape, for these groups of mutants, is conserved in very different experimental conditions is suggestive of a very strong and persistent effect, which in this instance is likely linked to cell growth and the cell cycle.

Few of our cell shape hits were annotated as round, or stubby by Hayles et al., yet the majority of those that were, are found within Cell Shape Cluster 2 ($^{7}/_{11}$ & $^{6}/_{8}$), additionally the class contains two of the three small mutants. Functional analysis of these 15 genes reveals strong enrichment for cell tip localised genes involved in defining the sites of cell growth (5), hence other genes within this group may also play a vital role in defining growth zones and may be of great interest for future research.

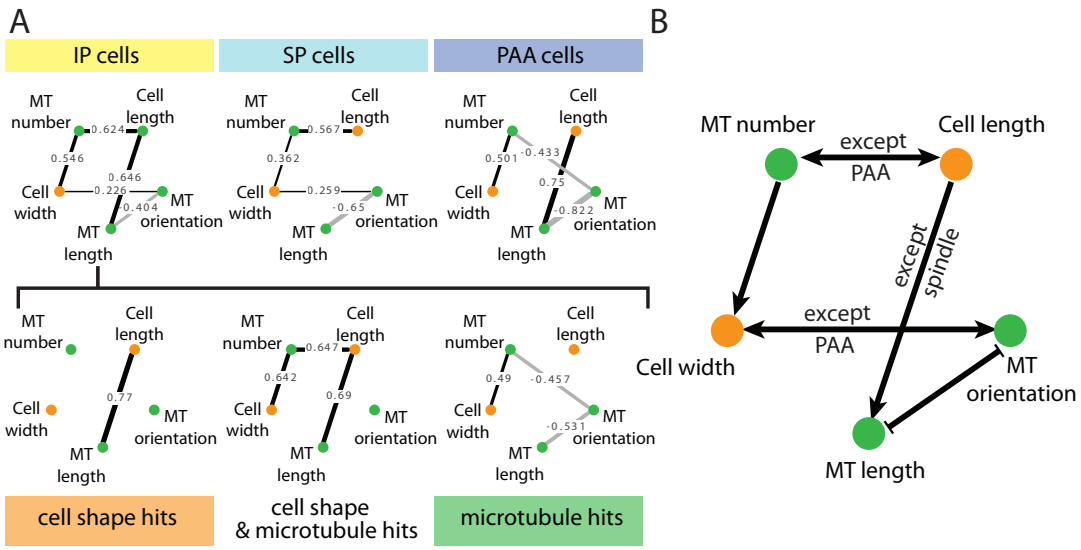

Figure 4.6: Cross-process Bayesian analysis of screening data - The results of Bayesian inference analysis across hits, used to examine correlations between selected cell shape and microtubule features to infer links between different parameters at difference cell cycle stages. **(A)** Direct analysis results sub-selected for different microtubule-determined cell cycle stages (top) or different hit lists (bottom). Edges represent significant inferred links (positive in black; negative in grey) with coefficients shown (edges do not arise directly from correlations). **(B)** A summary plot of all suggested links, directionality inferred manually from hit list based plots in **(A)**. Figure adapted from Graml et al. (2014).

4.4 Analysing effects across cell processes

Previous screens have typically focused on just one aspect of cell biology and have not been able to study separate processes simultaneously. Since we collected results about cell shape, microtubules and cell cycle progression together, it was possible to examine how these processes were related on a systemic level.

Whilst we could not reasonably look for connections between all parameters of these different processes, A. Chessel was able to use network analysis based upon Bayesian inference methods to indicate how a subset of prominent cell shape and microtubule features may be related to each other within cells (Collinet et al., 2010; Yu et al., 2004). From this we can gain a clearer view of how biological and physical effects interact to produce different phenotypes. Further analysis of findings like these may also help us to understand how different groups of genes

are able to indirectly affect seemingly unrelated cell processes.

This analysis focused particularly upon cell length and cell width, in addition to microtubule length, orientation and number. The results are reproduced in **Figure 4.6**. This analysis included specific cell populations, sub-divided by cell cycle stage and different hit lists. Whilst Bayesian analysis is able to suggest correlative links within a network, these connections are not directional, so it is impossible to suggest from this alone which features actually influence, or are influenced by, others. However, examining different sets of hits individually did allow us to make some progress in this area.

The two main directional connections we reported were; cell length affects microtubule length in non-spindle cells and microtubule number alters cell width. In the first case, we noticed that, whilst cell length and microtubule length retain a connection in cell shape hits and in the combined cell shape and microtubule hits, the connection is lost when examining the microtubule hits alone. This suggests that even when mutations affect cell shape, the connection to microtubule length remains, yet when microtubule organisation is perturbed the interaction with cell length is masked, meaning it no longer appears in the network. The converse is true for microtubule number and cell width, which is present in the analysis of both microtubule and cell shape & microtubule hits, but lost in cell shape hits.

4.4.1 Biological validation of Bayesian analysis

To support the results of the Bayesian analysis I performed a series of illustrative experiments to investigate some of the edges in the network and their directionality.

4.4.1.1 Cell length influences microtubule length

In the first of these experiments I focused on the link between cell length and microtubule length. Measurement of these properties in a wild-type cell population alone already suggested a correlation in which the average microtubule length of a cell increased proportionally to approximately 23% of the cell length. By combining information from wild-type cells with data from Cdc2 kinase modified cells

Strain	Cell length	MT length
wild-type	10.79 ± 2.37	5.01 ± 1.21
Cdc2-AS+	26.56 ± 4.86	9.67 ± 2.58
*tip1*Δ	11.58 ± 2.46	2.48 ± 0.78
wild-type	10.60 ± 1.76	4.96 ± 1.07
*klp6*Δ	10.44 ± 1.61	5.20 ± 0.86

Table 4.6: Relating cell length & microtubule length - Population average data (± s.d.) exploring the effects of varying cell length on microtubule length (top) and the reverse effect (bottom).

induced to enter cell cycle arrest with a non-hydrolysable ATP analogue (Cdc2-AS; Cipak et al. (2011)), I was able to examine this relationship over a greater range of cell lengths (**Table 4.6**; top, **Figure 4.7A**).

The Cdc2-AS strain includes an ATP-analogue sensitive kinase. These are well-established, simple kinase protein point mutations (Bishop et al., 2000). The vast majority of kinases act by binding the small molecule ATP and facilitating its hydrolysis to ADP, in the process attaching the removed phosphate to another target molecule, hence causing phosphorylation. Wild-type kinases are generally highly selective for ATP binding, possessing gatekeeper residues that regulate ATP binding.

Mutation of gatekeeper residues alters the ATP binding site, allowing ATP-like molecules to bind. Hence, in a cell with many kinases, only the analogue-sensitive mutant kinase will be able to bind to ATP-analogues, whilst all other kinases will make exclusive use of ATP. By introducing an ATP analogue that cannot be hydrolysed to an ADP analogue, it is possible to selectively prevent the kinase from acting. In the absence of the ATP analogue, the mutant kinase is still functional, hence analogue sensitive kinases are extremely useful for studying kinases that are essential for life. Several analogue-sensitive kinases in *S. pombe*, including Cdc2-AS, were initially reported in Cipak et al. (2011).

Considering cells from wild-type and Cdc2-AS populations together created a cell length range from 6 μm to 37 μm with average microtubule lengths per cell from 2.3 μm to 16.7 μm. On average, over this range, microtubule length increase was proportional to 28% of cell length increase.

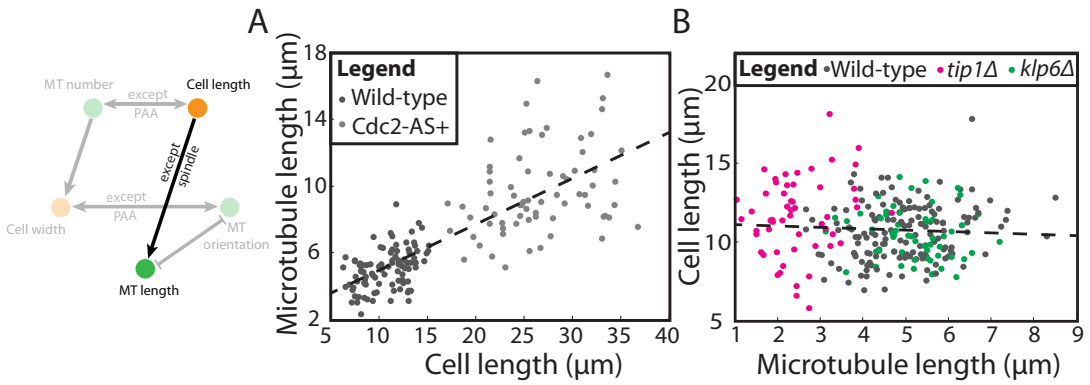

Figure 4.7: Cell length influences microtubule length - **(A)** Inducing elongated cells through cell cycle delay in Cdc2-AS cells treated with a non-hydrolysable ATP analogue (Cdc2-AS+; light grey) correlates with microtubule elongation. **(B)** Different deletion mutants (*tip1*Δ, magenta & *klp6*Δ, green), in which microtubule length is altered, do not show a correlated change in cell length. Note that axes have been drawn to adhere to the convention of displaying the independent variable on the horizontal axis, with the dependent variable vertical. Figure adapted from Graml et al. (2014).

In the converse experiment (**Table 4.6**; bottom, **Figure 4.7B**), deletion mutants for well-studied microtubule regulatory factors *tip1*Δ and *klp6*Δ (Erent et al., 2012; West et al., 2001), which respectively have shorter and longer microtubules, were used. I compared these again to wild-type, cells finding that microtubule length varied between 1.0 μm and 8.5 μm. In this experiment there was no marked shift in cell length with overall correlation showing a 0.09 μm reduction in cell length for every 1 μm increase in average microtubule length.

Logically, this relationship seems reasonable, microtubules are naturally constrained by the cell perimeter and typically undergo catastrophe shortly after contact with the cell ends (Drummond and Cross, 2000; Tran et al., 2001; Brunner and Nurse, 2000). Up to a point, longer cells will permit longer phases of polymerisation from microtubules and hence longer microtubules. Changes in microtubule length may to some extent alter cell length by affecting the delivery of polarity determinants but this link seems to be much less fundamental and may be dispensable.

Strain	MT number	Cell width
*mto1*Δ	0.5 ± 0.8	3.81 ± 0.30
wild-type	3.2 ± 0.8	3.90 ± 0.35
*ase1*Δ	5.6 ± 1.7	4.47 ± 0.32
*rga2*Δ	3.3 ± 1.0	3.39 ± 0.27
wild-type	3.2 ± 0.8	3.88 ± 0.26
*rga4*Δ	3.4 ± 0.8	4.41 ± 0.32

Table 4.7: Relating microtubule number & cell width - Population average data (± s.d.) exploring the effects of varying microtubule bundle number on cell width (top) and the reverse effect (bottom).

4.4.1.2 Microtubule number influences cell width

Bayesian analysis also indicated that varying microtubule number alters cell width. The number of microtubules, as assessed by the screen, refers to the number of microtubule bundles present in each cell. Deletion of gene for the microtubule bundler Ase1 made it possible to increase the number of bundles, whilst deleting gene for the nucleation factor Mto1 reduced the bundle number in most cells. Overall population-averaged microtubule bundle number increased by 5.1 bundles with a corresponding increase in average cell width of 17% (**Table 4.7**; top, **Figure 4.8A**).

Varying cell width made use of deletions in regulators of the rho-type GTPases, *rga4* and *rga2*, which respectively produce wider cells and narrower cells (Villar-Tajadura et al., 2008; Kokkoris et al., 2014; Kelly and Nurse, 2011). Whilst average cell width increased by over 30% between strains, average microtubule bundle number varied by less than 0.2 bundles (**Table 4.7**; bottom, **Figure 4.8B**).

This result is unexpected and may be of interest for further investigation. It is difficult to predict how this relationship may arise biologically. It may be that with a greater number of microtubule bundles there are more contact events between microtubules and the cell periphery that are not at the cell ends, which may lead to widening through incorrect deposition of growth factors. More bundles may also constitute more delivery of polarity factors to the cell ends resulting in cell wall expansion at a higher rate relative to cell growth, leading to cell widening.

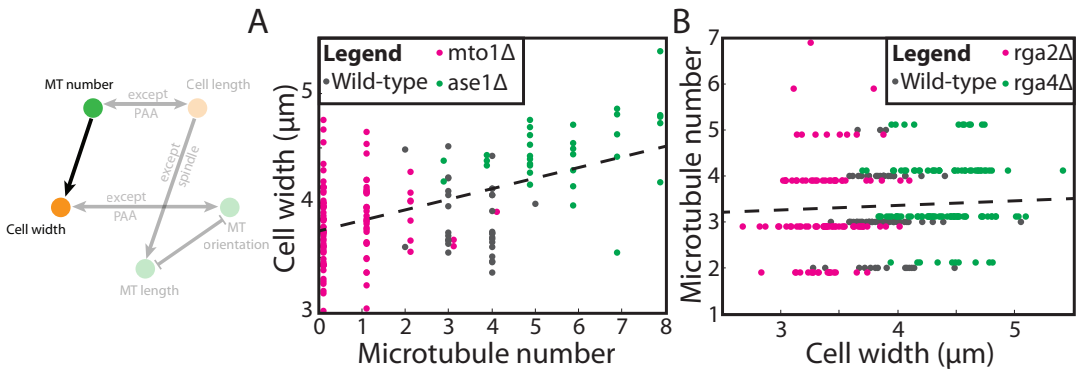

Figure 4.8: Microtubule bundle number influences cell width - **(A)** Effect of varying microtubule bundle number on cell width. Microtubule bundles are reduced relative to wild-type (grey) by *mto1*Δ (magenta) and increased by *ase1*Δ (green). **(B)** Effect of varying cell width on microtubule bundle number, illustrated by *rga2*Δ (magenta; narrow cells) and *rga4*Δ (green; wide cells) relative to wild-type. For clarity, data points from different datasets have been artificially offset along the microtubule number axes. Trendlines were plotted using unadjusted data. Note that axes have been drawn to adhere to the convention of displaying the independent variable on the horizontal axis, with the dependent variable vertical. Figure adapted from Graml et al. (2014).

Without further research it is difficult to offer a precise explanation. However, it is worth noting that Bayesian analysis indicates that, whatever the connection, it is independent of microtubule length and orientation, which may suggest a more subtle effect dependent upon changes in microtubule dynamics.

4.4.1.3 Microtubule number, microtubule length & cell length

Microtubule dynamics suggests an inverse connection between microtubule number and microtubule length, yet no such connection was observed in the Bayesian analysis. Microtubule number was found to influence microtubule length only via cell length and then the relationship was positive. Population averaged data from the genomic screen also showed that a positive relationship did exist (**Figure 4.9A**). By colour coding this correlation based upon cell length A. Chessel was able to show that, for any given average cell length, the relationship between microtubule length and microtubule number was weakly negative and hence the direct connection did not appear in the Bayesian results.

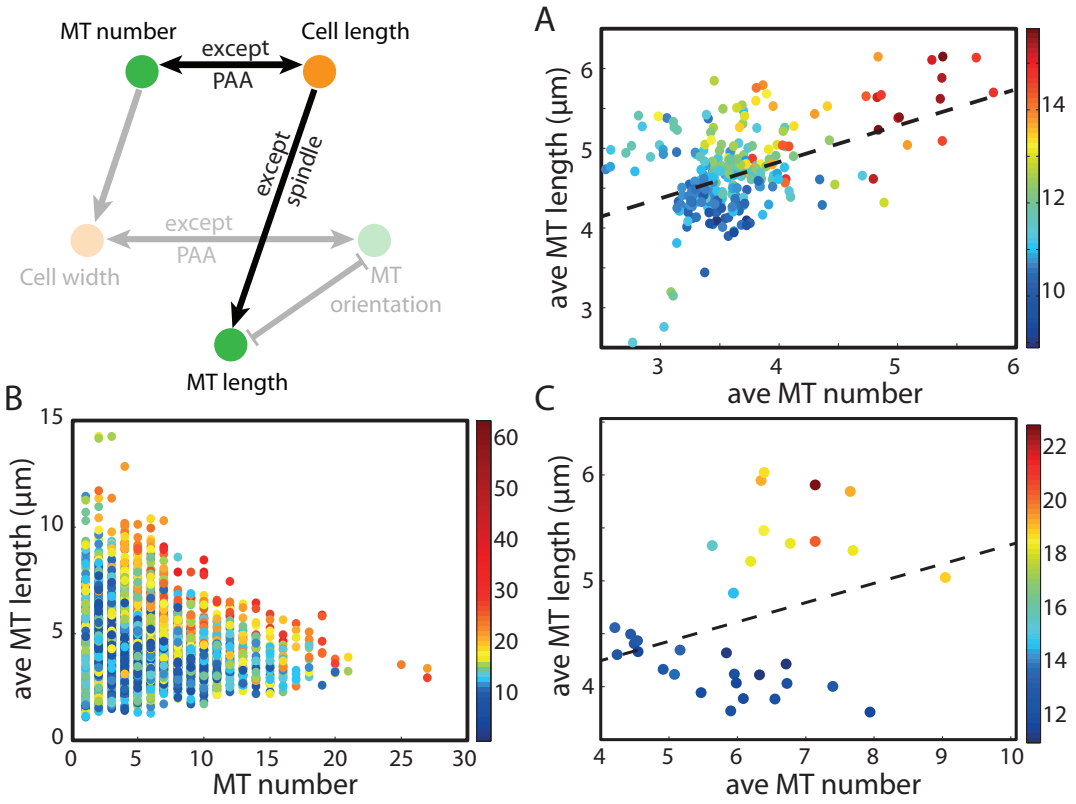

Figure 4.9: Cell length relates microtubule bundle number to microtubule length - Comparing microtubule bundle number to microtubule length with colours representing (average) cell lengths. **(A)** Data from genome-wide screening plotting the average values for each mutant. **(B)** Data from a plate of elongated wild-type cells, plotting cells individually. **(C)** as in **(B)** but using average values for each population. **(A)** & **(C)** adapted from Graml et al. (2014). Coloured bars show cell length values in μm.

I was able to further investigate this relationship by using our automated imaging and computational analysis procedure to study a plate of wild-type cells treated to arrest the cell cycle and adopt different cell lengths. To do this, part of a 96-well plate was prepared and imaged containing wild-type cells and Cdc2-AS cells. Wild-type cells were either untreated or treated with 3 mM HU to arrest the cell cycle and elongate the cells. Cdc2-AS cells were also elongated, by treatment with the non-hydrolysable ATP analogue. This produced cells with a broad range of lengths, microtubule numbers and microtubule lengths.

Using data from individual cells to analyse microtubule length, linked to microtubule number via cell length, showed a negative correlation between the two

factors that was independent of cell length (**Figure 4.9B**). However, these results were dominated by the data from untreated wild-type cells, so appeared more like a dataset already filtered by cell length, and were not representative of the full scale of cell length variation.

Working with A. Chessel, I found that the same was true for the overall screening data. Wild-type-length cells dominated the results when cells were considered individually. Thus biasing the overall trend towards representing a very narrow range of cell lengths. In the plate mentioned in the previous paragraph, and in the whole screen, cells with deviant cell lengths were generally longer than wild-type and so had greater issues with correct computational segmentation. In addition, images of longer cells generally contained fewer usable cells per image, hence their poor representation in these cell-based comparisons.

The Bayesian analysis itself was based upon averaged data from each mutant population. Examining trends in the equivalent averaged data from the plate of elongated cells, provides a more balanced representation of different cell lengths and shows the predicted positive correlation dependent upon cell length (**Figure 4.9C**). Hence, over a range of cell lengths, correlation between microtubule length and number is positive, whilst, over similar cell lengths, the relationship is subtly negative. This is likely related to the availability of tubulin in different cells. A longer cell with a larger cell volume will likely have a bigger pool of tubulin from which to construct microtubules, meaning both more and longer microtubules.

4.5 Online community resources

Overall this screen has produced a large amount of image based data, which cannot possibly be examined and investigated by this lab alone. As such, we have worked to make these results accessible to the wider scientific community through a variety of resources, which will permit others to access both raw and processed data and perform their own data mining activities. In addition to contributing comments on general phenotypes to PomBase, we have also produced two resources specific to this screen, referred to as SYSGRO and Mineotaur.

4.5.1 Annotations in PomBase

PomBase is a curated online resource managed by a consortium including members at the University of Cambridge, European Bioinformatics Institute (EBI) and University College London (UCL). During this screen we worked closely with consortium members Val Wood and Midori Harris to develop compatibility between our screening results and tools available through PomBase.

In particular, PomBase incorporates data from the fission yeast phenotype ontology (FYPO) , spanning both population and cell phenotypes (Harris et al., 2013). Our descriptions of different mutants contributed particularly to the descriptions of cell phenotypes. From 262 hits, I was able to generate 493 FYPO annotations, now included in PomBase alongside the publication of Graml et al. (2014).

FYPO is constrained by the use of specific descriptors of cell shape, microtubule organisation and cell cycle progression, which meant it was not always possible to offer a precise description of our findings for each mutant within the FYPO framework. As such, each hit was first assigned a general FYPO term highlighting an abnormal phenotype for that cell process, these were:

- FYPO: 0002197 – viable vegetative cell with abnormal cell shape
- FYPO: 0003625 – abnormal microtubule cytoskeleton during mitotic interphase
- FYPO: 0002736 – abnormal mitotic cell cycle phase

This represented 364 of the final FYPO annotations submitted. For these terms, every hit was also given an approximate measure of penetrance. Penetrance was assessed based on what proportion of screening rounds a mutant was called as a hit for compared to the number of times it was analysed. In accordance with PomBase guidelines, mutants called as hits in more than 80% of the datasets analysed were assigned ‘High’ penetrance, whilst less than 80% was ‘Medium’ penetrance. PomBase recommends ‘Low’ penetrance for rates below 20% but since we implemented a 35% cut-off (see **Section 3.4.2**) for high-confidence hits, this term was not used.

Further annotation of cell cycle progression hits was determined to be potentially misleading. Existing ontology terms in this area are based upon more typical approaches to studying cell cycle, which do not depend upon microtubule pattern

changes. As such, describing our observed phenotypes on the basis of specific cell cycle stages, whilst demonstrably comparable, may not be wholly accurate.

The full list of genes annotated with specific FYPO terms discussed below can be found in **Appendix Chapter A**.

4.5.1.1 Specific cell shape ontology annotations

I was able to reasonably assign six additional ontology terms to selected cell shape mutants. These were FYPO: 0001492 (elongated cells; 39 hits), FYPO: 0002106 (stubby; 20 hits), FYPO: 0002112 (curved; 2 hits), FYPO: 0002380 (spheroid; 1 hit), FYPO: 0002903 (pear-shaped/skittle; 9 hits), FYPO: 0003595 (S-shaped/kinky; 16 hits). Not all shape hits were assigned one of these additional annotations, some were assigned several. Additional annotations were only added to the most distinct hits in these classes. Whilst the same classifications could have been applied to other mutants, it was decided that a conservative approach was preferable to retain clarity and avoid producing an excessive number of overly detailed annotations. An alternative that was considered, would have been to include precise numerical annotations for every shape mutant, based upon the probabilistic measurements of shape classes.

These additional shape ontology annotations were assigned measures of penetrance and expressivity. Penetrance was indicative of the proportion of cells showing a specific phenotype and expressivity marked the severity of this phenotype in individual cells.

The average probability of a specific cell shape occurring in each mutant population forms an approximately normal distribution around the wild-type. Mutants falling outside the 99% one-tailed confidence interval measured from all non-hit mutants were given a specific cell shape phenotype annotation. Since the results of the classifiers already enriched for specific cell shape mutants relative to wild-type it was possible to use a particularly high threshold for this comparison.

Assessing penetrance and expressivity required examining the cell shape class annotations for all individual cells from a specific mutant. The mutants selected as strongly demonstrating a specific shape class generally showed a bimodal distribution. This is interpreted as some cells having a strong phenotype whilst other remain close to wild-type. The higher the separation between the two modes, the

stronger the phenotype in some cells, and so the higher the value of expressivity assigned ('High', 'Medium' & 'Low'). The proportion of cells in each part of the distribution could then be used to assess penetrance. Again, penetrance was divided into 'High', 'Medium' & 'Low' as described above.

4.5.1.2 Specific microtubule ontology annotations

I made use of three additional microtubule ontology annotations. These were FYPO: 0000233 (long; 17 hits), FYPO: 0002760 (short; 7 hits) and FYPO: 0002401 (more; 18 hits). Again, many hits did not receive additional annotations, whilst some received more than one.

Hits to be annotated were selected as being outside the 95% confidence interval defined for non-hits. Note that no microtubule hits showed a sufficient reduction in average microtubule number to fall below this threshold, hence no hits were annotated with fewer microtubules. Again, expressivity and penetrance were assigned on the basis of distributions from individual cells within each mutant population.

4.5.2 Publishing raw image data – SYSGRO

Figure 4.10: SYSGRO logo - See **Appendix Chapter B** for full views of the SYSGRO online interface. (Logo artwork is my own)

Work by A. Chessel produced an open access online resource at `www.sysgro.org` (Graml et al., 2014) that allows direct access to the analysis results for all screening data, including the results of hit selection procedures for all three cell processes. In addition, this resource displays images for all 262 hits and allows access to them through the open microscopy environment (OME; `www.openmicroscopy.org`) tool OMERO ((Allan et al., 2012)), where it is also possible to visualise the results of image segmentation to identify cells.

As well as providing end-user guidance during development of SYSGRO, I used HTML and CSS to design a visual interface that is appealing and intuitive. This tool is designed to allow biologists, with no technical background, to examine our

results for any gene-deletion they may be interested in. In addition, the website has been designed to permit easy, large-scale data mining for those with the computational skills to make full use of this capability.

4.5.3 Intuitive data mining – Mineotaur

Figure 4.11: Mineotaur logo - See **Appendix Chapter B** for full views of the Mineotaur online interface. (Logo artwork is my own)

Mineotaur (paper under review) was developed by B. Antal as a way to create informative graphics from any subset of screening data using an interactive graphical user interface to access a Neo4j graphical database (`neo4j.com`). This eliminates the need for specialist skills in accessing and querying large databases and provides familiar outputs and summaries of the data collected.

The results of this screen were used to develop and prototype this approach to data mining and presentation (unpublished demo link: `demo.mineotaur.org`), which will be generalised and made available for use with other large datasets through a dedicated website.

The tool can create single feature histograms or scatter plots across two features. Features include all cell shape and microtubule features, as well as cell shape classes. Results can be sub-filtered by microtubule pattern from cell cycle progression analysis and on the basis of different hit types. Results can be queried to highlight or filter specific mutants, show trendlines and produce statistics for distributions. In addition multiple plots can be saved for comparison, plots can be downloaded as images and raw data used in graphs can be downloaded for more detailed investigation. Again, Mineotaur is able to support direct online access to the raw data to support large-scale data mining.

I was involved in guiding the development of Mineotaur and testing its implementation. I have also used Mineotaur in parts of the data processing and analysis presented in this chapter, particularly investigations of feature and shape class distributions, on a gene-by-gene and cell-by-cell level, as part of FYPO assignments for PomBase.

4.6 Life after screening

In this chapter, I have explored the 262 hits identified through multi-process, high-throughput microscopy screening and highlighted many different groups of genes, as well as functional groups, complexes & pathways that provide interesting, unexpected and exciting opportunities for further research. At this stage, however, I chose to focus on just one of these many outcomes to pursue further and to examine in greater detail the biology that had led to certain genes appearing as hits in this screen.

I personally found the presence of many DNA damage response related genes (DDR hits) within both the cell shape and microtubule hit lists very interesting. Throughout the preparation and analysis of this screen, this particular group of genes had repeatedly appeared as consistently selected factors, with conserved phenotypes and a strong propensity for phenotypic clustering. Some previous evidence had suggested a link between microtubules and the DDR (Baschal et al., 2006; Lee et al., 2011; Xie et al., 2011). In addition, we have identified several papers reporting a clinical link between destabilisation of microtubules and more effective cancer treatment (Baumgart et al., 2012; Blagosklonny et al., 2000; Lee et al., 2010). Since cancer cells often have highly unstable genomes and a compromised DDR, this suggested the possibility of a conserved mechanism linking microtubules and DDR, with potential long-term medical benefits (Lord and Ashworth, 2012; Hosoya and Miyagawa, 2014).

As a result, the next chapter will focus specifically on my findings relating to the relationship between the DNA damage response and the microtubule cytoskeleton. But first it seems necessary to offer some background on the DNA damage response, another vital, highly conserved cell process.

4.7 An introduction to the DNA damage response

From a biochemical point of view, life exists to perpetuate DNA. Over time, evolution has produced bigger and more elaborate DNA genomes (Brown, 2002). These genomes are under constant threat from DNA damage. Incorrectly repaired DNA can lead to mutations, changes in the DNA sequence, and result in

dysfunctional genes that may ultimately lead to disease and death (Jackson and Bartek, 2009; Rass et al., 2007; Ciccia and Elledge, 2010). In the endless competition of life, it is the fittest, the most well-adapted, that survives. This necessitates genetic variation to create diversity, but it also demands high-fidelity reproduction and maintenance of DNA to ensure individual survival and reproductive success.

The need to preserve genetic information has provided the evolutionary pressure for organisms – particularly those with large, complex genomes – to develop mechanisms to protect their DNA and ensure its accurate reproduction (Friedberg, 2006). Whilst some of this responsibility lies with the polymerases that facilitate DNA synthesis (Kunkel and Soni, 1988; Kunkel et al., 1987; Goldsby et al., 2001), other mechanisms act, not just to ensure proper DNA duplication during S phase of the cell cycle, but to preserve DNA structure at all times (Friedberg, 2006). These are the DNA repair and signalling mechanisms, collectively referred to as the DNA damage response.

DNA damage can be classified into two groups: Single-stranded DNA (ssDNA) lesions affect just one side of the DNA double helix, leaving the other strand as a perfect template for repair (Caldecott, 2008; Watson, 2008). This typically consists of chemical modification or substitution of one or a few DNA bases. More dramatic effects result when both strands of the DNA helix are damaged, often leading to chromosome breaks, so-called double strand breaks (DSBs) (Khanna and Jackson, 2001; Jackson, 2002). These can take two forms, those where both strands are broken close together with little or no overhanging single-stranded DNA, blunt DSBs. The term DSB is most commonly applied to these lesions. Some other causes of DNA damage can lead to breaks with more extensive ssDNA regions at each of the broken ends, these are particularly linked to failures in DNA replication events (Shrivastav et al., 2008; Roos and Kaina, 2013).

Whilst the response to DNA damage must logically include the induction of mechanisms to directly repair the damage, it is equally important to initiate other responses to ensure suitable time and resources for DNA repair and an appropriate response in the event of continued failure (Roos and Kaina, 2013; Gobbini et al., 2013; Smith et al., 2010) . As such, DNA damage activates the coordinated DDR, which halts the cell cycle, delaying the onset of cell division and has the power to activate permanent cell senescence or cell death (**Figure 4.12**; Roos and Kaina (2013)).

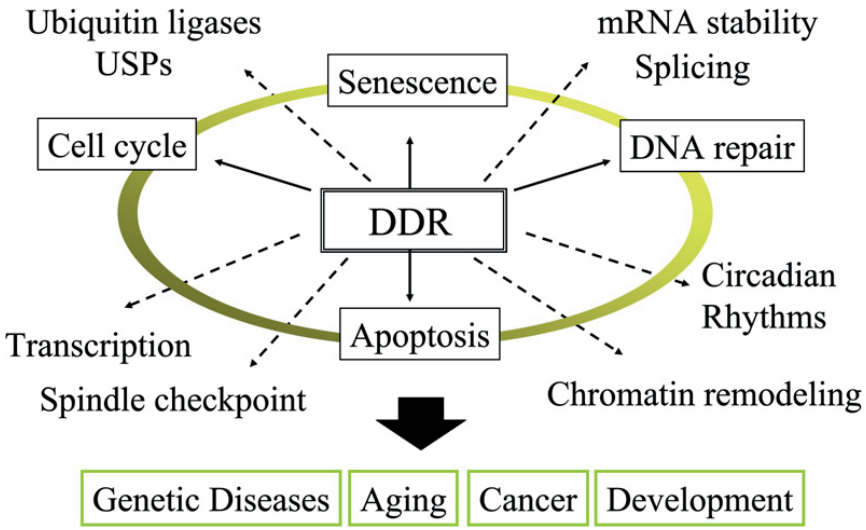

Figure 4.12: Consequences of the DNA damage response - The DNA damage response (DDR) has evolved to coordinate across many key cell processes. It ensures rapid, reliable maintenance of genome integrity through many cycles of cell division. Many processes are affected by the DNA damage response. Figure reproduced from Harper and Elledge (2007). Note: USPs are ubiquitin-sensitive proteases.

There are five main mechanisms of DNA repair in most eukaryotic cells. Three of these, nucleotide excision repair (Kamileri et al., 2012), base excision repair (Wallace, 2014) & mismatch repair (Jiricny, 2013), oversee repair of ssDNA lesions. The two remaining mechanisms, homologous recombination (HR; Li and Heyer (2008)) and non-homologous end joining (NHEJ; Lieber (2010)) resolve DSBs (**Figure 4.15**). Another mechanism, microhomology-mediated end joining (MMEJ), also exists (McVey and Lee, 2008), it has many similarities to NHEJ but requires a limited amount of homology between DNA ends.

4.7.1 Causing DNA damage

DNA molecules are vast and chemically complex. Maintaining perfect DNA, especially within a living cell that is tightly packed with thousands of reactive chemical species, is practically impossible. Many causes of DNA damage have been identified, with combined estimates saying that each human cell may be subject to as many as 1 000 000 DNA insults per day (Lodish, 2008). It has also been estimated that, at steady-state, a mammalian cell may have over 40 000 unre-

solved DNA errors (Helbock et al., 1998; Swenberg et al., 2011; Nakamura and Swenberg, 1999).

Damage has two primary sources, exogenous and endogenous (Friedberg et al., 2004; Helleday et al., 2014). Exogenous sources of DNA damage can include electromagnetic radiation, mutagenic chemicals and viruses and can originate from natural or man-made sources. Since these causes originate outside the body, they can be affected by habitats and lifestyle, but cannot be completely avoided (Doll and Peto, 1981). Endogenous DNA damage is the result of events within a living cell, and is completely unavoidable (Epe, 2002). Common sources include DNA replication errors and the production of reactive oxygen species as part of essential metabolic processes. Mitochondrial DNA is distinctly more prone to mutation than nuclear DNA due to its more direct exposure to the oxidative respiration pathway, a major source of reactive species (Yakes and Van Houten, 1997; Richter et al., 1988).

Whilst most of these factors will not immediately cause changes in the DNA sequence and can permit a cell to remain functional, issues arise when these cells undergo division in the presence of unresolved DNA damage (Ganem and Pellman, 2012; Lodish, 2008). This may also explain the tendency for complex organisms to maintain only a small number of well-protected dividing stem cells in their mature stages, rather than permit any cell the capacity for continued cell division.

Damaged DNA bases are prone to being mis-read by the DNA replication machinery and damage in the sugar-phosphate DNA backbone can result in DSBs after DNA replication. Unresolved DNA damage can lead to a number of different illnesses, although cell death and immune system mechanisms may still act to prevent this (Roos and Kaina, 2013; Nowsheen and Yang, 2012). Many age-related diseases, particularly cancer, start with the accumulation of damaged DNA (Harper and Elledge, 2007; Lord and Ashworth, 2012; Bartek and Lukas, 2001). The older we get the greater the chance that errors in DNA can occur and go unresolved, hence the typical linkage to old age.

All forms of DNA damage typically lead to cell cycle arrest, preventing the replication and division of damaged DNA. Damage to DNA can lead to arrest through initiation of cell cycle checkpoints. Checkpoints act to arresting cell cycling and promote DNA repair (see **Section 1.6.3**).

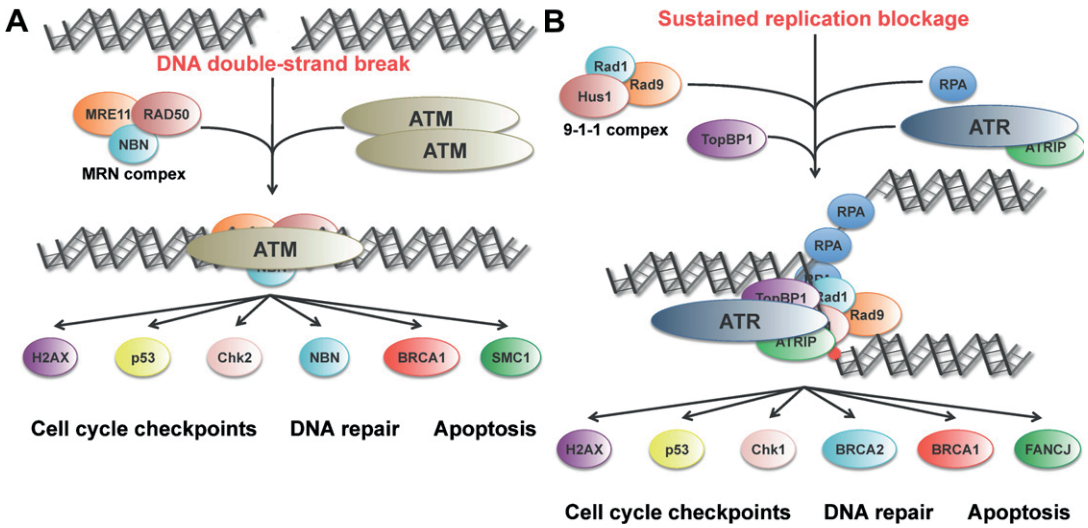

Figure 4.13: Responses to different DSBs - The factors involved in initiating a DNA damage response following different types of DSB. **(A)** Blunt DSBs are directly compatible with MRN binding, leading to ATM activation. **(B)** Replication blockage leaves DNA ends with exposed ssDNA, this binds RPA-like proteins and recruits ATR via ATRIP. Figure from Roos and Kaina (2013).

Checkpoints can be activated in response to DNA damage or failed DNA replication (Smith et al., 2010; Gobbini et al., 2013). The direct response to DNA damage is activated in response to a wide array of insults, particularly from radiation exposure or chemical damage, which can directly be detected as damage without involving DNA replication. Other forms of DNA damage are only discovered during DNA replication, where they may cause polymerase stalling, this can include thymidine dimers from UV exposure, or breaks in one strand of DNA. This is only identified when the DNA fails to replicate correctly.

4.7.2 Initiating the DNA damage response

DSBs are typically detected by DNA end binding complexes MRN (Mre11-Rad50-Nbs1 in metazoa and *S. pombe*, called MRX, Mre11-Rad50-Xrs2 in *S. cerevisiae*; Lisby et al. (2004)) and Ku (a Ku70/Ku80 heterodimer; Lisby et al. (2004)). It is thought that these complexes can only bind DNA by threading onto exposed DNA ends, which are only apparent at DSBs (**Figure 4.13A**; Lamarche et al. (2010)).

Although Ku is typically present during all DSB repair pathways, and may have a role in associating DNA ends prior to religation, it is only known to be functionally significant in NHEJ events where it acts to recruit the catalytic subunit of the DNA-dependent protein kinase (DNA-PK^{cs}; Featherstone and Jackson (1999)).

MRN has roles in bridging between DNA ends and provides a platform for other DNA damage response factors (Lamarche et al., 2010). In particular, MRN allows the recruiting of the key DNA damage checkpoint kinase ataxia telangiectasia mutated (ATM; Tel1 in *S. pombe*), which acts in concert with a secondary kinase CHK2 (Cds1 in *S. pombe*) to phosphorylate and activate a wide array of DNA repair and cell cycle arrest factors (Smith et al., 2010; Gobbini et al., 2013). In addition ATM and CHK2 affect chromatin modification and arrangement, sustain DNA damage response signalling and permit repair factors to access the DNA. One of the key chromatin modifications, often used as a marker for sites of DNA damage, is the phosphorylation of the H2A histone variant H2AX, referred to as (γH2AX; Rogakou et al. (1998); Cortez et al. (1999)). Whilst yeast homologues of H2AX are unknown, a similar phosphorylation event is reported to occur on the standard histone H2A proteins (Hta1 & Hta2 in *S. pombe*; Nakamura et al. (2004)).

MRN also acts more specifically in HR, recruiting CtIP (Ctp1 in *S. pombe*). Mre11 and CtIP, both nucleases, promote resection of the DNA ends to form long 3′ ssDNA overhangs (Limbo et al., 2007). These ends also occur as a result of failed DNA replication and are ideal templates for HR.

In cells, unprotected ssDNA is extremely prone to damage as part of the defence mechanisms that exist against viral invasion. Hence, ssDNA on the ends of chromosomes must be protected. At broken DNA ends, ssDNA is rapidly sequestered by replication protein A (RPA), which also binds to ssDNA during DNA replication (**Figure 4.13B**; Wold (1997); Zou and Elledge (2003)). The interaction of many RPA proteins with ssDNA forms a nucleoprotein filament, which promotes HR.

The RPA filament provides an ideal platform for the recruitment of the ATR-ATRIP complex (ATM-related kinase & ATR interacting protein; Rad3 and Rad26 in *S. pombe*; Zou and Elledge (2003)). ATR has similar roles to ATM and typically acts in concert with CHK1 (Chk1 in *S. pombe*; Gobbini et al. (2013); Smith et al. (2010)). Optimal CHK1 activation also requires the DNA-binding complex RAD9-RAD1-HUS1 (Rad9-Rad1-Hus1 in *S. pombe*), which recruits Claspin (Mrc1 in *S. pombe*) and TopBP1 (Rad4 in *S. pombe*; (Smith et al., 2010)).

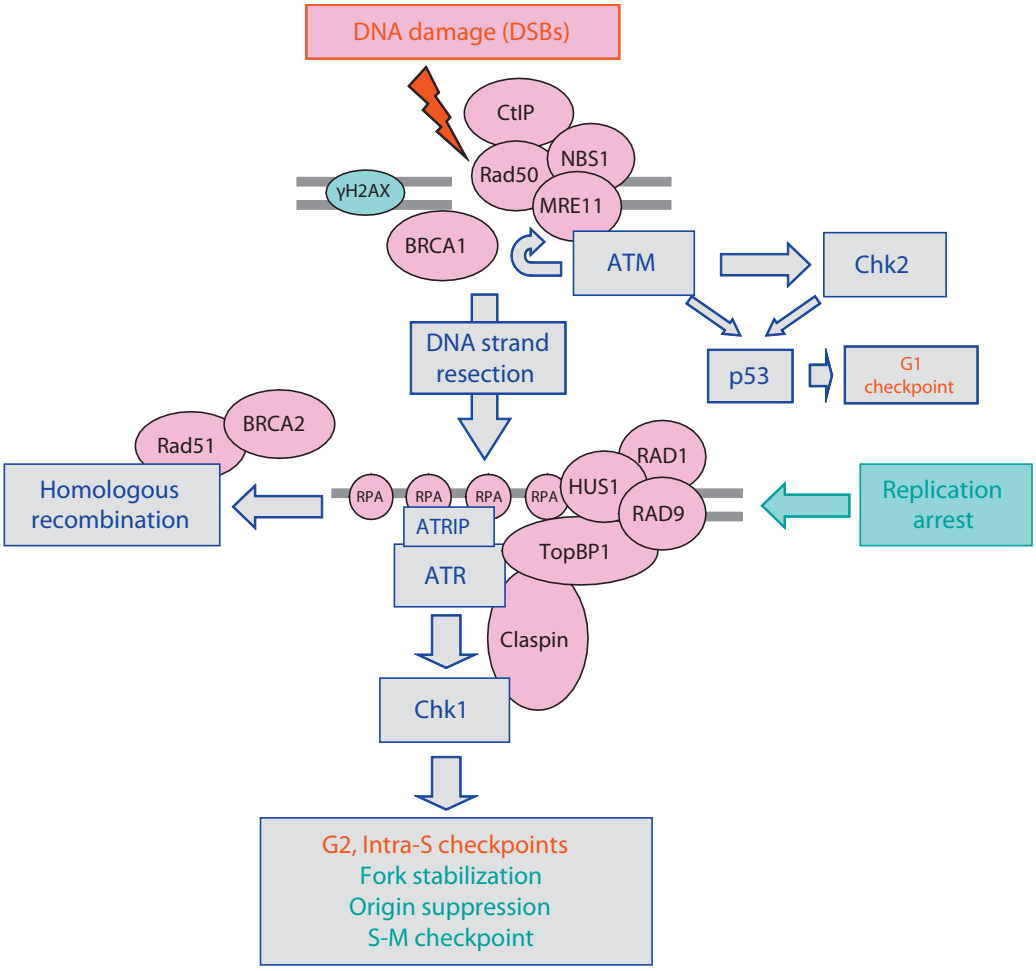

Figure 4.14: DNA end processing to permit homologous recombination - Although blunt ended DSBs can be resolved through NHEJ, they can also be processed by Mre11 and CtIP to give ends suitable for HR. In the process, the DNA damage signalling shifts from being mediated by ATM-CHK2 to ATR-CHK1. Figure from Smith et al. (2010).

It should be noted, that the above describes the stereotyped view of this network in mammalian cells. There is evidence for extensive cross-talk and interconversion between the early stages of the two DNA damage responses, with both ATM and ATR becoming active in the event of enough severe or prolonged damage (Gobbini et al., 2013). In particular, at certain stages of the cell cycle, it can be preferable to repair DSBs using HR rather than NHEJ, favouring DNA end resection and ATR-mediated signalling (**Figure 4.14**; Langerak and Russell (2011)). HR is less error-prone than NHEJ, so preferable in S/G2 phases when a homolo-

gous DNA template exists to facilitate repair by HR. Conversely, NHEJ is generally favoured in G1.

Whilst ATM, ATR, CHK1 and CHK2 are all conserved across species, their roles and interactions seem to differ (Rhind and Russell, 2000). In both *S. pombe* and *S. cerevisiae* responses to both DNA damage and replication failure are primarily thought to be coordinated by the ATR homologues, which demonstrate variable interaction with the CHK1 and CHK2 homologues (Limbo et al., 2011). In *S. pombe*, it seems that replication issues, and later cell cycle phases may favour interaction of Rad3 with Cds1, whilst Chk1 is primarily employed in the early cell cycle (Rhind and Russell, 2000).

In short, damage to DNA, whether direct or via DNA replication, leads to activation of the four checkpoint kinases (Smith et al., 2010). These kinases activate the DNA damage response pathways, which remodel chromatin to allow access to damaged DNA, arrest the cell cycle to prevent propagation of damaged DNA and activate & recruit DNA repair factors to bring about the repair of DNA. Dysfunction in elements of these pathways have two main possible outcomes, a failure to delay cell division, resulting in more extensive DNA damage, probably leading to cell death, or alternatively a prolonged cell cycle delay due to reduced efficiency of the DNA damage response.

4.7.3 Arresting the cell cycle

Arresting the cell cycle prevents the cell from initiating division until genome duplication is complete and all damage lesions have been resolved (Elledge, 1996; Kastan and Bartek, 2004; Lukas et al., 2004). It is much easier to resolve damage prior to division, as cell division can convert some DNA lesions into more drastic DNA damage and makes effective repair more difficult, due to the reduction of DNA content. In some cases, where repair is incomplete or incorrect, a chromosome may be torn between two cells as they divide, preventing cells from receiving a complete genome compliment. There can be many outcomes from this situation, all resulting in genome damage or cell death.

Primarily, the arrest of the cell cycle occurs at the G2/M transition (Lobrich and Jeggo, 2007), immediately before commitment to cell division, although some organisms are able to initiate a G1/S arrest mediated by CHK1/CHK2 activating

the stress-response coordinator protein, p53 (Lin et al., 1992; Rhind and Russell, 2000). The G2/M arrest also responds to the checkpoint kinases, which inhibit the activity of CDC25 (Cdc25 in *S. pombe*; Furnari et al. (1999); Raleigh and O'Connell (2000)).

CDC25 is a phosphatase enzyme that removes inhibitory phosphorylations from the key CDK1/cyclinB (Cdc2/Cdc13 in *S. pombe*) complex that drives entry into mitotic M phase (Coleman and Dunphy, 1994). DNA damage triggering the DNA damage response leads to cell cycle arrest at G2/M by inhibiting CDC25, maintaining inhibition of CDK1 and prolonging the G2 cell cycle phase. Additionally, in *S. pombe* the checkpoint kinases can activate the WEE1-like kinase, Mik1, which functionally opposes CDC25 and hence further prevents the G2-M transition.

4.7.4 Repairing DSBs by HR and NHEJ

The two major DSB repair mechanisms have been particularly closely studied and relate to many of the DDR hits identified in the screen, as such they will be the focus of this section. In addition, it should be noted that these mechanisms have also been co-opted to other specific roles within organisms. HR plays a part in the resolution of chiasmata during meiotic cell division (Longhese et al., 2009), whilst NHEJ is important in the immune system for generating antibody diversity through V(D)J recombination (Jung and Alt, 2004).

Whilst NHEJ requires little pre-processing of DSBs, HR requires ssDNA at the broken ends and the presence of a sister chromosome or chromatid to use as a repair template (Smith et al., 2010). Hence HR is well-suited to the resolution of collapsed DNA replication forks, whilst NHEJ can act more rapidly to repair blunt DSBs.

DNA repair through NHEJ is a highly error-prone but versatile means to repair DSBs, as it requires very little to successfully repair DNA. NHEJ has the great benefit of being able to repair any DSB without the need for any overlapping homology between ends, or the use of a homologous template strand. However, this means that it will randomly rejoin any chromosome ends, without any consideration for the results (Betermier et al., 2014; Ferguson and Alt, 2001).

Repairs by NHEJ are excellent for maintaining overall genome integrity, but can have unexpected side-effects. At the very least, the suite of polymerases (Pols

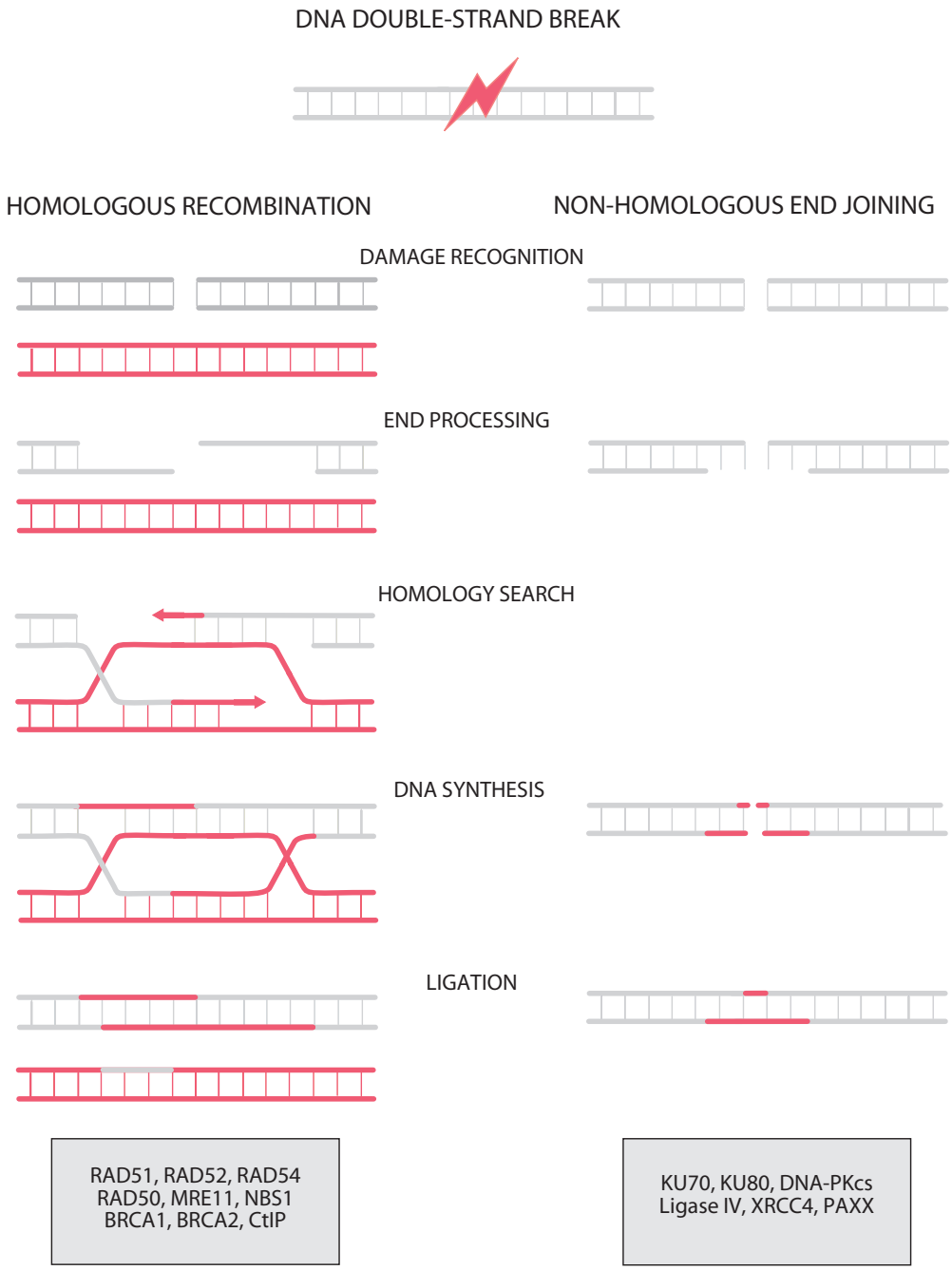

Figure 4.15: DNA repair mechanisms from chromosome breaks - An overview of the two main DNA repair mechanisms for chromosome breaks. Homologous recombination (HR; left), requires extensive end processing and uses a homologous chromosome or sister chromatid (red) as a template for re-sysnthesis across a chromosome break. This mechanism is stereotypically employed at sites of DNA replication blockage, where DNA ends are already compatible with recombination. Error rate is low. Non-homologous end joining (NHEJ; right) uses no template and is prone to errors. Key factors involved in each process are given in grey boxes below. Figure adapted from Houtgraaf et al. (2006), PAXX added in recognition of work in Ochi et al. (2015).

λ & μ) and putative nucleases recruited by Ku to remodel the DNA ends and make them compatible for religation, are likely to remove or add additional base pairs, disrupting regulatory sites or potentially greatly disrupting gene coding sequences (Alberts, 2002). At the very worst, the wrong chromosome ends can become joined together, leading to massive genome rearrangements, chromosomal translocations and gene fusions, which are direct causative agents of cancer (Ferguson and Alt, 2001). The final religation of DNA ends is performed by a protein complex containing DNA Ligase IV (Lig4 in *S. pombe*; Wilson et al. (1997)).

Repair by HR is somewhat more complex. Following resection of the DNA ends by MRN and CtIP, where necessary, additional factors EXO1 & DNA2 (Exo1 & Dna2 in *S. pombe*) are recruited to extend the regions of ssDNA around the DSB (Rhind and Russell, 2000; Li and Heyer, 2008; Jackson, 2002). The 3′ ssDNA overhangs, entwined with RPA polymers are the key to HR. RPA permits interaction with a complex consisting of several RecA-family recombinase factors, primarily RAD51 (Rad51 in *S. pombe*, also Rad55 & Rad57), the mediator protein RAD52 (Rad52 in *S. pombe*) and DNA remodellers RAD54 & RDH54 (Rad54 & Rdh54 in *S. pombe*; Holthausen et al. (2010)).

These proteins work together to identify and separate the two DNA strands of a homologous chromosome region on an intact sister chromatid or homologous chromosome (in diploid organisms), into which a 3′ overhang region of the broken DNA helix can be introduced (Haber et al., 2004; Symington, 2005). This process is known as strand invasion. The broken end is matched to complimentary sequences in the homologue and this is used to synthesise new sequence to replace and repair the damaged regions.

Different models exist to explain how the second DNA strand is then repaired, however a key step is typically the resolution of strand crossovers between the two DNA helices. These crossover regions, called Holliday junctions, are repaired by protein complexes called resolvases that cut and religate crossovers to give fully repaired DNA helices (Ip et al., 2008). How these junctions are repaired can vary and this is a key aspect of chiasmata resolution in meiosis. The EME1-MUS81 complex (Eme1-Mus81 in *S. pombe*) is thought to be responsible for Holliday junction resolution (Dehe et al., 2013).

DNA repair by NHEJ has been found to be the predominant DNA repair mechanism in mammalian cells (Sonoda et al., 2006; Liang et al., 1998). It is likely that, in addition to a long G1 phase, the larger genome, larger nuclear size, greater

chromosome number and more complex nuclear architecture, slow the process of HR by increasing the difficulty of finding an appropriate homologous template. Hence the potential for DNA errors arising from NHEJ is outweighed by the deleterious effects of waiting for HR. By contrast, DNA repair in yeasts (both *S. pombe* & *S. cerevisiae*) seems to be typically dominated by HR (Sonoda et al., 2006; Aylon and Kupiec, 2004), even though they often propagate as haploid organisms and so lack any possible DNA templates for HR in the G1 phase of the cell cycle. Notably, in *S. pombe*, this may go some way to explaining the contraction of the G1 cell cycle phase in favour of an extended G2 phase where HR once again becomes possible. The prominence of HR in these cells may also go some way to explaining the number of HR specific factors detected by the screen.

4.7.5 Senescence & cell death

Some DNA damage just cannot be repaired. After a cell enters cell cycle arrest it is given only a limited time to resume cycling or other mechanisms become activated to bring about more permanent solutions (Roos and Kaina, 2013). Cellular senescence puts a cell into a physiological state that means it can no longer undergo division. Although this state is common in multi-cellular organisms – as a means of limiting the potential for cancer development – it is also thought to occur in ageing unicellular organisms (Powell et al., 2000; Henderson and Gottschling, 2008; Stephens, 2005). The alternative, cell death by apoptosis, also called cell suicide, is a more dramatic solution to persistent DNA damage. In particular, in multi-cellular organisms, apoptosis prevents cells from losing cell cycle control and becoming harmful (Roos and Kaina, 2013).

In mammalian cells, commitment to cell cycle exit is thought to be primarily controlled by p53, which accumulates over time due to inhibition of normal degradation processes (Hofseth et al., 2004). The outcome is also influenced by other stress factors within the cells, which typically activate signalling networks that converge on p53. Whilst p53 is thought to be absent in yeasts, apoptotic responses have been observed (Burhans et al., 2003).

4.8 DNA damage response hits

This overview of the canonical processes involved in resolving DNA breaks has already included several of the 22 DDR hits. This includes elements of the MRN complex (Mre11, Rad50), ssDNA binding proteins (Rad51, Rad55, Rad57) and repair proteins, including the endonuclease Ctp1, helicases (Rdh54, Rrp2, Srs2) and the primase-associated factor Mcl1. More surprisingly, the list also includes the ATM kinase, Tel1, which has some reported links to DNA repair in *S. pombe*. Less directly, hits also include transcription regulators and histone modifiers (Ccq1, Gcn5, Png1, Set1). Several factors also control protein activity through post-translational modification (Ppk26, Pof3) and mRNA/protein turnover (Cdt2, Cid12, Csn1, Csn2).

Notably, a number of these hits (e.g. Rad51, Rad55, Rad57) are known to be specifically involved in mediating repair by homologous recombination. Although, as already mentioned, this is thought to be the preferred repair mechanism in *S. pombe*, these hits may not be indicative of a phenotypic response to HR specifically. The nature of these hits suggests a reduced ability to repair DNA damage, leading to increased background levels of damage in the population. This is supported by an increased sensitivity to DNA damaging agents in most ($^{18}/_{22}$) of these hits, including $^{16}/_{22}$ sensitive to hydroxyurea (HU) (Hayles et al., 2013).

5 Investigation of DNA Damage Hits

"Great men are forged in fire. It is the privilege of lesser men to light the flame."
—THE WAR DOCTOR (*The Day of the Doctor*, 2013)

The DDR hits represented a relatively large group of hits, that cluster phenotypically, span both cell shape and microtubules and were identified as hits stably across many screening rounds. As covered in the cluster analysis sections of **Chapter 4**, whilst elongation of cells may have been predicted in these mutants, alterations in microtubule organisation were unexpected.

5.1 DDR hits elongate some cells and microtubules

In total 22 genes with links to the DNA damage response were detected by our screen, of which 13 were hits for both cell shape and microtubule organisation.

Initial observation of screening images depicting DDR hits, showed that a proportion of cells are longer than wild-type in all populations. I also noticed that these cells typically had longer microtubules, many of which made contact with the cortex at the cell ends (**Figure 5.1**). This is by contrast to wild-type cells where microtubules will typically contact the cell ends but then rapidly depolymerise and hence only one microtubule bundle is typically seen in contact with the cell tips at any one time (Tischer et al., 2009; Sagolla et al., 2003).

This observation was reinforced by the cluster analysis (**Table 5.1**), where the majority ($^{9}/_{16}$; 56%) of DDR hits fell into Cell Shape Cluster 4 (elongated cells). These hits constituted ⅕ (20%) of the 44 genes in this cluster.

Less obviously, some DDR hits occurred in Cell Shape Cluster 2 ($^{6}/_{16}$; 38%) encompassing 9% of the 66 gene cluster. These hits primarily show enrichment in stubby cells, which are disproportionately wide for their length. Three of these

Gene Name	Genome ID	*H.s.* Homologue	Cell Shape		Microtubule	
			Cluster	Detection Rate	Cluster	Detection Rate
ccq1	*SPCC188.07*		4	8/8 (100%)	1	6/6 (100%)
cdt2	*SPAC17H9.19c*	DTL	4	5/5 (100%)	1	4/4 (100%)
cid12	*SPCC663.12*			1/14 (7%)	4	5/12 (42%)
csn1	*SPBC215.03c*	GPS1	2	8/8 (100%)	1	5/7 (71%)
csn2	*SPAPB17E12.04c*	COPS2	2	6/8 (75%)	7	5/7 (71%)
ctp1	*SPCC338.08*	RBBP1	4	4/8 (50%)	1	5/8 (63%)
gcn5	*SPAC1952.05*	KAT2A/B		3/10 (30%)	1	5/10 (50%)
mcl1	*SPAPB1E7.02c*	WDHD1	4	7/7 (100%)	1	6/6 (100%)
mre11	*SPAC13C5.07*	MRE11	4	8/8 (100%)	1	5/7 (71%)
png1	*SPAC3G9.08*	ING4	2	7/7 (100%)	5	2/4 (50%)
pof3	*SPCC338.16*	STIP1	4	9/10 (100%)	1	7/10 (70%)
ppk26	*SPBC336.14c*	PAN3	2	4/6 (67%)		1/5 (20%)
rad50	*SPAC1556.01c*	RAD50	4	7/8 (88%)	1	5/6 (83%)
rad51	*SPAC644.14c*	RAD51		4/12 (33%)	1	4/9 (44%)
rad55	*SPAC3C7.03c*	RAD51B/D	4	8/10 (80%)	1	10/10 (100%)
rad57	*SPAC20H4.07*	XRCC3	2	8/9 (89%)		2/8 (25%)
rdh54	*SPAC22F3.03c*	RAD54B		0/7 (0%)	4	6/6 (100%)
rrp2	*SPBC23E6.02*	HLTF		1/5 (20%)	5	2/5 (40%)
set1	*SPCC306.04c*	SETD1A/B	4	6/8 (75%)	8	5/8 (63%)
srs2	*SPAC4H3.05*	SRS2	5	4/10 (40%)		3/10 (30%)
tel1	*SPCC23B6.03c*	ATM		1/9 (11%)	3	3/8 (38%)
ubi1	*SPAC11G7.04*	UBA52	2	4/7 (57%)	7	4/6 (67%)

Table 5.1: DDR hits - List of all genes proposed as high-confidence DDR hits for cell shape and/or microtubules, showing how the genes clustered and the frequency of detection across screening rounds. Note that detection rates for these mutants are often high and genes primarily fall into Cell Shape Cluster 4 ($^{9}/_{16}$) or 2 ($^{6}/_{16}$) and Microtubule Cluster 1 ($^{11}/_{19}$). If a cluster number is not shown then that gene is not a hit for that process. Non-hit detection rates are shown for completeness.

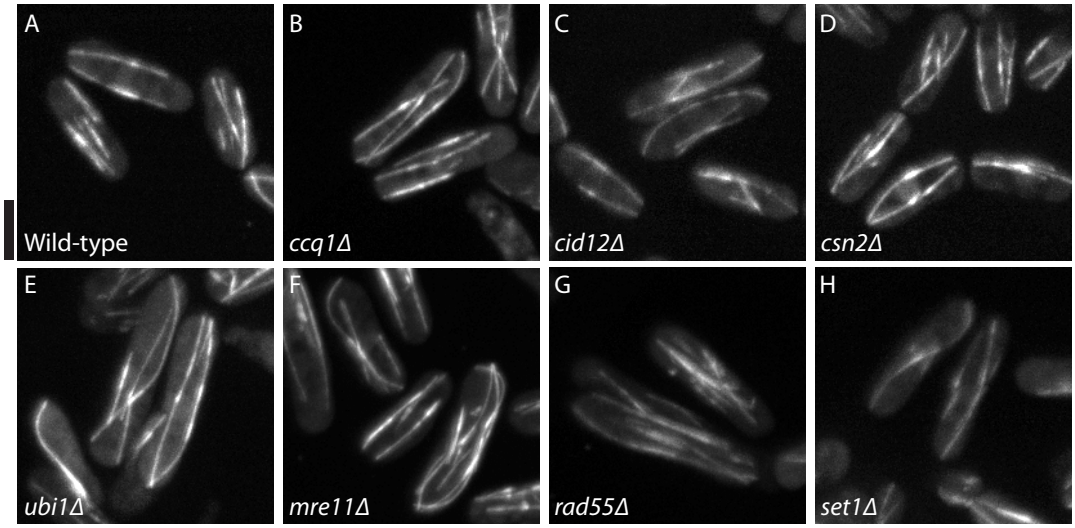

Figure 5.1: Example DDR hit microtubule phenotypes - A collection of images from high-throughput screening showing the GFP-labelled microtubule arrays of selected deletion mutants reported to affect the DNA damage response.

hits; *png1*, *csn1* and *ubi1* cluster particularly closely and show a secondary enrichment for elongated cells, which is not shared with the majority of hits in the cluster.

Most ($^{11}/_{19}$; 58%) DDR hits with microtubule phenotypes are found within Microtubule Cluster 1, (longer, more variable microtubule length). Here, DNA damage hits represent 22% of the 50 genes within the cluster. Within the cluster, seven of the genes (*ccq1*, *ctp1*, *mcl1*, *mre11*, *rad50*, *rad51*, *rad55*) are directly hierarchically linked, suggesting particularly strong phenotypic similarity.

There was also a high overlap between the DNA damage genes in these major clusters. Eight genes in Cell Shape Cluster 4 were also in Microtubule Cluster 1.

Intuitively, an elongated microtubule phenotype suggests a mechanism which stabilises microtubules and maybe promotes assembly, or at the very least suppresses catastrophe. However, because the precise form of the microtubule array is the product of dynamic equilibrium – a series of stochastic events – there are other potential explanations for this observed phenotype, warranting a more detailed investigation of the effect.

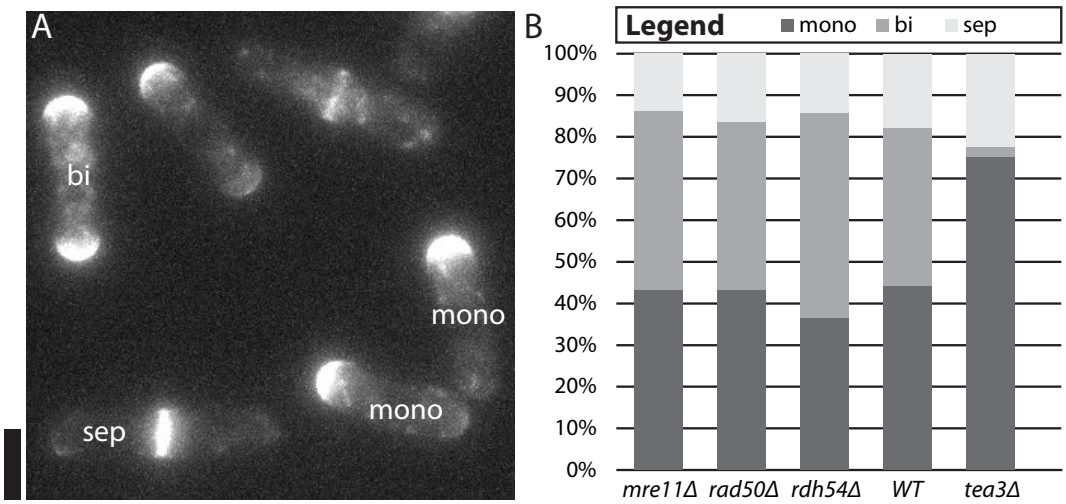

Figure 5.2: DNA damage and cell polarity - **(A)** Example RFP-Bgs4 localisation in cells undergoing monopolar growth (mono; pre-NETO) bipolar growth (bi; post-NETO) and septation (sep). **(B)** Bar plots comparing the population average polarity states of different hits related to DNA damage with wild-type and positive control *tea3*Δ populations.

5.2 DDR hits do not have altered cell polarity

A paper by Kume et al. (2011) provided a potential connection between the DNA replication checkpoint and microtubule stabilisation in *S. pombe*. The paper reported that activation the checkpoint kinase Cds1 (CHK2 homologue), by overexpression, polymerase deletion or HU treatment, induces NETO delay mediated by calcineurin and dephosphorylation of Tip1 (CLIP170 homologue). The regulation of Tip1 led to reduced microtubule dynamic activity and unusual accumulation of the cell tip localised polarity factor Tea1. Since Tip1 deletion is known to have a destabilising effect on microtubules, it may be a good candidate to explain the altered microtubule organisation in our hits.

If this response were active in the DNA damage-related hits, we would expect to see a similar delay in the NETO cell polarity transition in DDR hits, which are defective in DNA repair. This would be reflected in an increased proportion of monopolar cells in the mutant populations. I assessed the polarity of different mutants by examining the localisation of RFP-labelled β-glucan synthase (RFP-Bgs4), an enzyme involved in cell wall synthesis at areas of growth that can be used as a live reporter of cell growth (Dodgson et al., 2010).

In wild-type cells, an average 44% of cells were found to be monopolar (**Figure 5.2**). Deletion of the *tea3* gene (*tea3*Δ) is known to strongly delay the NETO transition leading to 75% monopolarity (Arellano et al., 2002). Examination of three DDR hits *mre11*Δ, *rad50*Δ and *rdh54*Δ showed no deviation from wild-type (monopolarity 43.3%, 43.2% & 36.6% respectively).

These findings suggested the pathway reported by Kume et al. (2011) is not likely to be responsible for the phenotypes observed in our hits.

5.3 Inducing a DNA damage response

5.3.1 Hydroxyurea treatment causes microtubule elongation

Since this group of hits are all involved in the DDR, I decided to investigate whether a similar phenotype could be induced by causing DNA repair in wild-type cells.

Typical DNA damage experiments in this organism have commonly used 10-15 mM HU to induce DNA damage (Tischer et al., 2009; Drummond and Cross, 2000; Selvanathan et al., 2010). HU induces DNA damage by preventing the production of deoxynucleotide triphosphates (dNTPs). HU targets ribonucleotide reductase, which is necessary for the reduction reaction that forms dNTPs from NTPs (Elford, 1968). DNA polymerases require dNTPs to construct DNA and so during the subsequent DNA synthesis phase they rapidly exhaust the existing dNTP pool and are unable to complete genome duplication. The collapse of incomplete DNA replication forks creates a variety of DNA lesions and initiates the DDR.

I performed initial experiments using 3 mM or 15 mM doses of HU to explore the influence of different levels of DNA damage. Cells were treated for nine hours before imaging, with a new dose of HU added after every three hours to counteract adaptation to the drug (Parker et al., 1997). As expected, microtubules appear to became longer upon cell treatment with HU (**Figure 5.3A-C**). Conspicuously, at higher doses, many microtubules could be seen to become disproportionately elongated, contacting or curving around the cell ends (**Figure 5.3C**).

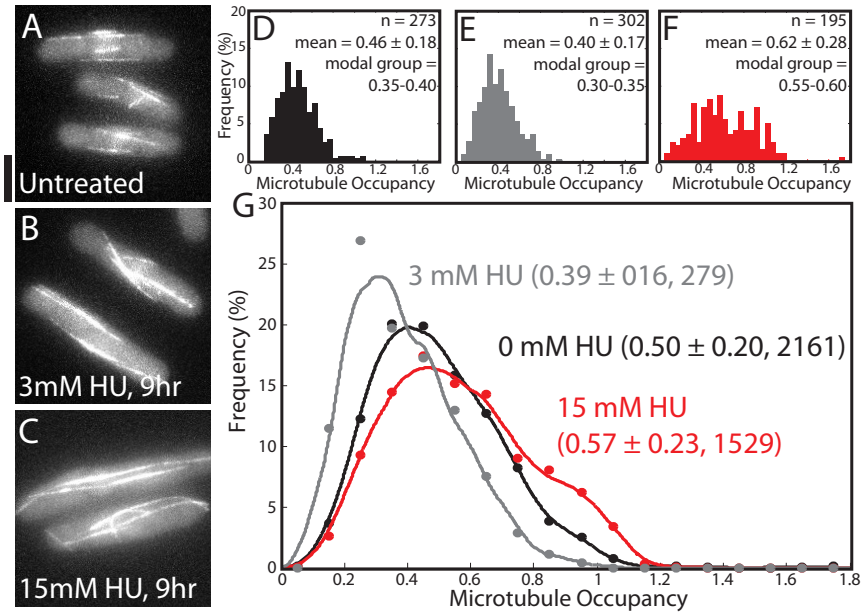

Figure 5.3: The microtubule response to DNA damage by HU - **(A)-(C)** Low-throughput images comparable to **Figure 5.1**, showing the effects of treating GFP-Atb2 wild-type cells with different doses of HU for nine hours. **(D)-(F)** Histograms showing the corresponding effect of these treatments on microtubule occupancy – the microtubule length relative to the length of the cell. **(G)** Pooled data across multiple experiments of cells treated with HU for 6 hours showing the same response. Points represent histogram bars of width 0.1, lines represent a kernel density function fitted to the histogram data to permit easy overlay of plots. Labels show mean (± s.d.) and number of microtubules measured. Full data presented in **Table 5.2**.

DNA damage also causes cell cycle arrest. Hence, *S. pombe* cells treated with HU become longer (Fantes, 1977). Since microtubule catastrophe is often caused by contact with the cell ends, it is expected that microtubules should become longer proportional to the cell length. This was exactly as expected for cells treated with 3 mM HU (**Figure 5.3G**), where cells elongated from an average 10.57 ± 1.80 μm to 24.05 ± 3.98 μm (127% increase) with a lesser increase in microtubule length from 5.15 ± 1.96 μm to 9.85 ± 3.80 μm (91% increase). Microtubule elongation is expected to fall short of increasing cell length because, as cells elongate, it becomes progressively more likely that microtubules will stochastically undergo catastrophe before reaching the cell ends (Mitchison and Kirschner, 1984a).

	Time			
HU Dose	2hr	4hr	6hr	9hr
0 mM	0.50 ± 0.20 (2161)			
3 mM	N/A	N/A	0.39 ± 0.16 (279)	0.42 ± 0.18 (93)
10 mM	N/A	N/A	0.50 ± 0.21 (818)	N/A
15 mM	0.55 ± 0.23 (299)	0.54 ± 0.21 (575)	0.57 ± 0.23 (1529)	0.54 ± 0.23 (650)

Table 5.2: Effect of variable HU dosage - Average (± s.d.) microtubule occupancy measurements from wild-type populations subjected to different doses of HU for variable lengths of time. Results are aggregated from many separate experiments with number of measurements per condition shown in parentheses.

By contrast, cells treated with 15 mM HU undergo disproportionate microtubule elongation, achieving a similar cell length as 3 mM treated cells (21.89 ± 5.11 μm; 107%) but with a 127% increase in microtubule length (11.71 ± 5.52 μm).

To assess the disproportionate elongation of microtubules, I created a measure of microtubule occupancy (**Figure 5.3D-F**), representing the relative length of each microtubule bundle to the cell. An average microtubule in an untreated cell has an occupancy of approximately one half the cell length (0.50 ± 0.20), which falls in 3 mM treated cells (0.42 ± 0.18; KS-test; p<0.001) but is increased in 15 mM treated cells (0.54 ± 0.23; p<0.001).

In addition, in the initial investigation, more than 40% of 15 mM treated cells ($^{27}/_{63}$) featured microtubules which curved around the cell end. This was not observed in untreated or 3 mM HU-treated cells ($^{0}/_{108}$, $^{0}/_{83}$). Microtubule bundle number was also found to increase from an average 2.84 ± 0.85 μm to 3.87 ± 1.19 μm (35%; KS-test p<0.001) in 3 mM treated cells and 3.55 ± 1.22 μm (25%; p=0.02) in 15 mM treatments.

5.3.2 Dose and time dependence of HU treatment

Since 3 mM HU and 15 mM HU treatments over 9 hours showed different effects on the microtubule array, I went on to look at other HU treatment conditions in wild-type cells to better validate and understand the initial results.

The collected results for wild-type cells suggest a rapid dose-dependent response to HU treatment (Table 5.2). Even after just 2 hours exposed to 15 mM HU, cells showed a notable increase in microtubule occupancy when compared directly to untreated populations. Conversely, 3 mM populations showed a consistent reduction. A mild effect is apparent in 10 mM treatments, which is sufficient to restore occupancy to a level similar to untreated cells. Wild-type cells treated with different HU doses, for the same length of time, demonstrated a similar amount of cell elongation. After six hours, average cell lengths were between 17.4 and 19.0 μm, reaching 21.9 to 24 μm after nine hours.

For practical reasons, unless otherwise indicated, from this point cells were treated with HU for 6 hours, rather than 9 hours.

5.4 Other elongated cells do not alter microtubules

5.4.1 Cdc2-AS arrested cells

To validate that change in microtubule length was a result of HU treatment, cells were also elongated using an analogue sensitive *cdc2* cyclin-dependent kinase mutant (Cdc2-AS; Cipak et al. (2011)) . As mentioned in **Section 4.4.1.1**, Cdc2-AS cells, when exposed to a non-hydrolysable ATP-analogue, arrest cell cycle progression, primarily at the G2/M transition, although some G1/S arrest has also been reported (Coudreuse and Nurse, 2010). As such, Cdc2-AS is not perfectly comparable to HU treatment, where cells would arrest in S phase. However, microtubules are reported to maintain consistent organisation from septation, typically in early S phase, through to early M phase, therefore it is still reasonable to make comparisons between HU treatment and Cdc2-AS arrest (Hayles and Nurse, 2001; Sawin and Tran, 2006).

Untreated Cdc2-AS cells should initially directly comparable to wild-type cells, including a comparable cell length (9.58 $\pm$ 2.20 μm), microtubule length (4.80 $\pm$ 1.99 μm) and occupancy (0.50 $\pm$ 0.19).

Cdc2-AS cells, when treated with a non-hydrolysable ATP analogue, arrest the cell cycle and show progressive cell elongation. After just six hours, they become comparable in length to cells treated with 15 mM for 9 hours, with an average

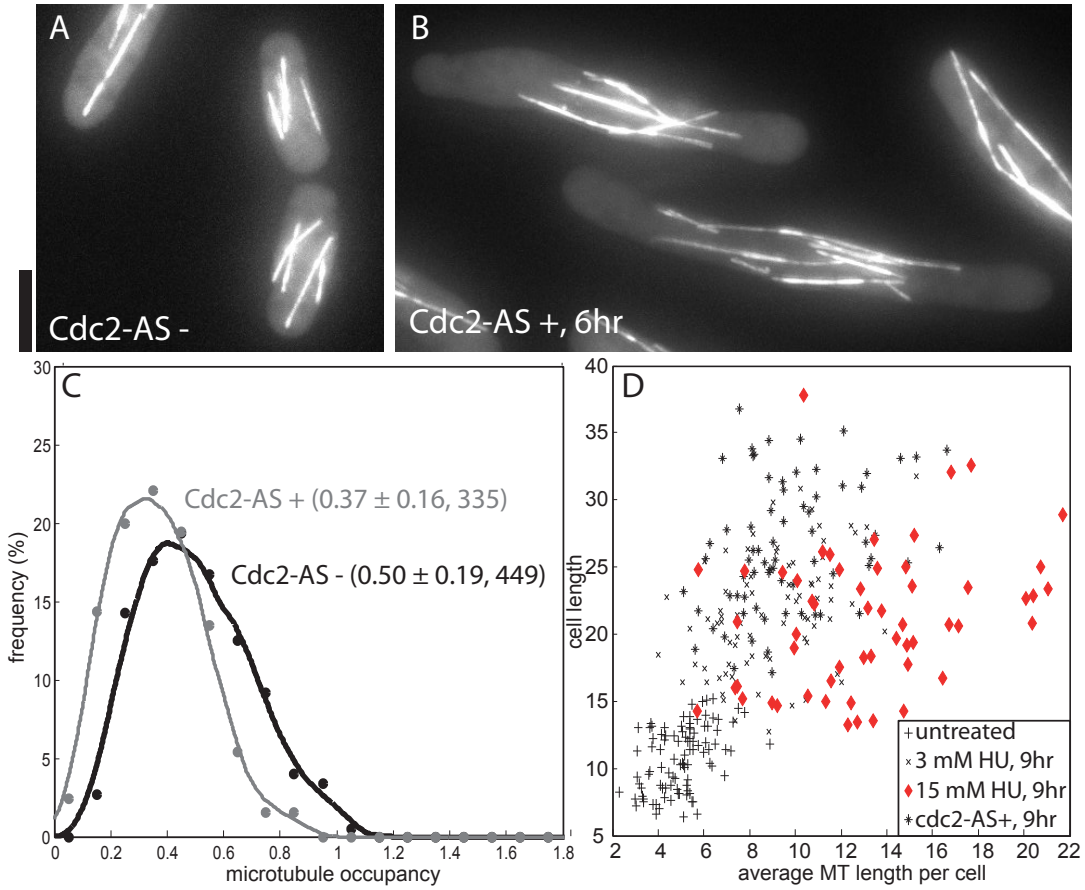

Figure 5.4: Microtubules in other elongated cells - Analogue-sensitive *cdc2* mutant cells (Cdc2-AS), both untreated **(A)** and treated with an ATP analogue for 6 hours **(B)**, showing interphase microtubule arrays. **(C)** The corresponding measurements of microtubule occupancy in untreated and treated cells pooled across experiments (KS-test; p<0.001). Mean (± s.d.) and number of datapoints are given. **(D)** Comparison of cell length and average microtubule length per cell in untreated, 3 mM HU and 15 mM HU-treated cells, from **Figure 5.3**, against Cdc2-AS cells treated for 9 hours.

length of 24.44 ± 4.60 μm (a 142% increase). The difference in time to reach a similar cell length may primarily be explained by the different points of cell cycle arrest between these two datasets, but may also suggest a slowing of growth in HU-treated cells. Most HU-treated cells will go through an additional round of division before arresting, as such they may be expected to be around 7 μm shorter. Elongated Cdc2-AS cells only attained a microtubule length of 9.43 ± 4.06 μm (a 96% increase) and occupancy of 0.37 ± 0.16 (KS-test; p<0.001 compared to untreated Cdc2-AS cells). In addition, the average number of microtubule bundles

per cell increased, on treatment with ATP analogue, from 3.30 ± 0.87 to 5.15 ± 1.26 (56%)

If treated for nine hours, Cdc2-AS cells were measured at 26.56 ± 4.86 μm long with an occupancy of 0.36 ± 0.16. As shown in **Figure 5.4** the relative length of microtubules to cells is approximately linear through untreated, 3 mM HU and Cdc2-AS analogue treated cells (Average microtubule bundle length is consistently ≈51% of cell length), whilst average microtubule bundles in 15 mM HU-treated cells are 59% of cell length.

Hence, when *S. pombe* cells enter cell cycle arrest, induced by low dose HU treatment or Cdc2-AS treatment, the cells become progressively longer at a rate that exceeds elongation of their microtubule bundles. By contrast, when treated with high doses of HU, microtubule elongation is disproportionate to cell growth and many microtubules contact the cell ends, or bend around them. This disproportionate elongation of microtubules indicates enhanced stabilisation of the tubulin polymers in 15mM HU-treated cells.

5.4.1.1 Co-treatment with ATP-analogue and HU

When Cdc2-AS cells were exposed to the non-hydrolysable ATP-analogue and 15 mM HU together, the cells were found to phenocopy cells treated with just analogue, producing long cells (22.24 ± 9.75 μm) with low microtubule occupancy (0.35 ± 0.17) after a six hour treatment. Since Cdc2-AS predominantly blocks cells in early M phase (Coudreuse and Nurse, 2010), whilst HU-induced cell cycle arrest is dependent upon DNA synthesis in S phase, this supports the idea that cells must undergo cell division before being affected by HU. It also demonstrates that the microtubule elongation phenotype depends upon HU-induced cell cycle arrest and is not due to some other effect of HU presence in cells.

5.4.2 Phleomycin-treated cells

Phleomycin, an antibiotic drug related to bleomycin, causes DNA damage to cells in a mechanism distinct from HU. Where HU depletes dNTPs preventing DNA synthesis, phleomycin directly induces double stranded breaks in DNA (Hecht,

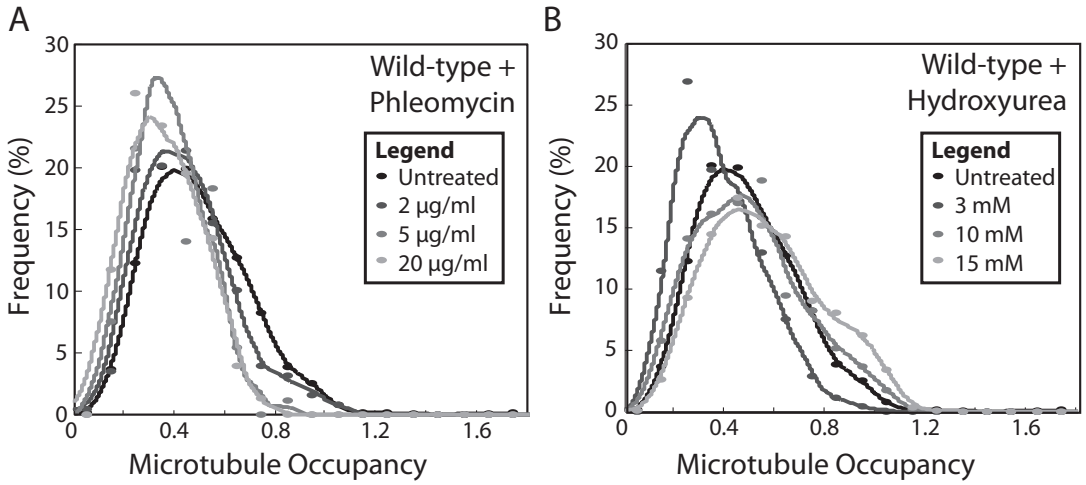

Figure 5.5: The effect of phleomycin on microtubules - Microtubule occupancy kernel density plots for wild-type cells treated with **(A)** phleomycin or **(B)** HU.

2000). Initially, I worked with phleomycin as a possible means for inducing DNA-damage linked microtubule stabilisation, separate to the use of HU. However, I was unable to demonstrate a response to phleomycin treatment (Figure 5.5). Doses tested ranged from 2 μg/mL to 10 μg/mL (Belenguer et al., 1995). Cells treated with phleomycin responded in a similar manner to Cdc2-AS cells, undergoing more rapid elongation (average cell length 23.19 $\pm$ 6.39 μm after six hours) than those treated with HU, whilst showing significant reduction in microtubule occupancy (KS-test; $p<0.01$).

5.5 Characterising the microtubule response to HU

Having identified a dose-dependent response to HU treatment, I performed other experiments to validate and better characterise the nature of this response.

5.5.1 HU treatment increases tubulin concentration

The use of GFP-labelled proteins to visualise cell structures directly makes it possible to try and quantify the amount of labelled protein present in cells by measuring GFP fluorescence intensity. I have attempted to use measurements of

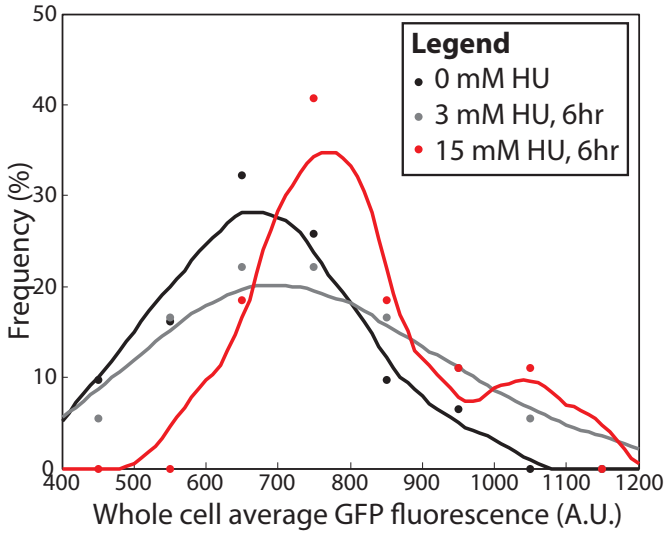

Figure 5.6: Total GFP-Atb2 cell content - Kernel densty plots of total cell fluorescence signal in wild-type cells treated with different doses of HU. Values reported are averaged across experiments, after subtraction of autoflourescence measured from GFP-negative cells in the same images.

GFP-Atb2 intensity to assess the total tubulin levels and to examine microtubule number within microtubule bundles, for cells under different conditions.

5.5.1.1 Total cell tubulin content

The total GFP-Atb2 fluorescence within untreated and 15 mM HU-treated cells was assessed using mixed samples of cells, where cells lacking GFP (dark cells) were grown alongside GFP-positive (light) cells and imaged together under the same conditions. Sum projections of z-stacks were used to ensure the full fluorescence output was captured in images.

Compared across samples in the same experiment, the average level of autofluorescence measured from dark cells was found to be highly consistent, although fluorescence levels did vary between experiments.

In one example experiment, the average autofluorescence level per pixel in dark cells was measured as 2807 ± 69 in untreated cells and 2894 ± 92 in treated cells. A significant rise in autofluorescence would most likely indicate an increase in cell death. The comparatively mild increase observed here suggests that cell death

is minimal after 15 mM HU treatment for six hours. By comparison, untreated GFP-Atb2 wild-type cells gave an average signal of 3471 ± 177, ≈664 levels above autofluorescence. When treated with 15 mM HU, intensity rose to 3887 ± 370, ≈993 above autofluorescence and an average 50% increase in atb2 density relative to untreated cells.

Across all experiments, 15 mM HU treatment was found to lead to an increase in average cell fluorescence signal of between 20% and 50%. In all cases this fluorescence increase was found to be significant (KS-test; $p<0.02$). Additionally, an experiment looking at 3 mM HU treatment showed a lesser increase in fluorescence level (10%; **Figure 5.6**), but was not statistically significant ($p=0.46$).

There are several possible explanations for this effect. Most obviously, this suggests an increase in the production of tubulin, or a reduction in its degradation, leading to an overall increase in levels. As this work only examines GFP-Atb2, other tubulins may not be affected – indeed *nda2* expression may actually be reduced, as it is able to compensate for changes in Atb2 (Adachi et al., 1986). Conversely, this may be symptomatic of a more general increase in cell protein content, that is not specifically linked to tubulin. It seems likely, given the observation of microtubule stabilisation that, at the very least there is an increase in available tubulin dimers available for microtubule polymerisation.

5.5.1.2 Microtubule bundle density

Average fluorescence intensity measurements collected along microtubule bundles, from z-stacks using a maximum projection, should be reflective of the amount of Atb2 tubulin present at each point along the bundle. I assumed this to be indicative of the number of individual microtubules present in a bundle. Alternatively GFP fluorescence may be influenced by a change in relative abundance of the two α-tubulin isoforms within the microtubule lattice, as expression of *nda2* is known to be able to compensate for altered levels of *atb2* expression (Adachi et al., 1986). These values were standardised by subtraction of autofluorescence signal from regions of the cytoplasm containing no polymerised microtubules.

Analysis of the average microtubule bundle fluorescence relative to untreated cells, across all experiments, showed a ≈52% increase in fluorescence intensity in cells treated with 3 mM HU. However at higher doses, even 10 mM HU, this was lost again. Comparing microtubule bundle intensity values within separate

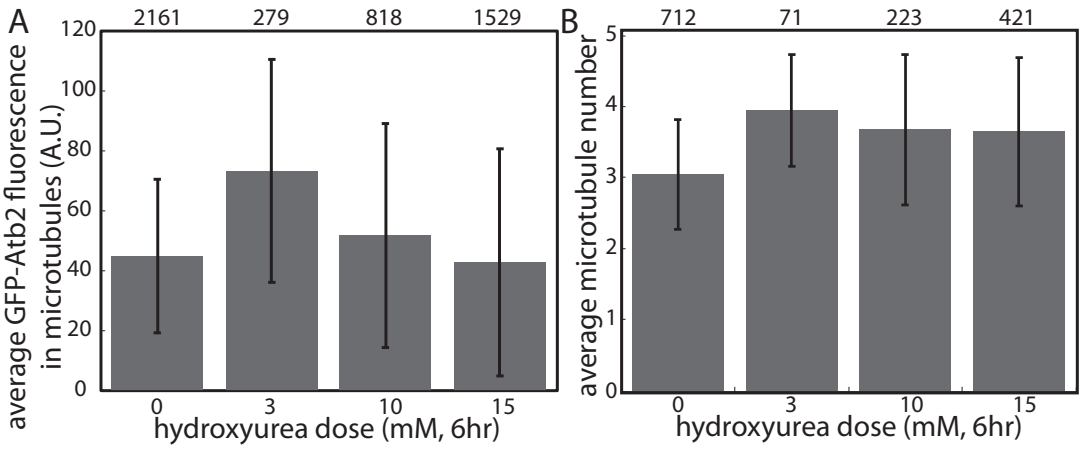

Figure 5.7: GFP-Atb2 incorporation in microtubule bundles - **(A)** Background subtracted GFP-Atb2 fluorescence in microtubules, measured after 6 hours treated with various HU doses. Values are assumed to be reflective of the average number of microtubules per bundle. As fluorescence values vary between experiments, values from within one experiment are shown. Error bars represent standard deviation between microtubules. **(B)** Microtubule bundle number measured under the same conditions. Error bars represent standard deviation between individual cells across all experiments. Number of measurements taken are given above each bar.

experiment, yields the same pattern (**Figure 5.7A**): showing significant increases in 3 mM (41-63%, KS-test $p<0.01$) and not 10 mM ($p>0.50$) or 15 mM ($p>0.10$) HU-treated cells.

A slight increase in number of microtubule bundles per cell, specific to 3 mM HU-treated cells is also observed, although this is likely to be an effect of the slightly increased average cell length of 3 mM HU-treated cells, relative to other treatments (**Figure 5.7B**). Overall these findings suggest an increase in microtubule polymer mass in 3 mM HU-treated cells despite no apparent increase in microtubule bundle lengths. As bundle lengths increase in higher HU doses, it is likely that the increased density of microtubules in 3 mM treated cells is converted to increased length in 10 mM and 15 mM treated cells. An alternative possibility is that 3 mM HU induces an increase in the proportion of Atb2 relative to Nda2 in microtubules, but that the normal ratio is then somehow restored upon more extreme HU treatment. Since microtubules in *atb2*Δ cells are known to be more sensitive to microtubule destabilising drugs (Adachi et al., 1986) this may suggest that increasing Atb2 helps to increase microtubule stability.

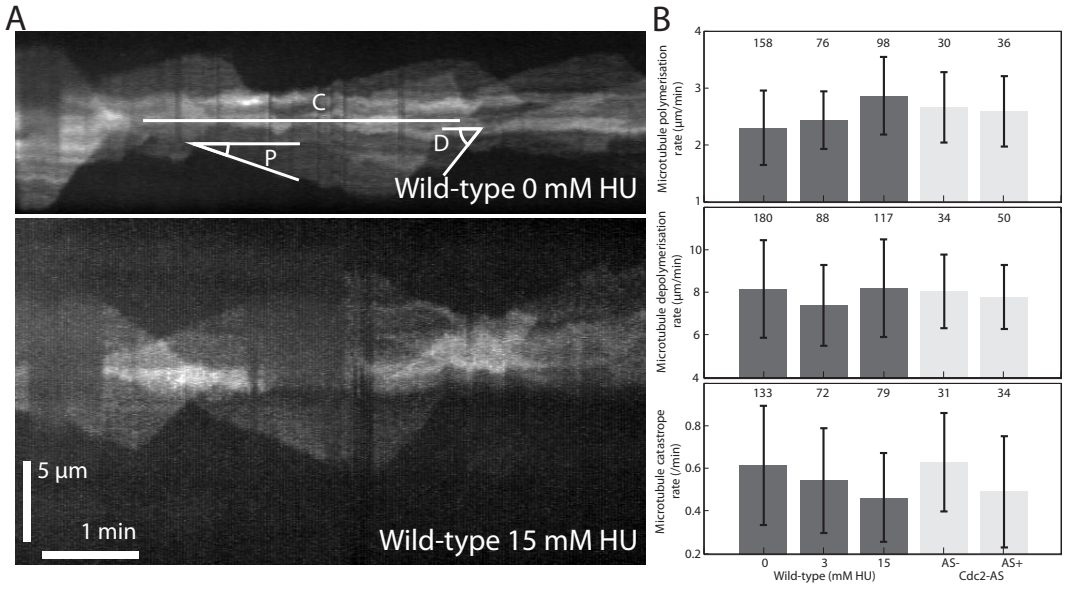

Figure 5.8: Microtubule dynamics in response to HU - **(A)** Example kymographs of an untreated (top) and 15 mM HU-treated (bottom) microtubule bundle. Examples of measuring polymerisation (P), depolymerisation (D) and catastrophe (C) are marked. **(B)** Bar charts of polymerisation (top), depolymerisation (middle) and catastrophe (bottom) rates for different HU doses. Cdc2-AS cells with (AS+) and without (AS-) analogue are shown for comparison. Error bars represent s.d.. Number of events measured are given above each bar.

5.5.2 HU treatment influences microtubule dynamics

It is possible to measure the individual dynamics of microtubules within bundles by creating kymographs of timelapse data. By imaging a single focal plane every 2 seconds for 10 minutes and manually adjusting the focus to track ends of microtubule bundles, I was able to evaluate polymerisation, depolymerisation and catastrophe rates for different populations of cells (Tran et al., 2001).

Kymographs consist of a time-resolved image, where the vertical axis represents the position in space along the microtubule bundle, whilst the horizontal axis represents position in time (**Figure 5.8A**). Using this display for a GFP-labelled microtubule bundle enables visualisation of individual microtubules as regions of changing fluorescence intensity. A polymerising microtubule appears as a slope rising towards the right, whilst depolymerisation appears as a, generally steeper, falling slope. The rates of these events can be calculated by measuring the incline of these slopes. The rate of catastrophe was assessed by measuring the length

Strain	Treatment	P (μm/min)	D (μm/min)	C (/min)
Wild-Type	0 mM	2.29 ± 0.66	8.14 ± 2.30	0.61 ± 0.28
Wild-Type	3 mM	2.43 ± 0.51	7.38 ± 1.90	0.54 ± 0.25
Wild-Type	15 mM	2.86 ± 0.68	8.19 ± 2.28	0.46 ± 0.21
Cdc2-AS	0	2.65 ± 0.62	8.03 ± 1.72	0.63 ± 0.23
Cdc2-AS	AS	2.59 ± 0.62	7.64 ± 1.50	0.49 ± 0.26

Table 5.3: Microtubule dynamics measurements - Average (± s.d.) changes in microtubule polymerisation (P), depolymerisation (D) and catastrophe (C) rates as measured from kymographs as shown in **Figure 5.8**.

of time (horizontal distance) that each microtubule persists for before initiating depolymerisation.

I found that wild-type cells treated with HU appear to show a dose-dependent change in microtubule polymerisation rate (**Figure 5.8B**; top). At 3 mM this effect is subtle (KS-test; p=0.05) but becomes much more pronounced after 15 mM treatment (p<0.001). The reduction in depolymerisation rate with 3 mM may also be significant (p=0.04; **Figure 5.8B**; middle).

As expected, there is an obvious reduction in average catastrophe rates (**Figure 5.8A**; bottom). This is primarily the result of cell elongation, leading to a reduction in cell tip-induced microtubule catastrophe. What is most surprising here is that the catastrophe rate in 15 mM HU-treated cells is lower than 3 mM HU-treated cells. Both of these populations have similar cell lengths but 15 mM HU cells have a higher polymerisation rate. This suggests that stochastic causes of catastrophe dominate in HU-treated cells, after 6 hours. Hence, the lower catastrophe rate in 15 mM HU cells is likely to be a side-effect of the increased polymerisation rate. Faster polymerisation typically suppresses catastrophe, theoretically because it helps to maintain the GTP-tubulin cap (Desai and Mitchison, 1997).

Whilst dominance of stochastic catastrophe in 3 mM HU cells is to be expected, since few microtubules are seen in contact with the cell ends, this is more surprising in 15 mM cells, where microtubules are able to reach the ends. This result may be indicative of microtubules becoming insensitive to cell end-induced catastrophe as a result of high dose HU treatment.

By comparison, Cdc2-AS cells, elongated by non-hydrolysable ATP analogue-induced cell cycle arrest, do not seem to alter their microtubule dynamics. A reduction in catastrophe rate is again observed, a result of the increased cell length.

It is also worth noting that my results support those reported elsewhere (Tran et al., 2001; Behrens and Nurse, 2002; Sagolla et al., 2003) for microtubule dynamics in *S. pombe*. One of the first attempts to measure this was by Drummond and Cross (2000), reporting polymerisation as 2-4 μm/min, depolymerisation as 2-7 μm/min and 1 catastrophe/min. Many of these previous attempts have relied upon exogenous expression of GFP-tubulin and often have imaged cells in water or minimal medium. As such I believe that my results should most accurately reflect the state of microtubules in true wild-type cells. In fact, the results reported here agree strongly with one of the more recent assessments of microtubule dynamics by Tischer et al. (2009). They reported average rates of 2.4 μm/min, 8.3 μm/min and 0.46 /min respectively.

5.6 Microtubule elongation is dependent on DDR kinases

As covered in detail in **Section 4.7**, the DDR is co-ordinated by a small network of serine/threonine kinases, which are highly conserved across species. In *S. pombe*, the DDR is thought to be initiated by the ATR homologue Rad3, which has some capacity to activate both checkpoint kinases CHK1 (Chk1) and CHK2 (Cds1) (Rhind and Russell, 2000). There is little evidence for the role of the ATM homologue Tel1 in the DDR Shiloh (2001); Zhao et al. (2003).

The DDR kinases in *S. pombe* are not essential and so deletions are possible. Three of these deletions (*rad3*Δ, *tel1*Δ and *cds1*Δ) were available in our collection. If the observed microtubule elongation in the DDR hits and HU-treated cells is directly due to the DDR then it is likely to depend upon these kinases. So the effects of HU treatment in DDR kinase deletion mutants, as well as in *rad26*Δ (the ATR interacting protein, ATRIP; (Cortez et al., 2001)) were investigated.

Unsurprisingly, some of these mutants, particularly *rad3*Δ, are highly sensitive to treatment with DNA damaging agents (Hayles et al., 2013). As such, many cells

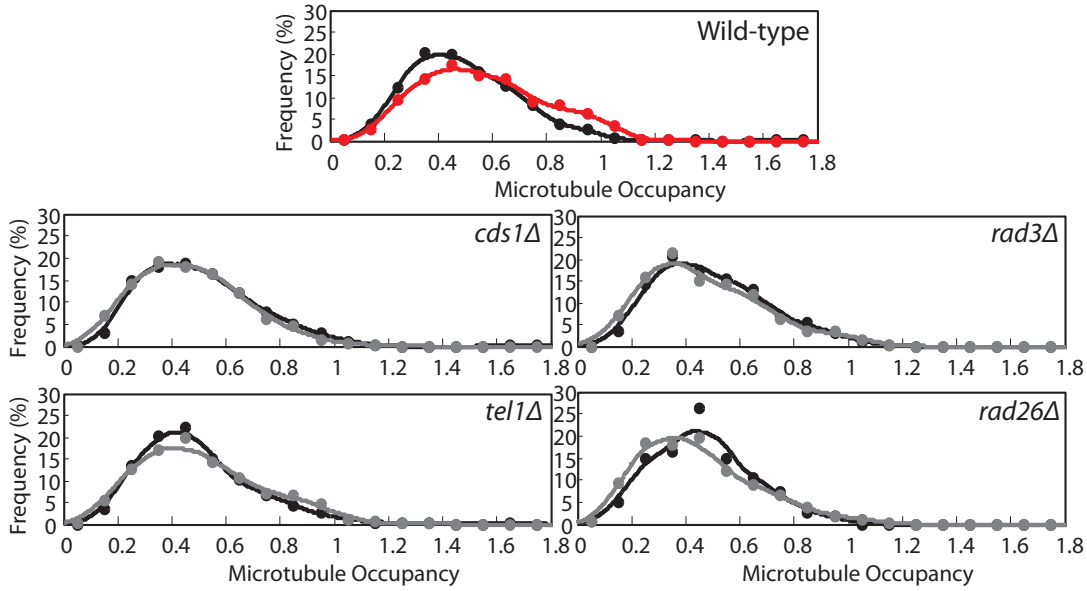

Figure 5.9: Response to HU in DDR kinase knockouts - Kernel density plots of microtubule occupancy for untreated cells (black) and 15 mM HU-treated cells after 6 hours (KS-test; p>0.05 in grey, p<0.05 in red) in DNA damage response kinase deletion mutants. Wild-type data is shown for comparison (top centre)

showed high levels of autofluorescence, abnormal cell morphology and/or defective cell division/septation phenotypes. For comparison, I focused exclusively on cells that had managed to maintain cell shape and microtubule organisation comparable to wild-type cells.

Interestingly, all deletion strains tested showed little or no increase in microtubule occupancy (**Table 5.4** and **Figure 5.9**). Similarly to Cdc2-AS cells, these mutants show cell growth over six hours that is much higher than the wild-type or *tip1*Δ cells. The lack of microtubule elongation in these mutant strains suggested that microtubule elongation in response to HU is mediated by the DDR kinases, most likely via Rad3 and Cds1, although Tel1 also seems to be required, despite not being widely reported to have a role in the DDR in *S. pombe* (Shiloh, 2001; Zhao et al., 2003). Subsequent work primarily makes use of *rad3*Δ and *cds1*Δ, as the well-established mediators of the *S. pombe* DDR.

Strain	**HU**	**n**	Cell Length (μm)	MT Length (μm)	Occupancy	MTs/cell
Wild-Type	-	2161	10.57 ± 1.8	5.15 ± 2	0.5 ± 0.2	3 ± 0.8
Wild-Type	+	1529	17.45 ± 3.4	9.78 ± 3.9	0.57 ± 0.2	3.6 ± 1
*rad3*Δ	-	283	10.99 ± 1.9	5.26 ± 2.1	0.49 ± 0.2	2.9 ± 0.8
*rad3*Δ	+	191	21.01 ± 5	10.25 ± 4.4	0.50 ± 0.2	3.7 ± 1
*rad26*Δ	-	367	10.82 ± 1.8	5.01 ± 2.0	0.47 ± 0.2	3.5 ± 0.9
*rad26*Δ	+	608	20.72 ± 4.8	9.11 ± 4.1	0.45 ± 0.2	4.1 ± 1.3
*tel1*Δ	-	553	11.18 ± 2.3	5.37 ± 2.0	0.49 ± 0.2	3.2 ± 0.8
*tel1*Δ	+	613	19.35 ± 4.3	9.69 ± 4.2	0.51 ± 0.2	3.8 ± 1.1
*cds1*Δ	-	654	11.24 ± 2.1	5.37 ± 2.0	0.49 ± 0.2	3.1 ± 0.8
*cds1*Δ	+	335	19.92 ± 3.2	9.34 ± 4.2	0.47 ± 0.2	3.4 ± 1.0

Table 5.4: HU treatment of key DDR factors - Average (± s.d.) changes in cell length, microtubule length, occupancy and microtubule bundle number in strains deleted for key DNA damage response kinases and co-factors. Cells were either measured without treatment (-) or treated with 15 mM HU for 6 hours (+) prior to imaging.

5.7 Screening for microtubule factors that respond to DNA damage

Having shown that DDR kinase activity appears to be a necessary precursor to microtubule elongation in response to HU treatment. The next step was to investigate possible targets for these kinases which could potentially affect microtubule stability. I started by examining the effect of deleting known microtubule regulatory proteins on the response to 15 mM HU.

A small, but non-exhaustive, group of proteins have been reported to affect microtubule stability in *S. pombe*, many of these are non-essential and deletion strains are readily available.

5.7.1 Candidate microtubule regulating proteins

Seven candidate proteins were considered as known microtubule associated factors which may regulate microtubule elongation/stability.

- Tea1 – Polarity factor involved in defining growth zones. Delivered to cell tips by microtubules. Deletion leads to microtubule elongation (Behrens and Nurse, 2002; Feierbach et al., 2004; Glynn et al., 2001; Mata and Nurse, 1997).
- Tea2 – Kinesin-like protein responsible for delivery of microtubule-stabilising and polarity factors to microtubule +ends and cell tips respectively. Deletion leads to shorter microtubules (Browning et al., 2000).
- Tip1 – CLIP170 homologue, binds to microtubule +ends, delivered by Tea2. Deletion leads to shorter microtubules (Brunner and Nurse, 2000; Busch and Brunner, 2004).
- Mal3 – EB1 homologue, binds to microtubule +ends. Deletion severely shortens microtubules (des Georges et al., 2008; Katsuki et al., 2009; Beinhauer et al., 1997; Sandblad et al., 2006).
- Klp6 – Microtubule destabilising kinesin protein. Acts in concert with Klp5 (not available). Deletion leads to microtubule elongation (Erent et al., 2012; West et al., 2001).
- Dis1 – TOG homologue. Microtubule-associated factor required for microtubule stabilisation upon kinetochore capture during mitosis. Known to associate with microtubules during interphase but currently no known function. (Ohkura et al., 1988)
- Amo1 – Nuclear rim protein. Over-expression causes cells to produce one, large hyperstable microtubule bundle. Deletion may cause slight microtubule elongation (Pardo and Nurse, 2005).

5.7.2 Microtubule elongation in candidate mutants

As for the DDR kinases, these factors were investigated using fluorescence microscopy to look for the ability to stabilise microtubules in response to 15 mM HU

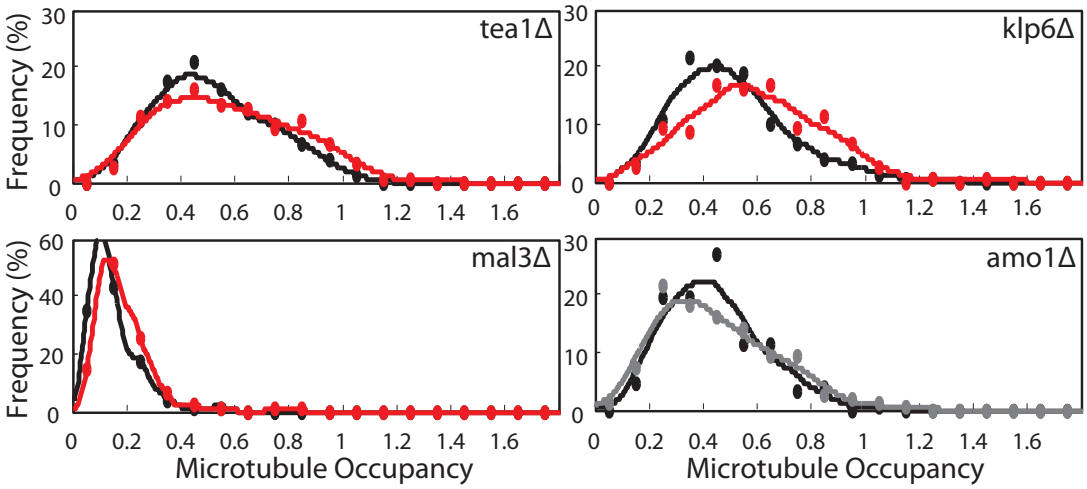

Figure 5.10: Effect of HU on microtubule occupancy - Examples of microtubule occupancy kernel density plots for four different microtubule regulator deletion strains. Note that, despite differences in untreated microtubule occupancies (black), all strains show a tendency towards higher microtubule occupancy when treated with 15 mM HU (red; KS-test; $p<0.05$), except for *amo1*Δ (grey; $p>0.05$). Average data and number of microtubules measured for these populations are given in **Table 5.5**.

(**Table 5.5**; example graphs shown in **Figure 5.10**). Of the candidate proteins initially considered, six demonstrate a response to HU treatment that is comparable to wild-type, with microtubule length increasing disproportionately to cell length. For these strains microtubule occupancy increased by between 15% and 30% comparable to the 20% to 30% change observed in wild-type populations.

The *amo1*Δ strain was the only candidate that appeared to respond differently to the wild-type. As indicated (**Table 5.5**), this strain dd not show a significant increase in microtubule occupancy. In addition, as for the DDR kinase deletion strains, *amo1*Δ showed comparable microtubule length to wild-type in treated and untreated cells but produced longer cells after six hours of HU treatment.

5.7.3 Computational search for DDR kinase targets

Targets for the DDR kinases have been well-studied in a number of contexts (Matsuoka et al., 2007; Tanaka et al., 2001; Chapman et al., 1999). The kinase target consensus sequence for the ATM/ATR kinases is particularly well-established

Strain	HU	n	Cell Length (μm)	MT Length (μm)	Occupancy	MTs/cell
Wild-type	-	108	11.43 ± 1.7	5.06 ± 1.8	0.44 ± 0.18	3.0 ± 0.8
Wild-type	+	209	15.96 ± 3.8	9.18 ± 3.3	0.59* ± 0.23	3.5 ± 1.3
*tea1*Δ	-	167	11.49 ± 1.9	5.93 ± 2.4	0.52 ± 0.2	3.5 ± 0.8
*tea1*Δ	+	154	14.96 ± 3	8.77 ± 3.6	0.60* ± 0.2	3.5 ± 0.9
*tea2*Δ	-	156	10.55 ± 2.1	2.4 ± 1.1	0.24 ± 0.1	3.3 ± 0.8
*tea2*Δ	+	201	15.58 ± 4	4.23 ± 2.1	0.28* ± 0.1	3.7 ± 1.0
*tip1*Δ	-	166	11.58 ± 2.5	2.44 ± 1.2	0.22 ± 0.1	3.1 ± 0.7
*tip1*Δ	+	169	18.53 ± 4.8	4.7 ± 2.5	0.25* ± 0.1	4.1 ± 1.3
*mal3*Δ	-	163	10.42 ± 1.6	1.53 ± 0.9	0.15 ± 0.1	3.1 ± 0.8
*mal3*Δ	+	199	16.65 ± 4.9	2.89 ± 1.5	0.18* ± 0.1	3.9 ± 1.1
*klp6*Δ	-	186	10.44 ± 1.6	5.12 ± 1.8	0.50 ± 0.2	3.3 ± 1.0
*klp6*Δ	+	200	19.14 ± 3.7	11.2 ± 4.5	0.59* ± 0.2	3.8 ± 1.0
*dis1*Δ	-	162	11.12 ± 1.4	4.78 ± 1.9	0.43 ± 0.2	3.5 ± 0.7
*dis1*Δ	+	176	19 ± 4.2	10.44 ± 4.1	0.55* ± 0.2	3.7 ± 0.9
*amo1*Δ	-	183	11.57 ± 2.6	5.02 ± 1.9	0.44 ± 0.2	2.8 ± 0.8
*amo1*Δ	+	269	22.08 ± 4.9	9.61 ± 4	0.45 ± 0.2	4.0 ± 1.0

Table 5.5: HU treatment of microtubule regulating factors - Average (± s.d.) changes in cell length, microtubule length, occupancy and microtubule bundle number in strains deleted for proposed microtubule regulators. Cells were either measured without treatment (-) or treated with 15 mM HU for 6 hours (+) prior to imaging. Asterisks (*) indicate HU treated samples with microtubule occupancies significantly ($p<0.05$) greater than their untreated counterparts.

(Kim et al., 1999; O'Neill et al., 2000). The core sequence typically includes a target serine or threonine directly followed by a glutamine residue (SQ/TQ), and targets often include clusters of these SQ/TQ target sites (Traven and Heierhorst, 2005). In addition, ATM/ATR favour SQ/TQ sites with hydrophobic or negatively charge amino acids at the -1 and -3 positions, and disfavour sites with nearby positively charged residues (Kim et al., 1999; O'Neill et al., 2000).

With this in mind, I created a code using MATLAB to search all protein sequences deposited in PomBase for SQ/TQ sites and assess their favourability and enrichment within different proteins. Favourability for a specific SQ/TQ site is de-

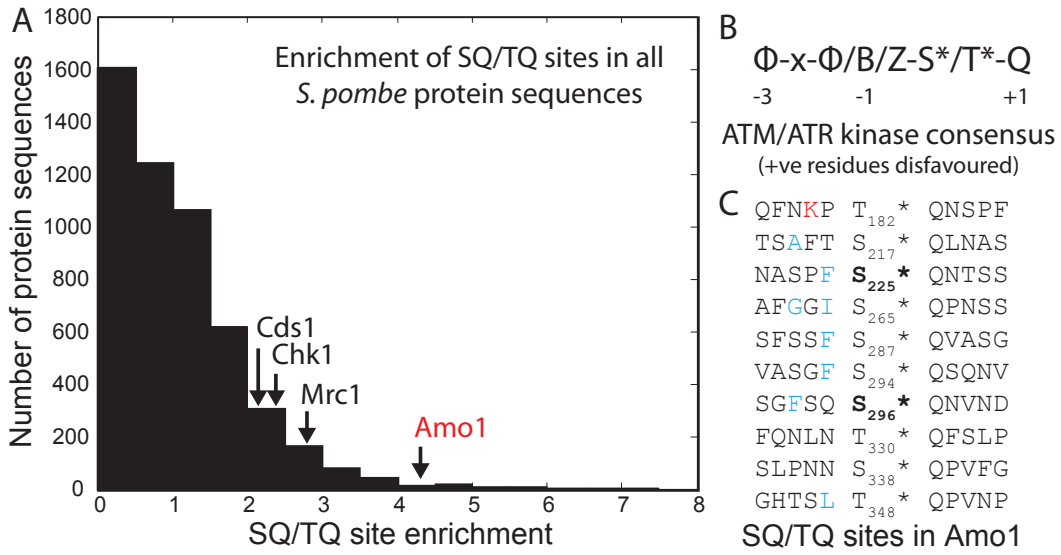

Figure 5.11: Identification of SQ/TQ sites in Amo1 - An overview of computational sequence analysis of the Amo1 protein sequence to identify potential ATM/ATR kinase target sites. **(A)** Histogram of SQ/TQ dipeptide enrichment, relative to a random sequence, for 5145 *S. pombe* proteins, indicating the position of known kinase targets (Mrc1, Chk1 & Cds1) and Amo1. **(B)** The broader consensus sequence for ATM/ATR targets (Kim et al., 1999; O'Neill et al., 2000), with phospho-residue indicated by asterisks (*). Φ (phi) represents hydrophobic residues, B is Asp/Asn and Z is Glu/Gln. Positive charges (Lys/Arg) are disfavoured in these regions. **(C)** Sequences surrounding SQ/TQ dipeptides in Amo1 highlighting positive determinants (blue) and negative ones (red). Numbers denote the position of the phospho-residue in the Amo1 sequence. The two most favourable sites, according to J. Carballo, are shown in bold.

termined by the surrounding residues; the sequence context (**Figure 5.11B**). SPCC737.08 contained the most SQ/TQ sites, with 28 across 4717 residues. Enrichment was assessed in comparison to the probability of adjacent SQ or TQ residues occurring in a randomly generated protein sequence ($2(1/20)^2 = 0.005$). The protein with the highest enrichment was Vma10 (SPBC1289.05c) with 4 in 108 residues, however the context of these sites makes them unfavourable ATM/ATR targets.

Three well-characterised targets of Rad3 in *S. pombe* are Mrc1, Chk1 and Cds1 (Tanaka et al., 2001; Chapman et al., 1999; Tanaka and Russell, 2004), which have respective SQ/TQ enrichments of 2.75 (14 in 1019), 2.42 (6 in 496) and

2.17 (5 in 460). If ranked according to enrichment, these proteins are 240^{th}, 362^{nd} and 493^{rd} of the 5145 sequences analysed, of which 3915 contain at least one SQ/TQ site (**Figure 5.11A**).

Searching for SQ/TQ sites, focusing on 29 known microtubule regulators, revealed only 8 with an enrichment score above 2, of which only three (Dis1, Tea2 and Amo1) are known to influence microtubule length. Of these, Dis1 is unlikely to be a target for phosphorylation, as 6 of 10 SQ/TQ motifs include unfavourable sequence elements and none of the remaining four contain enhancing motifs. Of 9 sites in Tea2, three have positive context. Amo1 also contains three sites with positive context (**Figure 5.11C**), has 10 sites overall and has the highest enrichment (4.21). Examining these sites more closely also indicates strong clustering, with 9 sites in less than 150 residues (217-348). For comparison, Traven and Heierhorst (2005) report SQ/TQ clusters with densities as low as 8 sites in 302 residues.

Following this investigation, collaboration with Dr Jesus Carballo (University of Sussex, UK), led to more detailed examination of the Amo1 sequence identifying six plausible ATM/ATR target motifs, with two sites (225 and 296) being particularly strong candidates.

This analysis focuses specifically on phosphorylation by ATM/ATR-type kinases directly. Performing a similar analysis for targets of the checkpoint kinases was less straightforward. Blasius et al. (2011) used an analogue sensitive CHK1 mutant and mass spectrometry analysis to propose a potential sequence favoured by CHK1. They reported a preference for positively charged residues at the -3 and -4 positions, a direct conflict with sites targeted by ATM/ATR.

Application of the same MATLAB code shows that there are only three of these sites in the Amo1 sequence (enrichment <1). However, the paper also reports that checkpoint phosphorylation sites are complex and only 120 of 268 identified target sequences include this particular consensus. Furthermore, this investigation only applies to CHK1 in human cells, consensus may vary between species and may also differ in CHK2/Cds1.

These findings suggested that Amo1 may be a strong candidate for mediating a link between the DDR kinases and the microtubule cytoskeleton, most likely through direct phosphorylation by ATM/ATR. In addition to the previous results

showing that microtubules in *amo1*Δ cells do not become stabilised in response to DNA damage, this suggested that Amo1 may be worthy of more detailed study.

5.8 Amo1 as a mediator between DNA damage and microtubules

From here I went on to investigate what is already known about Amo1 and further explore whether it might actually be responsible for the microtubule response to HU reported above.

5.8.1 Previously published work

Amo1 was identified by Pardo and Nurse (2005) in an over-expression screen for microtubule regulators. The initial screen reported a microtubule phenotype with one long, bright microtubule bundle per cell. Under the conditions used, *amo1*Δ cells grew slower than wild-type and showed a very mild propensity (8%) for bending.

In immunofluorescence images of cells expressing *gfp-atb2* from an exogenous site *amo1*Δ cells were reported to have fewer, longer microtubule bundles than wild-type. Microtubules in *amo1*Δ were also shown to be more resistant to depolymerisation by carbendazim (MBC), thiabendazole (TBZ) & cold treatments (Note that, although MBC and TBZ have historically been treated as equivalent, TBZ induces transient actin depolymerisation and cell growth arrest in addition to the microtubule destabilisation that is common to both MBC and TBZ (Sawin and Snaith, 2004)). Although *amo1*Δ was not seen to affect chromosome segregation, a reduced mitotic index was observed and over-expression led to mis-segregated chromosomes.

Attempts to establish a role for Amo1 in stabilising microtubules were complicated by its localisation on the nuclear envelope. Known microtubule-stabilising factors are typically active at the +ends near the cell tips, so-called +TIP proteins (e.g. Mal3, Tip1). Amo1 is a relatively low abundance protein, but has not been shown to localise away from the nuclear periphery. Pardo et al. were unable to show a role for Amo1 in microtubule nucleation, a more typical activity for factors localised

at the nuclear rim. There was also no evidence for Amo1 affecting microtubule anchoring to the nuclear membrane, *amo1*Δ cells also did not show altered microtubule polymerisation or depolymerisation rates but did spend more time in contact with the cell tips.

Pardo et al. went on to show that Amo1 does not affect microtubule loading of several microtubule associated factors, including Klp5, Tea2, Tip1 as well as nucleation factors Alp4 and Mod20 (Mto1). In contrast to weak sequence homology, they also provided evidence against a role for Amo1 as a nuclear pore complex (NPC) component.

More recently, Asakawa et al. (2014) have again proposed the idea of Amo1 as a NPC component, based primarily upon sequence analysis and localisation. Meanwhile, Hasan et al. (2014) also used sequence analysis to identify Amo1 as a putative RNA-binding protein containing a zinc-finger (zf-CCCH) motif (proposed binding consensus: UAUGAU). Transcriptome analysis of *amo1*Δ revealed a total of 44 mRNAs affected by Amo1 loss. Unfortunately, for the purposes of my investigations, none of the mRNAs identified have any known links to microtubules. Since this paper was published towards the end of the research reported here, there has been little opportunity to pursue these findings any further experimentally.

5.8.2 The effect of *amo1* deletion on cell tubulin content

Measuring whole cell tubulin levels, using GFP fluorescence, in *amo1*Δ cells showed a comparable, or sometimes greater, increase to wild-type (see **Section 5.5.1.1**, KS-test; p=0.02) when treated with 15 mM HU (28-46%; p<0.001) (**Figure 5.12A**). Increases were also seen consistently in *cds1*Δ (14-31%; p<0.09), but were less significant. Similarly *rad3*Δ, varied between a 16% increase and 6% decrease in GFP fluorescence levels. However, *rad3*Δ results are based upon very few data points, due to the poor survival of this strain in HU. This suggests that, whilst Amo1 affects microtubule bundle length in response to HU, it still experiences an increase in tubulin content, comparable to, or greater than the change observed in wild-type cells. By contrast, Cds1 and Rad3 appear to be at least partially required to facilitate increased tubulin.

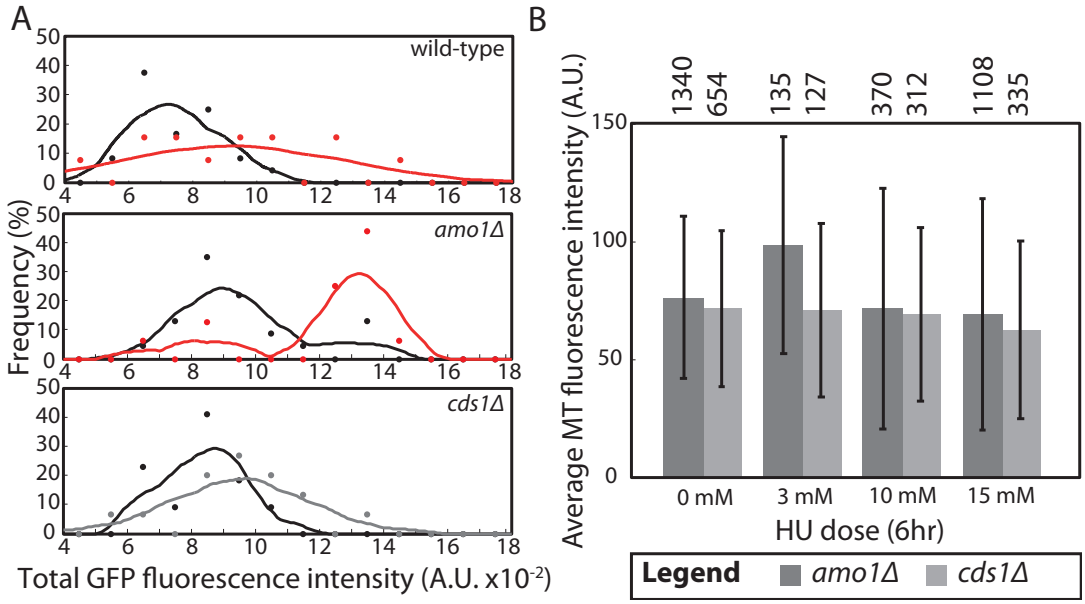

Figure 5.12: GFP-Atb2 levels in *amo1*Δ and *cds1*Δ - **(A)** Kernel density plots of total GFP fluorescence, measured for whole cells after subtraction of background fluorescence, as measured in equivalent GFP-negative cells, in one example experiment. Shown are wild-type (top) *amo1*Δ (middle) and *cds1*Δ (bottom), including untreated populations (black) and 15 mM HU-treated populations with significant (red; KS-test; $p<0.05$) or insignificant (grey) changes. Comparable wild-type data averaged across many experiments is presented in **Figure 5.7A**. **(B)** Average (± s.d.) microtubule fluorescence intensity measurements from one example experiment comparing *amo1*Δ (dark grey) and *cds1*Δ (light grey). Number of measurements taken are given above each bar.

Examination of GFP fluorescence levels in microtubules seems to mirror the results for total tubulin fluorescence (**Figure 5.12B**). When comparing microtubule bundles from HU-treated and untreated cells in the same experiment, *amo1*Δ demonstrated a 29% increase in average fluorescence after 3 mM HU (KS-test; $p<0.001$), which was subsequently lost with higher doses. Examination of *cds1*Δ showed no change at 3 mM, 10 mM or 15 mM HU ($p>0.54$).

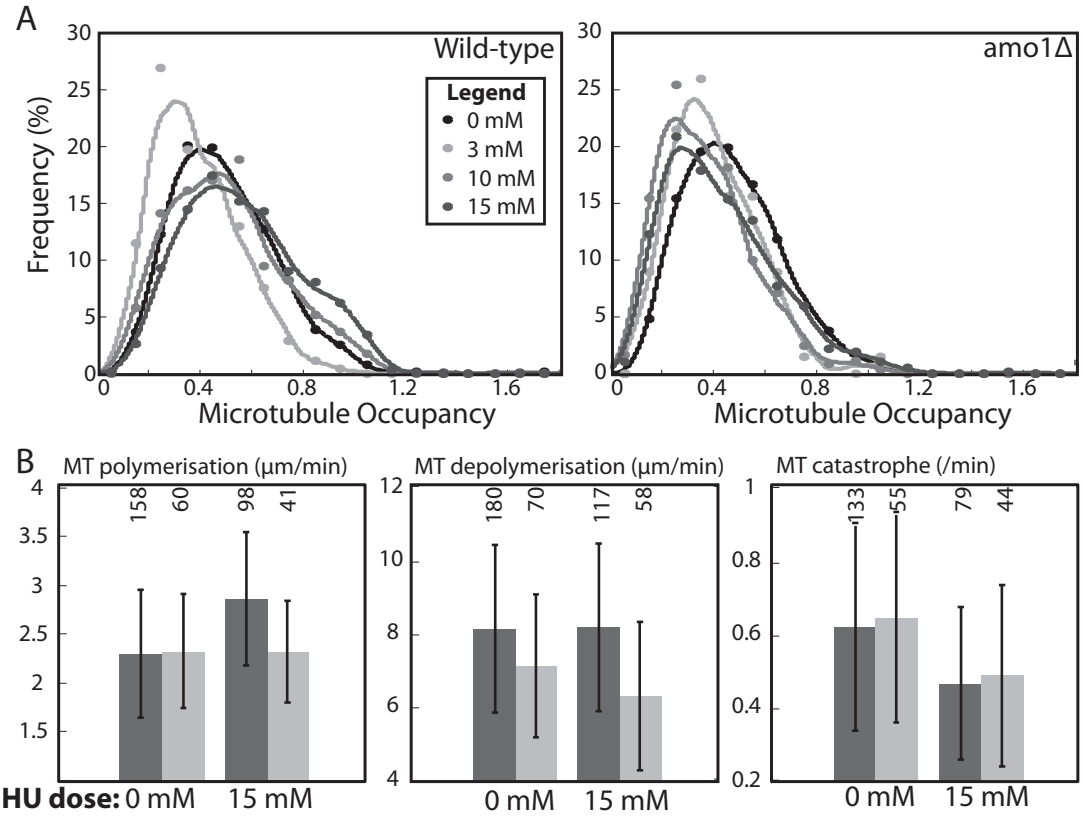

Figure 5.13: Comparison of *amo1*Δ to wild-type - **(A)** The different effect of 3, 10 and 15 mM HU treatment for 6 hours, on microtubule occupancy in wild-type cells (left) and *amo1*Δ (right). **(B)** Paired bar charts representing microtubule polymerisation (left), depolymerisation (middle) and catastrophe (right) rates from kymographs of wild-type cells (dark grey) and *amo1*Δ cells (light grey).

5.8.3 Microtubule dynamics are unchanged in HU treated *amo1*Δ cells

I have already shown that *amo1*Δ does not elongate microtubules in response to 15 mM HU over 6 hours. The same can also be shown to be true for different doses (**Figure 5.13A**) and durations of HU treatment (not shown). In wild-type cells, treatments of 10 mM HU and 15 mM HU result in a pattern of microtubule occupancy comparable to untreated cells, yet, in *amo1*Δ cells, the pattern of occupancy, in response to any dose of HU, is comparable to wild-type cells treated with 3 mM HU. Occupancy appears reduced, as cells elongate beyond the capacity of dynamic microtubules to keep up.

Examining the properties of microtubule dynamics in *amo1*Δ cells (**Figure 5.13B**) reveals a reduction (KS-test; p=0.027) in microtubule depolymerisation rate relative to wild-type cells. This effect is present in untreated cells but becomes more pronounced after HU treatment (p<0.001), although the change from untreated to treated cells is not significant (p=0.11).

More strikingly, whilst untreated *amo1*Δ cells maintained a polymerisation rate almost identical to wild-type (2.32 ± 0.59 μm/min), there was no increase observed after HU treatment (2.31 ± 0.52 μm/min). The rate of catastrophe in *amo1*Δ was comparable to wild-type before and after HU treatment.

5.8.4 Amo1 relocalises in response to HU

One outstanding puzzle of Amo1, which was reinforced by the results presented above, was the ability for it to influence microtubule dynamics near the cell ends from the nuclear envelope. In an attempt to explore this, I obtained an Amo1-GFP strain to study the localisation of Amo1. As previously reported Asakawa et al. (2014), Amo1 has comparatively (by comparison to, say, Atb2) low abundance but localises to the nuclear envelope in an inhomogeneous distribution. I was unable to observe any instances of Amo1 localising near to cell tips either in the absence or presence of HU.

However, many (≈85%) cells treated with HU showed confinement of Amo1 to specific sections (**Figure 5.14A**). This sometimes corresponded with the appearance of a large vacuole-like structure around the opposite side of the nucleus. This structure was visible in transmitted light images but showed no fluorescent signal. Unlike vacuoles that become apparent during cell death, this structure was much larger and did not have a high level of autofluorescence.

To assess the specificity of this observation, I also tried looking at localisation of Cut11-GFP, a more well-known nuclear envelope protein (West et al., 1998). Cut11 also becomes disrupted as a result of HU treatment (**Figure 5.14B**), which therefore suggests that this effect is a more general rearrangement of the nuclear membrane and not due to some specific aggregation of Amo1 proteins alone. It may be possible that, since these proteins both have proposed links to the NPCs, this represents a rearrangement of the pores and not necessarily the entire nuclear membrane.

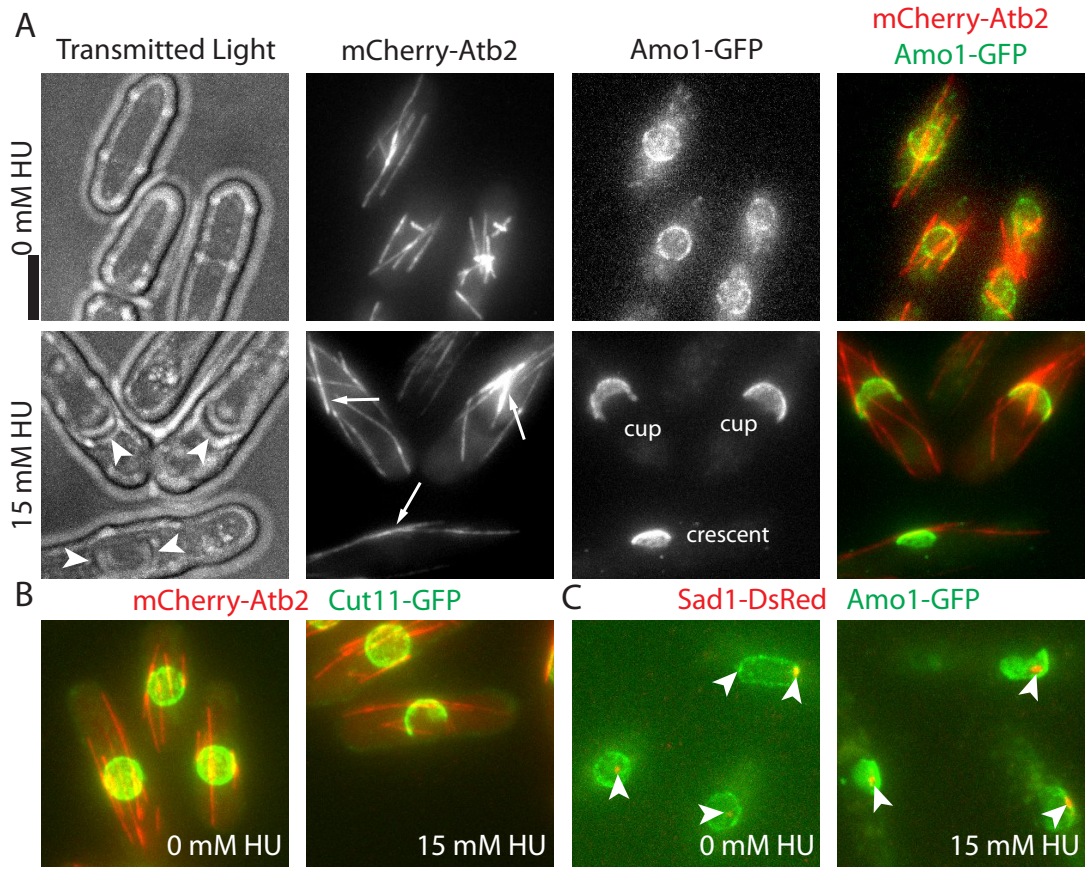

Figure 5.14: Amo1 localisation in response to HU - **(A)** Localisation of Amo1-GFP in untreated (top row) and 15 mM HU-treated (bottom row) cells. Note how, when treated with HU, Amo1-GFP no longer localises to all parts of the nuclear periphery, generally corresponding with microtubule positions (arrows). Note also, apparent distortions in transmitted light images corresponding to the area of undecorated nuclear periphery (arrowheads). **(B)** Cut11-GFP shows similar nuclear localisation to Amo1-GFP in both untreated (left) and 15 mM HU-treated (right) cells. **(C)** When Amo1-GFP is disrupted by 15 mM HU treatment, it always co-localises with Sad1-DsRed, a fluorescently-labelled marker of the SPB position (arrowheads). Scale bar represents 5μm.

Furthermore, of 224 microtubule bundles (mCh-Atb2) assessed in HU-treated cells with relocalised Amo1, ≈79% coincided with the areas of the nuclear envelope labelled with Amo1-GFP. Since these regions typically took the form of a crescent, cup or occasionally ring covering less than half of the nuclear surface, it seems possible that microtubules favourably interact with the Amo1-positive regions. This was also investigated by labelling the SPB using Sad1-DsRed, to pin-

point the location of the SPB, which also acts as an iMTOCs. Each cell contained a single Sad1-DsRed point of which 100% (51/51) coincided with Amo1-GFP (**Figure 5.14C**).

The finding that Amo1 and possibly other nuclear membrane factors gather together in one region of the nuclear envelope and that this appears to correlate with the position of the SPB, as well as the points where most microtubule bundles contact the nucleus, may suggest a benefit for DNA repair or the DNA damage response of concentrating the microtubule points of contact with the nucleus into just one region.

5.8.5 Attempts to verify Amo1 phosphorylation

As mentioned in **Section 5.7.3**, phosphorylation targets of the ATM/ATR kinases are well-studied. There are even antibodies available that are specific to phosphorylated SQ/TQ motifs. I attempted to examine whether SQ/TQ phosphorylation could be observed on Amo1 by performing a protein pull-down and western blot assay. Amo1-GFP cells were treated with 15 mM HU for 0, 2, 4 & 6 hours before being lysed.

I have been unable to produce definitive results by using this approach, despite various adaptations to the method, including changing lysis methods to preserve phosphoproteins, changes to the membrane blocking method and use of anti-GFP beads to enrich for GFP labelled proteins. One reason for this is probably the low abundance of Amo1 in cells, making it difficult to extract a sufficient amount for visualisation. Western blotting for phosphorylated residues is also generally difficult as phosphorylations can be unstable and easily lost. In addition, not all Amo1 in a cell is likely to be phosphorylated, further reducing the maximum possible signal. Since Amo1 may also be a protein with strong links to the nuclear membrane, it may also respond poorly to cell lysis and protein extraction.

Some blots for Amo1-GFP have produced faint double bands in the 50-64 kDa range (**Figure 5.15A**), which seem too small to be Amo1-GFP ($\approx$78 kDa). These blots included over 5 mg protein for each precipitation reaction, used low blocking stringency (1% BSA) and long exposure times (>1 hour). These bands may be Amo1-GFP as they are not apparent in blots using other strains but the size seems too small, there is no obvious reason for a double band and the protein

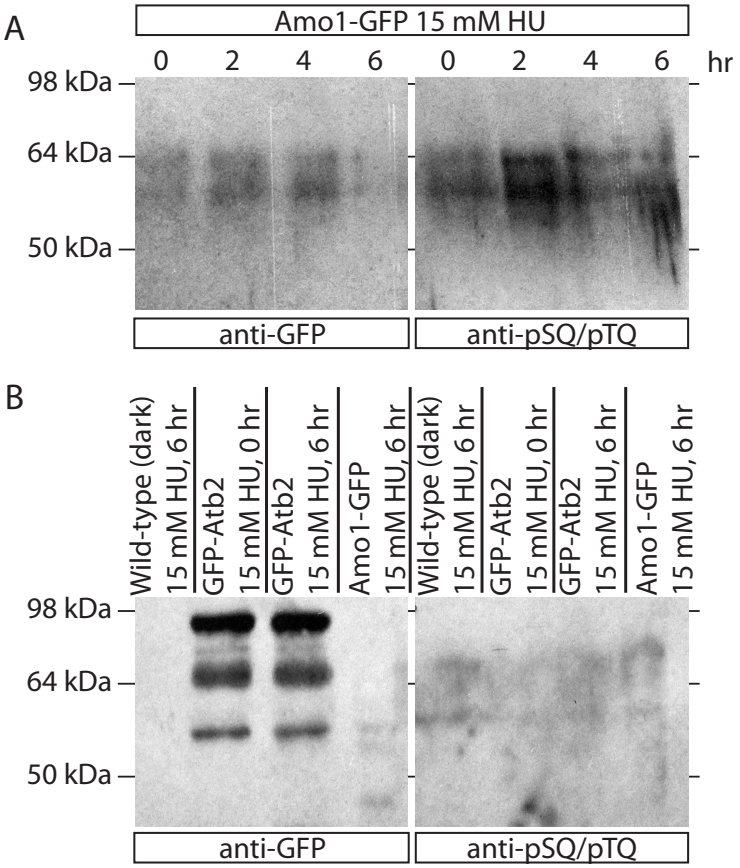

Figure 5.15: Attempts to show phosphorylation of Amo1 - **(A)** Western blot using anti-GFP to detect Amo1-GFP in cells treated with 15 mM HU for different lengths of time. Duplicate samples were run on the same gel, cut and probed with different antibodies (left & right frames). Exposure time ≈60 min. **(B)** Western blot testing Anti-GFP efficacy in detecting the GFP-Atb2. Extra bands are likely due to overloading of the gel. Exposure time ≈15 min. GFP-Atb2 is clearly detected (lanes 2 & 3) but not GFP-Amo1 (lane 4). Anti-pSQ/TQ is an antibody specific to sites of ATM/ATR-mediated phosphorylation. Extracts were enriched for GFP-labelled proteins using anti-GFP magnetic beads before loading onto gels.

would have to be at least partially phosphorylated even in untreated cells. Yet, if this is Amo1-GFP then it seems very probable that it is subject to SQ/TQ phosphorylation, likely a direct result of Rad3 activity.

A control experiment to test the efficacy of anti-GFP bead protein precipitation and the use of the anti-GFP detection antibody, compared the signal from a dark wild-type strain (PN557), a GFP-Atb2 strain (MS1404) and the Amo1-GFP strain (**Figure 5.15B**). This shows that GFP proteins are strongly detected in this

Strain	HU	n	Cell Length (μm)	MT Length (μm)	Occupancy	MTs/cell
*nup37*Δ	-	105	11.39 ± 2.3	5.35 ± 1.8	0.48 ± 0.2	3.3 ± 0.8
*nup37*Δ	+	97	21.29 ± 3.9	10.61 ± 4.4	0.52 ± 0.3	3.9 ± 1.1
*nup40*Δ	-	145	11.23 ± 1.7	6.04 ± 2	0.54 ± 0.2	3.1 ± 0.8
*nup40*Δ	+	127	19.2 ± 5.3	10.86 ± 4.9	0.58 ± 0.2	3.5 ± 1
*nup60*Δ	-	140	11.73 ± 2	5.73 ± 2.1	0.49 ± 0.2	3 ± 0.7
*nup60*Δ	+	78	22.62 ± 4.2	10.74 ± 4.4	0.48 ± 0.2	3.7 ± 0.9

Table 5.6: HU treatment of nuclear pore proteins - Average (± s.d.) changes in cell length, microtubule length, occupancy and microtubule bundle number in strains deleted for NPC components.

method, suggesting that issues with Amo1 relate to its low abundance. From this I conclude that future experiments should make use of even larger quantities of protein input, in the hope of recovering sufficient quantities of GFP-Amo1 for clear visualisation. Further testing should also be performed to ensure the efficacy of the pSQ/TQ antibody.

5.8.6 Examination of nuclear pore proteins

As mentioned above, the Amo1 sequence shows little homology to other known proteins. In their paper Asakawa et al. (2014) report finding some amino acid sequence similarity between Amo1, Nup42/Rip1 in *S. cerevisiae* and NUPL2/hCG1 a human nuclear pore protein. The NPC is a very large (125 MDa) and complex structure, its constituent proteins are called nucleoporins and generally have poor conservation between species, so it is not unusual for homology to be low between orthologues.

This proposed function for Amo1 led me to examine whether other nucleoporins may have a similar effect to Amo1 on the microtubule response to HU treatment. Unfortunately, nothing is known about where Amo1 might localise within NPCs so it is difficult to predict which other nucleoporins may play a similar role. A review from Bukata et al. (2013) reports that the *S. cerevisiae* homologue Nup42 is part of the external cytoplasmic periphery of the NPC, whilst the human homologue NUPL2 (labelled hCG1) is part of the cytoplasmic face of the pore itself. Of the

31 nuclear pore proteins reported by Asakawa et al. (2014), 16 were reported to be non-essential. Unfortunately none of the non-essential proteins are known to be cytoplasmic. Since there was limited time to pursue this, I decided to proceed by investigating three other nucleoporins, with available deletion mutants, from different NPC structures. The proteins selected were:

- Nup37 – Part of the Nup107-Nup160 ring. This major subcomplex forms the cytoplasmic side of a collar between the nuclear envelope and the pore itself and has roles in NPC assembly and RNA transport.

- Nup40 – Part of the Nup93 subcomplex, also involved in pore assembly and anchoring of the pore itself within the membrane. Primarily internal to the nucleus.

- Nup60 – Part of the nuclear basket structure on the nucleoplasmic face of NPCs.

I have completed one preliminary study of these proteins, examining microtubules in cells deleted for each protein, in the presence and absence of 15 mM HU over six hours. Whilst these results are only preliminary, they do provide interesting results (**Table 5.6**). None show an increase in microtubule occupancy on the scale of wild-type but both *nup37*Δ and *nup40*Δ show some microtubule elongation (9% & 7%; KS-tests; p=0.70, 0.13), whereas *nup60*Δ shows no change (p=0.93).

Although these results are not particularly conclusive, this may suggest that fully functional NPCs are an important part of the microtubule response to HU treatment and deletion of NPC components may have partial effects on the magnitude of this response. Whilst this does little to validate the view that Amo1 is a nuclear pore component, it may suggest that its role is in some way linked to these structures. Further experiments are needed to study other NPC mutants and more conclusively establish links to the DDR and Amo1.

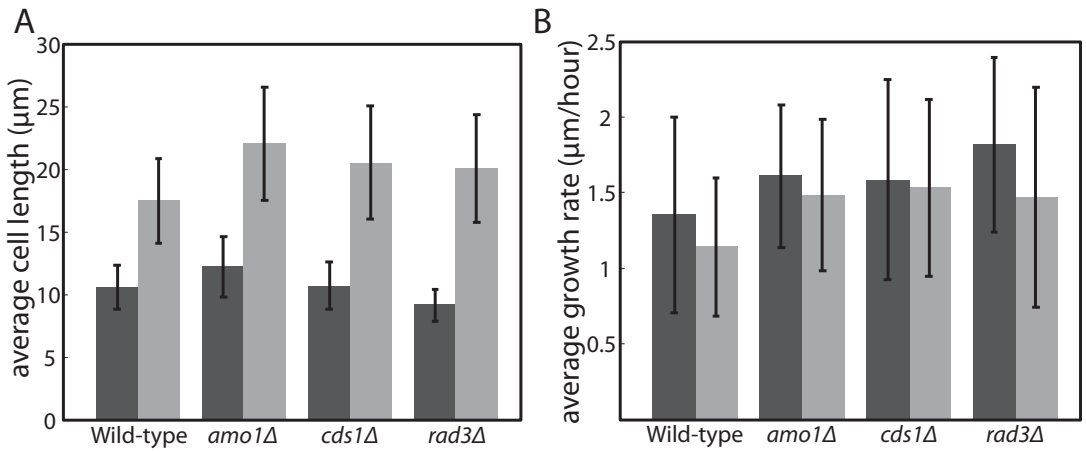

Figure 5.16: Growth rate responses to HU - **(A)** Average cell length, measured from static images for wild-type and key deletion mutants, aggregated across several experiments as in **Table 5.4**. **(B)** Average cell growth rate, as measured from timelapse images taken every 10 minutes over 6 hours. In both cases untreated (dark grey) and 15 mM HU-treated (light grey) cells were studied.

5.9 Further aspects of the microtubule response to HU

5.9.1 HU induces reduced cell growth rate in wild-type cells

Although it is apparent that an active reorganisation of microtubules is required to give the observed relative increase in microtubule length when treated with HU, this was complicated by differences in average cell lengths under different conditions. The change in average wild-type cell length after 6 hour 15 mM HU treatment was just 6.87 μm, whilst for *cds1*Δ, *rad3*Δ and *amo1*Δ it was 9.80, 10.95 & 9.80 μm respectively (**Figure 5.16A**). Although *S. pombe* cells are reported to have a doubling time of 2½ hours (Carlson et al., 1999; Mitchison and Nurse, 1985) – during which, cells are expected to grow approximately 7 μm – this is measured at 32℃ and is highly temperature sensitive. At room temperature we would expect cells to grow significantly slower.

Notably, most deletion mutants studied (e.g. *tea1*Δ, *tip1*Δ, *mal3*Δ) showed a similar or lower rate of average length change to wild-type (5.00-7.20 μm). Surpris-

ingly, some others had a higher rate of average cell length increase (e.g. *dis1*Δ, 7.90 μm and *klp6*Δ, 8.70 μm) but also showed corresponding microtubule elongation, meaning that microtubule occupancy still increased. This suggests that the absence of a microtubule response to HU treatment may also be linked to a change in cell growth rate.

To investigate whether HU treatment actually caused a change in growth rate of wild-type cells, I performed timelapse imaging of cells every 10 minute over 6 hour periods at room temperature. This was directly comparable to the imaging conditions of previous experiments. I then measured the length of cells throughout the video as they underwent growth and (in some cases) division (**Figure 5.16B**).

On average, I found that wild-type cells gained an average 1.36 μm/hour suggesting a doubling time just over 5 hours (310 min). In contrast to the findings of Pardo et al., *amo1*Δ cells, as well as *cds1*Δ and *rad3*Δ grew slightly faster (1.61, 1.58 & 1.81 μm/hour).

When treated with HU, wild-type cells did slow down, reducing growth by ≈19% to 1.14 μm/hour (KS-test; p=0.01). The *amo1*Δ and *cds1*Δ cells showed some reduction but these were not significant (1.48 & 1.53 μm/hour, p=0.06 & 0.38). Unexpectedly, *rad3*Δ cells slowed growth much the same as wild-type (24% reduction to 1.47 μm/hour). This contradicts measurements of cell length that show *rad3*Δ cells gaining on average over 10μm in just six hours. However, as previously mentioned, *rad3*Δ experiences high levels of cell death in response to HU treatment, which may explain this unexpected result. Many of the *rad3*Δ cells imaged may slow growth prior to cell death, whilst the few that survive continue at a higher growth rate.

Although these mutant strains do not appear longer than wild-type during normal growth, due to having a more similar growth rate and an implied higher division rate, they are able to grow at a rate that is 28-34% higher than wild-type when treated with 15 mM HU, resulting in a greater increase in length over the same period of time.

5.9.2 Microtubule stabilisation does not influence survival

In their paper Hayles et al. (2013) reported that *amo1*Δ showed a mild sensitivity to low dose HU (2.75 mM - 5.5 mM) over 24-48 hours when grown on agar plates.

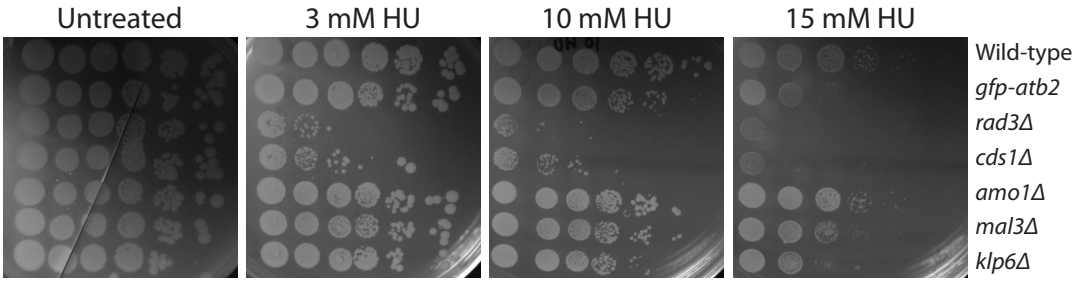

Figure 5.17: Sensitivity to HU - Wild-type and mutant strains exposed to 0, 3 mM, 10 mM & 15 mM HU for 72 hours on YES+agar plates, to explore sensitivity to HU treatment.

They went on to examine this using microscopy to show that a small number (<15%) of cells produce a cut phenotype after 10 hours treated with 11 mM HU in minimal medium and then fixed.

I also examined the growth of several strains on agar plates using 3 mM, 10 mM & 15 mM HU (**Figure 5.17**). At 3 mM *cds1*Δ and *rad3*Δ already showed severe loss of viability in-line with previous findings, including Hayles et al. There was no obvious effect on *amo1*Δ. Even at higher doses there was little distinction between *amo1*Δ and wild-type. Notably *klp6*Δ, which was included for comparison as another microtubule regulator, seems more sensitive to these higher doses of HU. There is also a noticeable difference between the HU sensitivity of the true wild-type strain and the strain carrying GFP-Atb2, which is the only strain included carrying a fluorescent construct.

An interesting result from this investigation is that *amo1*Δ cell survival in the presence of HU appears to be unaffected by the absence of Amo1 and hence the lack of microtubule stabilisation. This would appear to suggest that microtubule stabilisation is not critical for effective DNA repair. Yet, if this is that case, it is unclear why this response exists. It is possible that the benefit of microtubule stabilisation is subtle and only needed to ensure long term viability in the presence of DNA damaging agents over many generations i.e. to improve the efficiency or accuracy of DNA repair.

The sensitivity of the GFP-Atb2 wild-type strain is concerning as it highlights that fluorescent labelling can have some effects on cell physiology. In this case, the presence of GFP on Atb2 may serve to partially inhibit its incorporation into microtubules. As explored previously, microtubules containing more Atb2 relative to Nda2 are often more stable (Adachi et al., 1986). As such, this may serve to show

that microtubule stability can have some impact on cell viability, in that GFP-Atb2 microtubules are putatively less stable and the resulting cells are more sensitive to DNA damage than unlabelled wild-type cells.

5.9.3 A putative role for Ase1 in responding to DNA damage

Microtubule bundles are typically thought to include one overlap region near the cell centre where all microtubule -ends are gathered and held together by the crosslinker protein Ase1 (Loiodice et al., 2005; Janson et al., 2005). Although, detailed study proposes that bundles are more varied and not all microtubule -ends are located close to the nucleus at all times (Höög et al., 2007). During imaging of microtubule dynamics for kymographs, I noticed that the bundles in elongated cells seemed to undergo a lot of fragmentation and reassembly. It seemed that individual microtubules were spanning several regions of microtubule bundling, which were not being gathered together into a single point. I hypothesised that this may mean the observed elongation of microtubules was actually the result of rearrangement within bundles and not elongation of the microtubules themselves.

If this were the case, then microtubules in *ase1*Δ cells should not become longer upon 15 mM HU treatment. In addition, I examined Ase1-GFP cells to look for fragmentation or elongation of the Ase1-positive microtubule overlap region.

As predicted, microtubule occupancy did not show a significant increase (0.33 $\pm$ 0.15 to 0.35 $\pm$ 0.18; **Figure 5.18A**). In addition, as with *cds1*Δ and others, the change in average length over 6 hours was also higher than wild-type (21.5 $\pm$ 5.5 μm to 33.0 $\pm$ 5.7 μm). A preliminary examination of the extent of Ase1-GFP decoration on microtubules showed no change, with Ase1 covering approximately $^1/_3$ of total microtubule bundle length in each cell, whether untreated (0.34 $\pm$ 0.22) or HU-treated (0.32 $\pm$ 0.22; **Figure 5.18B**). The most apparent change was a shift in the number of Ase1 marked regions per microtubule bundle **Figure 5.18C**. In both cases, bundles had 0-3 Ase1 sections. However, whilst 70% of untreated cells had only one Ase1 region, only 55% did after HU treatment.

More data is needed to verify whether this is significant, it may be that the increase in number of Ase1 regions is simply due to the increase in cell length meaning that it takes longer for new microtubules to be collected into the central microtubule overlap regions. Hence, more microtubules include secondary Ase1

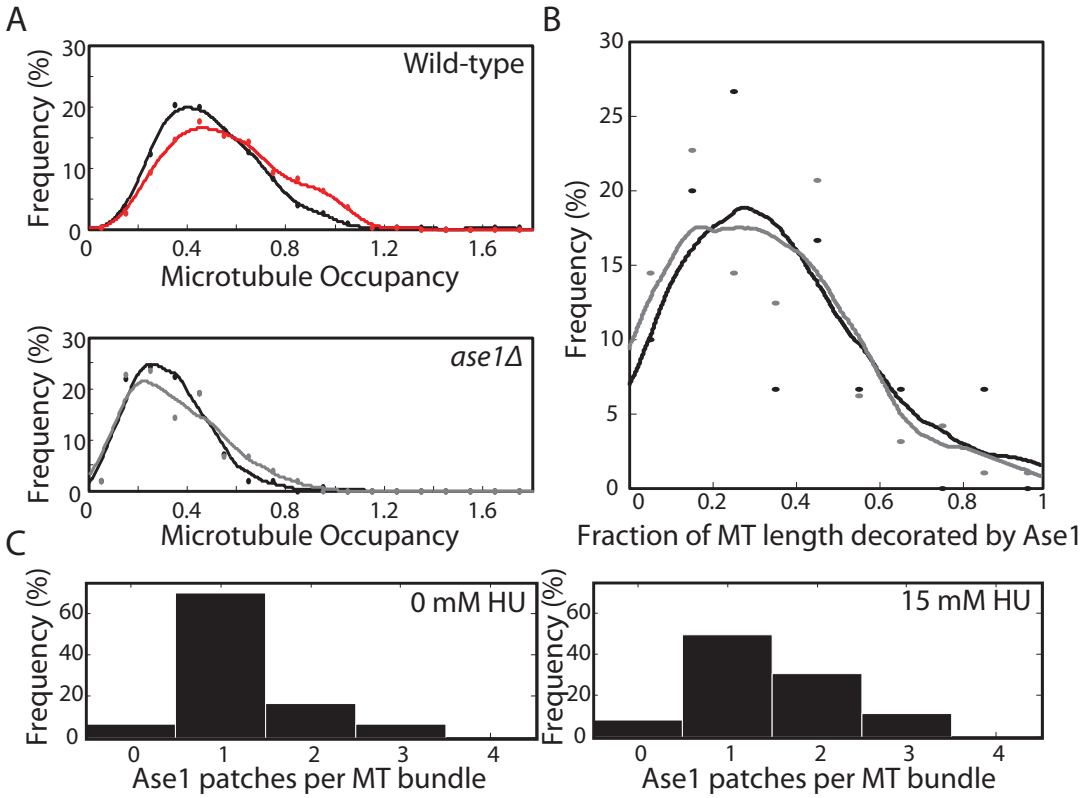

Figure 5.18: The role of Ase1 in response to HU - **(A)** Microtubule occupancy for wild-type (top) and *ase1*Δ (bottom). Untreated (black), HU-treated (grey; KS-test; p>0.05), HU-treated showing significant increase (red; p<0.05). **(B)** Fraction of microtubule length (mCh-Atb2) coated by Ase1-GFP in untreated (black) and HU-treated (grey) wild-type cells. **(C)** Histograms of number of Ase1 labelled regions per microtubule bundle in untreated (left) and HU-treated (right) cells. All HU-treated cells were treated with 15 mM HU for 6 hours.

marked regions. Examination of Ase1-GFP after 3 mM HU treatment and time-lapse imaging of Ase1 patch migration along microtubule bundles would help to confirm these findings.

5.9.4 Potential involvement of Mtr1 in responding to DNA damage

Towards the end of the work shown here, Carlier-Grynkorn et al. (2014) reported that deletion of the gene *SPCC132.01c* (*Mtr1*) was able to influence microtubule dwell time at the cell ends and could partially rescue microtubule destabilisation

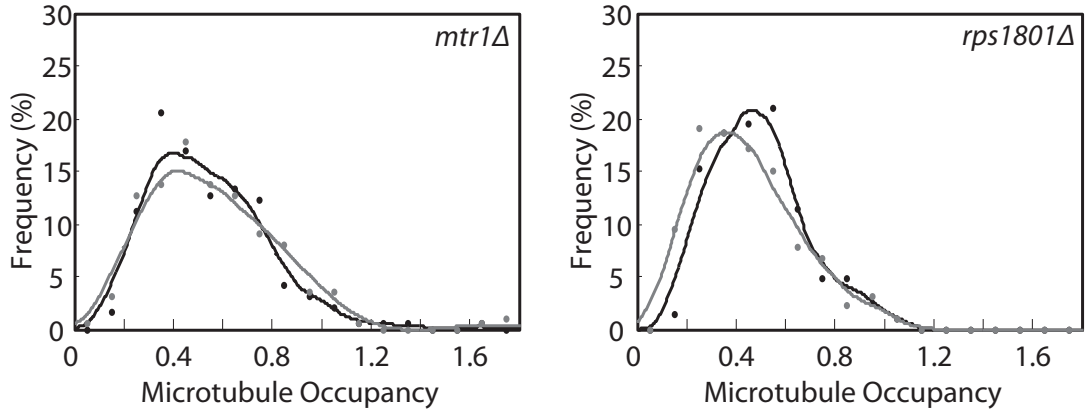

Figure 5.19: Testing the response to HU in *mtr1*Δ & *rps1801*Δ - Microtubule occupancy for untreated cells (black) and 15 mM HU-treated cells after 6 hours (grey; KS-test; p>0.05) in *mtr1*Δ & *rps1801*Δ populations.

in *mal3*Δ. The gene was identified as affecting microtubules in a screen of genes with proteins carrying an SxIP motif, which is common to many Mal3/EB1 interactors. Surprisingly Mtr1 has a general cytoplasmic localisation and was not reported to localise to microtubules with any specificity. Mtr1 also has sequence homology to elements of the ribosomal quality control complex and the paper went on to show that *rps1801* deletion was able to phenocopy *mtr1*Δ.

In the paper, similar dynamic analyses to the methods used in **Section 5.5.2** were employed to examine *mtr1*Δ. Their major finding is an extension of the length of time microtubule tips spend in contact with the cell end before initiating catastrophe (dwell-time, t-test; $p<10^{-5}$). They also report subtle reduction in polymerisation rate (p=0.01) and catastrophe rate (p<0.01).

Whilst I have not been able to study these genes fully, I have again tested their deletions for response to 15 mM HU treatment. Both of these proteins, after repeated testing, consistently show no response to HU treatment (**Figure 5.19**). Microtubule occupancy in *mtr1*Δ does not vary from untreated cells (KS-test; p=0.48), whilst *rps1801*Δ shows a shift towards lower microtubule occupancy (p=0.02) comparable to *amo1*Δ. In line with **Section 5.9.1**, these strains also show respective average cell length elongation of 8.70 and 10.64 μm over six hours. It is also worth noting that neither protein is likely to be a good candidate for direct ATM/ATR phosphorylation at SQ/TQ sites.

I would recommend exploring Mtr1 and Rps1801 further by examining dwell-time

in more detail in combination with *cds1*Δ, *amo1*Δ, as well as exploring microtubule dynamics of HU-treated *mtr1*Δ/*rps1801*Δ cells.

5.10 The microtubule response to DNA damage in *Homo sapiens*

In the process of preparing the results of the screen and the preliminary results relating to the DDR hits for publication, a collaboration with Dr Laura Wagstaff in the lab of Dr Eugenia Piddini (Gurdon Institute, Cambridge, UK) was undertaken to explore the possibility of a conserved link between DNA damage and microtubule organisation. The first results in this study, from L. Wagstaff and E. Piddini, are reported in Graml et al. (2014) and reproduced here in **Figure 5.20**.

Visual study of these images suggested a response to DNA damage, observed as formation of dense microtubule bundles around the nucleus, in cells exposed to 30 J/m^2 UVC radiation (**Figure 5.20A**). Further quantification of microtubules in these images is difficult due to the complexity of the microtubule network in higher eukaryotic cells. Unlike in *S. pombe* it was impossible to manually or computationally isolate and measure individual microtubules from the considerably more complex microtubule network.

Exposing microtubules to low temperatures (4℃ PBS, 10 min) before fixation is known to favour depolymerisation, greatly reducing and simplifying the microtubule networks within cells (Kirschner et al., 1974). Using this approach it was possible to more easily visualise microtubules and attempt to quantify the effect of UVC exposure (**Figure 5.20B**). The microtubule networks in these images were skeletonised by L. Wagstaff to create a skeleton view of the microtubule networks with each element reduced to just one pixel wide. Computational measurement these networks by A. Chessel found that the number of junctions, may provide a measure of the microtubule extent in these cells. The number of junctions is defined the number of places where microtubules came together or branched, showed an increase as a result of UV treatment and provided evidence for greater length and/or number of microtubules following DNA damage.

Immunostaining for acetylated-tubulin in cold-treated cells provided a second measure based upon the extent of remaining microtubules in these cells. Acetylation

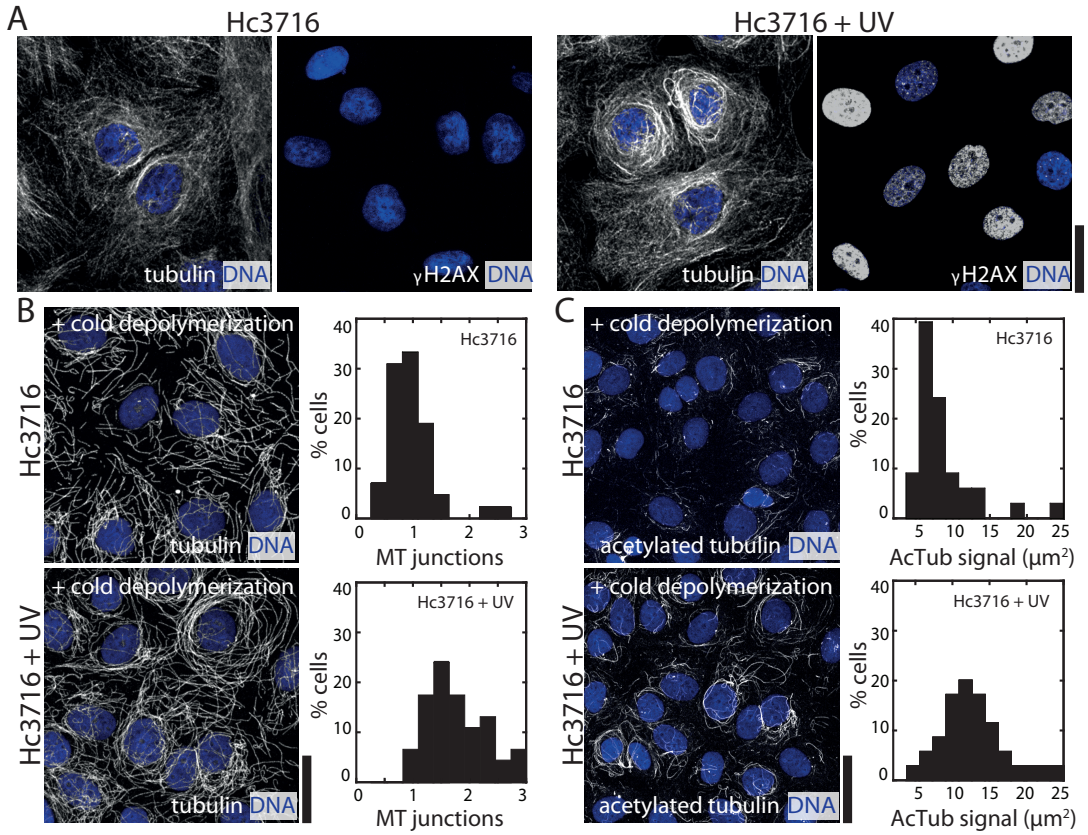

Figure 5.20: Microtubule response to UV in human cells - **(A)** Immunofluorescence images comparing microtubule arrays (panels 1 & 3) in human cells (Hc3716-hTERT) in the absence (left) and presence (right) of DNA damage induced by exposure to 30J/m^2 ultraviolet subtype C (UVC) radiation. Separate images of cells subjected to the same treatment are shown, stained for γH2AX (panels 2 & 4), a marker of DNA damage. **(B)** Quantification of the effect of UVC exposure on number of microtubule intersection points (junctions) in Hc3716 cells, after partial microtubule depolymerisation by 4℃ treatment for 10 min. **(C)** Quantification of acetylated tubulin immunofluorescent signal under the same conditions. Figure from Graml et al. (2014).

marks only a subset of microtubules, which are typically held to be particularly stable or long-lived (Lawson and Carazo Salas, 2013; Westermann and Weber, 2003; Wloga and Gaertig, 2010; Janke and Bulinski, 2011). Visualising just acetylated tubulin gives a reduced view of the microtubule network, which is easier to evaluate (**Figure 5.20C**).

At this stage I took over this work, hoping to further investigate the similarities between the responses in *S. pombe* and *Homo sapiens* cells.

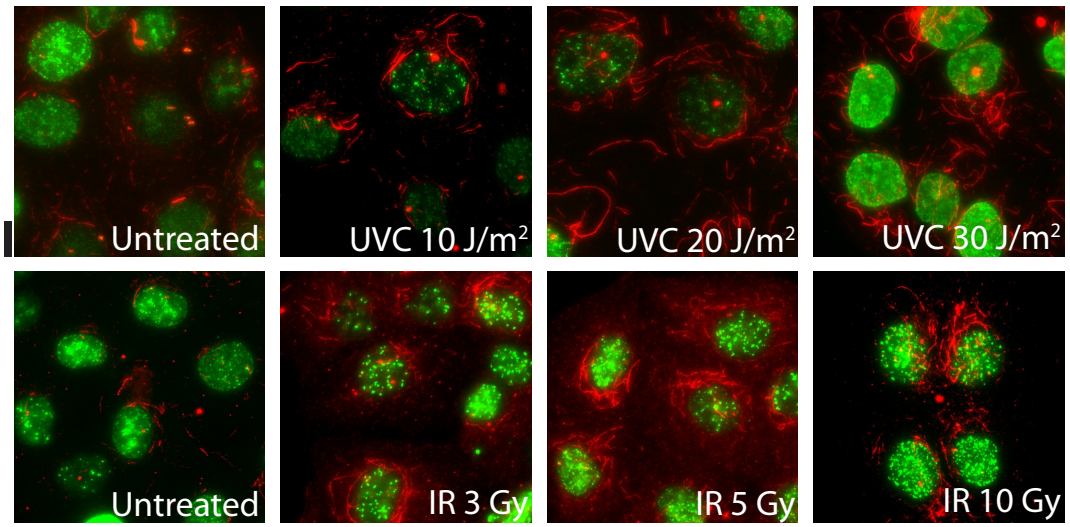

Figure 5.21: Example images of human cells exposed to UVC or IR - Example images of Hc3716-hTERT cells exposed to varying doses of UVC radiation or ionising radiation (IR), showing DNA damage marker γH2AX (green) and acetylated tubulin (red). Scale bar represents 10 μm.

Further investigation of the data from Graml et al. led to the conclusion that variation in the level of DNA damage may be reducing the significance of our results. Cells subjected to the same treatments may not necessarily have the same magnitude of DNA response. Untreated cells may experience DNA damage randomly from the environment and treated cells may be subject to variation in levels of exposure, as seen in **Figure 5.20A**, panel 4.

Co-staining cells for γH2AX immunofluorescence and either tubulin or acetylated tubulin allowed direct comparison of DNA damage and the microtubule response. Hence, in most subsequent investigations, I co-stained for γH2AX and acetylated tubulin. Acetylated tubulin already seemed to be the most useful stain for image analysis and had the added benefit of being a compatible antibody with γH2AX staining.

5.10.1 UVC exposure appears to stabilise microtubules in a dose-dependent manner

I found that the simplest method of analysis for these images was a visual comparison of proportion of cells with only stubs of microtubules remaining after 4℃ treatment, against cells which retained distinct microtubule arrays. Similarly, Pardo and Nurse (2005) also assessed microtubule stabilisation in *amo1*Δ *S. pombe* cells by counting the proportion of cells that retained microtubules after 4℃ treatment. Cells were judged to have retained microtubule arrays if they included multiple microtubules with a length greater than the diameter of the cell nucleus and several branches or junction points.

Despite this straightforward approach to microtubule assessment, there was extensive variation between experiments. Yet it was still possible to identify trends between different treatments, allowing combination of data from across experiments. Variation is likely to be the result of changing cell confluence between experiments, as well as changes in the extent of microtubule depolymerisation induced by 4℃. In all cases, the proportion of cells retaining observable microtubule arrays after 30 J/m^2 UVC treatment was higher than untreated cells.

In different experiments 11-52% of untreated cells retained microtubule arrays, averaging 31% ($^{243}/_{786}$) of cells across eight experiments. On average, almost twice as many cells treated with 30 J/m^2 UVC retained acetylated microtubules (57%; $^{204}/_{357}$) across five experiments (**Figure 5.21**; top row). This distinction became more apparent when results were filtered based upon γH2AX fluorescence signal. Only 25% ($^{145}/_{569}$) of γH2AX-negative untreated cells retained microtubules, whilst 59% ($^{156}/_{266}$) of 30 J/m^2 UVC cells did. Individual experiments varied, showing an increase in microtubule array retention of between 1.5- and 3.9-fold from untreated to UVC treated cells.

Examining other UVC treatments, showed a dose-dependent response in line with that observed for HU treatment in *S. pombe*. Whilst 10 J/m^2 exposure resulted in an average 39% ($^{53}/_{137}$; 1.00- to 1.02-fold) increase in cells with microtubule arrays, across two experiments, 20 J/m^2 had an average 56% ($^{92}/_{164}$; 1.3- to 1.6-fold). Notably, an experiment which included a 100 J/m^2 treatment appeared to show no further increase above the 30 J/m^2 response (64%; $^{59}/_{92}$).

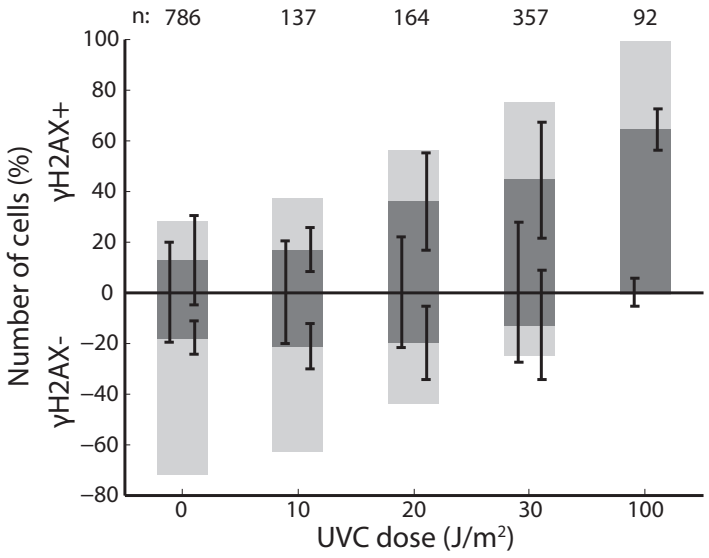

Figure 5.22: Change in γH2AX and microtubule stability in response to UVC treatment - Percentage of cells with strong γH2AX staining (above axis) or without (below) following exposure to different levels of UVC. Bars are divided into cells retaining microtubules after 4℃ treatment (dark grey) and lacking microtubules (light grey). Error bars show standard deviation between individual images across experiments.

The effect of filtering for γH2AX-positive cells became less noticeable as UVC dose increased and the proportion of cells with significant DNA damage rose (Figure 5.22). Across experiments, I found an average 26% of untreated cells with elevated γH2AX levels, of which 45% ($^{98}/_{217}$) retained microtubule arrays. Note that the proportion of γH2AX-negative cells with retained microtubules also seems to show some increase with UVC dose, this may be due to ambiguity in the distinction of γH2AX-negative vs γH2AX-positive cells or may suggest that the microtubule response to DNA damage is not exclusively linked to DNA repair mechanisms that are H2AX linked.

Hence, it appears that when Hc3716-hTERT cells are treated with UVC, this causes an expected increase in DNA damage, as measured by γH2AX staining. Interestingly, those cells that show high levels of DNA damage also included acetylated microtubule arrays with a higher degree of resistance to cold-induced depolymerisation.

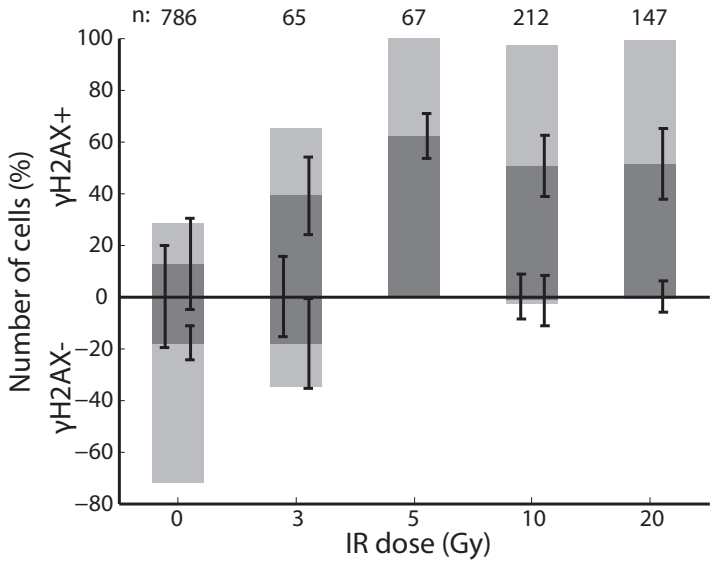

Figure 5.23: Change in γH2AX and microtubule stability in response to IR treatment - Percentage of cells with strong γH2AX staining (above axis) or without (below) following exposure to different levels of IR. Bars are divided into cells retaining microtubules after 4℃ treatment (dark grey) and lacking microtubules (light grey). Error bars show standard deviation between individual images across experiments.

5.10.2 IR exposure induces a more dramatic change in microtubule stability

Exposing DNA to UVC radiation is thought to cause a wide array of different lesions which make understanding of the cellular responses to damage difficult to dissect. Treatment of cells with IR is generally found to more specifically induce blunt DSBs and activate reportedly ATM-mediated responses in mammalian cells (Abraham, 2003). Previous comparisons have found IR dosage of 10 Gy to have roughly equivalent cytotoxicity to 10 J/m^2 UVC, with 12 Gy comparable to 30 J/m^2 (Chandler et al., 2006; Heffernan et al., 2007).

Across four experiments, 52% of cells, exposed to 10 Gy IR, retained acetylated-tubulin microtubule arrays (^{11}⁄$_{212}$; 1.5- to 2.6-fold increase over wild-type) after 4℃ treatment (**Figure 5.21**; bottom row). An experiment exploring lower IR doses found a 1.6-fold increase after just 3 Gy and 1.7-fold increase after 5 Gy. 20 Gy treatment was found to elevate microtubule retention by 1.4- to 2.2-fold across three experiments (**Figure 5.23**).

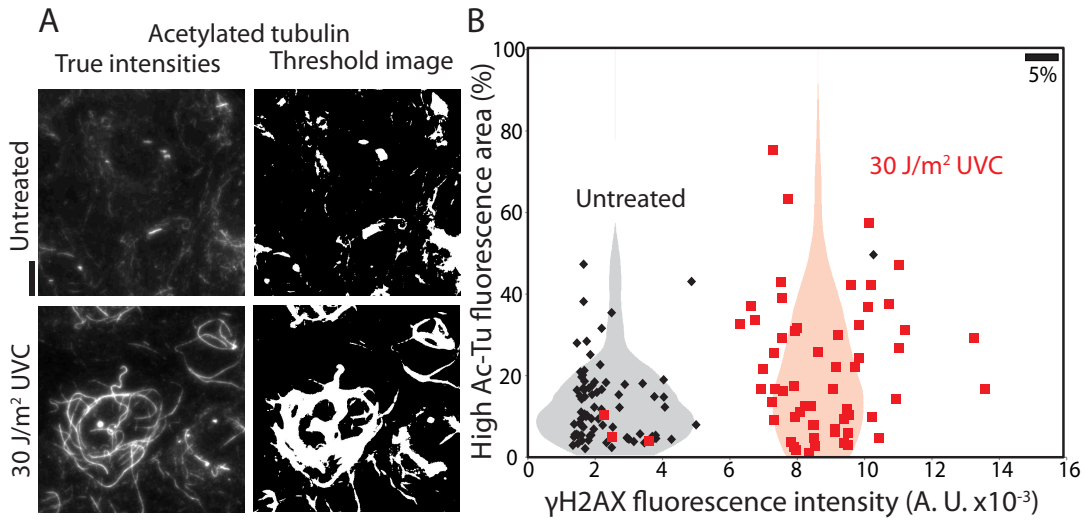

Figure 5.24: Detecting microtubules by thresholding - **(A)** Example images of acetylated tubulin (left) and corresponding thresholded images (right), used to quantify acetlyated microtubule extent around nuclei. Scale bar is 10 μM. **(B)** Example experiment showing clear shift in microtubule extent from untreated (black) to UVC irradiated cells (red). Points are superimposed onto kernel density plots showing distribution of Ac-Tu areas in both populations, positioned at the average γH2AX point for each population. Note there is no clear correlation between γH2AX intensity and acetylated tubulin extent in individual cells. Scale bar is equivalent to 5% of each cell population in the kernel density plots.

Overall it seems that, in these cells, there is a stronger response to IR exposure than UVC, with the response to UVC being more noticeably dose-dependent.

5.10.3 Attempts to quantify the microtubule network

The quantitative measures reported in Graml et al. have been commented on as being abstract and indirect measures of the extent of microtubules. By contrast, whilst visual assessment of microtubule arrays, as explored above, has proven effective, it is not a wholly objective or informative measure of microtubule retention. I have made attempts to uncover a simple, yet informative way to measure microtubules in images of Hc3716-hTERT cells, although I have been unable to find any one measure that consistently agrees with the visual results.

Analysing microtubule networks in human cells was complicated by the use of

fixed cells and immunofluorescence, which both create an extra degree of variation between and within experiments. The extent of permiabilisation, efficacy of fixation and ease of antibody access can vary greatly between cells, resulting in differences in fluorescent signal intensities. This created issues in using fluorescence intensity as a read-out for microtubule quantity and also complicated the use of thresholds to segment images. Thresholding approaches were also confounded by the inhomogeneity of background fluorescence within the cells, primarily due to variation in cell thickness.

Using the tubulin or acetylated tubulin channels it was possible to visually distinguish cell outlines and manually create a mask for each image, to outline the cells and exclude any unoccupied regions of an image. I then directly measured the fluorescence signal within these masks, to gain an idea of microtubule extent within cells. In these cases a greater distinction could generally be observed when more microtubules were present in the cytoplasm. As such, greater distinction was generally possible when staining for total tubulin without 4℃ treatment.

In an example experiment, which appeared to agree with visual assessment, exposure to 30 J/m^2 UVC caused an increase in average tubulin fluorescence, from 2774 ± 471 to 4295 ± 947 (55%; KS-test; p<0.001). Similarly, acetylated tubulin also increased, from 1523 ± 233 to 2455 ± 541 (61%; p<0.001). Treatment at 4℃, actually appeared to eliminate the effect of UVC treatment on tubulin levels in these cells; 1288 ± 231 to 1289 ± 172 (p=0.78). Although a distinction remained in levels of acetylated tubulin; 1140 ± 102 to 1367 ± 187 (19%; p<0.001).

However, in other experiments, it seemed that some samples acquired a much stronger fluorescence signal than others, although this was not reflected in the visual assessment of the cells. In one case, average untreated tubulin levels were measured at 10720 ± 2547, relative to treated cells at 2079 ± 232. However, noticeably, the fluorescence levels in these untreated samples were found to differ greatly relative to all others, with background levels an average 1.4-fold above normal and maximum intensities frequently saturated at 32760 relative to an average maximum of just 7216 ± 2998 under the same imaging conditions.

In images of cells co-stained for γH2AX, I attempted more direct comparisons on a cell-by-cell basis. It would not have been possible to efficiently segment cells on the basis of these images, so I developed methods that focused specifically on the area around each nucleus. Typically this involved applying thresholds to the DAPI channel to create a mask separating nuclei from background. The nuclei

mask could then be used to measure level of γH2AX as a proxy for extent of DNA damage in each cell. Expanding each nuclear mask radially by 5 μm made it possible to measure the amount of acetylated tubulin fluorescence in the area around the nucleus.

One issue with this approach arose from the variation in absolute tubulin fluorescence intensities between samples, discussed above. Hence, a variant approach involved applying a second threshold to binarise the acetylated tubulin channel to cancel out effects of varying fluorescence intensity and directly study microtubule extent. However, this was also ineffective, as different thresholds were needed for each image. In addition, again, the fluorescence intensities, which thresholds were based on, were highly heterogeneous. Whilst focusing on the area close to the nucleus mitigates some variation due to cell thickness, intensities also varied based upon position of cells within each image. As such, each threshold had to be subjectively placed to give a compromise that approximated the microtubules present in each image (**Figure 5.24A**). Even in 4℃ treated acetylated tubulin images, this was still difficult to achieve accurately.

These methods also included a lot of approximations, contributing to variability in the results. A nuclear mask expansion of 5 μm was chosen as a way to focus on areas close to the nucleus, but often nuclei were closer together than this or were less than 5 μm from the cell boundaries. As such, measurements were not always taken from entirely within the cytoplasm. In addition, to be consistent, the same thresholds should be used throughout each experiment, however the variation in fluorescence intensity between images made this impossible. Furthermore, since absolute fluorescence levels varied through the cells, each threshold was a compromise between missing some microtubules and including background pixels.

In the process of this investigation, I found that even the fluorescence signal for γH2AX could vary significantly between experiments, despite comparable treatments and visually similar phenotypes. In one experiment, average nuclear γH2AX fluorescence levels in untreated cells were approximately 2400 ± 1300, rising to 8600 ± 2000 after 30 J/m^2 UVC DNA damage (**Figure 5.24B**). Conversely, another experiment showed a much more subtle shift from 1900 ± 800 to 2500 ± 1000. With such variation, it seems that any simple methods of quantifying these samples based upon flourescence intensity or thresholds are unlikely to succeed.

Notably, the direction of change in γH2AX intensity was consistent throughout samples, despite the dramatic change in magnitude. In samples where it was possible to distinguish cells on the basis of γH2AX, it was possible to use the above methods to demonstrate a corresponding increase in microtubule extent.

Whilst these methods produced sound results in some experiments, none were consistent across all experiments, despite comparable visual results. A more complex, automated, computational approach based upon dynamic thresholding or machine learning methods, as employed during the screen, is likely to be needed to provide a robust solution to this problem.

The variability between UVC exposure experiments may also relate to the nature of the experimental set-up employed. The UVC source for these experiments is a custom constructed device, which shows variation in intensity over time but also does not give equivalent radiation doses across the whole sample. It also requires that all cells be stressed by the removal of medium during treatment, which the IR device does not. Whilst measures were taken to control for the variation introduced by this device – changes in exposure time to adjust for varying intensity and use of γH2AX staining to detect variation in damage induction – it would aid the clarity of future experimental results to seek to employ more reliable sources of DNA damage.

To conclude, these results suggest that inducing DNA damage in Hc3716-hTERT cells, through either UVC or IR treatment, leads to increased resistance of microtubule to cold-induced depolymerisation. This effect has proven difficult to quantify by appears to occur more strongly in response to IR treatments, providing some suggestion that this effect may be primarily mediated by the ATM kinase in mammalian cells.

6 Discussion

"Do what I do. Hold tight and pretend it's a plan!"
—THE 11TH DOCTOR (*The Doctor, the Widow & the Wardrobe*, 2011)

6.1 Results overview

I set out to complete the work started by X. Studera and V. Graml, to perform a computationally analysed, high-throughput, image-based screen of cell shape and microtubule organisation in the fission yeast *S. pombe*. By adapting their initial screening method, I performed a second genome-wide screen of 3004 gene knock-out mutants and a large number of internal controls. During the data analysis stage of this process, we realised that it was possible to add measurement of cell cycle progression to this investigation. From the outcomes of these two screens, 763 genes were proposed as being phenotypically distinct and so were selected for further screening. I performed eight rounds of rescreening on the selected mutants, supplemented by a further eight rounds of imaging for some mutants where initial data quality was poor. From this 262 high-confidence hits were proposed.

Hierarchical clustering of hits by phenotype, combined with investigation of existing functional annotations, revealed several groups of apparently related hits with novel connections to cell shape, microtubules or cell cycle progression. These groups warrant further investigation. I have also explored the location of these hits within the genome and reported a small number of hits with potential influence on microtubule function due to interactions within the genome, not as a result of the activity of the gene products. I went on to provide biological evidence to support the findings of Bayesian inference analysis of screening data, illustrating apparent causal links between major features of the microtubule network and cell shape, suggesting a complex and bidirectional interaction between these processes.

I have pursued the findings of this screen into a detailed investigation of a tightly functionally and phenotypically linked group of hits with reported roles in the DDR. Induction of the DDR has led me to conclude that certain forms of severe or prolonged DNA damage induce elongation and apparent stabilisation of microtubule bundles. This effect appears to be linked to, but not a direct result of, an increase in total tubulin content of cells. I show that DNA-damaged cells have faster microtubule polymerisation, which depends upon the DNA damage kinases and the reported microtubule regulator Amo1. I suggest that Amo1 is a direct target for the kinases Rad3 and/or Tel1 and that the microtubule response to DNA damage may be linked to the relocalisation of nuclear envelope proteins. I have also provided some evidence to suggest that this response may require the microtubule bundler Ase1 or the newly reported ribosome-linked microtubule destabiliser, Mtr1.

Finally, my work using cultured human cells shows evidence for a microtubule stabilisation aspect of the DDR. Visual analysis of these cells shows increased density of microtubule networks and an ability to resist cold-induced depolymerisation.

6.2 Reflection on screening

Poor reproducibility is an acknowledged drawback in high-throughput screening of all types (Barr and Bakal, 2012). When working with thousands of individual samples simultaneously, it is impossible to maintain the standards of precision that are expected when working with just a few. Additionally, it is demanding on time and resources to perform enough repetitions of an experiment to be considered rigorous.

Reproducibility is probably even more of an issue in the case of image-based screening, where the data collected is intrinsically complex, includes an element of subjectivity and is difficult to subject to automated analysis. Conversely, image data allows for high-content screening, studying many different properties and parameters in parallel. This gives results that are far more interesting and useful than a simple readout of, say, the capacity for different mutants to survive under different conditions.

Screens can be validated in many ways, it is logical to check for expected results, for example known microtubule regulators. Similarly, the phenotypic clustering of

functionally related groups goes some way to demonstrating that these genes are probably true hits. If many genes that are all parts of the same pathway give the same result then it is reasonable to infer that the pathway to which those genes all belong is somehow responsible for the observed outcome. Yet the ability to independently reproduce a specific result many times remains the best form of validation of any experiment.

Initial comparison between the two genome-wide screens demonstrated that reproducibility within our screens was, as expected, poor (≈16%), however the reoccurrence of certain genes and gene groups, demonstrated that this screening approach is effective. It was, however, infeasible to continue repeated genomic screens to stabilise the results.

The approach developed here addresses the need for repeats in image-based screening, by compromising between the desire to be as comprehensive as possible and the demands of practicality. Without including controls, ten complete genomic screens, of the scale used here, would have required an absolute minimum eight months of continuous, 24 hour, filming, with additional time needed for data analysis. This would have required over 80 Tb of data storage. By sub-selecting mutants based upon initial results, we were theoretically able to capture the majority of mutants with interesting phenotypes, whilst minimising effort wasted on exploring negative results. It is, however, obvious that these results are not wholly comprehensive, as well-known genes are not found in these hit lists.

Whilst repeat screening was effective, it would have been excessive, given the number of variables involved, to assume that true hits would be reliably detected in 100% of screening repeats. Variation in biological conditions, in addition to chances of unnoticed cross-contaminations and inaccuracies in computational image analysis, may all have slight effects. This is before considering natural biological variation within populations and the effects of partial phenotypic penetrance – where a distinct phenotype is only observable in some cells. As such, we devised criteria for hit selection across screening repeats based upon the accuracy of detection of the well-characterised, but subtle, phenotypes arising from *tea1*Δ. Notably, a total of 61 hits were detected 100% of the time for at least one of the three processes studied. Of these, 14 were always detected for both cell shape and microtubules, three of which are part of the DDR hit group.

What I have demonstrated is that partial-repeat screening is a viable method for economically collecting accurate, image-based screening data. Use of this

approach requires positive controls, with subtle phenotypes that can be used to estimate a reasonable level of reproducibility for determining high-confidence hits. Even an apparently low threshold of 35% was effective at filtering out a large number (66%) of candidates to produce a greatly reduced high-confidence hit list, which shows enrichment for known factors and groups of functionally related genes.

6.2.1 Use of the screening method

The procedures established by V. Graml, X. Studera & myself have subsequently been employed by two further projects in the lab, both currently unpublished. One, a co-localisation screen, explores relationships between gene-deletions and GFP-labelled genes, for a small number of known cell polarity factors (Dodgson et al., manuscript in preparation). The other, currently underway, is another genome-wide screen for factors affecting cell polarity and changes in polarity in *S. pombe* as it progresses through the cell cycle. This screen utilises the cyclin Cdc13 as a marker of cell cycle stage and the cell wall synthesis enzyme Bgs4 as a marker for regions of cell growth. Both of these projects have repeated the methods as described here, with adjustments to the data analysis stages to fit with the different project definitions and biological readouts.

One notable change in these subsequent screens, is the inclusion of the PEM-2 genetic system for reliable crossing of *S. pombe* strains as reported in Roguev et al. (2007). This approach uses a cycloheximide drug sensitivity cassette within the h^- mating locus to ensure the destruction of any remaining diploid cells, following spore germination. It also removes any h^- haploid cells, ensuring more genetically homogeneous populations. This is an approach that we were unaware of at the commencement of the screen reported here.

In the future, it should be possible to adapt many of the same tools to other biological contexts. It is our goal to be able to use this screen as a model for application to live image-based screens of cultured mammalian cells. This transition poses many new issues, primarily relating to computational analysis of the increased complexity and variation within mammalian cells. Experimental adaptations will also be needed to address their different environmental requirements and growth

rates. However, the lessons learnt from screening in *S. pombe* will inform future screen development and provide insights into potential problem areas and possible solutions.

6.2.2 Potential extension of this screen

This screen has already yielded a large number of results and detailed biological investigation of findings could continue for years. These results have the potential to produce a large number of interesting and diverse research questions, as is the nature of screening. However, our interest is primarily in providing large-scale community resources, as such it is important for us to try and be as comprehensive as possible in our work.

As has already been alluded to, the results of this screen, published in Graml et al. (2014) and reported here, are based upon the second version of the KO library from Bioneer. This is known to be incomplete, encompassing only 84% of all non-essential genes in *S. pombe*. The third version of the library was made available in early 2012, adding 304 new strains (93% coverage). An upgrade (v2v3 upgrade), containing all additions between version 2 and version 3, which also included 243 'upgraded' strains, also exists. The upgraded strains were deletions of genes that were also available in version 2 but had somehow been improved upon in the version 3 release. I have already generated images for the complete v2v3 upgrade, which are awaiting analysis. This will undoubtedly add more hits to our results.

In addition, during 2014, an independent consortium of labs, led by the laboratory of Professor Kathy Gould (Vanderbilt University, TN, USA), produced three further plates, of 281 deletion strains, which are reported to complete the coverage of all non-essential genes. We also have access to this resource, but it has not yet been added to this screen.

6.2.2.1 Screening for microtubule dynamics

An initial aspect of my project was to explore the effect of deletions on microtubule dynamics. As such, the second genomic screen attempted to collect approximate

microtubule dynamic data, by collecting two time points separated by 20 seconds, throughout the entire screen.

Comparison of the two images should have made it possible to estimate rates of microtubule polymerisation and depolymerisation, as well as giving potential estimates of dynamic features such as dwell times at the cell tips. With large enough numbers of cells, it should be possible – as with our cell cycle progression analysis – to employ ergodic arguments to overcome the limitations of just two time points. This would make it possible to predict microtubule dynamics in all strains with sufficient accuracy to propose more microtubule hits for investigation.

This particular study was halted due to lack of available computational expertise to process the data. Whilst image segmentation and feature extraction should have been identical to the rest of this screen, it would have been necessary to create algorithms to precisely align and compare different time points (Baker and Matthews, 2001; Zitova and Flusser, 2003). Images tended to drift by a few pixels from one time to the next, and would need to be automatically realigned before comparisons could be made.

Visually, image registering is trivial. However, computationally registration is more complex. The ever-changing microtubules cannot be relied upon for image alignment and computationally detected cell outlines also change between images. Due to slight variation in illumination and image capture, the computer will not necessarily assign precisely the same outline to the same cell, even in images separated by a brief time difference. As such, the computer does not have any straightforward, fixed points of reference to use to align two images. A more complex approach would most likely be required.

As a proof-of-principle, I have manually aligned images, generated during screening, and demonstrated that a single, 20 second time step has the potential to show enough variation in microtubules for data extraction and comparison between different strains (**Figure 6.1**). However, this task remains to be tackled computationally.

Assuming that this is pursued in the future, it may be necessary to complete another genome-wide screen. This is because dynamics have only been imaged once, subsequent refilms will also need to be considered. It is likely that this will be a reduced task, as many hits for dynamics are likely to also be hits from our

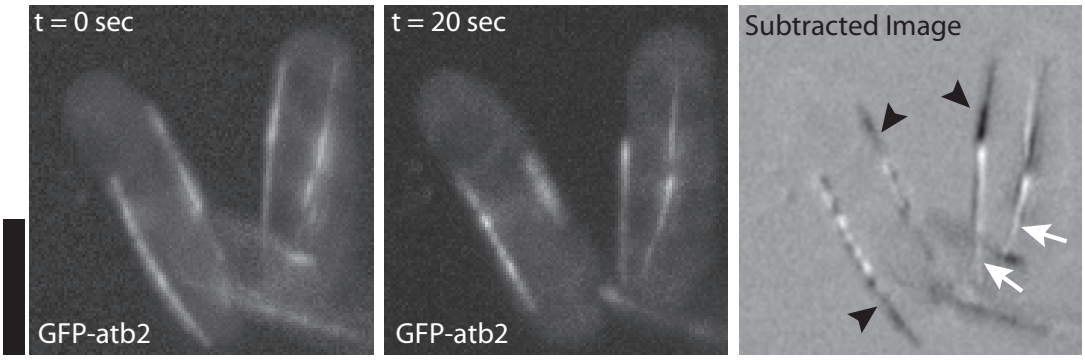

Figure 6.1: Proof-of-principle image for high-throughput microtubule dynamics - Two maximum projected image stacks of the same wild-type cells, expressing *GFP-atb2*, filmed 20 seconds apart. The subtracted image (right) shows microtubule growth over the time period in white (arrows) and microtubule catastrophe in black (arrowheads). Areas where black and white are closely adjacent suggest that the microtubule bundle position has changed between frames. Scale bar represents 5μm.

static microtubule screen, although it may still be of interest to investigate, in a high-throughput context, how their static and dynamic phenotypes are related.

A more condensed approach to high-throughput study of microtubule dynamics would focus on the 186 microtubule hits from this screen, many of which are likely to create their phenotype as a result of affecting microtubule dynamics. This screen could specifically investigate how microtubule dynamics are affected in each microtubule hit. This should be an experimentally minimal project, consisting of just 2 or 3 plates per repeat (depending on the need for controls), but will provide a valuable supplement to the screen as presented here. Once analysis of such a screen becomes computationally possible, I would view this as being an extremely important addition to the results presented here, as it will hopefully further validate the results of clustering, may help to identify distinct groups within clusters and could add strength to the functionally related gene groups already identified within clusters. It will also offer a wealth of information on how different hits influence microtubule organisation and where to start looking for these connections.

6.2.3 Reasons to keep believing in the unknown

The probabilistic nature of successful hit detection that has already been explored (**Section 3.4.2**) provides strong evidence to suggest that our hit lists are by no means comprehensive. In particular, if we consider mutants with subtle phenotypes, akin to *tea1*Δ, there is a 42% (0.65^2) chance that it would not be detected in either of our two genome-wide screens and so would be excluded from further investigation.

Even for the 58% we would expect to identify, they would, by definition, have only a 50% chance of reaching the 35% detection rate threshold required to be called a high-confidence hit. By this token, we may expect at least some of the 501 mutants that were refilmed but not classified as high-confidence hits to also be of potential interest for further investigation.

The results of this screen provide a lot of leads to the control and regulation of cell shape and the microtubule cytoskeleton; showing that both are much more complex and tightly connected to other cellular processes than may have been expected. Whilst we have been able to implicate many genes in these three processes, there is still much to be done to show what the hits do and to identify whether any are directly involved in defining cell shape and microtubule organisation, or whether they are functionally parts of distinct pathways that act indirectly.

Whilst our broad view of connections between distinct processes is enlightening and lends value to the holistic, non-reductionist approach to studying biological systems, we have not yet addressed some of the more detailed questions. Of particular interest may be the 26 previously unknown genes implicated as hits in this screen; these should be verified and studied in more detail to establish whether any are suitable candidates for elaborating how cell shape is defined and maintained and understanding the complexities of *in vivo* microtubule dynamics.

Furthermore, *S. pombe* is just one biological system, selected for its simplicity. It is well-known that the cell wall prevents this species from exhibiting the morphological plasticity present in animal cells and that many common microtubule properties, such as rescue and pausing, are not commonly observed here (Sawin and Tran, 2006). As such, even if the results of this screen did demonstrate perfect coverage of the factors involved in the three processes studied, it is still not

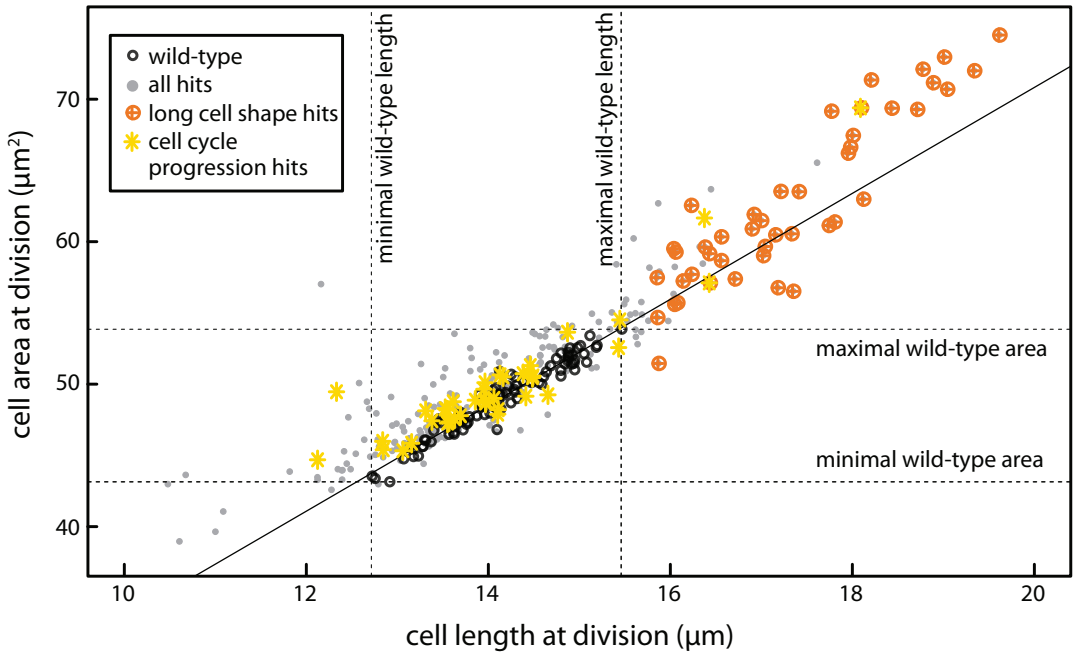

Figure 6.2: Comparison of long hits and cell cycle progression hits - Graph of the length and area of all hits by comparison to wild-type, highlighting cell cycle progression hits (yellow) and long hits (orange). Notably these groups do not seem to correlate. Figure adapted from Graml et al. (2014).

possible to claim that a comprehensive list of cell shape and microtubule regulators has been attained.

Our cell cycle progression hits are certainly far from comprehensive, particularly due to the highly stringent method with which they were selected. However, they do offer some insights into the workings of the *S. pombe* cell cycle, which may have a significant impact on the field.

Primarily, as reported in Graml et al. (2014), we show that these hits affect cell cycle progression but, contrary to classical *S. pombe* cell cycle regulators, do not alter average cell length at division (Hayles et al., 2013; Carlson et al., 1999). Of the 44 cell shape hits in Cell Shape Cluster 4 (long cells), only two (*apl4*Δ & *dph3*Δ) were also cell cycle progression hits. In total, only 5 of the 35 cell cycle progression hits had average cell lengths at division considered to be outside the wild-type 95% confidence interval (**Figure 6.2**).

A second observation, from the cell cycle progression hits, was a strong inverse correlation between the proportion of cells in a population that had interphase mi-

crotubules and the proportion of cells with a PAA. If we stick with our assumption of ergodicity, this suggests that PAA duration is reduced when interphase is prolonged. This may be reflective of the previously reported size-control checkpoints at the end of G1 and G2 (Fantes, 1977; Fantes and Nurse, 1978; Mitchison, 2003). If this is the case, it implies that the transition from PAA to interphase microtubule organisation must be linked to the G1/S cell cycle transition. Alternatively, it is possible that the PAA to IP microtubule state transition is not directly coupled to the G1/S cell cycle transition and hence the timing of these events can vary independently.

The observation of a cell cycle-linked compensation between interphase and PAA is unexpected. The G1/S checkpoint has previously been thought to be cryptic in wild-type cells; almost always inactive because cells are already large enough at the end of G1 to fulfil the requirements of the checkpoint (Abraham, 2003). Hence, it was believed that the G1/S checkpoint could only become active in cells induced to undergo premature mitosis, producing shorter cells at G1. As most of the cell cycle progression hits show longer interphase stages, it would be expected that the G1/S control would remain inactive at all times. However, our findings suggest that some mutant cells accelerate progression through the early cell cycle. This suggests that, under normal circumstances, a mechanism, possibly the G1/S checkpoint, must exist that delays the G1/S transition.

These findings suggest two possible explanations and roles for the genes involved. Either, most of these hits have lost a mechanism that typically prolongs the early cell cycle, leading to initially shorter cells, which then arrest at the end of G2 to acquire sufficient mass for division. Or, these mutations may cause a delay at the end of G2, which is then compensated for by acceleration through the early cell cycle to ensure that normal cell length at division is maintained. In both cases, the length of a cell in mitosis remains normal, whilst we would predict a reduction in the length at cytokinesis. In the second case, it should be noted that the initiation of a compensation mechanism would have to be a direct response to the extension of the previous interphase and could clearly not be mediated by cell length.

These cell cycle progression hits have suggested that we cannot always simply use cell length as a proxy for cell cycle progression in *S. pombe* and some processes may exist, and impact upon wild-type cells, that cannot be identified or studied through typical cell cycle methods.

Further work in this area should initially remove the assumption of ergodicity, by studying mutants over time and using more direct markers of cell cycle stages and progression. If the same patterns are still observed, then these hits should be examined for cell cycle dependent changes of localisation or activity. Inducible activation or silencing of some of these genes may also help to clarify where they act in the cell cycle. Complementary mutations, in known genes regulating cell cycle checkpoints, may also offer guidance of where in the cell cycle these genes are most active and where currently unknown processes might exist.

6.3 Linking DNA damage and microtubules

Connections between microtubules and the genome are well-known, at least during cell division, where microtubules form the spindle that is necessary for division of chromosomes (Alberts, 2002; Lodish, 2008). Yet, the transition between interphase and spindle microtubule arrays in any species is significant, requiring SPB duplication, altered MTOC activities, reorientation of microtubule nucleation and massive changes in microtubule dynamics. In *S. pombe*, this is further complicated by the occurrence of closed mitosis, where the nuclear envelope remains present throughout cell division (Guttinger et al., 2009). Yet, the interaction between DNA and microtubules in interphase is not as well-studied and this new connection was quite unexpected.

Whilst I have attempted to provide some preliminary indications of how DNA damage is able to influence microtubules, the precise signalling network involved remains to be established. The localisation of Amo1 to the nuclear envelope may suggest that it has a key role to play in connecting events in the nucleus to cytoplasmic responses. My data, together with previously findings linking Amo1 and nuclear pore complexes (Asakawa et al., 2014) or RNA processing (Hasan et al., 2014), may suggest that these factors are important for regulating signal transmission through the nuclear envelope. The exact roles played by Amo1 in this process remain to be fully explored.

What is perhaps more pressing, is why persistent DNA damage, especially as a result of HU treatment, leads to microtubule stabilisation. There are several plausible explanations for this response:

6.3.1 Stable microtubules form no spindles

The first hypothesis suggests that stabilisation of interphase microtubules simply acts as a redundant security measure, preventing cells from restructuring microtubules into a spindle until all DNA damage is resolved. It is notable that during the cell cycle, several independent and redundant mechanisms are employed in different transitions to ensure that the fidelity of the cell cycle is maintained (Elledge, 1996; Santamarina et al., 2008; Diffley, 2010). It would thus not be totally unreasonable to assume that, in addition to all of the central cell cycle regulators, a separate mechanism exists that specifically prevents spindle formation in the presence of DNA damage. This seems especially reasonable given that it is the separation of chromosomes by the spindle that is the point in the cell cycle where irreversible genome damage can occur, if DNA repair is incorrect or incomplete (Hardwick et al., 1999; Lara-Gonzalez et al., 2012).

This hypothesis could be best tested by examining the sensitivity of checkpoint defective mutants to microtubule destabilising drugs. Even under normal conditions there would likely be an increase in sensitivity and microscopically more cells should be observed with a cut phenotype due to errors in karyokinesis.

6.3.2 Longer microtubules support longer cells

My second idea suggests that this response is an adaptation to cell elongation as a result of cell cycle arrest. The stabilisation of microtubules may allow them to continue to occupy the majority of the cell volume in elongated cells. This may help to more reliably maintain cell shape (Chang and Martin, 2009; Hayles and Nurse, 2001). This idea originates from the observation that *amo1*Δ and short microtubule mutants (e.g. *tip1*Δ) seem more prone to developing severe curvature, or branching, when treated with HU (**Figure 6.3**). Measuring the abundance of branching, or severity of curvature, should provide an easy experimental test for this hypothesis.

In addition, longer microtubules should make it easier to maintain the cell nucleus close to the cell centre, an important requirement for reliable cell division upon reentry into the cell cycle (Chang et al., 1996; Chang and Nurse, 1996). However, this explanation is more specific to *S. pombe*, so would not explain the apparent conservation to human cells.

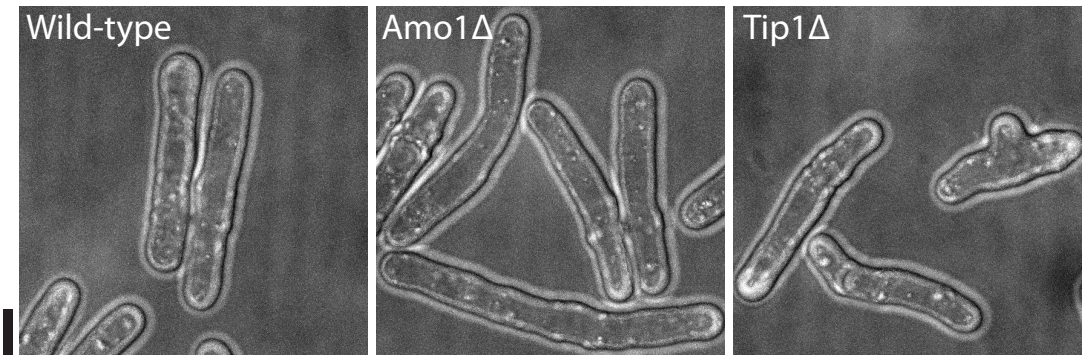

Figure 6.3: Elongating microtubules may preserve cell shape - Comparative images of 15 mM HU-treated cells after 6 hours of treatment. Wild-type cells elongate microtubules and seem more able to maintain straight cell after elongation. Cells which do not elongate microtubules (*amo1*Δ) and cells that have highly unstable microtubules (*tip1*Δ) show a greater propensity for bent or branched cells. Branched wild-type cells have never been observed under these conditions. Scale bar represents 5 μm.

A variant of this idea suggests that the stabilisation of microtubules also helps to restrict cell growth. This may help to conserve energy and resources as well as making it easier for cells to recommence division accurately upon checkpoint exit. This is supported by the observation that wild-type cells are shorter and demonstrate a more marked reduction in cell growth rate compared to mutants that do not activate the microtubule response.

It is also interesting to note that some mutants appeared to have much longer cells but still showed a wild-type-like elongation of microtubules, yet the converse (short microtubules and shorter cells) was not seen. This may support the idea that the microtubule response is upstream of the slowing of cell growth. It is known that microtubule ends deposit growth factors at the cell ends each time they make contact and undergo catastrophe (Browning et al., 2003; Behrens and Nurse, 2002; Dodgson et al., 2013). It may thus seem that, by stabilising microtubules, cells limit the delivery of these factors and hence delay growth.

Conversely, stable microtubules may provide a more constant delivery pathway for factors that inhibit cell growth, although there is little evidence for the existence or activity of such factors, particularly in association with microtubules. Unpublished findings from other members of the lab propose that Tea3 may play such an inhibitory role, which is necessary for the transition between monopolar and

bipolar growth during the cell cycle (Geymonat et al., manuscript in revision).

6.3.3 Microtubules promote DNA repair by rocking the nucleus

The final concept derives from the observation of highly dynamic microtubule activity in association with *S. pombe* meiosis (Yamamoto et al., 1999; Yamamoto and Hiraoka, 2001). These rapid microtubule motions have some parallels to the response I have identified.

When microtubules contact the cell ends they push against them. Since the microtubules are anchored to the nucleus this tends to push the nucleus away from the cell end being contacted. Normally, the balance of microtubules pushing against each cell end are thought to help maintain the position of the nucleus at the cell centre (Tran et al., 2001). During meiosis, the same effect occurs but much more vigorously, the result is a constant rocking of the nucleus (Yamamoto and Hiraoka, 2001). This is suggested to promote chromosome cross-overs and resolution by speeding the search for homologous chromosome regions and promoting more stringent DNA repair.

This idea may be supported by the observation of the relocalisation of Amo1 in response to DNA damage, causing it to focus into part of the nuclear periphery, apparently in conjunction with the iMTOCs. Notably, microtubules during meiosis appear to focus their points of contact with the nucleus into one region (Ding et al., 1998), which likely helps to ensure that microtubules drive coherent motion of the nucleus within cells and do not jeopardise nuclear integrity. This theory could easily be explored further by examining nuclear motion over time in DNA damaged cells relative to untreated or extended Cdc2-AS cells.

Since DNA repair by HR is similar to crossing over in meiosis, the associated microtubule activities may also have some similarities. However, if this explanation were totally valid we would expect strains that do not stabilise microtubules to show increased sensitivity to DNA damage, which does not always seem to be the case. This could be further assessed by investigating synergistic effects between microtubule destabilisation and DNA damaging agents.

6.3.4 Evidence from other research

Several other groups have recently produced findings that highlight the links between DNA damage and microtubules. Although none have yet suggested that DNA damage may alter microtubule dynamics, they do highlight that the dynamic actions of microtubules appear to aid in DNA repair, specifically through HR.

6.3.4.1 Nuclear rocking promotes DNA repair

Results from J. Zhurinsky (personal correspondence) reported that rocking of the nucleus by microtubule activities in *S. pombe* promotes DNA repair by HR, as suggested in **Section 6.3.3**. However, their results did not explore any change to microtubules in response to DNA damage that may help to facilitate repair.

6.3.4.2 Altered microtubule:nuclear interaction promotes DNA repair in *H. sapiens*

Research reported by Larrieu et al. (2014) supports the idea that microtubules may influence the repair of DNA damage. They identify a drug for treatment of laminopathies (genetic illnesses that compromise nuclear integrity), which targets a lysine acetyl transferase called NAT10.

NAT10 has known effects on histones and microtubules (Shen et al., 2009), and Larrieu et al. report that drug-induced NAT10 inhibition reduces the level of DNA damage in laminopathic cells. They state that this effect appears to be due to a weakening of the microtubule attachment to the nuclear membrane. If this is correct, it is possible to infer that altering microtubule dynamics, or at least nuclear attachment, can affect DNA repair.

NAT10 is conserved in *S. pombe* as Nat10, which provides a potential start point for further investigation of these findings. If *nat10*Δ phenocopies *amo1*Δ in response to DNA damage, it may suggest that, beyond simple alteration of microtubule attachment to the nucleus, Nat10 is a key factor in the altered microtubule dynamics reported here. Conversely, whilst Amo1 is not conserved to *H. sapiens*, if findings suggesting a role for Amo1 in relation to NPCs are correct, then

suppression of nuclear pore activity, through siRNA, may be similarly effective at reducing DNA damage in laminopathic cells.

6.3.4.3 Damaged DNA becomes mechanically linked to microtubules via LINC complexes

There is more direct support for the role of microtubules in the DDR in *S. pombe* from Swartz et al. (2014). Their work explores nuclear envelope bridging proteins – which span the nuclear envelope, linking cytoplasmic cytoskeleton to the nucleoplasm – of potential interest here in helping to understand how signalling from DNA damage comes to influence microtubules and how microtubules may then come to affect DNA repair.

In meiosis, association of chromosomes with a linker of nucleoskeleton and cytoskeleton (LINC) protein complex of SUN and KASH domain proteins (Sad1 and Kms2 in *S. pombe*), is known to aid resolution of chiasmata (Yoshida et al., 2013). Swartz et al. found that, in S/G2 of mitosis, persistent DNA damage foci also associate with Sad1, which then favours the association of Sad1 with Kms1 (a different KASH protein). They show that, when DNA repair by HR is compromised, these Sad1-Kms1 foci accumulate in cells. The same result is also observed in *mto1*Δ mutants or when microtubules are depolymerised.

Swartz et al. suggest that, when DNA damage is easily repaired, the activation of ATR kinase is minimal and this response is not activated. When rapid repair is prevented, or damage is persistent, then damage sites associate with Sad1-Kms1. This suppresses repair by NHEJ in favour of HR, hence in HR defective mutants damage accumulates. Association with Sad1-Kms1 allows mechanical linkage of damaged DNA to microtubules. This aids the search for homologous regions, through motion of the nucleus, and hence speeds HR. They also report that *kms1*Δ mutants do not experience sensitivity to DNA damage-inducing drugs, and are even able to rescue the sensitivity of HR defective mutants (including DDR hits *rad51*Δ and *rad55*Δ). They state that this is because the loss of the Sad1-Kms1 association, prevents damaged DNA from becoming committed to repair by HR and hence repair by NHEJ is favoured.

Furthermore, the study of Kms1 potentially offers an explanation of why Amo1 is apparently not HU sensitive, although there are differences between Amo1 and

Kms1, primarily in their localisation. Where Kms1 accumulates in a small number of foci, Amo1 is found more widely across the nuclear envelope, even in DNA damaged cells. Further experiments should explore whether Amo1 and Kms1 show some degree of co-localisation, since Amo1 has already been shown to partially co-localise with Sad1 foci in DNA damaged cells. In addition, this research adds support to the idea of a meiosis-like microtubule motion, that can be triggered in mitotic interphase in response to DNA damage (see **Section 6.3.3**).

Interestingly, the association of DNA damage foci with SUN proteins has been implicated in aiding DNA repair in both *S. cerevisiae* (Kalocsay et al., 2009; Oza et al., 2009) and mice (Lei et al., 2012), suggesting that this response is conserved across species.

Again, this does not prove the existence of an active microtubule response to DNA damage, but does show that stable microtubules favour DNA repair and Swartz et al. even propose that accelerated microtubule dynamics may speed repair. This also highlights that cells can employ active measures, in response to DNA damage, that promote association between DNA and microtubules. Interestingly, the response reported by Swartz et al. mirrors my own findings in proposing a two stage response to DNA damage, depending on severity and persistence of DNA damage.

The links to this study could be explored further by investigating the response of microtubules to DNA damage in *kms1*Δ. Note that *kms1*Δ was not a part of the version 2 KO library, so is not present in the screen. However, it is part of the v2v3 upgrade. Assuming Kms1 and Amo1 functions are closely related, I would still expect *kms1*Δ to give no phenotype in cells lacking DNA damage. The findings of Swartz et al. also indicate that loss of Mto1 should be investigated in DNA damaged cells. Since *kms1*Δ, like *amo1*Δ, did not show sensitivity to HU – apparently due to a preferential switch to NHEJ repair – it will be interesting to explore whether *amo1*Δ can also rescue the HU sensitivity of DDR hit deletion mutants (*rad51*Δ and *rad55*Δ).

Swartz et al. made use of methyl methanesulfonate (MMS) as the primary means of inducing DNA damage, so exploring my current results in this context would also be of interest. Assuming that the two-step response to DNA damage reported by Swartz et al. correlate with the different responses to HU dose that I have identified here, it may also be interesting to examine the nuclear localisation of DNA damage/Sad1/Kms1 foci in cells treated with different HU doses. Studies

using HO exonuclease to induce targeted DNA damage could also be enlightening.

6.4 A mechanism for the microtubule response to DNA damage

In wild-type cells, I have identified a response that leads to an increase in average microtubule bundle occupancy within cells through an increase in microtubule polymerisation rate that is activated by DNA damage under very specific conditions. This response appears to be specifically linked to DNA replication arrest and DNA repair by HR. The response can be induced by HU treatment but not phleomycin and appears to be activated in a dose-dependent manner, requiring a minimum dose of HU before becoming noticeable.

The pathway that links the DDR to microtubules is dependent upon the DDR kinases, most notably Rad3 and Cds1, but apparently also Tel1. I have also shown that the gene *amo1*, which has been previously linked to microtubule organisation, is also necessary to elongate microtubule bundles in response to DNA damage.

6.4.1 Conclusions from wild-type cells

I have observed that HU-treated cells appear to show a dose-dependent increase in average tubulin content per unit volume, as judged by GFP-Atb2 fluorescence. An increase in tubulin content may help to explain the increased number of microtubule bundles I have observed in all elongated cells. To explore this, it would be necessary to examine the total tubulin fluorescence of Cdc2-AS cells for comparison. However, this cannot be a purely cell length-dependent response, as the increase in tubulin levels is more pronounced in 15 mM HU-treated cells, which are on average shorter than 3 mM HU-treated cells.

The increase in tubulin content appears to also permit an increase in number of microtubules per microtubule bundle, as assessed by average GFP-Atb2 fluorescence within microtubule bundles in 3 mM HU-treated cells. Average microtubule

bundle fluorescence intensity appears to then fall in synchrony with the elongation of microtubule bundles at higher doses of HU, although total tubulin levels continue to rise. The true number of microtubules per bundle could potentially be studied in more detail by exploring the variation in fluorescence intensity along bundles.

These results correlate well with my investigation of microtubule dynamics, which shows a dose-dependent increase in polymerisation rate and a correlated reduction in catastrophe rate in response to high dose HU treatment. Increased tubulin availability in the cytoplasm would result in more rapid tubulin polymerisation. This in turn contributes to the suppression of catastrophe, potentially through maintenance of the GTP-tubulin cap. Catastrophe is also reduced due to cell elongation, which reduces the frequency of catastrophes induced by contact between a microtubule and the cell end. The dose-dependence of these changes in dynamics is likely a function of the changes in total tubulin level and the fact that the increased microtubule bundle density in 3 mM tubulin cells will also limit the availability of free tubulin dimers, as more polymerising microtubule ends are competing for them.

Overall, this suggests a sensitive response to DNA damage that increases tubulin production, either directly through increased tubulin synthesis and/or suppressed tubulin breakdown. At higher doses of DNA damage, a second response becomes active that further promotes microtubule polymerisation, whilst apparently reducing the number of microtubules per bundle and hence the number of individual microtubules per cell.

6.4.2 Conclusions from mutants that do not stabilise microtubules

The DDR kinase mutants *cds1*Δ and *rad3*Δ do not seem to initiate a tubulin response to DNA damage. Cells typically show only a slight increase in tubulin content. This smaller increase may be reflective of the increase in tubulin content solely linked to cell elongation theorised above. As expected, *cds1*Δ and *rad3*Δ also do not show any increase in GFP-Atb2 fluorescence in microtubule bundles upon treatment with 3 mM HU. This may be a direct result of the absence of these DDR kinases, or may be an indirect result of the lack of available free tubulin.

The response of *amo1*Δ is less apparent. These cells do increase total tubulin content, comparable to wild-type cells. They also show the same pattern of microtubule fluorescence intensity as wild-type, increasing at 3 mM HU then falling at higher doses. Yet, the loss of microtubule bundle density at higher HU doses in *amo1*Δ cannot be explained by microtubule elongation. Most interestingly, *amo1*Δ appears to decouple the apparent increased availability of tubulin in these cells from changes in microtubule dynamics. Although total tubulin content is apparently increased, there is no change in microtubule polymerisation rate. The observed reduction in microtubule catastrophe rate may then be explained wholly by the increased length of *amo1*Δ cells.

6.4.3 Possible functions for Amo1

As little is known about the true function of Amo1, there are several possible explanations for how *amo1*Δ may have its effects on microtubules and microtubule dynamics. Notably, *amo1*Δ microtubule activity only appears to differ from wild-type at higher doses of HU, hence its function is probably only relevant at these doses. As such, it is reassuring that, in all ways studied, *amo1*Δ behaves like wild-type when treated with 3 mM HU. This should be investigated further, through study of *amo1*Δ microtubule dynamics and whole cell fluorescence after 3 mM HU treatment.

The initial Amo1 paper (Pardo and Nurse, 2005) makes it clear that a straightforward role for Amo1 in microtubule regulation is impossible. Over-expression and deletion of Amo1 are phenotypically similar, both producing fewer, longer microtubules. The phenotype is slightly more severe in Amo1 over-expression, where most cells retain just one microtubule bundle. Note that the similarity between these phenotypes makes it difficult to determine whether the phenotype observed in wild-type cells treated with 15 mM HU is linked to increased or decreased Amo1 activity.

Deletion of Amo1 was found to have no effect on microtubule polymerisation or depolymerisation rates but did increase stability and delay microtubule catastrophe at cell ends. Fusion and fragmentation of bundles was also found to be similar. They did find that *amo1*Δ *tea1*Δ cells have greater difficulty in maintaining

proper cell shape, although I have been unable to show a role for *tea1*Δ in affecting DDR-induced microtubule stability. This may, however, support the idea that the observed microtubule response helps to maintain correct cell shape.

My results have not perfectly reflected those previously published for *amo1*Δ; I do not report a pronounced microtubule phenotype in untreated cells. However, cells in Pardo et al. were grown under very different conditions and fixed for imaging, so cannot be expected to be entirely comparable.

Based upon my results, the potential roles of Amo1 in response to DNA damage seem to breakdown into either increasing the availability of free tubulin in the cytoplasm or promoting microtubule polymerisation through addition of new tubulin dimers. These outcomes may either be directly or indirectly due to the actions of Amo1.

6.4.3.1 Amo1 increases free tubulin availability

Since the GFP-tubulin level in *amo1*Δ shows that GFP-Atb2 is still being produced and is present in the cytoplasm, I suggest that tubulin may not be folding correctly or forming dimers, so therefore is not available for integration into microtubules. Since correct folding and dimerisation of tubulin is much more challenging than for GFP, it is possible that the observed increase in GFP fluorescence does not reflect availability of correctly folded, usable tubulin. Increased production of tubulin in response to DNA damage would plausibly require additional factors to aid protein folding.

This suggests the presence of stress-responsive chaperonins, activated by DNA damage, or increased tubulin transcription, that could facilitate the production of functional tubulin dimers (Liang and MacRae, 1997; Young et al., 2003; Simons et al., 2004). The features of Amo1 make it unlikely that it directly fulfils this role, as it lacks any sequence/domain characteristics of chaperones and would be expected to have a different localisation. However, it may still influence the availability of such chaperones. This may support evidence that proposes Amo1 as a nucleoporin or RNA-binding protein, both of which could functionally regulate the synthesis or stress-induced relocalisation of chaperones.

A related hypothesis suggests that Amo1 may somehow affect the tubulin-GTP cycle. A delay in nucleotide exchange by free tubulin dimers, due to the absence

of a hypothetical guanosine-nucleotide exchange factor (GEF), would also serve to reduce the effective tubulin availability for microtubule synthesis. Although, again, Amo1 appears to lack any of the necessary domains to plausibly act directly in this role.

Alternatively, free tubulin dimers may be present and complete but not readily accessible. Certain proteins, such as stathmin, act to sequester free tubulin (Jourdain et al., 1997; Amos and Schlieper, 2005). It may be that much of the observed free tubulin in 15 mM HU *amo1*Δ cells is sequestered in this way, suggesting that Amo1 mediates a response to release tubulin from sequestration. However, currently no tubulin sequestering proteins are known in *S. pombe*.

6.4.3.2 Amo1 promotes tubulin polymerisation

Polymerisation of microtubules can also be promoted by aiding addition of tubulin dimers to the growing microtubule ends. Amo1 may be involved in a process that specifically aids the recruiting of tubulin to microtubules in response to DNA damage. Whilst its location makes it unlikely that it directly enacts this effect, it may have a role in loading factors onto microtubules for transport, as proposed by Pardo and Nurse (2005). Whilst they were unable to identify any such factors in their publication, this does not comprehensively rule-out this mechanism.

This hypothesis may also be relevant to the preliminary data reported for *mtr1*Δ. Whilst Mtr1 is apparently not a microtubule-stabilising agent, but acts counter to Mal3, it may be that, in wild-type cells, Amo1 is able to block loading of Mtr1 in a DDR-dependent manner, and thus microtubule elongation is enacted by Mal3 in the absence of competition by Mtr1. However, the results from *mtr1*Δ appear to more closely reflect *amo1*Δ cells than wild-type cells, when treated with 15 mM HU. Mtr1 localisation also appears to be uniform throughout the cytoplasm, so may not require microtubule loading. Furthermore, although subtle, due to short microtubule lengths, elongation of microtubules in response to DNA damage is apparently still present in *mal3*Δ, which does not fit with this concept.

One further possibility is that Amo1 somehow regulates the access of a tubulin-modifying enzyme to tubulin dimers. This post-translational modification of tubulin may then be able to have the effect of facilitating microtubule polymerisation, or at least stabilising existing microtubules (Wloga and Gaertig, 2010; Westermann and Weber, 2003; Janke and Bulinski, 2011). An example candidate for this could

be the lysine acetyltransferase, Nat10, in line with the findings of Larrieu et al. (2014).

6.4.3.3 Amo1 is much more complicated

One final possibility is that Amo1 has much more indirect and complex effects, which are particularly difficult to predict. If Amo1 is a nucleoporin or RNA-binding protein as suggested (Asakawa et al., 2014; Hasan et al., 2014), its phenotype may be the result of changes in many different proteins. The analysis of its RNA-binding capacity suggested no target genes that would be expected to affect microtubules, based on current knowledge. This list also did not include any enrichment for microtubule hits from our screen. However, this does not completely rule out the possibility that the *amo1*Δ phenotype is the result of altered RNA levels in the cell. Similar logic applies for a nuclear pore function, although without much more investigation it is difficult to comment further.

6.4.4 A role for Ase1 and bundle organisation?

On the basis of only limited information it is difficult to reach any conclusions regarding the effect of *ase1*Δ on the ability of microtubules to respond to DNA damage. Since all other data seem to suggest that microtubules do alter their dynamics in response to DNA damage and that this change is in-keeping with an increase in average microtubule length, there is no apparent need for a change in bundling.

As Höög et al. (2007) previously proposed, microtubule bundles in untreated wild-type cells may consist of a mosaic of Ase1-bundled cells, and not be as centrally focused as previously thought. This would suggest that changes in Ase1 distribution in elongated cells may simply be a result of longer cells with longer microtubules. However, this still does not provide an explanation of why I do not observe increased length of individual microtubules in *ase1*Δ.

Bundled microtubules may be needed to mediate consistent microtubule elongation, especially if this is dependent upon delivery of factors to cell ends. This may support theories in which Amo1-loaded factors are transported along microtubules to the +ends. Bundled microtubules may be more effective in such a

mechanism, as they may aid motor processivity by offering more points of microtubule contact for motor proteins (Furuta and Toyoshima, 2008). In accordance with the mosaic model of microtubule bundles, bundling would also be necessary to provide a continuous transport pathway from the cell centre. In addition, bundled microtubules will more accurately deliver cargoes to the cell ends, as microtubule orientation within cells is much stronger when microtubules are bundled by Ase1 (Janson et al., 2007; Daga et al., 2006; Carazo-Salas and Nurse, 2006).

Much more investigation is needed to reliably confirm whether Ase1 is relevant to this process and the role it might have. This will start with repeats of previous experiments and investigation of the positioning of Ase1-GFP in *amo1*Δ cells when treated with different doses of HU. It may also be interesting to study changes in the distribution of the motor protein Klp2, which is responsible for the relative positioning of microtubules prior to bundling by Ase1. If the function of Klp2 is affected by HU treatment it may add weight to the idea that microtubule arrangements, as well as microtubule dynamics, are altered by 15 mM HU.

6.4.5 Model summary

Whilst many aspects of this response remain poorly defined, I will attempt to propose a preliminary model for the response of microtubules to DNA damage by HU (**Figure 6.4**).

Initiation of the DNA damage response in *S. pombe*, which typically favours repair by HR, is signalled by the activation of DDR kinases. Primarily, the ATR homologue (Rad3) leads to activation of the checkpoint kinase (Cds1).

In less severe cases of DNA damage, these kinases initiate a response that apparently includes an increase of tubulin in the cytoplasm, through unknown mechanisms. This leads to an increase in microtubule bundle density but no detectable changes in microtubule polymerisation rate or microtubule bundle length.

More extensive DNA damage, initiates the same increase in tubulin, but apparently also initiates a procedure that increases microtubule polymerisation, restricts individual microtubule number and leads to overall elongation of microtubule bundles. This response apparently requires Amo1, which computationally appears to be an ideal candidate for targeting by the ATM/ATR kinases. It is probable, that if it is subject to phosphorylation by Rad3 and/or Tel1 then it may also

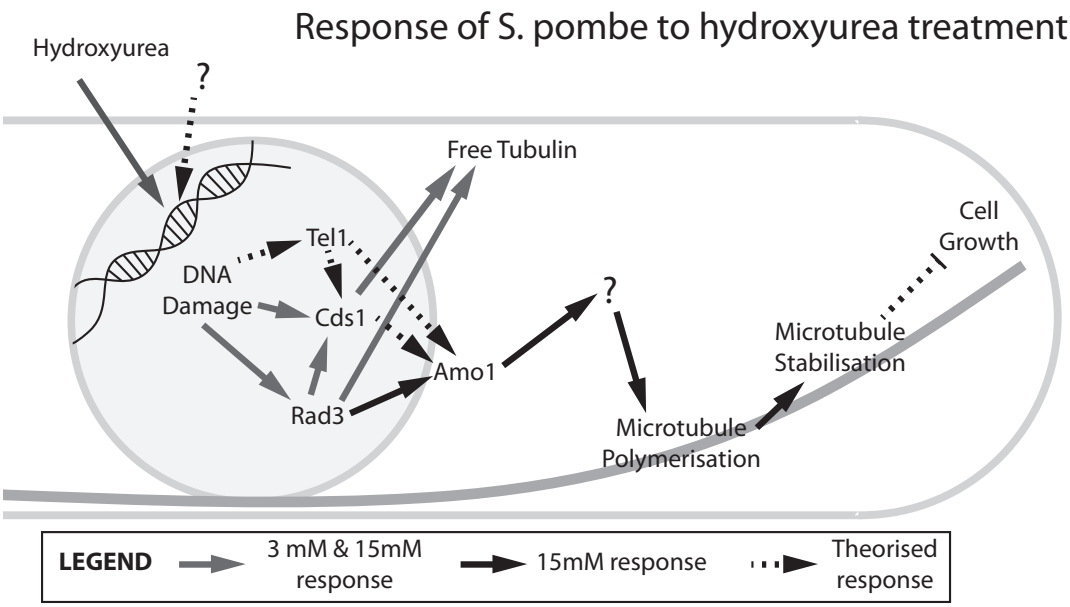

Figure 6.4: Proposed model for microtubule response to DNA damage in *S. pombe* - Treatment of *S. pombe* with HU initiates microtubule responses. At low doses the level of tubulin is increased leading to an increase in microtubule bundle density. This appears to depend upon the DDR kinases Rad3, Cds1 and possibly Tel1. The kinases are also active at higher HU doses, where microtubule elongation and increased polymerisation rate are observed. This secondary response seems to also require the presence of Amo1. Measurements of cell length suggest that this response may contribute to slowing of cell growth.

be a target for the checkpoint kinases (primarily Cds1 in *S. pombe*). Whether this activates or suppresses Amo1 activity is difficult to determine.

Results suggest that DDR-induced changes in Amo1 may then, most likely indirectly, affect microtubule organisation via Mtr1/Rps1801 and possibly also Ase1. A process which blocks Mtr1 function could cause microtubule elongation, whilst Ase1 may influence microtubule bundle organisation. On the basis of studying growth rate changes and measuring cell elongation in different mutants, I suggest that, at least partially, the function of microtubule elongation is to slow cell growth during cell cycle arrest.

6.5 Further experiments in *S. pombe*

Many unanswered questions, several of them deeply significant, remain in the exploration of this apparently new pathway linking DNA damage to microtubules. Perhaps most apparent are the role of Amo1 in this process, how this function relates to other functions proposed elsewhere and the microtubule factor(s) that most probably exist further along this pathway. In the long run, the possible link between microtubule elongation and cell growth is also a major area for research.

First, it is important to further validate the results as presented here. Quantification of fluorescence signal, in particular, needs further work. Techniques such as fluorescence assisted cell sorting (FACS) or quantitative western blotting are likely to be necessary to stably confirm my reported changes in protein abundance. There is also plenty of scope for more investigation of microtubule dynamics, it will be important to examine how both *cds1*Δ and *rad3*Δ behave dynamically, in addition to the previously mentioned investigation of *amo1*Δ with 3 mM HU.

Whilst extremely time-consuming, assessment of microtubule dynamics changes in response to HU treatment may be the most conclusive way of validating which factors are involved in this response. As such, to be completely rigorous, it will be necessary to investigate dynamics in many other contexts. It would also be interesting to compare microtubule dynamics in cells treated with HU and other agents. Confirmation of the absence of a response in phleomycin-treated cells should be a priority. However, I believe a broader screen of external factors that induce cell stress should be considered. The significance of the response to HU treatment can only be fully recognised if it can also be demonstrated in other contexts. In particular, treatments that are known to slow cell growth are likely to be of interest.

Identifying more factors involved in mediating this response may take several different approaches. I have screened several candidates affecting microtubule stability, as seen in **Table 5.5**: this could be expanded to include all known microtubule regulators. Given the observed microtubule phenotype however, it is unlikely that anything interesting will come of this – unless changes in microtubule nucleation turn out to be relevant. Alternatively, all microtubule hits could be investigated for responses to HU. This could even be extended to another genome-wide screen for drug response. This would serve to explore cell growth

and polarity factors, potentially revealing whether microtubule elongation results in reduced cell growth. If Amo1 is functioning as an RNA-binding protein, it may also be interesting to study the products of transcripts influenced by Amo1, as one of these may be particularly functionally significant in understanding the affect Amo1 has on microtubules.

Of course it is also important to investigate the reasons why cells induce microtubule stabilisation in response to DNA damage. This will include examining how this response aids cell fitness, especially since loss of microtubule stabilisation in *amo1*Δ has no obvious detrimental effect on cell viability.

The obvious test here is to reduce microtubule stability and study the effect this has on cell viability and speed of DNA repair. Discovering the function of microtubule stabilisation should start with assessment of cell curving and branching in different contexts. Assessment of nuclear displacement from the cell centre is also an easy follow-up experiment. For these tests, Cdc2-AS is an obvious choice, since it is an artificial means of cell elongation that demonstrably elongates cells without any microtubule response. Further examination of, say, *tip1*Δ, as a short microtubule mutant, should also be performed. If, as mentioned above, it is possible to identify other stress factors that also initiate the same response, this may provide further insights into the purpose of this response and its effects.

Other issues relate to the targeting of Amo1 by ATM/ATR, which has proven biologically difficult to demonstrate. Since I have computationally identified several potential phosphorylation sites of Amo1, it may be possible to examine this interaction by creating phospho-null and phospho-mimic mutants of Amo1 that would be independent of ATM/ATR activity. This should, at least, show whether Amo1 is subject to direct regulation by these kinases. Another point of interest is the possible involvement of nucleoporins in this response. Further examination of the response to HU in a wider range of nucleoporin mutants is needed to prove whether they do have a role in linking DNA damage and microtubules. More rigorous investigation of the link between Amo1 and nucleoporins is also outstanding.

Also of interest is the apparent increase in whole-cell tubulin content in response to DNA damage and the decoupling of tubulin availability and microtubule dynamics in *amo1*Δ cells. One of the first questions to address here is the cause of elevated tubulin: is there increased transcription, translation or a reduction in degradation? This could involve quantification of tubulin transcripts and study of their association with ribosomes through microarray analysis. In addition, changes in

tubulin half-life could be studied through blocking protein synthesis. Depending on the results of these studies, it may also be necessary to extend this to investigate post-translational modification of the tubulin proteins.

Understanding decoupling in *amo1*Δ cells will first require a deeper understanding of the mechanism of action of Amo1. On the basis of theories suggested here, it may be possible to use over-expression of different factors to attempt a rescue of this decoupling. If tubulin turns out to be being synthesised faster but is not being appropriately formed into dimers then over-expression of, say, the prefoldin chaperones, may help to recover the effect. Similarly, if there are fewer microtubule-stabilising factors loaded onto microtubules in this mutant, then over-expression of Mal3 or Tip1 may provide a solution.

6.6 DNA damage & microtubules in human cells

My investigation of human cells is still in the early stages and there is much more work to be done. I have provided evidence that DNA damage in human cells also causes an increase in polymerised microtubule mass and microtubule stability. This response appears to be initiated both by UVC- and IR-induced DNA damage. Since it appears that this response is much more sensitive to IR treatment than UVC, this suggests that the response is primarily ATM-mediated in these cells, although direct kinase inhibition will be needed to confirm this.

I have considered several means for the quantification of microtubules in human cells but have been unable to provide a method that is stably as conclusive as visual phenotype assessment. This will need to be a top priority for continuation of this work.

6.6.1 Conserved pathways without conserved proteins

A key point to consider in the transition of this study from *S. pombe* to *H. sapiens* is the role of non-conserved proteins in a conserved response. Since Amo1 does not have a sequence homologue in humans, either an alternative mechanism or a functional homologue is required.

If Amo1 is a nucleoporin then parts of it are reported to show weak homology to NUPL2 (hCG1), similarly, as a CCCH-type Zn-finger RNA-binding protein, there are many possible homologues in the human genome. Nucleoporins are particularly known for poor sequence conservation between species due to their need for functional plasticity. Similarly the diversity of RNA-binding proteins limit the ability to identify them from sequence alone (Asakawa et al., 2014; Cronshaw et al., 2002; Huang et al., 2010). It is notable that, throughout evolution, functional conservation of proteins is much higher than sequence conservation. In the first instance, this is because many amino acids can be easily substituted for chemically similar ones without significant effects on protein function (Barnes, 2007). This is particularly true of proteins with few structural elements, where flexibility may be the most significant conserved element.

As we saw from our screening hits, functionally related groups of proteins may often be more significant than individual genes. Even if certain genes in a pathway were missed, it was possible to suggest that the whole pathway has an influence on cell shape or microtubules. This reasoning may also apply here: Amo1 may be dispensable through evolutionary time, but its functional network remains, in the form of other proteins. Learning more about the functional context of Amo1 may help discover how its role is conserved in human cells.

Similarly, the DDR network has been reported to vary greatly between species (Rhind and Russell, 2000). Whilst, in this instance, the proteins themselves appear to be strongly conserved, they show functional plasticity, changing the stimuli they respond to and the effectors they target. Yet, ultimately this highly adaptable network has the same effect, helping cells survive stressful conditions. Hence, it is possible to consider that, although both species show microtubule stabilisation, the constituent elements of the underlying mechanism may vary.

6.6.2 Further work in *H. sapiens*

My work in human cells has focused on Hc3716-hTERT cells, a key continuation of this work will be to investigate whether the same response can be observed in other cells and whether the same relative sensitivities to UVC and IR are observed. It would also be greatly beneficial to identify an intuitive, quantitative measure of microtubule stabilisation, which may also then be informative of the biological processes involved.

A first step in dissecting the mechanism in human cells may involve chemical inhibition of the DDR kinases in an attempt to isolate which are involved, what stimuli are involved and to more specifically isolate the types of DNA lesions required. For example, caffeine treatment is reported to specifically inhibit ATM kinase (Blasina et al., 1999). If caffeine is found to suppress microtubule stabilisation then it would confirm the inference, from IR sensitivity, that ATM is the primary driver of microtubule stabilisation in human cells.

Further investigations are less predictable but will require knock-outs or known-downs of different factors to study their effect on microtubules. These studies should potentially focus on known microtubule regulators. If nucleoporins in *S. pombe* continue to be of interest, it may also be interesting to study the effect of impaired nuclear pore function in human cells. Similarly, homologues of targets of Amo1 RNA-binding in *S. pombe* could be considered. A screen for factors that do not stabilise microtubules may even be possible, although not on a comprehensive genome-wide scale.

6.7 Wider impact of findings

Scientifically speaking, the impact of this work is in its contribution to the scientific community. This screen has provided vast amounts of new image data, which are openly available for mining and analysis by anyone. The potential for advancement from investigating such a dataset is huge. I have also proposed several highly interesting groups of genes, from the hits selected by our analysis, which may provide enlightening insights into the relationship between different processes within cells.

In addition, the methodological contributions from this screen are significant. We have provided the first rigorous methods for identifying hits from image-based screening and simultaneous study of multiple cell processes. Continued development and use of this method, by our lab and others, will serve to expand the variety of available high-throughput phenotypic data, spanning the full range of biological processes. This also provides a start-point from which to develop more elaborate screening approaches to study more complex biological systems, most specifically mammalian tissue culture.

Our finding that cell cycle progression hits do not elongate cells – thought to be typical for cell cycle regulators in *S. pombe* – may open a new door into our understanding of how cells regulate the cell cycle. This may provide many new avenues of study and could highlight new key areas of cell cycle control, even in well-studied model organisms.

The link between the DNA damage/stress responses and microtubule stability in interphase is also scientifically fascinating. It highlights the need for more extensive study of microtubules during interphase and acts as a demonstration that all cell processes are tightly interlinked in complex networks. In particular, examination of the reason for this response may add to our understanding of DNA repair and the processes that determine which repair mechanisms are favoured and how cells ensure that repairs are made correctly and as rapidly as possible.

From a wider societal viewpoint, the primary outcome of this study is the finding that DNA damage is linked to the microtubule cytoskeleton through a specific, regulated mechanism of biological factors, which is conserved in humans. Several clinical findings have previously indicated that destabilisation of microtubules is synergistic with therapeutic agents in the treatment of cancer, which allows for selective sensitisation of cancer cells to radio- or chemotherapeutic interventions (Baumgart et al., 2012; Blagosklonny et al., 2000; Lee et al., 2010). Since the development of cancer is critically dependent upon errors in genome repair, a more detailed understanding of the connections between DNA damage and microtubules may impact our ability to treat cancer more effectively and with fewer debilitating side-effects.

Abbreviations

γ-TuRC	γ-tubulin ring complex
atb2	α-tubulin 2
ATM	ataxia telangiectasia mutated kinase
ATR	ATM-related kinase
ATRIP	ATR interacting protein
BSA-FAF	bovine serum albumin – fatty acid free
Carb	Non-selective antibacterial drug
Cdc2-AS	analogue sensitive Cdc2 kinase strain
CDK	cyclin dependent kinase
CHK1	Checkpoint kinase 1 (spChk1)
CHK2	Checkpoint kinase 2 (spCds1)
DDR	DNA damage response
DNA-PK^{cs}	DNA-dependent protein kinase, catalytic subunit
dNTP	deoxynuclotide triphosphate
DSB	double strand break
DsRed	red fluorophore
EMM(-N)	Edinburgh minimal medium (minus Nitrogen)
eMTOC	equatorial microtubule organising centre
ERA	ergodic rate analysis
FACS	fluorescence assisted cell sorting
FBS	fetal bovine serum
FIJI	Fiji is just ImageJ – Open source image processing software
FYPO	fission yeast phenotype ontology
G0	quiescence/senescence cell state
G1	gap 1 cell cycle phase
G2	gap 2 cell cycle phase
G418	Selective drug for Kan resistance
GEF	guanosine-nucleotide exchange factor
GFP/eGFP	(enhanced) green fluorescent protein
GWAS	genome-wide association studies
H2AX	Histone 2A variant X
HBM	hepatocyte basal medium
Hc3716	immortalised non-cancer human cell line
HCS	high-content screening
hEGF	human epidermal growth factor
HR	homologous recombination
hTERT	human telomerase reverse transcriptase
HU	hydroxyurea
iMTOC	interphase microtubule organising centre
indel	genetic insertion or deletion

ABBREVIATIONS

IP Interphase microtubule pattern

IP2 post-septation, interphase microtubule pattern in conjoined cells

IR ionising radiation

KO total gene knock out

KS Kolmogorov-Smirnov

Ku Ku70/Ku80 heterodimer

LINC linker of nucleoskeletion and cytoskeleton

liquidator 96-tip manual pipette system

M mitosis cell cycle phase

MAP microtubule associated protein

MBC methyl 1H-benzimidazole-2-ylcarbamate (carbendazim); microtubule depolymerising drug

mCherry red fluorophore

MMEJ microhomology-mediated end joining

MMS methyl methanesulfonate

MRN Mre11-Rad50-Nbs1 complex

MTOC microtubule organising centre

Nat clonNAT; selective drug for Nat resistance

NETO old end take-off

NHEJ non-homologous end joining

NN neural network

NPC nuclear pore complex

OD optical density

OETO old end take-off

OME open microscopy environment

OMERO OME online image management tools

ORF open reading frame

PAA post-anaphase array microtubule pattern

phenoprint phenotypic fingerprint

QMS quantitative morphology score

RCI remote control interface

RFP red fluorescent protein

RNAi RNA interference

RPA replication protein A

S synthesis cell cycle phase

SNP single nucleotide polymorphism

SP Spindle microtubule pattern

SPB spindle pole body

SQ/TQ dipeptide target sequences for ATM/ATR kinases

ssDNA single-stranded DNA

SVM support vector machine

TBZ thiabendazole; microtubule/actin depolymerising drug

TC treatment condition

TCA trichloroacetic acid

UVC ultraviolet radiation subtype C

v2v3 version 2 to version 3 Bioneer library upgrade

VBA Visual Basic for Applications

YES yeast extract & supplements

YFM yellow freezing medium

References

Abraham, R. T. Checkpoint signaling: epigenetic events sound the DNA strand-breaks alarm to the ATM protein kinase. *Bioessays*, 25(7):627–30, 2003.

Adachi, Y., Toda, T., Niwa, O., and Yanagida, M. Differential expressions of essential and nonessential alpha-tubulin genes in *Schizosaccharomyces pombe*. *Mol Cell Biol*, 6(6):2168–78, 1986.

Adams, D. S. Mechanisms of Cell-Shape Change - the Cytomechanics of Cellular-Response to Chemical Environment and Mechanical Loading. *Journal of Cell Biology*, 117(1):83–93, 1992.

Adams, M. D., Celniker, S. E., Holt, R. A., Evans, C. A., Gocayne, J. D., Amanatides, P. G., Scherer, S. E., Li, P. W., Hoskins, R. A., and Galle, R. F. The genome sequence of *Drosophila melanogaster*. *Science*, 287(5461):2185–2195, 2000.

Agrawal, N., Dasaradhi, P. V., Mohmmed, A., Malhotra, P., Bhatnagar, R. K., and Mukherjee, S. K. RNA interference: biology, mechanism, and applications. *Microbiol Mol Biol Rev*, 67(4): 657–85, 2003.

Akamatsu, Y., Murayama, Y., Yamada, T., Nakazaki, T., Tsutsui, Y., Ohta, K., and Iwasaki, H. Molecular characterization of the role of the *Schizosaccharomyces pombe nip1*+/*ctp1*+ gene in DNA double-strand break repair in association with the Mre11-Rad50-Nbs1 complex. *Mol Cell Biol*, 28(11):3639–51, 2008.

Akhmanova, A. and Hoogenraad, C. C. Microtubule plus-end-tracking proteins: mechanisms and functions. *Curr Opin Cell Biol*, 17(1):47–54, 2005.

Akhmanova, A. and Steinmetz, M. O. Tracking the ends: a dynamic protein network controls the fate of microtubule tips. *Nat Rev Mol Cell Biol*, 9(4):309–22, 2008.

Alao, J. P. and Sunnerhagen, P. Rad3 and Sty1 function in *Schizosaccharomyces pombe*: an integrated response to DNA damage and environmental stress? *Mol Microbiol*, 68(2):246–54, 2008.

Alberts, B. *Molecular biology of the cell*. Garland Science, New York, 4th edition, 2002.

Alfa, C. E., Booher, R., Beach, D., and Hyams, J. S. Fission yeast cyclin: subcellular localisation and cell cycle regulation. *J Cell Sci Suppl*, 12:9–19, 1989.

Allan, C., Burel, J. M., Moore, J., Blackburn, C., Linkert, M., Loynton, S., Macdonald, D., Moore, W. J., Neves, C., Patterson, A., Porter, M., Tarkowska, A., Loranger, B., Avondo, J., Lagerstedt, I., Lianas, L., Leo, S., Hands, K., Hay, R. T., Patwardhan, A., Best, C., Kleywegt, G. J., Zanetti, G., and Swedlow, J. R. OMERO: flexible, model-driven data management for experimental biology. *Nat Methods*, 9(3):245–53, 2012.

Amano, M., Nakayama, M., and Kaibuchi, K. Rho-kinase/ROCK: A key regulator of the cytoskeleton and cell polarity. *Cytoskeleton (Hoboken)*, 67(9):545–54, 2010.

Amos, L. A. and Schlieper, D. Microtubules and maps. *Adv Protein Chem*, 71:257–98, 2005.

Apodaca, G. Endocytic traffic in polarized epithelial cells: role of the actin and microtubule cytoskeleton. *Traffic*, 2(3):149–59, 2001.

Applegate, K. T., Besson, S., Matov, A., Bagonis, M. H., Jaqaman, K., and Danuser, G. plusTipTracker: Quantitative image analysis software for the measurement of microtubule dynamics. *J Struct Biol*, 176(2):168–84, 2011.

Arellano, M., Niccoli, T., and Nurse, P. Tea3p is a cell end marker activating polarized growth in *Schizosaccharomyces pombe*. *Curr Biol*, 12(9):751–6, 2002.

Arnal, I., Karsenti, E., and Hyman, A. A. Structural transitions at microtubule ends correlate with their dynamic properties in *Xenopus* egg extracts. *J Cell Biol*, 149(4):767–74, 2000.

Asakawa, H., Yang, H. J., Yamamoto, T. G., Ohtsuki, C., Chikashige, Y., Sakata-Sogawa, K., Tokunaga, M., Iwamoto, M., Hiraoka, Y., and Haraguchi, T. Characterization of nuclear pore complex components in fission yeast *Schizosaccharomyces pombe*. *Nucleus*, 5(2):149–62, 2014.

Aylon, Y. and Kupiec, M. New insights into the mechanism of homologous recombination in yeast. *Mutat Res*, 566(3):231–48, 2004.

Bakal, C. and Perrimon, N. Realizing the promise of RNAi high throughput screening. *Dev Cell*, 18(4):506–7, 2010.

Bakal, C., Aach, J., Church, G., and Perrimon, N. Quantitative morphological signatures define local signaling networks regulating cell morphology. *Science*, 316(5832):1753–6, 2007.

Baker, J. and Garrod, D. Epithelial cells retain junctions during mitosis. *J Cell Sci*, 104 (Pt 2): 415–25, 1993.

Baker, S. and Matthews, I. Equivalence and efficiency of image alignment algorithms. *2001 Ieee Computer Society Conference on Computer Vision and Pattern Recognition, Vol 1, Proceedings*, pages 1090–1097, 2001.

Bakkenist, C. J. and Kastan, M. B. Initiating cellular stress responses. *Cell*, 118(1):9–17, 2004.

Banks, P. Microtubules and vesicle migration in neurons. *Biochem Soc Trans*, 4(4):548–51, 1976.

Bao, S., Wu, Q., McLendon, R. E., Hao, Y., Shi, Q., Hjelmeland, A. B., Dewhirst, M. W., Bigner, D. D., and Rich, J. N. Glioma stem cells promote radioresistance by preferential activation of the DNA damage response. *Nature*, 444(7120):756–60, 2006.

Barnes, M. R. *Bioinformatics for geneticists : a bioinformatics primer for the analysis of genetic data*. Wiley, Chichester, England ; Hoboken, NJ, 2nd edition, 2007.

Barr, A. R. and Bakal, C. A direct look at RNAi screens. *Mol Syst Biol*, 8:580, 2012.

Bartek, J. and Lukas, J. Mammalian G1- and S-phase checkpoints in response to DNA damage. *Curr Opin Cell Biol*, 13(6):738–47, 2001.

Bartlett, J. S. and Stirling, D. *A Short History of the Polymerase Chain Reaction*, volume 226 of *Methods in Molecular Biology*, chapter 1, pages 3–6. Humana Press, 2003.

Baschal, E. E., Chen, K. J., Elliott, L. G., Herring, M. J., Verde, S. C., and Wolkow, T. D. The fission yeast DNA structure checkpoint protein Rad26ATRIP/LCD1/UVSD accumulates in the cytoplasm following microtubule destabilization. *BMC Cell Biol*, 7:32, 2006.

Basu, R. and Chang, F. Shaping the actin cytoskeleton using microtubule tips. *Curr Opin Cell Biol*, 19(1):88–94, 2007.

Baumgart, T., Klautke, G., Kriesen, S., Kuznetsov, S. A., Weiss, D. G., Fietkau, R., Hildebrandt, G., and Manda, K. Radiosensitizing effect of epothilone B on human epithelial cancer cells. *Strahlenther Onkol*, 188(2):177–84, 2012.

Beach, D. L., Thibodeaux, J., Maddox, P., Yeh, E., and Bloom, K. The role of the proteins Kar9 and Myo2 in orienting the mitotic spindle of budding yeast. *Curr Biol*, 10(23):1497–506, 2000.

Behrens, R. and Nurse, P. Roles of fission yeast *tea1p* in the localization of polarity factors and in organizing the microtubular cytoskeleton. *J Cell Biol*, 157(5):783–93, 2002.

Beinhauer, J. D., Hagan, I. M., Hegemann, J. H., and Fleig, U. Mal3, the fission yeast homologue of the human APC-interacting protein EB-1 is required for microtubule integrity and the maintenance of cell form. *J Cell Biol*, 139(3):717–28, 1997.

Belenguer, P., Oustrin, M. L., Tiraby, G., and Ducommun, B. Effects of phleomycin-induced DNA damage on the fission yeast *Schizosaccharomyces pombe* cell cycle. *Yeast*, 11(3):225–31, 1995.

Belmont, L., Mitchison, T., and Deacon, H. W. Catastrophic revelations about Op18/stathmin. *Trends Biochem Sci*, 21(6):197–8, 1996.

Ben-Ze'ev, A. *Cell Shape, the Complex Cellular Networks, and Gene Expression*, chapter 2, pages 23–53. Springer US, 1985.

Bermudes, D., Hinkle, G., and Margulis, L. Do Prokaryotes Contain Microtubules. *Microbiological Reviews*, 58(3):387–400, 1994.

Betermier, M., Bertrand, P., and Lopez, B. S. Is non-homologous end-joining really an inherently error-prone process? *PLoS Genet*, 10(1):e1004086, 2014.

Bishop, A. C., Ubersax, J. A., Petsch, D. T., Matheos, D. P., Gray, N. S., Blethrow, J., Shimizu, E., Tsien, J. Z., Schultz, P. G., Rose, M. D., Wood, J. L., Morgan, D. O., and Shokat, K. M. A chemical switch for inhibitor-sensitive alleles of any protein kinase. *Nature*, 407(6802):395–401, 2000.

Blagosklonny, M. V., Robey, R., Bates, S., and Fojo, T. Pretreatment with DNA-damaging agents permits selective killing of checkpoint-deficient cells by microtubule-active drugs. *J Clin Invest*, 105(4):533–9, 2000.

Blasina, A., Price, B. D., Turenne, G. A., and McGowan, C. H. Caffeine inhibits the checkpoint kinase ATM. *Curr Biol*, 9(19):1135–8, 1999.

Blasius, M., Forment, J. V., Thakkar, N., Wagner, S. A., Choudhary, C., and Jackson, S. P. A phospho-proteomic screen identifies substrates of the checkpoint kinase Chk1. *Genome Biol*, 12(8):R78, 2011.

Blattner, F. R., Plunkett, r., G., Bloch, C. A., Perna, N. T., Burland, V., Riley, M., Collado-Vides, J., Glasner, J. D., Rode, C. K., Mayhew, G. F., Gregor, J., Davis, N. W., Kirkpatrick, H. A., Goeden, M. A., Rose, D. J., Mau, B., and Shao, Y. The complete genome sequence of Escherichia coli K-12. *Science*, 277(5331):1453–62, 1997.

Booher, R. and Beach, D. Interaction between *cdc13+* and *cdc2+* in the control of mitosis in fission yeast; dissociation of the G1 and G2 roles of the *cdc2+* protein kinase. *EMBO J*, 6(11): 3441–7, 1987.

Bornens, M. Organelle positioning and cell polarity. *Nat Rev Mol Cell Biol*, 9(11):874–86, 2008.

Boudreau, N. J. and Jones, P. L. Extracellular matrix and integrin signalling: the shape of things to come. *Biochem J*, 339 (Pt 3):481–8, 1999.

Bouissou, A., Verollet, C., Sousa, A., Sampaio, P., Wright, M., Sunkel, C. E., Merdes, A., and Raynaud-Messina, B. γ-Tubulin ring complexes regulate microtubule plus end dynamics. *J Cell Biol*, 187(3):327–34, 2009.

Boutros, M. and Ahringer, J. The art and design of genetic screens: RNA interference. *Nat Rev Genet*, 9(7):554–66, 2008.

Boutros, M., Kiger, A. A., Armknecht, S., Kerr, K., Hild, M., Koch, B., Haas, S. A., Paro, R., and Perrimon, N. Genome-wide RNAi analysis of growth and viability in *Drosophila* cells. *Science*, 303(5659):832–5, 2004.

Bratman, S. V. and Chang, F. Stabilization of overlapping microtubules by fission yeast CLASP. *Dev Cell*, 13(6):812–27, 2007.

Brown, P. O. and Botstein, D. Exploring the new world of the genome with DNA microarrays. *Nat Genet*, 21(1 Suppl):33–7, 1999.

Brown, S. D. and Balling, R. Systematic approaches to mouse mutagenesis. *Curr Opin Genet Dev*, 11(3):268–73, 2001.

Brown, T. A. *Genomes*. Wiley-Liss, New York, 2nd edition, 2002.

Browning, H., Hayles, J., Mata, J., Aveline, L., Nurse, P., and McIntosh, J. R. Tea2p is a kinesin-like protein required to generate polarized growth in fission yeast. *J Cell Biol*, 151(1):15–28, 2000.

Browning, H., Hackney, D. D., and Nurse, P. Targeted movement of cell end factors in fission yeast. *Nat Cell Biol*, 5(9):812–8, 2003.

Brun, L., Rupp, B., Ward, J. J., and Nedelec, F. A theory of microtubule catastrophes and their regulation. *Proc Natl Acad Sci U S A*, 106(50):21173–8, 2009.

Brunner, D. and Nurse, P. CLIP170-like tip1p spatially organizes microtubular dynamics in fission yeast. *Cell*, 102(5):695–704, 2000.

Bukata, L., Parker, S. L., and D'Angelo, M. A. Nuclear pore complexes in the maintenance of genome integrity. *Curr Opin Cell Biol*, 25(3):378–86, 2013.

Burhans, W. C., Weinberger, M., Marchetti, M. A., Ramachandran, L., D'Urso, G., and Huberman, J. A. Apoptosis-like yeast cell death in response to DNA damage and replication defects. *Mutat Res*, 532(1-2):227–43, 2003.

Burns, F. J. and Tannock, I. F. On the existence of a G0-phase in the cell cycle. *Cell Tissue Kinet*, 3(4):321–34, 1970.

Busch, K. E. and Brunner, D. The microtubule plus end-tracking proteins mal3p and tip1p cooperate for cell-end targeting of interphase microtubules. *Curr Biol*, 14(7):548–59, 2004.

Butler, L. C., Blanchard, G. B., Kabla, A. J., Lawrence, N. J., Welchman, D. P., Mahadevan, L., Adams, R. J., and Sanson, B. Cell shape changes indicate a role for extrinsic tensile forces in *Drosophila* germ-band extension. *Nature Cell Biology*, 11(7):859–U181, 2009.

Bütschli, O. Studien Ãijber die ersten EntwicklungsvorgÃď nge der Eizelle, die Zelltheilung und die Conjugation der Infusorien. 1876.

Cabeen, M. T. and Jacobs-Wagner, C. Bacterial cell shape. *Nat Rev Microbiol*, 3(8):601–10, 2005.

Cadart, C., Zlotek-Zlotkiewicz, E., Le Berre, M., Piel, M., and Matthews, H. K. Exploring the function of cell shape and size during mitosis. *Dev Cell*, 29(2):159–69, 2014.

Caldecott, K. W. Single-strand break repair and genetic disease. *Nat Rev Genet*, 9(8):619–31, 2008.

Carazo-Salas, R. and Nurse, P. Sorting out interphase microtubules. *Mol Syst Biol*, 3:95, 2007.

Carazo-Salas, R. E. and Nurse, P. Self-organization of interphase microtubule arrays in fission yeast. *Nat Cell Biol*, 8(10):1102–7, 2006.

Carlier-Grynkorn, F., Ji, L., Fraisier, V., Lombard, B., Dingli, F., Loew, D., Paoletti, A., Ronot, X., and Tran, P. T. Fission yeast mtr1p regulates interphase microtubule cortical dwell-time. *Biol Open*, 3(7):591–6, 2014.

Carlson, C. R., Grallert, B., Stokke, T., and Boye, E. Regulation of the start of DNA replication in *Schizosaccharomyces pombe*. *J Cell Sci*, 112 (Pt 6):939–46, 1999.

Carthew, R. W. Adhesion proteins and the control of cell shape. *Curr Opin Genet Dev*, 15(4): 358–63, 2005.

Carvalho, P., Tirnauer, J. S., and Pellman, D. Surfing on microtubule ends. *Trends Cell Biol*, 13 (5):229–37, 2003.

Cava, F., Kuru, E., Brun, Y. V., and de Pedro, M. A. Modes of cell wall growth differentiation in rod-shaped bacteria. *Curr Opin Microbiol*, 16(6):731–7, 2013.

Cavalier-Smith, T. The origin of cells: a symbiosis between genes, catalysts, and membranes. *Cold Spring Harb Symp Quant Biol*, 52:805–24, 1987a.

Cavalier-Smith, T. The origin of eukaryotic and archaebacterial cells. *Ann N Y Acad Sci*, 503: 17–54, 1987b.

Chandler, D. S., Singh, R. K., Caldwell, L. C., Bitler, J. L., and Lozano, G. Genotoxic stress induces coordinately regulated alternative splicing of the p53 modulators MDM2 and MDM4. *Cancer Res*, 66(19):9502–8, 2006.

Chang, F. and Martin, S. G. Shaping fission yeast with microtubules. *Cold Spring Harb Perspect Biol*, 1(1):a001347, 2009.

Chang, F. and Nurse, P. How fission yeast fission in the middle. *Cell*, 84(2):191–4, 1996.

Chang, F., Woollard, A., and Nurse, P. Isolation and characterization of fission yeast mutants defective in the assembly and placement of the contractile actin ring. *J Cell Sci*, 109 (Pt 1): 131–42, 1996.

Chapman, C. R., Evans, S. T., Carr, A. M., and Enoch, T. Requirement of sequences outside the conserved kinase domain of fission yeast Rad3p for checkpoint control. *Mol Biol Cell*, 10(10): 3223–38, 1999.

Chavali, S., Barrenas, F., Kanduri, K., and Benson, M. Network properties of human disease genes with pleiotropic effects. *BMC Syst Biol*, 4:78, 2010.

Chernyatina, A. A., Guzenko, D., and Strelkov, S. V. Intermediate filament structure: the bottom-up approach. *Curr Opin Cell Biol*, 32C:65–72, 2015.

Chia, J., Goh, G., Racine, V., Ng, S., Kumar, P., and Bard, F. RNAi screening reveals a large signaling network controlling the Golgi apparatus in human cells. *Mol Syst Biol*, 8:629, 2012.

Ciccia, A. and Elledge, S. J. The DNA damage response: making it safe to play with knives. *Mol Cell*, 40(2):179–204, 2010.

Cipak, L., Zhang, C., Kovacikova, I., Rumpf, C., Miadokova, E., Shokat, K. M., and Gregan, J. Generation of a set of conditional analog-sensitive alleles of essential protein kinases in the fission yeast *Schizosaccharomyces pombe*. *Cell Cycle*, 10(20):3527–32, 2011.

Coetzee, K., Kruge, T. F., and Lombard, C. J. Predictive value of normal sperm morphology: a structured literature review. *Hum Reprod Update*, 4(1):73–82, 1998.

Coleman, T. R. and Dunphy, W. G. Cdc2 regulatory factors. *Curr Opin Cell Biol*, 6(6):877–82, 1994.

Collinet, C., Stoter, M., Bradshaw, C. R., Samusik, N., Rink, J. C., Kenski, D., Habermann, B., Buchholz, F., Henschel, R., Mueller, M. S., Nagel, W. E., Fava, E., Kalaidzidis, Y., and Zerial, M. Systems survey of endocytosis by multiparametric image analysis. *Nature*, 464(7286): 243–9, 2010.

Consortium, C. Genome sequence of the nematode *C. elegans*: a platform for investigating biology. *Science*, 282(5396):2012–8, 1998.

Cooper, G. M. and Hausman, R. E. *The cell : a molecular approach*. Sinauer Associates, Sunderland, Mass., 6th edition, 2013.

Cortez, D., Wang, Y., Qin, J., and Elledge, S. J. Requirement of ATM-dependent phosphorylation of brca1 in the DNA damage response to double-strand breaks. *Science*, 286(5442):1162–6, 1999.

Cortez, D., Guntuku, S., Qin, J., and Elledge, S. J. ATR and ATRIP: partners in checkpoint signaling. *Science*, 294(5547):1713–6, 2001.

Cotta-Ramusino, C., McDonald, r., E. R., Hurov, K., Sowa, M. E., Harper, J. W., and Elledge, S. J. A DNA damage response screen identifies RHINO, a 9-1-1 and TopBP1 interacting protein required for ATR signaling. *Science*, 332(6035):1313–7, 2011.

Coudreuse, D. and Nurse, P. Driving the cell cycle with a minimal CDK control network. *Nature*, 468(7327):1074–9, 2010.

Cronshaw, J. M., Krutchinsky, A. N., Zhang, W., Chait, B. T., and Matunis, M. J. Proteomic analysis of the mammalian nuclear pore complex. *J Cell Biol*, 158(5):915–27, 2002.

Daga, R. R., Lee, K. G., Bratman, S., Salas-Pino, S., and Chang, F. Self-organization of microtubule bundles in anucleate fission yeast cells. *Nat Cell Biol*, 8(10):1108–13, 2006.

Dammermann, A., Desai, A., and Oegema, K. The minus end in sight. *Curr Biol*, 13(15):R614–24, 2003.

Darwin, C. *On the origin of the species by means of natural selection, or, The preservation of favoured races in the struggle for life*. J. Murray, London„ 1859.

Darwin, C. and Wallace, A. R. *On the tendency of species to form varieties; and on the perpetuation of varieties and species by natural means of selection*. Journal of the proceedings of the Linnean Society, v 3, no 9. [Linnean Society of London], London, 1858.

Davies, P. F. and Tripathi, S. C. Mechanical stress mechanisms and the cell. An endothelial paradigm. *Circ Res*, 72(2):239–45, 1993.

Davy, A. and Robbins, S. M. Ephrin-A5 modulates cell adhesion and morphology in an integrin-dependent manner. *EMBO J*, 19(20):5396–405, 2000.

De Robertis, E. and Franchi, C. M. The submicroscopic organization of axon material isolated from myelin nerve fibers. *Quarterly Journal of Experimental Physiology*, 98(3):269–76, 1953.

Dehe, P. M., Coulon, S., Scaglione, S., Shanahan, P., Takedachi, A., Wohlschlegel, J. A., Yates, J. R., Llorente, B., Russell, P., and Gaillard, P. H. Regulation of Mus81-Eme1 Holliday junction resolvase in response to DNA damage. *Nat Struct Mol Biol*, 20(5):598–603, 2013.

Dehmelt, L. and Halpain, S. The MAP2/Tau family of microtubule-associated proteins. *Genome Biol*, 6(1):204, 2005.

Delphin, C., Bouvier, D., Seggio, M., Couriol, E., Saoudi, Y., Denarier, E., Bosc, C., Valiron, O., Bisbal, M., Arnal, I., and Andrieux, A. MAP6-F Is a Temperature Sensor That Directly Binds to and Protects Microtubules from Cold-induced Depolymerization. *Journal of Biological Chemistry*, 287(42):35127–35138, 2012.

des Georges, A., Katsuki, M., Drummond, D. R., Osei, M., Cross, R. A., and Amos, L. A. Mal3, the *Schizosaccharomyces pombe* homolog of EB1, changes the microtubule lattice. *Nat Struct Mol Biol*, 15(10):1102–1108, 2008.

Desai, A. and Mitchison, T. J. Microtubule polymerization dynamics. *Annu Rev Cell Dev Biol*, 13: 83–117, 1997.

Desai, A., Verma, S., Mitchison, T. J., and Walczak, C. E. Kin I kinesins are microtubule-destabilizing enzymes. *Cell*, 96(1):69–78, 1999.

Diez-Silva, M., Dao, M., Han, J., Lim, C. T., and Suresh, S. Shape and Biomechanical Characteristics of Human Red Blood Cells in Health and Disease. *MRS Bull*, 35(5):382–388, 2010.

Diffley, J. F. The many faces of redundancy in DNA replication control. *Cold Spring Harb Symp Quant Biol*, 75:135–42, 2010.

Dimitrov, A., Quesnoit, M., Moutel, S., Cantaloube, I., Pous, C., and Perez, F. Detection of GTP-tubulin conformation in vivo reveals a role for GTP remnants in microtubule rescues. *Science*, 322(5906):1353–6, 2008.

Ding, D. Q., Chikashige, Y., Haraguchi, T., and Hiraoka, Y. Oscillatory nuclear movement in fission yeast meiotic prophase is driven by astral microtubules, as revealed by continuous observation of chromosomes and microtubules in living cells. *J Cell Sci*, 111 (Pt 6):701–12, 1998.

Ding, R., McDonald, K. L., and McIntosh, J. R. Three-dimensional reconstruction and analysis of mitotic spindles from the yeast, *Schizosaccharomyces pombe*. *J Cell Biol*, 120(1):141–51, 1993.

Dixon, S. J., Fedyshyn, Y., Koh, J. L., Prasad, T. S., Chahwan, C., Chua, G., Toufighi, K., Baryshnikova, A., Hayles, J., Hoe, K. L., Kim, D. U., Park, H. O., Myers, C. L., Pandey, A., Durocher, D., Andrews, B. J., and Boone, C. Significant conservation of synthetic lethal genetic interaction networks between distantly related eukaryotes. *Proc Natl Acad Sci U S A*, 105(43):16653–8, 2008.

Dodgson, J., Brown, W., Rosa, C. A., and Armstrong, J. Reorganization of the growth pattern of *Schizosaccharomyces pombe* in invasive filament formation. *Eukaryot Cell*, 9(11):1788–97, 2010.

Dodgson, J., Chessel, A., Yamamoto, M., Vaggi, F., Cox, S., Rosten, E., Albrecht, D., Geymonat, M., Csikasz-Nagy, A., Sato, M., and Carazo-Salas, R. E. Spatial segregation of polarity factors into distinct cortical clusters is required for cell polarity control. *Nat Commun*, 4:1834, 2013.

Doll, R. and Peto, R. The causes of cancer: quantitative estimates of avoidable risks of cancer in the United States today. *J Natl Cancer Inst*, 66(6):1191–308, 1981.

Drechsel, D. N. and Kirschner, M. W. The minimum GTP cap required to stabilize microtubules. *Curr Biol*, 4(12):1053–61, 1994.

Dresdner, R. D. and Katz, D. F. Relationships of mammalian sperm motility and morphology to hydrodynamic aspects of cell function. *Biol Reprod*, 25(5):920–30, 1981.

Drubin, D. G. and Nelson, W. J. Origins of cell polarity. *Cell*, 84(3):335–44, 1996.

Drummond, D. R. and Cross, R. A. Dynamics of interphase microtubules in *Schizosaccharomyces pombe*. *Curr Biol*, 10(13):766–75, 2000.

Dudley, A. M., Janse, D. M., Tanay, A., Shamir, R., and Church, G. M. A global view of pleiotropy and phenotypically derived gene function in yeast. *Mol Syst Biol*, 1:2005 0001, 2005.

Duggan, D. J., Bittner, M., Chen, Y., Meltzer, P., and Trent, J. M. Expression profiling using cDNA microarrays. *Nat Genet*, 21(1 Suppl):10–4, 1999.

Edge, M. D., Green, A. R., Heathcliffe, G. R., Meacock, P. A., Schuch, W., Scanlon, D. B., Atkinson, T. C., Newton, C. R., and Markham, A. F. Total synthesis of a human leukocyte interferon gene. *Nature*, 292(5825):756–62, 1981.

Effler, J. C., Kee, Y. S., Berk, J. M., Tran, M. N., Iglesias, P. A., and Robinson, D. N. Mitosis-specific mechanosensing and contractile-protein redistribution control cell shape. *Curr Biol*, 16 (19):1962–7, 2006.

Effler, J. C., Iglesias, P. A., and Robinson, D. N. A mechanosensory system controls cell shape changes during mitosis. *Cell Cycle*, 6(1):30–5, 2007.

Eisenberg, D., Marcotte, E. M., Xenarios, I., and Yeates, T. O. Protein function in the post-genomic era. *Nature*, 405(6788):823–6, 2000.

Eisenberg, D. S., Kuriyan, J., and Richards, F. M. Advances in Protein Chemistry. *Adv Protein Chem*, 59, 2002.

Elford, H. L. Effect of hydroxyurea on ribonucleotide reductase. *Biochem Biophys Res Commun*, 33(1):129–35, 1968.

Elledge, S. J. Cell cycle checkpoints: preventing an identity crisis. *Science*, 274(5293):1664–72, 1996.

Epe, B. Role of endogenous oxidative DNA damage in carcinogenesis: what can we learn from repair-deficient mice? *Biol Chem*, 383(3-4):467–75, 2002.

Erent, M., Drummond, D. R., and Cross, R. A. *S. pombe* kinesins-8 promote both nucleation and catastrophe of microtubules. *PLoS One*, 7(2):e30738, 2012.

Evans, L., Mitchison, T., and Kirschner, M. Influence of the centrosome on the structure of nucleated microtubules. *J Cell Biol*, 100(4):1185–91, 1985.

Evans, T., Rosenthal, E. T., Youngblom, J., Distel, D., and Hunt, T. Cyclin: a protein specified by maternal mRNA in sea urchin eggs that is destroyed at each cleavage division. *Cell*, 33(2): 389–96, 1983.

Evensen, L., Link, W., and Lorens, J. B. Image-based high-throughput screening for inhibitors of angiogenesis. *Methods Mol Biol*, 931:139–51, 2013.

Fan, J., Griffiths, A. D., Lockhart, A., Cross, R. A., and Amos, L. A. Microtubule minus ends can be labelled with a phage display antibody specific to alpha-tubulin. *J Mol Biol*, 259(3):325–30, 1996.

Fantes, P. A. Control of cell size and cycle time in *Schizosaccharomyces pombe*. *J Cell Sci*, 24: 51–67, 1977.

Fantes, P. A. and Nurse, P. Control of the timing of cell division in fission yeast. Cell size mutants reveal a second control pathway. *Exp Cell Res*, 115(2):317–29, 1978.

Featherstone, C. and Jackson, S. P. Ku, a DNA repair protein with multiple cellular functions? *Mutat Res*, 434(1):3–15, 1999.

Feierbach, B., Verde, F., and Chang, F. Regulation of a formin complex by the microtubule plus end protein tea1p. *J Cell Biol*, 165(5):697–707, 2004.

Ferenz, N. P., Gable, A., and Wadsworth, P. Mitotic functions of kinesin-5. *Semin Cell Dev Biol*, 21(3):255–9, 2010.

Ferguson, D. O. and Alt, F. W. DNA double strand break repair and chromosomal translocation: lessons from animal models. *Oncogene*, 20(40):5572–9, 2001.

Fish, J. L., Dehay, C., Kennedy, H., and Huttner, W. B. Making bigger brains-the evolution of neural-progenitor-cell division. *J Cell Sci*, 121(Pt 17):2783–93, 2008.

Flemming, W. Zur Kenntniss der Zelle und ihrer Theilungs-Erscheinungen. 1878.

Fletcher, D. A. and Mullins, R. D. Cell mechanics and the cytoskeleton. *Nature*, 463(7280): 485–92, 2010.

Foley, E. A. and Kapoor, T. M. Microtubule attachment and spindle assembly checkpoint signalling at the kinetochore. *Nat Rev Mol Cell Biol*, 14(1):25–37, 2013.

Forsburg, S. L. The art and design of genetic screens: yeast. *Nat Rev Genet*, 2(9):659–68, 2001.

Franker, M. A. and Hoogenraad, C. C. Microtubule-based transport - basic mechanisms, traffic rules and role in neurological pathogenesis. *J Cell Sci*, 126(Pt 11):2319–29, 2013.

Fraser, A. G., Kamath, R. S., Zipperlen, P., Martinez-Campos, M., Sohrmann, M., and Ahringer, J. Functional genomic analysis of *C. elegans* chromosome I by systematic RNA interference. *Nature*, 408(6810):325–30, 2000.

Friedberg, E. C., McDaniel, L. D., and Schultz, R. A. The role of endogenous and exogenous DNA damage and mutagenesis. *Curr Opin Genet Dev*, 14(1):5–10, 2004.

Friedberg, E. C. *DNA repair and mutagenesis*. ASM Press, Washington, D.C., 2nd edition, 2006.

Friedman, A. and Perrimon, N. Genome-wide high-throughput screens in functional genomics. *Curr Opin Genet Dev*, 14(5):470–476, 2004.

Fu, C., Jain, D., Costa, J., Velve-Casquillas, G., and Tran, P. mmb1p Binds Mitochondria to Dynamic Microtubules. *Current Biology*, 21(17):1431–1439, 2011.

Fuchs, F., Pau, G., Kranz, D., Sklyar, O., Budjan, C., Steinbrink, S., Horn, T., Pedal, A., Huber, W., and Boutros, M. Clustering phenotype populations by genome-wide RNAi and multiparametric imaging. *Mol Syst Biol*, 6:370, 2010.

Fuerstenberg, S., Broadus, J., and Doe, C. Q. Asymmetry and cell fate in the *Drosophila* embryonic CNS. *Int J Dev Biol*, 42(3):379–83, 1998.

Fujita, A., Vardy, L., Garcia, M. A., and Toda, T. A fourth component of the fission yeast gamma-tubulin complex, Alp16, is required for cytoplasmic microtubule integrity and becomes indispensable when gamma-tubulin function is compromised. *Mol Biol Cell*, 13(7):2360–73, 2002.

Fukushige, T., Siddiqui, Z. K., Chou, M., Culotti, J. G., Gogonea, C. B., Siddiqui, S. S., and Hamelin, M. MEC-12, an alpha-tubulin required for touch sensitivity in *C. elegans*. *J Cell Sci*, 112 (Pt 3):395–403, 1999.

Furnari, B., Blasina, A., Boddy, M. N., McGowan, C. H., and Russell, P. Cdc25 inhibited in vivo and in vitro by checkpoint kinases Cds1 and Chk1. *Mol Biol Cell*, 10(4):833–45, 1999.

Furuta, K. and Toyoshima, Y. Y. Minus-end-directed motor Ncd exhibits processive movement that is enhanced by microtubule bundling in vitro. *Curr Biol*, 18(2):152–7, 2008.

Galperin, M. Y. and Koonin, E. V. Who's your neighbor? New computational approaches for functional genomics. *Nat Biotechnol*, 18(6):609–13, 2000.

Ganem, N. J. and Pellman, D. Linking abnormal mitosis to the acquisition of DNA damage. *J Cell Biol*, 199(6):871–81, 2012.

Gao, Y., Vainberg, I. E., Chow, R. L., and Cowan, N. J. Two cofactors and cytoplasmic chaperonin are required for the folding of alpha- and beta-tubulin. *Mol Cell Biol*, 13(4):2478–85, 1993.

Gardner, M. K., Zanic, M., and Howard, J. Microtubule catastrophe and rescue. *Curr Opin Cell Biol*, 25(1):14–22, 2013.

Gerdes, J. M., Davis, E. E., and Katsanis, N. The vertebrate primary cilium in development, homeostasis, and disease. *Cell*, 137(1):32–45, 2009.

Giaever, G., Chu, A. M., Ni, L., Connelly, C., Riles, L., Veronneau, S., Dow, S., Lucau-Danila, A., Anderson, K., Andre, B., Arkin, A. P., Astromoff, A., El-Bakkoury, M., Bangham, R., Benito, R., Brachat, S., Campanaro, S., Curtiss, M., Davis, K., Deutschbauer, A., Entian, K. D., Flaherty, P., Foury, F., Garfinkel, D. J., Gerstein, M., Gotte, D., Guldener, U., Hegemann, J. H., Hempel, S., Herman, Z., Jaramillo, D. F., Kelly, D. E., Kelly, S. L., Kotter, P., LaBonte, D., Lamb, D. C., Lan, N., Liang, H., Liao, H., Liu, L., Luo, C., Lussier, M., Mao, R., Menard, P., Ooi, S. L., Revuelta, J. L., Roberts, C. J., Rose, M., Ross-Macdonald, P., Scherens, B., Schimmack, G., Shafer, B., Shoemaker, D. D., Sookhai-Mahadeo, S., Storms, R. K., Strathern, J. N., Valle, G., Voet, M., Volckaert, G., Wang, C. Y., Ward, T. R., Wilhelmy, J., Winzeler, E. A., Yang, Y., Yen, G., Youngman, E., Yu, K., Bussey, H., Boeke, J. D., Snyder, M., Philippsen, P., Davis, R. W., and Johnston, M. Functional profiling of the *Saccharomyces cerevisiae* genome. *Nature*, 418 (6896):387–91, 2002.

Giansanti, M. G., Gatti, M., and Bonaccorsi, S. The role of centrosomes and astral microtubules during asymmetric division of Drosophila neuroblasts. *Development*, 128(7):1137–45, 2001.

Gibbons, I. R. and Rowe, A. J. Dynein: A Protein with Adenosine Triphosphatase Activity from Cilia. *Science*, 149(3682):424–6, 1965.

Giepmans, B. N., Adams, S. R., Ellisman, M. H., and Tsien, R. Y. The fluorescent toolbox for assessing protein location and function. *Science*, 312(5771):217–24, 2006.

Glory, E. and Murphy, R. F. Automated subcellular location determination and high-throughput microscopy. *Dev Cell*, 12(1):7–16, 2007.

Glotzer, M. The 3Ms of central spindle assembly: microtubules, motors and MAPs. *Nat Rev Mol Cell Biol*, 10(1):9–20, 2009.

Glynn, J. M., Lustig, R. J., Berlin, A., and Chang, F. Role of bud6p and tea1p in the interaction between actin and microtubules for the establishment of cell polarity in fission yeast. *Curr Biol*, 11(11):836–45, 2001.

Gobbini, E., Cesena, D., Galbiati, A., Lockhart, A., and Longhese, M. P. Interplays between ATM/Tel1 and ATR/Mec1 in sensing and signaling DNA double-strand breaks. *DNA Repair (Amst)*, 12(10):791–9, 2013.

Goetz, S. C. and Anderson, K. V. The primary cilium: a signalling centre during vertebrate development. *Nat Rev Genet*, 11(5):331–44, 2010.

Goffeau, A., Barrell, B. G., Bussey, H., Davis, R. W., Dujon, B., Feldmann, H., Galibert, F., Hoheisel, J. D., Jacq, C., Johnston, M., Louis, E. J., Mewes, H. W., Murakami, Y., Philippsen, P., Tettelin, H., and Oliver, S. G. Life with 6000 genes. *Science*, 274(5287):546, 563–7, 1996.

Goldsby, R. E., Lawrence, N. A., Hays, L. E., Olmsted, E. A., Chen, X., Singh, M., and Preston, B. D. Defective DNA polymerase-delta proofreading causes cancer susceptibility in mice. *Nat Med*, 7(6):638–9, 2001.

Goldstein, L. S. and Yang, Z. Microtubule-based transport systems in neurons: the roles of kinesins and dyneins. *Annu Rev Neurosci*, 23:39–71, 2000.

Gonczy, P., Echeverri, C., Oegema, K., Coulson, A., Jones, S. J., Copley, R. R., Duperon, J., Oegema, J., Brehm, M., Cassin, E., Hannak, E., Kirkham, M., Pichler, S., Flohrs, K., Goessen, A., Leidel, S., Alleaume, A. M., Martin, C., Ozlu, N., Bork, P., and Hyman, A. A. Functional genomic analysis of cell division in *C. elegans* using RNAi of genes on chromosome III. *Nature*, 408(6810):331–6, 2000.

Goshima, G. and Scholey, J. M. Control of mitotic spindle length. *Annu Rev Cell Dev Biol*, 26: 21–57, 2010.

Goshima, G., Wollman, R., Goodwin, S. S., Zhang, N., Scholey, J. M., Vale, R. D., and Stuurman, N. Genes Required for Mitotic Spindle Assembly in *Drosophila* S2 Cells. *Science*, 316(5823): 417–421, 2007.

Gough, A. H. and Johnston, P. A. Requirements, features, and performance of high content screening platforms. *Methods Mol Biol*, 356:41–61, 2007.

Graham, C. F. and Morgan, R. W. Changes in the cell cycle during early amphibian development. *Developmental Biology*, 14(3):439–460, 1966.

Graml, V., Studera, X., Lawson, J. L., Chessel, A., Geymonat, M., Bortfeld-Miller, M., Walter, T., Wagstaff, L., Piddini, E., and Carazo-Salas, R. E. A genomic Multiprocess survey of machineries that control and link cell shape, microtubule organization, and cell-cycle progression. *Dev Cell*, 31(2):227–39, 2014.

Graml, V. M. *An automated, 3D image-based functional genomics screen for microtubule and cell shape regulators in fission yeast*. PhD thesis, ETH, 2012.

Greber, U. F. and Way, M. A superhighway to virus infection. *Cell*, 124(4):741–54, 2006.

Gregory, S. G., Barlow, K. F., McLay, K. E., Kaul, R., Swarbreck, D., Dunham, A., Scott, C. E., Howe, K. L., Woodfine, K., Spencer, C. C., Jones, M. C., Gillson, C., Searle, S., Zhou, Y., Kokocinski, F., McDonald, L., Evans, R., Phillips, K., Atkinson, A., Cooper, R., Jones, C., Hall, R. E., Andrews, T. D., Lloyd, C., Ainscough, R., Almeida, J. P., Ambrose, K. D., Anderson, F., Andrew, R. W., Ashwell, R. I., Aubin, K., Babbage, A. K., Bagguley, C. L., Bailey, J., Beasley, H., Bethel, G., Bird, C. P., Bray-Allen, S., Brown, J. Y., Brown, A. J., Buckley, D., Burton, J., Bye, J., Carder, C., Chapman, J. C., Clark, S. Y., Clarke, G., Clee, C., Cobley, V., Collier, R. E., Corby, N., Coville, G. J., Davies, J., Deadman, R., Dunn, M., Earthrowl, M., Ellington, A. G., Errington, H., Frankish, A., Frankland, J., French, L., Garner, P., Garnett, J., Gay, L., Ghori, M. R., Gibson, R., Gilby, L. M., Gillett, W., Glithero, R. J., Grafham, D. V., Griffiths, C., Griffiths-Jones, S., Grocock, R., Hammond, S., Harrison, E. S., Hart, E., Haugen, E., Heath, P. D., Holmes, S., Holt, K., Howden, P. J., Hunt, A. R., Hunt, S. E., Hunter, G., Isherwood, J., James, R., Johnson, C., Johnson, D., Joy, A., Kay, M., Kershaw, J. K., Kibukawa, M., Kimberley, A. M., King, A., Knights, A. J., Lad, H., Laird, G., Lawlor, S., Leongamornlert, D. A., Lloyd, D. M., et al. The DNA sequence and biological annotation of human chromosome 1. *Nature*, 441(7091): 315–21, 2006.

Griffiths, A. J. F. *An introduction to genetic analysis*. W.H. Freeman, New York, 7th edition, 2000.

Gruenbaum, Y. and Aebi, U. Intermediate filaments: a dynamic network that controls cell mechanics. *F1000Prime Rep*, 6:54, 2014.

Gu, Y., Rosenblatt, J., and Morgan, D. O. Cell cycle regulation of CDK2 activity by phosphorylation of Thr160 and Tyr15. *EMBO J*, 11(11):3995–4005, 1992.

Guttinger, S., Laurell, E., and Kutay, U. Orchestrating nuclear envelope disassembly and reassembly during mitosis. *Nat Rev Mol Cell Biol*, 10(3):178–91, 2009.

Haber, J. E., Ira, G., Malkova, A., and Sugawara, N. Repairing a double-strand chromosome break by homologous recombination: revisiting Robin Holliday's model. *Philos Trans R Soc Lond B Biol Sci*, 359(1441):79–86, 2004.

Hachet, O., Bendezu, F. O., and Martin, S. G. Fission yeast: in shape to divide. *Curr Opin Cell Biol*, 24(6):858–64, 2012.

Hagan, I. and Yanagida, M. Evidence for cell cycle-specific, spindle pole body-mediated, nuclear positioning in the fission yeast *Schizosaccharomyces pombe*. *J Cell Sci*, 110 (Pt 16):1851–66, 1997.

Hagan, I. M. The fission yeast microtubule cytoskeleton. *J Cell Sci*, 111 (Pt 12):1603–12, 1998.

Haimo, L. T. and Rosenbaum, J. L. Cilia, flagella, and microtubules. *J Cell Biol*, 91(3 Pt 2): 125s–130s, 1981.

Hamada, T. Microtubule organization and microtubule-associated proteins in plant cells. *Int Rev Cell Mol Biol*, 312:1–52, 2014.

Hammond, E. M., Dorie, M. J., and Giaccia, A. J. ATR/ATM targets are phosphorylated by ATR in response to hypoxia and ATM in response to reoxygenation. *J Biol Chem*, 278(14):12207–13, 2003.

Haralick, R. M. Statistical and Structural Approaches to Texture. *Proceedings of the Ieee*, 67(5): 786–804, 1979.

Hardwick, K. G., Li, R., Mistrot, C., Chen, R. H., Dann, P., Rudner, A., and Murray, A. W. Lesions in many different spindle components activate the spindle checkpoint in the budding yeast *Saccharomyces cerevisiae*. *Genetics*, 152(2):509–18, 1999.

Harold, F. M. To shape a cell: an inquiry into the causes of morphogenesis of microorganisms. *Microbiological Reviews*, 54(4):381–431, 1990.

Harper, J. W. and Elledge, S. J. The DNA damage response: ten years after. *Mol Cell*, 28(5): 739–45, 2007.

Harris, M. A., Lock, A., Bahler, J., Oliver, S. G., and Wood, V. FYPO: the fission yeast phenotype ontology. *Bioinformatics*, 29(13):1671–8, 2013.

Hartwell, L., Hood, L., and Goldberg, M. L. *Genetics: from genes to genomes*. Granite Hill Publishers, 2008.

Hartwell, L. H., Culotti, J., and Reid, B. Genetic Control of the Cell-Division Cycle in Yeast, I. Detection of Mutants. *Proceedings of the National Academy of Sciences*, 66(2):352–359, 1970.

Hasan, A., Cotobal, C., Duncan, C. D., and Mata, J. Systematic analysis of the role of RNA-binding proteins in the regulation of RNA stability. *PLoS Genet*, 10(11):e1004684, 2014.

Hayles, J. and Nurse, P. A journey into space. *Nat Rev Mol Cell Biol*, 2(9):647–56, 2001.

Hayles, J., Wood, V., Jeffery, L., Hoe, K. L., Kim, D. U., Park, H. O., Salas-Pino, S., Heichinger, C., and Nurse, P. A genome-wide resource of cell cycle and cell shape genes of fission yeast. *Open Biol*, 3(5):130053, 2013.

Hecht, S. M. Bleomycin: new perspectives on the mechanism of action. *J Nat Prod*, 63(1):158–68, 2000.

Heffernan, T. P., Unsal-Kacmaz, K., Heinloth, A. N., Simpson, D. A., Paules, R. S., Sancar, A., Cordeiro-Stone, M., and Kaufmann, W. K. Cdc7-Dbf4 and the human S checkpoint response to UVC. *J Biol Chem*, 282(13):9458–68, 2007.

Heggeness, M. H., Simon, M., and Singer, S. J. Association of mitochondria with microtubules in cultured cells. *Proc Natl Acad Sci U S A*, 75(8):3863–6, 1978.

Hehnly, H. and Stamnes, M. Regulating cytoskeleton-based vesicle motility. *FEBS Lett*, 581(11): 2112–8, 2007.

Heim, R., Cubitt, A. B., and Tsien, R. Y. Improved green fluorescence. *Nature*, 373(6516):663–4, 1995.

Heitz, M. J., Petersen, J., Valovin, S., and Hagan, I. M. MTOC formation during mitotic exit in fission yeast. *J Cell Sci*, 114(Pt 24):4521–32, 2001.

Helbock, H. J., Beckman, K. B., Shigenaga, M. K., Walter, P. B., Woodall, A. A., Yeo, H. C., and Ames, B. N. DNA oxidation matters: the HPLC-electrochemical detection assay of 8-oxo-deoxyguanosine and 8-oxo-guanine. *Proc Natl Acad Sci U S A*, 95(1):288–93, 1998.

Helfand, B. T., Mendez, M. G., Pugh, J., Delsert, C., and Goldman, R. D. A role for intermediate filaments in determining and maintaining the shape of nerve cells. *Mol Biol Cell*, 14(12):5069–81, 2003.

Helleday, T., Eshtad, S., and Nik-Zainal, S. Mechanisms underlying mutational signatures in human cancers. *Nat Rev Genet*, 15(9):585–98, 2014.

Henderson, K. A. and Gottschling, D. E. A mother's sacrifice: what is she keeping for herself? *Curr Opin Cell Biol*, 20(6):723–8, 2008.

Hennessy, K. M. and Botstein, D. Regulation of DNA replication during the yeast cell cycle. *Cold Spring Harb Symp Quant Biol*, 56:279–84, 1991.

Herrmann, H., Bar, H., Kreplak, L., Strelkov, S. V., and Aebi, U. Intermediate filaments: from cell architecture to nanomechanics. *Nat Rev Mol Cell Biol*, 8(7):562–73, 2007.

Hieter, P. and Boguski, M. Functional genomics: it's all how you read it. *Science*, 278(5338): 601–2, 1997.

Hiltmann, P. and Lory, P. On oxygen diffusion in a spherical cell with Michaelis-Menten oxygen uptake kinetics. *Bulletin of Mathematical Biology*, 45(5):661–664, 1983.

Himes, R. H., Jordan, M. A., and Wilson, L. The effects of glutaraldehyde on the bound nucleotide content and morphology of microtubules in vitro. *Cell Biol Int Rep*, 6(7):697–704, 1982.

Hirokawa, N. Kinesin and dynein superfamily proteins and the mechanism of organelle transport. *Science*, 279(5350):519–26, 1998.

Hirokawa, N., Noda, Y., Tanaka, Y., and Niwa, S. Kinesin superfamily motor proteins and intracellular transport. *Nat Rev Mol Cell Biol*, 10(10):682–96, 2009.

Hofseth, L. J., Hussain, S. P., and Harris, C. C. p53: 25 years after its discovery. *Trends Pharmacol Sci*, 25(4):177–81, 2004.

Holthausen, J. T., Wyman, C., and Kanaar, R. Regulation of DNA strand exchange in homologous recombination. *DNA Repair (Amst)*, 9(12):1264–72, 2010.

Holy, T. E. and Leibler, S. Dynamic instability of microtubules as an efficient way to search in space. *Proc Natl Acad Sci U S A*, 91(12):5682–5, 1994.

Höög, J. L., Schwartz, C., Noon, A. T., O'Toole, E. T., Mastronarde, D. N., McIntosh, J. R., and Antony, C. Organization of Interphase Microtubules in Fission Yeast Analyzed by Electron Tomography. *Developmental Cell*, 12(3):349–361, 2007.

Hooke, R. *Micrographia, or, Some physiological descriptions of minute bodies made by magnifying glasses*. Martyn and Allestry, London, 1665.

Horn, T., Sandmann, T., Fischer, B., Axelsson, E., Huber, W., and Boutros, M. Mapping of signaling networks through synthetic genetic interaction analysis by RNAi. *Nat Methods*, 8(4):341–6, 2011.

Hosoya, N. and Miyagawa, K. Targeting DNA damage response in cancer therapy. *Cancer Sci*, 105(4):370–88, 2014.

Houtgraaf, J. H., Versmissen, J., and van der Giessen, W. J. A concise review of DNA damage checkpoints and repair in mammalian cells. *Cardiovasc Revasc Med*, 7(3):165–72, 2006.

Huang, Y. F., Chiu, L. Y., Huang, C. C., and Huang, C. K. Predicting RNA-binding residues from evolutionary information and sequence conservation. *BMC Genomics*, 11 Suppl 4:S2, 2010.

Hughes, J. R., Meireles, A. M., Fisher, K. H., Garcia, A., Antrobus, P. R., Wainman, A., Zitzmann, N., Deane, C., Ohkura, H., and Wakefield, J. G. A microtubule interactome: complexes with roles in cell cycle and mitosis. *PLoS Biol*, 6(4):e98, 2008.

Huh, W. K., Falvo, J. V., Gerke, L. C., Carroll, A. S., Howson, R. W., Weissman, J. S., and O'Shea, E. K. Global analysis of protein localization in budding yeast. *Nature*, 425(6959):686–91, 2003.

Hunt, T. Cyclins and their partners: from a simple idea to complicated reality. *Semin Cell Biol*, 2 (4):213–22, 1991.

Ip, S. C., Rass, U., Blanco, M. G., Flynn, H. R., Skehel, J. M., and West, S. C. Identification of Holliday junction resolvases from humans and yeast. *Nature*, 456(7220):357–61, 2008.

Itakura, K., Hirose, T., Crea, R., Riggs, A. D., Heyneker, H. L., Bolivar, F., and Boyer, H. W. Expression in *Escherichia coli* of a chemically synthesized gene for the hormone somatostatin. *Science*, 198(4321):1056–63, 1977.

Iwaki, T., Onishi, M., Ikeuchi, M., Kita, A., Sugiura, R., Giga-Hama, Y., Fukui, Y., and Takegawa, K. Essential roles of class E Vps proteins for sorting into multivesicular bodies in *Schizosaccharomyces pombe*. *Microbiology*, 153(Pt 8):2753–64, 2007.

Jackson, S. P. Sensing and repairing DNA double-strand breaks. *Carcinogenesis*, 23(5):687–96, 2002.

Jackson, S. P. and Bartek, J. The DNA-damage response in human biology and disease. *Nature*, 461(7267):1071–8, 2009.

Janke, C. and Bulinski, J. C. Post-translational regulation of the microtubule cytoskeleton: mechanisms and functions. *Nat Rev Mol Cell Biol*, 12(12):773–86, 2011.

Janosi, I. M., Chretien, D., and Flyvbjerg, H. Structural Microtubule Cap: Stability, Catastrophe, Rescue, andThird State. *Biophysical Journal*, 83(3):1317–1330, 2002.

Janson, M. E., Setty, T. G., Paoletti, A., and Tran, P. T. Efficient formation of bipolar microtubule bundles requires microtubule-bound gamma-tubulin complexes. *J Cell Biol*, 169(2):297–308, 2005.

Janson, M. E., Loughlin, R., Loiodice, I., Fu, C., Brunner, D., Nedelec, F. J., and Tran, P. T. Crosslinkers and motors organize dynamic microtubules to form stable bipolar arrays in fission yeast. *Cell*, 128(2):357–68, 2007.

Jeffares, D. C., Rallis, C., Rieux, A., Speed, D., Prevorovsky, M., Mourier, T., Marsellach, F. X., Iqbal, Z., Lau, W., Cheng, T. M. K., Pracana, R., Mulleder, M., Lawson, J. L. D., Chessel, A., Bala, S., Hellenthal, G., O'Fallon, B., Keane, T., Simpson, J. T., Bischof, L., Tomiczek, B., Bitton, D. A., Sideri, T., Codlin, S., Hellberg, J. E. E. U., van Trigt, L., Jeffery, L., Li, J.-J., Atkinson, S., Thodberg, M., Febrer, M., McLay, K., Drou, N., Brown, W., Hayles, J., Salas, R. E. C., Ralser, M., Maniatis, N., Balding, D. J., Balloux, F., Durbin, R., and Bahler, J. The genomic and phenotypic diversity of *Schizosaccharomyces pombe*. *Nat Genet*, advance online publication, 2015.

Jiricny, J. Postreplicative mismatch repair. *Cold Spring Harb Perspect Biol*, 5(4):a012633, 2013.

Johannsen, W. *Elemente der exakten Erblichkeitslehre*. Gustav Fischer Jena, 1909.

Jolly, A. L. and Gelfand, V. I. Cytoplasmic microtubule sliding: An unconventional function of conventional kinesin. *Commun Integr Biol*, 3(6):589–91, 2010.

Jones, P. L., Schmidhauser, C., and Bissell, M. J. Regulation of gene expression and cell function by extracellular matrix. *Crit Rev Eukaryot Gene Expr*, 3(2):137–54, 1993.

Jorgensen, E. M. and Mango, S. E. The art and design of genetic screens: *Caenorhabditis elegans*. *Nat Rev Genet*, 3(5):356–69, 2002.

Jourdain, L., Curmi, P., Sobel, A., Pantaloni, D., and Carlier, M. F. Stathmin: a tubulin-sequestering protein which forms a ternary T2S complex with two tubulin molecules. *Biochemistry*, 36(36): 10817–21, 1997.

Jung, D. and Alt, F. W. Unraveling V(D)J recombination; insights into gene regulation. *Cell*, 116 (2):299–311, 2004.

Kafri, R., Levy, J., Ginzberg, M. B., Oh, S., Lahav, G., and Kirschner, M. W. Dynamics extracted from fixed cells reveal feedback linking cell growth to cell cycle. *Nature*, 494(7438):480–3, 2013.

Kalocsay, M., Hiller, N. J., and Jentsch, S. Chromosome-wide Rad51 spreading and SUMO-H2A.Z-dependent chromosome fixation in response to a persistent DNA double-strand break. *Mol Cell*, 33(3):335–43, 2009.

Kamileri, I., Karakasilioti, I., and Garinis, G. A. Nucleotide excision repair: new tricks with old bricks. *Trends Genet*, 28(11):566–73, 2012.

Kanoh, J., Francesconi, S., Collura, A., Schramke, V., Ishikawa, F., Baldacci, G., and Geli, V. The fission yeast spSet1p is a histone H3-K4 methyltransferase that functions in telomere maintenance and DNA repair in an ATM kinase Rad3-dependent pathway. *J Mol Biol*, 326(4):1081–94, 2003.

Kastan, M. B. and Bartek, J. Cell-cycle checkpoints and cancer. *Nature*, 432(7015):316–23, 2004.

Katsuki, M., Drummond, D. R., Osei, M., and Cross, R. A. Mal3 Masks Catastrophe Events in *Schizosaccharomyces pombe* Microtubules by Inhibiting Shrinkage and Promoting Rescue. *Journal of Biological Chemistry*, 284(43):29246–29250, 2009.

Kelly, D. E., Lamb, D. C., and Kelly, S. L. Genome-wide generation of yeast gene deletion strains. *Comp Funct Genomics*, 2(4):236–42, 2001.

Kelly, F. D. and Nurse, P. Spatial control of Cdc42 activation determines cell width in fission yeast. *Mol Biol Cell*, 22(20):3801–11, 2011.

Khanna, K. K. and Jackson, S. P. DNA double-strand breaks: signaling, repair and the cancer connection. *Nat Genet*, 27(3):247–54, 2001.

Khorana, H. G., Agarwal, K. L., Buchi, H., Caruthers, M. H., Gupta, N. K., Kleppe, K., Kumar, A., Otsuka, E., RajBhandary, U. L., Van de Sande, J. H., Sgaramella, V., Terao, T., Weber, H., and Yamada, T. Studies on polynucleotides. 103. Total synthesis of the structural gene for an alanine transfer ribonucleic acid from yeast. *J Mol Biol*, 72(2):209–17, 1972.

Khotanzad, A. and Hong, Y. H. Invariant Image Recognition by Zernike Moments. *Ieee Transactions on Pattern Analysis and Machine Intelligence*, 12(5):489–497, 1990.

Kikkawa, M., Ishikawa, T., Nakata, T., Wakabayashi, T., and Hirokawa, N. Direct visualization of the microtubule lattice seam both in vitro and in vivo. *J Cell Biol*, 127(6 Pt 2):1965–71, 1994.

Kim, D.-U., Hayles, J., Kim, D., Wood, V., Park, H.-O., Won, M., Yoo, H.-S., Duhig, T., Nam, M., Palmer, G., Han, S., Jeffery, L., Baek, S.-T., Lee, H., Shim, Y. S., Lee, M., Kim, L., Heo, K.-S., Noh, E. J., Lee, A.-R., Jang, Y.-J., Chung, K.-S., Choi, S.-J., Park, J.-Y., Park, Y., Kim, H. M., Park, S.-K., Park, H.-J., Kang, E.-J., Kim, H. B., Kang, H.-S., Park, H.-M., Kim, K., Song, K., Song, K. B., Nurse, P., and Hoe, K.-L. Analysis of a genome-wide set of gene deletions in the fission yeast *Schizosaccharomyces pombe*. *Nat Biotech*, 28(6):617–623, 2010.

Kim, S. T., Lim, D. S., Canman, C. E., and Kastan, M. B. Substrate specificities and identification of putative substrates of ATM kinase family members. *J Biol Chem*, 274(53):37538–43, 1999.

King, S. M. The dynein microtubule motor. *Biochim Biophys Acta*, 1496(1):60–75, 2000.

Kirkwood, T. B. Understanding the odd science of aging. *Cell*, 120(4):437–47, 2005.

Kirkwood, T. B. and Austad, S. N. Why do we age? *Nature*, 408(6809):233–8, 2000.

Kirschner, M. and Mitchison, T. Beyond self-assembly: from microtubules to morphogenesis. *Cell*, 45(3):329–42, 1986a.

Kirschner, M. W. and Mitchison, T. Microtubule dynamics. *Nature*, 324(6098):621, 1986b.

Kirschner, M. W., Williams, R. C., Weingart.M, and Gerhart, J. C. Microtubules from Mammalian Brain - Some Properties of Their Depolymerization Products and a Proposed Mechanism of Assembly and Disassembly. *Proceedings of the National Academy of Sciences of the United States of America*, 71(4):1159–1163, 1974.

Kline-Smith, S. L. and Walczak, C. E. Mitotic spindle assembly and chromosome segregation: refocusing on microtubule dynamics. *Mol Cell*, 15(3):317–27, 2004.

Knust, E. Control of epithelial cell shape and polarity. *Curr Opin Genet Dev*, 10(5):471–5, 2000.

Knust, E. Regulation of epithelial cell shape and polarity by cell-cell adhesion (Review). *Mol Membr Biol*, 19(2):113–20, 2002.

Koch, A. L. What size should a bacterium be? A question of scale. *Annu Rev Microbiol*, 50: 317–48, 1996.

Koepp, D. M., Harper, J. W., and Elledge, S. J. How the cyclin became a cyclin: regulated proteolysis in the cell cycle. *Cell*, 97(4):431–4, 1999.

Kokkoris, K., Gallo Castro, D., and Martin, S. G. The Tea4-PP1 landmark promotes local growth by dual Cdc42 GEF recruitment and GAP exclusion. *J Cell Sci*, 127(Pt 9):2005–16, 2014.

Kozubek, S., Lukasova, E., Amrichova, J., Kozubek, M., Liskova, A., and Slotova, J. Influence of cell fixation on chromatin topography. *Anal Biochem*, 282(1):29–38, 2000.

Krausz, E. High-content siRNA screening. *Mol Biosyst*, 3(4):232–40, 2007.

Krausz, E. and Korn, K. High-content siRNA screening for target identification and validation. *Expert Opin Drug Discov*, 3(5):551–64, 2008.

Kume, K., Koyano, T., Kanai, M., Toda, T., and Hirata, D. Calcineurin ensures a link between the DNA replication checkpoint and microtubule-dependent polarized growth. *Nat Cell Biol*, 13(3): 234–42, 2011.

Kunkel, T. A. and Soni, A. Exonucleolytic proofreading enhances the fidelity of DNA synthesis by chick embryo DNA polymerase-gamma. *J Biol Chem*, 263(9):4450–9, 1988.

Kunkel, T. A., Sabatino, R. D., and Bambara, R. A. Exonucleolytic proofreading by calf thymus DNA polymerase delta. *Proc Natl Acad Sci U S A*, 84(14):4865–9, 1987.

Lamarche, B. J., Orazio, N. I., and Weitzman, M. D. The MRN complex in double-strand break repair and telomere maintenance. *FEBS Lett*, 584(17):3682–95, 2010.

Lancaster, O. M., Le Berre, M., Dimitracopoulos, A., Bonazzi, D., Zlotek-Zlotkiewicz, E., Picone, R., Duke, T., Piel, M., and Baum, B. Mitotic rounding alters cell geometry to ensure efficient bipolar spindle formation. *Dev Cell*, 25(3):270–83, 2013.

Lander, E. S., Linton, L. M., Birren, B., Nusbaum, C., Zody, M. C., Baldwin, J., Devon, K., Dewar, K., Doyle, M., FitzHugh, W., Funke, R., Gage, D., Harris, K., Heaford, A., Howland, J., Kann, L., Lehoczky, J., LeVine, R., McEwan, P., McKernan, K., Meldrim, J., Mesirov, J. P., Miranda, C., Morris, W., Naylor, J., Raymond, C., Rosetti, M., Santos, R., Sheridan, A., Sougnez, C., Stange-Thomann, N., Stojanovic, N., Subramanian, A., Wyman, D., Rogers, J., Sulston, J., Ainscough, R., Beck, S., Bentley, D., Burton, J., Clee, C., Carter, N., Coulson, A., Deadman, R., Deloukas, P., Dunham, A., Dunham, I., Durbin, R., French, L., Grafham, D., Gregory, S., Hubbard, T., Humphray, S., Hunt, A., Jones, M., Lloyd, C., McMurray, A., Matthews, L., Mercer, S., Milne, S., Mullikin, J. C., Mungall, A., Plumb, R., Ross, M., Shownkeen, R., Sims, S., Waterston, R. H., Wilson, R. K., Hillier, L. W., McPherson, J. D., Marra, M. A., Mardis, E. R., Fulton, L. A., Chinwalla, A. T., Pepin, K. H., Gish, W. R., Chissoe, S. L., Wendl, M. C., Delehaunty, K. D., Miner, T. L., Delehaunty, A., Kramer, J. B., Cook, L. L., Fulton, R. S., Johnson, D. L., Minx, P. J., Clifton, S. W., Hawkins, T., Branscomb, E., Predki, P., Richardson, P., Wenning, S., Slezak, T., Doggett, N., Cheng, J. F., Olsen, A., Lucas, S., Elkin, C., Uberbacher, E., Frazier, M., et al. Initial sequencing and analysis of the human genome. *Nature*, 409(6822):860–921, 2001.

Langerak, P. and Russell, P. Regulatory networks integrating cell cycle control with DNA damage checkpoints and double-strand break repair. *Philos Trans R Soc Lond B Biol Sci*, 366(1584): 3562–71, 2011.

Lara-Gonzalez, P., Westhorpe, F. G., and Taylor, S. S. The spindle assembly checkpoint. *Curr Biol*, 22(22):R966–80, 2012.

Larrieu, D., Britton, S., Demir, M., Rodriguez, R., and Jackson, S. P. Chemical inhibition of NAT10 corrects defects of laminopathic cells. *Science*, 344(6183):527–32, 2014.

Laufer, C., Fischer, B., Billmann, M., Huber, W., and Boutros, M. Mapping genetic interactions in human cancer cells with RNAi and multiparametric phenotyping. *Nat Methods*, 10(5):427–31, 2013.

Lawson, J. L. and Carazo Salas, R. E. Microtubules: greater than the sum of the parts. *Biochem Soc Trans*, 41(6):1736–44, 2013.

Lawson, J. L. D. Pombe polarity: Identifying novel elements of microtubule organisation in fission yeast *Schizosaccharomyces pombe*. Master's thesis, University of Cambridge, 2011.

Lecuit, T. and Lenne, P. F. Cell surface mechanics and the control of cell shape, tissue patterns and morphogenesis. *Nature Reviews Molecular Cell Biology*, 8(8):633–644, 2007.

Lederberg, J. The transformation of genetics by DNA: an anniversary celebration of Avery, MacLeod and McCarty (1944). *Genetics*, 136(2):423–6, 1994.

Leduc, C. and Etienne-Manneville, S. Intermediate filaments in cell migration and invasion: the unusual suspects. *Curr Opin Cell Biol*, 32C:102–112, 2015.

Lee, H., Jeon, J., Ryu, Y. S., Jeong, J. E., Shin, S., Zhang, T., Kang, S. W., Hong, J. H., and Hur, G. M. Disruption of microtubules sensitizes the DNA damage-induced apoptosis through inhibiting nuclear factor kappaB (NF-kappaB) DNA-binding activity. *J Korean Med Sci*, 25(11): 1574–81, 2010.

Lee, K. J., Lin, Y. F., Chou, H. Y., Yajima, H., Fattah, K. R., Lee, S. C., and Chen, B. P. Involvement of DNA-dependent protein kinase in normal cell cycle progression through mitosis. *J Biol Chem*, 286(14):12796–802, 2011.

Lee, L., Tirnauer, J. S., Li, J., Schuyler, S. C., Liu, J. Y., and Pellman, D. Positioning of the mitotic spindle by a cortical-microtubule capture mechanism. *Science*, 287(5461):2260–2, 2000.

Lei, K., Zhu, X., Xu, R., Shao, C., Xu, T., Zhuang, Y., and Han, M. Inner nuclear envelope proteins SUN1 and SUN2 play a prominent role in the DNA damage response. *Curr Biol*, 22(17):1609–15, 2012.

Leptin, M. Morphogenesis. Control of epithelial cell shape changes. *Curr Biol*, 4(8):709–12, 1994.

Leuwenhoek, A. Observations upon the Callus of the Hands and Feet, by the Same Curious Gentleman. Translated by John Chamberlayne, Esq. *Philosophical Transactions*, 32(370-380): 156–161, 1722.

Leuwenhoek, A. V. An Extract of a Letter from Mr. Anth. Van Leuwenhoek, concerning Animalcules Found on the Teeth; Of the Scaleyness of the Skin. *Philosophical Transactions*, 17 (192-206):646–649, 1693.

Lewis, S. A., Tian, G., Vainberg, I. E., and Cowan, N. J. Chaperonin-mediated folding of actin and tubulin. *J Cell Biol*, 132(1-2):1–4, 1996.

Li, F., Long, T., Lu, Y., Ouyang, Q., and Tang, C. The yeast cell-cycle network is robustly designed. *Proc Natl Acad Sci U S A*, 101(14):4781–6, 2004.

Li, X. and Heyer, W. D. Homologous recombination in DNA repair and DNA damage tolerance. *Cell Res*, 18(1):99–113, 2008.

Liang, F., Han, M., Romanienko, P. J., and Jasin, M. Homology-directed repair is a major double-strand break repair pathway in mammalian cells. *Proc Natl Acad Sci U S A*, 95(9):5172–7, 1998.

Liang, P. and MacRae, T. H. Molecular chaperones and the cytoskeleton. *J Cell Sci*, 110 (Pt 13): 1431–40, 1997.

Lieber, M. R. The mechanism of double-strand DNA break repair by the nonhomologous DNA end-joining pathway. *Annu Rev Biochem*, 79:181–211, 2010.

Limbo, O., Chahwan, C., Yamada, Y., de Bruin, R. A., Wittenberg, C., and Russell, P. Ctp1 is a cell-cycle-regulated protein that functions with Mre11 complex to control double-strand break repair by homologous recombination. *Mol Cell*, 28(1):134–46, 2007.

Limbo, O., Porter-Goff, M. E., Rhind, N., and Russell, P. Mre11 nuclease activity and Ctp1 regulate Chk1 activation by Rad3ATR and Tel1ATM checkpoint kinases at double-strand breaks. *Mol Cell Biol*, 31(3):573–83, 2011.

Lin, D., Shields, M. T., Ullrich, S. J., Appella, E., and Mercer, W. E. Growth arrest induced by wild-type p53 protein blocks cells prior to or near the restriction point in late G1 phase. *Proc Natl Acad Sci U S A*, 89(19):9210–4, 1992.

Lisby, M., Barlow, J. H., Burgess, R. C., and Rothstein, R. Choreography of the DNA damage response: spatiotemporal relationships among checkpoint and repair proteins. *Cell*, 118(6): 699–713, 2004.

Liska, A. J., Popov, A. V., Sunyaev, S., Coughlin, P., Habermann, B., Shevchenko, A., Bork, P., and Karsenti, E. Homology-based functional proteomics by mass spectrometry: application to the *Xenopus* microtubule-associated proteome. *PROTEOMICS*, 4(9):2707–21, 2004.

Liu, Z., Persson, S., and Zhang, Y. The connection of cytoskeletal network with plasma membrane and the cell wall. *J Integr Plant Biol*, 57(4):330–40, 2015.

Lobrich, M. and Jeggo, P. A. The impact of a negligent G2/M checkpoint on genomic instability and cancer induction. *Nat Rev Cancer*, 7(11):861–9, 2007.

Lodish, H. F. *Molecular cell biology*. W.H. Freeman, New York, 6th edition, 2008.

Loiodice, I., Staub, J., Setty, T. G., Nguyen, N. P., Paoletti, A., and Tran, P. T. Ase1p organizes antiparallel microtubule arrays during interphase and mitosis in fission yeast. *Mol Biol Cell*, 16 (4):1756–68, 2005.

Longhese, M. P., Bonetti, D., Guerini, I., Manfrini, N., and Clerici, M. DNA double-strand breaks in meiosis: checking their formation, processing and repair. *DNA Repair (Amst)*, 8(9):1127–38, 2009.

Lord, C. J. and Ashworth, A. The DNA damage response and cancer therapy. *Nature*, 481(7381): 287–94, 2012.

Lu, M. S. and Johnston, C. A. Molecular pathways regulating mitotic spindle orientation in animal cells. *Development*, 140(9):1843–56, 2013.

Luders, J. and Stearns, T. Microtubule-organizing centres: a re-evaluation. *Nat Rev Mol Cell Biol*, 8(2):161–7, 2007.

Lukas, J., Lukas, C., and Bartek, J. Mammalian cell cycle checkpoints: signalling pathways and their organization in space and time. *DNA Repair (Amst)*, 3(8-9):997–1007, 2004.

Luo, L. Actin cytoskeleton regulation in neuronal morphogenesis and structural plasticity. *Annu Rev Cell Dev Biol*, 18:601–35, 2002.

Lydall, D. and Weinert, T. Yeast checkpoint genes in DNA damage processing: implications for repair and arrest. *Science*, 270(5241):1488–91, 1995.

Lynch, E. M., Groocock, L. M., Borek, W. E., and Sawin, K. E. Activation of the gamma-tubulin complex by the Mto1/2 complex. *Curr Biol*, 24(8):896–903, 2014.

Mack, G. J. and Compton, D. A. Analysis of mitotic microtubule-associated proteins using mass spectrometry identifies astrin, a spindle-associated protein. *Proc Natl Acad Sci U S A*, 98(25): 14434–9, 2001.

Mandelkow, E. and Mandelkow, E. M. Microtubules and microtubule-associated proteins. *Curr Opin Cell Biol*, 7(1):72–81, 1995.

Mardis, E. R. The impact of next-generation sequencing technology on genetics. *Trends Genet*, 24(3):133–41, 2008.

Martin, S. G. and Berthelot-Grosjean, M. Polar gradients of the DYRK-family kinase Pom1 couple cell length with the cell cycle. *Nature*, 459(7248):852–6, 2009.

Martin, S. G., McDonald, W. H., Yates, J. R., and Chang, F. Tea4p links microtubule plus ends with the formin for3p in the establishment of cell polarity. *Dev Cell*, 8(4):479–91, 2005.

Masui, Y. and Wang, P. Cell cycle transition in early embryonic development of *Xenopus laevis*. *Biol Cell*, 90(8):537–48, 1998.

Mata, J. and Nurse, P. *tea1* and the microtubular cytoskeleton are important for generating global spatial order within the fission yeast cell. *Cell*, 89(6):939–49, 1997.

Matsuoka, S., Ballif, B. A., Smogorzewska, A., McDonald, r., E. R., Hurov, K. E., Luo, J., Bakalarski, C. E., Zhao, Z., Solimini, N., Lerenthal, Y., Shiloh, Y., Gygi, S. P., and Elledge, S. J. ATM and ATR substrate analysis reveals extensive protein networks responsive to DNA damage. *Science*, 316(5828):1160–6, 2007.

Matsuyama, A., Arai, R., Yashiroda, Y., Shirai, A., Kamata, A., Sekido, S., Kobayashi, Y., Hashimoto, A., Hamamoto, M., Hiraoka, Y., Horinouchi, S., and Yoshida, M. ORFeome cloning and global analysis of protein localization in the fission yeast *Schizosaccharomyces pombe*. *Nat Biotechnol*, 24(7):841–7, 2006.

Matter, K. and Mellman, I. Mechanisms of cell polarity: sorting and transport in epithelial cells. *Curr Opin Cell Biol*, 6(4):545–54, 1994.

Matthiesen, R. Methods, algorithms and tools in computational proteomics: A practical point of view. *Proteomics*, 7(16):2815–2832, 2007.

McDaniel, D. P. and Roberson, R. W. Microtubules Are required for motility and positioning of vesicles and mitochondria in hyphal tip cells of Allomyces macrogynus. *Fungal Genet Biol*, 31 (3):233–44, 2000.

McDowall, M. D., Harris, M. A., Lock, A., Rutherford, K., Staines, D. M., Bahler, J., Kersey, P. J., Oliver, S. G., and Wood, V. PomBase 2015: updates to the fission yeast database. *Nucleic Acids Res*, 43(Database issue):D656–61, 2015.

McVey, M. and Lee, S. E. MMEJ repair of double-strand breaks (director's cut): deleted sequences and alternative endings. *Trends Genet*, 24(11):529–38, 2008.

Meischner, F. *Letter I; to Wilhelm His; Tübingen, February 26th, 1869*, volume 1F of *Die Histochemischen und Physiologischen Arbeiten von Friedrich Miesncher-Aus dem wissenschaftlichen Briefwechsel von F. Miescher*. C. W. Vogel, Leipzig, 1869.

Melan, M. *Overview of Cell Fixation and Permeabilization*, volume 34 of *Methods in Molecular Bilogy*, chapter 8, pages 55–66. Humana Press, 1995.

Melki, R., Vainberg, I. E., Chow, R. L., and Cowan, N. J. Chaperonin-mediated folding of vertebrate actin-related protein and gamma-tubulin. *J Cell Biol*, 122(6):1301–10, 1993.

Mendel, G. Experiments in plant hybridization (1865). *Verhandlungen des naturforschenden Vereins Brünn.) Available online: www. mendelweb. org/Mendel. html*, 1865.

Mercer, J., Snijder, B., Sacher, R., Burkard, C., Bleck, C. K., Stahlberg, H., Pelkmans, L., and Helenius, A. RNAi screening reveals proteasome- and Cullin3-dependent stages in vaccinia virus infection. *Cell Rep*, 2(4):1036–47, 2012.

Metzker, M. L. Sequencing technologies - the next generation. *Nat Rev Genet*, 11(1):31–46, 2010.

Meyer, F. Topographic Distance and Watershed Lines. *Signal Processing*, 38(1):113–125, 1994.

Mitchison, J. M. Growth during the cell cycle. *Int Rev Cytol*, 226:165–258, 2003.

Mitchison, J. M. and Nurse, P. Growth in cell length in the fission yeast *Schizosaccharomyces pombe*. *J Cell Sci*, 75:357–76, 1985.

Mitchison, T. and Kirschner, M. Dynamic instability of microtubule growth. *Nature*, 312(5991): 237–42, 1984a.

Mitchison, T. and Kirschner, M. Microtubule assembly nucleated by isolated centrosomes. *Nature*, 312(5991):232–7, 1984b.

Mitchison, T. J. Localization of an exchangeable GTP binding site at the plus end of microtubules. *Science*, 261(5124):1044–7, 1993.

Moseley, J. B., Mayeux, A., Paoletti, A., and Nurse, P. A spatial gradient coordinates cell size and mitotic entry in fission yeast. *Nature*, 459(7248):857–60, 2009.

Mott, J. D. and Werb, Z. Regulation of matrix biology by matrix metalloproteinases. *Curr Opin Cell Biol*, 16(5):558–64, 2004.

Munck, L., Pram Nielsen, J., Moller, B., Jacobsen, S., Sondergaard, I., Engelsen, S. B., Norgaard, L., and Bro, R. Exploring the phenotypic expression of a regulatory proteome-altering gene by spectroscopy and chemometrics. *Analytica Chimica Acta*, 446(1-2):169–184, 2001.

Mundt, K. E., Liu, C., and Carr, A. M. Deletion mutants in COP9/signalosome subunits in fission yeast *Schizosaccharomyces pombe* display distinct phenotypes. *Mol Biol Cell*, 13(2):493–502, 2002.

Murphy, M. P. Modulating mitochondrial intracellular location as a redox signal. *Sci Signal*, 5(242): pe39, 2012.

Musch, A. Microtubule organization and function in epithelial cells. *Traffic*, 5(1):1–9, 2004.

Nakamura, J. and Swenberg, J. A. Endogenous apurinic/apyrimidinic sites in genomic DNA of mammalian tissues. *Cancer Res*, 59(11):2522–6, 1999.

Nakamura, M. Microtubule nucleating and severing enzymes for modifying microtubule array organization and cell morphogenesis in response to environmental cues. *New Phytol*, 205(3): 1022–7, 2015.

Nakamura, T. M., Du, L. L., Redon, C., and Russell, P. Histone H2A phosphorylation controls Crb2 recruitment at DNA breaks, maintains checkpoint arrest, and influences DNA repair in fission yeast. *Mol Cell Biol*, 24(14):6215–30, 2004.

Nakayama, K. I. and Nakayama, K. Regulation of the cell cycle by SCF-type ubiquitin ligases. *Semin Cell Dev Biol*, 16(3):323–33, 2005.

Nelson, W. J. Cytoskeleton functions in membrane traffic in polarized epithelial cells. *Semin Cell Biol*, 2(6):375–85, 1991.

Nelson, W. J. Adaptation of core mechanisms to generate cell polarity. *Nature*, 422(6933):766–74, 2003.

Nelson, W. J., Hammerton, R. W., Wang, A. Z., and Shore, E. M. Involvement of the membrane-cytoskeleton in development of epithelial cell polarity. *Semin Cell Biol*, 1(5):359–71, 1990.

Neumann, B., Held, M., Liebel, U., Erfle, H., Rogers, P., Pepperkok, R., and Ellenberg, J. High-throughput RNAi screening by time-lapse imaging of live human cells. *Nat Methods*, 3(5): 385–90, 2006.

Neumann, B., Walter, T., Heriche, J. K., Bulkescher, J., Erfle, H., Conrad, C., Rogers, P., Poser, I., Held, M., Liebel, U., Cetin, C., Sieckmann, F., Pau, G., Kabbe, R., Wunsche, A., Satagopam,

V., Schmitz, M. H., Chapuis, C., Gerlich, D. W., Schneider, R., Eils, R., Huber, W., Peters, J. M., Hyman, A. A., Durbin, R., Pepperkok, R., and Ellenberg, J. Phenotypic profiling of the human genome by time-lapse microscopy reveals cell division genes. *Nature*, 464(7289):721–7, 2010.

Niccoli, T., Arellano, M., and Nurse, P. Role of Tea1p, Tea3p and Pom1p in the determination of cell ends in *Schizosaccharomyces pombe*. *Yeast*, 20(16):1349–58, 2003.

Niehl, A., Pena, E. J., Amari, K., and Heinlein, M. Microtubules in viral replication and transport. *Plant J*, 75(2):290–308, 2013.

Noatynska, A., Tavernier, N., Gotta, M., and Pintard, L. Coordinating cell polarity and cell cycle progression: what can we learn from flies and worms? *Open Biol*, 3(8):130083, 2013.

Nogales, E. Structural insights into microtubule function. *Annu Rev Biochem*, 69:277–302, 2000.

Nogales, E., Downing, K. H., Amos, L. A., and Lowe, J. Tubulin and FtsZ form a distinct family of GTPases. *Nat Struct Biol*, 5(6):451–8, 1998.

Noma, K. and Grewal, S. I. Histone H3 lysine 4 methylation is mediated by Set1 and promotes maintenance of active chromatin states in fission yeast. *Proc Natl Acad Sci U S A*, 99 Suppl 4: 16438–45, 2002.

Norbury, C. and Nurse, P. Animal cell cycles and their control. *Annu Rev Biochem*, 61:441–70, 1992.

Nowsheen, S. and Yang, E. S. The intersection between DNA damage response and cell death pathways. *Exp Oncol*, 34(3):243–54, 2012.

Nurse, P. Genetic-Control of Cell-Size at Cell-Division in Yeast. *Nature*, 256(5518):547–551, 1975.

Nurse, P. and Thuriaux, P. Regulatory genes controlling mitosis in the fission yeast *Schizosaccharomyces pombe*. *Genetics*, 96(3):627–37, 1980.

Obaya, A. J. and Sedivy, J. M. Regulation of cyclin-Cdk activity in mammalian cells. *Cell Mol Life Sci*, 59(1):126–42, 2002.

Ochi, T., Blackford, A. N., Coates, J., Jhujh, S., Mehmood, S., Tamura, N., Travers, J., Wu, Q., Draviam, V. M., Robinson, C. V., Blundell, T. L., and Jackson, S. P. DNA repair. PAXX, a paralog of XRCC4 and XLF, interacts with Ku to promote DNA double-strand break repair. *Science*, 347 (6218):185–8, 2015.

O'Connell, C. B. and Wang, Y. L. Mammalian spindle orientation and position respond to changes in cell shape in a dynein-dependent fashion. *Mol Biol Cell*, 11(5):1765–74, 2000.

Oheim, M. Advances and challenges in high-throughput microscopy for live-cell subcellular imaging. *Expert Opin Drug Discov*, 6(12):1299–315, 2011.

Ohkura, H., Adachi, Y., Kinoshita, N., Niwa, O., Toda, T., and Yanagida, M. Cold-sensitive and caffeine-supersensitive mutants of the *Schizosaccharomyces pombe* dis genes implicated in sister chromatid separation during mitosis. *EMBO J*, 7(5):1465–73, 1988.

Olmsted, J. B. and Borisy, G. G. Microtubules. *Annu Rev Biochem*, 42:507–40, 1973.

O'Neill, T., Dwyer, A. J., Ziv, Y., Chan, D. W., Lees-Miller, S. P., Abraham, R. H., Lai, J. H., Hill, D., Shiloh, Y., Cantley, L. C., and Rathbun, G. A. Utilization of oriented peptide libraries to identify substrate motifs selected by ATM. *J Biol Chem*, 275(30):22719–27, 2000.

Oppenheimer, D. G. Genetics of plant cell shape. *Curr Opin Plant Biol*, 1(6):520–4, 1998.

Oza, P., Jaspersen, S. L., Miele, A., Dekker, J., and Peterson, C. L. Mechanisms that regulate localization of a DNA double-strand break to the nuclear periphery. *Genes Dev*, 23(8):912–27, 2009.

Paluch, E. and Heisenberg, C. P. Biology and physics of cell shape changes in development. *Curr Biol*, 19(17):R790–9, 2009.

Panbianco, C. and Gotta, M. Coordinating cell polarity with cell division in space and time. *Trends Cell Biol*, 21(11):672–80, 2011.

Pardo, M. and Nurse, P. The nuclear rim protein Amo1 is required for proper microtubule cytoskeleton organisation in fission yeast. *J Cell Sci*, 118(Pt 8):1705–14, 2005.

Parker, A. E., Clyne, R. K., Carr, A. M., and Kelly, T. J. The *Schizosaccharomyces pombe rad11+* gene encodes the large subunit of replication protein A. *Mol Cell Biol*, 17(5):2381–90, 1997.

Patel, M. R. and Shen, K. Neurite extension: starting at the finish line. *Cell*, 137(2):207–9, 2009.

Pearce, A. K. and Humphrey, T. C. Integrating stress-response and cell-cycle checkpoint pathways. *Trends Cell Biol*, 11(10):426–33, 2001.

Pearson, C. G. and Bloom, K. Dynamic microtubules lead the way for spindle positioning. *Nat Rev Mol Cell Biol*, 5(6):481–92, 2004.

Pelkmans, L., Fava, E., Grabner, H., Hannus, M., Habermann, B., Krausz, E., and Zerial, M. Genome-wide analysis of human kinases in clathrin- and caveolae/raft-mediated endocytosis. *Nature*, 436(7047):78–86, 2005.

Pennacchio, L. A., Bickmore, W., Dean, A., Nobrega, M. A., and Bejerano, G. Enhancers: five essential questions. *Nat Rev Genet*, 14(4):288–95, 2013.

Pepperkok, R. and Ellenberg, J. High-throughput fluorescence microscopy for systems biology. *Nat Rev Mol Cell Biol*, 7(9):690–6, 2006.

Pereira, G. and Schiebel, E. Centrosome-microtubule nucleation. *J Cell Sci*, 110 (Pt 3):295–300, 1997.

Perlman, Z. E., Slack, M. D., Feng, Y., Mitchison, T. J., Wu, L. F., and Altschuler, S. J. Multidimensional drug profiling by automated microscopy. *Science*, 306(5699):1194–8, 2004.

Pidoux, A. L., LeDizet, M., and Cande, W. Z. Fission yeast *pkl1* is a kinesin-related protein involved in mitotic spindle function. *Mol Biol Cell*, 7(10):1639–55, 1996.

Piel, M. and Tran, P. T. Cell shape and cell division in fission yeast. *Curr Biol*, 19(17):R823–7, 2009.

Pilizota, T. and Shaevitz, J. Origins of *Escherichia coli* growth rate and cell shape changes at high external osmolality. *New Biotechnology*, 31:S46–S46, 2014.

Pines, J. Cyclins and cyclin-dependent kinases: take your partners. *Trends Biochem Sci*, 18(6): 195–7, 1993.

Pinsky, B. A. and Biggins, S. The spindle checkpoint: tension versus attachment. *Trends Cell Biol*, 15(9):486–93, 2005.

Pollard, T. D. and Cooper, J. A. Actin, a central player in cell shape and movement. *Science*, 326 (5957):1208–12, 2009.

Pon, L. A. Organelle transport: mitochondria hitch a ride on dynamic microtubules. *Curr Biol*, 21 (17):R654–6, 2011.

Powell, C. D., Van Zandycke, S. M., Quain, D. E., and Smart, K. A. Replicative ageing and senescence in *Saccharomyces cerevisiae* and the impact on brewing fermentations. *Microbiology*, 146 (Pt 5):1023–34, 2000.

Prendergast, F. G. and Mann, K. G. Chemical and physical properties of aequorin and the green fluorescent protein isolated from Aequorea forskalea. *Biochemistry*, 17(17):3448–53, 1978.

Pruyne, D. and Bretscher, A. Polarization of cell growth in yeast. *J Cell Sci*, 113 (Pt 4):571–85, 2000.

Pugacheva, E. N., Roegiers, F., and Golemis, E. A. Interdependence of cell attachment and cell cycle signaling. *Curr Opin Cell Biol*, 18(5):507–15, 2006.

Quarmby, L. Cellular Samurai: katanin and the severing of microtubules. *J Cell Sci*, 113 (Pt 16): 2821–7, 2000.

Ragkousi, K. and Gibson, M. C. Cell division and the maintenance of epithelial order. *J Cell Biol*, 207(2):181–8, 2014.

Raleigh, J. M. and O'Connell, M. J. The G(2) DNA damage checkpoint targets both Wee1 and Cdc25. *J Cell Sci*, 113 (Pt 10):1727–36, 2000.

Rass, U., Ahel, I., and West, S. C. Defective DNA repair and neurodegenerative disease. *Cell*, 130(6):991–1004, 2007.

Rauch, A., Bellew, M., Eng, J., Fitzgibbon, M., Holzman, T., Hussey, P., Igra, M., Maclean, B., Lin, C. W., Detter, A., Fang, R., Faca, V., Gafken, P., Zhang, H., Whiteaker, J., States, D., Hanash, S., Paulovich, A., and McIntosh, M. W. Computational Proteomics Analysis System (CPAS): an extensible, open-source analytic system for evaluating and publishing proteomic data and high throughput biological experiments. *J Proteome Res*, 5(1):112–21, 2006.

Rhind, N. and Russell, P. Chk1 and Cds1: linchpins of the DNA damage and replication checkpoint pathways. *J Cell Sci*, 113 (Pt 22):3889–96, 2000.

Richter, C., Park, J. W., and Ames, B. N. Normal oxidative damage to mitochondrial and nuclear DNA is extensive. *Proc Natl Acad Sci U S A*, 85(17):6465–7, 1988.

Rogakou, E. P., Pilch, D. R., Orr, A. H., Ivanova, V. S., and Bonner, W. M. DNA double-stranded breaks induce histone H2AX phosphorylation on serine 139. *J Biol Chem*, 273(10):5858–68, 1998.

Roguev, A., Wiren, M., Weissman, J. S., and Krogan, N. J. High-throughput genetic interaction mapping in the fission yeast *Schizosaccharomyces pombe*. *Nat Methods*, 4(10):861–6, 2007.

Rohn, J. L., Sims, D., Liu, T., Fedorova, M., Schock, F., Dopie, J., Vartiainen, M. K., Kiger, A. A., Perrimon, N., and Baum, B. Comparative RNAi screening identifies a conserved core metazoan actinome by phenotype. *J Cell Biol*, 194(5):789–805, 2011.

Roll-Mecak, A. and Vale, R. D. Making more microtubules by severing: a common theme of noncentrosomal microtubule arrays? *J Cell Biol*, 175(6):849–51, 2006.

Roll-Mecak, A. and McNally, F. J. Microtubule-severing enzymes. *Current Opinion in Cell Biology*, 22(1):96–103, 2010.

Roohvand, F., Maillard, P., Lavergne, J. P., Boulant, S., Walic, M., Andreo, U., Goueslain, L., Helle, F., Mallet, A., McLauchlan, J., and Budkowska, A. Initiation of hepatitis C virus infection requires the dynamic microtubule network: role of the viral nucleocapsid protein. *J Biol Chem*, 284(20):13778–91, 2009.

Roos, W. P. and Kaina, B. DNA damage-induced cell death: from specific DNA lesions to the DNA damage response and apoptosis. *Cancer Lett*, 332(2):237–48, 2013.

Roth, S. and Lynch, J. Axis formation: microtubules push in the right direction. *Curr Biol*, 22(13): R537–9, 2012.

Sagolla, M. J., Uzawa, S., and Cande, W. Z. Individual microtubule dynamics contribute to the function of mitotic and cytoplasmic arrays in fission yeast. *J Cell Sci*, 116(Pt 24):4891–903, 2003.

Salbreux, G., Charras, G., and Paluch, E. Actin cortex mechanics and cellular morphogenesis. *Trends Cell Biol*, 22(10):536–45, 2012.

Samejima, I., Miller, V. J., Rincon, S. A., and Sawin, K. E. Fission yeast Mto1 regulates diversity of cytoplasmic microtubule organizing centers. *Curr Biol*, 20(21):1959–65, 2010.

Sandblad, L., Busch, K. E., Tittmann, P., Gross, H., Brunner, D., and Hoenger, A. The *Schizosaccharomyces pombe* EB1 Homolog Mal3p Binds and Stabilizes the Microtubule Lattice Seam. *Cell*, 127(7):1415–1424, 2006.

Sanger, F. and Coulson, A. R. A rapid method for determining sequences in DNA by primed synthesis with DNA polymerase. *J Mol Biol*, 94(3):441–8, 1975.

Sanger, F., Air, G. M., Barrell, B. G., Brown, N. L., Coulson, A. R., Fiddes, C. A., Hutchison, C. A., Slocombe, P. M., and Smith, M. Nucleotide sequence of bacteriophage phi X174 DNA. *Nature*, 265(5596):687–95, 1977a.

Sanger, F., Nicklen, S., and Coulson, A. R. DNA sequencing with chain-terminating inhibitors. *Proceedings of the National Academy of Sciences of the United States of America*, 74(12): 5463–5467, 1977b.

Santamarina, M., Hernandez, G., and Zalvide, J. CDK redundancy guarantees cell cycle progression in Rb-negative tumor cells independently of their p16 status. *Cell Cycle*, 7(13):1962–72, 2008.

Sato, M., Dhut, S., and Toda, T. New drug-resistant cassettes for gene disruption and epitope tagging in *Schizosaccharomyces pombe*. *Yeast*, 22(7):583–91, 2005.

Sauer, G., Korner, R., Hanisch, A., Ries, A., Nigg, E. A., and Sillje, H. H. Proteome analysis of the human mitotic spindle. *Mol Cell Proteomics*, 4(1):35–43, 2005.

Saunders, T. E., Pan, K. Z., Angel, A., Guan, Y., Shah, J. V., Howard, M., and Chang, F. Noise reduction in the intracellular pom1p gradient by a dynamic clustering mechanism. *Dev Cell*, 22 (3):558–72, 2012.

Savage, C., Hamelin, M., Culotti, J. G., Coulson, A., Albertson, D. G., and Chalfie, M. mec-7 is a beta-tubulin gene required for the production of 15-protofilament microtubules in *Caenorhabditis elegans*. *Genes Dev*, 3(6):870–81, 1989.

Sawin, K. E. and Nurse, P. Regulation of cell polarity by microtubules in fission yeast. *J Cell Biol*, 142(2):457–71, 1998.

Sawin, K. E. and Snaith, H. A. Role of microtubules and tea1p in establishment and maintenance of fission yeast cell polarity. *J Cell Sci*, 117(Pt 5):689–700, 2004.

Sawin, K. E. and Tran, P. T. Cytoplasmic microtubule organization in fission yeast. *Yeast*, 23(13): 1001–14, 2006.

Sawin, K. E., Lourenco, P. C., and Snaith, H. A. Microtubule nucleation at non-spindle pole body microtubule-organizing centers requires fission yeast centrosomin-related protein mod20p. *Curr Biol*, 14(9):763–75, 2004.

Schenk, J., Wilsch-Brauninger, M., Calegari, F., and Huttner, W. B. Myosin II is required for interkinetic nuclear migration of neural progenitors. *Proc Natl Acad Sci U S A*, 106(38):16487–92, 2009.

Schiebel, E. gamma-tubulin complexes: binding to the centrosome, regulation and microtubule nucleation. *Curr Opin Cell Biol*, 12(1):113–8, 2000.

Schmoranzer, J. and Simon, S. M. Role of microtubules in fusion of post-Golgi vesicles to the plasma membrane. *Mol Biol Cell*, 14(4):1558–69, 2003.

Schneider, A., Sherwin, T., Sasse, R., Russell, D. G., Gull, K., and Seebeck, T. Subpellicular and flagellar microtubules of *Trypanosoma brucei brucei* contain the same alpha-tubulin isoforms. *J Cell Biol*, 104(3):431–8, 1987.

Schopf, J. W. Fossil evidence of Archaean life. *Philosophical Transactions of the Royal Society B-Biological Sciences*, 361(1470):869–885, 2006.

Schopf, J. W., Kudryavtsev, A. B., Czaja, A. D., and Tripathi, A. B. Evidence of archean life: Stromatolites and microfossils. *Precambrian Research*, 158(3-4):141–155, 2007.

Schuster, S. C. Next-generation sequencing transforms today's biology. *Nat Methods*, 5(1):16–8, 2008.

Sclafani, R. A. and Holzen, T. M. Cell cycle regulation of DNA replication. *Annu Rev Genet*, 41: 237–80, 2007.

Segal, M., Bloom, K., and Reed, S. I. Kar9p-independent microtubule capture at Bud6p cortical sites primes spindle polarity before bud emergence in *Saccharomyces cerevisiae*. *Mol Biol Cell*, 13(12):4141–55, 2002.

Selvanathan, S. P., Thakurta, A. G., Dhakshnamoorthy, J., Zhou, M., Veenstra, T. D., and Dhar, R. *Schizosaccharomyces pombe* Dss1p is a DNA damage checkpoint protein that recruits Rad24p, Cdc25p, and Rae1p to DNA double-strand breaks. *J Biol Chem*, 285(19):14122–33, 2010.

Sethian, J. A. *Level set methods and fast marching methods : evolving interfaces in computational geometry, fluid mechanics, computer vision, and materials science*. Cambridge monographs on applied and computational mathematics. Cambridge University Press, Cambridge, U.K. ; New York, 2nd edition, 1999.

Shah, J. V. Cells in tight spaces: the role of cell shape in cell function. *J Cell Biol*, 191(2):233–6, 2010.

Shelden, E. and Wadsworth, P. Observation and quantification of individual microtubule behavior in vivo: microtubule dynamics are cell-type specific. *J Cell Biol*, 120(4):935–45, 1993.

Shen, Q., Zheng, X., McNutt, M. A., Guang, L., Sun, Y., Wang, J., Gong, Y., Hou, L., and Zhang, B. NAT10, a nucleolar protein, localizes to the midbody and regulates cytokinesis and acetylation of microtubules. *Exp Cell Res*, 315(10):1653–67, 2009.

Shiloh, Y. ATM and ATR: networking cellular responses to DNA damage. *Curr Opin Genet Dev*, 11(1):71–7, 2001.

Shrivastav, M., De Haro, L. P., and Nickoloff, J. A. Regulation of DNA double-strand break repair pathway choice. *Cell Res*, 18(1):134–47, 2008.

Siegrist, S. E. and Doe, C. Q. Microtubule-induced cortical cell polarity. *Genes Dev*, 21(5):483–96, 2007.

Siller, K. H. and Doe, C. Q. Spindle orientation during asymmetric cell division. *Nat Cell Biol*, 11 (4):365–74, 2009.

Simons, C. T., Staes, A., Rommelaere, H., Ampe, C., Lewis, S. A., and Cowan, N. J. Selective contribution of eukaryotic prefoldin subunits to actin and tubulin binding. *J Biol Chem*, 279(6): 4196–203, 2004.

Simons, K. and Toomre, D. Lipid rafts and signal transduction. *Nat Rev Mol Cell Biol*, 1(1):31–9, 2000.

Simpson, J. C., Joggerst, B., Laketa, V., Verissimo, F., Cetin, C., Erfle, H., Bexiga, M. G., Singan, V. R., Heriche, J. K., Neumann, B., Mateos, A., Blake, J., Bechtel, S., Benes, V., Wiemann, S., Ellenberg, J., and Pepperkok, R. Genome-wide RNAi screening identifies human proteins with a regulatory function in the early secretory pathway. *Nat Cell Biol*, 14(7):764–74, 2012.

Singla, V. and Reiter, J. F. The primary cilium as the cell's antenna: signaling at a sensory organelle. *Science*, 313(5787):629–33, 2006.

Sivakumaran, S., Agakov, F., Theodoratou, E., Prendergast, J. G., Zgaga, L., Manolio, T., Rudan, I., McKeigue, P., Wilson, J. F., and Campbell, H. Abundant pleiotropy in human complex diseases and traits. *Am J Hum Genet*, 89(5):607–18, 2011.

Skotheim, J. M., Di Talia, S., Siggia, E. D., and Cross, F. R. Positive feedback of G1 cyclins ensures coherent cell cycle entry. *Nature*, 454(7202):291–6, 2008.

Slautterback, D. B. Cytoplasmic Microtubules. *J Cell Biol*, 18:367–88, 1963.

Sledz, C. A. and Williams, B. R. RNA interference in biology and disease. *Blood*, 106(3):787–94, 2005.

Small, J. V. The actin cytoskeleton. *Electron Microscopy Reviews*, 1(1):155–174, 1988.

Smith, J., Tho, L. M., Xu, N., and Gillespie, D. A. The ATM-Chk2 and ATR-Chk1 pathways in DNA damage signaling and cancer. *Adv Cancer Res*, 108:73–112, 2010.

Snell, V. and Nurse, P. Genetic analysis of cell morphogenesis in fission yeast–a role for casein kinase II in the establishment of polarized growth. *EMBO J*, 13(9):2066–74, 1994.

Snell, W. J., Pan, J., and Wang, Q. Cilia and flagella revealed: from flagellar assembly in Chlamydomonas to human obesity disorders. *Cell*, 117(6):693–7, 2004.

Sodeik, B., Ebersold, M. W., and Helenius, A. Microtubule-mediated transport of incoming herpes simplex virus 1 capsids to the nucleus. *J Cell Biol*, 136(5):1007–21, 1997.

Sommer, C. and Gerlich, D. W. Machine learning in cell biology - teaching computers to recognize phenotypes. *J Cell Sci*, 126(Pt 24):5529–39, 2013.

Sonoda, E., Hochegger, H., Saberi, A., Taniguchi, Y., and Takeda, S. Differential usage of non-homologous end-joining and homologous recombination in double strand break repair. *DNA Repair (Amst)*, 5(9-10):1021–9, 2006.

Spiegelman, B. M., Penningroth, S. M., and Kirschner, M. W. Turnover of tubulin and the N site GTP in Chinese hamster ovary cells. *Cell*, 12(3):587–600, 1977.

St Johnston, D. Moving messages: the intracellular localization of mRNAs. *Nat Rev Mol Cell Biol*, 6(5):363–75, 2005.

Stearns, T., Evans, L., and Kirschner, M. Gamma-tubulin is a highly conserved component of the centrosome. *Cell*, 65(5):825–36, 1991.

Stein, W. D. and Bonner, F. *Cell shape : determinants, regulation, and regulatory role*. Academic Press, San Diego, 1989.

Stephens, C. Senescence: even bacteria get old. *Curr Biol*, 15(8):R308–10, 2005.

Stephens, D. J. Functional coupling of microtubules to membranes - implications for membrane structure and dynamics. *J Cell Sci*, 125(Pt 12):2795–804, 2012.

Stolz, D. B. and Michalopoulos, G. K. Comparative effects of hepatocyte growth factor and epidermal growth factor on motility, morphology, mitogenesis, and signal transduction of primary rat hepatocytes. *J Cell Biochem*, 55(4):445–64, 1994.

Studera, X. E. *Establishment of a genome-wide, microscope-based functional genomics screen to identify microtubule regulators in fission yeast*. PhD thesis, ETHZ, 2012.

Su, Y., Meador, J. A., Geard, C. R., and Balajee, A. S. Analysis of ionizing radiation-induced DNA damage and repair in three-dimensional human skin model system. *Exp Dermatol*, 19(8): e16–22, 2010.

Subramanian, R., Wilson-Kubalek, E. M., Arthur, C. P., Bick, M. J., Campbell, E. A., Darst, S. A., Milligan, R. A., and Kapoor, T. M. Insights into antiparallel microtubule crosslinking by PRC1, a conserved nonmotor microtubule binding protein. *Cell*, 142(3):433–43, 2010.

Sutton, W. S. On the morphology of the chromosome group in Brachystola magna. *The Biological Bulletin*, 4(1):24–39, 1902.

Sutton, W. S. The chromosome in heredity. *The Biological Bulletin*, 4(5):231–250, 1903.

Swartz, R. K., Rodriguez, E. C., and King, M. C. A role for nuclear envelope-bridging complexes in homology-directed repair. *Mol Biol Cell*, 25(16):2461–71, 2014.

Swenberg, J. A., Lu, K., Moeller, B. C., Gao, L., Upton, P. B., Nakamura, J., and Starr, T. B. Endogenous versus exogenous DNA adducts: their role in carcinogenesis, epidemiology, and risk assessment. *Toxicol Sci*, 120 Suppl 1:S130–45, 2011.

Symington, L. S. Focus on recombinational DNA repair. *EMBO Rep*, 6(6):512–7, 2005.

Szankasi, P. and Smith, G. R. A single-stranded DNA exonuclease from *Schizosaccharomyces pombe*. *Biochemistry*, 31(29):6769–73, 1992.

Szankasi, P. and Smith, G. R. Requirement of *S. pombe* exonuclease II, a homologue of *S. cerevisiae* Sep1, for normal mitotic growth and viability. *Curr Genet*, 30(4):284–93, 1996.

Takeda, S., Gapper, C., Kaya, H., Bell, E., Kuchitsu, K., and Dolan, L. Local positive feedback regulation determines cell shape in root hair cells. *Science*, 319(5867):1241–4, 2008.

Tanaka, K. and Russell, P. Cds1 phosphorylation by Rad3-Rad26 kinase is mediated by forkhead-associated domain interaction with Mrc1. *J Biol Chem*, 279(31):32079–86, 2004.

Tanaka, K., Boddy, M. N., Chen, X. B., McGowan, C. H., and Russell, P. Threonine-11, phosphorylated by Rad3 and atm in vitro, is required for activation of fission yeast checkpoint kinase Cds1. *Mol Cell Biol*, 21(10):3398–404, 2001.

Tatebe, H., Shimada, K., Uzawa, S., Morigasaki, S., and Shiozaki, K. Wsh3/Tea4 is a novel cell-end factor essential for bipolar distribution of Tea1 and protects cell polarity under environmental stress in *S. pombe*. *Curr Biol*, 15(11):1006–15, 2005.

Taylor, D. L., Haskins, J. R., and Giuliano, K. A. *High content screening : a powerful approach to systems cell biology and drug discovery*. Methods in molecular biology,. Humana Press, Totowa, N.J., 2007.

Tepp, K., Mado, K., Varikmaa, M., Klepinin, A., Timohhina, N., Shevchuk, I., Chekulayev, V., Kuznetsov, A. V., Guzun, R., and Kaambre, T. The role of tubulin in the mitochondrial metabolism and arrangement in muscle cells. *J Bioenerg Biomembr*, 46(5):421–34, 2014.

Thery, M. and Bornens, M. Cell shape and cell division. *Curr Opin Cell Biol*, 18(6):648–57, 2006.

Thompson, D. W. *On growth and form*. University press, Cambridge Eng., 1917.

Tischer, C., Brunner, D., and Dogterom, M. Chapter 20: Automated spatial mapping of microtubule catastrophe rates in fission yeast. *Methods Cell Biol*, 89:521–38, 2008.

Tischer, C., Brunner, D., and Dogterom, M. Force- and kinesin-8-dependent effects in the spatial regulation of fission yeast microtubule dynamics. *Mol Syst Biol*, 5:250, 2009.

Toczyski, D. P. Methods for studying adaptation to the DNA damage checkpoint in yeast. *Methods Enzymol*, 409:150–65, 2006.

Tran, P. T., Marsh, L., Doye, V., Inoue, S., and Chang, F. A mechanism for nuclear positioning in fission yeast based on microtubule pushing. *J Cell Biol*, 153(2):397–411, 2001.

Traven, A. and Heierhorst, J. SQ/TQ cluster domains: concentrated ATM/ATR kinase phosphorylation site regions in DNA-damage-response proteins. *Bioessays*, 27(4):397–407, 2005.

Tsutsui, Y., Morishita, T., Natsume, T., Yamashita, K., Iwasaki, H., Yamao, F., and Shinagawa, H. Genetic and physical interactions between *Schizosaccharomyces pombe* Mcl1 and Rad2, Dna2 and DNA polymerase alpha: evidence for a multifunctional role of Mcl1 in DNA replication and repair. *Curr Genet*, 48(1):34–43, 2005.

Ursell, T. S., Nguyen, J., Monds, R. D., Colavin, A., Billings, G., Ouzounov, N., Gitai, Z., Shaevitz, J. W., and Huang, K. C. Rod-like bacterial shape is maintained by feedback between cell curvature and cytoskeletal localization. *Proc Natl Acad Sci U S A*, 111(11):E1025–34, 2014.

Vainberg, I. E., Lewis, S. A., Rommelaere, H., Ampe, C., Vandekerckhove, J., Klein, H. L., and Cowan, N. J. Prefoldin, a chaperone that delivers unfolded proteins to cytosolic chaperonin. *Cell*, 93(5):863–73, 1998.

Vale, R. D., Reese, T. S., and Sheetz, M. P. Identification of a novel force-generating protein, kinesin, involved in microtubule-based motility. *Cell*, 42(1):39–50, 1985.

van de Peppel, J. and Holstege, F. C. Multifunctional genes. *Mol Syst Biol*, 1:2005 0003, 2005.

van der Vaart, B., Akhmanova, A., and Straube, A. Regulation of microtubule dynamic instability. *Biochem Soc Trans*, 37(Pt 5):1007–13, 2009.

Varga, V., Helenius, J., Tanaka, K., Hyman, A. A., Tanaka, T. U., and Howard, J. Yeast kinesin-8 depolymerizes microtubules in a length-dependent manner. *Nat Cell Biol*, 8(9):957–62, 2006.

Vedrenne, C., Giroud, C., Robinson, D. R., Besteiro, S., Bosc, C., Bringaud, F., and Baltz, T. Two related subpellicular cytoskeleton-associated proteins in *Trypanosoma brucei* stabilize microtubules. *Mol Biol Cell*, 13(3):1058–70, 2002.

Venkatram, S., Tasto, J. J., Feoktistova, A., Jennings, J. L., Link, A. J., and Gould, K. L. Identification and characterization of two novel proteins affecting fission yeast gamma-tubulin complex function. *Mol Biol Cell*, 15(5):2287–301, 2004.

Venter, J. C., Adams, M. D., Myers, E. W., Li, P. W., Mural, R. J., Sutton, G. G., Smith, H. O., Yandell, M., Evans, C. A., Holt, R. A., Gocayne, J. D., Amanatides, P., Ballew, R. M., Huson, D. H., Wortman, J. R., Zhang, Q., Kodira, C. D., Zheng, X. H., Chen, L., Skupski, M., Subramanian, G., Thomas, P. D., Zhang, J., Gabor Miklos, G. L., Nelson, C., Broder, S., Clark, A. G., Nadeau, J., McKusick, V. A., Zinder, N., Levine, A. J., Roberts, R. J., Simon, M., Slayman, C., Hunkapiller, M., Bolanos, R., Delcher, A., Dew, I., Fasulo, D., Flanigan, M., Florea, L., Halpern, A., Hannenhalli, S., Kravitz, S., Levy, S., Mobarry, C., Reinert, K., Remington, K., Abu-Threideh, J., Beasley, E., Biddick, K., Bonazzi, V., Brandon, R., Cargill, M., Chandramouliswaran, I., Charlab, R., Chaturvedi, K., Deng, Z., Di Francesco, V., Dunn, P., Eilbeck, K., Evangelista, C., Gabrielian, A. E., Gan, W., Ge, W., Gong, F., Gu, Z., Guan, P., Heiman, T. J., Higgins, M. E., Ji, R. R., Ke, Z., Ketchum, K. A., Lai, Z., Lei, Y., Li, Z., Li, J., Liang, Y., Lin, X., Lu, F., Merkulov, G. V., Milshina, N., Moore, H. M., Naik, A. K., Narayan, V. A., Neelam, B., Nusskern, D., Rusch, D. B., Salzberg, S., Shao, W., Shue, B., Sun, J., Wang, Z., Wang, A., Wang, X., Wang, J., Wei, M., Wides, R., Xiao, C., Yan, C., et al. The sequence of the human genome. *Science*, 291(5507):1304–51, 2001.

Verde, F., Mata, J., and Nurse, P. Fission yeast cell morphogenesis: identification of new genes and analysis of their role during the cell cycle. *J Cell Biol*, 131(6 Pt 1):1529–38, 1995.

Verhey, K. J. and Gaertig, J. The tubulin code. *Cell Cycle*, 6(17):2152–60, 2007.

Villar-Tajadura, M. A., Coll, P. M., Madrid, M., Cansado, J., Santos, B., and Perez, P. Rga2 is a Rho2 GAP that regulates morphogenesis and cell integrity in *S. pombe*. *Mol Microbiol*, 70(4): 867–81, 2008.

Virchow, R. Cellular-Pathologie. *Archiv fÃijr pathologische Anatomie und Physiologie und fÃijr klinische Medicin*, 8(1):3–39, 1855.

Vorobjev, I., Malikov, V., and Rodionov, V. Self-organization of a radial microtubule array by dynein-dependent nucleation of microtubules. *Proc Natl Acad Sci U S A*, 98(18):10160–5, 2001.

Waki, K., Anno, K., Ono, T., Ide, T., Chayama, K., and Tahara, H. Establishment of functional telomerase immortalized human hepatocytes and a hepatic stellate cell line for telomere-targeting anticancer drug development. *Cancer Sci*, 101(7):1678–85, 2010.

Walczak, C. E. and Shaw, S. L. A MAP for bundling microtubules. *Cell*, 142(3):364–7, 2010.

Walker, R. A., O'Brien, E. T., Pryer, N. K., Soboeiro, M. F., Voter, W. A., Erickson, H. P., and Salmon, E. D. Dynamic instability of individual microtubules analyzed by video light microscopy: rate constants and transition frequencies. *J Cell Biol*, 107(4):1437–48, 1988.

Wallace, S. S. Base excision repair: a critical player in many games. *DNA Repair (Amst)*, 19: 14–26, 2014.

Wallenfang, M. R. and Seydoux, G. Polarization of the anterior-posterior axis of *C. elegans* is a microtubule-directed process. *Nature*, 408(6808):89–92, 2000.

Wasteneys, G. O. Microtubule organization in the green kingdom: chaos or self-order? *J Cell Sci*, 115(Pt 7):1345–54, 2002.

Watson, J. D. *Molecular biology of the gene*. Pearson/Benjamin Cummings ; Cold Spring Harbor Laboratory Press, San Francisco Cold Spring Harbor, N.Y., 6th edition, 2008.

Watson, J. D. and Crick, F. H. Molecular structure of nucleic acids. *Nature*, 171(4356):737–738, 1953.

Wells, W. A. and Bonetta, L. Microtubules shape the cell. *Journal of Cell Biology*, 169(4):553–553, 2005.

Welte, M. A. Bidirectional transport along microtubules. *Curr Biol*, 14(13):R525–37, 2004.

West, R. R., Vaisberg, E. V., Ding, R., Nurse, P., and McIntosh, J. R. *cut11*(+): A gene required for cell cycle-dependent spindle pole body anchoring in the nuclear envelope and bipolar spindle formation in *Schizosaccharomyces pombe*. *Mol Biol Cell*, 9(10):2839–55, 1998.

West, R. R., Malmstrom, T., Troxell, C. L., and McIntosh, J. R. Two related kinesins, *klp5*+ and *klp6*+, foster microtubule disassembly and are required for meiosis in fission yeast. *Mol Biol Cell*, 12(12):3919–32, 2001.

Westermann, S. and Weber, K. Post-translational modifications regulate microtubule function. *Nat Rev Mol Cell Biol*, 4(12):938–47, 2003.

Wiese, C. and Zheng, Y. Microtubule nucleation: gamma-tubulin and beyond. *J Cell Sci*, 119(Pt 20):4143–53, 2006.

Williams, D. R. and McIntosh, J. R. *mcl1+*, the *Schizosaccharomyces pombe* homologue of CTF4, is important for chromosome replication, cohesion, and segregation. *Eukaryot Cell*, 1(5):758–73, 2002.

Williams, D. R. and McIntosh, J. R. Mcl1p is a polymerase alpha replication accessory factor important for S-phase DNA damage survival. *Eukaryot Cell*, 4(1):166–77, 2005.

Williams, R. S., Dodson, G. E., Limbo, O., Yamada, Y., Williams, J. S., Guenther, G., Classen, S., Glover, J. N., Iwasaki, H., Russell, P., and Tainer, J. A. Nbs1 flexibly tethers Ctp1 and Mre11-Rad50 to coordinate DNA double-strand break processing and repair. *Cell*, 139(1): 87–99, 2009.

Wilson, T. E., Grawunder, U., and Lieber, M. R. Yeast DNA ligase IV mediates non-homologous DNA end joining. *Nature*, 388(6641):495–8, 1997.

Winzeler, E. A., Shoemaker, D. D., Astromoff, A., Liang, H., Anderson, K., Andre, B., Bangham, R., Benito, R., Boeke, J. D., Bussey, H., Chu, A. M., Connelly, C., Davis, K., Dietrich, F., Dow, S. W., El Bakkoury, M., Foury, F., Friend, S. H., Gentalen, E., Giaever, G., Hegemann, J. H., Jones, T., Laub, M., Liao, H., Liebundguth, N., Lockhart, D. J., Lucau-Danila, A., Lussier, M., M'Rabet, N., Menard, P., Mittmann, M., Pai, C., Rebischung, C., Revuelta, J. L., Riles, L., Roberts, C. J., Ross-MacDonald, P., Scherens, B., Snyder, M., Sookhai-Mahadeo, S., Storms, R. K., Veronneau, S., Voet, M., Volckaert, G., Ward, T. R., Wysocki, R., Yen, G. S., Yu, K., Zimmermann, K., Philippsen, P., Johnston, M., and Davis, R. W. Functional characterization of the *S. cerevisiae* genome by gene deletion and parallel analysis. *Science*, 285(5429):901–6, 1999.

Wloga, D. and Gaertig, J. Post-translational modifications of microtubules. *J Cell Sci*, 123(Pt 20): 3447–55, 2010.

Wold, M. S. Replication protein A: a heterotrimeric, single-stranded DNA-binding protein required for eukaryotic DNA metabolism. *Annu Rev Biochem*, 66:61–92, 1997.

Wollman, R. and Stuurman, N. High throughput microscopy: from raw images to discoveries. *J Cell Sci*, 120(Pt 21):3715–22, 2007.

Wollman, R., Cytrynbaum, E. N., Jones, J. T., Meyer, T., Scholey, J. M., and Mogilner, A. Efficient chromosome capture requires a bias in the 'search-and-capture' process during mitotic-spindle assembly. *Curr Biol*, 15(9):828–32, 2005.

Wood, V., Gwilliam, R., Rajandream, M. A., Lyne, M., Lyne, R., Stewart, A., Sgouros, J., Peat, N., Hayles, J., Baker, S., Basham, D., Bowman, S., Brooks, K., Brown, D., Brown, S., Chillingworth, T., Churcher, C., Collins, M., Connor, R., Cronin, A., Davis, P., Feltwell, T., Fraser, A., Gentles, S., Goble, A., Hamlin, N., Harris, D., Hidalgo, J., Hodgson, G., Holroyd, S., Hornsby, T., Howarth, S., Huckle, E. J., Hunt, S., Jagels, K., James, K., Jones, L., Jones, M., Leather, S., McDonald, S., McLean, J., Mooney, P., Moule, S., Mungall, K., Murphy, L., Niblett, D., Odell, C., Oliver, K., O'Neil, S., Pearson, D., Quail, M. A., Rabbinowitsch, E., Rutherford, K., Rutter, S., Saunders, D., Seeger, K., Sharp, S., Skelton, J., Simmonds, M., Squares, R., Squares, S., Stevens, K., Taylor, K., Taylor, R. G., Tivey, A., Walsh, S., Warren, T., Whitehead, S., Woodward, J., Volckaert, G., Aert, R., Robben, J., Grymonprez, B., Weltjens, I., Vanstreels, E., Rieger, M., Schafer, M., Muller-Auer, S., Gabel, C., Fuchs, M., Dusterhoft, A., Fritzc, C., Holzer, E., Moestl, D., Hilbert, H., Borzym, K., Langer, I., Beck, A., Lehrach, H., Reinhardt, R., Pohl, T. M., Eger, P., Zimmermann, W., Wedler, H., Wambutt, R., Purnelle, B., Goffeau, A., Cadieu, E., Dreano, S., Gloux, S., et al. The genome sequence of *Schizosaccharomyces pombe*. *Nature*, 415(6874): 871–80, 2002.

Wood, V., Harris, M. A., McDowall, M. D., Rutherford, K., Vaughan, B. W., Staines, D. M., Aslett, M., Lock, A., Bahler, J., Kersey, P. J., and Oliver, S. G. PomBase: a comprehensive online resource for fission yeast. *Nucleic Acids Res*, 40(Database issue):D695–9, 2012.

Wordeman, L. and Mitchison, T. J. Identification and partial characterization of mitotic centromere-associated kinesin, a kinesin-related protein that associates with centromeres during mitosis. *J Cell Biol*, 128(1-2):95–104, 1995.

Wu, M., Kalyanasundaram, A., and Zhu, J. Structural and biomechanical basis of mitochondrial movement in eukaryotic cells. *Int J Nanomedicine*, 8:4033–42, 2013.

Xie, P., Li, L., Xing, G., Tian, C., Yin, Y., He, F., and Zhang, L. ATM-mediated NuSAP phosphorylation induces mitotic arrest. *Biochem Biophys Res Commun*, 404(1):413–8, 2011.

Yakes, F. M. and Van Houten, B. Mitochondrial DNA damage is more extensive and persists longer than nuclear DNA damage in human cells following oxidative stress. *Proc Natl Acad Sci U S A*, 94(2):514–9, 1997.

Yamamoto, A. and Hiraoka, Y. How do meiotic chromosomes meet their homologous partners?: lessons from fission yeast. *Bioessays*, 23(6):526–33, 2001.

Yamamoto, A., West, R. R., McIntosh, J. R., and Hiraoka, Y. A cytoplasmic dynein heavy chain is required for oscillatory nuclear movement of meiotic prophase and efficient meiotic recombination in fission yeast. *J Cell Biol*, 145(6):1233–49, 1999.

Yang, J., Yu, Y., Hamrick, H. E., and Duerksen-Hughes, P. J. ATM, ATR and DNA-PK: initiators of the cellular genotoxic stress responses. *Carcinogenesis*, 24(10):1571–80, 2003.

Yeung, T., Georges, P. C., Flanagan, L. A., Marg, B., Ortiz, M., Funaki, M., Zahir, N., Ming, W., Weaver, V., and Janmey, P. A. Effects of substrate stiffness on cell morphology, cytoskeletal structure, and adhesion. *Cell Motil Cytoskeleton*, 60(1):24–34, 2005.

Yin, H., Pruyne, D., Huffaker, T. C., and Bretscher, A. Myosin V orientates the mitotic spindle in yeast. *Nature*, 406(6799):1013–5, 2000.

Yin, Z., Sadok, A., Sailem, H., McCarthy, A., Xia, X., Li, F., Garcia, M. A., Evans, L., Barr, A. R., Perrimon, N., Marshall, C. J., Wong, S. T., and Bakal, C. A screen for morphological complexity identifies regulators of switch-like transitions between discrete cell shapes. *Nat Cell Biol*, 15(7): 860–71, 2013.

Yoshida, M., Katsuyama, S., Tateho, K., Nakamura, H., Miyoshi, J., Ohba, T., Matsuhara, H., Miki, F., Okazaki, K., Haraguchi, T., Niwa, O., Hiraoka, Y., and Yamamoto, A. Microtubule-organizing center formation at telomeres induces meiotic telomere clustering. *J Cell Biol*, 200(4):385–95, 2013.

Young, J. C., Barral, J. M., and Ulrich Hartl, F. More than folding: localized functions of cytosolic chaperones. *Trends Biochem Sci*, 28(10):541–7, 2003.

Yu, J., Smith, V. A., Wang, P. P., Hartemink, A. J., and Jarvis, E. D. Advances to Bayesian network inference for generating causal networks from observational biological data. *Bioinformatics*, 20 (18):3594–603, 2004.

Zhao, H., Tanaka, K., Nogochi, E., Nogochi, C., and Russell, P. Replication checkpoint protein Mrc1 is regulated by Rad3 and Tel1 in fission yeast. *Mol Cell Biol*, 23(22):8395–403, 2003.

Zheng, Y., Wong, M. L., Alberts, B., and Mitchison, T. Nucleation of microtubule assembly by a gamma-tubulin-containing ring complex. *Nature*, 378(6557):578–83, 1995.

Zhou, C., Seibert, V., Geyer, R., Rhee, E., Lyapina, S., Cope, G., Deshaies, R. J., and Wolf, D. A. The fission yeast COP9/signalosome is involved in cullin modification by ubiquitin-related Ned8p. *BMC Biochem*, 2:7, 2001.

Zitova, B. and Flusser, J. Image registration methods: a survey. *Image and Vision Computing*, 21 (11):977–1000, 2003.

Zou, L. and Elledge, S. J. Sensing DNA damage through ATRIP recognition of RPA-ssDNA complexes. *Science*, 300(5625):1542–8, 2003.

A Screening Lists

"Spoilers"

—RIVER SONG (*Forest of the Dead*, 2008)

Tables

Table A.1: Hit candidates – 763 genes, which were suggested as hits from either of two genome-wide screens described in **Chapter 3**. All were filmed at least an additional 8 times during refilming. Some (92, indicated by *) were then re-refilmed a further 8 times to improve coverage.

GenomeID	Name	GenomeID	Name	GenomeID	Name	GenomeID	Name
SPCC63.02c	*aah3*	*SPBC1652.02**	*aap1*	*SPBC359.05*	*abc3*	*SPBC409.10*	*ade7*
*SPAC14C4.09**	*agn1*	*SPCC736.11*	*ago1*	*SPAPB1A10.12c*	*alo1*	*SPBC15D4.10c*	*amo1*
SPCC4G3.02	*aph1*	*SPCP1E11.06*	*apl4*	*SPAC144.06*	*apl5*	*SPCC622.17*	*apn1*
SPAPJ760.02c	*app1*	*SPAC30D11.05*	*aps3*	*SPBC1539.08*	*arf6*	*SPAC4G9.10*	*arg3*
SPAC23D3.09	*arp42*	*SPBC13G1.08c*	*ash2*	*SPBC27.02c*	*ask1*	*SPBC15D4.07c*	*atg9*
SPAC4G8.11c	*atp10*	*SPBC29A3.10c*	*atp14*	*SPBC31F10.15c*	*atp15*	*SPAC23C4.11*	*atp18*
SPBC16G5.11c	*bag101*	*SPCC18B5.01c**	*bfr1*	*SPAC24C9.07c**	*bgs2*	*SPBC215.02*	*bob1*
*SPCC970.10c**	*brl2*	*SPBC25B2.06c*	*btb2*	*SPCC1223.13*	*cbf12*	*SPBC1105.04c*	*cbp1*
SPAC25G10.02	*cce1*	*SPCC188.07*	*ccq1*	*SPBC29A10.01*	*ccr1*	*SPCC31H12.08c*	*ccr4*
SPAC1556.04c	*cdd1*	*SPAC17H9.19c**	*cdt2*	*SPAC8C9.03*	*cgs1*	*SPCC663.12*	*cid12*
SPBC16A3.18	*cip1*	*SPAC1B3.17*	*clr2*	*SPBC800.03**	*clr3*	*SPBC428.08c*	*clr4*
SPAC56F8.04c	*coq2*	*SPAC1687.12c**	*coq4*	*SPCC4G3.04c*	*coq5*	*SPAC1296.02*	*cox4*
SPAC16C9.05	*cph1*	*SPAC2F7.07c*	*cph2*	*SPAC3A11.02*	*cps3*	*SPBC215.03c*	*csn1*
SPAPB17E12.04c	*csn2*	*SPAC17A2.09c*	*csx1*	*SPCC338.08*	*ctp1*	*SPBC19C2.13c*	*ctu2*
SPAC31A2.11c	*cuf1*	*SPBC32F12.05c*	*cwf12*	*SPAC30D11.09*	*cwf19*	*SPAC21E11.05c*	*cyp8*
SPBC36.04	*cys11*	*SPAC25B8.01*	*dap1*	*SPAC17A5.02c*	*dbr1*	*SPBC646.17c*	*dic1*
SPAC4F8.01	*did4*	*SPAC8E11.03c*	*dmc1*	*SPBC12C2.08*	*dnm1*	*SPBC651.05c*	*dot2*
*SPBC839.15c**	*ef1a-c*	*SPBC336.03*	*efc25*	*SPAC3C7.08c*	*elf1*	*SPAC688.11**	*end4*
SPAC23D3.10c	*eng2*	*SPCC622.16c*	*epe1*	*SPBC30B4.08*	*eri1*	*SPBC2D10.13*	*est1*
*SPBC1105.05**	*exg1*	*SPAC17A5.14*	*exo2*	*SPAC926.09c*	*fas1*	*SPBC336.01*	*fbh1*
SPCC1235.05c	*fft2*	*SPAC1F7.08*	*fio1*	*SPBC16G5.15c*	*fkh2*	*SPBC3E7.10*	*fma1*
SPBC14C8.03	*fma2*	*SPBC1683.09c*	*frp1*	*SPAC6F12.03c*	*fsv1*	*SPAC1F8.06**	*fta5*
SPCC1902.01	*gaf1*	*SPAC140.02*	*gar2*	*SPAC1952.05*	*gcn5*	*SPAC13G6.06c*	*gcv2*
SPBC211.06	*gfh1*	*SPBC1683.08*	*ght4*	*SPBC1348.14c*	*ght7*	*SPCC1753.02c*	*git3*
SPBC32H8.07	*git5*	*SPCC736.04c*	*gma12*	*SPAC343.04c*	*gnr1*	*SPAC23H3.13c*	*gpa2*
SPAC4F10.20	*grx1*	*SPCC965.07c*	*gst2*	*SPAC1751.01c*	*gti1*	*SPCC4G3.09c*	*gyp3*
SPAC26F1.09	*gyp51*	*SPAC1F5.07c*	*hem14*	*SPAC1805.06c**	*hem2*	*SPAC24B11.13*	*hem3*
SPBC31F10.14c	*hip3*	*SPBC418.01c*	*his4*	*SPBC725.09c**	*hob3*	*SPAC222.07c*	*hri2*
*SPAC3G6.01**	*hrp3*	*SPAC3H1.11*	*hsr1*	*SPCC132.02*	*hst2*	*SPBC839.07*	*ibp1*
SPAC6G10.08	*idp1*	*SPAC222.04c*	*ies6*	*SPBP35G2.07*	*ilv1*	*SPBC19G7.16*	*iws1*
SPAC1002.05c	*jmj2*	*SPCC1322.06*	*kap113*	*SPBC1271.12*	*kes1*	*SPBC4F6.06**	*kin1*
SPAC664.10	*klp2*	*SPAC144.14*	*klp8*	*SPBC2G2.01c*	*liz1*	*SPAC1D4.11c**	*lkh1*
SPAC22F3.06c	*lon1*	*SPBC146.09c**	*lsd1*	*SPAC2F3.15*	*lsk1*	*SPBC16A3.03c*	*lyn1*
SPAP7G5.04c	*lys1*	*SPAC343.16*	*lys2*	*SPAC17C9.02c*	*lys7*	*SPAC1834.08*	*mak1*
*SPAC18G6.15**	*mal3*	*SPAPB1E7.02c*	*mcl1*	*SPBC216.02*	*mcp5*	*SPAC17A5.04c*	*mde10*
*SPAC17G8.05**	*med20*	*SPAC1782.11*	*met14*	*SPBC14C8.05c*	*meu17*	*SPBC409.11*	*meu18*
SPAC25H1.05	*meu29*	*SPAC9.05*	*mfh1*	*SPBC27.06c*	*mgr2*	*SPBC1D7.04**	*mlo3*
SPAC1527.01	*mok11*	*SPBC16D10.05*	*mok13*	*SPAC13G7.13c*	*msa1*	*SPAC8F11.03**	*msh3*
SPBC902.06	*mto2*	*SPCC11E10.03*	*mug1*	*SPAC56F8.14c*	*mug115*	*SPCC645.11c*	*mug117*
SPBC19C2.06c	*mug124*	*SPAC11G7.06c*	*mug132*	*SPCC1919.11*	*mug137*	*SPAC3A12.03c*	*mug145*
SPAC3H1.03	*mug151*	*SPBC1604.01*	*mug158*	*SPAC11H11.02c*	*mug162*	*SPBC25B2.07c*	*mug164*
SPBPB2B2.02	*mug180*	*SPAC6G9.03c*	*mug183*	*SPAC22H12.01c*	*mug35*	*SPCC1393.07c*	*mug4*
SPCC584.12	*mug42*	*SPCC31H12.02c**	*mug73*	*SPBC1D7.03*	*mug80*	*SPBC13G1.10c*	*mug81*
*SPBC3E7.15c**	*mug83*	*SPBC146.13c*	*myo1*	*SPAC4A8.05c**	*myp2*	*SPAC3H8.09c*	*nab3*
SPCC364.06	*nap1*	*SPBC23G7.04c*	*nif1*	*SPAC8F11.09c*	*nnt1*	*SPBC23E6.03c*	*nta1*
SPCC18B5.07c	*nup61*	*SPAC17A2.05*	*osm1*	*SPBP4H10.03*	*oxa102*	*SPBC16E9.12c*	*pab2*
SPBC32F12.06	*pch1*	*SPAC21E11.03c**	*pcr1*	*SPCC790.02**	*pep3*	*SPBC725.07*	*pex5*
SPBC30D10.16	*pha2*	*SPBC3B8.02*	*php5*	*SPBC11B10.10c*	*pht1*	*SPAC3C7.06c*	*pit1*
SPBC106.10	*pka1*	*SPBC713.11c*	*pmp3*	*SPBC31E1.02c*	*pmr1*	*SPBC19C2.02*	*pmt1*
SPAC3G9.08	*png1*	*SPAC29E6.01*	*pof11*	*SPCC338.16*	*pof3*	*SPAC17G6.17*	*pof8*
SPAC2F7.03c	*pom1*	*SPBC21B10.05c*	*pop3*	*SPBP4H10.04*	*ppb1*	*SPAC3H1.13*	*ppk13*
*SPAC890.03**	*ppk16*	*SPBC336.14c*	*ppk26*	*SPCC1223.11**	*ptc2*	*SPAC2G11.07c*	*ptc3*

Continued on next page

Table A.1 – continued from previous page

GenomeID	Name	GenomeID	Name	GenomeID	Name	GenomeID	Name
SPAC11G7.02	*pub1*	*SPBC16E9.11c*	*pub3*	*SPBC1921.06c*	*pvg3*	*SPAC5D6.07c*	*pxa1*
SPAC57A7.08	*pzh1*	*SPBC16C6.08c*	*qcr6*	*SPCC1682.01*	*qcr9*	*SPBC3E7.08c*	*rad13*
SPAC13C5.07	*rad32*	*SPAC1556.01c*	*rad50*	*SPCC613.12c*	*raf1*	*SPBC1778.02*	*rap1*
SPAC22F3.03c	*rdh54*	*SPBC1198.11c*	*reb1*	*SPAC25G10.04c*	*rec10*	*SPBC32F12.02*	*rec14*
SPAC1952.15c	*rec24*	*SPBC2D10.06*	*rep1*	*SPBC2F12.11c*	*rep2*	*SPAC1782.08c*	*rex3*
SPAC19A8.10	*rfp1*	*SPAC26A3.09c**	*rga2*	*SPBC17F3.01c**	*rga5*	*SPAC16.01*	*rho2*
SPBC1734.06	*rhp18*	*SPCP25A2.02c*	*rhp26*	*SPAC644.14c**	*rhp51*	*SPAC15A10.03c**	*rhp54*
SPAC3C7.03c	*rhp55*	*SPAC20H4.07*	*rhp57*	*SPCC11E10.08*	*rik1*	*SPBC1685.11*	*rlp1*
SPCC1259.03	*rpa12*	*SPAPYUG7.04c*	*rpb9*	*SPCC31H12.04c*	*rpl1202*	*SPCC576.11**	*rpl15*
SPCC364.03	*rpl1702*	*SPBC11C11.07*	*rpl1801*	*SPAC26A3.04*	*rpl2002*	*SPAC959.08**	*rpl2102*
SPBC29B5.03c	*rpl26*	*SPAC9G1.03c*	*rpl3001*	*SPAC3H5.10**	*rpl3202*	*SPBC1921.01c*	*rpl3701*
SPCC1223.05c	*rpl3702*	*SPAPB17E12.05*	*rpl3703*	*SPAC15E1.03*	*rpl42*	*SPAC3H5.12c*	*rpl501*
SPAC3H5.07	*rpl702*	*SPAC1F7.13c*	*rpl801*	*SPAC4G9.16c*	*rpl901*	*SPAC637.10c*	*rpn10*
SPBC3B9.13c	*rpp102*	*SPBP8B7.06*	*rpp201*	*SPBC23G7.15c**	*rpp202*	*SPBP22H7.08**	*rps1002*
SPAC31G5.03	*rps1101*	*SPCC962.04*	*rps1201*	*SPBC1685.02c*	*rps1202*	*SPBC839.05c*	*rps1701*
SPCC24B10.09	*rps1702*	*SPBC16D10.11c*	*rps1801*	*SPAC22A12.04c*	*rps2201*	*SPAC1805.11c*	*rps2602*
SPBC1685.10	*rps27*	*SPAC19B12.04*	*rps3001*	*SPBC19G7.03c*	*rps3002*	*SPAC328.10c**	*rps502*
*SPAC521.05**	*rps802*	*SPBC23G7.12c*	*rpt6*	*SPBC1734.15*	*rsc4*	*SPAC4C5.02c*	*ryh1*
SPCC1840.03	*sal3*	*SPBC23E6.08*	*sat1*	*SPBC2G2.03c**	*sbh1*	*SPAC16E8.09*	*scd1*
SPAC22H10.07	*scd2*	*SPBC18H10.04c*	*sce3*	*SPBC119.06*	*sco1*	*SPBC3B9.15c*	*scp1*
*SPBC776.04**	*sec2302*	*SPAC5D6.05*	*sep11'*	*SPCC306.04c*	*set1*	*SPAC22E12.11c*	*set3*
SPBP8B7.07c	*set6*	*SPCC297.04c*	*set7*	*SPAC3C7.09*	*set8*	*SPAC31A2.13c**	*sft1*
SPAC15A10.15	*sgo2*	*SPAC1F5.09c*	*shk2*	*SPCC16C4.01*	*sif2*	*SPAC12G12.15*	*sif3*
SPAPYUG7.02c	*sin1*	*SPBC16H5.11c*	*skb1*	*SPBC19C2.14*	*smd3*	*SPAC29B12.04*	*snz1*
SPAC3A11.09	*sod22*	*SPBC30B4.04c*	*sol1*	*SPAC29B12.03*	*spd1*	*SPAC4F10.11**	*spn1*
SPAC24C9.15c	*spn5*	*SPCC188.12*	*spn6*	*SPAC1F7.01c**	*spt6*	*SPBC354.05c*	*sre2*
SPCC1322.08	*srk1*	*SPAC4H3.05*	*srs2*	*SPAC13G7.02c*	*ssa1*	*SPAC3G9.04*	*ssu72*
SPAC20G4.07c	*sts1*	*SPBC27.08c*	*sua1*	*SPCC576.13*	*swc5*	*SPAC23H3.05c*	*swd1*
SPAC11E3.01c	*swr1*	*SPAC7D4.04*	*taf1*	*SPBC32F12.11*	*tdh1*	*SPCC1223.06**	*tea1*
SPBC1604.20c	*tea2*	*SPAC6G10.02c*	*tea3*	*SPBC1706.01**	*tea4*	*SPCC23B6.03c*	*tel1*
SPAC23H4.10c	*thi4*	*SPAC26H5.10c*	*tif51*	*SPBC1289.09*	*tim21*	*SPAC3C7.12*	*tip1*
SPAC343.15	*tit1*	*SPBC27B12.10c*	*tom7*	*SPAC6B12.12*	*tom70*	*SPBC30D10.10c**	*tor1*
SPAC31A2.02	*trm112*	*SPAC22F3.13*	*tsc1*	*SPBC800.07c*	*tsf1*	*SPBC800.05c*	*tub1*
SPAC18B11.10	*tup11*	*SPAC630.14c*	*tup12*	*SPCC126.06*	*twf1*	*SPAC11G7.04*	*ubi1*
*SPCC1682.12c**	*ubp16*	*SPBC1703.12*	*ubp9*	*SPCC895.09c*	*ucp12*	*SPAC20H4.10*	*ufd2*
SPAC17A5.07c	*ulp2*	*SPAC16C9.06c*	*upf1*	*SPAC57A10.12c*	*ura3*	*SPBC4B4.07c*	*usp102*
*SPCC550.14**	*vgl1*	*SPAC767.01c**	*vps1*	*SPAC824.05*	*vps16*	*SPBC4B4.06*	*vps25*
SPAC1B3.07c	*vps28*	*SPAC1142.07c*	*vps32*	*SPBC3B9.09*	*vps36*	*SPAC1783.02c*	*vps66*
SPBC409.07c	*wis1*	*SPAC9G1.02*	*wis4*	*SPAC9E9.13*	*wos2*	*SPCC1450.08c*	*wtf16*
SPAC31F12.01	*zds1*	*SPBC1718.07c**	*zfs1*	*SPAC23C11.14*	*zhf1*	*SPAC25G10.03*	*zip1*
SPCC1442.16c	*zta1*	*SPBC1778.01c**	*zuo1*	*SPAC1006.03c*		*SPAC1039.03*	
*SPAC1039.04**		*SPAC1071.04c*		*SPAC1093.03*		*SPAC10F6.04**	
SPAC11D3.04c		*SPAC11D3.07c*		*SPAC11E3.13c*		*SPAC12B10.03*	
SPAC12G12.07c		*SPAC139.01c*		*SPAC13C5.04*		*SPAC13G7.03*	
SPAC13G7.11		*SPAC14C4.06c**		*SPAC14C4.10c**		*SPAC1565.07c*	
SPAC15E1.02c		*SPAC1610.02c*		*SPAC1635.01*		*SPAC1687.08*	
SPAC1687.14c		*SPAC1687.19c*		*SPAC1687.23c*		*SPAC16A10.03c*	
SPAC16C9.01c		*SPAC16E8.01*		*SPAC16E8.08*		*SPAC16E8.13*	
SPAC1705.02		*SPAC1782.05**		*SPAC17A5.08*		*SPAC17A5.09c*	
SPAC17A5.16		*SPAC17C9.14*		*SPAC17G6.15c*		*SPAC17H9.06c*	
SPAC17H9.08		*SPAC17H9.13c*		*SPAC1834.10c*		*SPAC18G6.05c*	
SPAC1952.02		*SPAC1952.09c*		*SPAC19B12.06c*		*SPAC19G12.04*	
SPAC19G12.09		*SPAC1B1.04c**		*SPAC1B3.15c*		*SPAC1F3.03*	
SPAC1F5.03c		*SPAC1F5.05c*		*SPAC1F7.09c*		*SPAC20H4.02**	
SPAC20H4.05c		*SPAC227.01c**		*SPAC227.05*		*SPAC227.10*	
SPAC227.11c		*SPAC227.17c*		*SPAC22A12.06c*		*SPAC22E12.01*	
SPAC22H10.11c		*SPAC23A1.14c*		*SPAC23A1.16c**		*SPAC23C11.06c*	
SPAC23C11.10		*SPAC23C4.06c*		*SPAC23G3.05c*		*SPAC23H3.11c*	
SPAC23H3.12c		*SPAC24C9.12c*		*SPAC24H6.10c*		*SPAC25B8.04c*	

Continued on next page

Table A.1 – continued from previous page

GenomeID Name	GenomeID Name	GenomeID Name	GenomeID Name
*SPAC25B8.19c**	*SPAC25G10.01*	*SPAC26A3.17c*	*SPAC26H5.05*
SPAC27D7.06	*SPAC27D7.10c*	*SPAC27E2.03c*	*SPAC29A4.13*
SPAC29A4.20	*SPAC29B12.08*	*SPAC29B12.12*	*SPAC29E6.10c*
SPAC2C4.10c	*SPAC2E12.03c*	*SPAC2E1P3.04*	*SPAC2F3.02**
SPAC2F3.12c	*SPAC2F7.17*	*SPAC2G11.10c*	*SPAC2H10.01*
SPAC30.02c	*SPAC30C2.04*	*SPAC30C2.08*	*SPAC30D11.01c*
SPAC30D11.06c	*SPAC31G5.19*	*SPAC323.01c*	*SPAC323.05c*
SPAC328.04	*SPAC32A11.02c*	*SPAC343.20*	*SPAC3A11.03*
SPAC3A11.13	*SPAC3A12.06c*	*SPAC3A12.13c*	*SPAC3C7.04*
SPAC3C7.13c	*SPAC3F10.17*	*SPAC3G9.05*	*SPAC3H1.05*
SPAC3H1.07	*SPAC3H1.08c*	*SPAC3H5.11*	*SPAC3H8.02*
SPAC3H8.04	*SPAC3H8.05c*	*SPAC3H8.07c*	*SPAC458.02c**
*SPAC4F10.02**	*SPAC4F10.04**	*SPAC4F10.19c*	*SPAC4G8.07c*
SPAC4G8.08	*SPAC57A7.12*	*SPAC57A7.13*	*SPAC589.05c*
SPAC589.07c	*SPAC589.09*	*SPAC5H10.04*	*SPAC5H10.09c*
SPAC630.10	*SPAC637.09*	*SPAC644.07**	*SPAC664.03*
SPAC688.03c	*SPAC688.14*	*SPAC694.02*	*SPAC6C3.02c*
SPAC6C3.05	*SPAC6C3.08*	*SPAC6F6.13c*	*SPAC6G10.06**
SPAC6G9.14	*SPAC6G9.16c*	*SPAC750.06c*	*SPAC823.10c*
*SPAC824.02**	*SPAC869.10c*	*SPAC890.05*	*SPAC8C9.19*
SPAC8E11.10	*SPAC8F11.02c*	*SPAC8F11.08c*	*SPAC922.04**
SPAC977.05c	*SPAC977.11*	*SPAC9E9.15*	*SPAC9G1.07*
SPAC9G1.08c	*SPAP14E8.02*	*SPAP27G11.02*	*SPAP7G5.03*
SPAP8A3.12c	*SPAPB17E12.08*	*SPAPB1A10.08*	*SPAPB24D3.03*
SPBC106.03	*SPBC106.07c*	*SPBC119.16c*	*SPBC1198.03c*
SPBC1271.07c	*SPBC1289.06c*	*SPBC1289.16c*	*SPBC12C2.03c*
SPBC12C2.04	*SPBC1348.01**	*SPBC1348.02*	*SPBC13A2.04c*
SPBC13G1.02	*SPBC14C8.04*	*SPBC14F5.10c*	*SPBC15D4.01c*
SPBC15D4.05	*SPBC15D4.06*	*SPBC15D4.09c*	*SPBC1604.09c*
SPBC1604.12	*SPBC1604.16c*	*SPBC1683.11c*	*SPBC16A3.06*
SPBC16A3.10	*SPBC16D10.08c*	*SPBC16E9.15*	*SPBC16G5.02c*
SPBC16G5.07c	*SPBC16G5.09*	*SPBC16G5.17*	*SPBC16H5.14c*
SPBC1703.11	*SPBC1709.09*	*SPBC1734.07c*	*SPBC1773.01*
*SPBC1773.02c**	*SPBC1773.08c*	*SPBC17A3.03c*	*SPBC17A3.05c**
SPBC17D11.03c	*SPBC17G9.02c*	*SPBC1861.05*	*SPBC1861.07*
*SPBC18A7.02c**	*SPBC18E5.01*	*SPBC18E5.05c*	*SPBC18E5.07*
SPBC18E5.13	*SPBC18H10.07*	*SPBC1921.04c*	*SPBC1921.07c*
*SPBC19C2.10**	*SPBC19C7.01**	*SPBC19F8.03c*	*SPBC1A4.04*
SPBC1D7.01	*SPBC20F10.05*	*SPBC20F10.07**	*SPBC215.01*
SPBC21B10.13c	*SPBC21C3.02c*	*SPBC21C3.14c*	*SPBC21D10.08c*
SPBC21H7.04	*SPBC21H7.06c*	*SPBC23E6.02*	*SPBC23E6.10c*
SPBC23G7.06c	*SPBC24C6.10c**	*SPBC25B2.01*	*SPBC25B2.08*
SPBC25D12.06	*SPBC25H2.15**	*SPBC25H2.16c*	*SPBC27B12.05**
SPBC28E12.02	*SPBC29A10.06c*	*SPBC29A10.10c*	*SPBC29A10.12*
SPBC29A3.13	*SPBC2A9.03*	*SPBC2A9.07c*	*SPBC2D10.16**
SPBC2F12.03c	*SPBC31F10.10c**	*SPBC31F10.12*	*SPBC31F10.17c*
SPBC32F12.07c	*SPBC32F12.12c*	*SPBC32H8.01c*	*SPBC337.11*
SPBC342.03	*SPBC354.10*	*SPBC365.11*	*SPBC36B7.02*
SPBC3B8.04c	*SPBC3B8.05*	*SPBC3B9.05*	*SPBC3D6.06c*
SPBC3D6.13c	*SPBC3E7.09*	*SPBC3H7.03c*	*SPBC3H7.07c*
SPBC3H7.10	*SPBC3H7.13*	*SPBC405.02c*	*SPBC409.17c*
SPBC409.19c	*SPBC428.06c*	*SPBC530.05*	*SPBC543.08*
SPBC56F2.08c	*SPBC609.03*	*SPBC651.09c*	*SPBC660.06*
SPBC660.10	*SPBC660.17c*	*SPBC685.03*	*SPBC691.04*
SPBC691.05c	*SPBC6B1.03c*	*SPBC725.01*	*SPBC725.04*
SPBC83.05	*SPBC839.02*	*SPBC887.02*	*SPBC8D2.12c*
SPBC8E4.03	*SPBC902.03*	*SPBC902.04*	*SPBC947.01*
SPBC947.08c	*SPBC947.09**	*SPBC9B6.07*	*SPBCPT2R1.01c*
*SPBP16F5.05c**	*SPBP19A11.02c*	*SPBP22H7.06**	*SPBP35G2.04c*

Continued on next page

APPENDIX A

Table A.1 – continued from previous page

GenomeID	Name	GenomeID	Name	GenomeID	Name	GenomeID	Name
SPBP35G2.11c		*SPBP4H10.16c*		*SPBP8B7.09c*		*SPBP8B7.13*	
SPBP8B7.18c		*SPBPB10D8.06c*		*SPBPB10D8.07c*		*SPBPB2B2.12c**	
SPBPB2B2.14c		*SPBPB7E8.01*		*SPCC1020.09*		*SPCC1020.11c*	
SPCC1020.12c		*SPCC1183.11*		*SPCC11E10.04*		*SPCC11E10.06c*	
SPCC1259.04		*SPCC1259.08*		*SPCC132.01c*		*SPCC1322.02*	
SPCC1322.03		*SPCC1442.02*		*SPCC1442.11c*		*SPCC1442.17c*	
SPCC1450.03		*SPCC162.02c*		*SPCC162.11c*		*SPCC1672.04c*	
SPCC16C4.20c		*SPCC1739.04c*		*SPCC1739.06c**		*SPCC1739.07*	
SPCC1739.08c		*SPCC1840.05c*		*SPCC1906.02c*		*SPCC1919.03c*	
SPCC1919.04		*SPCC1919.05*		*SPCC1919.12c*		*SPCC23B6.01c*	
SPCC24B10.08c		*SPCC24B10.11c*		*SPCC24B10.12*		*SPCC24B10.15*	
SPCC24B10.16c		*SPCC24B10.19c*		*SPCC24B10.22*		*SPCC285.13c*	
*SPCC320.04c**		*SPCC330.03c*		*SPCC338.14*		*SPCC417.12*	
SPCC4B3.01		*SPCC4B3.07*		*SPCC4B3.13*		*SPCC4F11.03c**	
SPCC548.04		*SPCC550.07*		*SPCC550.09*		*SPCC553.08c*	
SPCC569.04		*SPCC584.11c*		*SPCC594.05c**		*SPCC622.12c*	
SPCC645.12c		*SPCC663.15c*		*SPCC70.02c*		*SPCC70.04c*	
SPCC736.02		*SPCC736.09c*		*SPCC737.03c*		*SPCC737.07c*	
SPCC74.02c		*SPCC777.02*		*SPCC794.03*		*SPCC825.05c*	
*SPCC830.06**		*SPCC895.06*		*SPCC965.06*		*SPCC970.02*	
SPCP31B10.04		*SPCP31B10.05*		*SPCPB16A4.05c*			

Table A.2: Hit lists – 262 high-confidence cell shape, microtubule & cell cycle progression (CCP) hits reported from the screen described in **Chapter 3** and published in Graml et al. (2014). Entrez IDs were used for functional annotation using DAVID. Bioneer locations are given for version 2 of the library. Hits are assigned a percentage as the number of screen repeats where they were a hit over the total number of repeats analysed. Hits annotated visually by X. Studera are also indicated. Conservation was assessed using data provided by PomBase.

Hits			Bioneer		Cell Shape			Microtubules			CCP		Conservation		
Name	GenomeID	EntrezID	Plate	Well	Hit (%)	Cluster	Visual	Hit (%)	Cluster	Visual	Hit (%)	Cluster	*S. cerevisiae*	Vertebrates	Humans
aah3	*SPCC63.02c*	2539415	12	G11	100	1		40	3				•		
abo1	*SPAC31G5.19*	2543084	6	B2	67	2							•	•	•
ada2	*SPCC24B10.08c*	2539174	9	E6				71	2				•	•	•
ago1	*SPCC736.11*	2539403	9	D4				40	6					•	•
amk2	*SPCC1919.03c*	2539130	9	F1	67	3							•	•	•
apl4	*SPCP1E11.06*	2539311	12	F12	100	4		100	1		50	1	•	•	•
apl5	*SPAC144.06*	2542857	29	H4				50	3				•	•	•
aps3	*SPAC30D11.05*	2542114	14	A2				57	3				•	•	•
are2	*SPCP1E11.05c*	2538854	12	E12	40	2							•	•	
arf6	*SPBC1539.08*	2539937	2	D6	75	1		86	1				•	•	•
arp42	*SPAC23D3.09*	2541496	5	E10	63	2		57	2				•	•	
ash2	*SPBC13G1.08c*	2539667	14	A12				44	8				•	•	•
bag101	*SPBC16G5.11c*	2539843	22	C3				40	5				•	•	
bob1	*SPBC215.02*	2540664	11	A3				100	7				•	•	•
brl2	*SPCC970.10c*	2539307	9	D5	100	4	•						•	•	
cao2	*SPBC1289.16c*	2539624	14	G11				71	5					•	
cbp1	*SPBC1105.04c*	2539971	12	C6				71	3	•	50	2			•
ccq1	*SPCC188.07*	2539352	16	A2	100	4	•	100	1				•		
ccr1	*SPBC29A10.01*	2541038	22	A11	50	2		100	6	•	67	2	•	•	•
ccr4	*SPCC31H12.08c*	2538913	17	B11	86	2							•	•	•
cdt2	*SPAC17H9.19c*	2542374	16	G12	100	4		100	1					•	•
cgi121	*SPCC24B10.12*	2539388	24	C6							40	2	•	•	•
cgs1	*SPAC8C9.03*	2543351	3	D8	43	2							•	•	•
cid12	*SPCC663.12*	2539423	24	G6				42	7					•	
clr3	*SPBC800.03*	2540821	13	E4	70	2							•	•	
clr5	*SPAC29B12.08*	2542669	31	A4				43	7						
coq5	*SPCC4G3.04c*	2539510	32	G10				43	6				•	•	•
cph1	*SPAC16C9.05*	2542318	10	H9	100	4	•	75	8	•			•	•	•
cph2	*SPAC2F7.07c*	2541422	23	H10	100	4		100	1				•	•	•
cps3	*SPAC3A11.02*	2543054	16	E5	56	2		44	5				•		
csc4	*SPAC2C4.10c*	2542650	30	D6	63	2							•		
csn1	*SPBC215.03c*	2540352	26	C1	100	2		71	1					•	•
csn2	*SPAPB17E12.04c*	3361420	2	B4	75	2		71	2					•	•
csx1	*SPAC17A2.09c*	2542151	13	A8	100	4	•	63	8	•			•	•	
ctp1	*SPCC338.08*	2538706	21	F10	50	4	•	63	1				•	•	
ctu2	*SPBC19C2.13c*	2540896	20	G5	43	4							•	•	
cuf1	*SPAC31A2.11c*	2543198	20	A5	100	4		75	1	•			•		
cwf12	*SPBC32F12.05c*	2540230	17	G7	40	5							•	•	•
cys11	*SPBC36.04*	2540946	32	E6	50	2		50	6		40	2	•	•	
dbp7	*SPBC21H7.04*	2540518	11	H4							43	2	•	•	•
dep1	*SPBC21C3.02c*	2540595	16	B3	78	4		100	1				•	•	
did4	*SPAC4F8.01*	2543521	23	D11	50	2		40	5				•	•	•
dip1	*SPBC24C6.10c*	2540504	25	E3	100	2							•	•	
dph3	*SPAC8F11.02c*	2543434	29	C1	50	4		43	8		50	1	•	•	•

Continued on next page

Table A.2 – continued from previous page

Name	GenomeID	EntrezID	Plate	Well	Hit (%)	Cluster	Visual	Hit (%)	Cluster	Visual	Hit (%)	Cluster	*S. cerevisiae*	Vertebrates	Humans
ebs1	*SPBC2F12.03c*	2540346	15	F3				40	8					•	
ecm6	*SPCC1020.11c*	2538978	30	F2	38	1		38	6				•	•	•
efc25	*SPBC336.03*	2540248	8	A2	100	2	•	40	3				•	•	•
elf1	*SPAC3C7.08c*	2543082	12	B4							40	2	•		
elp2	*SPCC895.06*	2538986	30	E1				43	7				•	•	•
elp3	*SPAC29A4.20*	2541614	17	A3	100	4		100	8	•			•	•	•
elp4	*SPCC11E10.06c*	2538987	27	C9	100	4	•	100	1				•	•	•
elp6	*SPBC3H7.10*	2540979	30	E9	100	4	•	100	8	•			•	•	
end4	*SPAC688.11*	2543336	17	H4	100	2	•						•	•	•
erd1	*SPAC227.01c*	2541909	18	A8	100	5		100	1				•	•	
erp2	*SPAC17A5.08*	2542439	30	C12				40	3	•			•	•	•
exo2	*SPAC17A5.14*	2542204	26	D12				50	4				•	•	•
fft2	*SPCC1235.05c*	2539045	8	G11				38	5				•	•	•
fkh2	*SPBC16G5.15c*	2539703	21	F4				100	3	•			•	•	•
gar2	*SPAC140.02*	2542869	10	H10							38	1	•	•	
gas5	*SPAC11E3.13c*	2542989	20	G10				40	3				•		
gcn5	*SPAC1952.05*	2542513	23	A10				50	1				•	•	•
gdh1	*SPCC622.12c*	2539147	18	G6	40	2							•	•	
gfh1	*SPBC211.06*	2540667	18	F3				80	7					•	
git3	*SPCC1753.02c*	2538770	15	A10				40	5				•		
gma12	*SPCC736.04c*	2539101	20	G2				43	8				•		
gpa2	*SPAC23H3.13c*	2541720	14	B7	75	2	•						•	•	
hem14	*SPAC1F5.07c*	2541631	16	C1	75	2		43	7				•	•	•
iws1	*SPBC19G7.16*	2540721	28	G11							40	3	•	•	•
kap113	*SPCC1322.06*	2538800	28	A4				50	1				•	•	•
liz1	*SPBC2G2.01c*	2540342	15	G3				38	5				•	•	
lon1	*SPAC22F3.06c*	2541875	11	A1				63	5				•	•	•
lsd1	*SPBC146.09c*	2539805	7	G3	50	2								•	
mak1	*SPAC1834.08*	2542119	26	G6				44	5						
mal3	*SPAC18G6.15*	2542123	5	H4				100	2	•	56	4	•	•	•
mcl1	*SPAPB1E7.02c*	2543387	22	E9	100	4		100	1				•	•	•
med20	*SPAC17G8.05*	2542421	1	C9	100	4	•	100	1	•			•	•	
met14	*SPAC1782.11*	2542359	1	B9	71	1		80	1				•	•	
meu29	*SPAC25H1.05*	2542722	16	F6	100	1							•		
meu34	*SPAC3A12.03c*	2543036	6	C3				38	5				•	•	
mft1	*SPCC24B10.11c*	2539006	19	F12				43	1				•	•	
mga2	*SPAC26H5.05*	2542701	12	B3	88	2							•		
mms1	*SPAC3H8.05c*	2543633	11	A7	44	4		78	1				•		
mok11	*SPAC1527.01*	3361410	9	E12				63	5						
mpg2	*SPBC13G1.02*	2539751	9	E9				40	5					•	•
mpn1	*SPAC23C11.10*	2542061	1	G2	43	2		57	6				•	•	
mre11	*SPAC13C5.07*	2542757	4	H10	100	4		71	1				•	•	•
msy1	*SPCC1183.11*	2539051	13	A12				38	5						
mug132	*SPAC11G7.06c*	2543018	16	B5	86	2							•		
mug81	*SPBC13G1.10c*	2539673	10	A4				40	5				•	•	•
myo1	*SPBC146.13c*	2539659	12	G6	100	2	•						•	•	
naa30	*SPBC15D4.06*	2539835	2	G6				57	6				•	•	•
nab3	*SPAC3H8.09c*	2543638	13	E9	90	2		44	2				•		
nif1	*SPBC23G7.04c*	2540468	12	B8				100	5				•		
oxa102	*SPBP4H10.03*	2539811	4	B2				40	7				•	•	
pac10	*SPAC3H8.07c*	2543378	10	A11				100	7	•	50	4	•	•	•
pcr1	*SPAC21E11.03c*	2542047	24	D7							40	3	•	•	•
pep3	*SPCC790.02*	2539053	29	A1	100	4		100	1				•	•	•
pex5	*SPBC725.07*	2541112	16	D3				40	5				•	•	•
pfd1	*SPBC1D7.01*	2540765	10	A6				100	7	•			•	•	
php5	*SPBC3B8.02*	2540133	16	H7	43	3	•						•	•	•

Continued on next page

Table A.2 – continued from previous page

Name	GenomeID	EntrezID	Plate	Well	Hit (%)	Cluster	Visual	Hit (%)	Cluster	Visual	Hit (%)	Cluster	*S. cerevisiae*	Vertebrates	Humans
pit1	*SPAC3C7.06c*	2543071	13	D9	67	1							•	•	
pka1	*SPBC106.10*	2539781	7	G1	71	2		50	1				•	•	•
pmp3	*SPBC713.11c*	2541129	8	F6							40	3	•		
pmt1	*SPBC19C2.02*	2540766	32	A10	44	4		44	8					•	•
png1	*SPAC3G9.08*	2543454	6	H4	100	2	•	50	1	•			•	•	
pof3	*SPCC338.16*	2539527	12	D11	90	4	•	70	1	•			•	•	
pom1	*SPAC2F7.03c*	2541889	13	B4	50	2					63	4		•	•
pop3	*SPBC21B10.05c*	2540645	7	C9	88	2		100	6		43	2	•	•	•
ppk13	*SPAC3H1.13*	2543440	6	D5				40	5				•	•	•
ppk26	*SPBC336.14c*	2540231	8	B2	67	2							•	•	•
pub1	*SPAC11G7.02*	2541818	4	F9	89	2	•						•	•	•
pxa1	*SPAC5D6.07c*	2541884	21	F2							50	3	•	•	
qcr6	*SPBC16C6.08c*	2540140	16	D7				38	5				•	•	•
rad50	*SPAC1556.01c*	2541635	13	H1	88	4	•	83	1	•			•	•	•
rad51	*SPAC644.14c*	2543580	6	C8				44	1	•			•	•	•
rad55	*SPAC3C7.03c*	2543685	19	G3	80	4	•	100	1	•			•	•	
rad57	*SPAC20H4.07*	2542007	3	E5	89	2							•	•	•
ral2	*SPBC21.05c*	2540760	15	D2	100	2	•						•		
rdh54	*SPAC22F3.03c*	2541798	5	F8				100	7				•	•	•
red1	*SPAC1006.03c*	2543254	11	G10				38	5					•	
rep1	*SPBC2D10.06*	2540433	3	H11							50	1	•	•	
rep2	*SPBC2F12.11c*	2540341	7	A12	80	4		75	1				•	•	
rga2	*SPAC26A3.09c*	2542682	13	E7	78	4							•	•	•
rpl1702	*SPCC364.03*	2539013	28	B4	50	3							•	•	•
rpl2102	*SPAC959.08*	2543337	30	H7	43	2							•	•	•
rpl3001	*SPAC9G1.03c*	2542848	10	G11				60	1				•	•	
rpl3702	*SPCC1223.05c*	2538715	8	D11				40	5	•			•	•	•
rpl502	*SPBC11C11.09c*	2539680	21	B12							38	2	•	•	•
rpl801	*SPAC1F7.13c*	5802952	28	A5				40	1		50	2	•	•	•
rpl901	*SPAC4G9.16c*	2543380	26	E3	100	2							•	•	•
rpn10	*SPAC637.10c*	2543682	18	B1	44	2		43	5				•	•	•
rps1002	*SPBP22H7.08*	3361259	2	D12	40	3	•	56	1				•	•	•
rps1701	*SPBC839.05c*	2541229	24	G4	38	1							•	•	•
rps1702	*SPCC24B10.09*	2539331	4	G3							60	2	•	•	•
rps2201	*SPAC22A12.04c*	2541838	31	F2	45	3							•	•	•
rrf1	*SPBC1709.09*	2540194	10	E5				60	6				•	•	
rrp2	*SPBC23E6.02*	2540464	9	F9				40	5				•	•	
rsc4	*SPBC1734.15*	2539999	30	E11	43	5		86	2				•	•	•
rtr1	*SPAC23A1.16c*	2542005	27	A12	100	4							•	•	•
rxt2	*SPBC428.06c*	2540689	30	F6	60	4		75	1				•		
ryh1	*SPAC4C5.02c*	2543529	23	H5				57	6				•	•	•
sal3	*SPCC1840.03*	2539387	15	G10	100	4	•	100	1				•	•	•
sat1	*SPBC23E6.08*	2540531	7	G9				43	6				•	•	•
sbh1	*SPBC2G2.03c*	2540282	28	B9	89	4		75	1				•	•	
scd2	*SPAC22H10.07*	2541726	5	F9	63	2	•						•		
sce3	*SPBC18H10.04c*	2540528	4	H5	75	5		38	8				•	•	•
sco1	*SPBC119.06*	2539826	7	C2				50	6				•	•	•
sec2302	*SPBC776.04*	2541164	29	C6	67	4	•						•	•	•
sep11	*SPAC5D6.05*	2541925	19	B5	100	4	•	100	1	•			•	•	
ser2	*SPBC3H7.07c*	2540968	10	A12				40	8				•	•	•
set1	*SPCC306.04c*	2538762	11	G9	75	4		63	8				•	•	•
sft1	*SPAC31A2.13c*	2542585	25	C11	100	2	•						•		
sgf29	*SPBC1921.07c*	2540787	24	B9	43	1							•	•	
shd1	*SPAC16E8.01*	2542338	26	C6	100	2							•		
sin1	*SPAPYUG7.02c*	2542972	14	H10	100	2		100	6				•	•	
slx9	*SPAPB21F2.03*	2543463	2	A5				50	7				•		

Continued on next page

Table A.2 – continued from previous page

Name	GenomeID	EntrezID	Plate	Well	Hit (%)	Cluster	Visual	Hit (%)	Cluster	Visual	Hit (%)	Cluster	*S. cerevisiae*	Vertebrates	Humans
snz1	*SPAC29B12.04*	2542689	25	A8				57	5		100	2	•		
sol1	*SPBC30B4.04c*	2540318	15	D4				38	5				•		
spf1	*SPCC594.05c*	2539023	20	D9	50	4		73	1				•	•	
spo7	*SPAC6G9.04*	2541456	6	D9				40	5				•	•	
srs2	*SPAC4H3.05*	2543577	29	E1	40	5							•	•	
ssa1	*SPAC13G7.02c*	2542875	11	G11				40	5				•	•	
sts1	*SPAC20G4.07c*	2541740	18	C11				50	6				•	•	
swd1	*SPAC23H3.05c*	2541776	19	G2	75	4	•	80	8				•	•	•
tdh1	*SPBC32F12.11*	2540547	19	B10				40	6				•	•	•
tea1	*SPCC1223.06*	2539047	8	F11	38	3		50	4	•			•	•	•
tea2	*SPBC1604.20c*	2539857	24	A2	57	3	•	100	2	•			•	•	•
tea3	*SPAC6G10.02c*	2542619	13	E6	80	1							•	•	
tea4	*SPBC1706.01*	2539642	12	F7				60	2				•		
tel1	*SPCC23B6.03c*	2539209	10	C5				38	5				•	•	•
tip1	*SPAC3C7.12*	2543044	6	A4				100	2	•			•	•	
tlg2	*SPAC823.05c*	2543436	23	F12				67	6				•	•	•
tom7	*SPBC27B12.10c*	2540502	31	B7	60	2	•	60	6	•			•	•	
trm112	*SPAC31A2.02*	2541708	1	E3	100	1	•				40	1	•	•	•
trp1322	*SPCC1322.03*	2539071	12	G10	38	2		80	3		50	2			
tsf1	*SPBC800.07c*	2540692	28	F7				80	7					•	•
tup11	*SPAC18B11.10*	2542299	16	E2				50	8				•		
tup12	*SPAC630.14c*	2543402	19	E5	100	5		88	1				•		
twf1	*SPCC126.06*	2539064	8	A12							43	1	•	•	•
ubi1	*SPAC11G7.04*	2541768	23	A9	57	2		67	1				•	•	•
ulp2	*SPAC17A5.07c*	2542268	20	D11				38	5				•	•	•
upf1	*SPAC16C9.06c*	2542327	5	E1	40	5							•	•	•
upf3	*SPAC13G7.03*	2542908	1	G7				38	8				•	•	•
ura3	*SPAC57A10.12c*	2542781	13	A10	63	2							•	•	•
vac7	*SPBP8B7.13*	2541367	33	A5	89	2							•		
vps1	*SPAC767.01c*	2542724	10	B7				43	3				•	•	
vps16	*SPAC824.05*	2541533	29	D2	90	4		83	1				•	•	•
vps25	*SPBC4B4.06*	2540828	2	B11	80	2		50	6				•	•	•
vps32	*SPAC1142.07c*	2542922	20	E10	100	2		50	4				•	•	•
vps36	*SPBC3B9.09*	2540981	17	C8	64	2		43	5				•	•	•
vps66	*SPAC1783.02c*	2542362	24	F7				63	6	•	63	1	•	•	
wis1	*SPBC409.07c*	2541055	16	F2	67	2		38	2				•	•	•
yox1	*SPBC21B10.13c*	2540309	10	B2				40	1				•	•	
ypa1	*SPAC4F10.04*	2543619	32	H11	100	2		100	1				•	•	
ypa2	*SPAC1782.05*	2542349	5	H1	38	2	•						•	•	•
zds1	*SPAC31F12.01*	2543190	31	G10	50	1							•		
zfs1	*SPBC1718.07c*	2539958	25	F2	36	1		64	5				•	•	•
zip1	*SPAC25G10.03*	2542707	5	G11							40	2	•		
	SPAC12B10.10	2543030	22	G2				44	1				•		
	SPAC14C4.10c	2541421	25	F9	43	2								•	
	SPAC15E1.02c	2542758	20	C11				43	5						
	SPAC1610.02c	3361520	26	A6	38	2		75	6		50	2	•	•	
	SPAC1687.08	2542803	28	A7				38	5				•		
	SPAC16E8.08	2542328	1	G8	57	1							•		
	SPAC1F3.03	2542372	28	C10	56	2		60	6				•	•	
	SPAC1F5.05c	2541432	29	C9	78	2							•	•	
	SPAC227.10	2541498	5	C8				100	7				•	•	•
	SPAC227.17c	2541488	29	A7	56	2	•	50	6	•			•		
	SPAC22H10.11c	2541730	14	D6				75	1				•		
	SPAC27D7.06	2542075	3	F6	67	4		80	1				•	•	•
	SPAC27E2.03c	2541434	6	A1				40	3				•	•	
	SPAC30.02c	2542458	11	C4	78	4		57	1				•	•	•

Continued on next page

Table A.2 – continued from previous page

Name	GenomeID	EntrezID	Plate	Well	Hit (%)	Cluster	Visual	Hit (%)	Cluster	Visual	Hit (%)	Cluster	*S. cerevisiae*	Vertebrates	Humans
	SPAC323.05c	2542476	18	A6	38	1	•						•	•	•
	SPAC328.04	2543208	6	D2	44	2							•	•	•
	SPAC343.20	2543162	1	F3				40	6				•		
	SPAC3A11.13	2543106	24	F8							40	3	•	•	•
	SPAC3A12.13c	2543108	26	B10	70	2							•	•	
	SPAC3F10.17	2541634	32	C3	43	3		43	1				•	•	•
	SPAC4G8.07c	2543535	19	D4				40	3				•	•	
	SPAC589.09	2542218	6	F7				50	5				•	•	•
	SPAC5H10.04	2541543	20	E8				38	5				•		
	SPAC5H10.09c	2542731	19	C5				38	5				•		
	SPAC630.10	2543414	27	B5	43	5		100	1				•	•	
	SPAC664.03	2543560	31	D10	100	4		71	8	•			•	•	•
	SPAC6C3.08	2542919	9	D12				38	6				•	•	•
	SPAC6G9.14	2542056	10	G5	80	2		43	3				•	•	
	SPAC823.10c	2543361	11	B4				40	6		44	2	•	•	•
	SPAC890.05	2543532	19	A6				43	5				•	•	•
	SPAC8C9.19	5802920	2	A3	89	2		50	6	•	50	1	•		
	SPAP14E8.02	2542021	30	A10	78	2							•		
	SPAPB1A10.08	2543374	32	G4				50	7				•		
	SPBC106.07c	2540058	28	F11				57	6	•	50	1	•	•	
	SPBC1604.12	2539702	20	F8				38	8				•		
	SPBC16A3.10	2539940	16	E1				50	5				•	•	•
	SPBC16E9.15	2540124	2	D7				83	3	•				•	
	SPBC16G5.07c	2539877	14	G12	56	4		100	8					•	•
	SPBC1734.07c	2539876	10	A2				50	5				•	•	•
	SPBC17A3.05c	2540130	15	D1	100	4		100	1					•	•
	SPBC1861.05	2539763	7	H6				60	6	•					
	SPBC18H10.07	2540647	2	C8	70	4	•	43	8					•	
	SPBC19C2.10	2540758	7	C7	100	1								•	•
	SPBC19F8.03c	2540702	11	B1	36	1							•	•	•
	SPBC20F10.07	2540703	19	A9				40	3				•	•	•
	SPBC25B2.08	2540628	30	E12	60	2							•		
	SPBC25H2.15	2540619	19	E9	44	3							•	•	•
	SPBC29A10.12	2540542	2	D9				50	3					•	•
	SPBC29A10.16c	2540533	28	A9				43	5				•	•	
	SPBC409.19c	2540958	10	E2	38	2							•	•	
	SPBC543.08	2540872	28	E7				50	1				•	•	
	SPBC685.03	2541090	22	D12				38	5				•		
	SPBC691.04	2541136	17	C9				63	4	•			•	•	
	SPBC8D2.12c	2541235	19	C11							38	2	•	•	•
	SPBP35G2.04c	2541288	26	A4	38	2							•		
	SPBP8B7.18c	2541373	12	C10				38	5				•		
	SPBPB7E8.01	2541357	15	H7							40	2	•		
	SPCC1450.03	2539316	23	H1	100	4	•	100	1	•			•	•	
	SPCC1672.04c	2538939	29	E6				50	5				•	•	•
	SPCC24B10.19c	2538907	13	D12				38	5				•		
	SPCC553.08c	2539293	10	C11	88	4	•	100	1	•			•	•	•
	SPCC584.11c	2538896	11	A10	67	2		71	6				•		
	SPCC645.12c	2538818	26	D9							50	3	•		
	SPCC965.06	2539573	9	B5	50	2		71	6					•	•

Table A.3: Hit FYPO annotations – As discussed in **Section 4.5.1** all hits were assigned a general FYPO annotation. In addition 129 more detailed assignments were made, as listed below.

GenomeID	Name	GenomeID	Name	GenomeID	Name	GenomeID	Name
CELL SHAPE PHENOTYPES							
FYPO:0000233 – long cytoplasmic microtubules							
SPCP1E11.06	*apl4*	*SPAC2F7.07c*	*cph2*	*SPAC31A2.11c*	*cuf1*	*SPAC29A4.20*	*elp3*
SPCC11E10.06c	*elp4*	*SPBC3H7.10*	*elp6*	*SPAC227.01c*	*erd1*	*SPCC790.02*	*pep3*
SPBC19C2.02	*pmt1*	*SPBP22H7.08*	*rps1002*	*SPBC2G2.03c*	*sbh1*	*SPAC5D6.05*	*sep11*
SPBC800.07c	*tsf1*	*SPAC824.05*	*vps16*	*SPAC30.02c*		*SPBC17A3.05c*	
SPCC1450.03							
FYPO:0001492 – long cytoplasmic microtubules							
SPAC13C5.07	*mre11*	*SPAC1556.01c*	*rad50*	*SPAC16C9.05*	*cph1*	*SPAC17A2.09c*	*csx1*
SPAC17G8.05	*med20*	*SPAC17H9.19c*	*cdt2*	*SPAC227.01c*	*erd1*	*SPAC23A1.16c*	*rtr1*
SPAC23H3.05c	*swd1*	*SPAC27D7.06*		*SPAC2F7.07c*	*cph2*	*SPAC30.02c*	
SPAC31A2.11c	*cuf1*	*SPAC3C7.03c*	*rad55*	*SPAC3G9.08*	*png1*	*SPAC3H8.05c*	*mms1*
SPAC4F10.04	*ypa1*	*SPAC5D6.05*	*sep11*	*SPAC664.03*		*SPAC824.05*	*vps16*
SPAPB1E7.02c	*mcl1*	*SPBC17A3.05c*		*SPBC21C3.02c*	*dep1*	*SPBC2G2.03c*	*sbh1*
SPBC3H7.10	*elp6*	*SPBC428.06c*	*rxt2*	*SPBC776.04*	*sec2302*	*SPCC11E10.06c*	*elp4*
SPCC1450.03		*SPCC1840.03*	*sal3*	*SPCC188.07*	*ccq1*	*SPCC306.04c*	*set1*
SPCC338.08	*ctp1*	*SPCC338.16*	*pof3*	*SPCC553.08c*		*SPCC594.05c*	*spf1*
SPCC790.02	*pep3*	*SPCC970.10c*	*brl2*	*SPCP1E11.06*	*apl4*		
FYPO:0002106 – viable stubby vegetative cell							
SPAC1142.07c	*vps32*	*SPAC11G7.02*	*pub1*	*SPAC1782.05*	*ypa2*	*SPAC22H10.07*	*scd2*
SPAC23H3.13c	*gpa2*	*SPAC26H5.05*	*mga2*	*SPAC31A2.13c*	*sft1*	*SPAC3A11.02*	*cps3*
SPAC4G9.16c	*rpl901*	*SPAC637.10c*	*rpn10*	*SPAC688.11*	*end4*	*SPAC8C9.19*	
SPBC146.13c	*myo1*	*SPBC19C2.10*		*SPBC21.05c*	*ral2*	*SPBC24C6.10c*	*dip1*
SPBC336.03	*efc25*	*SPBC336.14c*	*ppk26*	*SPBC36.04*	*cys11*	*SPCP1E11.05c*	*are2*
SPBC1604.20c	*tea2*	*SPBP22H7.08*	*rps1002*				
FYPO:0002380 – viable spheroid vegetative cell							
SPBC19C2.10							
FYPO:0002903 – viable pear-shaped vegetative cell							
SPAC11G7.02	*pub1*	*SPAC25H1.05*	*meu29*	*SPAC31A2.02*	*trm112*	*SPAC323.05c*	
SPAC688.11	*end4*	*SPBC19C2.10*		*SPBC336.03*	*efc25*	*SPBC36.04*	*cys11*
SPCC63.02c	*aah3*						
FYPO:0003595 – S-shaped cell							
SPAC17G8.05	*med20*	*SPAC17H9.19c*	*cdt2*	*SPAC23A1.16c*	*rtr1*	*SPAC2F7.07c*	*cph2*
SPAC5D6.05	*sep11*	*SPAC630.14c*	*tup12*	*SPAC824.05*	*vps16*	*SPBC17A3.05c*	
SPBC21C3.02c	*dep1*	*SPBC428.06c*	*rxt2*	*SPCC1450.03*		*SPCC1840.03*	*sal3*
SPCC553.08c		*SPCC790.02*	*pep3*	*SPCC970.10c*	*brl2*	*SPCP1E11.06*	*apl4*
MICROTUBULE PHENOTYPES							
FYPO:0002401 – microtubules present in greater numbers							
SPCP1E11.06	*apl4*	*SPAC17H9.19c*	*cdt2*	*SPAC2F7.07c*	*cph2*	*SPAC227.01c*	*erd1*
SPAC17G8.05	*med20*	*SPCC790.02*	*pep3*	*SPAC3G9.08*	*png1*	*SPBC21B10.05c*	*pop3*
SPBC428.06c	*rxt2*	*SPCC1840.03*	*sal3*	*SPBC2G2.03c*	*sbh1*	*SPAC5D6.05*	*sep11*
SPAPYUG7.02c	*sin1*	*SPAC23H3.05c*	*swd1*	*SPAC824.05*	*vps16*	*SPAC4F10.04*	*ypa1*
SPBC17A3.05c		*SPCC1450.03*					
FYPO:0002760 – short cytoplasmic microtubules							
SPBC1105.04c	*cbp1*	*SPBC16G5.15c*	*fkh2*	*SPAC18G6.15*	*mal3*	*SPBC1604.20c*	*tea2*
SPAC3C7.12	*tip1*	*SPCC1322.03*	*trp1322*	*SPCC584.11c*			

B Community Resource Images

"I'll give you a fiver if you can tell me what the hell it is,
'cause I haven't got the foggiest."
—ROSE TYLER (*Fear Her*, 2006)

Figures

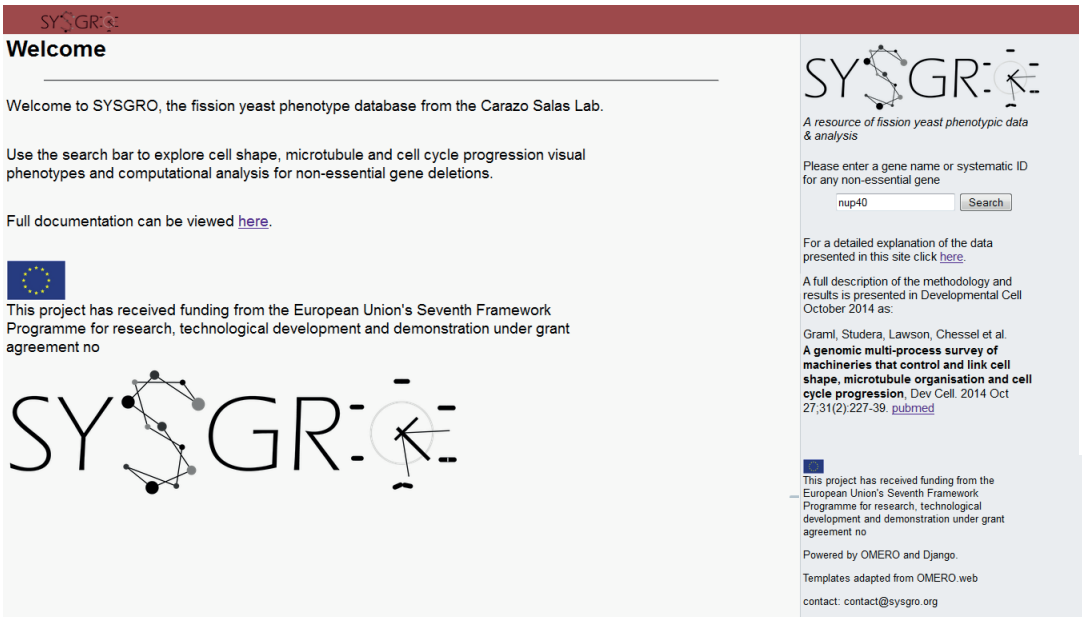

Figure B.1: SYSGRO homepage - Entry page for the SYSGRO website as accessed directly from the web. Tripartite page layout adapted by A. Chessel from OMERO templates. I created page layout and content using direct CSS & HTML programming, SYSGRO graphics created by me in Adobe Illustrator.

Csn2 (SPAPB17E12.04c)

find this gene on PomBase

COP9/signalosome complex subunit Csn2

Overview

Genes detected as hits are reported here, in each case the number of experimental repeats that were called a hit and the total number of repeats analysed are given.

Representative Images

Representative high-throughput Images of Csn2Δ atb2-GFP

Click images for full view. In viewer select 'show ROI' to highlight cells used for analysis.

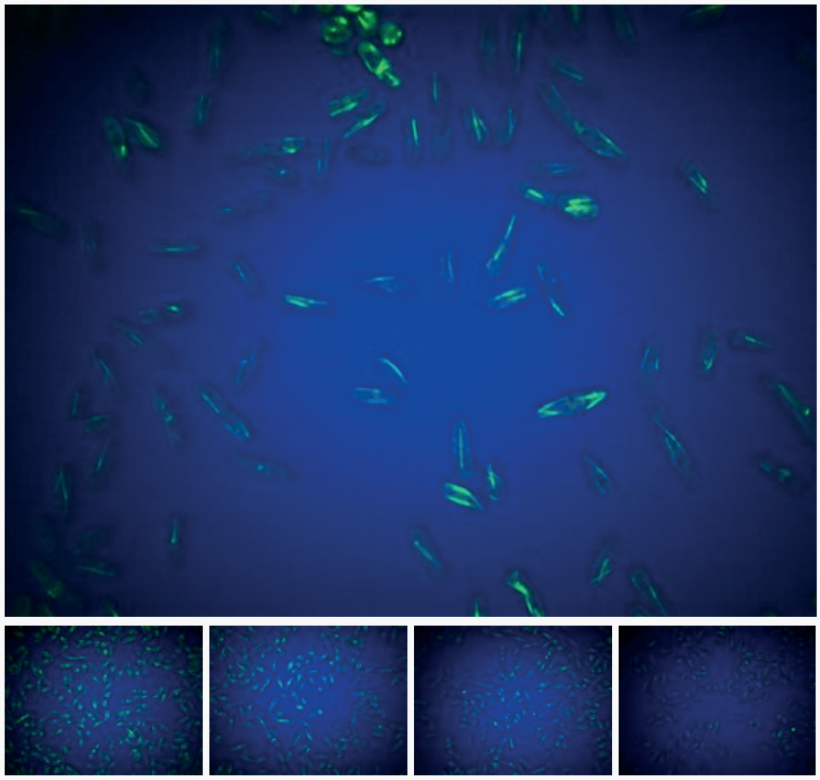

Screening Results

The results from phenotypic analysis of images as shown above. Reported hits are shown with ✔ and non-hits are shown with ✖

Genes may be called as cell shape and microtubule hits by one of two methods, a p-value based single feature method or a multiparametric profile based method. The results of each are given separately below. In all cases, the single feature with the lowest p-value is also given even when the method does not call a hit. For a full list of features please see the published article.

Cell Shape ✔

N	Hit?	Multiparametric	Single feature	Strongest feature
220	True	None	True	width, widthLeft, widthRight
68	True	None	True	width
149	True	None	True	width
137	True	None	True	width
166	True	None	True	width
34	None	None	None	width
176	True	None	True	width
53	None	None	None	width

Figure B.2: Continued on next page...

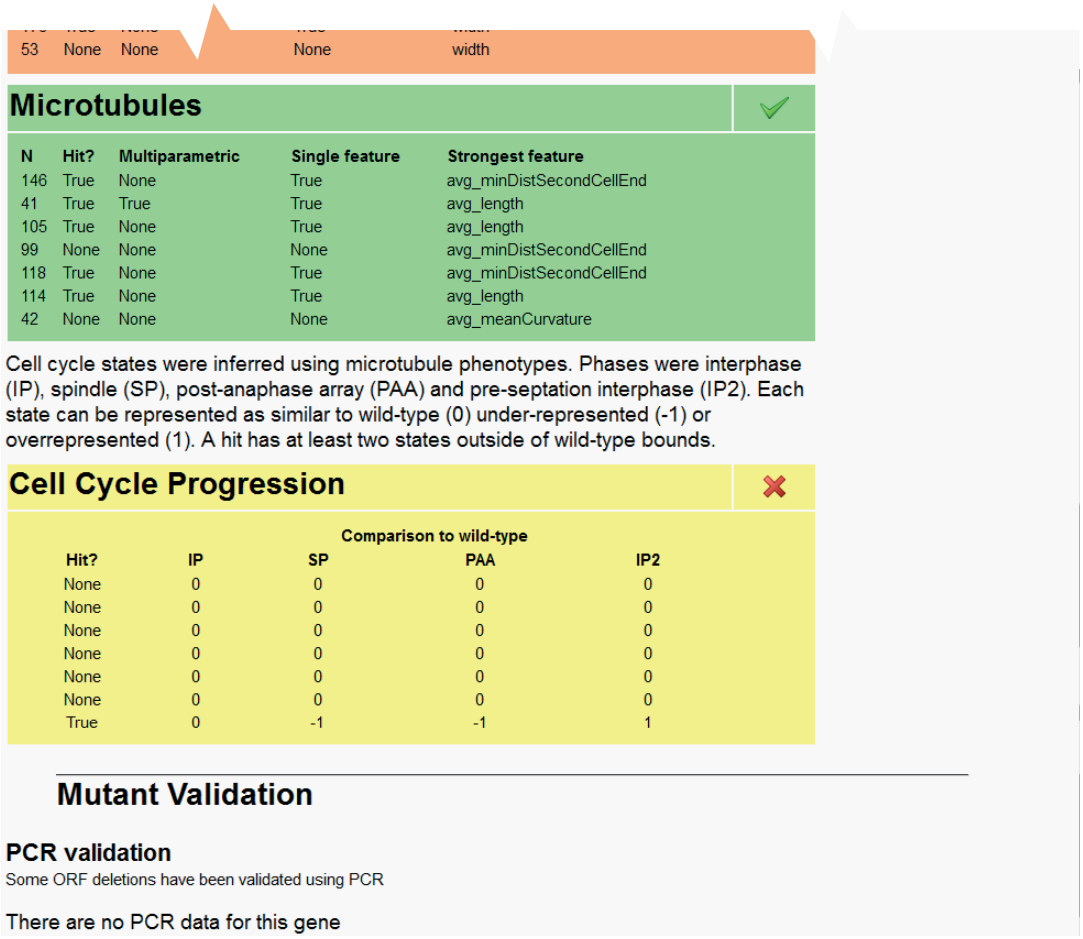

53	None	None	None	width

Microtubules

N	Hit?	Multiparametric	Single feature	Strongest feature
146	True	None	True	avg_minDistSecondCellEnd
41	True	True	True	avg_length
105	True	None	True	avg_length
99	None	None	None	avg_minDistSecondCellEnd
118	True	None	True	avg_minDistSecondCellEnd
114	True	None	True	avg_length
42	None	None	None	avg_meanCurvature

Cell cycle states were inferred using microtubule phenotypes. Phases were interphase (IP), spindle (SP), post-anaphase array (PAA) and pre-septation interphase (IP2). Each state can be represented as similar to wild-type (0) under-represented (-1) or overrepresented (1). A hit has at least two states outside of wild-type bounds.

Cell Cycle Progression

	Comparison to wild-type			
Hit?	IP	SP	PAA	IP2
None	0	0	0	0
None	0	0	0	0
None	0	0	0	0
None	0	0	0	0
None	0	0	0	0
None	0	0	0	0
True	0	-1	-1	1

Mutant Validation

PCR validation

Some ORF deletions have been validated using PCR

There are no PCR data for this gene

Figure B.2: SYSGRO hit page - Continued from previous page. Example page for a gene that is a hit in Graml et al. (2014). Contributions as in **Figure B.1**, data extracted from database and integrated into layout by A. Chessel. Images handled by OMERO.

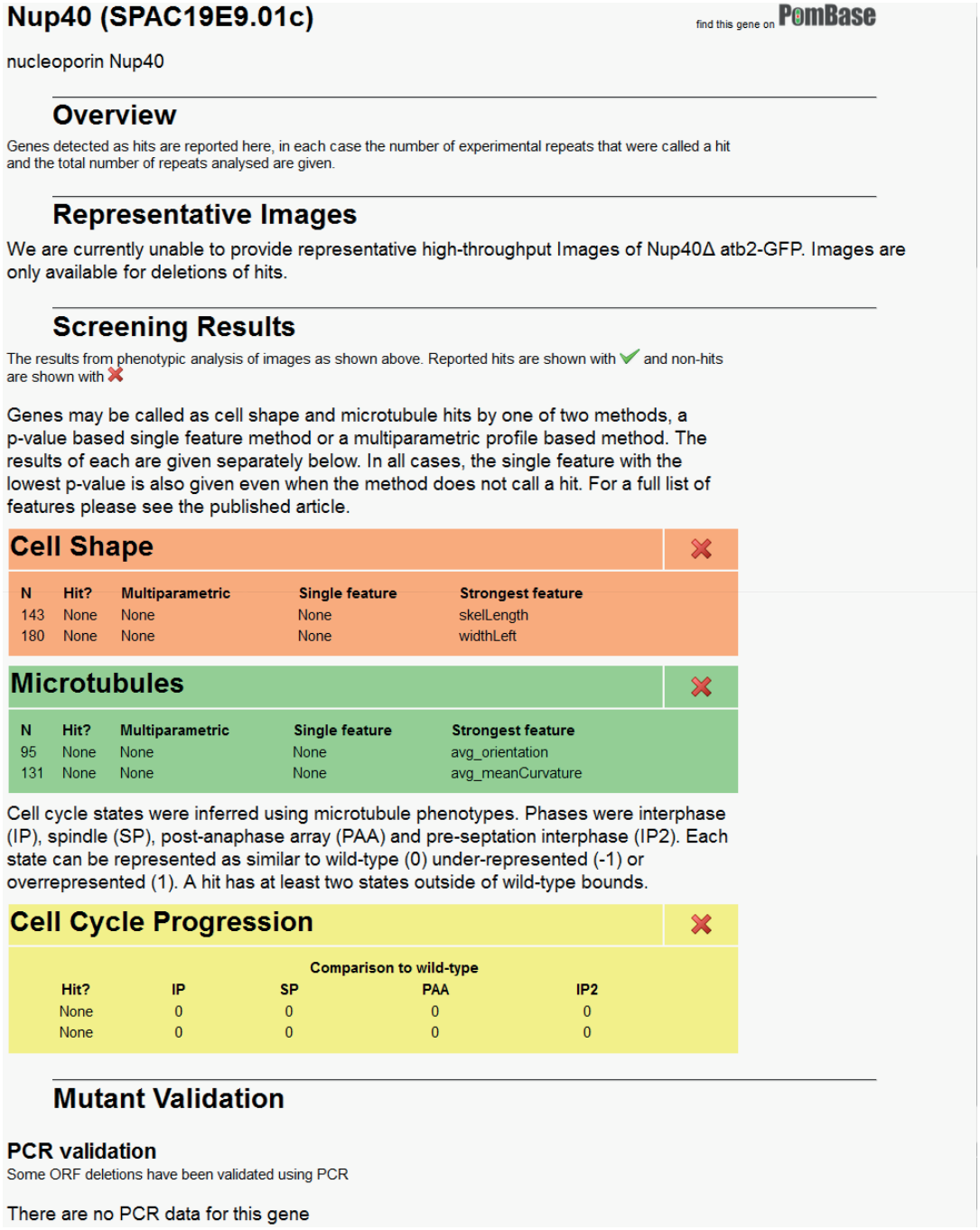

Nup40 (SPAC19E9.01c)

find this gene on PomBase

nucleoporin Nup40

Overview

Genes detected as hits are reported here, in each case the number of experimental repeats that were called a hit and the total number of repeats analysed are given.

Representative Images

We are currently unable to provide representative high-throughput Images of Nup40Δ atb2-GFP. Images are only available for deletions of hits.

Screening Results

The results from phenotypic analysis of images as shown above. Reported hits are shown with ✔ and non-hits are shown with ✖

Genes may be called as cell shape and microtubule hits by one of two methods, a p-value based single feature method or a multiparametric profile based method. The results of each are given separately below. In all cases, the single feature with the lowest p-value is also given even when the method does not call a hit. For a full list of features please see the published article.

Cell Shape ✖

N	Hit?	Multiparametric	Single feature	Strongest feature
143	None	None	None	skelLength
180	None	None	None	widthLeft

Microtubules ✖

N	Hit?	Multiparametric	Single feature	Strongest feature
95	None	None	None	avg_orientation
131	None	None	None	avg_meanCurvature

Cell cycle states were inferred using microtubule phenotypes. Phases were interphase (IP), spindle (SP), post-anaphase array (PAA) and pre-septation interphase (IP2). Each state can be represented as similar to wild-type (0) under-represented (-1) or overrepresented (1). A hit has at least two states outside of wild-type bounds.

Cell Cycle Progression ✖

	Comparison to wild-type			
Hit?	IP	SP	PAA	IP2
None	0	0	0	0
None	0	0	0	0

Mutant Validation

PCR validation

Some ORF deletions have been validated using PCR

There are no PCR data for this gene

Figure B.3: SYSGRO non-hit page - Example page for a gene that is not a hit in Graml et al. (2014) but that is present in the KO library. Contributions as in **Figure B.1**, data extracted from database and integrated into layout by A. Chessel.

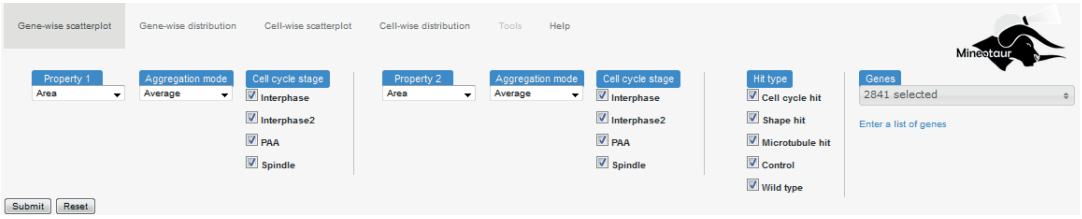

Figure B.4: Mineotaur options page - Demo landing page for Mineotaur datamining tool, providing options on which graphs to plot, data to use and filters to apply. Developed and implemented by B. Antal, with contribution of graphics from myself.

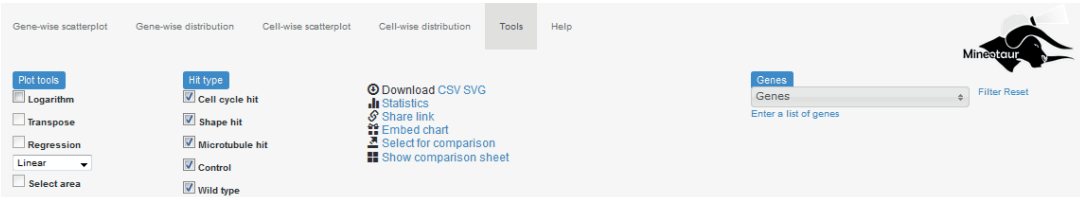

Figure B.5: Mineotaur graph menus - Page header bar for Mineotaur datamining tool demo, providing options on adjustments/additions to plotted graphs and means to extract graphs or raw data for use in other contexts. Contributions as in **Figure B.4**.

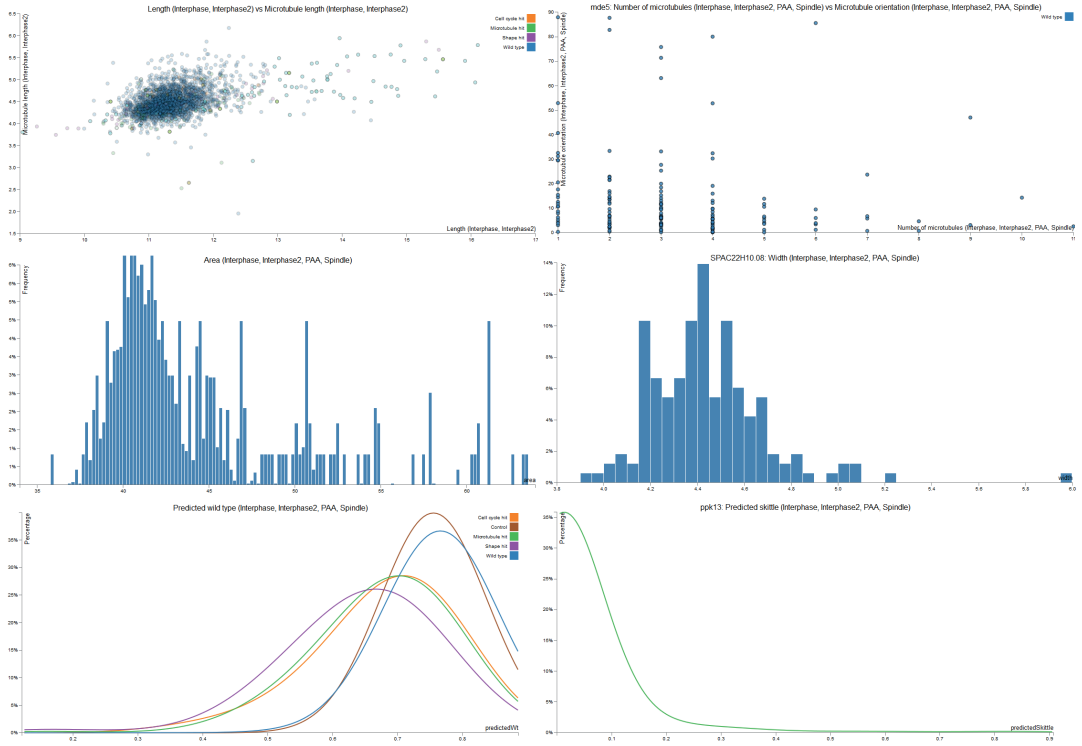

Figure B.6: Mineotaur graphs - Example graphs generated using screening data from **Chapter A**. Graphs on the left show the population data for each strain as a single data point (gene-wise). Graphs on the right plot each cell individually for one mutant strain. Mineotaur is capable of scatter plots (top), histograms (middle) and kernel density plots (bottom). Contributions as in **Figure B.4**.

C Publications

"Is there a word for total screaming genius that sounds modest and just a tiny bit sexy?"
—CLARA OSWALD (*Asylum of the Daleks*, 2012)

Papers

1736 Biochemical Society Transactions (2013) Volume 41, part 6

Microtubules: greater than the sum of the parts

Jonathan L.D. Lawson* **and Rafael E. Carazo Salas*[1]**
*The Gurdon Institute, University of Cambridge, Tennis Court Road, Cambridge CB2 1QN, U.K.

Abstract

The post-genomic era has produced a variety of new investigation technologies, techniques and approaches that may offer exciting insights into many long-standing questions of scientific research. The microtubule cytoskeleton is a highly conserved system that shows a high degree of internal complexity, is known to be integral to many cell systems and functions on a fundamental level. After decades of study, much is still unknown about microtubules *in vivo* from the control of dynamics in living cells to their responses to environmental changes and responses to other cellular processes. In the present article, we examine some outstanding questions in the microtubule field and propose a combination of emerging interdisciplinary approaches, i.e. high-throughput functional genomics techniques, quantitative and super-resolution microscopy, and *in silico* modelling, that could shed light on the systemic regulation of microtubules in cells by networks of regulatory factors. We propose that such an integrative approach is key to elucidate the function of the microtubule cytoskeleton as a complete responsive integral biological system.

Introduction: what was the question?

The post-genomic era has greatly expanded our knowledge of biology and has generated a host of new fields and technologies, permitting a holistic approach to study spatiotemporal control in biological systems [1]. Microtubules are highly multifunctional structural components of eukaryotic cells, directing and controlling cell motility, intracellular transport and chromosome segregation [2]. A considerable body of research over the last four decades has characterized numerous microtubule-regulating molecules across eukaryotes [3,4], yet the systemic and physiological aspects of microtubules in cells, such as how factors compete or collaborate to control microtubule dynamics and how they cross-regulate and co-ordinate with cell context, are still largely unexplained even in simple cell types. In the present article, we examine some outstanding questions and suggest how recent advances may help to address them.

Microtubule structure and polymerization

Microtubules are structurally complex. Each polymer forms from the reversible association of tubulin heterodimers, arranged in a pseudohelix of 13 laterally associated linear protofilaments with a longitudinal seam [4,5]. Other protofilament numbers occur *in vitro* [4] and rarely *in vivo* [6], although this is detrimental to transport functions, forcing cargo to follow unfavourable helical paths through the cytoplasm or skip between protofilaments [7,8]. Microtubules stochastically alternate between growth (polymerization) and shrinkage (depolymerization) phases, with 'plus' ends more active than 'minus' ends, a property dubbed 'dynamic instability' [9]. This property permits sampling of three-dimensional space, allowing microtubules to efficiently capture intracellular targets, such as mitotic kinetochores [10]. Dynamic instability is controlled by binding, hydrolysis and exchange of GTP by β-tubulin; tubulin-GTP favours polymerization, which activates GTP hydrolysis [11]. Hence GTP hydrolysis follows polymerization, causing most dimers in a tubule to be conformationally strained; a proposed 'GTP-cap' [12] maintains stability. Loss of the cap causes a switch to rapid depolymerization ('catastrophe'). A 'tubulin sheet' may also contribute to dynamics, as dimers polymerize on a flat sheet followed by tube closure. Catastrophe then occurs when the microtubule end closes [13]. The actual relevance of these physicochemical models *in vivo* remains largely unknown and unobserved. Similarly, although microtubule 'rescue' (recovery from shrinkage to growth) can occur, the mechanism that causes it remains unclear; some studies suggest that lattice discontinuities, where GTP hydrolysis has not occurred, may be required [14,15]. In general, the mechanistic basis of dynamic instability remains to be fully elucidated (Figure 1).

Regulation of microtubules in cells: the reductionist view

Although intrinsic physicochemical properties probably explain much of the dynamics, pattern and function of microtubules in cells, *in vivo* microtubule number, average length, connectivity and localization are thought to be modulated mostly by additional factors (Figure 2).

Nucleators control microtubule number and localization

Nucleators are highly conserved regulators of microtubule minus ends that either provide or activate a template

Key words: cytoskeleton, microtubule, post-genomic era, systems biology.
Abbreviations used: MAP, microtubule-associated protein; MTOC, microtubule-organizing centre; PTM, post-translational modification; +TIP, plus-end-tracking protein.
[1]To whom correspondence should be addressed (email cre20@cam.ac.uk).

Biochem. Soc. Trans. (2013) 41, 1736–1744; doi:10.1042/BST20130239

Figure 1 | **Outstanding questions in microtubule biology**

Many questions relating to microtubules in different contexts exist; however, most of them can be traced back to a few basic questions of *in vivo* dynamic instability and direct interactions with microtubule regulating factors. Generally, these consist of understanding microtubule nucleation, roles and functions of other 'satellite' factors, the microtubule rescue and paused states, understanding the structural aspects of the microtubule plus end, the mechanism of action of microtubule-severing factors and the responsiveness of the microtubule network as a whole to extrinsic cues. We show some of the possible, and potentially complementary, models that have been proposed to explain these features. References cited: Bouissou 2009 [15], Chretien 1995 [13], Cleveland 1981 [47], Dammermann 2003 [19], Dimitrov 2008 [14], Drechsel 1994 [12], Erickson and Stoffler 1996 [18], Hammond 2008 [57], Roll-Mecak 2010 [32], Samejima 2005 [21], Wiese 2006 [20], Zheng 1995 [16].

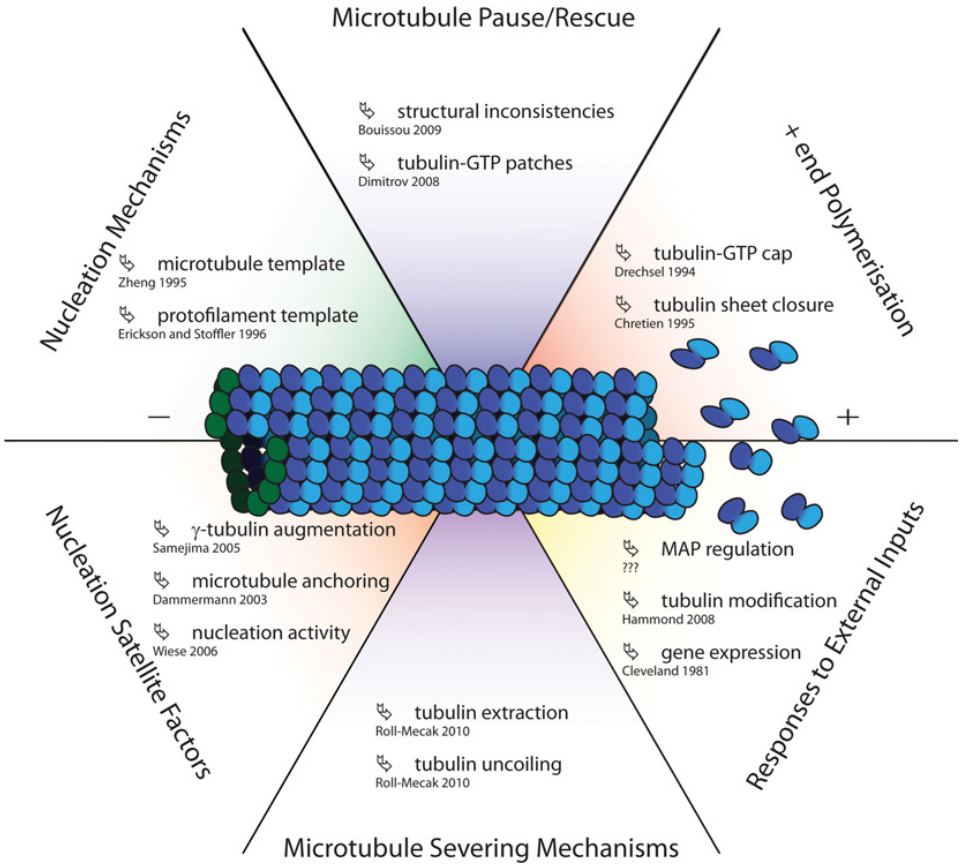

for protofilament organization. The most prominent is γ-tubulin [16–18], which forms complexes [e.g. γ-TuRC (γ-tubulin ring complex) in animal cells] that are thought to seed the tubulin arrangement required for initiating polymerization *de novo*. Other factors (e.g. centrosomin or ninein [19–21]) influence nucleation position and microtubule anchoring. Most eukaryotic cells possess nucleator-rich MTOCs (microtubule-organizing centres), including the centrosome, which act as foci for microtubule array organization [22]. However, 'secondary' MTOCs also occur [19,23], allowing cells to seed diverse functional microtubule arrays.

Stabilizing and destabilizing factors regulate length

Microtubule-stabilizing and -destabilizing factors operate by altering microtubule integrity, particularly at plus ends, thereby indirectly regulating microtubule length. There are two main classes of stabilizers: those that permeate the microtubule lattice {'classical' MAP (microtubule-associated protein) family [4]} and those that act through specific interaction with the plus ends, +TIPs (plus-end-tracking proteins) {e.g. EB1/2/3 (end-binding protein 1/2/3) or CLIP170 (cytoplasmic linker protein 170) [3,4,24]}. Different parts of these proteins associate with the luminal and external

Figure 2 | The major groups of known microtubule regulators and their general functions

Although others may exist, it seems likely that all MAPs will fall into one of a small number of functional groups on the basis of the way they influence microtubule organization. These can generally be judged to interact synergistically, competitively or neutrally depending on whether they serve to increase tubulin polymerization (nucleators, stabilizers and chaperones), decrease polymerization (destabilizers and severers) or simply reposition polymers (motors and bundlers). Different members of these groups may act on microtubules at different levels, altering expression of tubulin genes, influencing protein turnover and affecting the formation of dimers or polymers, as well as the overall cellular microtubule array.

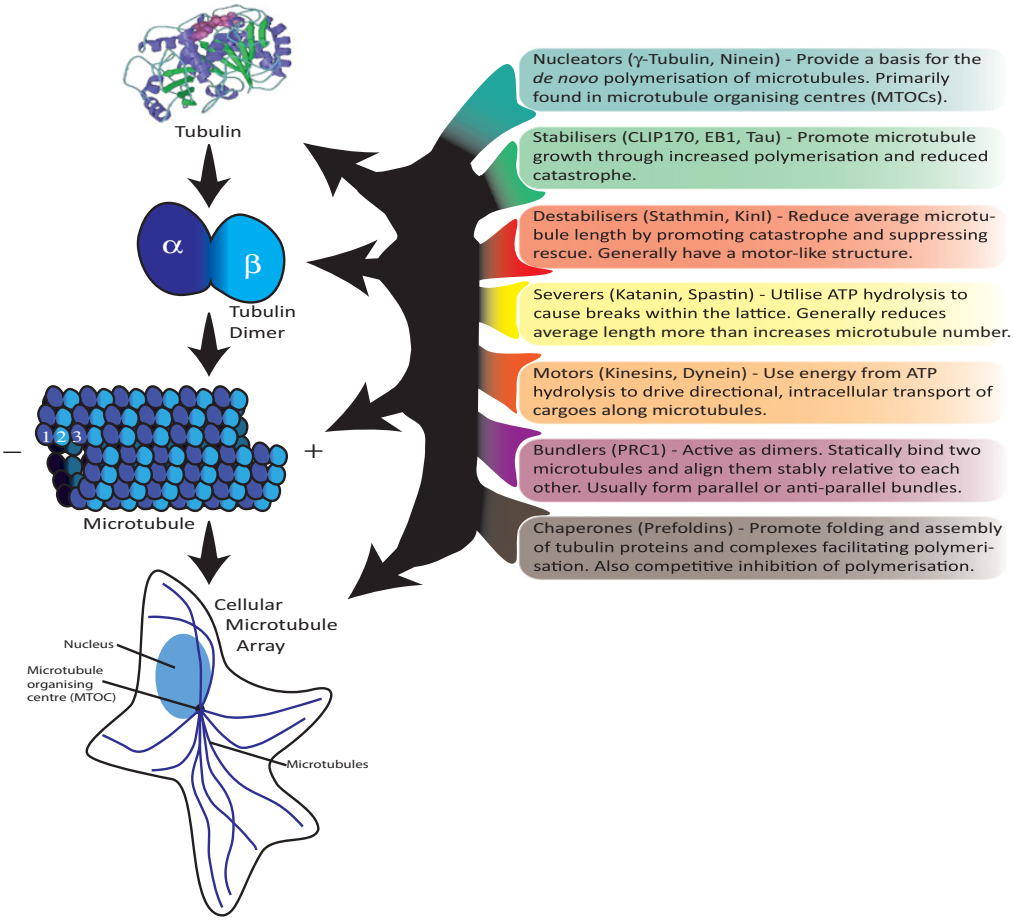

tubule faces, hence they probably co-assemble during polymerization and act from within. They have extended tails, which may affect microtubule spacing and cytoplasmic transport. +TIPs generally accumulate at polymerizing plus ends and undergo repeated cycles of association and dissociation as they track plus ends. Some utilize motor proteins (see below) for active delivery [25].

Microtubule destabilizers can induce catastrophe, in some cases (KinI) by inducing outward curvature of protofilaments through disruption of lateral associations [26–28]. Stathmin/Op18 [4,29] also induces catastrophe through protofilament bending. However, stathmin binding of free tubulin dimers occasionally permits it to promote polymerization.

Severing factors (katanin and spastin [30–32]) commonly destabilize microtubules by cutting microtubules in the middle of the lattice, creating two new microtubule ends. *In vitro*, this induces rapid catastrophe of the newly created plus end, lacking a GTP-cap, usually reducing microtubule length, but not microtubule number. The fate of severed microtubules in most systems remains unclear [32]. In rare cases, severing proteins may increase microtubule number, as reported in neurons [31,33].

The antagonism of stabilizers and destabilizers is necessary to permit global responses to intra- or extra-cellular inputs. For example, the stabilizer/destabilizer pair XMAP215/XKCM1, coupled to the cell cycle engine, approximates the microtubule dynamics seen in meiotic frog eggs [34].

Active and passive cross-linkers control microtubule pattern and localization

Microtubules can be relocated following nucleation by motor protein-mediated directional transport along cytoskeletal pathways. Kinesin motors [35] comprise 14 families (including KinI, above) with variable domain compositions and activities, but are typically dimeric and move unidirectionally, usually towards plus ends, with exceptions (Kin-14 kinesins are minus-end-directed). Dyneins comprise a second group of motors [35], remarkable for a higher processivity and favour rapid transit to minus ends. Dyneins are multiprotein complexes incorporating activity regulators (dynein light chains), microtubule associators ($p150^{glued}$ and $p135^{glued}$) and cargo interactors (Arp1 and dynamitin) [36]. Kinesins and dyneins may move microtubules relative to each other, thereby arranging the microtubule [37]. Motor-mediated transport is the basis of microtubule self-organization, an apparently universal mechanism of active microtubule patterning key to the robustness and plasticity of cellular structures, such as the mitotic spindle [37–39].

Bundler proteins form stable cross-links between adjacent microtubules, fixing them into specific relative positions [40]. Bundlers work closely with motor proteins to ensure proper arrangement of microtubules within cells and cellular domains. Most bundlers (e.g. Prc1/MAP65/Ase1 [41]), operate as dimers, binding two adjacent microtubules. This favours linear parallel or antiparallel arrays and imposes polarity on microtubule arrays. Co-operation or antagonism between motors and bundlers may also be a widespread mechanistic means to assemble specific microtubule structures [37,39,42].

Thus nucleators, stabilizers/destabilizers and cross-linkers constitute the biochemical arsenal employed by cells to pattern and modulate their microtubule behaviour, with each cell exploiting a specific recipe of regulatory factors suited to its needs.

Beyond reductionism: co-operation and consensus

Microtubule systems are much more than protein–protein interactions and dynamic instability. For example, microtubule-regulating proteins, especially tubulin itself, are subject to extensive convergent control through PTM (post-translational modification). Moreover, there are complex co-dependent ways in which these regulated proteins interact with each other, often in highly complex and dynamic systems needed to integrate several conflicting signals and generate a useful and concerted global response. This suggests that microtubule regulation is highly systemic and, that despite *in vitro* systems being informative about the function of specific regulators, understanding how microtubules are regulated in specific cell types may require non-classical means of investigation.

Regulating proteins: expression and epiproteomics

Controlling gene expression is often overlooked in the already complex study of microtubules. This has many facets; microtubules act as a cytoplasmic anchor for transcription factors, linking gene expression directly to microtubule dynamics [43–45]. Furthermore, it has been seen in 3T6 fibroblasts as well as in rat hepatocytes and enucleated mouse L929 cells that free tubulin suppresses its own synthesis post-transcriptionally [46–48]; this may help to maintain a near constant free tubulin concentration during polymerization, which could explain the necessity for additional factors *in vivo* to maintain dynamic instability. By contrast, in certain human cell lines such as Jurkat cells, it has been shown that the tubulin-binding protein stathmin/Op18 is able to stabilize tubulin mRNA [49], which may be an indirect effect for the sequestration of free tubulin by stathmin/Op18 binding. It should be noted that, although these processes are significant, the long timescale at which they take place is likely to render them negligible when considering regular microtubule dynamics or cell cycle transitions [50].

Other expression mechanisms are also known to influence tubulin levels and forms, including RNAi [51,52] and differential expression of tubulin isoforms [53], although little is known about the functional significance of different tubulins [54]. Furthermore, as may be expected, differentiation programs are also known to affect microtubule dynamics [55], with additional transcriptional influences hinted at in the results of phenotypic screens.

Most notably, microtubules are affected by the epiproteomics of tubulin; by analogy to the epigenetic histone code, this is the conglomerate effect of multiple PTMs on the proteins that make up microtubules [56,57]. PTMs of tubulin are extensive and complex [54,58,59]. Beyond the obvious phosphorylation, which is unusually rare on the already highly acidic tubulin, there are also examples of lysine acetylation [60–62], which seems to be associated with microtubule stability. Tubulin may be polyglutamylated or polyglycylated on glutamine residues, a complex and functionally poorly understood pair of competitive modifications [63,64], Most common is C-terminal tubulin modification, the initial and reversible loss of the terminal tyrosine [65] and the rarer successive irreversible removal of glutamate [66], both of which only affect polymerized tubulin.

The numerous enzymes required for these modifications are well known; of note is the role of the cell cycle kinase CDK1 (cyclin-dependent kinase 1) in phosphorylation [67] and histone modifiers HDAC6 (histone deacetylase 6) with Sirtuin2 in deacetylation [62,68], hinting at significant cross-talk between cell systems through PTMs. It should also be noted that known MAPs are subject to PTMs, especially phosphorylation in response to cell cycle [67,69,70] and environment sensing [71–74].

Combinatorial influence of factors and pathways on microtubules is unsurprising given the number of inputs they respond to on varied timescales. Whereas protein–protein interactions allow for rapid and continuous adaptation, PTMs provide a slower, but more consistent and rapidly reversible, intermediate that facilitates the easy integration of a great number of signals into one appropriate output. Meanwhile,

genetic regulation allows for long-term adaptation and specialization with targeted modification through RNAi and splicing modulation. Evolution of this highly complementary system ensures highly reliable control of microtubule organization despite its intrinsic unpredictability. With so much complexity, the necessity for a reductionist approach is clear and has provided good groundwork [4]; however, microtubules cannot simply be considered a sum of their parts, no matter how numerous.

Regulating the system: multiprotein complexes and consensus effects

Observation of labelled +TIPs show that they commonly form tightly knit clusters [3], with recent *in vivo* studies beginning to demonstrate that this permits rapid aggregation of activities into one consensus effect which rapidly responds to change [75,76]. Multifunctional particle activities range from anchoring to transport through microtubule regulation, self-regulation and localization, and growth regulation. This spatiofunctional coupling permits rapid responses to any number of inputs. The particles are thought to contain multiple and variable numbers of different proteins, which may be specific or stochastic, as has yet to be established. Some MAP clusters also seem to be self-organizing and maintain structure when deposited from a microtubule, as was recently observed in fission yeast (*Schizosaccharomyces pombe*) cells [77]. Structural study of MAPs indicates their propensity to co-associate in a relatively non-specific manner, necessary for clustering. Coiled-coil domains are prevalent in several groups of MAPs [3,78], suggesting protein–protein interaction [79]. Similarly, Kelch domain proteins incorporate a protein binding β-propeller [80], commonly associated with actin binding and cortical anchoring [80], but with suggested other roles too. Over 100 Kelch proteins, many with unknown functions, are thought to be encoded within the human genome.

Towards a holistic approach

Study of MAPs illustrates their co-dependence and extensive networks of interactions [3,4,75]. There is much evidence for this, ranging from co-localization of co-operative and competing factors, to analysis of protein–protein interaction motifs. In the present article, we have discussed aspects of microtubule regulation that are biologically relevant, but not immediately apparent from reductionist studies. Whereas there is some evidence for these, much is based upon hypothetical considerations. Consensus effects confound, confuse or conceal focused genetic studies as mutations may have seemingly little effect or may inadvertently affect numerous other factors. This is one of several elements that feed the discussion of indirect effects. To truly understand the components of microtubule regulatory complexes, we need ways to dissect their composite functions and identify specific roles, and furthermore we must understand their ever-changing individual states *in vivo*, including expression levels and epiproteomic state of modification. It is here that novel methods may be required.

From the parts to the whole: reconstructing the microtubule-regulatory network

A combination of classical investigations and three modern approaches seem particularly promising to advancing our understanding of the systemic regulation of microtubules *in vivo*. A few examples are detailed below (Figure 3).

Completing the parts lists

Decades of considerable work have identified diverse types of microtubule regulators, as detailed above. However, that 'parts' list is likely to be incomplete, and comprehensive knowledge is needed to address many outstanding questions and understand the clinical effects of microtubule perturbation. Although it is necessary to consider microtubule regulation as a whole, we must first identify all of the essential components.

High-throughput techniques have previously permitted thorough investigation of DNA and RNA expression and activity in a wide range of contexts. More recently, this has been extended to image-based and proteomic approaches, supported by computational analysis techniques, permitting more accurate and subtle feature detection, and pushing boundaries of our current technical capabilities [81,82]. Simultaneous study of a large number of gene localizations, mutant phenotypes, interactomes and environmental responses enables comprehensive rapid identification of new MAPs and begins the work of unveiling functional details. This all exists as an extension of genomic studies which provided complete lists of candidate gene products, and highlights the prevalence and significance of non-coding genes [83,84], which must logically also have roles in microtubule regulation.

One promising approach to identify novel factors is the use of microscopy-based high-throughput/high-content techniques as a way to systematically screen for outstanding regulators. Our laboratory (V.M. Graml, X.E. Studera, J.L.D. Lawson, A. Chessel, M. Geymonat, M. Bortfeld-Miller, T. Walter, L.J. Wagstaff, E. Piddini and R.E. Carazo Salas, unpublished work) has pioneered the development of such genome-wide screens looking for genes whose mutation affects microtubule organization, with preliminary results suggesting that hundreds of new possible microtubule-regulating genes are waiting to be investigated. Similar approaches to screen for genes whose disruption affect microtubule dynamics could be very important in the future to complete that 'parts list'. However, the speed of dynamic instability and need for extended filming currently puts this beyond common high-throughput approaches.

What the parts do and how they interact *in vivo*

Ideally, once we know which components are involved, a high-resolution visualization of their conformation and interactions live *in vivo* would make functional assignment easy. Currently, we can have extreme detail, through structural approaches from EM and X-ray crystallography, to more modern NMR and AFM approaches, but we cannot

Figure 3 | An overview of new approaches to holistic microtubule investigation

The future of microtubule investigation, in context within cells and in connection with other cellular systems, is dependent on some exciting new and emerging approaches to biological study. High-throughput studies, an extension of the genomic era, permit rapid identification of factors and inform on how they may bridge different pathways, but are vague on their roles and activity within the system. Super-resolution microscopy, coupled to synthetic fluorophores with photo-activatable/photoconvertible properties offer the ability to study protein interactions, positions and functionality, particularly with regard to the broad structural variation of the microtubule lattice *in vivo*, on a spatial and temporal scale that has not been previously possible. Finally, computer modelling is reaching the stage of being able to accurately simulate our understanding of live microtubule systems, providing an important sanity check on what we know and giving detailed feedback highlighting gaps in our understanding.

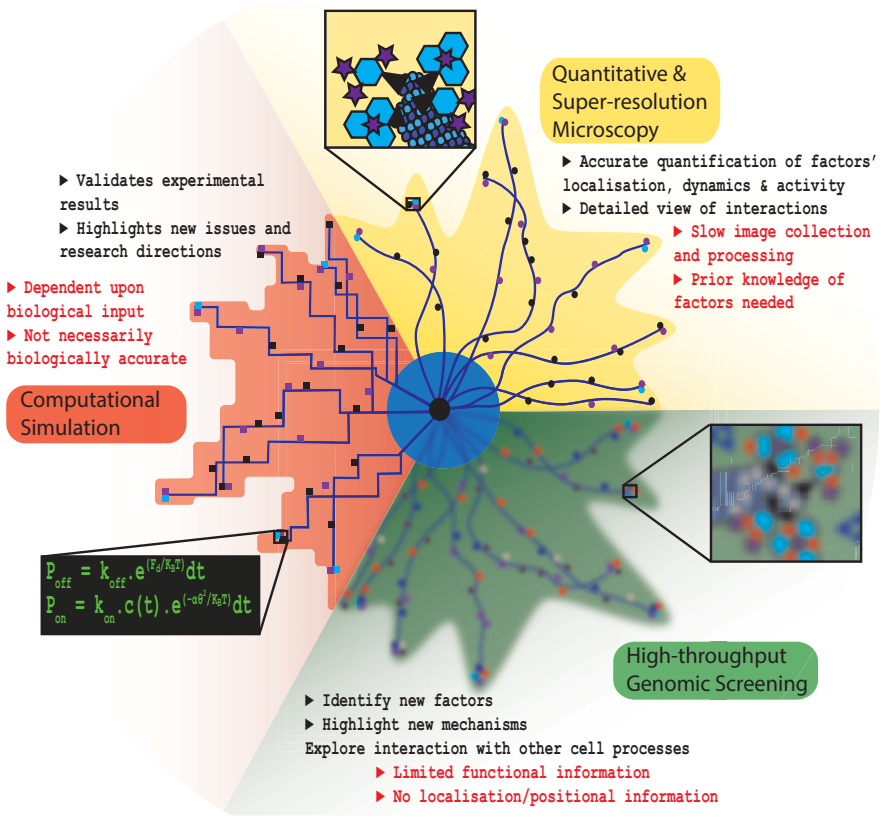

have it *in vivo*. Alternatively, we can have live imaging, but only to the resolution limits of light microscopy. Super-resolution imaging begins to offer a solution, using physical interference [SIM (structured illumination microscopy)] or computational interpolations [PALM (photo-activated localization microscopy)/STORM (stochastic optical reconstruction microscopy)] to visualize structures in the 10–100 nm range [85–87].

However, whereas super-resolution imaging is promising, it is currently time-consuming to collect sufficient images and requires extensive computational resources. This limits its usefulness in live systems [88,89], especially variable ones such as microtubules, which require rapid collection and processing of many images. Yet, with the current rate of technological progress, this may soon cease to be a limitation.

Furthermore, computational fitting allows atomic structures to be positioned into larger low-resolution images. With these techniques and enough processing power, we can envisage a complete atomic *in silico* approximation of whole organelles or even cells. This approach is highly dependent on guesswork and sufficient resolution and conformational details across several levels of investigation. These techniques are also highly dependent on newly developed fluorophores, particularly photoconvertible molecules, which themselves offer a wide range of new means of investigation [90–92].

The most promising aspect here is the potential to expand existing EM studies of the microtubule lattice [93] into dynamic study of live cells. Even with limited resolution, this offers many benefits for microtubule study. Most obviously, it may permit imaging of microtubule ends and the proposed tubulin sheet and tube closure [13]. We can then explore

structural features of other microtubule dynamic transitions and potentially elucidate the microtubule rescue and pause conformations.

Put your model where your mouth is

Improved computing power has been central to the groundwork and development of modern biological techniques. However, it also provides an important validation of our biological understanding, allowing us to create synthetic models based on what we know of the components and rules governing an organism. A model that poorly approximates life suggests that there is something important we are missing. Microtubule modelling has already proven highly effective with Cytosim [94,95]. As with many microtubule studies, this focuses on the highly conserved spindle structure, and shows a remarkably elegant system for bipolar spindle self-organization. Contrastingly, little work has been carried out to thoroughly probe the much more variable, but equally important, interphase arrays in different cellular contexts. Addressing this depends strongly on the modern techniques outlined above and will be validated by the capacity to accurately model different arrays *in silico*.

Outlook

We have aimed to highlight the outstanding questions in microtubule study, mention novel techniques that may be relevant and how they may be applied to providing a detailed and thorough image of microtubule regulation throughout the cell cycle and in different biological contexts. Microtubule biology is at a key stage and it seems to simply be a matter of time before we are able to rigorously identify MAPs, provide mechanistic details of their actions *in vivo* and ultimately demonstrate the elegant complexity of microtubule regulation that permits it to be so ubiquitous and multifunctional in eukaryotic life.

Acknowledgement

We thank M. Geymonat for carefully reading the paper before submission.

Funding

J.L.D.L. was supported by a Wellcome Trust Ph.D. studentship and R.E.C.S. was supported by a European Research Council (ERC) Starting Researcher Investigator Grant (SYSGRO).

References

1 Fuchs, F., Pau, G., Kranz, D., Sklyar, O., Budjan, C., Steinbrink, S., Horn, T., Pedal, A., Huber, W. and Boutros, M. (2010) Clustering phenotype populations by genome-wide RNAi and multiparametric imaging. Mol. Syst. Biol. **6**, 370
2 Olmsted, J.B. and Borisy, G.G. (1973) Microtubules. Annu. Rev. Biochem. **42**, 507–540
3 Akhmanova, A. and Hoogenraad, C.C. (2005) Microtubule plus-end-tracking proteins: mechanisms and functions. Curr. Opin. Cell Biol. **17**, 47–54
4 Amos, L.A. and Schlieper, D. (2005) Microtubules and maps. Adv. Protein Chem. **71**, 257–298
5 Evans, L., Mitchison, T. and Kirschner, M. (1985) Influence of the centrosome on the structure of nucleated microtubules. J. Cell Biol. **100**, 1185–1191
6 Desai, A. and Mitchison, T.J. (1997) Microtubule polymerization dynamics. Annu. Rev. Cell Dev. Biol. **13**, 83–117
7 Chrétien, D. and Wade, R.H. (1991) New data on the microtubule surface lattice. Biol. Cell **71**, 161–174
8 Wade, R.H., Chrétien, D. and Job, D. (1990) Characterization of microtubule protofilament numbers: how does the surface lattice accommodate? J. Mol. Biol. **212**, 775–786
9 Mitchison, T. and Kirschner, M. (1984) Dynamic instability of microtubule growth. Nature **312**, 237–242
10 Hayles, J. and Nurse, P. (2001) A journey into space. Nat. Rev. Mol. Cell Biol. **2**, 647–656
11 Carlier, M.F. and Pantaloni, D. (1982) Assembly of microtubule protein: role of guanosine di- and triphosphate nucleotides. Biochemistry **21**, 1215–1224
12 Drechsel, D.N. and Kirschner, M.W. (1994) The minimum GTP cap required to stabilize microtubules. Curr. Biol. **4**, 1053–1061
13 Chrétien, D., Fuller, S.D. and Karsenti, E. (1995) Structure of growing microtubule ends: two-dimensional sheets close into tubes at variable rates. J. Cell Biol. **129**, 1311–1328
14 Dimitrov, A., Quesnoit, M., Moutel, S., Cantaloube, I., Poüs, C. and Perez, F. (2008) Detection of GTP-tubulin conformation *in vivo* reveals a role for GTP remnants in microtubule rescues. Science **322**, 1353–1356
15 Bouissou, A., Vérollet, C., Sousa, A., Sampaio, P., Wright, M., Sunkel, C.E., Merdes, A. and Raynaud-Messina, B. (2009) γ-Tubulin ring complexes regulate microtubule plus end dynamics. J. Cell Biol. **187**, 327–334
16 Zheng, Y., Wong, M.L., Alberts, B. and Mitchison, T. (1995) Nucleation of microtubule assembly by a γ-tubulin-containing ring complex. Nature **378**, 578–583
17 Moritz, M. and Agard, D.A. (2001) γ-Tubulin complexes and microtubule nucleation. Curr. Opin. Struct. Biol. **11**, 174–181
18 Erickson, H.P. and Stoffler, D. (1996) Protofilaments and rings, two conformations of the tubulin family conserved from bacterial FtsZ to α/β and γ tubulin. J. Cell Biol. **135**, 5–8
19 Dammermann, A., Desai, A. and Oegema, K. (2003) The minus end in sight. Curr. Biol. **13**, R614–R624
20 Wiese, C. and Zheng, Y. (2006) Microtubule nucleation: γ-tubulin and beyond. J. Cell Sci. **119**, 4143–4153
21 Samejima, I., Lourenço, P.C., Snaith, H.A. and Sawin, K.E. (2005) Fission yeast mto2p regulates microtubule nucleation by the centrosomin-related protein mto1p. Mol. Biol. Cell **16**, 3040–3051
22 Bornens, M. (2002) Centrosome composition and microtubule anchoring mechanisms. Curr. Opin. Cell Biol. **14**, 25–34
23 Straube, A., Brill, M., Oakley, B.R., Horio, T. and Steinberg, G. (2003) Microtubule organization requires cell cycle-dependent nucleation at dispersed cytoplasmic sites: polar and perinuclear microtubule organizing centers in the plant pathogen *Ustilago maydis*. Mol. Biol. Cell **14**, 642–657
24 Glotzer, M. (2009) The 3Ms of central spindle assembly: microtubules, motors and MAPs. Nat. Rev. Mol. Cell Biol. **10**, 9–20
25 Browning, H. and Hackney, D.D. (2005) The EB1 homolog Mal3 stimulates the ATPase of the kinesin Tea2 by recruiting it to the microtubule. J. Biol. Chem. **280**, 12299–12304
26 Walczak, C.E. (2003) The Kin I kinesins are microtubule end-stimulated ATPases. Mol. Cell **11**, 286–288
27 Maddox, P.S. (2005) Microtubules: Kar3 eats up the track. Curr. Biol. **15**, R622–R624
28 Desai, A., Verma, S., Mitchison, T.J. and Walczak, C.E. (1999) Kin I kinesins are microtubule-destabilizing enzymes. Cell **96**, 69–78
29 Ravelli, R.B., Gigant, B., Gigant, B. and Knossow, M. (2004) Insight into tubulin regulation from a complex with colchicine and a stathmin-like domain. Nature **428**, 198–202
30 Quarmby, L. (2000) Cellular Samurai: katanin and the severing of microtubules. J. Cell Sci. **113**, 2821–2827
31 Salinas, S., Carazo-Salas, R.E., Proukakis, C., Schiavo, G. and Warner, T.T. (2007) Spastin and microtubules: functions in health and disease. J. Neurosci. Res. **85**, 2778–2782
32 Roll-Mecak, A. and McNally, F.J. (2010) Microtubule-severing enzymes. Curr. Opin. Cell Biol. **22**, 96–103

33 Roll-Mecak, A. and Vale, R.D. (2006) Making more microtubules by severing: a common theme of noncentrosomal microtubule arrays? J. Cell Biol. **175**, 849–851
34 Niethammer, P., Kronja, I., Kandels-Lewis, S., Rybina, S., Bastiaens, P. and Karsenti, E. (2007) Discrete states of a protein interaction network govern interphase and mitotic microtubule dynamics. PLoS Biol. **5**, e29
35 Hirokawa, N. (1998) Kinesin and dynein superfamily proteins and the mechanism of organelle transport. Science **279**, 519–526
36 Sakato, M. and King, S.M. (2004) Design and regulation of the AAA$^+$ microtubule motor dynein. J. Struct. Biol. **146**, 58–71
37 Vorobjev, I., Malikov, V. and Rodionov, V. (2001) Self-organization of a radial microtubule array by dynein-dependent nucleation of microtubules. Proc. Natl. Acad. Sci. U.S.A. **98**, 10160–10165
38 Bratman, S.V. and Chang, F. (2008) Mechanisms for maintaining microtubule bundles. Trends Cell Biol. **18**, 580–586
39 Carazo-Salas, R.E. and Nurse, P. (2006) Self-organization of interphase microtubule arrays in fission yeast. Nat. Cell Biol. **8**, 1102–1107
40 Subramanian, R., Wilson-Kubalek, E.M., Arthur, C.P., Bick, M.J., Campbell, E.A., Darst, S.A., Milligan, R.A. and Kapoor, T.M. (2010) Insights into antiparallel microtubule crosslinking by PRC1, a conserved nonmotor microtubule binding protein. Cell **142**, 433–443
41 Walczak, C.E. and Shaw, S.L. (2010) A MAP for bundling microtubules. Cell **142**, 364–367
42 Braun, M., Lansky, Z., Fink, G., Ruhnow, F., Diez, S. and Janson, M.E. (2011) Adaptive braking by Ase1 prevents overlapping microtubules from sliding completely apart. Nat. Cell Biol. **13**, 1259–1264
43 Pierreux, C.E., Nicolás, F.J. and Hill, C.S. (2000) Transforming growth factor β-independent shuttling of Smad4 between the cytoplasm and nucleus. Mol. Cell. Biol. **20**, 9041–9054
44 Ziegelbauer, J., Shan, B., Yager, D., Larabell, C., Hoffmann, B. and Tjian, R. (2001) Transcription factor MIZ-1 is regulated via microtubule association. Mol. Cell **8**, 339–349
45 Yamasaki, C., Tashiro, S., Nishito, Y., Sueda, T. and Igarashi, K. (2005) Dynamic cytoplasmic anchoring of the transcription factor Bach1 by intracellular hyaluronic acid binding protein IHABP. J. Biochem. (Tokyo) **137**, 287–296
46 Ben-Ze'ev, A., Farmer, S.R. and Penman, S. (1979) Mechanisms of regulating tubulin synthesis in cultured mammalian cells. Cell **17**, 319–325
47 Cleveland, D.W., Lopata, M.A., Sherline, P. and Kirschner, M.W. (1981) Unpolymerized tubulin modulates the level of tubulin mRNAs. Cell **25**, 537–546
48 Caron, J.M., Jones, A.L., Rall, L.B. and Kirschner, M.W. (1985) Autoregulation of tubulin synthesis in enucleated cells. Nature **317**, 648–651
49 Sellin, M.E., Holmfeldt, P., Stenmark, S. and Gullberg, M. (2008) Global regulation of the interphase microtubule system by abundantly expressed Op18/stathmin. Mol. Biol. Cell **19**, 2897–2906
50 Wittmann, T., Hyman, A. and Desai, A. (2001) The spindle: a dynamic assembly of microtubules and motors. Nat. Cell Biol. **3**, E28–E34
51 Kanakkanthara, A. and Miller, J.H. (2013) MicroRNAs: novel mediators of resistance to microtubule-targeting agents. Cancer Treat. Rev. **39**, 161–170
52 Kanakkanthara, A., Northcote, P.T. and Miller, J.H. (2012) βII-Tubulin and βIII-tubulin mediate sensitivity to peloruside A and laulimalide, but not paclitaxel or vinblastine, in human ovarian carcinoma cells. Mol. Cancer Ther. **11**, 393–404
53 McKean, P.G., Vaughan, S. and Gull, K. (2001) The extended tubulin superfamily. J. Cell Sci. **114**, 2723–2733
54 Westermann, S. and Weber, K. (2003) Post-translational modifications regulate microtubule function. Nat. Rev. Mol. Cell Biol. **4**, 938–947
55 Nechipurenko, I.V. and Broihier, H.T. (2012) FoxO limits microtubule stability and is itself negatively regulated by microtubule disruption. J. Cell Biol. **196**, 345–362
56 Verhey, K.J. and Gaertig, J. (2007) The tubulin code. Cell Cycle **6**, 2152–2160
57 Hammond, J.W., Cai, D. and Verhey, K.J. (2008) Tubulin modifications and their cellular functions. Curr. Opin. Cell Biol. **20**, 71–76
58 Wloga, D. and Gaertig, J. (2010) Post-translational modifications of microtubules. J. Cell Sci. **123**, 3447–3455
59 Garnham, C.P. and Roll-Mecak, A. (2012) The chemical complexity of cellular microtubules: tubulin post-translational modification enzymes and their roles in tuning microtubule functions. Cytoskeleton **69**, 442–463
60 L'Hernault, S.W. and Rosenbaum, J.L. (1985) *Chlamydomonas* α-tubulin is posttranslationally modified by acetylation on the ε-amino group of a lysine. Biochemistry **24**, 473–478
61 LeDizet, M. and Piperno, G. (1987) Identification of an acetylation site of *Chlamydomonas* α-tubulin. Proc. Natl. Acad. Sci. U.S.A. **84**, 5720–5724
62 Matsuyama, A., Shimazu, T., Sumida, Y., Saito, A., Yoshimatsu, Y., Seigneurin-Berny, D., Osada, H., Komatsu, Y., Nishino, N., Khochbin, S. et al. (2002) *In vivo* destabilization of dynamic microtubules by HDAC6-mediated deacetylation. EMBO J. **21**, 6820–6831
63 Rogowski, K., Juge, F., van Dijk, J., Wloga, D., Strub, J.M., Levilliers, N., Thomas, D., Bré, M.H., Van Dorsselaer, A., Gaertig, J. and Janke, C. (2009) Evolutionary divergence of enzymatic mechanisms for posttranslational polyglycylation. Cell **137**, 1076–1087
64 Wloga, D., Webster, D.M., Rogowski, K., Bré, M.H., Levilliers, N., Jerka-Dziadosz, M., Janke, C., Dougan, S.T. and Gaertig, J. (2009) TTLL3 is a tubulin glycine ligase that regulates the assembly of cilia. Dev. Cell **16**, 867–876
65 Hallak, M.E., Rodriguez, J.A., Barra, H.S. and Caputto, R. (1977) Release of tyrosine from tyrosinated tubulin. Some common factors that affect this process and the assembly of tubulin. FEBS Lett. **73**, 147–150
66 Lafanechere, L. and Job, D. (2000) The third tubulin pool. Neurochem. Res. **25**, 11–18
67 Fourest-Lieuvin, A., Peris, L., Gache, V., Garcia-Saez, I., Juillan-Binard, C., Lantez, V. and Job, D. (2006) Microtubule regulation in mitosis: tubulin phosphorylation by the cyclin-dependent kinase Cdk1. Mol. Biol. Cell **17**, 1041–1050
68 Hubbert, C., Guardiola, A., Shao, R., Kawaguchi, Y., Ito, A., Nixon, A., Yoshida, M., Wang, X.F. and Yao, T.P. (2002) HDAC6 is a microtubule-associated deacetylase. Nature **417**, 455–458
69 Maia, A.R., Garcia, Z., Kabeche, L., Barisic, M., Maffini, S., Macedo-Ribeiro, S., Cheeseman, I.M., Compton, D.A., Kaverina, I. and Maiato, H. (2012) Cdk1 and Plk1 mediate a CLASP2 phospho-switch that stabilizes kinetochore-microtubule attachments. J. Cell Biol. **199**, 285–301
70 Schofield, A.V., Gamell, C., Suryadinata, R., Sarcevic, B. and Bernard, O. (2013) Tubulin polymerization promoting protein 1 (Tppp1) phosphorylation by Rho-associated coiled-coil kinase (Rock) and cyclin-dependent kinase 1 (Cdk1) inhibits microtubule dynamics to increase cell proliferation. J. Biol. Chem. **288**, 7907–7917
71 Benseddik, K., Sen Nkwe, N., Daou, P., Verdier-Pinard, P. and Badache, A. (2013) ErbB2-dependent chemotaxis requires microtubule capture and stabilization coordinated by distinct signaling pathways. PLoS ONE **8**, e55211
72 Mizuno, K., Shiba, K., Okai, M., Takahashi, Y., Shitaka, Y., Oiwa, K., Tanokura, M. and Inaba, K. (2012) Calaxin drives sperm chemotaxis by Ca^{2+}-mediated direct modulation of a dynein motor. Proc. Natl. Acad. Sci. U.S.A. **109**, 20497–20502
73 Kumar, S., Xu, J., Perkins, C., Guo, F., Snapper, S., Finkelman, F.D., Zheng, Y. and Filippi, M.D. (2012) Cdc42 regulates neutrophil migration via crosstalk between WASp, CD11b, and microtubules. Blood **120**, 3563–3574
74 Lin, T.C., Gombos, L., Neuner, A., Sebastian, D., Olsen, J.V., Hrle, A., Benda, C. and Schiebel, E. (2011) Phosphorylation of the yeast γ-tubulin Tub4 regulates microtubule function. PLoS ONE **6**, e19700
75 Kumar, P. and Wittmann, T. (2012) +TIPs: SxIPping along microtubule ends. Trends Cell Biol. **22**, 418–428
76 Sato, M., Vardy, L., Angel Garcia, M., Koonrugsa, N. and Toda, T. (2004) Interdependency of fission yeast Alp14/TOG and coiled coil protein Alp7 in microtubule localization and bipolar spindle formation. Mol. Biol. Cell **15**, 1609–1622
77 Dodgson, J., Chessel, A., Yamamoto, M., Vaggi, F., Cox, S., Rosten, E., Albrecht, D., Geymonat, M., Csikasz-Nagy, A., Sato, M. and Carazo-Salas, R.E. (2013) Spatial segregation of polarity factors into distinct cortical clusters is required for cell polarity control. Nat. Commun. **4**, 1834
78 Wang, Y., Zhang, X., Zhang, H., Lu, Y., Huang, H., Dong, X., Chen, J., Dong, J., Yang, X., Hang, H. and Jiang, T. (2012) Coiled-coil networking shapes cell molecular machinery. Mol. Biol. Cell **23**, 3911–3922
79 Lupas, A. (1996) Coiled coils: new structures and new functions. Trends Biochem. Sci. **21**, 375–382
80 Adams, J., Kelso, R. and Cooley, L. (2000) The kelch repeat superfamily of proteins: propellers of cell function. Trends Cell Biol. **10**, 17–24
81 Neumann, B., Held, M., Liebel, U., Erfle, H., Rogers, P., Pepperkok, R. and Ellenberg, J. (2006) High-throughput RNAi screening by time-lapse imaging of live human cells. Nat. Methods **3**, 385–390
82 Neumann, B., Walter, T., Hériché, J.K., Bulkescher, J., Erfle, H., Conrad, C., Rogers, P., Poser, I., Held, M., Liebel, U. et al. (2010) Phenotypic profiling of the human genome by time-lapse microscopy reveals cell division genes. Nature **464**, 721–727
83 Lewis, B.P., Burge, C.B. and Bartel, D.P. (2005) Conserved seed pairing, often flanked by adenosines, indicates that thousands of human genes are microRNA targets. Cell **120**, 15–20

APPENDIX C

84 Friedman, R.C., Farh, K.K., Burge, C.B. and Bartel, D.P. (2009) Most mammalian mRNAs are conserved targets of microRNAs. Genome Res. **19**, 92–105
85 Huang, B. (2010) Super-resolution optical microscopy: multiple choices. Curr. Opin. Chem. Biol. **14**, 10–14
86 Schermelleh, L., Heintzmann, R. and Leonhardt, H. (2010) A guide to super-resolution fluorescence microscopy. J. Cell Biol. **190**, 165–175
87 Leung, B.O. and Chou, K.C. (2011) Review of super-resolution fluorescence microscopy for biology. Appl. Spectrosc. **65**, 967–980
88 Shao, L., Kner, P., Rego, E.H. and Gustafsson, M.G. (2011) Super-resolution 3D microscopy of live whole cells using structured illumination. Nat. Methods **8**, 1044–1046
89 Hensel, M., Klingauf, J. and Piehler, J. (2013) Imaging the invisible: resolving cellular microcompartments by superresolution microscopy techniques. Biol. Chem. **394**, 1097–1113
90 Li, W.H. and Zheng, G. (2012) Photoactivatable fluorophores and techniques for biological imaging applications. Photochem. Photobiol. Sci. **11**, 460–471
91 Lukinavicius, G. and Johnsson, K. (2011) Switchable fluorophores for protein labeling in living cells. Curr. Opin. Chem. Biol. **15**, 768–774
92 Wombacher, R. and Cornish, V.W. (2011) Chemical tags: applications in live cell fluorescence imaging. J. Biophotonics **4**, 391–402
93 Jánosi, I.M., Chrétien, D. and Flyvbjerg, H. (1998) Modeling elastic properties of microtubule tips and walls. Eur. Biophys. J. **27**, 501–513
94 Loughlin, R., Heald, R. and Nédélec, F. (2010) A computational model predicts *Xenopus* meiotic spindle organization. J. Cell Biol. **191**, 1239–1249
95 Loughlin, R., Wilbur, J.D., McNally, F.J., Nédélec, F.J. and Heald, R. (2011) Katanin contributes to interspecies spindle length scaling in *Xenopus*. Cell **147**, 1397–1407

Received 9 October 2013
doi:10.1042/BST20130239

eLIFE
elife.elifesciences.org

FEATURE ARTICLE

CUTTING EDGE

A network approach to mixing delegates at meetings

Delegates at scientific meetings can come from diverse backgrounds and use very different methods in their research. Promoting interactions between these 'distant' delegates is challenging but such interactions could lead to novel interdisciplinary collaborations and unexpected breakthroughs. We have developed a network-based 'speed dating' approach that allows us to initiate such distant interactions by pairing every delegate with another delegate who might be of interest to them, but whom they might never have encountered otherwise. Here we describe our approach and its algorithmic implementation.

FEDERICO VAGGI, TOMMASO SCHIAVINOTTO, JONATHAN LD LAWSON, ANATOLE CHESSEL, JAMES DODGSON, MARCO GEYMONAT, MASAMITSU SATO, RAFAEL EDGARDO CARAZO SALAS† AND ATTILA CSIKÁSZ-NAGY†

Scientists have been going to conferences for more than 450 years, but the basic format of talks followed by questions–with regular breaks for informal interactions over a drink or a meal–has remained largely the same. It is possible to foresee many ways in which conferences may evolve in the years ahead, but the main attraction is likely to remain the opportunity for scientists to meet and network, to develop ideas and collaborations, and to drink large amounts of tea, coffee and alcohol.

Compared to their 16th century ancestors, modern conferences are more inclusive than they have ever been, with diverse selections of delegates and speakers from around the world. However, the Q & A sessions after talks offer only limited opportunities for meaningful speaker-audience dialogue (***Moore, 2010***), and the discussion is often dominated by the senior scientists among the delegates. Although coffee breaks–the most productive part of scientific conferences (***Obris, 2008***; ***Stobbe et al., 2013***)—provide more junior scientists with an opportunity to network, there is plenty of scope for improving the level of interactions between the senior and junior delegates.

Thus, current conference formats pose two key, interrelated problems: 'breaking the ice' (i.e., making it easy for younger scientists to introduce themselves, and 'breaking the heat' (i.e., discouraging the key players from only networking with their peers, thereby excluding their junior colleagues). There is a third problem at interdisciplinary conferences due to a lack of natural topics of conversation between people working in very different areas of research, so like tends to stick with like.

Mixing delegates in a mutually interesting and novel way

Over the years conference organisers have tried many approaches to improve this state of affairs. There have been attempts at using web-based technologies to improve the interaction between the audience and the speakers, and to make social mixing easier and less intimidating. People have previously trialled virtual conferences, real-time

†These authors contributed equally to this work

Twitter feedback, and other web 2.0 technologies (***Ebner and Reinhardt, 2009***; ***Rigutto, 2013***). These approaches have been successful in some fields, particularly related to media and journalism (***Briggs, 2007***; ***Picard, 2009***), but they come with their own set of problems (***Boyd, 2009***) not the least a lack of technical know-how in the audience, particularly in the more academic fields.

There are also approaches to facilitate the formation of interest groups at conferences (***Canning et al., 2013***) and to help researchers identify potential collaborators from the web (***Schall, 2013***). The Mathematisches Forschungsinstitut Oberwolfach in Germany organizes weekly meetings where each participant has a napkin holder with her/his name on it, and at each meal the napkin holders are randomly distributed to each seat in the dining hall. Inspired by this, we recently developed an alternative, more 'engineered' approach to encouraging interactions at a meeting entitled Cell Polarity in the Systems Medicine Era, that was attended by 40 people. We call this approach interdisciplinary speed dating.

This was a satellite meeting that was held immediately after a larger meeting we organised at the Royal Society in London on the topic of cell polarity. In the smaller gathering the idea was to discuss in depth several topics brought up at the larger meeting in a more intimate setting, so all the delegates (a mix of junior group leaders, senior lab heads, and postdocs) were accommodated in the same building (at Chicheley Hall, which is about 50 miles north of London) to spend two days discussing science. Since the meeting was about cell polarity, the attendees consisted of a heterogeneous group of biophysicists, mathematical modellers, biochemists, in vivo researchers, and bioinformatics researchers. The combination of wide-ranging interests among the delegates, as well as the relatively small number of people attending, made this meeting an excellent test bed for our unorthodox conference approach.

To prepare for the satellite meeting we asked all the delegates to complete a short survey and eventually received responses from all but one delegate. In the survey, we asked the participants to state which methods they were familiar with from a list of 32 relevant methods, and to state which methods they wanted to learn more about (***Figure 1***). There was a wide variation between the number of methods known by the different delegates (ranging from 1 to 26, out of a total of 32; mean = 6.6, standard deviation = 4.4).

Next, we asked which of the other delegates they had previously collaborated with. Interestingly, only about half of the relationships were mutual (51%)—this difference is probably due to some delegates only counting scientists with whom they have published papers, and other delegates favouring a less formal definition. However, it was notable

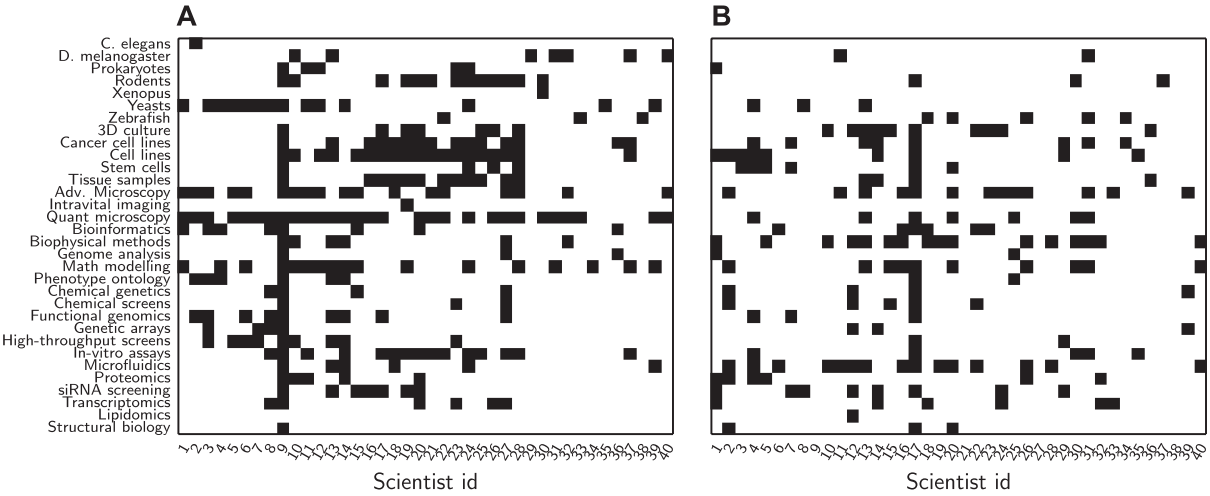

Figure 1. Data from initial survey sent to delegates. Prior to the meeting, we asked each delegate to choose, from a predetermined list, which methods they were familiar with, and which methods they wanted to learn more about. (**A**) Methods known by delegate. Each row represents a method and each column represents an individual delegate (names omitted for reasons of confidentiality). Delegates were most familiar with microscopy (both quantitative and advanced), cells (both cancer and stem) and mathematical modelling. This information was used to calculate the knowledge distance between delegates in ***Figure 3***. (**B**) Methods that delegates wanted to learn more about. The most popular methods were biophysical methods and microfluidic devices.

that the delegates formed a connected network, with every delegate having collaborated with at least one other delegate (***Figure 2A***). We did not observe any statistically significant links between the gender of the scientist (13 female and 27 male scientists attended) and the extent of methodological knowledge or collaboration experience.

At the conference

Over the two days of the conference, we dedicated two 90 minute sessions to speed dating. The first session consisted of five rounds of ice breakers in which each delegate was paired with another delegate with whom they had little in common (based on the methods they knew about and the people they had collaborated with). The intention was to cause the delegates to meet new and different people. Each round lasted 15 minutes, giving enough time for scientists to discuss their own work while still keeping the meetings brief and to the point. The atmosphere of the meetings was highly informal–coffee and refreshments were provided, and scientists had the choice to sit down at small tables or simply walk around near posters and discuss each other's results.

In these five encounters, we used two criteria to match the delegates (***Figure 3***). The first criterion was 'acquaintance distance'—the number of steps between the delegates on the collaboration graph based on their shared previous acquaintances. The second criterion was the 'knowledge similarity' between the two delegates in a pair–this number gave us a measure of how much knowledge the delegates had in common. We then added the inverse of the 'acquaintance distance' to the 'knowledge similarity'. We used a parameter α to determine how much weight to give to each criterion in the sum (***Figure 3C–F***): α = 0 meant that only 'acquaintance distance' was considered when matching the delegates; α = 0.5 meant that 'acquaintance distance' and 'knowledge similarity' were considered equally; and α = 1 meant that only 'knowledge similarity' was considered. Finally, pairings between delegates who had previously collaborated—that is, whose acquaintance distance was equal to 1—were forbidden.

For each round, we sought to find the 20 pairs that would minimize the sum of the two values. In other words, we wanted to form pairs of delegates who were far away from each other in the network and who had minimal overlap in their knowledge. This means that we were looking for 20 deep blue squares in the matrices in ***Figure 3***, subject to the constraint that we had to select one square (i.e., one delegate) from each column and from each row per round. This is a well-known problem in combinatorial optimization, and is called the Maximum-Weight Perfect Matching Problem (***Edmonds, 1965***); several polynomial-time exact algorithms exist for solving this problem (***Gabow and Tarjan, 1991***). Interestingly, the number of one-way collaborations (where one delegate reports a collaboration but the other does not) was significantly correlated with the number of methods known ($r = 0.38$, p-value = 0.015).

After the pairings for one round had been solved, we added a further constraint to prevent the same pairs being selected again in future rounds. Importantly, for each round we were solving for the optimal pairs which simultaneously maximized new knowledge gained for all scientists. This was a greedy strategy: choices made in early rounds introduced constraints (by reducing

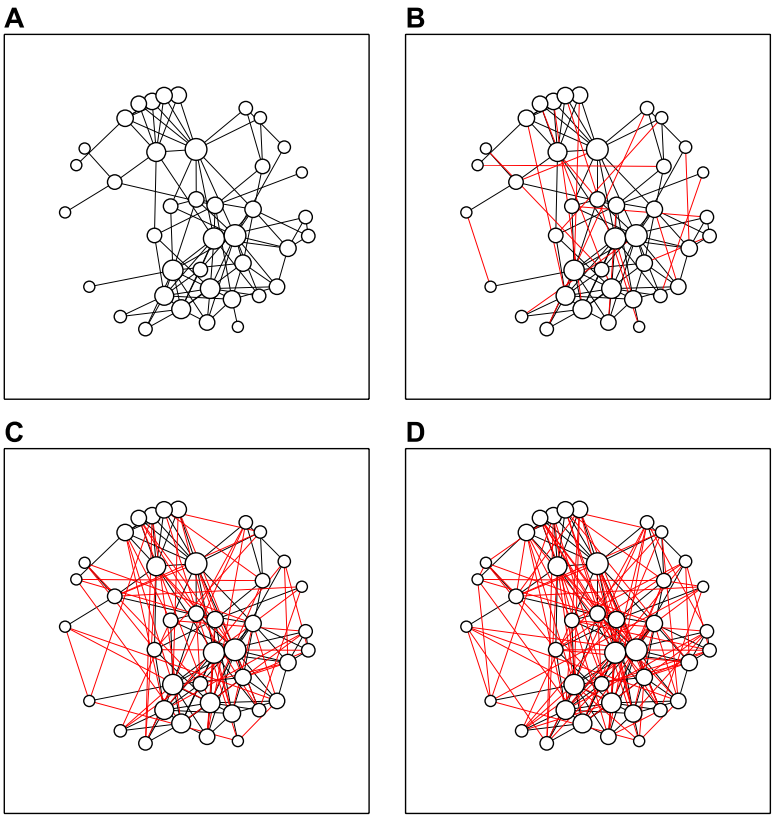

Figure 2. Speed dates increase network density. (**A**) The collaboration network before the meeting: some delegates already knew 10 or more other delegates, whereas others knew just one or two. (**B**) After the first round of speed dates, 20 new connections (shown in red) had been added to the network. (**C**, **D**) The network after three (**C**) and five (**D**) rounds of speed dates; α = 0.9.

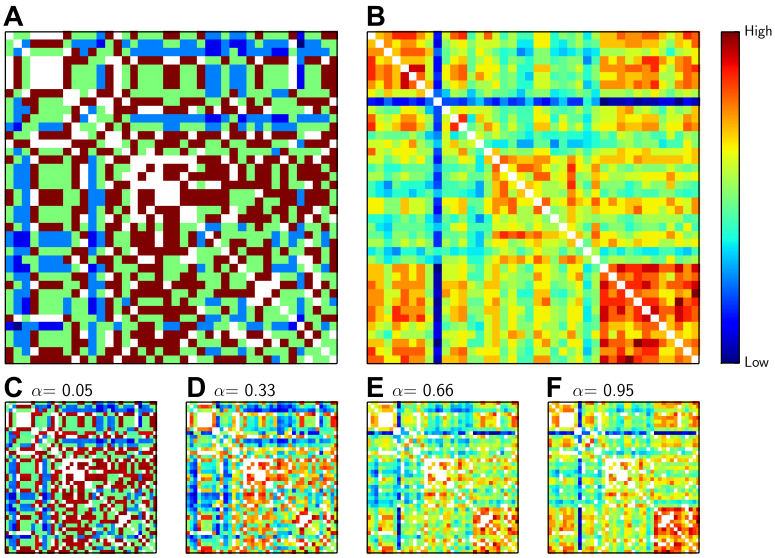

Figure 3. The distance between delegates. (**A**) Matrix showing the inverse of the 'acquaintance distance' between all pairs of delegates, who are arranged horizontally and vertically as in ***Figure 1***. (**B**) Matrix showing the 'knowledge similarity' between all pairs of delegates: similarity increases with the number of methods known in common by both candidates, and decreases with the number of methods that are only known by one. The inverse acquaintance distance (**A**) and the knowledge similarity (**B**) have both been normalized to have zero mean and unit variance so that they can be added together, suitably weighted by α. (**C**–**F**) The sum of inverse acquaintance distance and the knowledge similarity for pairs of delegates for different values of α. Colder colours such as blue indicate low similarity and high distance (see colour bar); hotter colours such as red and brown indicate the reverse; white squares not on the diagonal represent delegates who have previously collaborated. The similarity measure that we used (the Rogers and Tanimoto similarity measure) penalized pairs with low overlap, which led to the pronounced vertical and horizontal blue lines observed for the delegate familiar with 26 methods in **B**.

the number of possible pairs), which may prevent the algorithm from finding a best solution for later rounds. Hence a future improvement of this approach could be to modify the above implementation to maximise the sum of the distances across all rounds, instead of finding the optimal match on a per-round basis. In this manner, the solution would not need to decay through successive selection rounds.

To select an appropriate value of α, we simulated what would happen during five rounds of speed dating with four different values of this number. Since the meeting was quite small and the collaboration network was already quite dense to begin with, the average shortest path decreased quite rapidly, almost irrespective of the value of α (***Figure 4A***). However, the amount of new knowledge gained increased with the value of α (***Figure 4B***), so we used α = 0.9 when calculating pairs.

While the goal of the first five encounters was to match people who would not traditionally meet, the goal of the second round of encounters was to optimise the way people meet collaborators at conferences. Therefore, in the second round we sought to match delegates who were expert in particular methods with delegates wanting to learn about those methods (based on the data in ***Figure 1B***). We did this by computing a 'matching knowledge distance', which quantified how much the methods known by one participant resembled the methods sought by another and vice-versa. We then summed the inverse of the 'matching knowledge distance' with the 'acquaintances distance', again weighted by a parameter α, and sought to maximise this sum. This was a popular approach, with a large proportion (>50%) of the people who responded to the post-meeting questionaire indicating that this part of the meeting led to the establishment of new collaborations.

The code we used to generate the pairs for this paper is available on the github repository: https://github.com/FedericoV/conference_pairings. When using our approach for very large conferences, it will be important to investigate the use of heuristics that allow the calculation of near-optimal solutions in a fraction of the time, as the current exact algorithm has O(N^3) scaling (where N is the number of delegates at the meeting).

Conclusions and perspectives

When tweaking a successful idea, it is important to stay true to the original spirit and purpose one had in mind. Trying to improve scientific conferences, we sought to engineer a better way for scientists to become exposed to new ideas and unlikely conversation partners, meet potential collaborators, and learn more about specific methods they fancied. While our approach was decidedly unorthodox, our first attempt to implement it turned out much better than we expected: of the 24 delegates who commented on it in the post-meeting questionnaire, 21 (87.5%) were very enthusiastic and complimentary, and 12 mentioned that potential new collaborations were emerging from discussions at the meeting.

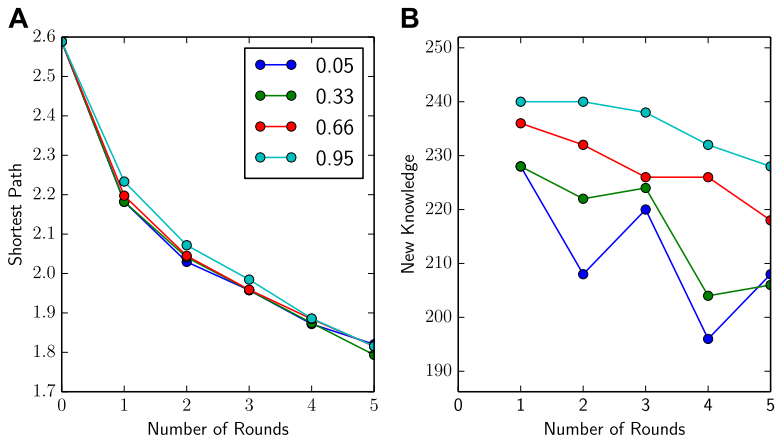

Figure 4. Increasing α increases new knowledge gained. (**A** and **B**) Average shortest path and new knowledge gained (i.e., the total number of new methods delegates were told about in a given round) vs number of rounds of speed dating for four different values of α. The shortest average path (**A**) fell quickly with the number of rounds of speed dating, almost irrespective of the value of α. However, new knowledge gained (**B**) increased with the value of α: this is to be expected because higher values of α mean that delegates are more likely to be paired with someone who can tell them about new methods.

Of course there is room for improvement. For example, quite a few of the delegates at our meeting were lab heads, so at larger meetings attended by a lot of junior scientists it would be interesting to use 'scientific seniority' as an additional criterion when calculating the distance between delegates with a view to pairing these junior scientists with senior figures in the field. Alternatively, everyone attending the meeting could be asked what they hope to get out of the meeting (e.g., to meet new people, to learn more about various methods, to meet lab heads who are recruiting, and so on), and then one could attempt to match everyone according to their own stated aims. We are eager to explore these and other applications of our approach in the future.

Acknowledgements

We thank the Royal Society and the staff at Chicheley Hall, especially T Wheeler, for their help. This work was supported by a Wellcome Trust PhD studentship (JLDL), a BBSRC Responsive Mode grant (REC-S, AC, MG, JD; BB/K006320/1), an European Research Council Starting Researcher Investigator Grant (REC-S, JD; SYSGRO), and a Human Frontier Science Program Young Investigator Grant (REC-S, ACN, MS; RGY0066/2009-C).

Federico Vaggi is in the Department of Computational Biology, Fondazione Edmund Mach, San Michele all'Adige, Italy
federico.vaggi@fmach.it
Tommaso Schiavinotto is at U-Hopper, Trento, Italy
Jonathan LD Lawson is at the Gurdon Institute and the Genetics Department, University of Cambridge, Cambridge, United Kingdom
Anatole Chessel is at the Gurdon Institute and the Genetics Department, University of Cambridge, Cambridge, United Kingdom
James Dodgson is at the Gurdon Institute and the Genetics Department, University of Cambridge, Cambridge, United Kingdom
Marco Geymonat is at the Gurdon Institute and the Genetics Department, University of Cambridge, Cambridge, United Kingdom
Masamitsu Sato is in the Department of Life Science and Medical Bioscience, Waseda University, Tokyo, Japan
Rafael E Carazo-Salas is at the Gurdon Institute and the Genetics Department, University of Cambridge, Cambridge, United Kingdom
cre20@cam.ac.uk
Attila Csikász-Nagy is in the Department of Computational Biology, Fondazione Edmund Mach, San Michele all'Adige, Italy, and the Randall Division of Cell and Molecular Biophysics and Institute of Mathematical and Molecular Biomedicine, King's College London, London, United Kingdom
attila.csikasz-nagy@fmach.it
Competing interests: The authors declare that no competing interests exist.
Published 04 February 2014

Notes

Rafael E Carazo-Salas and Attila Csikász-Nagy contributed equally to this work.

References

Boyd D. 2009. spectacle at Web2.0 Expo… from my perspective. http://www.zephoria.org/thoughts/archives/2009/11/24/spectacle_at_we.html
Briggs M. 2007. Journalism 2.0: how to survive and thrive. http://www.kcnn.org/images/uploads/Journalism_20.pdf
Canning S, Forster CRW, Readshaw NI. 2013. Formation of special interest groups. http://www.google.co.in/patents/US20110276629
Ebner M, Reinhardt W. 2009. Social networking in scientific conferences – Twitter as tool for strengthen a scientific community. http://www.scribd.com/doc/20363438/Social-networking-in-scientific-conferences---Twitter-as-tool-for-strengthen-a-scientific-community
Edmonds J. 1965. Paths, trees, and flowers. *Canadian Journal of Mathematics* **17**:449–467. doi: 10.4153/CJM-1965-045-4.
Gabow HN, Tarjan RE. 1991. Faster scaling algorithms for general graph matching problems. *Journal of the ACM* **38**:815–853. doi: 10.1145/115234.115366.

APPENDIX C

Moore A. 2010. Could virtual conferences change the face of scientific enquiry? - for the better? *BioEssays* **32**:737. doi: 10.1002/bies.201090032.

Obris HU. 2008. A rule of the game. *The Edge*. http://edge.org/conversation/a-rule-of-the-game

Picard RG. 2009. Blogs, tweets, social media, and the news business. *Nieman Foundation for Journalism at Harvard*. http://www.nieman.harvard.edu/reports/article/101884/Blogs-Tweets-Social-Media-and-the-News-Business.aspx

Rigutto C. 2013. How to engage a wider audience using Twitter at Scientific Conferences. http://www.academia.edu/5016060/How_to_engage_a_wider_audience_using_Twitter_at_Scientific_Conferences

Schall D. 2013. A multi-criteria ranking framework for partner selection in scientific collaboration environments. *Decision Support Systems*. doi: 10.1016/j.dss.2013.10.001.

Stobbe M, Mishra T, Macintyre G. 2013. Breaking the ice and forging links: the importance of socializing in research. *PLOS Computational Biology* **9**:e1003355. doi: 10.1371/journal.pcbi.1003355.

Developmental Cell
Resource

A Genomic Multiprocess Survey of Machineries that Control and Link Cell Shape, Microtubule Organization, and Cell-Cycle Progression

Veronika Graml,[1,2,3,6,7] Xenia Studera,[1,2,3,6,8] Jonathan L.D. Lawson,[1,2,6] Anatole Chessel,[1,2,6] Marco Geymonat,[1,2] Miriam Bortfeld-Miller,[3,9] Thomas Walter,[4] Laura Wagstaff,[1,5] Eugenia Piddini,[1,5] and Rafael E. Carazo-Salas[1,2,3,*]
[1]The Gurdon Institute, University of Cambridge, Tennis Court Road, Cambridge CB2 1QN, UK
[2]Genetics Department, University of Cambridge, Downing Street, Cambridge CB2 3EH, UK
[3]Institute of Biochemistry, ETH Zürich, Schafmattstrasse 18, HPM G16.2, Zürich 8093, Switzerland
[4]Institut Curie, Centre for Computational Biology, Centre de Recherche Unité 900, 26 Rue d'Ulm, 75248 Paris Cedex, France
[5]Zoology Department, University of Cambridge, Downing Street, Cambridge CB2 3EJ, UK
[6]Co-first author
[7]Present address: Deloitte Consulting AG, General Guisan-Quai 38, P.O. Box 2232, 8022 Zürich, Switzerland
[8]Present address: PriceSpective, 22 Tudor Street, London EC4Y 0AY, UK
[9]Present address: Institute of Microbiology, ETH Zurich, HCI F 428 Wolfgang-Paulistrasse 10, 8093 Zürich, Switzerland
*Correspondence: cre20@cam.ac.uk
http://dx.doi.org/10.1016/j.devcel.2014.09.005

SUMMARY

Understanding cells as integrated systems requires that we systematically decipher how single genes affect multiple biological processes and how processes are functionally linked. Here, we used multiprocess phenotypic profiling, combining high-resolution 3D confocal microscopy and multiparametric image analysis, to simultaneously survey the fission yeast genome with respect to three key cellular processes: cell shape, microtubule organization, and cell-cycle progression. We identify, validate, and functionally annotate 262 genes controlling specific aspects of those processes. Of these, 62% had not been linked to these processes before and 35% are implicated in multiple processes. Importantly, we identify a conserved role for DNA-damage responses in controlling microtubule stability. In addition, we investigate how the processes are functionally linked. We show unexpectedly that disruption of cell-cycle progression does not necessarily affect cell size control and that distinct aspects of cell shape regulate microtubules and vice versa, identifying important systems-level links across these processes.

INTRODUCTION

In many ways, the genomes of most organisms remain as black boxes, with the function of the majority of genes and gene products still unknown. This is the case foremost in humans, where, a decade after publication of the human genome sequence, we still have no direct experimental evidence of the function of over half of all the proteins it encodes (http://www.ebi.ac.uk/QuickGO/GAnnotation). Yet this is just the tip of the iceberg because many genes and proteins play roles in multiple biological processes, themselves functionally linked, with most of those multiple roles and links awaiting discovery.

Fission yeast (*Schizosaccharomyces pombe*) is excellently placed for that discovery, with a genome of ~4,900 protein coding genes (26.1% essential), 40% of which have a function only inferred from homology and another 20% completely uncharacterized (Aslett and Wood, 2006; Wood et al., 2002). Over the past four decades, classical genetic screening using *S. pombe* has allowed the discovery of numerous molecules and pathways controlling many essential eukaryotic processes thanks to the genetic tractability, simple morphology, and uniform growth and division pattern of *S. pombe* cells (Forsburg, 2003). Recently, a genome-wide library of knockout (KO) haploid strains—where each of 3,004 nonessential genes across the *S. pombe* genome was systematically deleted—became commercially available (Kim et al., 2010), opening the possibility to potentiate that discovery power using ultrasensitive image-based phenotypic screening strategies (Chia et al., 2012; Collinet et al., 2010; Cotta-Ramusino et al., 2011; Laufer et al., 2013; Mercer et al., 2012; Neumann et al., 2010; Rohn et al., 2011; Simpson et al., 2012; Yin et al., 2013).

Here, we used fission yeast to carry out a 3D image-based genomic screen monitoring cell shape, microtubule organization, and cell-cycle progression to find genes involved in these processes, identify genes controlling multiple processes, and determine how processes are functionally linked. We describe the identification, large-scale validation and quantitative annotation of 262 putative regulators, with 62% newly implicated in the processes studied and 35% implicated in more than one. As a result of in-depth validation of one hit class, we identify a conserved role of the DNA damage response in controlling microtubule stability, revealing a link between those two therapeutically relevant cell biological machineries. Moreover, by exploiting the richness of the multidimensional feature sets obtained from the screen, we investigate statistically and in detail the functional links across processes. We show that disruption of cell-cycle progression does not necessarily affect cell size

CellPress

Developmental Cell

Genes Linking Cell Cycle, Shape, and Microtubules

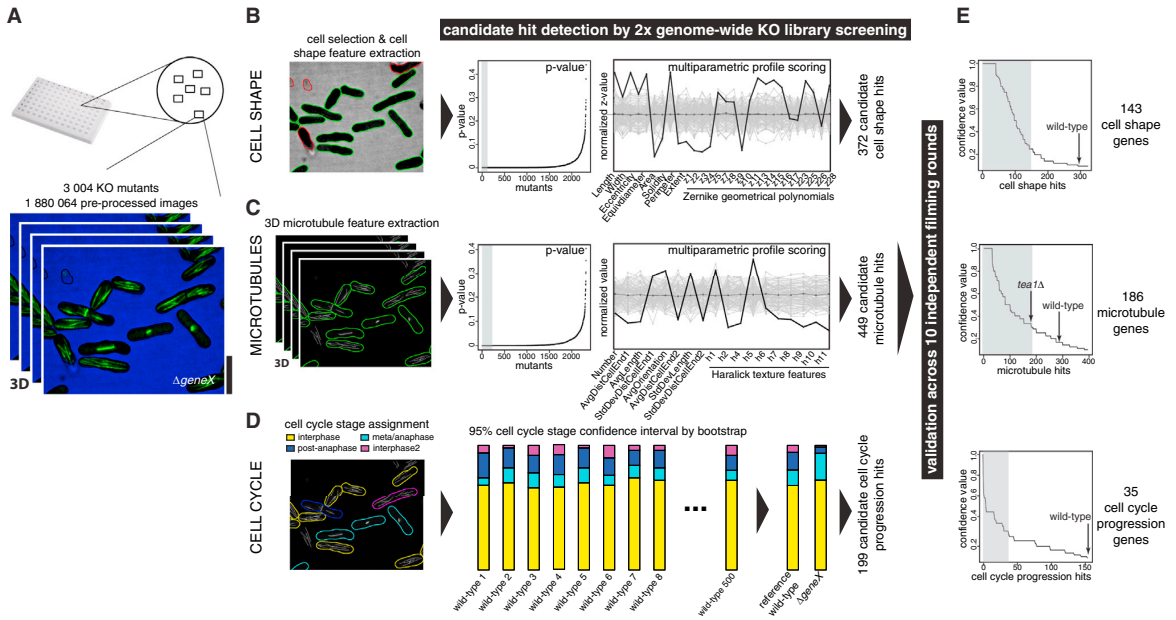

Figure 1. 3D Image-Based Multiprocess Screening Pipeline and Multiparametric Hit Detection

(A) A 2× genomic screen input; 3,004 gene KO strains were imaged in 96-well microplates. 3D z stack images were collected from six locations per well in two fluorescence channels to detect cell outlines and GFP-microtubules.

(B and C) Cell shape (B) and microtubule (C) hit detection strategy, using single feature p value measurements to detect extreme hits in one feature (left) or multifeature profile analysis to detect subtle changes across many features (right).

(D) Cell-cycle progression hit identification, by comparison for each mutant of the proportion of its cells assigned to each cell-cycle stage compared to a bootstrapped reference wild-type.

(E) 10-fold high-throughput hit validation using the strategies in (B)–(D). Hits were ranked based on the fraction of independent screening rounds where they were coincidently identified as hits (confidence value). Hits with ≥35% confidence value were subsequently analyzed.

Scale bar represents 10 μm. See also Figures S1–S6 and Tables S1, S2, and S3.

control and that the causal links between cell shape and microtubule regulation in *S. pombe* are directional and complex, with distinct cell shape and microtubule features having defined epistatic relationships in this species.

The multiprocess screen images and gene annotations are available online as a resource for the community at http://www.sysgro.org as well as linked to the centralized fission yeast repository PomBase http://www.pombase.org.

RESULTS AND DISCUSSION

Establishment of a 3D Image-Based, Yeast Phenotypic Profiling Pipeline

To carry out a multiprocess phenotypic screen in fission yeast, we developed a live cell, 3D fluorescence image-based phenotypic profiling pipeline combining automated high-resolution spinning disk confocal microscopy and large-scale, quantitative multiparametric image analysis. We used confocal microscopy and 3D (*xyz*) imaging to extract high-resolution subcellular information from individual yeast cells, allowing us to screen with high sensitivity and to obtain refined phenotypic cell biological annotations. Details of the experimental and computational implementation of the pipeline are described in the Experimental Procedures.

We chose to screen for genes controlling cell shape, microtubules, and cell-cycle progression because they are fundamental, well-studied processes for which an extensive, yet likely not exhaustive, list of regulators is known. In addition, all three processes can be monitored simultaneously in live cells expressing only fluorescently labeled tubulin, minimizing manipulation of their genetic background. Indeed, microtubules can be used as bona fide reporters of the cell-cycle state, as they take defined stereotypical patterns across the cell cycle (Hagan, 1998); in turn, cell shape can be simply monitored using extracellular fluorescent dyes (see below). Thus, we generated a version of the genome-wide KO library expressing GFP-tagged endogenous alpha tubulin 2 (GFP-Atb2; Figure 1 and Figure S1A available online), allowing us to visualize microtubules and cell-cycle stage "live" in all mutants. Because the different KO mutants arrayed in 96-well plates had different growth proficiencies compared to the wild-type (Kim et al., 2010), prior to imaging we used a serial dilution and manual repooling strategy to ensure all mutants grew exponentially and were hence physiologically comparable (Figure S1B; Protocol). Then, in preparation for high-throughput imaging, cells were immersed in Cascade blue dextran-containing fluorescent growth medium. This allowed visualization of live cell morphology without the need to express a cytoplasmic fluorophore (Figure 1). Thereafter, mutants in the 96-well plates

Developmental Cell
Genes Linking Cell Cycle, Shape, and Microtubules

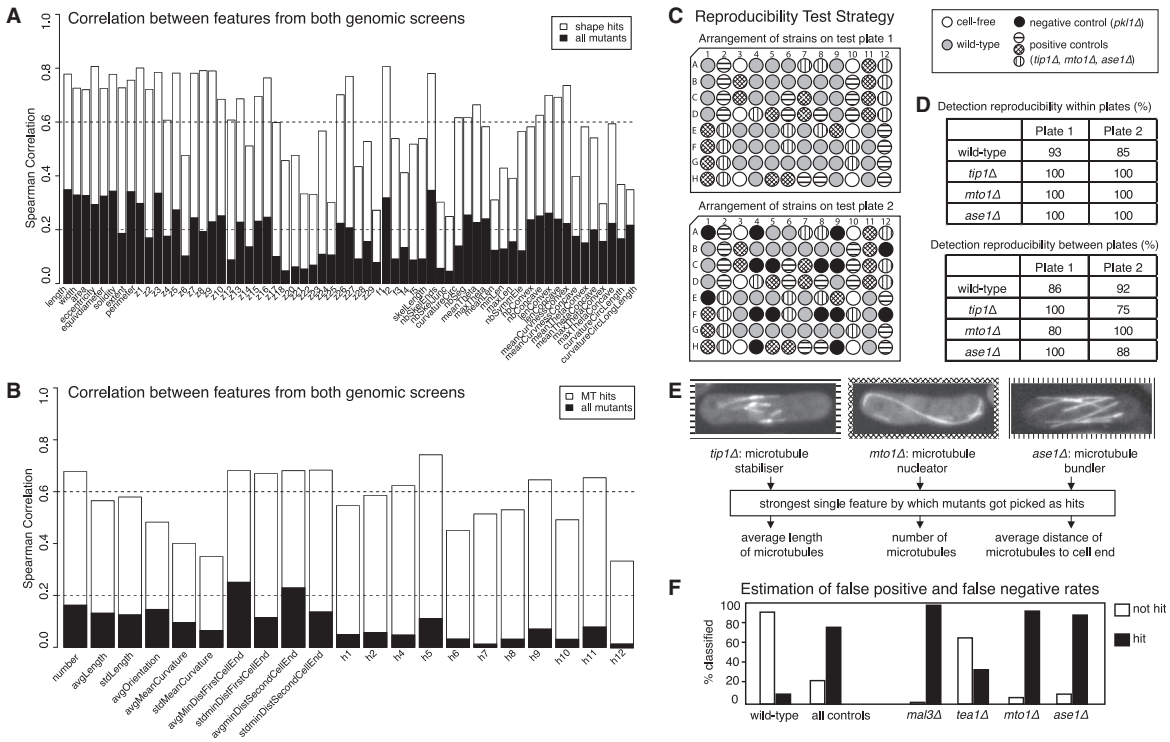

Figure 2. Quality Control

(A) Spearman correlation of cell shape features for all mutants and for cell shape hits between the two genomic screening rounds. Only features consistent between both screens were used for analysis.

(B) Similar to (A) for microtubule features.

(C) Arrangement of known microtubule mutants and wild-type cells in plates used in proof-of-method experiments, designed to test for plate location effects and reproducibility of positive and negative control phenotypes.

(D) Percentage of correct identification of mutant versus wild-type populations within and between test plates.

(E) Known mutants used and features for which they were picked.

(F) Rates of incorrect identification of a mutant as wild-type (false-negative rate) for four mutants versus the rate of incorrect identification of wild-type controls as mutant (false-positive rate).

were filmed with two-color (405 nm, 488 nm) automated high-throughput confocal microscopy at high magnification (60× 1.2NA) and in 3D (xy and 16 z planes), and their images computationally analyzed and phenotyped using custom-made image analysis software.

Quantitative Phenotyping of Cell Shape, Microtubules, and Cell-Cycle Stage

First, we segmented images in the Cascade blue channel, and extracted 57 shape and gray-level features from each 2D cell object (length, width, area, convexity, concavity, topological skeleton, fluorescence intensity along the object's contour, etc.; Figures 1B and 2A; Figure S2 and Table S1). Then, using Machine Learning (Jones et al., 2009; Sommer and Gerlich, 2013), specifically a Random Forest classifier trained with both wild-type shaped and strongly misshapen mutant cells, we identified and rejected poorly segmented objects and kept only well-segmented cells for further analysis (9.28% out-of-bag error rate).

Subsequently, we detected microtubules in the GFP channel xyz image stacks, reconstructed microtubule orientation within every cell in 3D, and extracted 24 geometrical and grey level microtubule features (number, length, fluorescence intensity, orientation, etc.; Figures 1C, 2B, and S3A–S3D; Table S2).

Finally, we identified the cell-cycle stage for each cell based on 3D microtubule pattern, using a four-class support vector machine classifier (Jones et al., 2009; Sommer and Gerlich, 2013),. The classifier, trained with wild-type cells and cells from four known microtubule mutants (lacking Tip1/CLIP170, Brunner and Nurse, 2000; Mto1/Centrosomin, Sawin et al., 2004; Ase1/PRC1, Loïodice et al., 2005; and Pkl1/Kinesin-14A, Troxell et al., 2001) distinguished four cell-cycle-related microtubule patterns: interphase microtubule array (IP; characteristic of G2 phase in our exponential growth conditions), metaphase spindle (SP; characteristic of M phase), postanaphase array (PAA; reflective of G1 phase), and postmitotic interphase microtubule array (called IP2 for "interphase2"; likely reflective of G1-S phases). The classifier accuracy was 93.78% across the wild-type and

CellPress

Developmental Cell

Genes Linking Cell Cycle, Shape, and Microtubules

four mutants combined, indicating that we could achieve robust cell-cycle stage assignment even when microtubules had an abnormal phenotype. This was partly thanks to the use of 3D microtubule features, which allowed a more accurate assignment of cell-cycle stage than 2D features (see Supplemental Experimental Procedures). The output was a signature of four scores reflecting the proportion of cells assigned to each cell-cycle stage, for each wild-type (typically 70% IP, 10% SP, 10% PAA, and 10% IP2) and mutant cell population, indicative of their cell-cycle progression characteristics (Figures 1D, S3E, and S3F).

Hit Detection, 10-Fold Validation, and Selection

We used two complementary strategies for detecting KO mutants with aberrant cell shape or microtubules (hits; Figures 1B, 1C, and S4). The first strategy identified mutants with a prominent alteration in a single feature (p value; Figure 1). The second strategy identified mutants with multiple subtle feature alterations (multiparametric profile scoring, Figure 1). In proof-of-principle experiments prior to screening, the use of both strategies combined led to highly consistent detection of the wild-type and of four known microtubule mutants within and across 96-well microplates (Figures 2C–2F), validating the quality and reproducibility of our hit detection strategy. The combined hit detection procedure was optimized independently for cell shape and microtubules based on the results of visual screening by a human observer of one genomic image data set (Figures S5 and S6).

To detect KO mutants (hits) with altered cell-cycle progression, we used bootstrap statistics to estimate the typical proportions of wild-type cells in each cell-cycle stage, scoring as hits KOs where at least two cell-cycle stages were statistically disproportionate with respect to the wild-type (i.e., under- or overrepresented; Figure 1D). That criterion ensured only detection of hits where general cell-cycle progression was affected. In particular, this allowed us to screen for genes distinct from classical cell-cycle regulators which, when mutated, often lead to checkpoint-mediated delay in just one cell-cycle stage or transition.

We grew, imaged, and computationally screened the entire library twice independently (Figures S1C–S1F), analyzing 1,880,064 images and making and analyzing 1,707,870 cell, 5,597,165 microtubule, and 1,607,406 cell-cycle stage assignments. This identified 372 cell shape hits, 449 microtubule hits, and 199 cell-cycle progression hits (note: hit identification for each process was independent of the others). To generate a high-confidence hit list, we then rescreened all hits at large-scale to obtain ten biologically independent screening rounds (also see the Protocol online) and ranked hits according to the fraction of repeats in which they were detected (confidence value; Figure 1E). Only hits with $\geq$35% confidence—the percentage corresponding to a well-established but weak phenotype hit (*tea1*Δ; Figure 2F) added as positive control in all repeats—were selected for further analysis. Altogether, this led to identification of 143 cell shape, 186 microtubules, and 35 cell-cycle progression high-confidence hit genes (Table S3) described next.

Genes and Pathways Controlling Cell Shape and Cell Size Control

Genes whose KO affected cell shape (cell shape genes; Figure 1E) included expected regulators of cell morphology, cell polarity and growth (Tea3, Pom1, Arf6, Rga2, Tea2, Sla2/End4, Myo1, Efc25, Scd2; for genes' annotations see http://www.pombase.org/) but also many genes related to a wide range of other processes such as trafficking or cell-cycle control, and 17 altogether unannotated genes. Forty-one percent (58/143) of genes implicated in cell shape regulation had not been previously reported as such, to our knowledge. Importantly, they were not identified in a recent visual screen of the *S. pombe* KO library (Hayles et al., 2013). This is likely due to the very different physiological conditions used in that study (nonexponential growth on solid medium) and our use of sensitive computational hit detection.

Similar to previously published studies (Bakal et al., 2007; Fuchs et al., 2010), cell shape hit classification was done using eight support vector machine classifiers trained to recognize eight basic phenotypic classes on an individual cell basis (Figures 3A, 3B, and S4A): stubby (wide), banana (curved), orb (round), kinky (S-shaped), long (elongated), skittle (with one side wider than the other), and T-shaped (branched). Classically, cell shape mutants are thought to display only one aberrant shape phenotype, such as being round or curved (Hayles et al., 2013). Surprisingly we found that, instead, all strains including the wild-type did not display only a single shape phenotype but rather could be defined as a mixture of those eight phenotypes (Figures 3A, 3B, and S4A). Thus, even within a genotypically uniform cell population, the genome allows *S. pombe* cells to explore multiple morphogenetic states. These might be brought about by cell-to-cell differences in the content of key shape-controlling proteins due, for example, to nonexact equipartition of cellular material—polarity landmarks, secretory machinery, cell wall composition/properties, etc.—between daughter cells at cell division or from stochastic gene expression.

Quantitatively, the most common aberrant cell phenotype was stubby (Figure 3C), indicating it may be the most general manifestation of compromised cell shape; conversely the least common was orb (i.e., completely nonpolarized), consistent with the finding that known genes whose disruption leads to complete rounding are essential (Hayles et al., 2013) and with the notion that complete loss of polarity may be incompatible with viability.

We clustered mutants based on their shape phenoprint and found that KOs of specific pathways shared characteristic morphological signatures (Figure 3D). One major cluster of predominantly stubby mutants comprised regulators of endocytosis and exocytosis (Vps25, Vps32, Vps36, Shd1, Dip1, Did4, Sla2/End4, and Sft1; likely involved in apical restriction of cellular growth zones), genes involved in ubiquitin/COP9 signalosome-mediated protein degradation (Csn1, Csn2, Pub1, and Ubi1), and several uncharacterized factors. Another major cluster comprised significantly longer mutants (note: cell elongation, usually associated with cell-cycle deregulation, was scored in our screen as a cell shape defect), corresponding to factors involved in the DNA damage response (DDR; Mre11, Rad50, Rad55, Set1, Ccq1, Cdt2, and Ctp1; the DDR leads to cell-cycle delay and cell elongation), transcriptional regulators (Cuf1 and Rep2), elongator complex subunits (Elp3, Elp4, Elp6, and Dph3; this complex has been involved in negatively regulating exocytosis), histone modifiers (Brl2, Cph1, Cph2, Dep1, and Rtx2), and other putative regulators.

Developmental Cell
Genes Linking Cell Cycle, Shape, and Microtubules

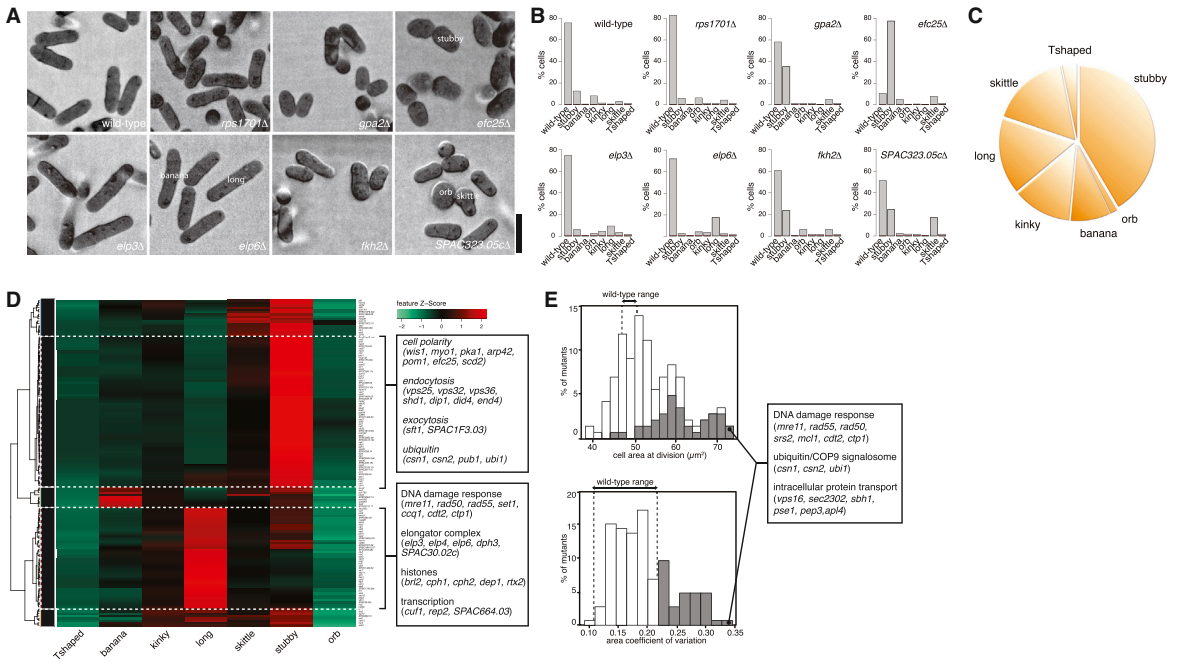

Figure 3. Cell Shape Genes and Deregulation of Cell Size Control

(A) Example cell shape hits.

(B) Corresponding cell shape hit shape profiles illustrating the comanifestation of multiple cell shape phenotypes within the genotypically uniform mutant populations.

(C) Phenotypic trait abundance (pie chart) illustrating the proportion of cells from all shape hit populations combined into stereotyped categories.

(D) Phenoprint clustering of cell shape hits based on the shape profiles in (B) and major functional gene ontology (GO) groups.

(E) Distributions of cell size at division (top) and its coefficient of variation (bottom) for cell shape mutants. Mutants with greater coefficient of variation than wild-type are shown in gray with selected gene names.

Scale bar represents 10 μm. See also Figures S2 and S4 and Tables S1 and S3.

We next asked whether, given their geometrical disruption, cell shape mutants properly control cell size. *S. pombe* cells are thought to need to reach a critical cell size at the G1/S and, most importantly, at the G2/M cell-cycle transition, when cells engage in cell division only after reaching twice their original size at birth (Mitchison, 2003). We calculated the average cell area (as a proxy for size) at mitosis by looking at cells containing a mitotic spindle and plotted distributions of the average area at mitosis for all hits (Figure 3E, top) and its coefficient of variation (Figure 3E, bottom). Ninety percent of cell shape hits had an area at division lower or higher than wild-type cells, which divide at an area of ~48 μm^2. This included KOs of factors known to be involved in cell size control such as Pom1 (Martin and Berthelot-Grosjean, 2009; Moseley et al., 2009). Strikingly, 30% had a higher coefficient of variation of the cell area than the 0.12–0.22 coefficient of the wild-type (gray, Figure 3E), indicative of lack of precision in cell size control at division. Interestingly, the latter was enriched for mutants in the ubiquitin/COP9 signalosome complex (implicated in cell-cycle and cell size control in *Drosophila melanogaster*; Björklund et al., 2006), DDR regulators, and various factors involved in intracellular protein transport. Because the COP9 complex regulates cullin activity in mammals and cullin (Cul-4) has been implicated in both cell-cycle control and the DDR (Hu et al., 2004), one possibility is that ubiquitin/COP9 and the DDR act on cell size control via the same pathway, possibly via their role in cell-cycle regulation. Alternatively, each may play a distinct role that needs to be further explored. Similarly, the role in size control of other factors identified needs to be clarified.

Genes and Pathways Associated with Characteristic Microtubule Signatures

Genes whose KO affected microtubules (microtubule genes; Figure 1E) included known microtubule regulators (Tea2, Tip1, and Mal3), mitochondrial factors, trafficking-related genes, and 19 altogether unannotated factors. Notably, 93.5% (174/186) of the genes implicated in microtubule regulation had not, to our knowledge, been previously reported as such. Mutants in those genes primarily led to deregulation of microtubule number, length, or orientation, with most KOs affecting several features simultaneously albeit in different proportions (Figure 4A). Microtubule length (encompassing the features: length, length variance, occupancy, occupancy variance; Figures 4B and 4C) was by far the most common quantitatively affected microtubule property, demonstrating that microtubule length per se is not essential for cell viability. In contrast, low microtubule number

CellPress

Developmental Cell

Genes Linking Cell Cycle, Shape, and Microtubules

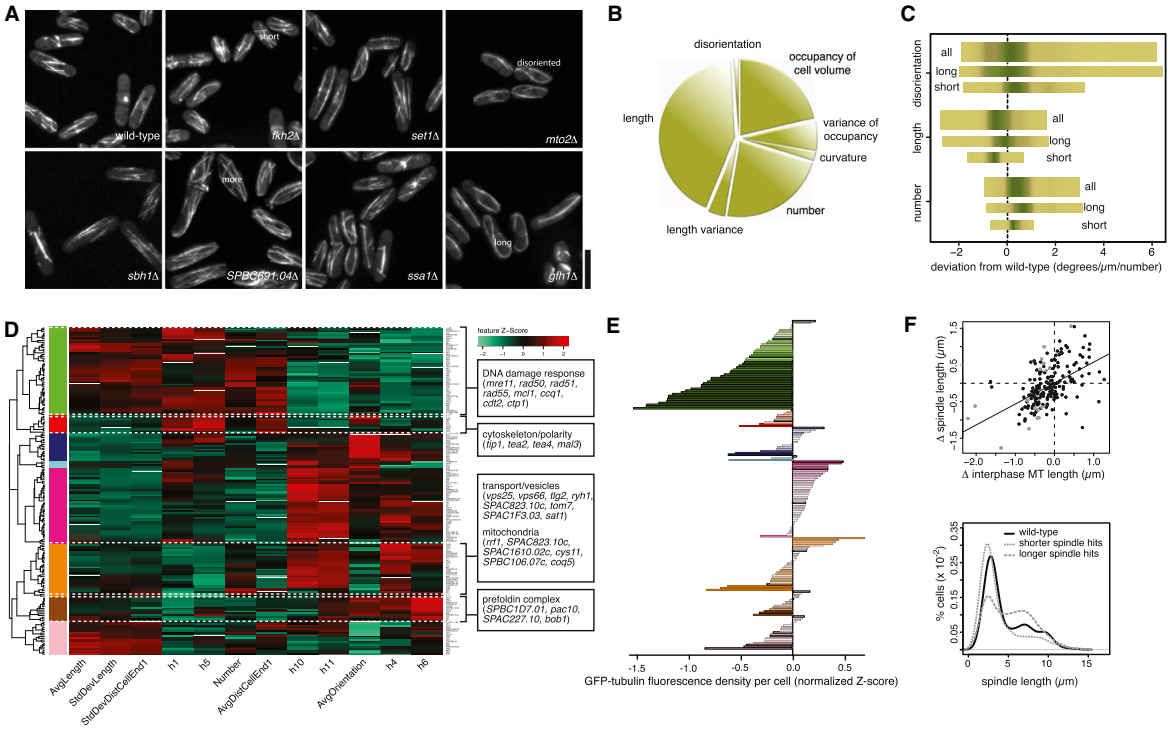

Figure 4. Genes Associated with Characteristic Microtubule Signatures

(A) Example microtubule hits.

(B) Phenotypic trait abundance (pie chart) illustrating the proportion of cells from all microtubule mutant cell populations combined displaying a significant phenotype in the features shown.

(C) Three significant features for all (top), only short (bottom) or only long (middle) mutants.

(D) Phenoprint clustering of microtubule hits based on extracted microtubule features and major functional GO groups.

(E) GFP-tubulin content. Average GFP-Atb2 fluorescence level per cell for each mutant is shown in (D) as a proxy for tubulin concentration with respect to the average wild-type value. Colors of the gene groups indicate which clusters from (D) they correspond to.

(F) Correspondence between interphase and mitotic phenotype. Top: comparison of interphase and spindle microtubule length changes for all microtubule hits. Grey: KOs with significantly altered spindle length (spindle hits). Bottom: percentage of cells with a given spindle length, for spindle hits with a spindle shorter/longer than wild-type (shorter/longer spindle hits). In all three classes of populations shown, cells accumulate with a short spindle, likely corresponding to prometaphase state during chromosome capture. Long spindle mutants (gray dashed) also accumulate cells with a longer spindle, which may indicate a delay during or on exiting anaphase B.

Scale bar represents 10 μm. See also Figures S3 and S4 and Tables S2 and S3.

was a very infrequent feature, consistent with the fact that microtubule nucleation is essential for cell viability.

Clustering of microtubule hits was done using a subset of 12 features selected by visual quality control to optimize for high interclass variability and low intraclass variability (i.e., to optimally group together KOs judged visually to have the same phenotype and assign to separate groups KOs with visually different phenotypes) and identified various pathways, each associated with a specific microtubule phenoprint (Figure 4D). Among the most prominent pathways we found were cytoskeleton/cell polarity (Tea2, Tip1, Tea4, Mal3; whose KO leads to short, disoriented microtubules), DDR (Mre11, Rad50, Rad51, Rad55, Mcl1, Ccq1, Cdt2, Ctp1; slightly elongated, hyperoriented microtubules), transport/vesicles and mitochondria (Vps25, Vps66, Tlg2, Ryh1, SPAC823.10c, Tom7, SPAC1F3.03, Sat1, and Rrf1, SPAC823.10c, SPAC1610.02c, Cys11, SPBC106.07c, Coq5; slightly more microtubules), and tubulin folding (the Prefoldin complex subunits SPBC1D7.01, Pac10, SPAC227.10, Bob1; fewer microtubules). We next assessed whether differences in tubulin content could account for the mutants' microtubule feature signatures by quantitating their intracellular GFP-Atb2 fluorescence. We found that, although many mutants displayed substantial differences in tubulin content compared to the wild-type, there was no obvious correlation between their microtubule feature signatures and GFP-tubulin fluorescence, suggesting that their microtubule phenotype arises from deregulation of microtubule assembly rather than tubulin content (Figure 4E). Interestingly, analysis of the hits' microtubule length in interphase versus mitosis revealed a correlation between the two in ~80% of cases (Figure 4F), indicating that many genes identified may also play a role in mitotic spindle control.

Developmental Cell
Genes Linking Cell Cycle, Shape, and Microtubules

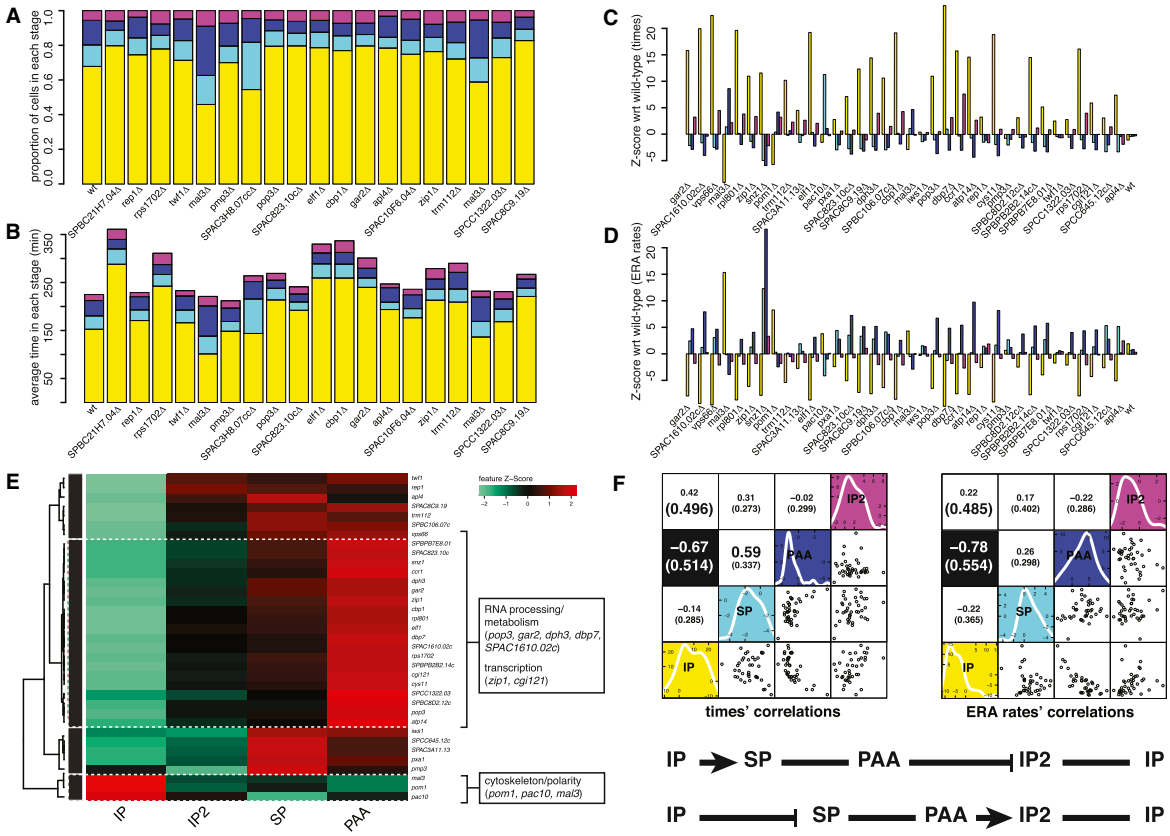

Figure 5. Cell-Cycle Progression Genes and Cell-Cycle Stage Correlation Analysis

(A) Proportional representation of the cell-cycle phases—interphase (yellow), spindle (light blue), PAA (blue), interphase 2 (purple)—for a selection of cell-cycle progression hits and a reference wild-type (WT).

(B) As in (A) but with distributions scaled by the doubling time of each mutant.

(C) *Z* score plot showing the significance of deviation from wild-type of cell-cycle stage durations for all hits.

(D) As in (C) for ergodic rate analysis (ERA)-derived progression rates.

(E) Phenoprint clustering based on hits' ERA rates and major functional GO groups.

(F) Correlation analysis among the four cell-cycle stages' durations and ERA progression rates. The graphs show correlation plots of the duration (left graph, bottom half) and rate (right graph, bottom half) of each cell-cycle stage against every other, for all hits. Spearman (and maximal information coefficient, in parentheses) correlation coefficients are shown for each combination in the top half of the graphs. Black boxes indicate significant anticorrelation between the duration and ERA rate of IP and PAA. The diagonal shows the distribution of *Z* score values for the durations (left) and ERA rates (right) across all hits, for each cell-cycle stage quantitated. A diagram representation of the implications of that anticorrelation for the overall cell-cycle is illustrated beneath (pointy arrows: accelerated progression; blunt arrows: delayed progression).

See also Figure S3 and Table S3.

Cell-Cycle Progression Genes Reveal Temporal Linkage between Nonconsecutive Cell-Cycle Phases

Genes whose KO affected cell-cycle progression (cell-cycle progression genes; Figure 1E) comprised a diverse range of factors and, as expected, did not include classical cell-cycle regulators. To look for interesting functional groups, we measured the cell-cycle duration of all cell-cycle progression hits. This allowed us to convert for each KO the proportions of cells in each cell-cycle stage into average times spent in each stage (Figures 5A and 5B). We then calculated the *Z* score of all four stage times (durations) with respect to the wild-type, for all hits (Figure 5C). Subsequently, we used ergodic rate analysis (ERA; Kafri et al., 2013) to estimate the average rate of progression from each cell-cycle stage to the next (i.e., the rate of exit from each stage) and calculated the ERA rates' *Z* score with respect to the wild-type rates for all cell-cycle progression hits (Figure 5D).

Clustering of the KOs based on their ERA rate *Z* scores (Figure 5E) revealed groups of factors whose KO mainly results in accelerated exit from: IP into SP (Mal3, Pom1, Pac10: cytoskeleton/polarity related), SP into PAA (for example Pxa1: intracellular trafficking; Tos4, Iws1: transcription), PAA into IP2 (the largest group, including Pop3, Gar2, Dph3, Dbp7; RNA processing and metabolism), and IP2 into IP (including Twf1, Apl4: actin and endocytosis). Genes from the first cluster could be involved

CellPress

Developmental Cell

Genes Linking Cell Cycle, Shape, and Microtubules

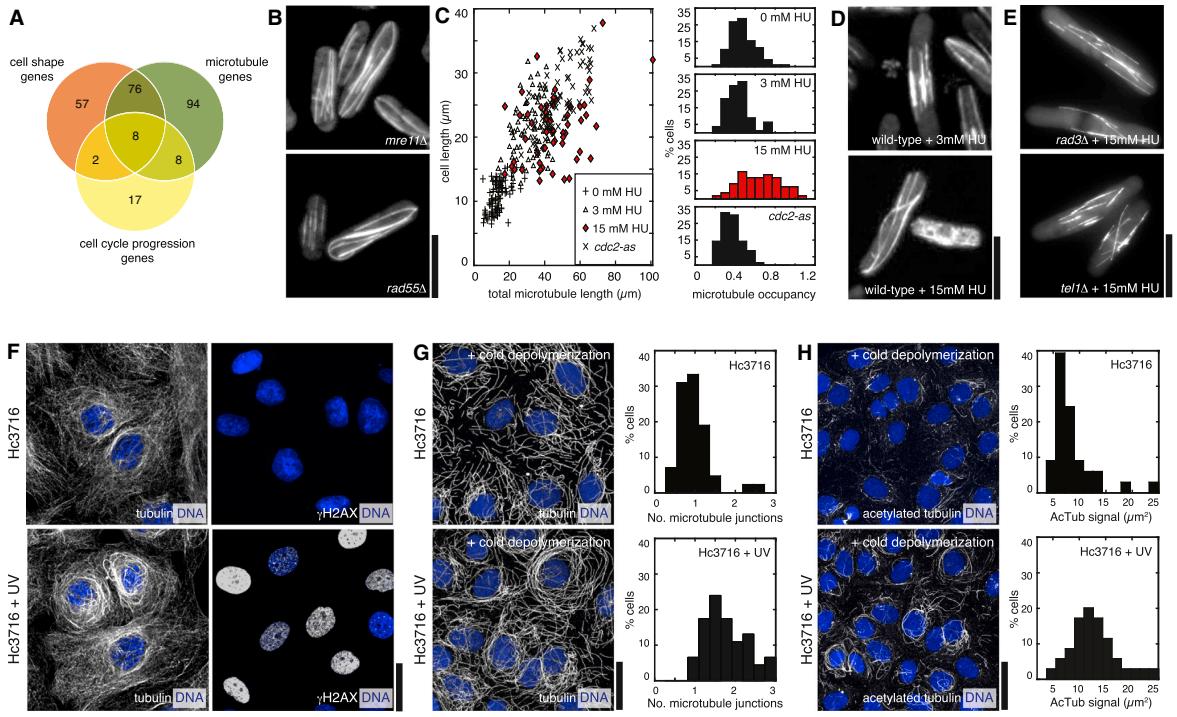

Figure 6. Genes Regulating Multiple Processes and Role of the DDR in Inducing Interphase Microtubule Stabilization

(A) Venn diagram illustrating cell shape, microtubule, and cell-cycle progression hits.

(B) The DNA repair defective mutants *mre11Δ* and *rad55Δ* display highly elongated microtubules.

(C) Hydroxyurea (HU) induces disproportionate microtubule elongation in wild-type cells. Microtubule occupancy is the ratio of average microtubule length to cell length. Contrary to 15 mM HU-treated cells, 3 mM HU-treated cells and cell-cycle-arrested *cdc2-as* cells do not disproportionately elongate microtubules.

(D) Images of 3 mM HU- (top) and 15 mM HU-treated cells (bottom).

(E) HU treatment does not induce enhanced microtubule stabilization in the DNA damage checkpoint mutants *rad3Δ* and *tel1Δ*.

(F) Left: effect on microtubules of UV-induced DNA damage in human cultured cells (Hc3716-hTERT). Right: γH2AX staining showing extent of DNA damage.

(G) Contrary to UV-untreated cells, UV-treated cells contain denser (right: quantitations) microtubule bundles that resist cold-induced depolymerization, indicative of microtubule stabilization.

(H) UV-treated cells contain significantly higher acetylated tubulin levels (right: quantitations) than UV-untreated cells.

Scale bars represent 10 μm.

in regulating the IP-SP transition via the Pom1 cell size control pathway (Martin and Berthelot-Grosjean, 2009; Moseley et al., 2009). Some genes from the fourth cluster could control the IP2-IP transition via regulation of the cytokinetic actomyosin ring (Rincon and Paoletti, 2012). It will be interesting to determine how all other genes, known and uncharacterized, are linked to cell-cycle progression control.

Analysis of correlations in durations/rates among the four cell-cycle stages (Spearman or maximal information coefficient; Reshef et al., 2011; Figure 5F) for our hits revealed a strong anticorrelation between IP and PAA, i.e., KOs with an extended IP tend to have a shorter PAA and vice versa. Because IP and PAA reflect G2- and G1-phases, respectively, this suggests that an accelerated G1/S transition (PAA-IP2 exit) causes delayed G2/M transition (IP-SP exit) and vice versa. Because *S. pombe* has been shown to possess two apparently independent cell size control mechanisms acting at G2/M (the dominant one) and G1/S (revealed in small *wee1-50* mutants; Fantes, 1977; Fantes and Nurse, 1978; Mitchison, 2003), which secure that nuclear division does not occur before cells reach a critical size, the observed anticorrelation might reflect compensation in cell-cycle progression caused by one of the mechanisms when the other fails. Interestingly, because the cell-cycle progression mutants identified here did not display altered size at cell division (Figure 6B and next section; contrary for example to *wee1-50* mutants), this suggests that both mechanisms exist and are active even in normally sized cells.

Genes Involved in Multiple Processes

Of the 262 genes identified for the three processes investigated, 168 (64%) were associated with a single process and 94 (36%) had multiple functional assignments (Figure 6A). Only ten (4%) genes were shared between cell shape and cell-cycle progression and 16 (6%) between microtubules and cell-cycle progression, implying that those processes are largely independent.

In contrast, 84 (32%) genes were shared between cell shape and microtubules, implying a potentially significant coregulation of both processes, as expected. These included factors involved

Developmental Cell
Genes Linking Cell Cycle, Shape, and Microtubules

CellPress

in cell morphogenesis and polarity (Aah3, Efc25, Tea2, Tip1), endocytosis (Did4, Vps25, Vps36, Snf7), but also transcriptional regulation (Pof3, Pmc6, Rep2, Rxt2, Tup12), chromatin remodeling (Rsc4, Set1, Arp42, Spp1, Swd1), and DDR (Mre11, Rad50, Rad55, Ctp1, Set1, Mcl1, Ubi1). Notably, 60/143 (42%) cell shape genes and 106/186 (57%) microtubule genes had a role in a single process alone. This implies that a link between cell shape and microtubule deregulation is not obligatory in cells and may be specific to particular machineries.

Future work will be needed to clarify which genes the associated with multiple processes actually correspond to factors that actively couple those processes.

The DDR Induces Stabilization of Interphase Microtubules

The largest functional group of KOs co-deregulating cell shape and microtubules was that of genes related to the DDR. Whereas the role of DDR genes in cell shape control (specifically in cell length and, hence, size control; Figures 3D and 3E) could be understood as resulting from DDR-induced cell-cycle arrest and elongation (Melo and Toczyski, 2002; Zhou and Elledge, 2000), a link between DDR and microtubules (Figure 4D) was unexpected and raised the question of whether DDR gene KOs lead to microtubule deregulation indirectly (via cell shape deregulation) or directly.

Therefore, we decided to investigate this link further and use this as a means to validate the predictions of our phenoprint clustering analysis. Inspection of cells lacking the DNA repair factors Mre11 and Rad55 revealed that in those mutants interphase microtubules are elongated compared to wild-type cells, often curling around cell ends, indicating increased microtubule stability (Figure 6B, quantitation not shown). In contrast, in cells lacking the ATR and ATM checkpoint kinases Rad3 and Tel1 microtubules were of wild-type length (not shown). This suggested that impaired DNA repair functions, and ensuing DDR arising from unrepaired DNA damage, may induce microtubule stabilization via the ATM/ATR pathway. To test this directly, we treated wild-type cells with different doses of hydroxyurea (HU) to induce the DDR in a primarily ATR-dependent manner, and we quantitated the effect of HU dosage on the average length of cellular microtubules and how it scales with cell length (microtubule occupancy). Cells untreated with HU displayed a range of microtubule lengths that varied proportionately with the wild-type range of cell lengths (Figure 6C, 0 mM HU). Similarly, following treatment with a low dose of HU, cells became elongated due to cell-cycle arrest and their microtubules became longer proportionally with cell length increase (Figures 6C and 6D top, 3 mM HU). In contrast, at a higher dose of HU, microtubules became disproportionately longer than cells, indicating an increase in microtubule stability induced specifically by the DDR (Figures 6C and 6D bottom, 15 mM HU). In agreement with this, in elongated G1- and G2-arrested *cdc2-as* mutant cells—where in principle no DDR activation occurs—microtubule elongation was also proportional to cell elongation (Figure 6C quantitations). Furthermore, the enhanced HU-induced microtubule stabilization was specifically DDR dependent, because microtubules did not become stabilized in cells lacking Rad3 or Tel1 treated with 15 mM HU (Figure 6E). Altogether, these data suggest that DNA damage induces microtubule lengthening in an ATR-dependent manner. To test whether this functional link is conserved, we then asked whether induction of DNA damage in human (Hc3716-hTERT) cells by UV treatment (30 J/m^2) also elicited a similar effect. We found that in those cells, induction of DDR often causes microtubules to organize in dense bundles around the cell nucleus (Figure 6F and not shown), suggestive of microtubule stabilization. To test this further, we then induced partial microtubule depolymerization by cold (4°C) treatment in both UV-untreated and UV-treated Hc3716 cells. We found that whereas not many UV-untreated cells contain thick bundles after cold depolymerization (1.22%, n = 575 cells; 15% of cell fields scored), many UV-treated cells still contain thick bundles (5.89%, n = 577 cells; 45% of cell fields scored) of much more connected microtubules (Figure 6G). In addition, microtubules in DDR-activated cells contain a much higher amount of acetylated tubulin (Figure 6H), indicative of increased microtubule stability (Hammond et al., 2008). We conclude that the DDR specifically induces stabilization of interphase microtubules, revealing a conserved link between the DDR and cytoskeletal control in cells. Although some links between those two machineries have been reported (Baschal et al., 2006; Lee et al., 2010, 2011; Xie et al., 2011), the conserved link described here points to a more general connection, whose exact physiological role and mechanistic details—in particular the cytoskeletal DDR target(s) involved—will need to be clarified. This might be of particular therapeutic relevance because a combination of cytostatic doses of DNA-damaging drugs with microtubule drugs has been shown to result in selective cytotoxicity and radiation/chemosensitization in some cancer cells (Baumgart et al., 2012; Blagosklonny et al., 2000; Lee et al., 2011).

Systems-Level Functional Relationships between Processes

One important aspect of our quantitative, multiprocess screening strategy is that it allowed us, beyond hit identification and phenotypic clustering, to obtain rich multidimensional feature sets characterizing all three processes simultaneously in cells, for hundreds of different KO conditions. Hence, we exploited the richness of those multidimensional feature sets to investigate statistically the systems-level functional relationships across processes.

We first turned to cell-cycle progression hits—selected as having at least two disproportionate cell-cycle stages with respect to the wild-type (Figure 1D)—and asked whether their cell-cycle progression defect quantitatively affected their cell size. Remarkably, we found that their cell size distribution—as assessed by measuring cells undergoing division—was indistinguishable from that of wild-type cells (Figure 7A). This is in contrast with mutants in conventional cell-cycle genes, which have traditionally been identified by virtue of their abnormal cell size phenotype, and indicates that the cell-cycle progression genes uncovered here likely constitute a mechanistically distinct class of cell-cycle regulators. Likewise and importantly, it demonstrates that disruption of cell-cycle progression does not necessarily affect cell size control.

We next turned to cell shape and microtubule hits and investigated dependencies between their features using Bayesian network analysis (Collinet et al., 2010; Yu et al., 2004). Like correlation analysis, Bayesian network analysis allows graphical

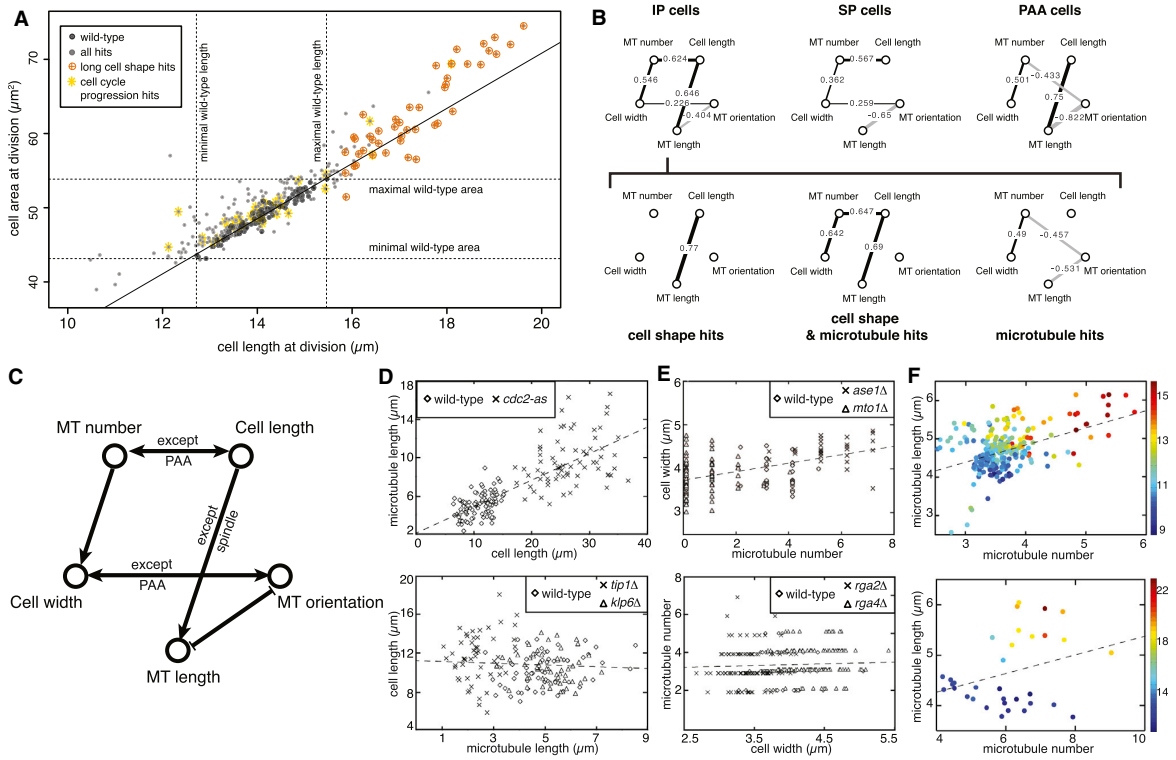

Figure 7. Systems-Level Functional Interactions between Processes

(A) Distribution of cell length and area at division for long cell shape hits (orange) versus cell-cycle progression hits (yellow). Note their lack of intersection. Wild-type controls (black) and other hits (gray) are shown, for comparison.

(B) Bayesian network inference graphs of the conditional correlation between cell shape and microtubule features across hits, filtered by cell-cycle stage (top row) or, for interphase cells only, subdivided by hitlist (cell shape and/or microtubule; bottom row). Correlation coefficients between variables are displayed on top of network edges (note that correlations were not directly used to obtain the networks).

(C) Diagram summarizing significant Bayesian causal links between cell shape and microtubule regulation in *S. pombe*.

(D) Causation between cell length and microtubule length. Top: plot of interphase cell length and microtubule length for wild-type and *cdc2-as* cells. Bottom: the inverse plot for cells with shorter (*tip1Δ*) or longer (*klp6Δ*) microtubules. Note that cell length influences specifically microtubule length, not the inverse.

(E) Causation between microtubule number and cell width. Top: plot of microtubule number against cell width for cells with more (*ase1Δ*) and fewer (*mto1Δ*) microtubules. Bottom: inverse plot for wider (*rga4Δ*) and narrower (*rga2Δ*) cells. To aid visualization, points have been artificially displaced along the microtubule number axis for different genotypes. Note that microtubule number influences specifically cell width, not the inverse.

(F) Plots of microtubule number against microtubule length colored by cell length (different colors signify different cell lengths), illustrating that correlation between these features is dependent upon cell length. Top: data from genomic screens; each point represents the average of all cells analyzed for a given mutant. Bottom: low-throughput validation using cells artificially elongated by cell-cycle arrest.

See also Figure S7.

representation of the probabilistic relationships between variables in a data set. However, in addition Bayesian networks allow inferring conditional dependencies between variables. Thus, two variables are disconnected in a Bayesian network graph if they are either independent or conditionally independent knowing one or several other variables. This allows inference of direct links between two variables, as opposed to indirect effects mediated or caused by a third variable.

We focused on five key features quantitated in our screen: microtubule number, microtubule length, microtubule (dis)orientation, cell length, and cell width. Using data from all cell shape and microtubule hits together, we constructed three Bayesian networks corresponding to three different cell-cycle stages (IP, SP, and PAA) by using for each network only cells in the corresponding cell-cycle stage, and compared edges between the networks. We found that, whereas specific pairs of features are interdependent in a consistently correlated or anticorrelated manner, many of those dependencies are cell-cycle stage-specific (Figure 7B, top three graphs; +, correlation; −, anticorrelation; Figure S7 illustrates the robustness of the analysis). For example, we found that cell length and microtubule number are always linked in cells except during postanaphase (PAA), when a profuse, radial microtubule network assembles in the cell middle. Similarly, cell width and microtubule (dis)orientation are always linked except in postanaphase, indicating that in this species not only interphase microtubule alignment but also

Developmental Cell
Genes Linking Cell Cycle, Shape, and Microtubules

mitotic spindle orientation relies mostly on cellular geometry (Théry et al., 2007). Instead, cell length and microtubule length are interdependent except during mitosis, indicating that mitotic spindle size is independent of cell size in this species (Wilbur and Heald, 2013).

We then constructed three different Bayesian networks using features from KOs deregulated in cell shape, microtubules or both (Figure 7B, bottom three graphs), and visually compared the networks to seek to infer directionality in the dependencies among features. We found that cell length and microtubule length are linked in hits deregulated in cell shape alone and in hits deregulated in both cell shape and microtubules. Instead, the two features are not linked in hits deregulated in microtubules only. We interpret this as implying that the causality is from cell length to microtubule length (e.g., increased cell length promotes increased microtubule length). Conversely and unexpectedly, we found that microtubule number and cell width are linked in microtubule-only hits and in cell shape and microtubule hits, but not in hits only deregulated in cell shape, leading us to interpret that the causality in this case is from microtubule number to cell width (e.g., increased microtubule number in cells promotes increased cell width). These results are summarized in Figure 7C.

To corroborate the inferred statistical relationships, we sought to externally validate some of its predictions. First, we looked at *cdc2-as* cells—which have altered cell length due to cell-cycle arrest—and found (Figure 6C) that, in this mutant, cell length changes induce proportional microtubule length changes (Figure 7D, top). In contrast, in mutants lacking the microtubule stabilizer Tip1/CLIP170 or the catastrophe-promoting kinesin-like protein Klp6/Kinesin-8—with, respectively, shorter and longer microtubules—microtubule length changes do not induce cell length changes (Figure 7D, bottom). Thus, cell length controls microtubule length and not the reverse, as predicted.

Second, we looked at mutants lacking the microtubule bundling protein Ase1/PRC1 or the microtubule nucleation factor Mto1/Centrosomin—with, respectively, a higher and lower number of microtubule bundles—and found that in those mutants, microtubule number changes induce cell width changes (Figure 7E, top). Instead and in contrast, in mutants lacking the Rho2 GTPase-activating protein Rga2 or the Cdc42/Rho2 GTPase-activating protein Rga4—narrower and wider than wild-type cells, respectively—cell width changes do not induce microtubule number changes (Figure 7E, bottom). Hence, microtubule number controls cell width and not the reverse, as inferred.

Third, we asked whether, as implied by the analysis, microtubule number and microtubule length are not directly linked. The absence of that direct link is interesting (despite the fact that microtubule number and length are known to be regulated by different machineries in cells) because one could expect both features to be somewhat dependent on one another, given that both rely on the common pool of tubulin available in each cell. In fact, plotting microtubule length versus number—both using the screen data set (Figure 7F, top) and external data from wild-type, 3mM HU-treated and *cdc2-as* cells for validation (Figure 7F, bottom)—showed a positive correlation between both features, implying a link between them. However, the correlation was absent among cells of similar length (Figure 7F). This demonstrates that, as predicted, microtubule number is not directly linked to microtubule length but rather both features are conditionally independent knowing cell length, i.e., they are coupled indirectly via the length of the cell.

Thus, the causal relationship between cell shape and microtubule regulation in *S. pombe* is directional and complex, with specific cell shape and microtubule features having defined epistatic relationships. Importantly, although our preliminary validation from Figures 7D–7F suggests that Bayesian analysis is indeed a useful predictor, given the partial and therefore potentially misleading nature of the parametrical description we have used, it will be crucial in the future to carefully validate the other predictions obtained using this approach.

Conclusions

In an effort to begin deciphering systematically how genes affect multiple cell biological processes and how processes are functionally linked, we carried out a quantitative multiprocess screen simultaneously monitoring three fundamental cell biological processes: cell shape, microtubule organization, and cell-cycle progression.

Our screen identified and annotated 262 genes, 131 of which were uncharacterized in *S. pombe* (of those, 29 had no predicted function in any species) and 131 had been described in the context of a different process, including six genes of the ubiquitin/elongator pathways not implicated in cell shape control; 39 membrane trafficking/mitochondrial genes, which we show are involved in microtubule regulation; and nine RNA processing/metabolism genes implicated in cell-cycle progression. We also probed in depth the systemic relationships among those three processes—identifying 94 genes regulating multiple processes and functional relationships linking defined aspects of such processes, in particular cell shape and microtubule control. This provides a rich, quantitative genomic data set available for further mining, validation, and mechanistic analysis by the scientific community (available at http://www.sysgro.org and http://www.pombase.org).

We extrapolate that an important gain in unexpected mechanistic insights could be obtained from multiprocess screening across an increasing range of cell biological processes, using simple unicellular systems with standardized/optimized genomic KO or siRNA/RNAi libraries (Collinet et al., 2010). A future challenge therefore lies in developing graphical and statistical modeling approaches (Nicolau et al., 2011; Singh et al., 2007) suited to cope with the very high dimensionality information generated by such screens, in particular to combine information from independent studies (Kemmer et al., 2009; Nicolau et al., 2011; Spalding et al., 2000; Troyanskaya et al., 2003) in a representable and interpretable manner. Such developments will be key to obtain a systemic picture of cell function and to better understand and predict synergistic or antagonistic interactions, including those among clinically relevant compounds (Horn et al., 2011).

EXPERIMENTAL PROCEDURES

Full methods are available in the Supplemental Experimental Procedures; specific standards for the synchronization and rescreening of thousands of parallel yeast strains are included in the Protocol.

CellPress

Developmental Cell

Genes Linking Cell Cycle, Shape, and Microtubules

Knockout Screen for Cell Shape, Microtubule, and Cell-Cycle Progression Genes

The Bioneer haploid deletion (knockout, KO) library v.2 (Bioneer, Korea) was modified to generate a GFP-tubulin expressing library (Dixon et al., 2008). KO mutants were grown exponentially for >48 hr and imaged in 96-well microplates (lectin-coated glass bottom, 10 μg/well) containing Cascade Blue Dextran-labeled YES medium (0.1 mg/ml). Two-color images were acquired using an automated OperaLX spinning-disk confocal microscope (Perkin Elmer) with 60× water-immersion objective (NA 1.2). Six stacks of 16 z planes 0.4 μm separation were collected for each well. The entire genomic KO library was filmed twice. Customized software was used for image analysis and feature extraction.

Hit Detection, Large-Scale Validation, and Bayesian Analysis

Cell shape or microtubule hits were KO strains with a: (1) low Kolmogorov-Smirnov p value relative to a mean wild-type for any one feature, or (2) significant Euclidean distance deviation from a mean wild-type across many features. Cell-cycle progression hits were KOs with the proportion of cells in greater than two 2-cell cycle stages outside the 95% bootstrap confidence interval of the corresponding wild-type stages. Genotypic and visual quality controls were done for corroboration. Hits were large-scale validated with ten times independent rescreening (see Protocol) and if picked in ≥35% of cases kept as high-confidence hits for analysis. Support vector machine classifiers assigned eight phenotypic classes to cell shape hits. ERA rates (Kafri et al., 2013) were calculated for cell-cycle progression hits. Clustering used R, functional GO assignments DAVID, Bayesian analysis, and the R package bnlearn (Scutari, 2010).

Investigation of DNA Damage Response and Microtubules

Yeasts were treated with HU 9 hr before filming and every 3 hr afterward and were imaged on lectin-coated MatTek dishes using a DeltaVision system (GE Healthcare). Hc3716-hTERT cells were grown to 70% confluence in Hepatocyte Medium Bullet Kit, exposed to 30 J/m^2 UVC, and grown for 8 hr before cold treatment or fixing. Immunostaining for β-tubulin or α-acetylated tubulin was done with ALEXAfluor-conjugated secondary antibodies, and DNA was DAPI-labeled. Cells were imaged with a Leica SP5 confocal microscope.

SUPPLEMENTAL INFORMATION

Supplemental Information includes Supplemental Experimental Procedures, seven figures, three tables, and one protocol and can be found with this article online at http://dx.doi.org/10.1016/j.devcel.2014.09.005.

AUTHOR CONTRIBUTIONS

R.E.C.-S. conceived/led the project and designed the general experimental and computational strategy. X.S. and M.B.M carried out preliminary experiments and generated the modified *S. pombe* haploid deletion library used. X.S. and J.L. carried out all experimental yeast work and imaging with continuous help from M.G. V.G. developed the image processing and large-scale analysis tools for screening and clustering with continuous help from A.C. A.C. carried out all Bayesian network inference work and ERA computation and correlation. T.W. contributed expertise in image analysis and data mining. R.E.C.-S. and E.P. designed the mammalian cell UV treatment experiments, and E.P. and L.W. carried out all mammalian cell work. R.E.C.-S. wrote the text with help from other coauthors.

ACKNOWLEDGMENTS

We thank Y. Barral, M. Peter, C. Wilson-Zbinden, D. Gerlich, G. Székely, P. Horvath, M. Held, D. Brunner, T. Makushok, J. Ellenberg, P. Nurse, J. Hayles, A. Sossick, C. Bradshaw, N. Samusik, S. Tooze, A. Csikász-Nagy, F. Vaggi, M. Sato, C. Schmidt, S. Jackson, J. Ahringer, D. St Johnston, V. Wood, P. Zegerman, E. Khabirova, C. Stocker, J. Pines, and the Carazo-Salas group for help and comments; A. Sossick and N. Lawrence for assistance with imaging; S. Jackson for antibodies (gamma-H2AX) and use of the UVC box; M. Sato for *S. pombe* strains; and J. Pines, S. Jackson, P. Horvath, F. Navarro, and E. Miska for critical reading of the manuscript. This work was supported by a European Research Council Starting Researcher Investigator grant (to R.E.C.-S.; SYSGRO), a SystemsX.ch Interdisciplinary PhD grant (to R.E.C.-S.; 2009-026), a Swiss National Foundation Project Grant (to R.E.C.-S.; 3100A0_120656/1), a Human Frontier Science Program Young Investigator grant (to R.E.C.-S. and A.C.; HFSP RGY0066/2009-C), a Biological Sciences Research Council Responsive Mode grant (to R.E.C.-S.; BB/K006320/1), an Isaac Newton Trust research grant (to R.E.C.-S.; 10.44(n)), a Wellcome Trust PhD studentship (to J.L.D.L.), a University Research Fellowship from the Royal Society (to E.P.; UF0905080), and a Cancer Research UK Programme Grant (to E.P.; A12460).

Received: November 2, 2013
Revised: April 21, 2014
Accepted: August 19, 2014
Published: October 27, 2014

REFERENCES

Aslett, M., and Wood, V. (2006). Gene Ontology annotation status of the fission yeast genome: preliminary coverage approaches 100%. Yeast *23*, 913–919.

Bakal, C., Aach, J., Church, G., and Perrimon, N. (2007). Quantitative morphological signatures define local signaling networks regulating cell morphology. Science *316*, 1753–1756.

Baschal, E.E., Chen, K.J., Elliott, L.G., Herring, M.J., Verde, S.C., and Wolkow, T.D. (2006). The fission yeast DNA structure checkpoint protein Rad26ATRIP/LCD1/UVSD accumulates in the cytoplasm following microtubule destabilization. BMC Cell Biol. *7*, 32.

Baumgart, T., Klautke, G., Kriesen, S., Kuznetsov, S.A., Weiss, D.G., Fietkau, R., Hildebrandt, G., and Manda, K. (2012). Radiosensitizing effect of epothilone B on human epithelial cancer cells. Strahlentherapie und Onkologie. Organ der Deutschen Rontgengesellschaft *188*, 177–184.

Björklund, M., Taipale, M., Varjosalo, M., Saharinen, J., Lahdenperä, J., and Taipale, J. (2006). Identification of pathways regulating cell size and cell-cycle progression by RNAi. Nature *439*, 1009–1013.

Blagosklonny, M.V., Robey, R., Bates, S., and Fojo, T. (2000). Pretreatment with DNA-damaging agents permits selective killing of checkpoint-deficient cells by microtubule-active drugs. J. Clin. Invest. *105*, 533–539.

Brunner, D., and Nurse, P. (2000). CLIP170-like tip1p spatially organizes microtubular dynamics in fission yeast. Cell *102*, 695–704.

Chia, J., Goh, G., Racine, V., Ng, S., Kumar, P., and Bard, F. (2012). RNAi screening reveals a large signaling network controlling the Golgi apparatus in human cells. Mol. Syst. Biol. *8*, 629.

Collinet, C., Stöter, M., Bradshaw, C.R., Samusik, N., Rink, J.C., Kenski, D., Habermann, B., Buchholz, F., Henschel, R., Mueller, M.S., et al. (2010). Systems survey of endocytosis by multiparametric image analysis. Nature *464*, 243–249.

Cotta-Ramusino, C., McDonald, E.R., 3rd, Hurov, K., Sowa, M.E., Harper, J.W., and Elledge, S.J. (2011). A DNA damage response screen identifies RHINO, a 9-1-1 and TopBP1 interacting protein required for ATR signaling. Science *332*, 1313–1317.

Dixon, S.J., Fedyshyn, Y., Koh, J.L., Prasad, T.S., Chahwan, C., Chua, G., Toufighi, K., Baryshnikova, A., Hayles, J., Hoe, K.L., et al. (2008). Significant conservation of synthetic lethal genetic interaction networks between distantly related eukaryotes. Proc. Natl. Acad. Sci. USA *105*, 16653–16658.

Fantes, P.A. (1977). Control of cell size and cycle time in Schizosaccharomyces pombe. J. Cell Sci. *24*, 51–67.

Fantes, P.A., and Nurse, P. (1978). Control of the timing of cell division in fission yeast. Cell size mutants reveal a second control pathway. Exp. Cell Res. *115*, 317–329.

Forsburg, S.L. (2003). Overview of Schizosaccharomyces pombe. Current Protocols in Molecular Biology *64*, 13.14.1–13.14.3.

Fuchs, F., Pau, G., Kranz, D., Sklyar, O., Budjan, C., Steinbrink, S., Horn, T., Pedal, A., Huber, W., and Boutros, M. (2010). Clustering phenotype populations by genome-wide RNAi and multiparametric imaging. Mol. Syst. Biol. *6*, 370.

Developmental Cell
Genes Linking Cell Cycle, Shape, and Microtubules

Hagan, I.M. (1998). The fission yeast microtubule cytoskeleton. J. Cell Sci. *111*, 1603–1612.

Hammond, J.W., Cai, D., and Verhey, K.J. (2008). Tubulin modifications and their cellular functions. Curr. Opin. Cell Biol. *20*, 71–76.

Hayles, J., Wood, V., Jeffery, L., Hoe, K.L., Kim, D.U., Park, H.O., Salas-Pino, S., Heichinger, C., and Nurse, P. (2013). A genome-wide resource of cell cycle and cell shape genes of fission yeast. Open biology *3*, 130053.

Horn, T., Sandmann, T., Fischer, B., Axelsson, E., Huber, W., and Boutros, M. (2011). Mapping of signaling networks through synthetic genetic interaction analysis by RNAi. Nat. Methods *8*, 341–346.

Hu, J., McCall, C.M., Ohta, T., and Xiong, Y. (2004). Targeted ubiquitination of CDT1 by the DDB1-CUL4A-ROC1 ligase in response to DNA damage. Nat. Cell Biol. *6*, 1003–1009.

Jones, T.R., Carpenter, A.E., Lamprecht, M.R., Moffat, J., Silver, S.J., Grenier, J.K., Castoreno, A.B., Eggert, U.S., Root, D.E., Golland, P., and Sabatini, D.M. (2009). Scoring diverse cellular morphologies in image-based screens with iterative feedback and machine learning. Proc. Natl. Acad. Sci. USA *106*, 1826–1831.

Kafri, R., Levy, J., Ginzberg, M.B., Oh, S., Lahav, G., and Kirschner, M.W. (2013). Dynamics extracted from fixed cells reveal feedback linking cell growth to cell cycle. Nature *494*, 480–483.

Kemmer, D., McHardy, L.M., Hoon, S., Rebérioux, D., Giaever, G., Nislow, C., Roskelley, C.D., and Roberge, M. (2009). Combining chemical genomics screens in yeast to reveal spectrum of effects of chemical inhibition of sphingolipid biosynthesis. BMC Microbiol. *9*, 9.

Kim, D.U., Hayles, J., Kim, D., Wood, V., Park, H.O., Won, M., Yoo, H.S., Duhig, T., Nam, M., Palmer, G., et al. (2010). Analysis of a genome-wide set of gene deletions in the fission yeast Schizosaccharomyces pombe. Nat. Biotechnol. *28*, 617–623.

Laufer, C., Fischer, B., Billmann, M., Huber, W., and Boutros, M. (2013). Mapping genetic interactions in human cancer cells with RNAi and multiparametric phenotyping. Nat. Methods *10*, 427–431.

Lee, H., Jeon, J., Ryu, Y.S., Jeong, J.E., Shin, S., Zhang, T., Kang, S.W., Hong, J.H., and Hur, G.M. (2010). Disruption of microtubules sensitizes the DNA damage-induced apoptosis through inhibiting nuclear factor κB (NF-κB) DNA-binding activity. J. Korean Med. Sci. *25*, 1574–1581.

Lee, K.J., Lin, Y.F., Chou, H.Y., Yajima, H., Fattah, K.R., Lee, S.C., and Chen, B.P. (2011). Involvement of DNA-dependent protein kinase in normal cell cycle progression through mitosis. J. Biol. Chem. *286*, 12796–12802.

Loïodice, I., Staub, J., Setty, T.G., Nguyen, N.P., Paoletti, A., and Tran, P.T. (2005). Ase1p organizes antiparallel microtubule arrays during interphase and mitosis in fission yeast. Mol. Biol. Cell *16*, 1756–1768.

Martin, S.G., and Berthelot-Grosjean, M. (2009). Polar gradients of the DYRK-family kinase Pom1 couple cell length with the cell cycle. Nature *459*, 852–856.

Melo, J., and Toczyski, D. (2002). A unified view of the DNA-damage checkpoint. Curr. Opin. Cell Biol. *14*, 237–245.

Mercer, J., Snijder, B., Sacher, R., Burkard, C., Bleck, C.K., Stahlberg, H., Pelkmans, L., and Helenius, A. (2012). RNAi screening reveals proteasome- and Cullin3-dependent stages in vaccinia virus infection. Cell Reports *2*, 1036–1047.

Mitchison, J.M. (2003). Growth during the cell cycle. Int. Rev. Cytol. *226*, 165–258.

Moseley, J.B., Mayeux, A., Paoletti, A., and Nurse, P. (2009). A spatial gradient coordinates cell size and mitotic entry in fission yeast. Nature *459*, 857–860.

Neumann, B., Walter, T., Hériché, J.K., Bulkescher, J., Erfle, H., Conrad, C., Rogers, P., Poser, I., Held, M., Liebel, U., et al. (2010). Phenotypic profiling of the human genome by time-lapse microscopy reveals cell division genes. Nature *464*, 721–727.

Nicolau, M., Levine, A.J., and Carlsson, G. (2011). Topology based data analysis identifies a subgroup of breast cancers with a unique mutational profile and excellent survival. Proc. Natl. Acad. Sci. USA *108*, 7265–7270.

Reshef, D.N., Reshef, Y.A., Finucane, H.K., Grossman, S.R., McVean, G., Turnbaugh, P.J., Lander, E.S., Mitzenmacher, M., and Sabeti, P.C. (2011). Detecting novel associations in large data sets. Science *334*, 1518–1524.

Rincon, S.A., and Paoletti, A. (2012). Mid1/anillin and the spatial regulation of cytokinesis in fission yeast. Cytoskeleton (Hoboken) *69*, 764–777.

Rohn, J.L., Sims, D., Liu, T., Fedorova, M., Schöck, F., Dopie, J., Vartiainen, M.K., Kiger, A.A., Perrimon, N., and Baum, B. (2011). Comparative RNAi screening identifies a conserved core metazoan actinome by phenotype. J. Cell Biol. *194*, 789–805.

Sawin, K.E., Lourenco, P.C., and Snaith, H.A. (2004). Microtubule nucleation at non-spindle pole body microtubule-organizing centers requires fission yeast centrosomin-related protein mod20p. Current biology: CB *14*, 763–775.

Scutari, M. (2010). Learning Bayesian Networks with the bnlearn R Package. J. Stat. Softw. *35*, 1–22.

Simpson, J.C., Joggerst, B., Laketa, V., Verissimo, F., Cetin, C., Erfle, H., Bexiga, M.G., Singan, V.R., Hériché, J.K., Neumann, B., et al. (2012). Genome-wide RNAi screening identifies human proteins with a regulatory function in the early secretory pathway. Nat. Cell Biol. *14*, 764–774.

Singh, G., Mémoli, F., and Carlsson, G.E. (2007). Topological methods for the analysis of high dimensional data sets and 3d object recognition. Eurographics Symposium on Point-Based Graphics *22*, 91–100.

Sommer, C., and Gerlich, D.W. (2013). Machine learning in cell biology - teaching computers to recognize phenotypes. J. Cell Sci. *126*, 5529–5539.

Spalding, D.J.M., Harker, A.J., and Bayliss, M.K. (2000). Combining high-throughput pharmacokinetic screens at the hits-to-leads stage of drug discovery. Drug Discov. Today *5* (12, Suppl 1), 70–76.

Théry, M., Jiménez-Dalmaroni, A., Racine, V., Bornens, M., and Jülicher, F. (2007). Experimental and theoretical study of mitotic spindle orientation. Nature *447*, 493–496.

Troxell, C.L., Sweezy, M.A., West, R.R., Reed, K.D., Carson, B.D., Pidoux, A.L., Cande, W.Z., and McIntosh, J.R. (2001). pkl1(+)and klp2(+): Two kinesins of the Kar3 subfamily in fission yeast perform different functions in both mitosis and meiosis. Mol. Biol. Cell *12*, 3476–3488.

Troyanskaya, O.G., Dolinski, K., Owen, A.B., Altman, R.B., and Botstein, D. (2003). A Bayesian framework for combining heterogeneous data sources for gene function prediction (in Saccharomyces cerevisiae). Proc. Natl. Acad. Sci. USA *100*, 8348–8353.

Wilbur, J.D., and Heald, R. (2013). Mitotic spindle scaling during Xenopus development by kif2a and importin α. eLife *2*, e00290.

Wood, V., Gwilliam, R., Rajandream, M.A., Lyne, M., Lyne, R., Stewart, A., Sgouros, J., Peat, N., Hayles, J., Baker, S., et al. (2002). The genome sequence of Schizosaccharomyces pombe. Nature *415*, 871–880.

Xie, P., Li, L., Xing, G., Tian, C., Yin, Y., He, F., and Zhang, L. (2011). ATM-mediated NuSAP phosphorylation induces mitotic arrest. Biochem. Biophys. Res. Commun. *404*, 413–418.

Yin, Z., Sadok, A., Sailem, H., McCarthy, A., Xia, X., Li, F., Garcia, M.A., Evans, L., Barr, A.R., Perrimon, N., et al. (2013). A screen for morphological complexity identifies regulators of switch-like transitions between discrete cell shapes. Nat. Cell Biol. *15*, 860–871.

Yu, J., Smith, V.A., Wang, P.P., Hartemink, A.J., and Jarvis, E.D. (2004). Advances to Bayesian network inference for generating causal networks from observational biological data. Bioinformatics *20*, 3594–3603.

Zhou, B.B., and Elledge, S.J. (2000). The DNA damage response: putting checkpoints in perspective. Nature *408*, 433–439.

The genomic and phenotypic diversity of *Schizosaccharomyces pombe*

Daniel C Jeffares[1], Charalampos Rallis[1], Adrien Rieux[1,2], Doug Speed[1,2], Martin Převorovský[3], Tobias Mourier[4], Francesc X Marsellach[1], Zamin Iqbal[5], Winston Lau[1], Tammy M K Cheng[6], Rodrigo Pracana[1], Michael Mülleder[7], Jonathan L D Lawson[8,9], Anatole Chessel[7], Sendu Bala[10], Garrett Hellenthal[1,2], Brendan O'Fallon[11], Thomas Keane[10], Jared T Simpson[10,17], Leanne Bischof[12], Bartlomiej Tomiczek[1], Danny A Bitton[1], Theodora Sideri[1], Sandra Codlin[1], Josephine E E U Hellberg[1], Laurent van Trigt[1], Linda Jeffery[6], Juan-Juan Li[6], Sophie Atkinson[1], Malte Thodberg[4], Melanie Febrer[13], Kirsten McLay[13], Nizar Drou[13], William Brown[14], Jacqueline Hayles[6], Rafael E Carazo Salas[8,9], Markus Ralser[7,15,16], Nikolas Maniatis[1], David J Balding[1,2,17], Francois Balloux[1,2], Richard Durbin[10] & Jürg Bähler[1,2]

Natural variation within species reveals aspects of genome evolution and function. The fission yeast *Schizosaccharomyces pombe* is an important model for eukaryotic biology, but researchers typically use one standard laboratory strain. To extend the usefulness of this model, we surveyed the genomic and phenotypic variation in 161 natural isolates. We sequenced the genomes of all strains, finding moderate genetic diversity ($\pi = 3 \times 10^{-3}$ substitutions/site) and weak global population structure. We estimate that dispersal of *S. pombe* began during human antiquity (~340 BCE), and ancestors of these strains reached the Americas at ~1623 CE. We quantified 74 traits, finding substantial heritable phenotypic diversity. We conducted 223 genome-wide association studies, with 89 traits showing at least one association. The most significant variant for each trait explained 22% of the phenotypic variance on average, with indels having larger effects than SNPs. This analysis represents a rich resource to examine genotype-phenotype relationships in a tractable model.

Although the standard laboratory strain of *S. pombe* has been extensively studied, genetic variation and phenotypic diversity have been analyzed only in preliminary ways[1–3]. Remarkably little is known about the evolutionary history or ecology of this model organism. It was first described in East African millet beer in 1893, and the standard laboratory strain was isolated from French wine in 1924 (ref. 4). Natural isolates have also been collected from vineyards in Sicily and cachaça (a sugarcane spirit) in Brazil and have been found to contribute to the microbial ecology of kombucha (fermented tea)[1,5,6]. The diverse origins of these natural isolates (**Fig. 1a** and **Supplementary Table 1**) suggest that this yeast species is now widely distributed.

To further describe *S. pombe*, we analyzed the genetic and phenotypic variation in natural isolates. Because the natural environment is not known, we collected all isolates available from the major stock centers and those given to us by microbial ecologists (**Supplementary Table 1**). These 161 strains had been collected over the last 100 years, in over 20 countries across the globe, primarily from cultivated fruit or various fermentations. Notably, the strains of known origin had been associated with human activities, providing little information about the natural environment of the species.

RESULTS

Variation and population structure

We sequenced the genome of all strains to at least 18-fold coverage, with a median of 76-fold coverage. To facilitate the detection of genetic variants, we mapped reads to the reference genome[7]. Mapping was comprehensive and accurate owing to the small, non-repetitive

[1]Department of Genetics, Evolution and Environment, University College London, London, UK. [2]University College London Genetics Institute, University College London, London, UK. [3]Department of Cell Biology, Faculty of Science, Charles University in Prague, Prague, Czech Republic. [4]Natural History Museum of Denmark, University of Copenhagen, Copenhagen, Denmark. [5]Wellcome Trust Centre for Human Genetics, Oxford, UK. [6]Cell Cycle Laboratory, Cancer Research UK London Research Institute, London, UK. [7]Department of Biochemistry, University of Cambridge, Cambridge, UK. [8]Department of Genetics, University of Cambridge, Cambridge, UK. [9]Gurdon Institute, University of Cambridge, Cambridge, UK. [10]Wellcome Trust Sanger Institute, Cambridge, UK. [11]Associated Regional and University Pathologists, Inc. University of Utah, Salt Lake City, Utah, USA. [12]Commonwealth Scientific and Industrial Research Organisation (CSIRO) Mathematics, Informatics and Statistics, North Ryde, New South Wales, Australia. [13]Genome Analysis Centre, Norwich, UK. [14]Centre for Genetics and Genomics, University of Nottingham, Nottingham, UK. [15]Cambridge Systems Biology Centre, University of Cambridge, Cambridge, UK. [16]Division of Physiology and Metabolism, Medical Research Council (MRC) National Institute for Medical Research, London, UK. [17]Present addresses: Ontario Institute for Cancer Research, Toronto, Ontario, Canada (J.T.S.) and School of Biosciences and School of Mathematics and Statistics, University of Melbourne, Melbourne, Queensland, Australia (D.J.B.). Correspondence should be addressed to D.C.J. (d.jeffares@ucl.ac.uk) or J.B. (j.bahler@ucl.ac.uk).

Received 8 July 2014; accepted 14 January 2015; published online 9 February 2015; doi:10.1038/ng.3215

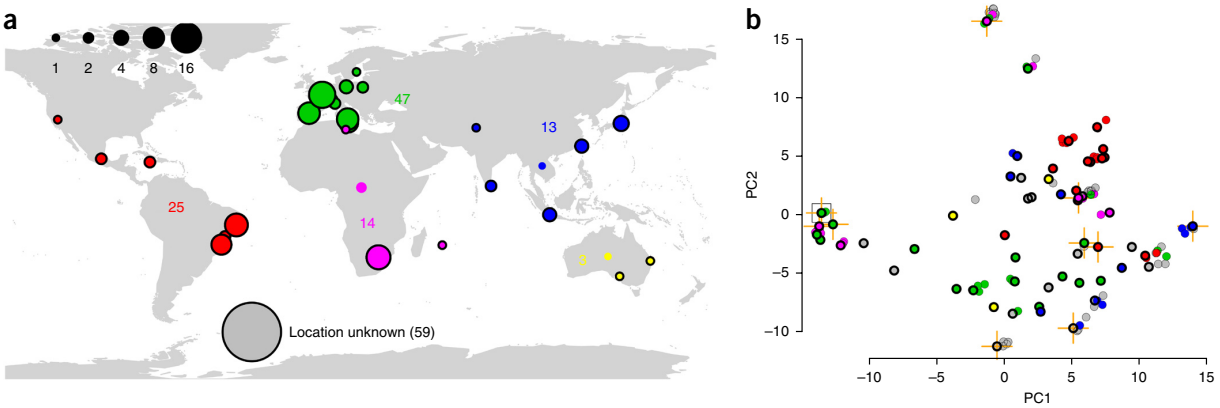

Figure 1 An overview of the strain collection. (**a**) Geographical origins of all 161 strains analyzed. Colored circles indicate the original sources of the strains used in this study, with circle sizes indicating the number of strains obtained from each site (the scale is illustrated with black circles). Strains for which only an approximate source is known (for example, Africa) lack a black border. (**b**) Principal-component projection of the 'drift distance' between strains determined using the 752 unlinked SNPs (Online Methods). The color scheme is as in **a**. Leupold's 972 reference strain is indicated with an open black square; strains that are members of the group of 57 non-redundant strains have a black border; strains known to contain large structural inversions[2] are indicated with an orange cross. PC, principal component.

nature of the genome, allowing us to query 93% of the genome with high confidence (11.8 Mb of 12.6 Mb). We identified 172,935 high-quality SNPs, 14,508 small indels and 1,048 long terminal repeat (LTR) insertions (**Table 1**).

Initial analysis identified 25 clusters of near-identical strains that differed by <150 SNPs (**Supplementary Fig. 1a**). As most clusters were isolated from a single location, they probably derive from isolated, mitotically reproducing populations or from repeat depositions of the same strain to stock centers. By excluding such 'clonal' strains, we identified a set of 57 strains that each differed by ≥1,900 SNPs, which included 99.6% of the SNPs identified for all strains. The average pairwise diversity (π) within these 57 strains was 3.0×10^{-3} substitutions/site (3 SNPs/kb), slightly lower than the diversity within the budding yeast *Saccharomyces cerevisiae* ($\pi = 5.7 \times 10^{-3}$)[8,9]. Flow cytometry indicated that all but one (JB1207/NBRC10570) of these strains were haploid. Also, 34 of 39 strains were homothallic (containing both mating types), and all 57 strains were prototrophic (able to grow on the same minimal medium as the reference strain).

To describe the relatedness among these 57 strains, we analyzed SNPs in the nuclear genome. Some strains carry large inversions and translocations[2,10], which bias estimates of population structure when large regions of chromosomes are inherited without recombination[11]. Therefore, we selected a set of 752 SNPs that were close to linkage equilibrium (pairwise $r^2 < 0.5$) and were distributed relatively evenly across the genome (**Supplementary Fig. 1b**), the use of which better suits population genetic models that assume no linkage between variants. Principal-component analysis with these SNPs showed weak clustering of strains by geography (**Fig. 1b**). Moreover, a pattern of genetic isolation by distance was evident, with genetic and physical distances being weakly but significantly correlated ($P = 9.9 \times 10^{-5}$; **Supplementary Fig. 1c**). This result suggests that there is some global population structure, which has been obscured by recent dispersal and intermixing of some strains.

To examine whether the observed genetic isolation had resulted in any reproductive isolation, we measured spore viability for 43 crosses that spanned the range of genetic distances, avoiding crosses that involved known structural variants[2]. We found a significant correlation between genetic distance and spore viability (Pearson's $r = 0.52$, $P = 6.5 \times 10^{-4}$; **Supplementary Fig. 1d**). This result suggests that these strains have accumulated sufficient genetic differences for reproductive barriers to emerge. Chromosomal rearrangements also contribute to reproductive isolation[10,12].

The budding yeast *S. cerevisiae* shows strong clustering of strains, determined both by geography and cultural uses[8,13]. To assess the situation for *S. pombe*, we applied the unsupervised genetic clustering methods Admixture[14] and fineSTRUCTURE[15], which do not take into account the geographical origin of the strains, to uncover any genetically differentiated populations. Both clustering methods identified between two and five populations that were consistent with those identified by principal-component analysis (**Supplementary Fig. 2a–c**). These results and further phylogenetic analysis showed that these groups were interbreeding populations, rather than clonally isolated lineages (**Supplementary Fig. 2d**). The F_{ST} values (representing the proportion of between-population genetic variance) for

Table 1 Genetic variation discovered in *S. pombe* strains

Annotation	Bases[a]	Genome (%)[a]	SNPs	Indels	LTRs
Genome	12,591,251	100	172,935	14,508	1,048
Exon	7,204,824	57.2	78,567	882	41
Synonymous, frame conserving	–	–	46,624	882	–
Nonsynonymous, frameshift	–	–	31,441	453	–
Pseudogene	38,896	0.3	254	19	0
Stop gain or loss	–	–	230	–	–
Start gain or loss	–	–	18	–	–
5′ or 3′ UTR	3,270,717	26	**48,839**	**6,947**	**298**
No annotation	1,851,692	14.7	**35,306**	**4,464**	**598**
Non-canonical noncoding RNA	1,722,785	13.7	**27,866**	**2,851**	**223**
Intron	213,282	1.7	**3,709**	**570**	4
Transposon LTR	76,038	0.6	806	66	–
Canonical noncoding RNA	60,235	0.5	291	26	4

Variant counts that are enriched (above what is expected for the percentage of the genome) are shown in bold.
[a]The number of bases and percentage of nucleotides annotated refers to the reference genome.

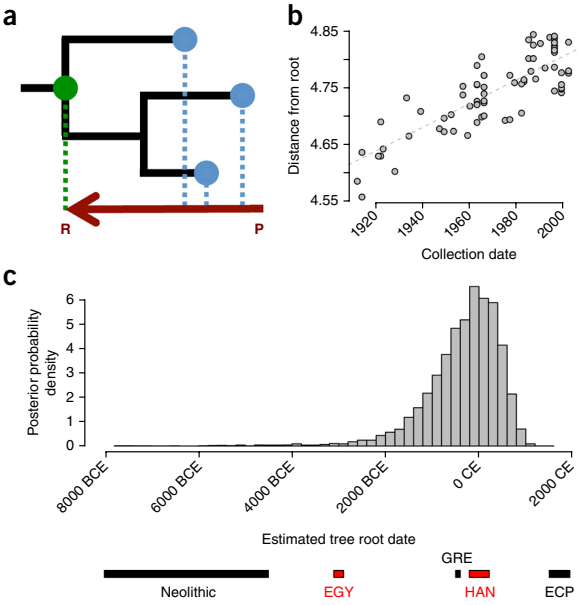

Figure 2 Recent dispersal of *S. pombe*. (**a**) Calibration of tree nodes using dated tips. With a collection of sequences sampled over various times (blue dots) up until the present day (P), we can jointly estimate the phylogenetic tree topology (black branches), the rate of evolution and the age of any node in the tree, including the root representing the most recent common ancestor of all strains (R; green dot). (**b**) Root-to-tip distances (mutations/site × 10^{-3}) correlate with collection date ($P < 1 \times 10^{-16}$), indicating that the data have reasonable predictive power. Distances were estimated using BEAST[35] from mitochondrial data for the 81 strains where collection dates were available; statistical details are provided in the Online Methods. The gray line shows the linear model. (**c**) Historical context of dispersal. The posterior probability distribution for time to the most recent common ancestor of the 81 collection-dated strains estimated using BEAST. The mean estimate was 340 BCE (95% confidence interval = 1875 BCE–1088 CE). Approximate historical periods are shown for context: ECP, European colonial period (~1500–1940 CE); HAN, Han dynasty in China (206 BCE–220 CE); GRE, Classical Greece (500 BCE–400 BCE); EGY, First Dynasty of ancient Egypt (3190 BCE–2800 BCE); Neolithic, Neolithic era (10,00 BCE–4,500 BCE).

the five-population clustering ranged between 0.22 and 0.59 (mean of 0.40) for different pairwise comparisons, indicating considerable genetic differences among these five connected clusters.

Dating the global dispersal of *S. pombe*

Although *S. pombe* now appears to be globally distributed, we have no ecological or historical context to this dispersal, except that most strains were isolated from brewed beverages. The available strains were collected between 1912 and 2002, which allowed us to estimate the age of every node in the phylogenetic tree from the mitochondrial genomes, including the root (the most recent common ancestor of all strains) (**Fig. 2a**). Modeling of the evolutionary rate showed that our data had predictive power (**Fig. 2b**), and we estimated the ancestor of all strains to have lived ~2,300 years ago (~340 BCE; **Fig. 2c**). We deduced a similar timeline from the nuclear genome sequences (**Supplementary Note**). This estimate points to an evolutionarily recent worldwide dispersal, perhaps associated with the spreading of technologies for brewing or other fermentations[16]. In comparison, it has been estimated that domesticated strains of *S. cerevisiae* dispersed 8,000–10,000 years ago, consistent with a Neolithic expansion[17]. Furthermore, our analysis provided a mean estimate of 1623 CE for the arrival of *S. pombe* in the Americas (95% confidence interval = 1422–1752 CE), coincident with European colonialism there, which began in 1492 CE. Notably, isolates from the Americas also showed the highest genetic similarity (**Fig. 1b** and **Supplementary Note**). Taken together, these findings suggest a recent European origin for *S. pombe* in the Americas.

Genetic diversity and genome function

Genetic variation data also contain signals of selection, which can be used to describe genome function. For example, both background selection and adaptive evolution reduce diversity most strongly in genetic elements that contribute to cell function. A consistent reduction in diversity is therefore a signature of functional elements, as reflected in the biased distribution of SNPs and indels (**Table 1**). Variation was significantly higher in the terminal 100 kb of all chromosomes and in centromeric regions (Mann-Whitney *U* test, $P = 1.5 \times 10^{-21}$ and 3.2×10^{-7}, respectively) (**Fig. 3a**). These regions are unusual in that they contain no essential genes, have an excess of pseudogenes (19% versus 0.2% in the whole genome), have an excess of LTR insertions and show low gene expression during vegetative growth, stationary phase and meiotic differentiation (**Supplementary Fig. 3**).

To systematically explore the relationship between genetic diversity and genome function, we calculated Watterson's θ (measuring nucleotide diversity) for the following annotation classes (**Fig. 3b**): protein-coding exons, introns, canonical RNAs (rRNAs, tRNAs, small nucleolar and small nuclear RNAs), long noncoding RNAs (lncRNAs), UTRs (of protein-coding transcripts) and the 15% of the genome not annotated as any of the preceding. Within exons, we calculated θ for one-fold-degenerate sites (where all changes to the DNA sequence lead to changes in the protein sequence) and four-fold-degenerate sites (where all changes to the DNA sequence result in the same protein sequence). Although polymorphisms at four-fold-degenerate sites are not truly neutral, they are subject to much weaker selection[18]. As expected, protein-coding exons were the least diverse regions of the genome (**Fig. 3b**). Additionally, 5′ and 3′ UTRs and introns were all significantly less diverse than four-fold-degenerate sites, suggesting substantial evolutionary selection at post-transcriptional levels of gene regulation. Analysis of SNP and indel median minor allele frequencies (MAFs) within windows showed consistent results (**Supplementary Fig. 4a**,**b**). Although lncRNAs appeared to be subject to little or no purifying selection overall, further analyses showed that the 20% of lncRNAs that were most highly expressed were subject to detectable purifying selection (**Supplementary Fig. 4c**–**e**). These findings indicate that purifying selection is dominated by protein-coding genes, including their UTRs. As a consequence, we would expect fewer genetic variants to remain in gene-dense regions. Consistent with this idea, θ was strongly negatively correlated with protein-coding exon density, with outliers mainly derived from telomeric regions that lack essential genes (**Fig. 3c**).

Variation in transposon insertions and gene content

Transposons create another source of genomic variation, which may contain signatures of evolutionary processes. *S. pombe* has only one family of mobile elements, the Tf-type LTR retrotransposons[19]. The reference genome contains only 13 full-length Tf elements but also has several hundred solo LTR fragments that indicate the sites of previous insertions. These elements are transcribed at low levels[20] and thus may be actively propagating. To examine this possibility, we

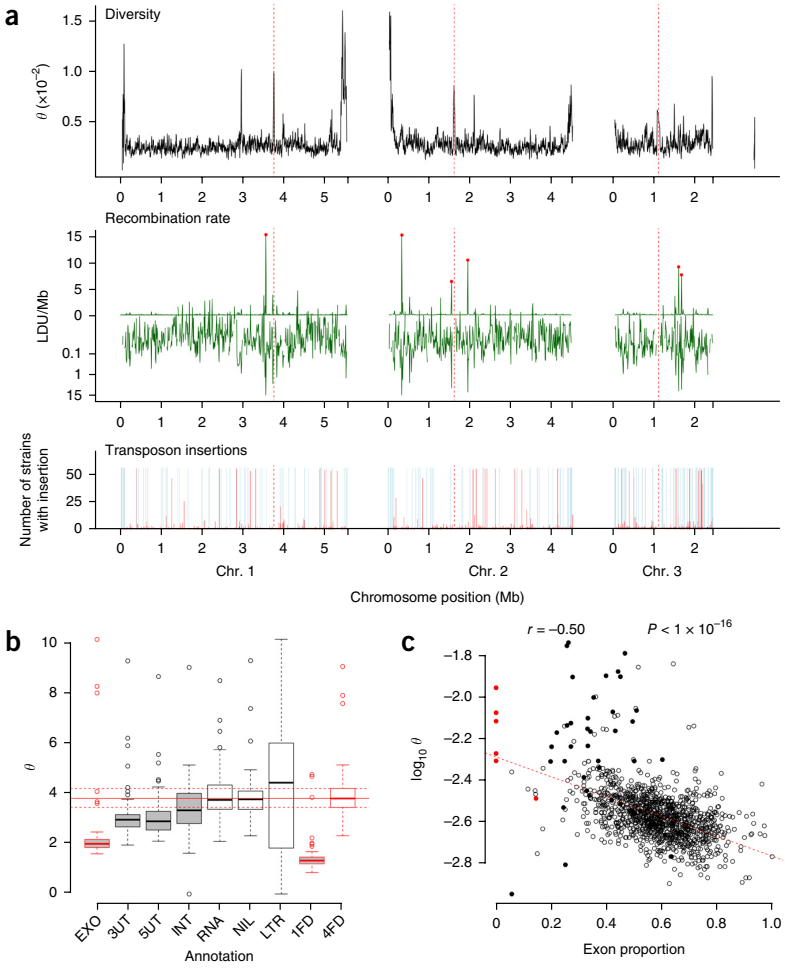

Figure 3 Relationships between genetic diversity and genome function. (**a**) Main features of diversity in the genome, with chromosome scale on the *x* axis and the mitochondrial genome on the right edge. Top, diversity (Watterson's θ) calculated using SNPs. Middle, recombination rate (scale, LDU/Mb × 10^{-3} above the *x* axis and log(1 + LDU/Mb) below the *x* axis). The six major recombination hotspots are indicated with red dots. Bottom, sites of Tf family LTR insertion (insertions present in all strains are shown in light blue) in the group of 57 non-clonal strains. (**b**) Diversity described by genome annotation. Distribution of Watterson's θ values for each centile of the genome, using only sites annotated as exons (EXO), 5′ and 3′ UTRs (5UT and 3UT), introns (INT), lncRNAs (RNA), unannotated regions (NIL), LTRs of Tf2 family transposons (LTR), and onefold-degenerate (1FD) and fourfold-degenerate (4FD) sites in exons. Protein-coding categories have red borders. The horizontal red lines correspond to the median and interquartile range for fourfold-degenerate sites; annotation classes with diversity significantly lower than the diversity for this proxy for neutral sites are shaded gray. One-sided paired Mann-Whitney *U* test *P* values in comparison to the fourfold-degenerate sites were as follows: exons, UTRs and onefold-degenerate sites, $P < 2 \times 10^{-16}$; introns, $P = 1 \times 10^{-6}$; lncRNAs, unannotated regions and LTRs, $P > 0.05$ (whiskers define the most extreme data points up to 1.5 times the interquartile range). (**c**) Diversity is negatively correlated with exon density. Diversity (θ) is plotted against the proportion of each window annotated as protein-coding exons, determined for 10-kb genomic windows. The Spearman's rank correlation and significance are shown above. Filled red circles, centromeric regions; filled black circles, telomeric regions (terminal 100 kb).

searched for new insertions of Tf elements in the 56 non-clonal strains and determined which reference LTRs were present in the other non-clonal strains. We located 1,048 LTR insertions, of which 78% were not present in the reference genome. Consistent with previous studies showing that Tf element insertions are targeted to RNA polymerase II (Pol II)-bound promoters[21,22], we observed a sharp peak of insertions upstream of transcription start sites (**Supplementary Fig. 5**) and few insertions in exons (**Table 1**). The majority of the insertions (593 loci; 57%) were present only in a single strain, suggesting recent transposon integration and loss.

Transposon integration has been proposed to occur during cellular stress[23,24]. To examine this model, we analyzed Tf element insertions within intergenic regions containing one promoter and one terminator, as these insertions allowed us to determine which promoter had been targeted by the insertion. Analysis of this set of 998 insertion sites upstream of 354 genes showed that insertions were more abundant upstream of genes with high Pol II occupancy, suggesting that the level of gene expression is a main determinant for Tf element insertion. Insertions were also enriched upstream of genes without introns, which tend to be rapidly regulated[25], and of Sty1-activated stress-response genes[26] (**Supplementary Table 2**). These observations corroborate the experimental finding that stress response genes are targeted by Tf insertions[22] and support the model that transposon integration occurs during stress but also preferentially occurs in highly expressed genes.

To gauge how much our collection differed in gene content, we used *de novo* assemblies of the 57 non-redundant strains to identify genes that were present in at least one strain but not present in the well-annotated reference strain. We created predictions of protein-coding genes for each strain from the assembly and attempted to locate similar genes in the reference strain genome. The strains were highly similar in their gene content; for example, 95% of the predicted encoded peptides from the divergent strain JB758 could be aligned to a reference protein with >95% identity. Curation identified only 17 putative new proteins, including 9 with strong supporting evidence (**Supplementary Table 3**). The majority of these new proteins were most similar to the products of genes from *Ascomycete* fungi, including 12 for which we could identify orthologs in related *Schizosaccharomyces* species by BLASTP (*e* value < 1×10^{-20}), suggesting ancient ancestry and subsequent gene loss in the reference strain. A notable exception was a protein most similar to the OsmC family from the plant-pathogenic enterobacterium *Brenneria salicis*, with highly conserved OsmC sequences being present in 29 of the 57 strains. This finding may reflect horizontal gene transfer, raising the possibility of an ecological association between *S. pombe* and plants.

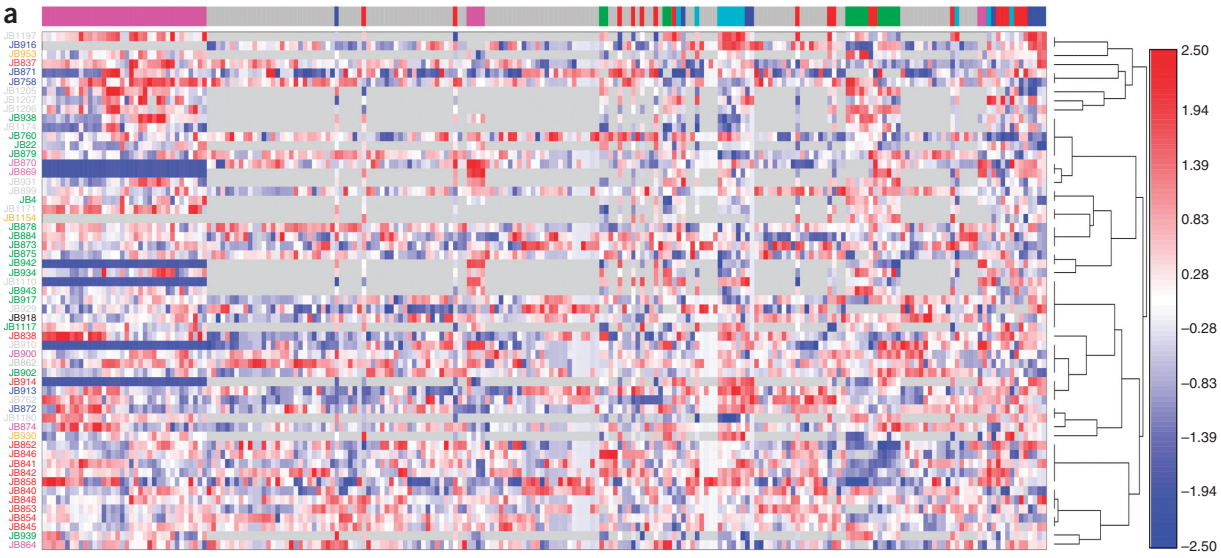

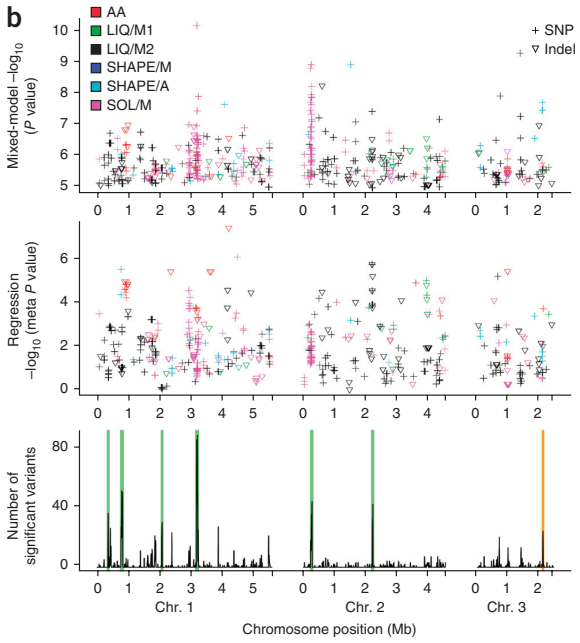

Figure 4 Phenotypes and genome-wide associations. (**a**) Phenotypic variation of all 57 non-clonal strains, with strains in rows and phenotypes in columns. Phenotype values are normalized, according to the scale on the right; missing data are represented by gray shading. The colored panel above indicates the category of phenotype measurement. Categories are amino acid concentrations (AA; red), growth on liquid media from this study (LIQ/M1; green), growth on liquid media[2] (LIQ/M2; black), manual (SHAPE/M; blue) and automated (SHAPE/A; cyan) determinations of shape phenotypes, and growth on solid media (SOL/M; magenta). Phenotypes are hierarchically clustered using phenotype values, and strains are clustered according to their genetic relatedness using the tree on the right inferred by fineSTRUCTURE. Strain names are colored according to geographical origin, as in **Figure 1a**. All phenotypes were measured for at least two biological replicates; values shown are generally the medians from biological and technical repeats (Online Methods). (**b**) Top, variants that were associated with one or more traits using the mixed-model GWAS. Variants are colored by phenotype category (as in **a**). Middle, the meta *P* values from linear regression within populations for the variants significant in our primary GWAS. Bottom, the total number of variants passing the significance threshold in each 10,000-nt window of the genome. Six hotspots (≥30 variants/10 kb) are indicated with green vertical bars. The orange bar shows the location of a hotspot discovered in an independent expression quantitative trait locus (eQTL) study[36]. *P*-value thresholds for the mixed model were derived from permutations of traits (Online Methods).

Distribution of recombination

Meiotic recombination is a source of diversity that influences natural selection and also reflects population history. Recombination events are initiated via double-stranded breaks (DSBs) that occur preferentially at hotspots in the *S. pombe* genome[27,28]. To examine the distribution of recombination, we estimated the historical recombination rate by constructing genetic maps with distances in linkage disequilibrium units (LDUs)[29]. The estimated recombination rate was zero for genomic regions spanned by 87% of the SNPs and was distributed log normally within the 13% of sites showing recombination (**Supplementary Fig. 6a**). Six regions with very high historical recombination rates were evident (rates above the 99.99th percentile; **Fig. 3a**). These hotspots showed a weak relationship with regions of high DSB activity (Spearman's rank $\rho = 0.25$, $P = 5.2 \times 10^{-16}$), but only 52% of the most recombinogenic SNPs were in DSB hotspots (**Supplementary Note**). As in other species, recombination positively correlated with genetic diversity (Spearman's $\rho = 0.43$, $P = 3.2 \times 10^{-57}$) and was primarily located away from genes (**Supplementary Fig. 6b**,**c**). For example, exons cover 57% of the genome, but only 26% of the 1,000 sites with the highest recombination were in exons. The result of the low-recombination regions is that, on average, LD (r^2) declines to 50% within 21 kb (**Supplementary Fig. 6d**). Hence, *S. pombe* has long haplotypes in comparison to eukaryotes of similar genome size and gene density; for example, LD in the budding yeasts *S. cerevisiae* and *Saccharomyces paradoxus* declines to 50% within 3–11 kb and 9 kb, respectively[8,9].

Phenotypic variation and genome-wide association studies

Model organisms have been used extensively to describe the complex genetics of quantitative traits[30,31], a task that is far more difficult in

less tractable species such as humans. It was clear that our collection contained variation in quantitative traits, both from previous studies[1,2] and our observation that some strains showed differences in cell shape and size (**Supplementary Fig. 7**). To extend these data, we measured 74 quantitative traits using 5 methods selected to sample a large variety of different phenotypes: (i) manual and (ii) automated measurements of cell shape and size, (iii) multiple growth parameters in minimal and rich liquid media, (iv) colony sizes on solid media under 42 different nutrient, drug and environmental conditions and (v) mass spectrometry measurements of intracellular amino acid concentrations. In combination with previous data[2], we analyzed 9,383 measurements for 223 phenotypes (an average of 164 values per strain) (**Fig. 4a** and **Supplementary Table 4**).

To assess the feasibility of using these data for GWAS, we estimated the heritability of each of these phenotypes using LDAK software[32], which considers additive genetic contributions without accounting for genetic interactions. These narrow-sense heritability estimates were significantly greater than zero for 130 of the 223 phenotypes, including for phenotypes for which data were gathered using all methods ($P < 0.05/220$; **Supplementary Fig. 8a** and **Supplementary Table 5**). Amino acid concentrations were among the most heritable phenotypes, indicating a high metabolic diversity with little contribution from genetic interactions (which are not measured by narrow-sense heritability). Analysis of trait measurements from biological and technical replicates also showed that the availability of data from replicates substantially increased the power of GWAS by reducing the non-genetic component of variance (**Supplementary Fig. 8b**).

GWAS would also be challenging if quantitative traits were clustered according to the population structure of the strains, as they are in budding yeast[33]. To examine this possibility, we tested each trait for significant differences in value among the five populations defined by Admixture. Only 19 of the 223 quantitative traits were significantly differentiated ($P < 0.05/220$), showing that traits are usually not stratified by population (**Supplementary Fig. 9a**).

Because our traits were highly heritable and infrequently stratified by population, we applied GWAS to search for the genetic variants associated with each of 223 quantitative traits. We used a mixed model[34], including all SNP and indel variants with minor allele counts ≥5 (108,105 SNPs and 8,543 indels). Mixed-model linear regression accounts for unequal relatedness between individuals. Using trait-specific significance thresholds with a 5% family-wise error rate for each trait, we discovered 1,419 variants that were significantly associated with at least one phenotype (1,239 SNPs and 180 indels; **Fig. 4b** and **Supplementary Table 6**). Genomic inflation factors (the median of the observed test statistic divided by the median expected test statistic) indicated that the mixed model was accounting well for unequal strain relatedness (**Supplementary Fig. 9a**,**b**). As an additional critical test of these associations, we divided the 57 non-clonal strains into 3 subpopulations (with 12, 26 and 17 members, defined by Admixture[14]) and examined each of the 1,419 variants for significant association using linear regression. Despite the small sample sizes, 67 of these variants were nominally associated with the trait and replicated in at least one additional subpopulation ($P < 0.05$; **Fig. 4b** and **Supplementary Note**).

Overall, we found that 1% of SNPs and 2% of indels were significantly associated with one or more traits (χ^2 test, $P = 3.0 \times 10^{-15}$). Associated indels also explained higher proportions of trait variance (**Supplementary Fig. 9c**), consistent with indels being more destructive variants. Many of the indels used in the GWAS were in the UTRs of coding transcripts (**Supplementary Fig. 9d**), which we showed are subject to selective constraint, suggesting that indels contribute to phenotypic change by altering gene regulation.

For 89 of the 223 traits examined, at least one variant passed the significance threshold. We considered the most significant variants to be the most likely candidates for causal variants. These 89 variants (72 SNPs and 18 indels) showed no bias for any genomic regions (**Supplementary Fig. 9d**) and explained 12–60% of trait variance, consistent with the expectation that the small sample size would have power to detect only variants of large effect. As for any GWAS, although estimates are globally unbiased, the largest estimates are likely to reflect a combination of genetic and stochastic effects and so tend to overestimate the true genetic variance explained, a bias known as winner's curse. In this study, the stochastic component of traits was well controlled by the use of replicate measurements (**Supplementary Fig. 8b**), which mitigates such bias.

Because of the extensive LD in this collection, many variants will be significant because they are in LD with a causal variant. To locate further variants that were independently associated with traits, we reapplied the mixed model for each of these 89 traits, conditioning on the most significant variant. This approach uncovered 18 additional associated variants (10 SNPs and 8 indels; **Supplementary Table 6**). These conditional hits explained 12–50% of the remaining trait variance.

The distribution of variants passing the significance threshold included six hotspots that harbored multiple variants associated with several different phenotypes (**Fig. 4b**). The most prominent of these hotspots contained 89 variants associated with 6 traits (**Supplementary Fig. 10a**), including the 3 most significant variants (3 SNPs, all in perfect LD with each other, all with $P = 7 \times 10^{-11}$). These polymorphisms were associated with growth in $MgCl_2$ and fell in the intergenic region between *nsk1* (encoding a microtubule-binding protein) and *sod2* (encoding a predicted manganese superoxide dismutase).

To experimentally validate this association, we crossed two strains that showed clear differences for this trait and contained the alternative haplotypes. We grew the pool of F_1 progeny in the presence and absence of $MgCl_2$. Sequencing of this pool showed a bias for the expected allele, supporting a role for this variant in these two genetic backgrounds (**Supplementary Fig. 10b**,**c**). These results provide experimental support for a causal role for this variant or the tightly linked SNPs. As a first step toward identifying the gene(s) affected by these SNPs, we compared the growth of the standard laboratory strain to that of strains with either *nsk1* or *sod2* deleted. Both deletion strains were sensitive to $MgCl_2$ (**Supplementary Fig. 10d**), consistent with the haplotype affecting a bidirectional promoter between *nsk1* and *sod2*.

DISCUSSION

In conclusion, this study contributes to the understanding of *S. pombe* in several areas. Our analysis is limited by the available strains collected from human-associated samples that share a relatively recent common ancestor. However, we show that GWAS are feasible with this strain collection and uncover a large number of potential causal variants. The effectiveness of GWAS, despite the low number of strains, was probably enabled by the relatively small genome and the quantitative phenotyping under tightly controlled conditions, which is obviously not possible with humans. We expect that the rich natural genetic and phenotypic variation presented here will provide a valuable resource to understand the complexities and subtleties of genetic architecture and genome function in this model species.

URLs. Gene List Analyzer, http://128.40.79.33/cgi-bin/GLA/GLA_input; FlowJo, http://www.flowjo.com/.

METHODS

Methods and any associated references are available in the online version of the paper.

Accession codes. Sequence data are archived in the European Nucleotide Archive under study accessions PRJEB2733 and PRJEB6284. All SNPs and indels were submitted to NCBI dbSNP under accessions 974514578–974688138 (SNPs) and 974702618–974688139 (indels).

Note: Any Supplementary Information and Source Data files are available in the online version of the paper.

ACKNOWLEDGMENTS

We thank L. Clissold, H. Musk, D. Baker and R. Davey for their contributions to sequencing, H. Levin for discussions about transposons, and J. Mata and S. Marguerat for comments on the manuscript. This work was supported by a Wellcome Trust Senior Investigator Award to J.B. (grant 095598/Z/11/Z), by the Wellcome Trust to S.B., T.K., J.T.S. and R.D., by grant 260801-BIG-IDEA from the European Research Council (ERC) and grant BB/H005854/1 from the Biotechnology and Biological Sciences Research Council (BBSRC) to A.R. and F.B., by UK Medical Research Council grant G0901388 to D.S. and D.J.B., by a Cancer Research UK Postdoctoral Fellowship to T.M.K.C., by an ERC Starting Grant (SYSGRO) to R.E.C.S., a Wellcome Trust PhD studentship to J.L.D.L. and BBSRC grant BB/K006320/1 to R.E.C.S. and A.C., by a Wellcome Trust grant (RG 093735/Z/10/Z) and ERC Starting Grant 260809 to M.R. (M.R. is a Wellcome Trust Research Career Development and Wellcome-Beit Prize Fellow), by Czech Science Foundation grant P305/12/P040 and Charles University grant UNCE 204013 to M.P. and by Cancer Research UK to L.J. and J.H.

AUTHOR CONTRIBUTIONS

D.C.J. coordinated all analyses, isolated DNA for sequencing, analyzed and filtered SNP calls, conducted diversity analysis and GWAS and drafted the manuscript. C.R. produced phenotype data for growth on various solid media and growth rates in liquid media. A.R. conducted analysis of dating using mitochondrial data. D.S. conducted GWAS. M.P. analyzed all phenotype data. T.M. identified LTR transposon insertions and analyzed transposon insertion data. F.X.M. conducted crosses for the analysis of spore viability. Z.I. produced indel calls with Cortex. W.L. conducted analysis of recombination rate, LD decay and principal-component analysis for distance between strains. T.M.K.C. assisted with phenotype and population analysis. R.P. analyzed Cortex and GATK indel calls. M.M. conducted amino acid profiling. J.L.D.L. and A.C. produced automated measures of cell morphology. S.B. aligned reads and produced GATK SNP calls. G.H. analyzed population structure using fineSTRUCTURE. B.O'F. estimated the time to the most recent common ancestor from the nuclear genome using ACG. T.K. identified LTR transposon insertions. J.T.S. produced *de novo* assemblies. L.B. developed the custom Workspace workflow Spotsizer. B.T. assisted with sequence analysis. D.A.B. assisted with analysis of new genes. T.S. assisted with strain verification. S.C. produced images of wild strains and assisted with strain verification. J.E.E.U.H. assisted with SNP validation. L.v.T. and M.T. assisted with LTR validation. L.J. and J.-J.L. assisted with manual measures of cell morphology and FACS. S.A. produced gene expression data. M.F., K.M. and N.D. assisted with sequencing. W.B. initiated and assisted with strain collection. J.H. coordinated manual measures of cell morphology and FACS. R.E.C.S. coordinated automated measures of cell morphology. M.R. coordinated amino acid profiling. N.M. conducted analysis of recombination and LD and advised on aspects of diversity and GWAS. D.J.B. advised on GWAS. F.B. advised on population structure and supervised A.R. R.D. facilitated sequencing. J.B. contributed to the initiation and development of the project and financed the Bähler laboratory.

COMPETING FINANCIAL INTERESTS

The authors declare no competing financial interests.

1. Gomes, F.C.O. *et al.* Physiological diversity and trehalose accumulation in *Schizosaccharomyces pombe* strains isolated from spontaneous fermentations during the production of the artisanal Brazilian cachaça. *Can. J. Microbiol.* **48**, 399–406 (2002).
2. Brown, W.R.A. *et al.* A geographically diverse collection of *Schizosaccharomyces pombe* isolates shows limited phenotypic variation but extensive karyotypic diversity. *G3* **1**, 615–626 (2011).
3. Fawcett, J.A. *et al.* Population genomics of the fission yeast *Schizosaccharomyces pombe*. *PLoS ONE* **9**, e104241 (2014).
4. Osterwalder, A. *Schizosaccharomyces liquefaciens* n.sp., eine gegen freie schweflige Säure widerstandsfähige Gärhefe. *Mitt. Geb. Lebensmittelunters. Hyg.* **15**, 5–28 (1924).
5. Florenzano, G., Balloni, W. & Materassi, R. Contributo alla ecologia dei lieviti *Schizosaccharomyces* sulle uve. *Vitis* **16**, 38–44 (1977).
6. Teoh, A.L., Heard, G. & Cox, J. Yeast ecology of Kombucha fermentation. *Int. J. Food Microbiol.* **95**, 119–126 (2004).
7. Wood, V. *et al.* The genome sequence of *Schizosaccharomyces pombe*. *Nature* **415**, 871–880 (2002).
8. Liti, G. *et al.* Population genomics of domestic and wild yeasts. *Nature* **458**, 337–341 (2009).
9. Schacherer, J., Shapiro, J.A., Ruderfer, D.M. & Kruglyak, L. Comprehensive polymorphism survey elucidates population structure of *Saccharomyces cerevisiae*. *Nature* **458**, 342–345 (2009).
10. Avelar, A.T., Perfeito, L., Gordo, I. & Godinho Ferreira, M. Genome architecture is a selectable trait that can be maintained by antagonistic pleiotropy. *Nat. Commun.* **4**, 2235 (2013).
11. Seich Al Basatena, N.-K., Hoggart, C.J., Coin, L.J. & O'Reilly, P.F. The effect of genomic inversions on estimation of population genetic parameters from SNP data. *Genetics* **193**, 243–253 (2013).
12. Zanders, S.E. *et al.* Genome rearrangements and pervasive meiotic drive cause hybrid infertility in fission yeast. *eLife* **3**, e02630 (2014).
13. Cromie, G.A. *et al.* Genomic sequence diversity and population structure of *Saccharomyces cerevisiae* assessed by RAD-seq. *G3* **3**, 2163–2171 (2013).
14. Alexander, D.H., Novembre, J. & Lange, K. Fast model-based estimation of ancestry in unrelated individuals. *Genome Res.* **19**, 1655–1664 (2009).
15. Lawson, D.J., Hellenthal, G., Myers, S. & Falush, D. Inference of population structure using dense haplotype data. *PLoS Genet.* **8**, e1002453 (2012).
16. Hornsey, I.S. *A History of Beer and Brewing* (The Royal Society of Chemistry, 2003).
17. Fay, J.C. & Benavides, J.A. Evidence for domesticated and wild populations of *Sacchoromyces cerevisiae*. *PLoS Genet.* **1**, 66–71 (2005).
18. Zhou, T., Gu, W. & Wilke, C.O. Detecting positive and purifying selection at synonymous sites in yeast and worm. *Mol. Biol. Evol.* **27**, 1912–1922 (2010).
19. Bowen, N.J., Jordan, I.K., Epstein, J.A., Wood, V. & Levin, H.L. Retrotransposons and their recognition of pol II promoters: a comprehensive survey of the transposable elements from the complete genome sequence of *Schizosaccharomyces pombe*. *Genome Res.* **13**, 1984–1997 (2003).
20. Mourier, T. & Willerslev, E. Large-scale transcriptome data reveals transcriptional activity of fission yeast LTR retrotransposons. *BMC Genomics* **11**, 167 (2010).
21. Kwon, E.-J.G. *et al.* Deciphering the transcriptional-regulatory network of flocculation in *Schizosaccharomyces pombe*. *PLoS Genet.* **8**, e1003104 (2012).
22. Guo, Y. & Levin, H.L. High-throughput sequencing of retrotransposon integration provides a saturated profile of target activity in *Schizosaccharomyces pombe*. *Genome Res.* **20**, 239–248 (2010).
23. Guo, Y. *et al.* Integration profiling of gene function with dense maps of transposon integration. *Genetics* **195**, 599–609 (2013).
24. Feng, G., Leem, Y.-E. & Levin, H.L. Transposon integration enhances expression of stress response genes. *Nucleic Acids Res.* **41**, 775–789 (2013).
25. Jeffares, D.C., Penkett, C.J. & Bähler, J. Rapidly regulated genes are intron poor. *Trends Genet.* **24**, 375–378 (2008).
26. Chen, D. *et al.* Global transcriptional responses of fission yeast to environmental stress. *Mol. Biol. Cell* **14**, 214–229 (2003).
27. Cromie, G.A. *et al.* A discrete class of intergenic DNA dictates meiotic DNA break hotspots in fission yeast. *PLoS Genet.* **3**, e141 (2007).
28. Fowler, K.R., Gutiérrez-Velasco, S., Martín-Castellanos, C. & Smith, G.R. Protein determinants of meiotic DNA break hot spots. *Mol. Cell* **49**, 983–996 (2013).
29. Maniatis, N. *et al.* The first linkage disequilibrium (LD) maps: delineation of hot and cold blocks by diplotype analysis. *Proc. Natl. Acad. Sci. USA* **99**, 2228–2233 (2002).
30. Liti, G. & Louis, E.J. Advances in quantitative trait analysis in yeast. *PLoS Genet.* **8**, e1002912 (2012).
31. Mackay, T.F.C. Epistasis and quantitative traits: using model organisms to study gene-gene interactions. *Nat. Rev. Genet.* **15**, 22–33 (2014).
32. Speed, D., Hemani, G., Johnson, M.R. & Balding, D.J. Improved heritability estimation from genome-wide SNPs. *Am. J. Hum. Genet.* **91**, 1011–1021 (2012).
33. Warringer, J. *et al.* Trait variation in yeast is defined by population history. *PLoS Genet.* **7**, e1002111 (2011).
34. Listgarten, J. *et al.* Improved linear mixed models for genome-wide association studies. *Nat. Methods* **9**, 525–526 (2012).
35. Drummond, A.J., Suchard, M.A., Xie, D. & Rambaut, A. Bayesian phylogenetics with BEAUti and the BEAST 1.7. *Mol. Biol. Evol.* **29**, 1969–1973 (2012).
36. Clément-Ziza, M. *et al.* Natural genetic variation impacts expression levels of coding, non-coding, and antisense transcripts in fission yeast. *Mol. Syst. Biol.* **10**, 764 (2014).

ONLINE METHODS

Sequencing and quality control. All strains are described in **Supplementary Table 1**. Strains were sequenced with either 54-nt or 100-nt paired-end Illumina reads. A summary of read data is provided in **Supplementary Table 7**. To verify that strain identity was correct at various stages in the project, we genotyped 30 SNPs (that would distinguish all 57 non-clonal strains with at least 2 allelic differences) in the 161 extracts used for sequencing, replicate extracts of the 57 non-clonal strains, extracts from stocks obtained directly from stock centers and extracts made from cultures picked from the ROTOR phenotyping plate. Only 2 of the 232 sets of genotypes were not as expected, and neither of these were members of the 57 non-clonal strains. All of the extracts from cultures grown on ROTOR plates were as expected.

Read mapping and SNP and indel calling. Reads were mapped to the *S. pombe* 972 *h*⁻ reference genome (May 2011 version)[7] with Stampy (v1.0.17)[18,37]. After detection of possible indel sites, alignments were realigned with the Genome Analysis Toolkit (GATK) IndelRealigner.

SNPs were called with the GATK UnifiedGenotyper and filtered using custom parameters (available on request). Indels were identified using the GATK HaplotypeCaller[38] and Cortex[39], both with filtering using custom parameters. Cortex and HaplotypeCaller call sets were generated by merging any two indels from each set that were positioned within 3 nt of each other, were within a 30% length range and differed by a maximum of one minor allele count.

SNP and indel validation. To estimate the false discovery rate and sensitivity of SNP calling, we sequenced ~20 paired-end shotgun clones from each of 4 strains with increasing genetic distance from the reference strain using an ABI capillary machine. Reads were then mapped to the reference genome using BWA mem[40]. We then manually examined 85 windows of the genome using the Integrated Genomics Viewer (IGV) tool[41]. These windows included 47,619 nt of mappable regions and 182 known SNPs. We found that all of the SNPs were valid, whereas 17 were discovered in alignments that were not called by our SNP calling pipeline (8.5% false negative rate).

To estimate the false discovery rate of indel calling, we manually inspected the Illumina read alignments at 100 indels called in the same 4 strains, choosing indels that were dispersed across all chromosomes. Only four of these calls were false positives (4% false discovery rate for calling indels). A total of seven indels corresponded to at least one strain with an incorrect allele call.

Locating Tf retrotransposons. We used RetroSeq[42] to locate insertions in the 57 strains that were not present in the reference strain. As LTR insertions are highly targeted in *S. pombe*[22], we used the soft-clipped, unaligned parts of sequence reads covering the insertion sites to distinguish between independent insertions at closely situated genomic sites, collating 1,474 predicted insertions into 820 insertion events. We assessed the target site duplication sizes from the soft-clipped reads. We used PCR to verify 90 of the RetroSeq predictions: 56 of these produced a product in both the reference and alternate strain, and 80% (45/56) of these confirmed the insertion with high confidence, whereas 93% (52/56) confirmed the insertion with at least medium-level confidence.

To determine which reference LTR elements were present in each wild strain, we used delly (version 0.0.6)[43] to locate deletions in the same position as a reference LTR sequence. Genes targeted by LTR insertions were identified by only considering LTR insertions between genes arranged in tandem (neighboring genes in the same orientation). Gene features were analyzed by the Gene List Analyzer (F. Schubert, S. Khadayate and J.B., unpublished data). The presence/absence and positions of all LTR insertions are provided in **Supplementary Table 8**. Detailed information about the PCR validation of LTR insertions is provided in **Supplementary Table 9**.

Diversity analysis. Diversity estimates were calculated using Variscan[44]. For analysis with 10-kb windows, we excluded windows with fewer than 1,000 nt of reliably called sites. To compare different genome annotation classes, we used regions that were annotated exclusively as exon, intron, noncoding RNA, etc. Median MAF was calculated for all variants passing the significance threshold in 100 windows (126 kb long) for SNPs and in 50 windows (252 kb) for indels.

Recombination rate, hotspots and linkage disequilibrium maps. We used LDMAP[45] to construct LDU maps from the SNPs segregating in 46 unrelated strains that appeared to be a homogenous population in principal-component analysis, excluding SNPs with MAF < 0.05. We calculated the DSB rate (per microarray probe) from the data of Cromie *et al.*[27], as the median signal for all probes in a 7-probe window, using both replicates of the time point at 5 h (14 probes in all), divided by the median signal for probes in the 7-probe window for the time point at 0 h. For both recombination rate and the DSB rate, we then calculated the mean signal over non-overlapping 1-kb windows of the genome. Pairwise D' and r^2 values were calculated for all pairs of SNPs with MAF > 0.05 up to a distance of 250 kb, using LDMAP (for D')[45] and PLINK (for r^2)[46]. Mean values were calculated from ≥500,000 pairwise comparisons for each 1-kb window.

Population structure. For analysis tools that assume variants are independent, we used 752 SNPs that were unlinked (pairwise $r^2 < 0.5$; 'unlinked SNPs'). We used vcftools[47] to estimate the Weir and Cockerham weighted F_{ST} value, using all SNPs for all pairwise combinations of populations. Admixture (version 1.22)[14] was run with $k = 1$ to $k = 20$. ChromoPainter and fineSTRUCTURE[15] were run using only the 57 non-clonal strains on all SNPs using the recombination rate estimate. When using ChromoPainter, we first ran ten expectation-maximization iterations to infer the 'global mutation' and 'switch rate' parameters, averaged the inferred values for each across chromosomes with weighting by the number of SNPs and then performed a final ChromoPainter run using these weight-averaged values. Isolation by distance was calculated using geoDist values from the SoDA packages in R. See the **Supplementary Note** for more details.

Dating strain divergence with mitochondrial data. This analysis used only the 84 strains with recorded sampling dates, which contained 204 SNPs. The *Schizosaccharomyces cryophilus* mitochondrial genome (GenBank, ACQJ00000000.2, supercontig_3.27) was used as the outgroup, aligned to the *S. pombe* strains using Muscle[48].

We used PartitionFinder[49] to choose the optimal partitioning scheme ($k = 5$) and nucleotide substitution model. Phylogenetic analyses were performed with BEAST 1.7.4 (ref. 35) on both the five schemes obtained with PartitionFinder and the whole molecule. In the first case, substitution and clock models were unlinked and tree topology was assumed to be the same for the five schemes. Log-normal relaxed clocks were compared to strict clocks through the evaluation of Bayes factors. To do so, marginal likelihood was computed using both path and stepping-stone sampling methods[50]. To minimize demographic assumptions, we adopted a Bayesian skyline plot approach to integrate over different coalescent histories. Rate variation among sites was modeled with a discrete gamma distribution with four rate categories. Posterior distributions of parameters, including divergence times and substitution rates, were estimated by Markov chain Monte Carlo (MCMC) sampling in BEAST. For each analysis, we ran 4 independent a posteriori combined chains in which samples were drawn every 2,500 MCMC steps from a total of 25,000,000 steps, after a discarded burn-in of 2,500,000 steps. Convergence to the stationary distribution was assessed by inspection of posterior samples.

Estimation of time to the most recent common ancestor with nuclear DNA. To obtain estimates of the time to the most recent common ancestor for the nuclear genome, we produced independent runs of ACG[51] for the full mitochondrial genome and for 160 regions of the nuclear genome, each 20 kb in length. To ensure that background selection between the mitochondrial and nuclear genome fractions would be approximately similar, we selected nuclear regions to have an exon density of 50–60%, similar to the mitochondrial genome. To ease the computational burden and aid convergence of the chains, we randomly chose 15 of the samples for inclusion. For each region, an ACG run of 5×10^7 steps was conducted using a Metropolis-coupled MCMC scheme with 8 chains. The first 25% of steps were discarded as burn-in. We estimated posterior distributions of the parameters of the substitution matrix assuming the TN93 model[52] and the ancestral recombination graph (ARG), recombination rate, substitution rate and locations of recombination breakpoints from the data. Flat (uniform) priors were assumed for all parameters

except recombination rate, for which we employed an exponential prior with a mean of 100.0 recombinations per unit of branch length. Convergence of chains was assessed by visual examination of the likelihood of the data conditional on the ARG.

***De novo* assembly.** *De novo* assemblies were performed using SGA version 0.9.35 (ref. 53). Error correction used 41-mer frequencies to identify and correct sequencing errors. For the contig assembly step, the minimum overlap length was set to 65 bp for the strains with 100-nt reads. For strains with 54-nt reads, a minimum overlap of 45 bp was required instead. Evidence from a minimum of five read pairs was required to build contigs into a scaffold.

Locating new genes. To identify protein-coding genes that were present in wild strain(s) but not in the reference strain, we produced gene predictions from each *de novo* assembly with Augustus[54] using default parameters. We then compared each predicted protein to the *S. pombe* reference using BLAST+ (ref. 55), BLASTP, TBLASTN and BLASTN. Predictions of ≥100 amino acids in length that scored <80% identity in all BLAST searches were chosen as potential new genes (800 predicted peptides). We used Markov clustering[56] to group these peptides into 32 clusters of similar peptides and 5 singletons. We then aligned each cluster with Clustal Omega[57], produced a consensus sequence using Emboss cons and used this consensus sequence as a query for BLASTP searches against the *S. pombe* reference protein data set and the NCBI nr protein data set. We excluded potential new genes whose best BLAST hit in the nr data set was from *S. pombe* or the phage Φx174 (likely contamination). We retained the 17 potential new genes where the ratio of the nr BLASTP bit score to the *S. pombe* bit score was >1. To examine the conservation of the 17 potential new genes in other *Schizosaccharomyces* yeasts, we used each predicted protein (from each *S. pombe* strain) for the 17 putative most promising new genes to query the predicted proteins of *S. cryophilus*, *Schizosaccharomyces japonicus* and *Schizosaccharomyces octosporus* using BLASTP, accepting BLAST hits with *e* value < 1×10^{-20} in one or more species.

Phenotyping. A summary of all phenotype measurements is provided in **Supplementary Table 4**, and the specific approaches are described below.

Amino acid quantification. These are the phenotypes with the prefix "aaconc" in **Supplementary Tables 4** and **5**.

Triplicate cultures (1.6 ml) of each strain were grown for 8 h, cell extracts were prepared with 80 °C boiling ethanol, extracts were cleared of insoluble material by centrifugation and the supernatant was collected for liquid chromatography and tandem mass spectrometry analysis. Samples were analyzed on a liquid chromatography (Agilent 1290 Infinity) and tandem mass spectrometry (Agilent 6460) system. Amino acids were separated by hydrophilic interaction chromatography with gradient elution using an ACQUITY UPLC BEH amide column.

Amino acid concentrations were determined by external calibration. Dilution was corrected by probabilistic quotient normalization[58]. The average of the amino acid values from the triplicates was used for further analysis. For quality control, all values with a coefficient of variation greater than two times the overall coefficient of variation (median) were eliminated. For the 19 amino acids analyzed, the median coefficients of variation were between 0.07 and 0.21 (mean of 0.13).

Growth and stresses on solid media. These are the phenotypes with the prefix "smgrowth" in **Supplementary Tables 4** and **5**.

Strains were arrayed by a ROTOR robot (Singer Instruments) onto solid YES and EMM2 media at a 1,536-spot density, with each strain represented by 4 spots. Edges of plates and various interspersed positions were inoculated with the standard laboratory strain, as well as strains with known sensitivity (*atf1Δ* and *sty1Δ*) or resistance (*pka1Δ*).

Plates were incubated at 32 °C, and high-resolution images of the plates were acquired using a UVP Multi-DocIt transillumination system. Two biological replicates were performed. Quantification of colony size was performed using the custom Workspace package with the Spotsizer custom workflow (L.B., M.P., C.R., D.C.J. and Y. Arzhaev *et al.*, unpublished data). Colonies with microbial contaminations and misidentified colonies were discarded. Median colony size for each strain was calculated for each plate and replicate. Conditions or plates showing poor reproducibility were removed from further analysis. Colony size data for strains under each condition were normalized to growth on YES medium and then to the growth of the 972 h^- reference strain under the given condition. Two or more replicate plates were analyzed for 25 of the 43 conditions, and 1 plate was analyzed for all others. Plate values were the median colony size from the four colonies analyzed per strain. The median between-plate Pearson's correlation was 0.95.

Cell growth parameters and kinetics in liquid media. These are the phenotypes with the prefix "lmgrowth" in **Supplementary Tables 4** and **5**.

All 57 non-clonal strains were cultured in a Biolector microfermenter (m2p labs) in 1.5 ml of YES or EMM2 medium (Formedium) using flowerplates from m2p labs for 24 h at 32 °C, measuring light scattering every 10 min. Growth of each strain was repeated at least in duplicate. For each replicate of the optical density data points, we used the R grofit package[59] to determine all growth parameters. Two biological repeats of Biolector cultures were grown per strain. Correlations between biological repeats were typically >0.9, and all were above 0.884. All coefficients of variation (within a strain) were above 0.075 (median for all traits = 0.034).

Manual cell morphology characterization. These are the phenotypes with the prefix "shape1" in **Supplementary Tables 4** and **5**.

Strains were grown on plates with YES medium at 32 °C and allowed to form small colonies. Cells around the edge of at least five colonies were examined using a Zeiss Axioskop microscope with both 20× LD ACROPLAN 0.4 and 50× CF plan 0.55 objectives, and the cell phenotype was described. Using the 50× CF plan 0.55 objective with 2.5× Optivar, a representative colony was photographed with the Sony NEX 5N camera. For cultures in liquid media, strains were grown to mid-log phase and examined using a Zeiss Axioskop 40 microscope with a 63× Plan APOCHROMAT 1.4 oil immersion objective. Cell length and width were measured for a minimum of 30 septated cells using ImageJ. FACS analysis was carried out as described[60]. The percentage of cells with 1C, 2C, 2–4C and >4C DNA content was estimated using FlowJo. Replicate length and width measurements were the median values for at least 34 cells (median of 53), with median coefficients of variation of 0.07 in both cases.

Automated cell morphology analysis. These are the phenotypes with the prefix "shape2" in **Supplementary Tables 4** and **5**.

Cells were grown to mid-log phase in YES medium and imaged using the OperaLX (PerkinElmer) high-throughput microscope at 60× magnification. Images were then automatically preprocessed, segmented and analyzed to give 54 independent measurements of phenotypic features for all strains.

The occurrence of stereotypical *S. pombe* cell shape phenotypes (wild type, long, stubby, curved, branched, round, skittle and kinked) was assessed for each strain using SVM classifiers. This method is described fully in Graml *et al.*[61] where cells were imaged using 405-nm and 488-nm exposure channels with ten independent repeats. Here only the 405-nm channel and six repeats were needed.

The symmetrized Kullback-Leibler divergence between each strain and the reference strain was used as an additional quantitative trait (shape2.KL.Predicted.* in **Supplementary Table 4**), along with the length, width and ratio of the width of both sides of the cell ('cell asymmetry'). Up to six populations of cells were analyzed per strain. Because measurements were generally non-Gaussian, variation within populations was assessed using the median of absolute deviation (MAD) divided by the median. MAD values ranged from 0.04 (length) to 1.42 (ks.predicted.long), with an average of 0.87.

Heritability and genome-wide association studies. We used LDAK[32] to estimate the heritability of all traits. We report values based on quantile-normalized phenotypes (see below), but we also repeat estimates using raw values. Heritabilities estimated with raw values were strongly correlated with those from normally transformed values ($r = 0.69$, $P \leq 2.2 \times 10^{-16}$).

We performed mixed-model association analysis using Fast-LMM[34], version 2.07. The mixed model adds to the standard linear regression model a polygenic term, designed to 'soak up' the effects attributable to relatedness and population structure[62]. We first normalized each phenotype by replacing observed values with the corresponding quantile from a standard normal distribution. We excluded variants with fewer than five calls for the minor allele (MAF < 3.1%) and variants that had >5% missing calls. We estimated a trait-specific *P*-value threshold for each trait by permuting trait values for individuals 1,000 times, recording the lowest *P* value from Fast-LMM

analysis and using the 5% quantile (50th lowest value) as the threshold. Variants passing this threshold therefore had a 5% family-wise error rate. We also performed conditional analysis; for each of the 89 traits with at least one variant significantly associated in the primary mixed-model GWAS, we repeated the analysis, including as a covariate the genotypes for the most significant variant.

The genomic inflation factor (GIF) was calculated as GIF = $\text{median}\left(\chi^2_{\text{observed}}(P)\right)/\text{median}\left(\chi^2_{\text{expected}}(P)\right)$, and the adjusted GIF was calculated as $\text{GIF} = \text{median}\left(\chi^2_{\text{observed}}(P)\right)/\text{median}\left(\chi^2_{\text{permuted}}(P)\right)$, where $\chi^2_{\text{observed}}(P)$ is the statistic corresponding to the observed P value and $\chi^2_{\text{expected}}(P)$ is the statistic expected assuming that P values are distributed uniformly within [0, 1]. Here permuted P values were obtained by permuting trait values once for each of the 223 traits used for the GWAS. The expected median, assuming P values are uniformly distributed, is 0.454.

To validate the results from the association analyses, we split the 57 non-clonal strains into 3 data sets (3 populations defined by Admixture on the basis of 752 independent SNPs). Each data set was therefore a homogeneous group of relatively unrelated members. The 3 data sets had 12, 26 and 17 members, and 2 of the 57 strains were excluded because they were not members of any of the 3 populations. Association analysis was based on linear regression of every trait on each of the 1,567 markers that passed the GWAS significance threshold in the initial analysis using the pooled data and the mixed model. We then performed meta-analysis only on those variants that replicated (showed nominal statistical evidence of association in at least two of the three (k) data sets). The P values from the linear regression in each data set for the same trait and marker were combined using Fisher's combined probability test

$$\chi^2 = -2\sum_{i=1}^{k}\ln(P)$$

The meta P value was obtained for 6 degrees of freedom ($2k$).

A summary of all the signals validated using linear regression together with their meta P values and the P values from the pooled data using the mixed model is presented in **Supplementary Table 6**.

Statistics. All statistics were generated with R (ref. 63).

37. Lunter, G. & Goodson, M. Stampy: a statistical algorithm for sensitive and fast mapping of Illumina sequence reads. *Genome Res.* **21**, 936–939 (2011).
38. DePristo, M.A. *et al.* A framework for variation discovery and genotyping using next-generation DNA sequencing data. *Nat. Genet.* **43**, 491–498 (2011).
39. Iqbal, Z., Caccamo, M., Turner, I., Flicek, P. & McVean, G. *De novo* assembly and genotyping of variants using colored de Bruijn graphs. *Nat. Genet.* **44**, 226–232 (2012).
40. Li, H. & Durbin, R. Fast and accurate long-read alignment with Burrows-Wheeler transform. *Bioinformatics* **26**, 589–595 (2010).
41. Thorvaldsdóttir, H., Robinson, J.T. & Mesirov, J.P. Integrative Genomics Viewer (IGV): high-performance genomics data visualization and exploration. *Brief. Bioinform.* **14**, 178–192 (2013).
42. Keane, T.M., Wong, K. & Adams, D.J. RetroSeq: transposable element discovery from next-generation sequencing data. *Bioinformatics* **29**, 389–390 (2013).
43. Rausch, T. *et al.* DELLY: structural variant discovery by integrated paired-end and split-read analysis. *Bioinformatics* **28**, i333–i339 (2012).
44. Hutter, S., Vilella, A.J. & Rozas, J. Genome-wide DNA polymorphism analyses using VariScan. *BMC Bioinformatics* **7**, 409 (2006).
45. Lau, W., Kuo, T.-Y., Tapper, W., Cox, S. & Collins, A. Exploiting large scale computing to construct high resolution linkage disequilibrium maps of the human genome. *Bioinformatics* **23**, 517–519 (2007).
46. Purcell, S. *et al.* PLINK: a tool set for whole-genome association and population-based linkage analyses. *Am. J. Hum. Genet.* **81**, 559–575 (2007).
47. Danecek, P. *et al.* The variant call format and VCFtools. *Bioinformatics* **27**, 2156–2158 (2011).
48. Edgar, R.C. MUSCLE: multiple sequence alignment with high accuracy and high throughput. *Nucleic Acids Res.* **32**, 1792–1797 (2004).
49. Lanfear, R., Calcott, B., Ho, S.Y.W. & Guindon, S. Combined selection of partitioning schemes and substitution models for phylogenetic analyses. *Mol. Biol. Evol.* **29**, 1695–1701 (2012).
50. Baele, G., Li, W.L.S., Drummond, A.J., Suchard, M.A. & Lemey, P. Accurate model selection of relaxed molecular clocks in Bayesian phylogenetics. *Mol. Biol. Evol.* **30**, 239–243 (2013).
51. O'Fallon, B.D. ACG: rapid inference of population history from recombining nucleotide sequences. *BMC Bioinformatics* **14**, 40 (2013).
52. Tamura, K. & Nei, M. Estimation of the number of nucleotide substitutions in the control region of mitochondrial DNA in humans and chimpanzees. *Mol. Biol. Evol.* **10**, 512–526 (1993).
53. Simpson, J.T. & Durbin, R. Efficient *de novo* assembly of large genomes using compressed data structures. *Genome Res.* **22**, 549–556 (2012).
54. Stanke, M., Schoffmann, O., Morgenstern, B. & Waack, S. Gene prediction in eukaryotes with a generalized hidden Markov model that uses hints from external sources. *BMC Bioinformatics* **7**, 62 (2006).
55. Camacho, C., Coulouris, G. & Avagyan, V. BLAST+: architecture and applications. *BMC Bioinformatics* **10**, 421 (2009).
56. van Dongen, S. & Abreu-Goodger, C. Using MCL to extract clusters from networks. *Methods Mol. Biol.* **804**, 281–295 (2012).
57. Sievers, F. *et al.* Fast, scalable generation of high-quality protein multiple sequence alignments using Clustal Omega. *Mol. Syst. Biol.* **7**, 539 (2011).
58. Dieterle, F., Ross, A., Schlotterbeck, G. & Senn, H. Probabilistic quotient normalization as robust method to account for dilution of complex biological mixtures. Application in 1H NMR metabonomics. *Anal. Chem.* **78**, 4281–4290 (2006).
59. Kahm, M., Hasenbrink, G., Lichtenberg-Frate, H., Ludwig, J. & Kschischo, M. Grofit: fitting biological growth curves with R. *J. Stat. Softw.* **33**, 1–21 (2010).
60. Sazer, S. & Sherwood, S.W. Mitochondrial growth and DNA synthesis occur in the absence of nuclear DNA replication in fission yeast. *J. Cell Sci.* **97**, 509–516 (1990).
61. Graml, V. *et al.* A genomic multiprocess survey of machineries that control and link cell shape, microtubule organization, and cell-cycle progression. *Dev. Cell* **31**, 227–239 (2014).
62. Yu, J. *et al.* A unified mixed-model method for association mapping that accounts for multiple levels of relatedness. *Nat. Genet.* **38**, 203–208 (2006).
63. The R Core Team. *R: A Language and Environment for Statistical Computing* (R Foundation for Statistical Computing, 2013).